George H. Miley · S. Krupakar Murali

Inertial Electrostatic Confinement (IEC) Fusion

Fundamentals and Applications

Springer

Inertial Electrostatic Confinement (IEC) Fusion

George H. Miley • S. Krupakar Murali

Inertial Electrostatic Confinement (IEC) Fusion

Fundamentals and Applications

Springer

George H. Miley
Fusion Studies Lab
University of Illinois
Urbana, IL, USA

S. Krupakar Murali
Department of Electronics
and Communication Engineering
J. K. K. M. College of Technology
Erode District, TN, India

ISBN 978-1-4614-9337-2 ISBN 978-1-4614-9338-9 (eBook)
DOI 10.1007/978-1-4614-9338-9
Springer New York Heidelberg Dordrecht London

Library of Congress Control Number: 2013952954

Printed on acid-free paper

Springer is part of Springer Science+Business Media (www.springer.com)

Preface

This book is intended to provide the reader with an overview of the basics, the current experimental status, supporting theory and technology, and potential applications of Inertial Electrostatic Confinement (IEC) fusion.

The IEC is a unique approach to fusion in that electrically driven units offer a number of near-term "spin-off" applications. This is largely due to its simple construction and ability to provide a relatively high fusion rate in a small volume, i.e., at a low power level. Such operation is four or five orders of magnitude below energy "breakeven," but the application justifies the cost of the electrical input required to drive the fusion. Examples include a small neutron source for Neutron Activation Analysis (NAA) to determine impurities in ores or coal at the mine. Extension of that technology discussed in this book includes land mine detection, neutron radiography, clandestine material detection at air- and seaports, medical isotope production, plasma space propulsion, subcritical fusion–fission hybrid reactors, and tunable x-ray sources, to name a few. The simplicity of the IEC has made construction of experiments, often called "fusors," possible. A number of amateur scientists and high school students have built units in their garages. These garage-based "fusor" experiments typically used hydrogen or run at low voltages to avoid serious radiation (x-rays and neutrons) danger to the operator. These experiments are an important introduction to fusion for a number of young people, some of whom eventually make fusion science their careers. Devices with higher neutron rates have been studied at various universities and laboratories where radiation shielding and monitoring can be employed. Much of this work has been done in the United States and Japan and is documented in a long series of DOE-sponsored U.S.–Japan IEC workshops. Principle participants have been the Universities of Illinois and Wisconsin, Los Alamos National Laboratory (LANL), Kyoto University, Kobe University, and the Tokyo Institute of Technology. Other participants include researchers from the University of Maryland, University of Sydney, University of Missouri, along with the private company EMC^2. Much of the material in this book comes from presentations at these meetings, with emphasis on IEC studies at the Universities of Illinois and Wisconsin, which the authors are most familiar with.

To move the IEC from electrically driven units to fusion breakeven and a power producing fusion plant requires a basic change from beam–background neutral reactions to beam–beam fusion. While studies of magnetically insulated and actively cooled grids have been performed, the preferable approach is to replace physical grids with "virtual" electrodes, forming a deep potential well for ion confinement. Indeed this is along the lines originally proposed by Philo Farnsworth (the U.S. inventor of electronic television) in his IEC patent which discussed "poissors" (virtual electrodes). The feasibility for experimentally achieving such a state revolves around fundamental physics issues such as ion beam thermalization, ion upscattering out of the well, stability of this configuration, and the ratio of ion to electron "temperature" (average energy). Much work remains to resolve these issues. Still, if such an IEC mode can be achieved, the door would be opened to a highly non-Maxwellian fusion plant capable of using advanced fuels such as D–^{3}He and p–^{11}B as well as D–T and D–D. Due to its simple structure and theoretical capability to achieve breakeven and net power gain in small units, an experimental campaign to study this could be done faster and at much less cost than currently involved in the international effort to develop a Tokamak reactor based on magnetic confinement.

This book reviews some computational/theoretical studies focused on moving toward an IEC power unit, but many issues need more study to fully understand the physics involved. On the other hand, electronically-driven gridded devices for immediate applications are reasonably well understood. With that in mind, we have included chapters on the basic technology of such units, e.g., high-voltage stalk design, grid design and geometry, and other non-spherical geometries. Thus this book should be useful for developing IEC experiments in university laboratories for students as well as researchers. It is the hope of the authors that this book aid the growth of IEC fusion research aimed at near-term "spin-off" applications and ultimately a stand-alone fusion power plant.

Features of This Book

Chapter 1 discusses the background and basics of IEC fusion, as well as some experiments. IEC fusion offers many potential advantages, including simplified support structures and the ability to create non-Maxwellian plasmas that can be used with a variety of fusion fuels. The basic IEC approach is to create a potential well through electrostatic confinement of one of the plasma species in a dynamic (inertial) configuration. "Inertial" effects associated with dynamic motion of the confined species are essential to avoid plasma losses.

Chapter 2 discusses the theory of potential well traps in the IEC. It might seem that the two injection methods are similar. However, important differences occur due to the mass difference in the particles that are then effectively providing the inertia to electrostatically confine the other species. This difference is discussed through the analyses presented in this chapter. This chapter focuses on potential

well formation and fully ionized spherical IECs. Other geometries have also been studied to see whether such wells could be formed. One example is a gridded cylindrical device that can be viewed as a two-dimensional version of the spherical IEC. However, a spherical geometry has generally been favored due to the three dimensional convergence of the ion beam in the central core.

Chapter 3 discusses gas discharges in gridded IECs. Many experimental IEC devices employ a gas discharge between the grid and vacuum vessel wall (or outer grounded grid) as an ion source. In this chapter we examine some of the basic physics of such discharges and the resulting voltage–current characteristics in the IEC.

Chapter 4 discusses high-voltage stalk design for IECs. Stalk design is crucial for successful internal source IEC device operation. This is particularly true for applications where very high voltages are desired. The requirements for an "ideal" stalk design are listed.

Chapter 5 discusses IEC grid materials and construction. This chapter concentrates on grids for spherical IEC systems. The construction of the IEC grid is complex in that a number of factors contribute to grid performance relative to key issues such as neutron production and ion confinement times. In this chapter we discuss issues that affect the selection of the grid materials and methods for assembling a grid.

Chapter 6 covers effects of grid design and geometry in more detail. Grid geometry plays an important role in the performance of a gridded spherical IEC device because the ion recirculation, hence the reaction rate, is strongly affected by the orientation and size of openings in the cathode in grid design. Several aspects of the effect of grid design on IEC operational performance are discussed.

Chapter 7 discusses studies of space charge limited flow analysis. The classical analyses presented in this chapter are of interest for several reasons. First, these analyses are historic in providing initial insight into space charge effects in diodes carrying large currents. Second, they illustrate techniques originally employed to solve the equations involved. Third, to some extent, the limiting current prediction as a function of applied voltage and anode–cathode spacing roughly apply to the IEC behavior prior to the point where, with combined ion–electron currents, virtual electrodes are formed. The application of space charge limited flow concepts to an actual IEC experiment is discussed. In that case, issues of plasma flow convergence and the high density converged core become important aspects of the problem.

Chapter 8 discusses ion and electron current scaling issues related to how the fusion rate scales with the ion current in the ion-injected type IEC.

Chapter 9 discusses cylindrical and other IEC geometries. Spherical geometry has been widely used following Farnsworth's original studies that stressed the possibility of three-dimensional compression of recirculating beams in the central core of this geometry. This becomes a very important feature if the goal is net power production. However, in many other applications, less compression (e.g. two-dimensional compression in a cylindrical geometry) may be adequate. Indeed, a unique feature of the IEC is that we can adapt its geometry to a number of important near-term applications short of power production. In this chapter we

consider cylindrical, Jet extraction, dipole-assisted, and magnetically-coupled IEC geometries. These provide unique capabilities for various near-term commercial applications.

Chapter 10 discusses other IEC concepts and experiments. Here we have chosen a few experiments that have received attention and supplement discussions in Chaps. 1, 2, and 9, in order to explain some issues and status relative to gridded devices for near-term applications such as neutron sources and also to address some issues such as ion injection related to future fusion power units.

Chapter 11 discusses IEC diagnostics. A wide variety of plasma diagnostics can be applied to an IEC. However, the specific diagnostics incorporated are usually selected based on the objective of the research or application involved. The most common of diagnostics used in IEC research are discussed in this chapter. Emphasis is placed on how these diagnostics are modified for use in the IEC and on the interpretation of the measurements made.

Chapter 12 discusses potential applications. The ability to use the IEC for practical applications with operation well below energy breakeven is a unique attractive feature of this device. In this chapter we discuss some NAA applications, along with medical isotope production. With some increase in energy gain and power, an IEC neutron driven subcritical fission assembly for student labs seems feasible. We discuss that use in this chapter, along with more demanding use in future fusion–fission hybrid reactors. IEC fusion space propulsion, another future application, is discussed to stress the potential for high power-to-weight systems using the IEC.

Chapter 13 discusses reactor confinement theory and visions for an IEC power reactor. Various semi-analytic and computer simulations of plasma confinement in the potential traps created by various IEC devices are discussed, and key issues such as ion thermalization times, energy balances, and instabilities caused by deviations from equilibrium conditions are addressed.

Urbana, IL, USA — George H. Miley
Erode District, TN, India — S. Krupakar Murali

Acknowledgments

I (George Miley) started writing this book with an IEC fusion reactor in mind. However, when S. K. Murali joined the project, he pointed out the importance of covering the technology of gridded devices in order to push immediate applications and student experiments ahead. He added much of this very important information to the book, making the presentation much more useful to the community. I would like to thank my wife, Liz, my family, and my former students and colleagues who assisted me during my IEC fusion research. I am grateful to all of them for their support. Also, both authors are very grateful to Robyn Bachar for the extensive work she has done on this book. Her efforts included searching out many reference papers, proofing and editing text, formatting materials, and offering many constructive suggestions. Her work was essential for completion of this book. We would also like to thank our editor at Springer, Merry Stuber, for her hard work and her patience with this book.

I (S. Krupakar Murali) would like to first thank Dr. Miley for giving me the opportunity to work alongside him in preparation of this book. I would also like to once again thank Prof. Gerald Kulcinski, my thesis advisor, for having introduced me to this field in 1999. Prof. Kulcinski and Prof. John Santarius from the University of Wisconsin, Madison, have both been instrumental in shaping my understanding of IEC devices. They gave me a free hand in exploring my ideas while I was still a graduate student, and the encouragement they showered on me even when some of my experiments failed played a crucial role in the knowledge I had gathered in the field, and that ultimately led me to join Prof. Miley in preparing this book.

I would also like to thank my wife, Kasthuri, and our two children (Vaibhav, our son, and Gowri, our daughter) who helped push me to extremes to achieve my goals. My parents have always played a major role in shaping my life, and they have never stopped supporting, encouraging, and blessing me. My parents-in-law have extended much help while preparing this book, and kept me going even at times when things were difficult to handle, and they supported me in every way possible. I owe them a debt of gratitude for this. I would also like to thank my sister- and brother-in-law who have always encouraged me.

Prof. Miley and I would finally like to thank all our fellow researchers who have contributed to the progress of IEC technology. This book would not be possible without their hard work and dedication to the field. We strongly encourage them to continue their excellent work to help IEC technology achieve new heights.

We sincerely hope that this book will help the academic community in familiarizing students to various forms of radiation, their generation techniques using IEC reactors, and the related applications.

Contents

Chapter 1
Background, Basics, and Some IEC Experiments

1.1 Introduction

This book is dedicated to the field of inertial electrostatic confinement (IEC) fusion. Confinement of a hot plasma for fusion or plasma processing is difficult because the hot plasma prevents use of a material confinement vessel. IEC fusion is one of the various methods that can be used to confine a hot fusion plasma. As will be apparent from this book, IEC fusion offers many potential advantages, including simplified support structures and the ability to create non-Maxwellian plasmas that can be used with a variety of fusion fuels. However, a majority of fusion scientists are studying magnetic field confinement in the form of a closed torus (e.g., a Tokamak). Alternately, the fast pulsed approach used in laser fusion attempts to rapidly compress the plasma to an ultrahigh density, and the inertia of the ions maintains the high density long enough such that the fusion energy produced exceeds the input compression energy. Thus, this approach was termed inertial confinement fusion (ICF). These two approaches have led to current major fusion experiments: the international ITER Tokamak in France and the National Ignition Fusion (NIF) experiment using a laser at the Lawrence Livermore National Laboratory (LLNL). Both confinement approaches require very large and complex units, costing billions of dollars to construct. A number of alternate confinement concepts have been proposed with the objective of achieving smaller, less expensive power plants. Some also have the objective of burning "advanced fuels," defined loosely as any non-D–T fuels [1]. Examples include deuterium–deuterium (D–D), deuterium–helium-3 (D–^{3}He), and hyrdrogen–boron-11 (H–B^{11}). One objective of using such fuels is to minimize neutron production, thus neutron-induced radioactivity and damage in structural materials. A second objective is to reduce or eliminate the need for tritium handling and breeding, greatly simplifying the chamber blanket systems. Hydrogen–boron-11 (or H–B^{11}, often termed p–B^{11}) is ideal with a plentiful fuel supply and a reaction that produces three energetic alpha particles with no neutron (hence aneutronic). However, burning p–B^{11} generally requires very high ion temperatures (~ 170 keV vs. ~ 25 keV for D–T) and low electron temperatures ($<$ 1/5 the ion temperature),

G.H. Miley and S.K. Murali, *Inertial Electrostatic Confinement (IEC) Fusion: Fundamentals and Applications*, DOI 10.1007/978-1-4614-9338-9_1,

plus elimination of magnetic fields within the hot fusing plasma to minimize Bremsstrahlung and cyclotron radiation losses, respectively. The IEC is one of only a few alternate confinement approaches that theoretically offer the highly non-Maxwellian plasma conditions needed to burn $p–B^{11}$. Experimental demonstration of this is a key objective for IEC experiments but is very challenging, as discussed in later chapters.

Electrostatic confinement was largely ignored as a confinement approach in early fusion work due to Earnshaw's theorem [2]. This theorem states that an electrostatic field alone cannot confine a plasma. This is easily understood conceptually. If a plate with positive potential is placed at the edge of a plasma to confine ions, it attracts electrons, and as they move to neutralize the potential, the entire plasma is lost. In contrast, the IEC represents a dynamic situation (versus Earnshaw's steady-state analysis) where inertia of the recirculating ions in the potential well electrostatically confines the electrons, thus the name "inertial" electrostatic confinement.

The IEC, like other alternate confinements approaches, has not received sufficient funding to build breakeven experiments. Proponents of these approaches argue that such experiments could be done in smaller size facilities than ITER or NIF, costing less money and moving forward faster. However, a strategy to do that has not been developed by the DOE in the United States or in equivalent agencies elsewhere. As noted later, some private funding has been devoted to attempts to achieve $p–B^{11}$ fusion in alternate concepts, including the IEC.

Despite the uncertainty about achieving a practical power plant, the IEC in particular has received considerable attention in a number of laboratories because in its simplest form an IEC device can be built to achieve fusion for near-term applications such as a neutron source for neutron activation analysis (NAA). Such operation is generally over five orders of magnitude below breakeven, but the electric input cost is justified by the practical application.

1.1.1 Comments About Current Studies

Indeed, many young students and hobbyists have built IEC fusion devices in their garages. Such units have been referred to as "Farnsworth Fusors" after the inventor, Philo Farnsworth. Instructions for building these devices can be found on the Open Source Fusor Research Consortium website (www.fusor.net). At the same time, higher powered and well-instrumented versions have been constructed at various US universities (such as the Universities of Illinois, Wisconsin, and Maryland) and in Japan (Kyoto, Kobe, and the Tokyo Institute of Technology), and at Sydney University in Australia. One motivation has been to use either D–T, D–D, or $D–^3He$ fusion to provide a neutron, proton, or alpha particle source. Much of the discussion in this book is directed at this type of IEC device because such work is well advanced.

Another motivation for IEC studies in these institutions has been to ultimately develop a breakeven power plant. However, such an IEC unit requires a number of changes compared to the present electrically driven devices. First, as done in a few experiments, the ions must enter the IEC from an external source (versus an internal discharge) so that the neutral gas in the fusion vessel is removed to avoid ion–neutral fusion and energy loss by charge exchange (CX) collisions. Second, it must be shown that the highly non-Maxwellian condition of a near monoenergetic ion beam and "cold" electron background can be maintained against various instabilities. Third, internal grids must be removed (or magnetically protected and actively cooled) in favor of a virtual electrode configuration. These three key issues are still very much under active research, and final answers are not yet in. We will discuss these issues in more detail in later chapters. However, we begin with coverage of the science and technology associated with current gridded IEC devices using an internal plasma discharge to produce ions.

1.2 Gridded IEC Devices

Before considering details, it is helpful to obtain a rough idea of how this type of IEC works. For this purpose, we consider the experimental IEC device of Fig. 1.1. As shown in Fig. 1.1a, this "gridded"-type IEC has a spherical mesh grid suspended on a high-voltage feedthrough (or "stalk") in the center of a metal vacuum vessel. Figure 1.1b is a photograph of a typical IEC chamber of this type. The fusion "fuel," e.g., deuterium gas, is first fed into the chamber originally prepared at high vacuum, e.g., 10^{-7} Torr, to remove impurity gas. The fuel gas raises the chamber pressure to a few mTorr. Then the negative voltage on the grid (cathode) is raised into the several 10s of kV range, creating a plasma discharge between the grid and chamber

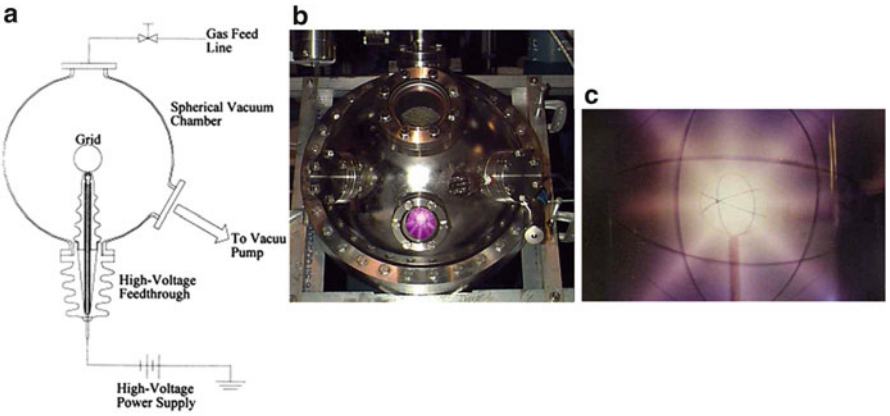

Fig. 1.1 Examples of a spherical IEC at the University of Illinois. (**a**) An illustration of the setup shown in the photo (**b**). (**c**) A photo of "Star" mode operation [5]

wall (electrically grounded). The high negative voltage on the grid extracts the ions from the plasma discharge, accelerating them toward the center of the grid at fusion-relevant energies. There, in principle, they collide and fuse, or if not, they proceed to the opposite side of the grid to a potential surface equal to their birth potential. There they stop and turn back, repeating the process. However, the operating chamber pressure must be relatively high to create the plasma discharge. Thus, the mean free path is low, with ion–neutral atomic fusion dominating over ion–ion fusion. In addition, some ions undergo fusion reactions directly with absorbed gas on the grid structure background materials, while others undergo charge exchange (CX) reactions. These CX reactions remove the high-energy ions from the system in the form of a high-energy neutral and leave behind a low-energy ion. These high-energy neutrals cause fusion elsewhere in the chamber. To add to the complexity of the ion interactions in these IEC devices, it must be remembered that the ion scattering cross section is larger than the fusion cross section. Thus, many ions and CX neutrals also scatter without reacting (fusing) [3, 4].

As discussed in detail later, the type of discharge created and the subsequent ion extraction is very dependent on the background pressure. Many IEC devices are run in the "Star" mode shown in Fig. 1.1c. This photograph of the discharge taken through the view port shows the "Star" mode discharge where ion beams are created that pass through the grid openings. This is important for long run times because ion bombardment of the grids, and hence grid wire sputtering, is minimized.

The dominance of scattering over fusion reactions is the central issue that must be overcome in all fusion confinement approaches. This forces the use of strong confinement so that the ions have many passes and hence a good probability of fusing before being lost from the fusion reaction chamber. In the IEC, multiple passes occur because the ions are trapped in the potential "well" created by negative bias on the grid. Viewed in another way, the ions extracted from the plasma discharge region between the grid and the wall can scatter and pass back through the grid, but they can only return to the same potential surface on which they were born. Thus, except for some that "up-scatter" in energy, they cannot reach the vessel wall. Instead, they stop and are accelerated by the grid potential back into the center of the grid. This then provides many "recirculations" through the center of the grid volume, where they have a finite probability of fusing or are lost by up-scattering in energy, CX, or intercepting the grid wire. If not for these loss channels, the ions would be trapped in the IEC potential well until they fused (see studies [6, 7] for more detail about the various plasma regimes encountered). These strong loss channels prevent the possibility of gaining a "breakeven" fusion condition in this regime of operation. To possibly do that, as already discussed, the use of an external ion source so that a very low background pressure can be maintained in the IEC chamber is essential. Alternately, other regimes such as used in the Polywell concept discussed later in this chapter may allow breakeven power. Short of going to a power unit, as already stressed, the internal plasma discharge ion source

IEC offers an electrically driven fusion source (running several orders of magnitude below breakeven) with many practical applications, such as a small neutron source.

Conditions needed for fusion breakeven can be described more quantitatively in terms of the confinement parameter, $n\tau$, where n is the ion density and τ is the confinement time. Also, the ion energy (or temperature, T) must be in the 20 or more keV range, assuming D–T fuel. For breakeven, J. Lawson developed his famous "criterion," $n\tau = 10^{14}$ cm^{-3}-s at $T > 15$ keV, for D–T fusion [8]. Here τ is the energy confinement time in seconds (s), n is the ion density in cm^{-3}, and T is the ion "temperature" or average energy. The Lawson criterion is independent of the confinement method, but does depend on the fuel via the selection of cross sections in the derivation. Magnetic confinement is generally limited to $n \sim 10^{14}$ cm^{-3} by pressure balance. Then a confinement time τ of ~ 1 s is required. For inertia confinement fusion (ICF) or "laser fusion," compression of targets can achieve $n \sim 10^{24}$, so a confinement time of only 10^{-10} s is needed (corresponding to the disassembly time of the compressed target). (For a general review of energy breakeven requirement for D–T fusion and other fuels like D–^{3}He and p–B^{11}, see reference [1].) In general, the Lawson parameter $n\tau$ and the temperature T required by such fuels are significantly higher than for D–T fuel.

1.3 IEC Fusion Reactor Issues

In principle, the ions focused on the center of the IEC can achieve a density of $n \sim 10^{16}$ cm^{-3} in a small central "core" region, giving a required confinement time of 10^{-2} s for D–T fusion breakeven. The ion "temperature" or average energy in the core region can easily be set at 80–100 keV near the peak of the fusion cross section for D–T reactions.

This core density estimate assumes the formation of such a high-density "core" due to the three-dimensional compression effect in spherical geometry. It also assumes a negligible background neutral pressure so that beam–beam fusion reactions dominate over beam–background or CX reactions. Cylindrical geometry with two-dimensional compression might also work but would have a lower core density, hence a longer confinement time requirement. Such a long lifetime criterion could be hard to achieve.

The confinement time can be restated in terms of the number of ion recirculations in the IEC potential well by dividing the well diameter by the average velocity of the recirculating ion. In later cases discussed in this book, this number is typically quite large, usually ~1,000 recirculations. Achievement of this large number of recirculations requires strong reduction of *all* of the loss channels noted earlier. Grid losses can be reduced by "Star" mode operation of Fig. 1.1c. In that case, the grid lifetime against sputtering-type erosion is greatly extended, and active cooling may be practical, as discussed in the IEC reactor design of reference [9].

The ideal, however, is the elimination of the grid altogether, which can be done via formation of virtual potential structures, originally proposed by Farnsworth and discussed in later sections here, and also in Chap. 2. Alternately, grids might be made highly transparent by using carbon nanotubes, as suggested by S. K. Murali and colleagues [10]. These highly transparent grids would then be very resilient to the harsh fusion environment. The temperature requirement also leads to a fundamental difference in the IEC physics versus other "thermonuclear" confinement approaches. (Note that "temperature" is not a proper term. It implies an equilibrium particle distribution, while the IEC is far from that with its beam-like ions. Thus, the reader should view "temperature" as the average energy of the ions.) Most ions in the IEC are born near the chamber wall, and they are accelerated to an energy close to the applied voltage on the grid during the extraction process. A reasonable estimate is that the ions reaching the fusion region in the center have an energy near 80 % of the grid voltage. Thus, it becomes quite easy to achieve the Lawson D–T threshold ion "temperature" requirement by applying a voltage of only ~ 25 kV. In fact, most IEC neutron sources operate at voltages $>$ 80 kV to achieve an ion energy range resulting in a higher fusion cross section.

In sharp contrast, magnetic thermonuclear fusion devices struggle to obtain a temperature in the 20-keV range. In that case, the entire plasma electron–ion population must be heated (versus direct ion acceleration in the IEC) due to the equilibrium distribution maintained in these plasmas. Another very important point is that Lawson assumed that the ions and electrons were in thermal equilibrium, at the same temperature, T. This is a reasonable approximation for magnetic confinement, but not so for the IEC. In the IEC, the electrons form a "distorted" Maxwellian distribution at an effective temperature well below that of the beam-like ions. Because electron energy loss processes such as radiation emission are serious, the Lawson temperature criterion must be modified for the IEC. A first rough estimate is that the $T_e/T_i < 1/3$ for D–T. (Here T_i and T_e are the ion and electron "temperatures," respectively.) Control of this ratio is a complex physics issue, involving the relative ion and electron source rates and energies and the potential well structure. In later sections of this chapter, we consider the use of p–B^{11} fuel in the IEC. This is very attractive because it provides all charged particle reaction products, making this a unique "aneutronic" system. Such a reactor represents a truly ideal system from an environmental and energy sustainability perspective. However, for such fuels, the Lawson criterion becomes much more demanding, increasing $n\tau$ by two orders of magnitude and T to ~ 150 kV. The IEC can operate at voltages to achieve this ion "temperature," but $n\tau$ remains very challenging. Radiation losses with the high z of boron are an additional hurdle. Elimination of the B-field with the IEC removes cyclotron radiation, but Bremsstrahlung remains an issue. As shown in reference [1], $T_e/T_i \lesssim 1/9$ becomes essential to minimize Bremsstrahlung radiation, such that p–B^{11} breakeven is possible.

Use of a temperature ratio is a very simplified representation. The radiation losses are quite sensitive to deviation in the actual energy distribution of the ions and electrons. For example, electron Bremsstrahlung emission primarily comes

from the high-energy "tail" of the electron distribution, while energy transfer with ions is dominated by the "foot" of the electron distribution. At high powers, interactions in these regions can become quite nonlinear, depleting or "burning out" the local populations in these regions. This effect causes energy losses to saturate and can be quite beneficial under some circumstances. However, the phenomena are complex to evaluate numerically, so little has been reported on it for IECs to date. In conclusion, the IEC remains one of a few alternate confinement concepts that offers a change of burning $p–B^{11}$.

1.4 IEC History

According to T. Dolan [11], Lavrent'ev [12] in the former Soviet Union first proposed electrostatic plasma confinement on June 22, 1950, and magnetic field enhancement of electrostatic plasma confinement in March of 1951. Similarly, in the United States, Philo Farnsworth conceived his ideas in the early 1950s and proposed experiments to the ITT corporation. According to R. Hirsch (2002, Consultant, Washington, DC, private communication), he did not make the information public until his patent was granted in 1966 [13]. Prior to his IEC fusion ideas, Farnsworth was credited with the invention of electronic television. The story of his life leading to that invention and some insight into his later focus on IEC fusion are discussed in several books, including reference [14].

Farnsworth proposed electrostatic plasma confinement for the production of fusion reactions, based upon his experience with spherical multipactor vacuum tubes. Hence, the credit for inventing this remarkable device is equally shared by the two scientists, one from the former Soviet Union and the other from the United States. As a note of interest, according to reference [14], controversy about possible prior work by a Russian inventor held up Farnsworth's basic patents on electronic television.

Around the time when IEC device was being conceived, the prime approaches to fusion being pursued worldwide were magnetic confinement and ICF. In fact, as already discussed, electrostatic confinement had been written off by most scientists due to Earnshaw's theorem. The IEC pioneers seemed to intuitively understand that this theorem assumed a steady state, so that if, as in IEC, the ions were dynamically moving and confined, they would electrostatically confine the electrons. Farnsworth went further and realized that in a spherical system, virtual electrodes would form an ultrahigh-density plasma region if the confined ions were focused at the center of the sphere [13].

Farnsworth [13] and Elmore et al. [15] envisioned the symmetric injection of electrons into an open, hollow, spherical anode, thus producing a negative electrostatic potential well at the center. This well would be capable of confining radially flowing ions, which would have a high density at the focus region in the center.

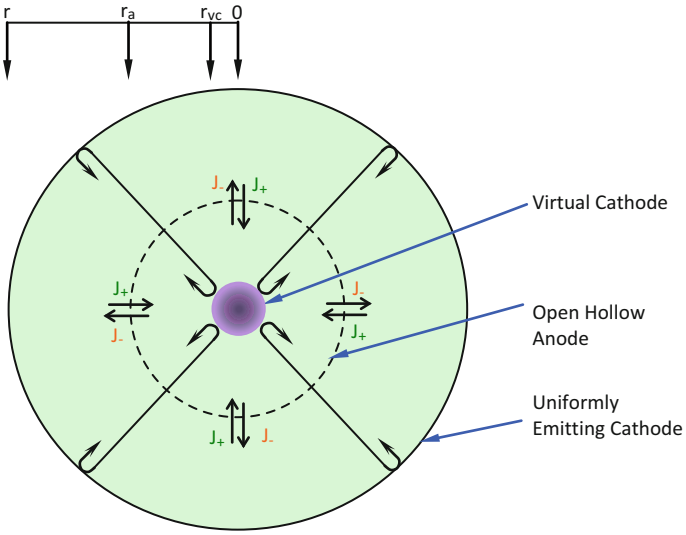

Fig. 1.2 Schematic showing typical electron orbits in a concentric spherical capacitor. Here r_{vc} is the virtual cathode radius, r_a is the anode radius, and r is the radius of the containment system [20]

1.4.1 Prior Virtual Electrode Studies

Farnsworth's and Elmore et al.'s concepts grew from and extended a variety of earlier studies related to space charge flow and virtual electrode formation. The theoretical analysis of saturated space charge flow was first carried out by Child [16] and was later enhanced by Langmuir [17–19] and others. Langmuir [20] analyzed the current flow into a concentric spherical capacitor and determined the shape of the potential well in the idealized model of such a system. This idealized model is shown in Fig. 1.2, where a real, uniformly emitting spherical cathode surrounds a hollow transparent anode. However, while the physics involved is similar to that in Farnsworth and Elmore, Tuck, and Watson's work, Langmuir had not considered developing a fusion reactor with this system.

With respect to Fig. 1.2, at steady state and a high electron current, a virtual cathode is formed at r_{vc} by the electron space charge within the anode. All of the radial flowing, monoenergetic electrons are reflected from this virtual cathode. For a highly transparent anode, the electron currents circulating through the anode will be much larger than the actual anode current, so that throughout the diode, the current flowing toward the central virtual cathode will be very nearly equal to that flowing out from the virtual cathode. Assuming these idealized conditions, the circulating current, the anode voltage, and the size of the virtual cathode were evaluated by Langmuir and are related as follows [20]:

$$I_c = \frac{29.34 \times 10^{-6} V^{\frac{3}{2}}}{\alpha^2}. \tag{1.1}$$

Here I_c is the algebraic sum of the inward and outward flowing electron currents (amperes), V is the potential (volts), and

$$\alpha = -0.3\gamma^2 + 0.075\gamma^3 - 0.0143\gamma^4 + \ldots, \tag{1.2}$$

where $\gamma = \log \frac{r}{r_c}$ and r_c is the virtual cathode radius. Various values of α^2 were derived in references [16–19].

Using one-dimensional simulations with time variations of a number of similar physical states, Dunn and Barnes [22] showed that an oscillating potential well persists with symmetric monoenergetic particle injection in a planar diode. However, when an energy spread was introduced to the injected particles, the oscillations are damped almost linearly with the spread. All oscillations were found to damp out after the initial start-up transient, even when monoenergetic electrons were injected. Using a two-dimensional code, Hockney [23] studied single species virtual electrode formation in cylindrical geometry and found that the virtual cathodes formed over a large current range were stable (i.e., no spatial, potential, or flutelike instabilities were found). The sizes of the virtual cathodes formed in Hockney's simulations corresponded closely to those indicated by the Langmuir analysis [16–19]. These simulations indicate that spherical virtual cathodes should be stable and should be free from the large-amplitude oscillations observed in the monoenergetic planar diodes [22–24]. While these various studies were aimed at the understanding of virtual electrode characteristics, the connection to creating fusion reactions was not made. However, in 1961 Budker [25] calculated the fusion reaction rate that could be attained by trapping ions in the negative electrostatic charge of an electron beam. While not as promising as Farnsworth's later work, this did provide a first look at the connection to fusion.

1.5 Recent IEC Studies

While Hirsch [21] worked with Farnsworth to demonstrate early success with IEC experiments, the concept received little study elsewhere as funding for magnetic and inertial confinement research exponentiated. Then in the late 1990s, R. W. Bussard revived the concept with the hybrid IEC magnetic approach termed HEPS, or "Polywell" [26, 27]. In this approach the electrons were confined in a nearly spherical magnetic field, forming a potential trap for ions. (Note the similarity to the original conceptual potential well discussed by Elmore et al. [15].) Upon invitation by R. W. Bussard to join this effort, one of the authors of this book, George H. Miley, undertook supporting experiments that were a variation of the original Hirsch approach. (The story of Miley's involvement and his interactions with Farnsworth, Hirsch, and Bussard are detailed in reference [28].) He used electrostatic grids to form a trap with a plasma discharge source for ions that then brought electrons in. The motivation was that this approach could result in a very attractive low-level neutron source for neutron activation analysis (NAA) applications and began

that development. Similar work was soon taken up in several other laboratories, including Los Alamos National Laboratory (LANL); University of Wisconsin, Madison; and Kyoto University. Meanwhile, Bussard's work continued with strong funding from the US Navy. However, due to fear of DOE interference, little was published or known about this until 2008, when Bussard made public appeals on YouTube to regain funding that had stopped just when the experiment achieved a major success. Funding resumed, but Bussard passed away shortly thereafter due to a long battle with cancer. The company, EMC^2, was still owned by Bussard's wife, Dollie. However, management of the technical work was then taken over by R. Nebel, who took leave from LANL. Subsequently EMC^2 was moved to San Diego under the leadership of J. Park, who had also worked with Nebel on the Los Alamos IEC. That effort is now in progress and represents the largest IEC-type power-oriented project in the United States or elsewhere.

While at LANL, Nebel and Barnes [29, 30] also came up with a unique alternate approach, termed the Periodically Oscillating Plasma Spheres (POPS) concept. Details of this concept and experiment will be provided in later chapters of this book. Meanwhile, laboratories elsewhere have continued working on gridded-type IEC neutron sources, while the University of Wisconsin has added an IEC proton source as an option using similar technology. These labs, including the University of Illinois at Urbana–Champaign, have fusion power as an ultimate goal but have mostly focused on their funded near-term "spin-off" projects.

At this point, the IEC still receives no funding from DOE, which remains focused on the Tokamak route to fusion power. Thus, with little funding, progress has been slow in answering the key question of whether or not the IEC can be developed for fusion power. If it can, the device would be simpler and smaller than a Tokamak, making it an extremely attractive option. In addition, as already noted, its beam-like reactions (highly non-Maxwellian) make the IEC very well suited for burning alternate ("advanced") fuels like D–^{3}He and p–B^{11}, which are much more environmentally favorable than conventional D–T fusion. In the meantime, the use of non-power producing IECs for other applications such as small neutron, proton, and x-ray sources has been amply demonstrated. Now, the issue is how well and in what applications such IEC sources can compete commercially with other options such as accelerator-target sources. IEC units licensed from the University of Illinois have been used commercially for neutron activation analysis (NAA) identification of impurities in ores by Daimler-Chrysler Aerospace Corporation in Germany. Thus, this can be claimed as the first commercial use of a fusing plasma.

1.6 Some IEC Basics

We begin by presenting the early theoretical study by Elmore, Tuck, and Watson [31]. That study addresses the key question of the fusion power density obtainable with potential well confinement. One of their basic assumptions is that the potential well that traps ions is "dug" by electrons. Certain added assumptions, e.g., well depth, were needed and finally they conclude that the system is unstable for ion

densities sufficiently high that appreciable thermonuclear yield is expected. They qualify this conclusion saying that "admittedly, a more thorough investigation is required to obtain a complete understanding of stability of this electrostatic device."

This result was quite negative for electron formation of potential wells but left the issue open by their statement that a more thorough investigation is required. Later, Bussard pursued this concept by introducing the Polywell device that uses a nearly spherical magnetic field to stabilize the potential well formed by electrons [26]. This represents a "hybrid" magnetic-IEC confinement system where electrons are confined by the magnetic field, forming the potential well which "traps" ions. Apparently, Bussard's view was that this added magnetic stabilization would overcome the earlier criticism by Elmore and colleagues. Subsequently, some of his simulations used particle-in-cell (PIC) methods to support the view that such a stabilized electron potential well would allow adequate density for attractive fusion densities.

However, the next IEC experiments following the Elmore et al. analysis (prior to Bussard's) in the United States were the Hirsch–Farnsworth experiments (2002, Consultant, Washington, DC, private communication, [13]) which used ion-injected (versus electron-injected) traps. This selection was driven by the desire to gain added stability by the large momentum of recirculating ions that form the potential well. More about ion versus electron injection routes will be discussed in later chapters. Next, it is important to review the multiple well ("poissors" solution) that Farnsworth–Hirsch found for ion-injected formation of potential wells in spherical geometry. This is described in the paper by Hirsch [32]. As seen from Fig. 1.3, monoenergetic ions with angular momentum "drag in" electrons to create "onion skin"-like nested potential wells around the center of the sphere, such that the ion density goes to infinity in a "zero" volume at the origin.

This is a very striking result that inspired these researchers to push on with this research. It, in effect, circumvents the Elmore et al. restriction by changing the potential well physics in a fundamental manner. Of course in practice, there will be a spread in energy and angular momentum, so one might expect a single potential well (versus the infinite poissors of Farnsworth) to form. Note that the single well trapping ions is formed by a virtual cathode while it is bounded by a virtual anode – thus, the terminology "double" potential well is applied to this configuration. The questions remaining then were (and still are) how deep can such a well be in practice and how high an ion density can be trapped in it? Various studies followed to study these issues more thoroughly using simulation codes.

Most of these studied retained a physical grid to aid formation of the ion trapping. For example, Black and Klevans [33] studied an ion-injected gridded IEC. They concluded that grid transparency and maintaining a spherical grid shape within a few percent were crucial issues. These results were somewhat encouraging, but prevention of grid deformation is a challenge in practice. A key point in their analysis was that the grid was treated as a surface with a given transparency. This ignored local perturbation of the potential surface by the grid openings. In practice, many grids in present devices were designed with larger

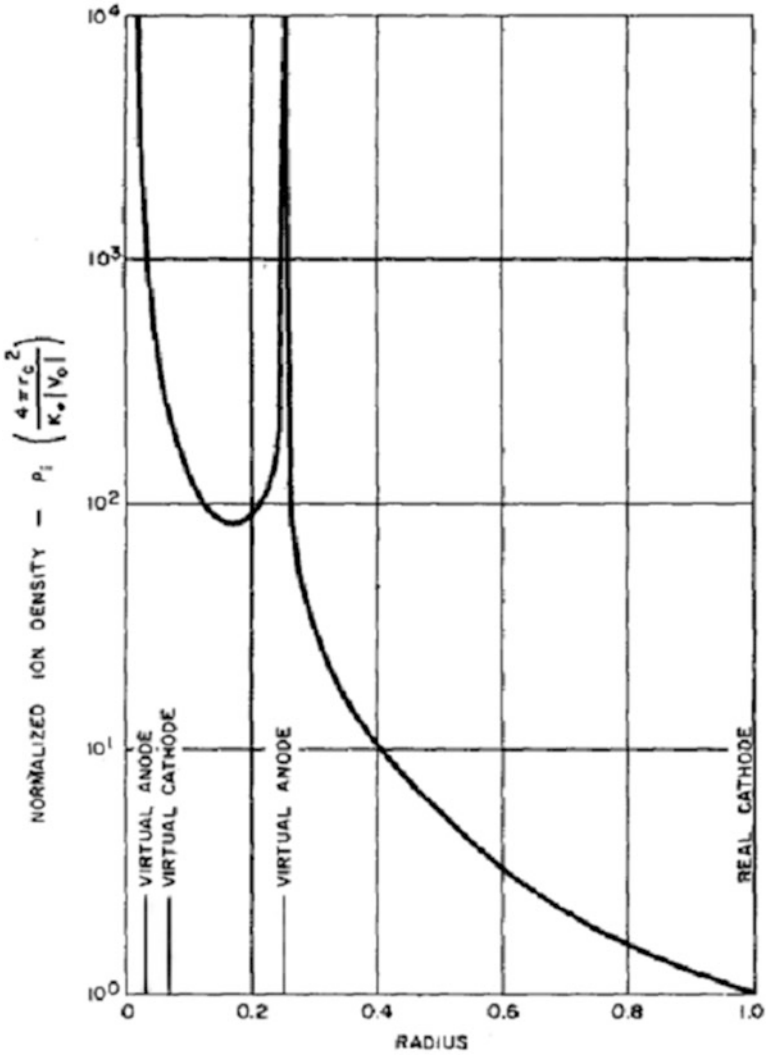

Fig. 1.3 Idealized potential structure calculated by Hirsch for monoenergetic ions with no angular momentum. The nested virtual anodes and cathodes observed were originally termed *poissors* by the inventor, Philo Farnsworth [21]

openings where the Black and Klevans approximation is not valid. Miley later showed that design of grids with larger openings provided the "Star" mode where ion beams passed through the center of the openings, greatly reducing grid collisions and making sphericity of the grid itself less important [34]. Also,

Murali showed in a sequence of experiments that while the symmetry of a grid with moderate size openings improved, so did the fusion rate, until a maximum fusion rate was achieved, beyond which there was no significant change with the improvement in grid symmetry [35]. Thus, such designs for grids are important for small neutron/proton source-type IEC devices. However, the assumption of grids fails to address the question of how a grid could survive in a power reactor or if they could be eliminated to use a potential well with virtual electrode formation (such as in Fig. 1.3). Some other efforts have studied retention of grids in a power reactor. Magnetic field protection techniques, active cooling, etc., are conceivable (e.g., see [29]).

Another question relates to the role of background gas in the IEC. When Miley moved to simplify the device for small neutron sources, he used the discharge between the grid and vessel to form the ions needed for acceleration and fusion. As already stressed, this inherently forces the use of a modest background neutral gas pressure of the fuel (typically deuterium) inside the reaction vessel. That in turn results in ion reactions with the background gas, becoming a dominant process in these IECs. Such interaction includes fusion itself, scattering, charge exchange, etc. This greatly changes the plasma physics of the IEC as opposed to the ideal of a potential well with "zero" background pressure.

Some key differences in the physics of such IECs were brought out by Tim Thorson in his experimental study described in [36]. He confirmed the conclusion that with higher background neutral pressures, convergence is not so important because fusion reactions occur throughout the plasma. However, he also pointed out that convergence may reduce the reactivity by forming a virtual anode that limits the central ion density. However, this space charge could, in theory, be overcome by proper introduction of electrons. In addition to the issue of beam–background fusion, Thorson stressed the importance of energetic ions undergoing charge exchange and being lost from the system.

Thorson's work and others on the small gridded systems at that time showed several important problems which are best understood by considering beam–background versus beam–beam fusion scaling. The fusion reaction rate (or neutron production rate, NPR) for beam–background reactions scales with density and pressure as

$$n_b \times n_{bk} < \sigma v > \sim n_b \times p < \sigma v > .$$

In contrast, beam–beam fusion simply scales as

$$n_b{}^2 < \sigma v > .$$

Here, n_b is the beam ion density per cm^3, n_{bk} is the background atoms per cm^3, p is background pressure, and $< \sigma v >$ is the fusion reactivity averaged over the appropriate beam–background or beam–beam velocity distribution function. Because much of the power going to the grid ends up in the ion beams, the fusion

rate per unit power can be much higher if beam–beam reactions are achieved. This, however, essentially requires elimination of the background pressure. If the ions are produced by electron ionization collisions with neutral gas during a plasma discharge between the grid and vacuum vessel wall, reduction of background gas pressure will also reduce the ion source, reducing the fusion reaction rate. Thus, it becomes apparent that to get the favorable beam–beam scaling, ions must be produced externally while differential pumping is employed to keep the main reaction chamber at very low background pressure. Indeed, without explicitly explaining that this was the reason, Hirsch used external ion "guns" in his early experiments at ITT labs. Miley, however, went back to the internal discharge ion source technique to simplify the device for portable neutron source applications. Then many others doing gridded IEC research also went in this direction. However, future IEC power devices will need to go back to external production of some type.

While earlier workers sought small grid openings designed to provide uniform ion flows for good core plasma convergence (stressed in the earlier papers already noted), Miley and colleagues disclosed that [34, 37] the "Star" mode could be produced with wider grid openings. In fact, Miley and colleagues identified that three key modes can be formed in gridded IECs depending on the pressure and grid openings. These are described as "Star," "central spot," and "halo" modes (illustrated in Fig. 1.4) [37]. These names are descriptive of the visual appearances of the visible light emitted from the discharges. All three modes are reproducible and stable; each is associated with a different potential well structure, hence neutron production rate. The "Star" mode has been used extensively in recent IECs designed as neutron sources. It is distinguished by microchannels or "spokes" radiating outward from a bright center spot, as seen in Fig. 1.5. As verified by magnetic deflection experiments, the spokes are primarily composed of ion beams aligned so that they pass through the center of the openings delineated by the grid wires. This mode is very efficient for neutron production, because the large effective grid transparency allows numerous passes of ions through the core before being intercepted by the grid or being lost through charge exchange. The "Star" mode is typically obtained at lower operating pressures (< 10 mTorr) and higher voltages (> 30 kV), using a carefully formed grid with good sphericity and high transparency (> 95 %). The "halo" (or "jet") mode occurs when one of the grid openings is slightly enlarged compared to the others. The "central spot" mode uses a grid with good sphericity but employs much smaller grid openings than in the "Star" mode.

A number of interesting variations on the basic gridded spherical IEC, such as shown in Figs. 1.5 and 1.6, have been studied in various laboratories. Each of these devices is aimed at operating at lower pressures and thus improving the efficiency of the device. In the next section we briefly describe some of these experiments.

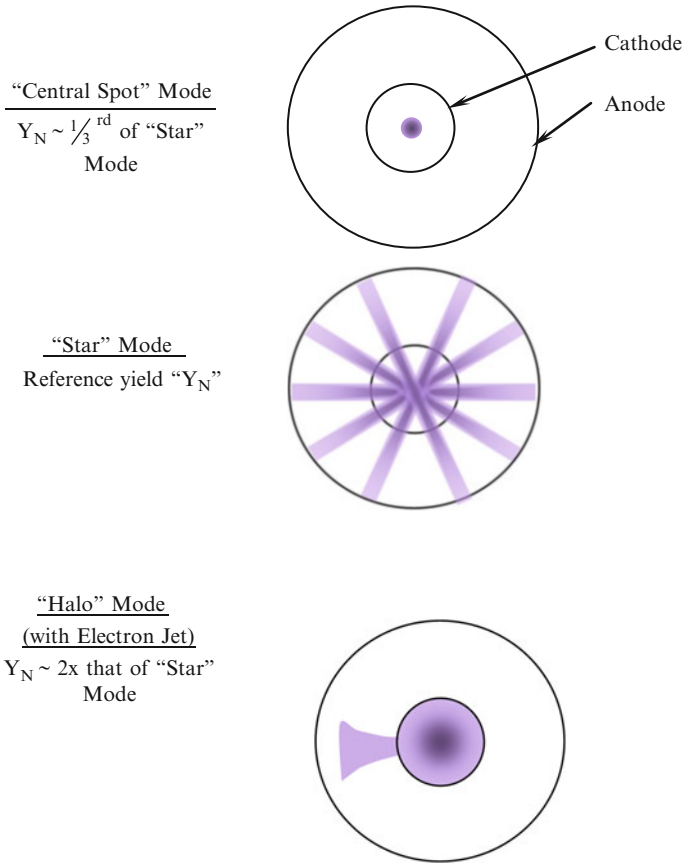

Fig. 1.4 Discharge modes in gridded devices identified by Miley [37]. The neutron yields, Y_N, possible with these modes are shown referenced to the "Star" mode as $1 \times Y_N$

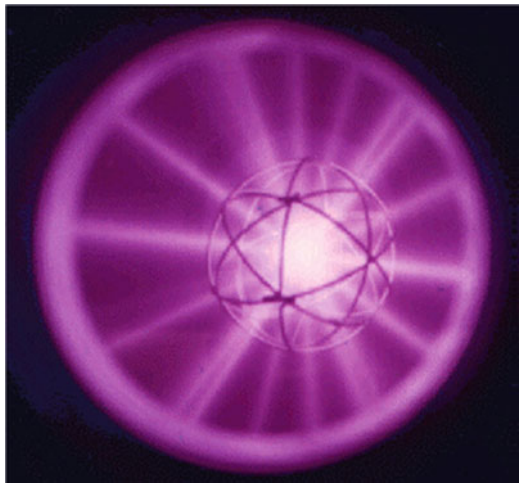

Fig. 1.5 Photo of "Star" mode seen through a reaction vessel port window [37]

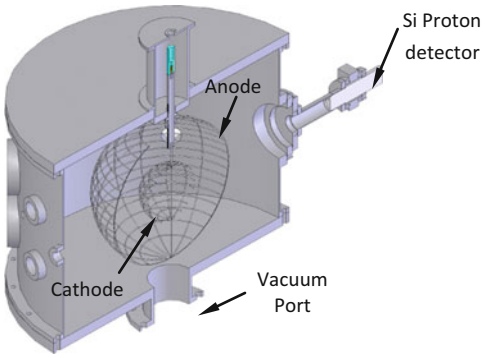

Fig. 1.6 Schematic of the IEC device (named Homer) at UW Madison. The cathode, anode, and the various detector ports are shown in the cross-sectional diagram [38]

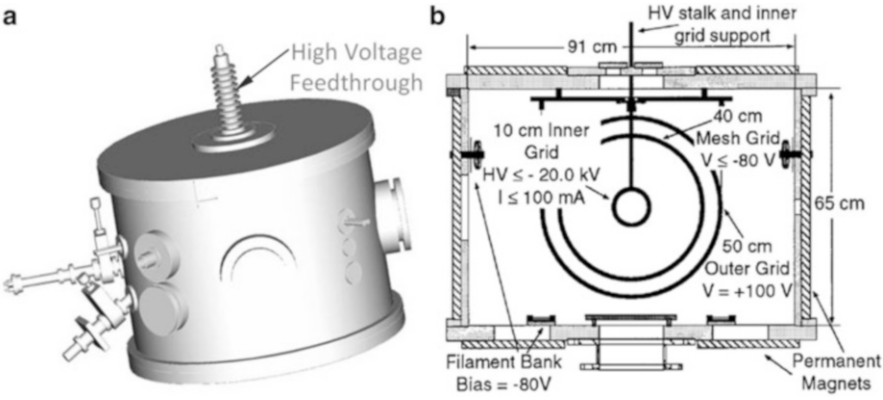

Fig. 1.7 (**a**) Schematic of the IEC device (named "Homer") at UW Madison. (**b**) The cross section of the Homer IEC device at UW Madison employing DC bias voltages [40]

1.6.1 Thorson's Triple Grid IEC Device

Thorson [39] used a triple grid arrangement with DC electric fields and a filament electron source to stabilize the IEC plasma as shown in Fig. 1.7.

One basic difference between the Homer-type device of Fig. 1.7 (see also Fig. 1.6) and the IEC devices at the University of Illinois shown in Fig. 1.5 is that the latter employed a spherical vacuum vessel as the anode. In contrast, the Homer device employs a spherical grid, but the vacuum chamber is cylindrical. In principle, the two should behave in the same way; however, great care must be taken when the outer anode is a grid to ensure that distortions by the grid mesh do not introduce asymmetries in the spherical shape of the anode. In the case of Homer, Thorson used the grid and cylindrical chamber to an advantage, as discussed next.

Thorson employed DC bias voltages and used filament electron sources to stabilize the operating parameters of the IEC device. In an attempt to improve the electron confinement close to the chamber walls, Thorson employed permanent

magnets. Prior to Thorson's work, there was very little experimental data on the generic behavior of the ion flow and flow convergence in IEC devices. He provided critical data, which in turn improved the fundamental understanding for all types of these systems. A flexible, gridded-electrode scheme was chosen for these experiments due to its relatively simple and inexpensive design, and electrostatic probes and visible imaging diagnostics were used to characterize the ion flow.

He reported the first detailed evaluation of the ion flow characteristics in the low-pressure, converged core regime of a spherically convergent ion focus [36]. Measurements of the electrostatic potential distribution throughout the Homer device show detailed agreement with a recirculating space charge-limited flow model and indicated that the ions dominate the system at the low pressures (~53 mPa) achieved. A virtual anode structure forms in the converged core due to the enhanced ion density in that region, but no evidence of multiple potential well structures was observed for the conditions under study. Camera imaging and plasma potential measurements in the core region showed that flow convergence improves with increasing voltage, pressure, potential well symmetry, and decreased current. Core density measurements show a factor of 10 increase in ion density in the core region (versus the outer chamber pressure). This increase agrees with a simple flow conservation model. Understanding the influence of the virtual anode on the flow dynamics is an important issue for high-density systems.

Prior to Thorson's work, it was generally thought that the deuterium–deuterium (D–D) fusion reactions observed in a spherical IEC device significantly exceeded the rate predicted by a collisionless flow model to support his conclusions. Thorson employed proton collimation measurements. He showed that a careful consideration of ion–neutral collisions and the trapped neutral density in the cathode accounted for the extra reactivity without invoking anomalous ion trapping in the converged core region [41]. The proton collimation experiments indicated that in Homer, the bulk of the observed reactivity originated outside the core region. Thorson also provided a classical flow model, where charge exchange collisional effects on the ions and the resulting fast neutral distribution are included. This model gave fusion rate estimates that are quantitatively consistent with the observed D–D fusion neutron production rate. In summary, Thorson's work provides important insight into IEC gas discharge physics.

1.6.2 Murali's Triple Grid RF-Based IEC Device

For the near-term applications to be commercially viable, it is important to improve the efficiency of the existing system. To this end, Murali [42] investigated various modes of operation (configurations) of the University of Wisconsin, Madison, Homer IEC device. Among other things, he showed that the use of a RF power supply connected to the outer grids (as shown in Fig. 1.8) provided an independent control over the cathode grid current by directly controlling the ionization fraction

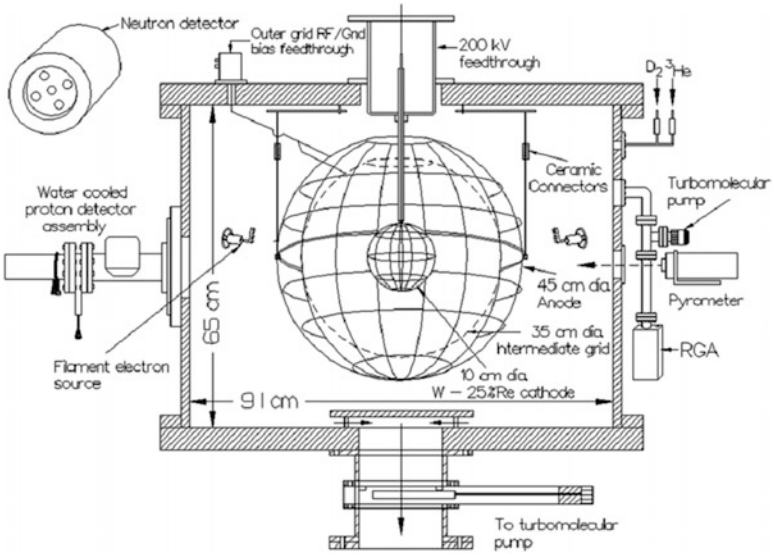

Fig. 1.8 Triple grid arrangement of the Homer device at UW Madison. Thorson used a DC bias on the outer grids, while Murali used RF power to generate selective ionization near the outer grid, improving device performance [35]

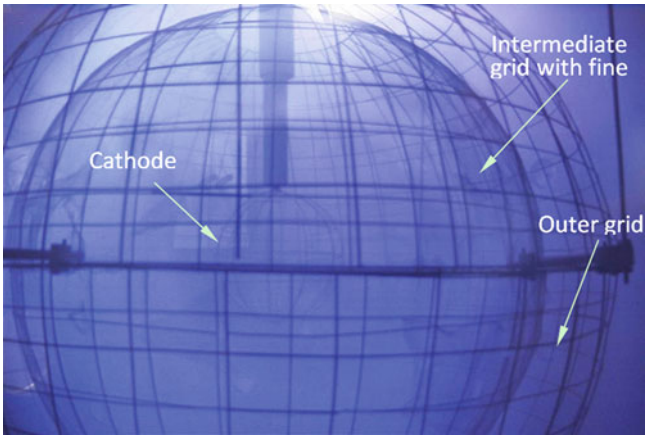

Fig. 1.9 Picture of Homer employing three grids with RF applied to the two outer grids. There is no bias on the cathode [43]

close to the boundary of the device (anode). This allowed stable operation of the device at various chamber pressures, mostly lower than pressures achieved by background ionization alone. Furthermore, this configuration evenly distributed the heat load around the cathode, thus preventing the thermionic emission from prematurely setting on the cathode grid. Figure 1.9 illustrates the RF power applied

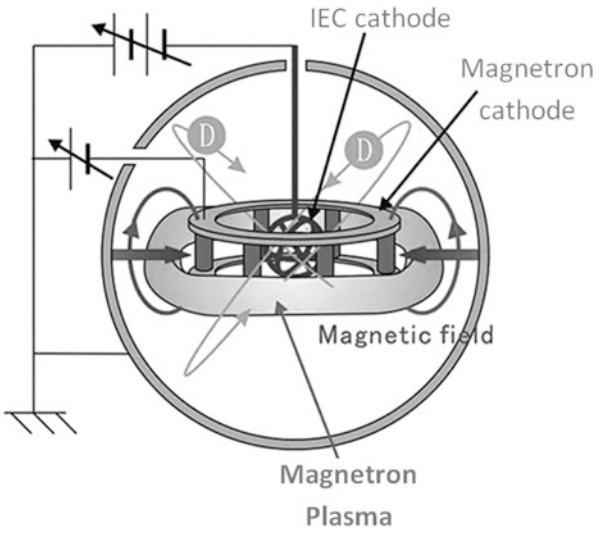

Fig. 1.10 Schematic for electrode arrangement in an RS-MIS-driven IEC device [48]

to the two outer grids in the absence of the cathode voltage showing the ionization of gases around the two outer grids (see also Fig. 1.10). The relatively low-pressure operation also improved the efficiency of the device, but the basic physics of operation did not change and the various loss mechanisms still persisted, only at a reduced rate.

1.6.3 The Ring-Shaped Magnetron Ion Source (RS-MIS)-Based IEC Device

The IEC devices at various universities in Japan [44, 45] initially employed gridded devices with internal discharge ion sources. However, Kai Masuda et al., from Kyoto University, developed a unique magnetron-based device that was aimed at lower pressure operation [46, 47]. The goal was to exploit the long mean free paths at low pressures to enhance the beam–beam interactions. Later, this configuration was extended to a set of magnetrons surrounding the cathode (shown in Fig. 1.10) [48]. This experiment was intended to reduce charge exchange by operating at much lower gas pressures (~ few millipascal) using an internal ring-shaped magnetron ion source (RS-MIS). The basic concept was to produce deuteron ions in a low-voltage (few kV), low-current (few mA) magnetron discharge using perpendicular electric and magnetic field vectors in the vicinity of the anode grid. Because the cathode grid is held at a lower potential than the magnetron cathode, electrons from the magnetron cathode are primarily accelerated toward the anode grid. As a result, most of the magnetron discharge occurs between the anode grid and the magnetron cathode. These source ions are then extracted using a traditional cathode

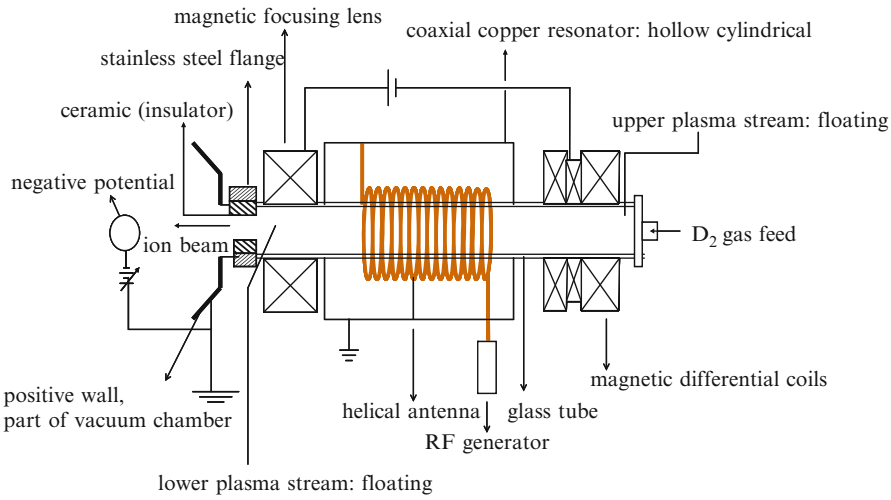

Fig. 1.11 Schematic of the UIUC RF gun injector for IEC experiments [49]

grid enclosing the concentric center of the system. While this configuration reduced CX losses, the ion source rate was also reduced, resulting in a maximum fusion reaction rate in the 10^4 n/s range versus ~10^8 n/s in other gridded units.

1.6.4 Miley's "Ion-Injected" Device

The key to developing an IEC power device is to use external ion "guns" to form and inject ions into the spherical IEC chamber. This mitigates the energy carried away by electrons, and differential pumping between the gun and chamber allows the high vacuum needed in the chamber. (Ion injection by external guns was originally used by Hirsch as already noted. Also, more recently other labs, such as the University of Wisconsin and University of Kyoto/Tokyo Institute of Technology, have started gun injection work, some of which is described in later chapters.) The ion formation is done in the high-pressure gun discharge region outside of the chamber. The objective is to find conditions where the IEC plasma can exist stably and has sufficient ion confinement time to approach power breakeven conditions. This approach will require a very precise control over the energy and angular momentum of injected ions, and a balanced supply of electrons is provided. A radio-frequency (RF) ion injector (or "gun") capable of such operation has already been developed [49]. A sketch of this design is shown in Fig. 1.11.

In this RF gun, a graded index magnetic field is used to increase the ionization efficiency. A key component is the magnetic focusing lens at the extraction port. This allows very efficient differential pumping between the high-pressure gun chamber and the low-pressure IEC chamber. It also provides some control of the angular velocity of entering ions.

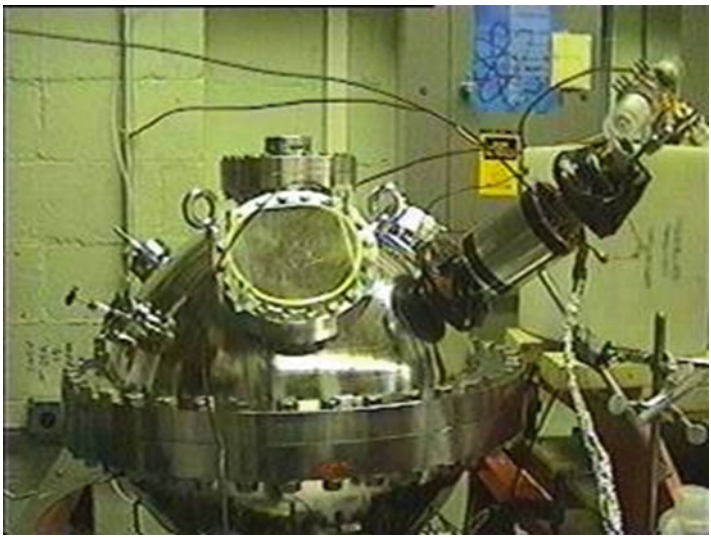

Fig. 1.12 RF gun attached to an IEC chamber in the UIUC laboratory [49]

The UIUC RF ion injector is shown attached to an IEC chamber in Fig. 1.12, and a photograph of the focal spot achieved with injection from this single injector is shown in Fig. 1.13 on page 22. Note that ion scattering off the central dense plasma "core" causes noticeable (but "faint") recirculating ion beams observed in the photograph of the discharge. With additional injectors, the recirculation pattern should become quite symmetric about the center. These studies did include differential pumping so that the number of recirculating passes, β, by an ion was very low, roughly two. The injected ion current, I, was about 50 mA. Still, based on measurements of neutrons emitted using deuterium fuel, the Q (fusion energy gain/energy in) was remarkable for such a small device, on the order of 10^{-6}. Based on these results, an aggressive breakeven experiment using this type of IEC with added ion injection "guns" might be considered.

1.6.5 Nebel–Barnes POPS Device

Theoretical studies by Barnes and Nebel [29] show that a small internal oscillating ion cloud may undergo a self-similar collapse in a harmonic oscillator potential formed by a uniform electron background. This then forms a dynamic IEC device, but with a quite different ion energy distribution versus the "conventional" beam-like one. This more Maxwellian-like distribution remains stable throughout the oscillations, eliminating stability issues for "conventional" beam–beam-type IECs. However, a key issue for this concept is how much plasma compression can be achieved by the POPS oscillations. Study [30] extended the prior study in a systematic fashion by developing a formalism that determines the required velocity

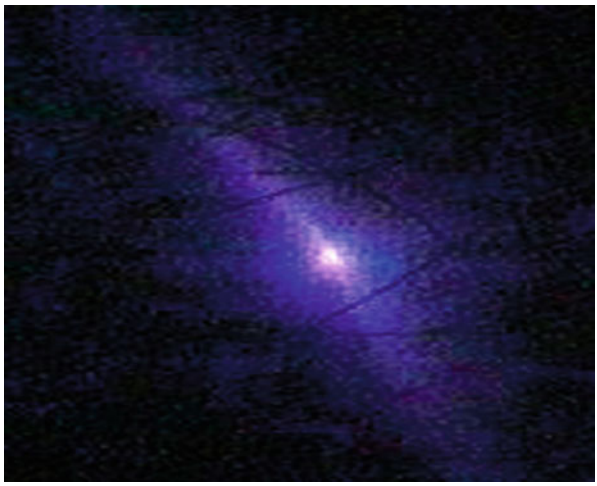

Fig. 1.13 Photo of center spot formation. The main beam observed is a direct path along the injector angle. Other faint light channels indicate beams for scattering of the central core region [49, 50]

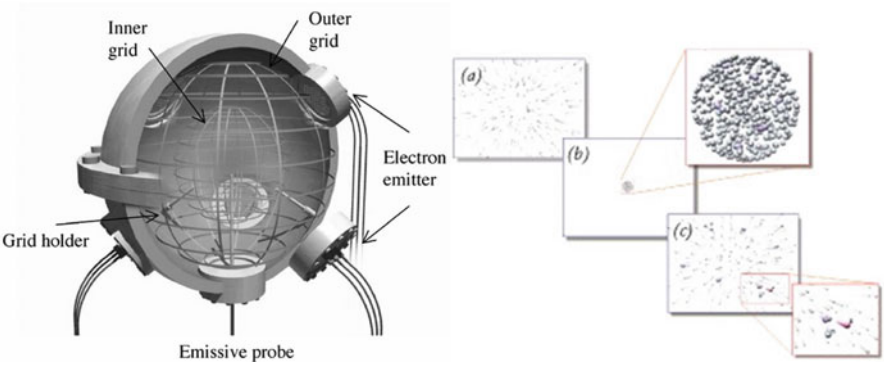

Fig. 1.14 Intense neutron source-electron (INS-e) device demonstrating the POPS concept at the Los Alamos National Lab. (**a**) Particles distributed spatially around the cathode but converged in velocity space. (**b**) Particles converging in space by distributed in velocity space. (**c**) Half a period later the particles return back to their original spatial distribution [5]

distribution of the injected electrons so space charge neutralization can be achieved. This formalism was then included as a boundary condition in a gridless particle code. Results from this complication indicate that although the formalism works well during the early phases of compression, when the compression increases, the solution bifurcates and becomes unphysical. Later studies in reference [51] show that by properly programming the distribution function of the injected electrons, it is possible to significantly improve the space dynamic charge neutralization and the plasma compression.

In support of these encouraging theoretical findings, some proof-of-principle experiments on POPS were done at LANL (Fig. 1.14). These have confirmed the

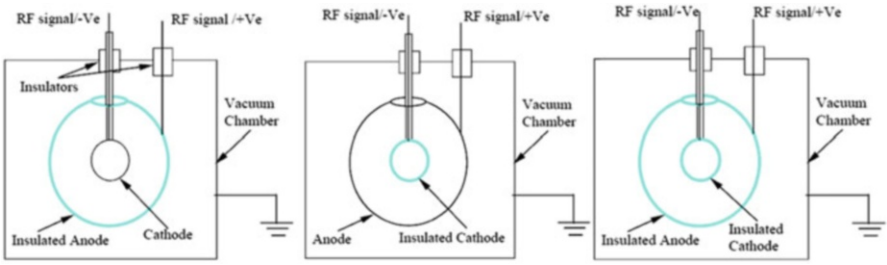

Fig. 1.15 Various configurations of Murali's high-pressure IEC operation. The voltages can also be reversed to have the ions move outward from the core

POPS-type oscillations through observation that the ions in the potential well exhibit resonance behavior when driven at the POPS frequency [52]. Excellent agreement between the observed POPS frequencies and the theoretical predictions was observed for a wide range of potential well depths and three different ion species. Practical applications of POPS require large plasma compressions which have not yet been done experimentally. Large compressions have been observed in particle simulations, although space charge neutralization remains an issue for such operation. Unfortunately, for various reasons research on POPS has not continued at high level of effort at LANL. Thus, the practicality of this concept remains an open question which deserves more research.

1.6.6 Murali's High-Pressure IEC Concept

In late 2012, Murali patented [53] a unique technology that relies on accelerating ions to fusion-relevant energies within one mean free path distance. This is achieved using pulsed high electrostatic fields at relatively high pressures. The major advantage of this technique is the potential of achieving higher fusion reaction rates with an improved efficiency. This device does not rely on the formation of any multiple potential wells and is relatively straightforward. Murali argued that it is relatively easy to produce very high voltages in comparison to generation of very high currents. However, high-voltage breakdown can become a show-stopping issue. In order to handle this problem, Murali suggested that the voltage be split between the two electrodes (as shown in Fig. 1.15) instead of applying all the voltage to a single electrode. This reduces the field stresses by half around each of the electrodes. Another problem associated with the use of very high voltage is that the electrons tend to arc from one electrode to the other without accelerating any ions. To solve this problem, Murali suggested that an insulator be placed between the two electrodes such that a direct path does not exist between the

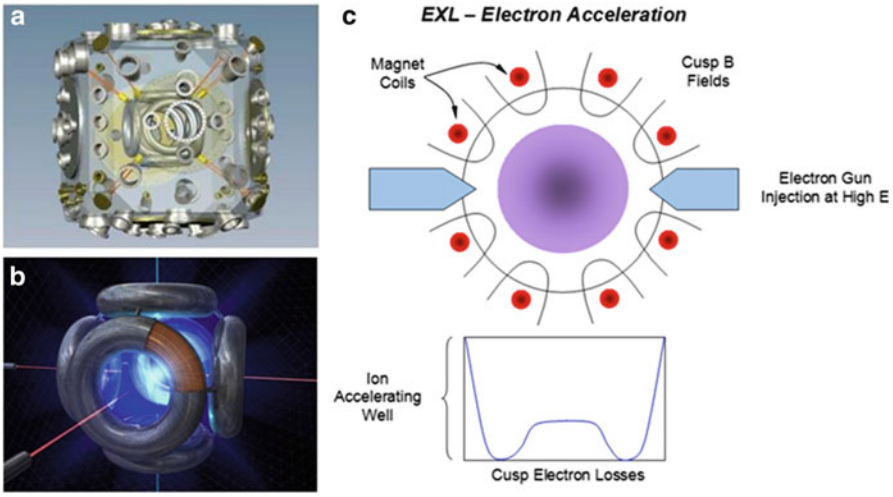

Fig. 1.16 (**a**) Bussard Polywell prototype design. (**b**) Picture of the cusp field confining the plasma and electrons being injected into the cusp fields. (**c**) The basic principle of operation showing the ions accelerating in the cusp fields generated by the magnet coils [53]

two electrodes (see Fig. 1.15). The only current that exists is the displacement current, allowing an isotropic acceleration of charged particles. To initiate the plasma, a RF source could also be used around the exterior of the chamber. Murali argued that such a device can achieve high fusion rates, offering near-term applications. This concept can also be extended to cylindrical geometry. Experimental demonstration of such operation is still required.

Because the discussions to this point have focused largely on gridded devices, next we briefly review a few other approaches, such as the Bussard HEPS concept and the Barnes–Nebel Penning trap.

1.6.7 Bussard HEPS (or Polywell) Concept

In Bussard's Polywell IEC, a simulated spherical magnetic field termed a "Polywell" is approximately obtained with a multipole cusp magnetic field as shown in Fig. 1.16 [26]. More about the theory of flows in this configuration is given in the paper by N. Krall [53], and some stability issues are addressed in the Wang and Krall paper [54]. Unique to this device is that the cathode is "virtual," and hence there is neither a grid-melting problem nor ion loss through collision with the cathode grid. One of the key physics revolves around electron losses from the poles in the cusp field. Krall and Bussard argue that a plasma "wiffle-ball" effect causes the loss cone angle to be reduced due to the high pressure developed in the IEC plasma. The issue still needs further experimental verification. The Polywell

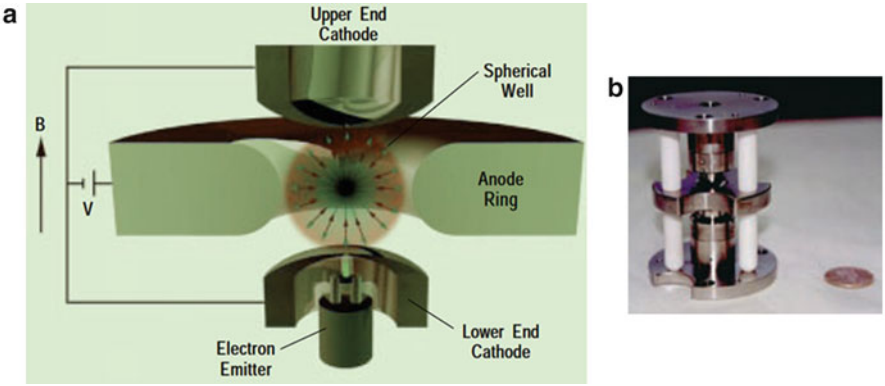

Fig. 1.17 (**a**) Schematic representation of the Penning trap showing the effective spherical well boundary and the reflected electron trajectories. (**b**) The trap used in the Penning trap experiments at Los Alamos National Lab. The quarter is placed next to the device for scaling purposes [56]

approach is very important, and it is currently pursued by R. Nebel's EMC^2 company in Santa Fe with significant DOD funding. More insights will be provided in later chapters of this book.

1.6.8 Barnes–Nebel Penning Trap

The Penning fusion (PF) concept developed by Barnes and Nebel et al. [55] uses a unique plasma confinement principle (shown in Fig. 1.17). In PF, a non-neutral electron plasma is confined in a modified Penning trap using applied magnetostatic and electrostatic fields. The electron space charge, in turn, electrostatically confines a minority, unmagnetized ion species. For fusion energy production, it is necessary to raise the applied voltages producing the confining electrostatic field to 100 kV or greater. Still, in a practically sized system, the electron density (and to a greater degree the ion density) falls short of that required to give a reasonable fusion reactivity. Still, PF provides important information about ion focusing, either in space or time, as a means of enhancing ion reactivity. The objective is to enhance the reactivity over that available with the background density. PF is strongly related to the IEC, and it attempts to address two limitations of the IEC. First, following the Bussard–Krall Polywell theory [26, 27], the grid is replaced by an electron cloud, which forms a virtual cathode. In this way, ion–grid collisions and associated limitations (such as secondary electron emission from the grid and grid heating) are avoided. Second, high rates of ion–ion collisions, which limit the theoretically achievable fusion gain Q (fusion power/input power) to around unity, are avoided to some extent with this type of well. However, issues of electron loss and cone losses, radiation damage of the magnets and cooling, and the ability to circumvent the Elmore et al. density limit remain open questions.

1.7 Summary

The basic IEC approach is to create a potential well through electrostatic confinement of one of the plasma species in a dynamic (inertial) configuration. "Inertial" effects associated with dynamic motion of the confined species are essential to avoid plasma losses predicted for systems by Earnshaw. The two primary approaches can be termed "ion injected" or "electron injected," with the "injected" species being the one forming the potential well. In order to maintain the well, the second species brought in with the injected one must not completely neutralize the plasma, i.e., the IEC plasma is inherently "quasi-neutral." This well provides trapping and convergence of the ions "streaming" toward the center of the trap region, forming a dense fusing plasma there. The objective for a power reactor is to obtain ion beam–beam collisions in this central core. For neutron/proton production, satisfactory reaction rates can come from beam–background collisions. However, this scaling with injected current would require excessive input power for a practical power producing unit. Thus, beam–beam scaling of the reaction rate as the current squared (or higher powers as noted earlier may be possible due to nonlinear effects) is essential. The vision of a power reactor seeks a "zero" background pressure and thus generally involves an external ion source with acceleration into the trap at ultralow pressure to obtain beam–beam collisions. As described earlier, this changes the details of the physics just discussed for an ideal "zero" background pressure device. The issue of whether the trap should be formed by ion injection or by "digging a well" with electrons remains open but involves stability and reaction volume (focusing) optimization issues.

As seen, a wealth of information has been developed in studies of gridded IEC devices. However, the beam–background fusion used in these devices involves important differences in physics compared to what is needed for future beam–beam IEC reactors. Most notable is the need to maintain an extremely low background pressure to prevent interactions with background neutrals. Further, physical grids are subject to damage at high power levels. As pointed out, some studies show grids can survive at modest powers. But, for aggressive power units such as the $p–B^{11}$ plant, they must be replaced with virtual electrode surfaces creating a deep potential well for ion confinement. Ion up-scattering out of the well must be minimized while electron temperatures are suppressed. These issues will be discussed further in later chapters.

References

1. Miley GH (1973) Fusion energy conversion. American Nuclear Society, La Grange
2. Earnshaw S (1842) On the nature of the molecular forces which regulate the constitution of the luminiferous ether. Trans Camb Philos Soc 7:97–112
3. Ashley RP, Kulcinski GL, Santarius JF, Krupakar Murali S, Piefer G, Radel R (2001) Steady-state D–^{3}He proton production in an IEC fusion device. Fusion Technol Ill 39(2):546–551

4. Tomiyasu K, Santarius JF, Kulcinski GL (2003) Numerical simulation for UW-IEC device. In: 6th U.S.-Japan IEC workshop, Tokyo, 21–23 Oct
5. Miley GH, Stubbers R, Yang Y, Webber J, Shaban Y (2004) Advances in IEC technology for a portable neutron/proton source. In: 14th Pacific Basin nuclear conference, Mar
6. Krupakar Murali S (2004) Diagnostic study of steady state advanced fuel (D–D and D–^{3}He) fusion in an IEC device. Ph.D. dissertation, University of Wisconsin, Madison
7. Krupakar Murali S, Cipiti BB, Santarius JF, Kulcinski GL (2006) Study of fusion regimes in an inertial electrostatic confinement device using the new eclipse disc diagnostic. Phys Plasmas 13:053111
8. Lawson JD (1957) Some criteria for a power producing thermonuclear reactor. Proc Phys Soc B 70:6
9. Chacon L, Miley G (1998) Inertial electrostatic confinement ^{3}He breeder for D–^{3}He satellite systems. Fusion Technol 33:182–209
10. Krupakar Murali S et al (2006) Carbon nanotubes in IEC fusion reactors. In: ANS annual meeting, Reno, 4–8 June
11. Dolan TJ (1994) Magnetic electrostatic plasma confinement. Plasma Phys Control Fusion 36:1539–1593
12. Lavrent'ev OA et al (1963) Jenergiya i plotnost'ionov v jelektromagnitnoj lovushke. Ukrain Fiz 8:440–445
13. Farnsworth PJ (1966) Electric discharge device for producing interaction between Nuclei. US Patent 3,258,402
14. Stashower D (2002) The boy genius and the mogul: the untold story of television. Harper Collins Press, New York
15. Elmore WC, Tuck JL, Watson KM (1959) On the inertial-electrostatic confinement of a plasma. Phys Fluids 2(3):239
16. Child CD (1911) Discharge from hot CaO. Phys Rev 32:493
17. Langmuir I (1913) The effect of space charge and residual gases on thermionic currents in high vacuum. Phys Rev 2:450
18. Langmuir I (1914) Thermionic currents in high vacuum. I. Effect of space charge. Physik Z 15:348
19. Langmuir I (1923) The effect of space charge on the potential distribution and thermionic current between parallel plate electrodes. Phys Rev 21:419
20. Langmuir I, Blodgett KB (1924) Currents limited by space charge between concentric spheres. Phys Rev 24:49–59
21. Hirsch RL (1968) Experimental studies of a deep, negative, electrostatic potential well in spherical geometry. Phys Fluids 11(11):2486
22. Barnes C, Dunn DA (1967) State of the art of inertial electrostatic containment. ITT Industrial Laboratories, Fort Wayne, App. VA
23. Hockney RW (1967) Two-dimensional computer experiments on inertial confinement. Bull Am Phys Soc 13:290
24. Birdsall CK, Bridges WB (1966) Electron dynamics of diode regions. Academic, New York
25. Budker GI (1961) Plasma physics and the problem of controlled thermonuclear reactions I. Pergamon Elmsford, New York, pp 295–301
26. Bussard RW (1991) Some Physics considerations of magnetic inertial-electrostatic confinement: a new concept for spherical converging-flow fusion. Fusion Technol 19(2):273–293
27. Krall NA (1992) The Polywell^{TM}: a spherically convergent ion focus concept. Fusion Technol 22(1):42–49
28. Miley GH (2013) Life at the center of the energy crisis: a technologist's search for a black swan. Word Scientific Publishing, Singapore
29. Nebel RA, Barnes DC (1998) The periodically oscillating plasma sphere. Fusion Technol 34:28–45
30. Barnes DC, Nebel RA (1998) Stable, thermal equilibrium, large-amplitude, spherical plasma oscillations in electrostatic confinement devices. Phys Plasmas 5:2498

31. Elmore W, Tuck J, Watson K (1959) On the inertial-electrostatic confinement of a plasma. Phys Fluids 2(3):239–246
32. Hirsch RL (1967) Inertial-electrostatic confinement of ionized fusion gases. J Appl Phys 38:4522–4534
33. Black WM, Klevans EH (1974) Theory of potential-well formation in an electrostatic confinement device. J Appl Phys 45(6):2502–2511
34. Miley GH, Gu Y, DeMora JM, Stubbers RA, Hochberg TA, Nadler JH, Anderl RA (1997) Discharge characteristics of the spherical inertial electrostatic confinement (IEC) device. IEEE Trans Plasma Sci 25(4):733–739
35. Krupakar Murali S, Cipiti BB, Santarius JF, Kulcinski GL (2008) Study of ion flow dynamics in an inertial electrostatic confinement (IEC) device through sequential grid construction. Phys Plasmas 15:122702
36. Thorson TA, Durst RD, Fonck RJ, Wainwright LP (1997) Convergence electrostatic potential, and density measurements in a spherical convergent ion focus. Phys Plasmas 4(1):4–5
37. Miley GH et al (1993) Inertial-electrostatic confinement neutron proton source. In: Third international conference on dense 2-pinches, AIP conference proceedings, vol 299, pp 675–689
38. University of Wisconsin-Madison. Inertial electrostatic confinement fusion. http://iec.neep.wisc.edu. Accessed 10 May 2013
39. Thorson TA, Durst RD, Fonck RJ, Wainwright LP (1997) Convergence, electrostatic potential, and density measurements in a spherically convergent ion focus. Phys Plasmas 4(1):4
40. Thorson TA (1998) Ion flow and fusion reactivity characterization of a spherically convergent ion focus. Ph.D. thesis, University of Wisconsin-Madison, Madison
41. Thorson TA, Durst RD, Fonck RJ, Sontag AC (1998) Fusion reactivity characterization of a spherically convergent ion focus. Nucl Fusion 38(4):495–507
42. Krupakar Murali S, Santarius JF, Kulcinski GL (2009) Study of various modes of operation of an IEC device. J Fusion Energy 28(3):314. doi:10.1007/s10894-009-9243-6
43. Krupakar Murali S, Santarius JF, Kulcinski GL (2010) Effects of displaced grids on the fusion reactivity of an inertial electrostatic confinement device. J Fusion Energy 29:256–260
44. Yamamoto Y, Hasegawa M, Ohnishi M, Yoshikawa K, Inoue N (1997) Preliminary studies of potential well measurement in inertial electrostatic confinement fusion experiments. In: 17th IEEE/NPSS symposium on fusion engineering. doi:10.1109/FUSION.1997.687733
45. Ohnishi M, Yamamoto Y, Hasegawa M, Yoshikawa K, Miley GH (1998) Study on an inertial electrostatic confinement fusion as a portable neutron source. Fusion Eng Des 42:207–211
46. Masuda K et al (2003) Performance characteristics of an inertial electrostatic confinement fusion device with magnetron discharge. In: 20th IEEE/NPSS symposium on fusion engineering. doi:10.1109/FUSION.2003.1426725
47. Takamatsu T, Masuda K, Kyunai T, Toku H, Yoshikawa K (2006) Inertial electrostatic confinement fusion device with an ion source using a magnetron discharge. Nucl Fusion 46:142–148
48. Masuda K et al (2010) Cathode grid current dependence of D(d, n)3He reaction rates in an inertial electrostatic confinement device driven by a ring-shaped magnetron ion source. Plasma Phys Control Fusion 52(9):095010
49. Miley GH, Shaban Y, Yang Y (2004) RF ion gun injector in support of fusion ship II research & development. In: El-Genk MS (ed) STAIF 2004, AIP conference proceeding, vol 699, 8–11 Feb, pp 406–412
50. Shaban YR, Miley GH (2002) Practical ion source for high fusion yield in inertial electrostatic confinement. Blt. ANS, 15th Topical Mtg. On the Technology of Fusion Energy, Washington, DC, 17–21 Nov, pp 58–59
51. Park J, Nebel RA, Stange S, Krupakar Murali S (2005) Experimental observation of a periodically oscillating plasma sphere in a gridded inertial electrostatic confinement device. Phys Rev Lett 95:015003

52. Park J, Nebel RA, Stange S, Krupakar Murali S (2005) Periodically oscillating plasma sphere. Phys Plasmas 12:056315
53. Krupakar Murali S (2013) Systems and methods for accelerating particles. Patent application number: PCT/IB2012/054717
54. Wong SK, Krall NA (1993) A nonlocal theory of counterstreaming ion instability. Phys Fluids B 5(6):1706–1714
55. Barnes DC, Nebel RA, Turner L (1991) Production and application of dense Penning trap plasmas. Phys Fluids B Plasma Phys 5:3651
56. Schauer MM, Mitchell TB (P-24), Barnes DC (XCM) (1995–1996) Los Alamos National Lab, Physics Division, Progress Report, Chapter 2, pp 84–87

Chapter 2
Theory of Well Potential Traps in the IEC

2.1 Introduction

As described in Chap. 1, there are two basic types of IECs: ion injected or electron injected. The difference can be easily envisioned by examining Fig. 2.1. There the grid is held at a positive voltage relative to ground. Thus electrons are accelerated (injected) inward, making this an electron-injected type IEC. If the voltage on the grid is reversed, ions created in a plasma discharge between the grid and the walls are extracted and accelerated inward, creating an ion-injected type IEC.

It might seem that the two injection methods are similar. However, important differences occur due to the mass difference in the particles that are then effectively providing the inertia to electrostatically confine the other species. This difference will become more apparent in the analyses in this chapter. From a practical point of view, work by Farnsworth and Hirsch focused on ion-injected type IECs. The Bussard "Polywell" uses a magnetic field to confine electrons that create the potential trap which in turn accelerates ions inward. Thus, in effect, it too is an "ion-injected" type IEC. There are a number of variations of these two extremes, some of which will be discussed here. One word of caution – "injection" is a somewhat misleading terminology. If either electrons or ions are generated externally, a zero energy as they enter at the grounded chamber wall is desired to avoid their passing through the grid and simply hitting the opposite wall.

In this chapter, we concentrate on well potential formation in a spherical IEC. This discussion assumes that the ion source is such that a neutral background gas is not required, i.e., a fully ionized plasma is assumed. In contrast, as discussed in Chap. 1, almost all experiments to date have had a significant background neutral pressure, such that most fusion reactions occur between the ion beam and background neutrals. However, the plasma case analyzed here represents an ideal for future devices designed for higher power fusion operations where fusion reactions are ion beam–beam type. In that case, the reaction rate scales as the ion beam density squared. Because the input power mainly goes into ion beam formation, the beam density squared scaling allows higher fusion rates per unit power than linear

G.H. Miley and S.K. Murali, *Inertial Electrostatic Confinement (IEC) Fusion: Fundamentals and Applications*, DOI 10.1007/978-1-4614-9338-9_2,

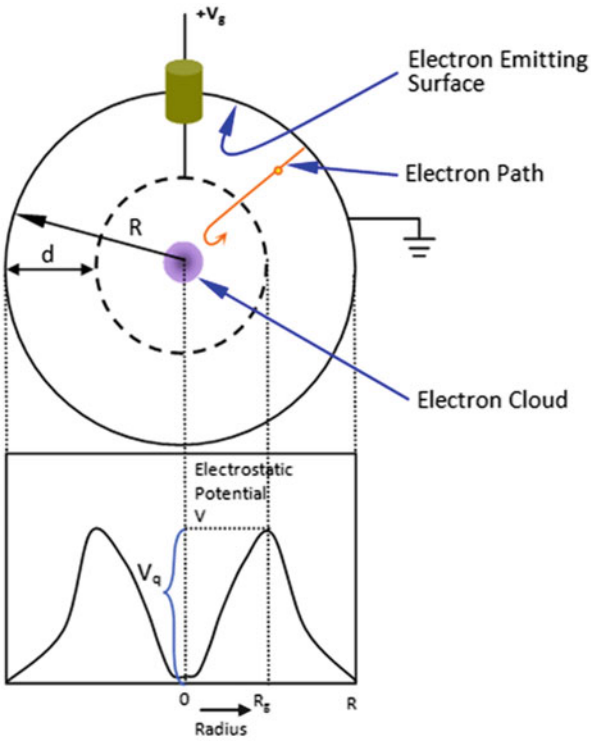

Fig. 2.1 Schematic representation of the "electron-injected" spherical device analyzed by Elmore et al. [1]

scaling. Also, charge exchange energy losses are essentially eliminated without background neutrals.

We begin by considering a conceptual illustration of the multiple well potentials first predicted by Farnsworth in Fig. 1.3 in Chap. 1. Figure 2.2a shows the potential diagram created by the cathode grid held at a negative potential relative to the vessel wall. This configuration automatically forms a well potential trap for ions. Because the objective is to accelerate an ion to its highest velocity as it passes through the center "core" of the device, the ion would ideally be born at the highest potential possible, i.e., very near to the wall. However, if ions are created by a plasma discharge between the grid and the wall, ions will be born over a range of potentials corresponding to the range of values between the wall and the cathode. This immediately brings up two key issues for IEC operation. First, if ions are "injected," a method must be developed to bring them into the grounded chamber at a potential slightly below ground or to cause them to lose energy in passing through the cathode grid (e.g., by collisions) such that they fall into this trap. Second, if a gas discharge is used, some method, such as electron source near the wall, is desirable to increase the ionization rate in that region. The point is that ions born near the wall (ground) gain a higher velocity versus the ones born elsewhere in the region between the grid and the wall. At the other extreme, an ion born near the cathode grid gains very little velocity. Here we will assume as shown in Fig. 2.2a that the

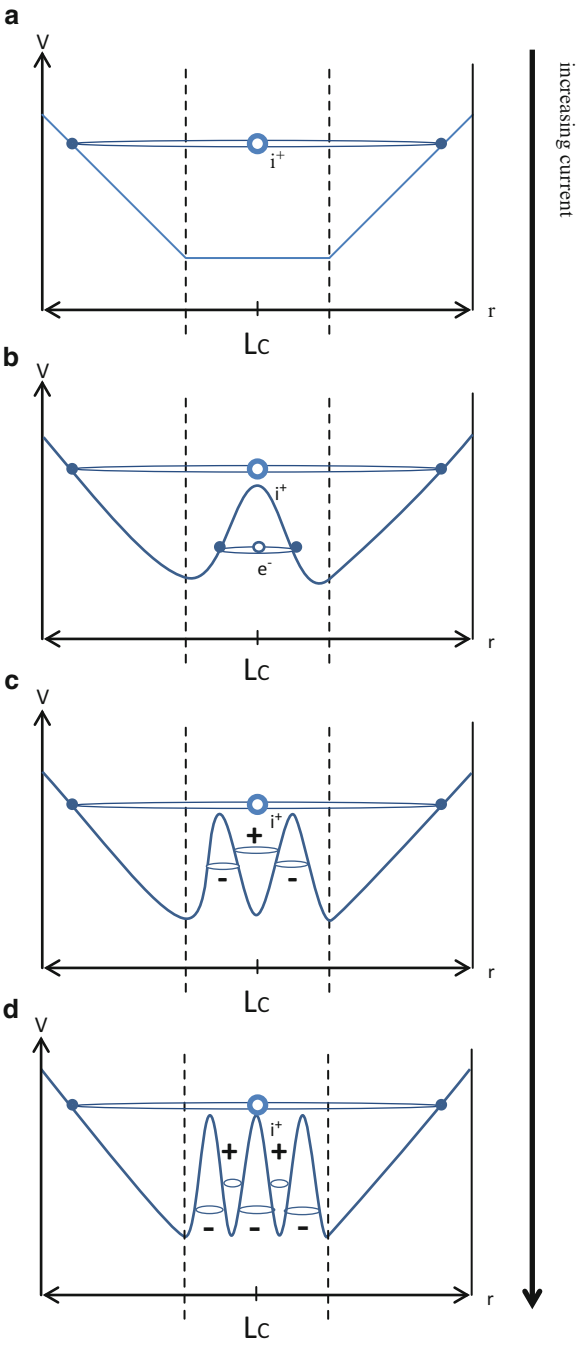

Fig. 2.2 Illustration of the formation of multiple well potentials in a spherical IEC as a function of increasing current in going from (**a**) to (**d**)

ions are produced at a potential surface near the wall. If the ion source rate is low, i.e., the ion current is low, the associated space charge created will not affect the potential, and the ion will circulate in the trap until it collides with the grid or suffers a collision with another ion such that its energy is increased, causing it to upscatter out of the potential trap (see Fig. 2.2a). However if the ion current is increased, the ion density will significantly increase near the center region of the spherical device due to a three-dimensional compression (or focusing) of the ion current in the center region. This will cause the corresponding formation of a virtual anode due to the high positive charge density in that region (see Fig. 2.2b). As the ion source rate continues to increase, the space charge can approach the value of the potential surface of the circulating ions, whereupon it will cause ions to be reflected before reaching the center virtual anode. However, the virtual anode serves as a well potential trap for electrons that are drawn into that region and circulate within this trap, much as the ions do in the outer trap. They in turn have a high density at the center line due to tight focusing in the spherical geometry. This results in the formation of a virtual cathode at the center line as shown in Fig. 2.2c. Ions are trapped in the well potential. Then, as illustrated in Fig. 2.2d, a new virtual anode is formed. In principle, this process could continue giving the nested "onion skin"-like virtual electrodes shown earlier in Fig. 1.3. As already noted, Farnsworth termed these nested well potentials "Poissors." However, in practice, as pointed out earlier, due to the ion energy spread in angular momentum effects, the potential trap formed by electrons (such as shown in Fig. 2.2c) is all that might be expected. Such a configuration leads to a maximum fusion reaction rate within each of the three ion traps, and that has been confirmed in measurements by Gu et al. [2] as described next.

Gu studied the fusion rate profiles to infer the potential trap profile [2]. This is based on the way the well potential profile affects the fusion reaction rate profile, as shown conceptually in Fig. 2.3.

In their experimental study, Gu and Miley [2] used a microchannel proton collimator to map out the fusion reaction rate profile as a function of ion current. The protons recorded were the 3.0-MeV protons created in D–D reactions. Gu et al. first studied the well potential and fusion reaction rate relationship using a computer simulation code (IXL) that solves the collisionless Vlasov equation and Poisson's equation in spherical coordinates [3]. That study confirmed that "practical" spreads in ion energy and angular momentum limit the number of spatially alternating wells to two (termed here a "double well" and illustrated in Fig. 2.3c). This double well is composed of a positive well by ions converging at the focal spot in the spherical cathode, with a negative well formed by electrons focused inside the positive well due to the virtual anode. While this double well falls short of the multiple well "Poissor" structure originally envisioned by Farnsworth, as a practical matter, it is capable of efficiently trapping ions within the virtual anode, much as hoped for in multiple wells. Thus the double well provides an attractive goal for future IEC devices designed for increased fusion rates. Due to this ion-trapping effect, the radial distribution of the fusion reaction rate density provides a means of distinguishing the double well profile.

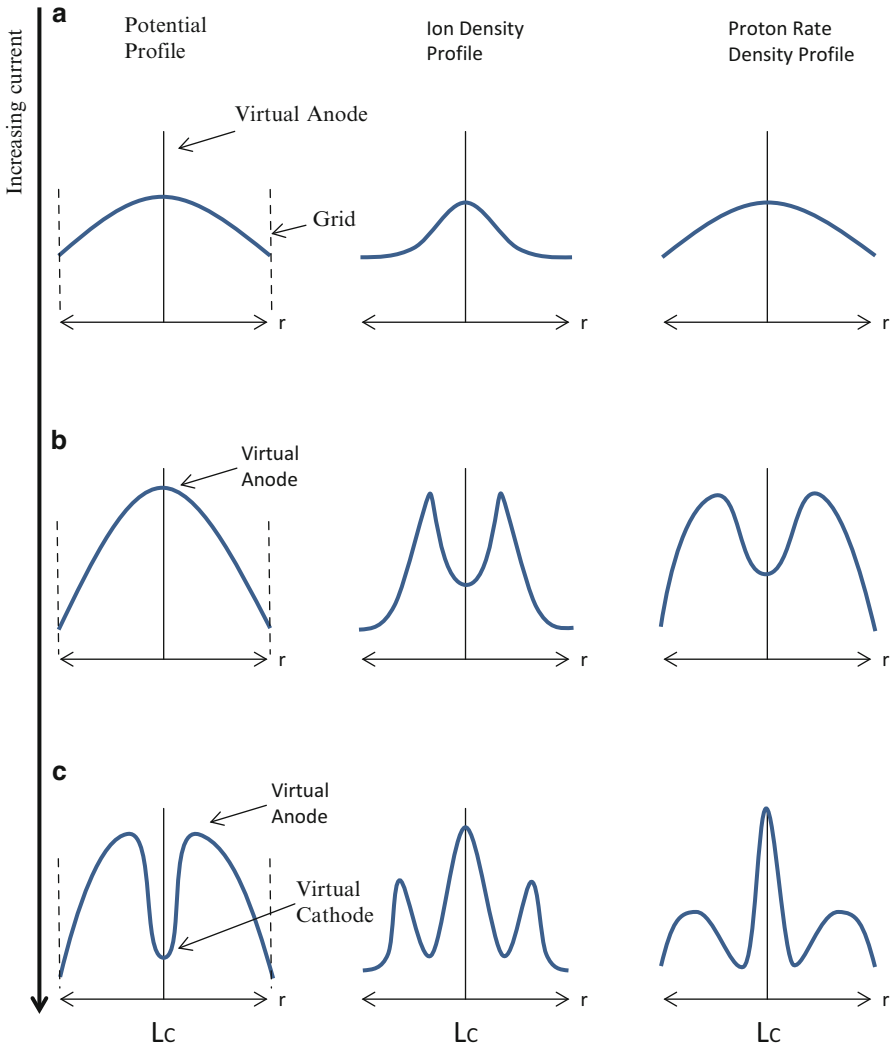

Fig. 2.3 An illustration of the changes in (**a**) proton rate density, (**b**) ion density, and (**c**) potential profile as the ion current increases [2]

The relation between the proton source-rate density profile and the well potential structure is delineated in Fig. 2.3 as a function of ion current. A fixed voltage is assumed in these figures. Note that the well potential properties follow the same pattern as shown earlier in Fig. 2.2, but now the corresponding fusion rate profiles are added to the right of the potential plots. The progression toward a double well is associated with increasing the ion current going from 2.3a to c. At low-ion current (such as in Fig. 2.3a), where the space charge potential at the center is low, a single sharp peak in the reaction rate density occurs there. As the height of this positive

potential peak increases in Fig. 2.3, ions are repulsed, causing a distinct "dip" in the reaction rate density peak at the center. However, as the ion current is further increased in Fig. 2.3c, the resulting virtual anode accelerates and focuses electrons in the center of the positive well, creating a potential "double well" (corresponding to the earlier Fig. 2.2c). Consequently, a distinctive peak in the reaction rate density suddenly appears in the middle of the dip in the reaction rate density profile due to the fusion of ions trapped by the double well. While the amplitudes of the various profiles will vary, the trends depicted will occur regardless of whether beam–beam or beam–background neutral-type fusion reactions dominate. Thus, these characteristics are quite general.

Because of the distinct reaction rate density behavior illustrated by Fig. 2.3, the experimental observance of two proton source-rate peaks (Fig. 2.3c) uniquely signals the existence of a double well potential. In addition, as discussed by Gu et al. [2], analysis of the reaction rate peak amplitudes can provide a reasonable estimate of the well depth.

Now that we have obtained a conceptual picture of well potential formation processes and the corresponding effect on the fusion reaction rate, we move on to review theoretical studies of this well potential formation in more detail.

An early theoretical analysis of IECs was carried out by Elmore, Tuck, and Watson [1]. At this point we present and extend their analysis because it leads to analytical solutions that illustrate the electrostatic structure of an IEC. The various assumptions employed in this analysis (and in other analytical solutions) limit the accuracy of the result. Thus, numerical methods such as discussed in Chap. 13 have been used for more realistic solutions. In their analysis, Elmore, Tuck, and Watson assumed electrons were injected radially inward with an energy of eV_o at the surface of a sphere. The electrons were then assumed to be stopped by their mutual repulsion near the center of the IEC and be reflected back toward the outer surface (analogous to the case for ion injection shown earlier in Fig. 2.2). The corresponding electrostatic potential within the sphere was shown earlier in Fig. 2.1. Elmore, Tuck, and Watson argued that a well potential of depth V_o will exist at the center, so positive ions of energy $\varepsilon_i < eV_o$ are confined within the well.

For reasonable confinement a well depth of $V_o \cong 100$ keV was assumed. This corresponds to an ion energy near the peak of the fusion cross section for D–T fusion reactions. Elmore and colleagues assumed all particles have radial motion (no angular momentum), neglected scattering collisions, and background neutrals (i.e., represents a fully ionized plasma), and potential surfaces were taken to be spherically symmetric (i.e., perturbations due to the "stalk" fixed to the grid to both hold it mechanically and supply a voltage to it). In a high vacuum where the electron mean free path is large compared to the grid diameter, an electron can make a number of passes before it collides with the grid and is lost. Owing to these recirculations, the effective space charge current given by the input current is multiplied by the average number of recirculations an electron makes. In other words, if an electron makes γ oscillations (across the grid), then the internal electron current drawn to the grid would be γ times the current drawn to the grid.

The suitable equation for describing the electrostatic equilibrium of such a potential distribution is the Poisson's equation. The electrostatic equilibrium of such a system is computed for two situations where the plasma has (1) a zero temperature and (2) a finite temperature. We now proceed to solve it for the zero plasma temperature assumption.

The Poisson's equation that describes the system in static operation is

$$\frac{1}{r^2}\frac{\partial}{\partial r}\left(r^2\frac{\partial V}{\partial r}\right) = -4\pi[\rho_i - \rho_e]. \tag{2.1}$$

Here i represents an ion and e represents an electron, ρ_i, ρ_e are the respective charge densities, and $\pm\nu_e$, $\pm\nu_i$ are the radial velocities at a given radius r. The total electron current (I_e) directed outward (and hence inward as well) is given by

$$I_e \equiv 4\pi r^2\left(\frac{\rho_e}{2}\right)\nu_e, \quad \text{and, similarly,} \quad I_i \equiv 4\pi r^2\left(\frac{\rho_i}{2}\right)\nu_i. \tag{2.2}$$

where the subscript e represents electrons and i represents ions. Conservation of energy requires that

$$\frac{1}{2}m_e{\nu_e}^2 - eV = \varepsilon_{oe}, \quad \text{and}$$

$$\frac{1}{2}m_i{\nu_i}^2 + eV = \varepsilon_{oi}. \tag{2.3}$$

Here m_e is the electron mass, m_i is the ion mass, e is the electron charge, and V is the electrostatic potential; ε_{oe} and ε_{oi} are the total energies, respectively, of an electron and ion.

A convenient dimensionless variable, W_e, associated with the electron energy, was proposed by P. T. Farnsworth [4] to simplify the analysis. He defined

$$W_e = \frac{\frac{1}{2}m_e{v_e}^2}{\Lambda}. \tag{2.4}$$

Here Λ is a constant parameter that has the dimensions of energy which will be determined later in the derivation. Solving for the radial velocities gives

$$v_e = \left(\frac{2\Lambda}{m_e}\right)^{\frac{1}{2}}W^{\frac{1}{2}} \text{ and } v_i = \left(\frac{2\Lambda}{m_i}\right)^{\frac{1}{2}}[W_o - W]^{\frac{1}{2}}, \tag{2.5a}$$

where

$$W_o \equiv \frac{1}{\Lambda}[\varepsilon_{0e} + \varepsilon_{0i}]. \tag{2.5b}$$

Equation 2.2 may be solved for ρ_e and ρ_i in terms of ν_e and ν_i, which in turn may be eliminated with Eq. 2.5a. We then obtain

$$4\pi e[\rho_i - \rho_e] = -\frac{2eI_e}{\left(\frac{2\Lambda}{m_e}\right)^{\frac{1}{2}}}\frac{1}{r^2}\left[\frac{1}{W^{\frac{1}{2}}} - \frac{G_0}{[W_0 - W]^{\frac{1}{2}}}\right], \tag{2.6a}$$

where G_0 is a function of the ion to electron current ratio:

$$G_0 \equiv \frac{I_i}{I_e}\left(\frac{m_i}{m_e}\right)^{\frac{1}{2}}. \tag{2.6b}$$

Returning to the Poisson's Equation 2.1 and setting $e\left(\frac{\partial V}{\partial r}\right) = \Lambda\left(\frac{\partial W}{\partial r}\right)$, we then obtain

$$\frac{\partial}{\partial r}\left(r^2\frac{\partial W}{\partial r}\right) = \frac{1}{W^{\frac{1}{2}}} - \frac{G_0}{[W_0 - W]^{\frac{1}{2}}}, \tag{2.7}$$

if we define the parameter Λ as

$$\Lambda^{\frac{1}{2}} = \sqrt{2}eI_e(m_e)^{\frac{1}{2}}. \tag{2.8}$$

For convenience, this equation can be expressed in terms of the independent variable

$$z \equiv \ln\frac{r}{r_o}. \tag{2.9}$$

Here r_o is a parameter which is characteristic of the "width" of the central region of the well potential. Equation 2.7 then becomes

$$\frac{d^2W}{dz^2} + \frac{dW}{dz} = \frac{1}{W^{\frac{1}{2}}} - \frac{G_0}{[W_0 - W]^{\frac{1}{2}}}, \tag{2.10}$$

with the boundary condition

$$\frac{\partial W}{\partial z} = 0 \quad \text{for } z = 0. \tag{2.11}$$

This equation represents a convenient form for the original Poisson's equation given in Eq. 2.1. A solution to Eq. 2.10 is most easily obtained for the simplest case, where $G_o = 0$, i.e., where the ion current is zero. For example, Elmore, Tuck, and Watson found for this case that with a well potential of depth $V_o \cong 100$ keV and

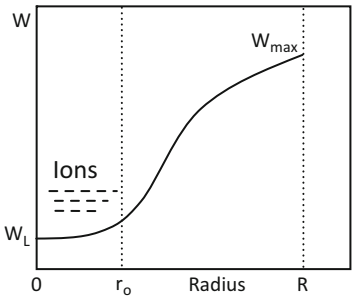

Fig. 2.4 The confinement of ions near the center "core" of the IEC well potential [4]

radius $r_o \cong 1$ cm can be maintained in a sphere 1 m in diameter with an electron current $(1/\nu)\, I_e \cong 100$ A.

However, this result poses some serious problems. The center of the well potential is restricted to a very small volume compared with the total volume within the sphere. Thus the volume of the confined fusion plasma is quite small, limiting the total fusion power level. This restriction occurred, however, by assuming that the electrons have no angular momentum about the center of the sphere. In fact, the electrons will develop transverse motion from scattering (deflection) by the accelerating grid and from scattering against the ions. While that will increase the central core fusing volume, the electron current must be increased to fill the volume at the high currents involved, and questions about instabilities must be studied. Indeed, one reason the Bussard "Polywell" IEC employs magnetic confinement of the electrons is to stabilize the electron well potential over a larger central volume.

Next, we consider Eq. 2.10 for the case when $G_o \geq 0$. If we integrate Eq. 2.10 outward from $z = 0$, W will increase from its value W_L at $z = 0$. As $W \rightarrow W_o$, the second term will dominate on the right-hand side of Eq. 2.10, causing W to start decreasing again. Thus, W never reaches the value W_o. This means that the well potential depth never becomes large enough to confine ions at W_o (see Eq. 2.5). Physically, this means that the ion charge density always dominates the electron charge density. This difficulty arises because the ions have all been given a single energy ε_{oi} as specified by Eq. 2.3. On the other hand, if the ions are injected with a distribution of energies ε_{oe} or if they are injected sufficiently slowly for a wider distribution to develop due to scattering, this issue may be resolved. Indeed, Elmore and colleagues state that it may be possible to have a system for which W is not bounded from above by the ion charge density. This issue of satisfying boundary conditions is common in such problems; e.g., it is encountered again in Hirsch's analysis of an ion-injected system [5]. The region found by his analysis where the boundary condition is satisfied and is presented graphically in Fig. 2.4.

2.2 Ion Velocity Distribution

Elmore and colleagues also studied the effect of electron angular momentum on ion velocity distribution in the system. Following various approximations, they concluded that the cumulative effect of small-angle scattering of electrons on electrons and ions will give a small displacement from the core size for zero angular momentum. However, they found that it was probably not large enough to be serious. On the other hand, they found ion collisions may cause the ions to relax into a roughly Maxwellian form that can be represented as a radial Maxwell distribution. This is employed to evaluate the fusion reactivity $\langle \sigma \upsilon \rangle$ in the following fusion power calculations. Under these conditions the intrinsic difficulty of obtaining sufficient ion density remains. (For details of this derivation, see reference [1].)

If the ions are distributed according to a Maxwell distribution with temperature θ, then the ion density as a function of r will be

$$n_i \approx n^o \exp\left(-\frac{eV}{\theta}\right) \cong \left[n_o{}' \exp\left(\frac{W_L}{\rho}\right)\right] \exp\left(-\frac{W}{\rho}\right), \tag{2.12}$$

with

$$\rho = \frac{\theta}{\Lambda}, \tag{2.13}$$

and W_L is the value of W at $r = r_o$. Here n_o and $n_o{}'$ are constants, $n_o{}'$ being the density at $r = r_o$. On the other hand, for only radial velocities and for the distribution of ε_{oi} values $P(\varepsilon_{oi})\, d\varepsilon_{oi}$, the distribution function in r and υ_i space is

$$f(r, \upsilon_i) = \frac{C}{r^2} P\left(\frac{1}{2} m_i {\upsilon_i}^2 + eV\right), \tag{2.14}$$

with

$$n_i(r) = \int f(r, \upsilon_i) d\upsilon_i. \tag{2.15}$$

For our subsequent discussions, we shall take

$$n(r) = n_o {r_o}^2 \frac{\exp\left(-\frac{W}{\rho}\right)}{r^2}. \tag{2.16}$$

Equation 2.16 corresponds to a radial Maxwell distribution and is viewed as a "conservative approach" relative to the optimum performance of the electrostatic system.

The distribution function of Eq. 2.16 will be used rather than Eq. 2.12 for the present calculations. The reason for this is mathematical. With Eq. 2.16 we can obtain the parameters of an "optimum system" in closed form. Because the ratio $(r_o/r)^2$ is limited in its variation in a practical device, we do not expect any appreciable difference in the operation of the two systems given by Eqs. 2.12 and 2.16. Finally, Eq. 2.16 is in any case optimistic for the behavior of the device. That is, the intrinsic difficulty is to obtain a sufficient ion density for thermonuclear reactions at the center and, at the same time, a low enough ion density elsewhere that the charge density remains negative. With the new distribution function of Eq. 2.16, we may rederive the appropriate Poisson's equation. In place of Eq. 2.11, we now obtain

$$\frac{d^2W}{dz^2} + \frac{dW}{dz} = \frac{1}{W^{\frac{1}{2}}} - G\ \exp\left(-\frac{W}{\rho}\right), \tag{2.17}$$

where

$$G \equiv \frac{2\pi n_o e r_o^2}{I_e}\left(\frac{2\Lambda}{m_e}\right)^{\frac{1}{2}}. \tag{2.18}$$

Here Λ is defined by Eq. 2.8.

Next we discuss how this system of equations restricts the fusion power density. Then we turn to subsequent studies by Farnsworth and Hirsch and review how they treat this ion density limit to obtain a more promising result.

2.3 Conditions for Maximum Thermonuclear Power

In this section we summarize Elmore and colleagues' evaluation of the maximum fusion power allowed in their model of the electron-injected potential trap.

The power input P_i to the device is the grid current times the grid voltage, divided by γ, the number of times an average electron goes into the control region of the device, or

$$P_i = \frac{1}{\gamma} I_e V_g, \tag{2.19}$$

where I_e and V_g are expressed in esu.

The thermonuclear power output P_o is

$$P_o = \left[\frac{4\pi}{3} r_o^3\right] \times \left[\frac{n_o^2}{4} < \sigma_{DT} v >_{avg} \Delta\varepsilon\right]. \tag{2.20}$$

Here $\frac{4\pi}{3}r_o^3$ is the active volume in which reactions occur; $< \sigma_{DT}\upsilon >_{avg}$ is the product of relative velocity and the D–T reaction cross section averaged over a Maxwellian velocity distribution for the ions (here we assume D–T reactions instead of D–D reactions as they have a larger cross section, giving a higher fusion power); and $\Delta\varepsilon$ is the energy liberated in a D–T reaction and is taken as

$$\Delta\varepsilon = 15 \text{ MeV}, \tag{2.21}$$

and

$$\frac{n_o^2}{4} = n_D n_T. \tag{2.22}$$

Here n_D and n_T are the respective densities of deuterons and tritons.

Equation 2.20 is subject to a geometric correction factor of order unity, because $\frac{4\pi}{3}r_o{}^3$ gives only an approximate value for the reaction volume. Then the ratio of fusion power out to the input power, P_o/P_i, must exceed unity for breakeven. This ratio is given by

$$\frac{P_o}{P_i} = \frac{n_o^2 r_o^3 \left[\frac{\pi}{3}\Delta\varepsilon < \sigma\upsilon >_{avg}\right]}{I_e V_g} v > 1. \tag{2.23}$$

The largest ion density for which ion containment is possible corresponds to the largest value of G in Eq. 2.17 for which W is not bounded from above. This case was illustrated earlier in Fig. 2.4, where the ions are shown as confined to the bottom of the potential well.

To analyze this further, Eq. 2.17 is multiplied by $p = \frac{dW}{dz}$ giving us

$$\frac{dW}{dz}\left(\frac{d^2W}{dz^2} + \frac{dW}{dz}\right) = \frac{d}{dz}\left(\frac{p^2}{2}\right) + p^2 = \frac{dW}{dz}\left(\frac{1}{W^{\frac{1}{2}}} - G\exp\left(-\frac{W}{\rho}\right)\right). \tag{2.24}$$

With $W = W_L$ and $p = 0$ at $z = 0$, we integrate out from $z = 0$ to obtain

$$\begin{aligned}\frac{p^2}{2} + \int_0^z p^2 dz &= \int_{W_L}^{W}\left[\frac{1}{W^{\frac{1}{2}}} - G\ \exp\left(-\frac{W}{\rho}\right)\right]dW \\ &= \left\{2\left[W^{\frac{1}{2}} - (W_L)^{\frac{1}{2}}\right] - \rho G\left[\exp\left(-\frac{W_L}{\rho}\right) - \exp\left(-\frac{W}{\rho}\right)\right]\right\}.\end{aligned} \tag{2.25}$$

Because $\int p^2 dz > 0$, we have

$$\frac{p^2}{2} \geq \left\{ 2\left[W^{\frac{1}{2}} - (W_L)^{\frac{1}{2}} \right] - \rho G \left[\exp\left(-\frac{W_L}{\rho} \right) - \exp\left(-\frac{W}{\rho} \right) \right] \right\} \equiv F(W). \quad (2.26)$$

Clearly, *F(W)* must be positive for all $W_L < W < W_{\max}$. This implies an upper limit on G. Because of the range of parameters involved (for confinement $W_{\max} >> \rho$), it will suffice to take

$$\begin{aligned} W_L &= 0, \\ W_{\max} &= \infty. \end{aligned} \quad (2.27)$$

Hence we now have from Eq. 2.26

$$F(W) = 2\left\{ 2W^{\frac{1}{2}} - \rho G \left[1 - \exp\left(-\frac{W}{\rho} \right) \right] \right\}. \quad (2.28)$$

Now the least value of F is given by

$$\frac{dF}{dW} = 0. \quad (2.29)$$

Defining a root $W = W_R$, the condition Eq. 2.26 implies that

$$F(W_R) \geq 0. \quad (2.30)$$

If we write

$$Q = \rho^{\frac{1}{2}} G, \quad (2.31)$$

then Eq. 2.29 becomes

$$1 = Qx \times \exp\left(-x^2\right). \quad (2.32)$$

Here $x^2 \equiv (1/\rho) W_R$. Then the equation $F(W_R) = 0$ gives

$$Q = \frac{2x}{1 - \exp(-x^2)} \quad (2.33)$$

The solution of Eqs. 2.32 and 2.33 is

$$Q = \rho^{\frac{1}{2}} G_{\max} \approx \pi$$

or

$$G \leq \left(\frac{\Lambda}{\theta} \right)^{\frac{1}{2}} \pi. \quad (2.34)$$

If we now substitute Eq. 2.18 in Eq. 2.34, we find

$$n_o \leq \left(\frac{m_e}{\theta}\right)^{\frac{1}{2}} \frac{I_e}{2^{\frac{3}{2}} e {r_o}^2}. \tag{2.35}$$

This result provides the upper limit on the ion density n_o in the central "core" region of the spherical system.

The power ratio from Eq. 2.23 will be greatest if we use the largest possible ion density, given by making Eq. 2.35 an equality. Substituting into Eq. 2.23 for n_o, we obtain

$$\frac{m_e}{\theta} \frac{{I_e}^2}{e^2 r_0} \frac{\left[\frac{\pi}{24} \Delta\varepsilon \langle\sigma v\rangle_{avg}\right]}{I_e V_g} > \frac{1}{\gamma}. \tag{2.36}$$

Next, we set

$$eV_g \cong 5\theta, \tag{2.37}$$

where θ is the average ion temperature. The value of eV_g cannot be much less than this, or the ions will not be confined. In addition, a larger value cannot be used because of the inequality Eq. 2.36. Now, substituting Eq. 2.37 into Eq. 2.36, we obtain

$$\frac{\pi}{120} \frac{m_e I_e \Delta\varepsilon}{e r_0} \frac{\langle\sigma v\rangle_{avg}}{\theta^2} > \frac{1}{\gamma}. \tag{2.38}$$

The next step is to find the temperature where $\theta = \theta_o$, which maximizes the ratio

$$\frac{\langle\sigma v\rangle_{avg}}{\theta^2}.$$

As shown in reference [4], this occurs for D–T reactions when

$$\begin{aligned} &\theta \cong 40 \text{ keV}, \\ &\langle\sigma v\rangle_{avg} \cong 7.2 \times 10^{-16} \text{cm}^3/\text{s}. \end{aligned} \tag{2.39}$$

Substituting these values into the inequality 2.38, we find

$$I_e > 10^{25} \frac{r_o}{\gamma} \text{esu}, \tag{2.40}$$

or

$$I_{amp} > 10^{16} \frac{r_o}{\gamma} \text{ A}.$$

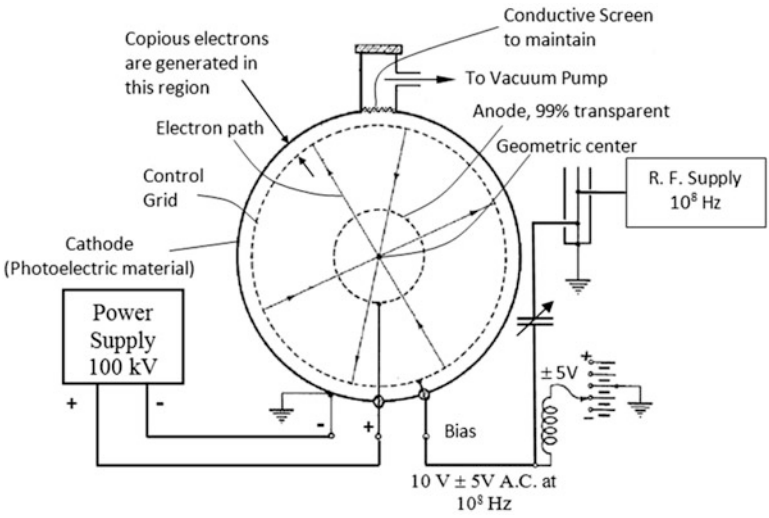

Fig. 2.5 IEC geometry proposed by P. T. Farnsworth [6]

From earlier discussion, it may be found that $\frac{r_o}{\gamma}$ is roughly 10^{-2}. Hence, from this analysis, it may be concluded that currents of the order of 10^{14} A are required for successful operation of the IEC described. This is an enormous current and practically impossible to realize, at least in the geometry considered. Even pulsed operation of the device might not be able to reach this current. Therefore, a system employing electrons injected into a transparent grid to confine ions seems to be impractical for useful fusion power. However, Elmore and colleagues conclude with the statement that other configurations and assumptions are still open for analysis. And that is what Philo Farnsworth attempted to do in his pioneering study of IEC fusion discussed next.

2.3.1 The Farnsworth "Fusor"

Farnsworth proposed a space charge device for producing nuclear reactions (shown in Fig. 2.5). He first proposed that the electric fields within the space charge would oscillate the ions resulting in collisions of particles and thus producing nuclear fusion. His design used concentrically arranged cathode and anode elements, the anode being electron permeable and supported within the cathode element. Farnsworth's design is very similar to the one analyzed by Elmore, Tuck, and Watson but with some subtle differences. One is that Farnsworth proposed a space charge buildup at the center causing a virtual cathode. Furthermore, he stated that ions are formed in the anodic space (inside the anode) through electron collisions

with background neutrals. Such ions fall through the negative virtual well potential resulting in their acceleration to high fusion–relevant energies.

Farnsworth argued that a virtual cathode potential, almost the same potential as that of the cathode, can be established within the anode through space charge buildup. This, he concluded, would be possible with the application of a 100-kV and 1,500-A electron current. In this case, the instantaneous space current, including both inward and outward flow, is related to the cathode current by the following series:

$$I_{space} = I_{cathode} \sum_{0}^{\gamma} \eta^{\gamma}, \tag{2.41}$$

where

$$\eta \equiv \frac{A_O}{A_{anode}}. \tag{2.42}$$

Here A_O is the open anode area, A_{anode} is the total anode area, and γ is the number of trips through the anode in both directions made by an electron that started at the cathode.

The variation in space current with time may be found by determining the electron transit time t for an electron between its inner and outer limits of travel, because this determines how often it passes the anode. Then the current at a specified time T is determined by substituting

$$\gamma = \frac{T}{t}. \tag{2.43}$$

The relation between the anode current and cathode current is then given as

$$I_{anode} = I_{cathode}(1 - \eta) \sum_{0}^{\gamma} \eta^{\gamma}. \tag{2.44}$$

From Eqs. 2.42 and 2.44, we obtain

$$I_{anode} = I_{space} \times (1 - \eta). \tag{2.45}$$

Hence, the actual space current in the device is many times greater than the anode current by a factor corresponding to $1/(1-\eta)$. Therefore, for $\eta = 99$ %, this factor is 100 giving anode current of only 15 A needed to supply the 1,500-A space current requirement. Assuming a spherical symmetry in the creation of the space charge, Farnsworth claimed that it is possible with this space charge flow to produce the desired nonuniform potential distribution in a space enclosed by a permeable equipotential surface (anode).

In order to obtain a copious electron current from the cathode, Farnsworth suggested that the cathode be built with either aluminum or with copper, having its interior coated with aluminum. Such a material would emit copious amounts of

electrons when bombarded with UV radiation. As the gas atoms (in a previously evacuated cathode and then filled with a fusion gas mixture, e.g., D–T) diffuse into the anode and into the paths of the converging electrons, collision of the electrons with the neutral atoms results in positive ion formation. Farnsworth then argued that if it were assumed that an ion is born or created in that part of the anodic space where the potential difference with respect to the geometric center (shown earlier in Fig. 2.5) is 50 kV, the ion will be accelerated toward the center. An inherent assumption here is that there are few electrons in the vicinity where the ion velocity is low as it reverses direction, avoiding recombination. As previously discussed, the ion will then be trapped between the well potential formed by the potential surface it is born on. Thus, it will oscillate along radial paths through the center. The length of such a path is determined by the potential surface location where the ion was born.

The ions born in the regions adjacent to the anode surface (shown in Fig. 2.5) will accelerate toward the zero potential geometric center with a high acceleration and velocity. All of these ions traversing the geometric center contribute to the high ion density that develops in the "core" region. For the case of 50 kV applied to the grid, the largest contribution to this ion density is attributable to those ions possessing energy in excess of 30 keV, which are presumably ~ 95 % of the total ions in consideration. A rough estimate of the space of heavy ion concentration is that it has a radius around 1 mm. Some of the more slowly moving ions will recombine with an electron near the center and thereby reduce to a neutral atom that tends to drift outwardly. They then will either be reionized with the probability of reappearance of ions of higher energy, or they will escape from the anodic space and be lost. Such reionization of neutral atoms will result in loss of average ion energy or loss from radiation. However, Farnsworth proposed that through intelligent selection of the potential distribution, one could achieve the desired energy ion concentration, $\geq$ 95 %, close to the center.

In short, a sequence of alternating (negative and positive) space charge buildup was proposed by Farnsworth. Such space charges represented either a virtual cathode (negative space charge) or a virtual anode (positive space charge). Farnsworth named this structure as "Poissors" and was illustrated earlier in Fig. 1.3 in Chap. 1.

The Poissor structure formed by monoenergetic radially directed ions and electrons consists of an infinite number of nested well potentials. However, Farnsworth acknowledged that their number would actually be quite limited in practice due to the velocity spread in the ion and electron distributions and also their nonzero angular momentum. This occurs because the points where either the ions or electrons reverse their direction of motion do not lie on mathematically thin surfaces causing the virtual anodes and cathodes or sheaths to have a finite radial thickness. As soon as the distance between a virtual anode and the adjacent virtual cathode approaches this thickness, they will merge and the process of developing alternate virtual electrode ceases.

However, Farnsworth expected the formation of more than one virtual electrode in devices that reduce the velocity spread of ions and electrons. Taking this idea further, he suggested that introducing ions from outside (such as with ion guns) so as to render the ion velocities more uniform, combined with improved electron grid optics to limit

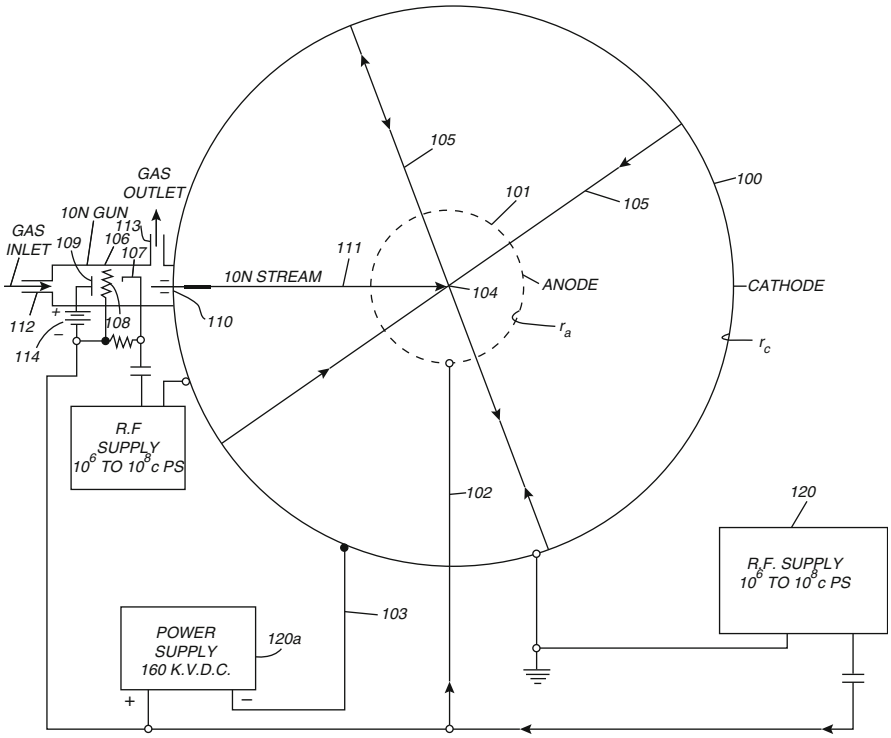

Fig. 2.6 Modification of the IEC design of Fig. 2.5 to add an ion gun, remove the outer grid, and include RF for bunching [6]

their angular momentum, would increase the volume of the ion trap. This idea was picked up on and implemented by Hirsch with his injected ion gun device [6].

2.3.2 *Farnsworth's "Modulation" Concept*

Assuming an ion density of 10^{18} particles/cc in the small volume at the core of the IEC, Farnsworth calculated that if an ion makes 10^6 trips across the core, the probability that the ion will be deflected greater than 8° of arc is only 10 %. He argued that even small deflections greater than the 8° arc would not result in nonradial motion of the ions as they are deflected very near the center, causing the new ion path to be radial as well. Moreover, he suggested the possibility of ion bunching at the core, much like the electrons bunching in a Klystron. To accomplish such bunching, he suggested that the position of the virtual cathode could be shifted radially at a frequency corresponding to the ion oscillatory period. He considered several methods for such a "modulation." One method for shifting the virtual cathode used a radio-frequency voltage between the cathode and anode, as illustrated in Fig. 2.6.

Another method for modulating the cathode is to modulate the ion gun with a radio-frequency voltage from the RF power supply, thus modulating the ion intensity in the ion beam. Assuming that modulation of the anode and cathode is used with a radio-frequency voltage of approximately 150 V in a sine wave profile, the intensity of electron space current converging on the center would also vary periodically, resulting in the oscillatory shifting movement of the virtual cathode as explained previously. As a consequence, the potential gradient accelerating the ions through the center would vary periodically, imparting a corresponding velocity change to the oscillating ions. This will result in some ions traveling faster than others with the consequence that the faster ions will overtake and "bunch" with the slower ions as the center is approached. The ion density in the center is thereby increased. In other words, the ion species that are initially distributed in space are converged a quarter period later at the center (spatially converged) but are then distributed in velocity space at the center.

Such operation provides a very high fusion rate that depends on the square of the density. Depending on the repetition rate, this could lead to a high time average reaction rate. Alternately some applications, e.g., types of neutron activation analysis, favor pulsed neutron production. One of the first studies to incorporate ideas from Farnsworth's bunching concept was done by Edwards [8] at the University of Illinois, and these concepts were extended and incorporated into the Periodically Oscillating Plasma Sphere (POPS) studied by Nebel and Barnes [7]. POPS operation was subsequently experimentally verified. It is truly pioneering on the part of Farnsworth to have intuitively foreseen this kind of behavior of the ions.

Interestingly, Farnsworth made many other pioneering suggestions for optimized operation of the IEC device and some are now being investigated, e.g., the use of vanes instead of wires to build the central cathode [6]. This would help radiate the heat load while reducing the footprint of the cathode wires thus improving the life of the cathode considerably. Another suggestion was the use of boron nitride for constructing the insulating material in the anode stalk; this material has one of the highest standoff voltages and is also easily machineable.

Operation of Farnsworth's IEC concept can be further evaluated by analysis of the ion and electron flow toward the center of the device. The laws by which charged particles move toward the center in a spherically symmetric field have been described by Langmuir and Blodgett as given by Eq. 1.1 in Chap. 1. This equation was originally derived for single species (electrons). However, if ions are present, G_o, defined in Eq. 2.6b, can be introduced. In the following, we change the nomenclature, using λ in the place of G_o, as done in the Farnsworth analysis.

$$\lambda = G_o = \frac{I_i}{I_e}\left(\frac{m_i}{m_e}\right)^{\frac{1}{2}}. \tag{2.46}$$

Farnsworth argued that the space charge formula can be used unchanged, but the denominator of Eq. 1.1 in the new case is now termed as μ^2, which is calculated as a different function of the radius than is α^2. As will become apparent, the term α^2 also

depends upon the factor λ. The quantity λ was introduced by Langmuir [9] wherein it was shown that λ (called α in Langmuir's paper) cannot exceed the value of unity if the ions are injected at the anode. Thus, for the present analysis, Eq. 1.1 is replaced with the following:

$$I_e = \frac{29.34 \times 10^{-6} V^{\frac{3}{2}}}{\mu^2}. \tag{2.47}$$

Here μ is a new function of r/r_c, given in Table 2.1. This table lists the values of ${\mu_a}^2$ and ${\alpha_a}^2$, that is, the values of μ^2 and α^2, respectively, at the anode position as functions of r_a/r_c and with λ as a parameter.

The intermediate values of μ^2 may easily be calculated by dividing Eq. 1.1 by 2.47. This gives (the ratio of electron current in the absence of ions to the electron current in the presence of ions) as follows:

$$\frac{I_{eo}}{I_e} = \frac{\mu^2}{\alpha^2} = \frac{{\mu_a}^2}{{\alpha_a}^2}. \tag{2.48}$$

Here α^2 is obtained mathematically and μ is summarized in Table 2.1.

Consider a small uniform, high-density "core" region at the center of a Poissor-like structure. The ion density in this region is n_o, while its radius is r_o. Taking the maximum cross section of the D–T reaction, the power output of this small region would be given by

$$P_o \approx 10^{-26} {n_o}^2 {r_o}^3 \quad \text{W}. \tag{2.49}$$

Here W corresponds to Eq. 2.4. Further, assuming that the center density is related to an ion current I_o, at r_o by

$$n_o = \frac{I_o}{4\pi {r_o}^2 v_o e}, \tag{2.50}$$

The fusion power output becomes

$$P_o \approx 2 \times 10^{-8} \frac{{I_o}^2}{r_o} \quad \text{W}. \tag{2.51}$$

Here I_o is expressed in amperes. Equation 2.51 emphasizes the fact that the "active" volume in an electrostatic machine would be small, high-density core region rather than a large, moderate-density region, as in most magnetic devices. In a one-meter radius device, a central-region size of $r_o = 0.1$ cm seems reasonable. At that size Eq. 2.51 indicates a total current of 2×10^5 A at $P_o = 10$ kW. This result was encouraging, and Farnsworth decided to undertake corresponding experimental work.

Table 2.1 Various values of α^2 and μ^2 summarized with λ (always < 1) as the parameter

			λ=0.2		λ=0.4		λ=0.6		λ=0.8		λ=1	
$\frac{r_a}{r_c}$ or $\frac{r_c}{r_a}$	α_a^2	$-\alpha_a^2$	μ_a^2	$(-\mu_a)^2$	μ_a^2	$(-\mu_a)^2$	μ_a^2	$(-\mu_a)^2$	μ_a^2	$(-\mu_a)^2$	μ_a^2	$(-\mu_a)^2$
1.6	0.1688	0.2968	0.1330	0.2520	0.0972	0.2071	0.0614	0.1623	0.0255	0.1174	–	0.0730
1.8	0.2480	0.5020	0.2067	0.4431	0.1654	0.3842	0.1240	0.3258	0.0827	0.2664	0.0414	0.2075
2.0	0.3260	0.7500	0.2790	0.6760	0.2321	0.6019	0.1852	0.5278	0.1382	0.5213	0.0913	0.3798
2.2	0.4020	1.0360	0.3497	0.9463	0.2975	0.8566	0.2452	0.7668	0.1930	0.6771	0.1407	0.5874

Note: Here r_a is the anode radius, r_c is the cathode radius, α_a is the value of α when $r = r_a$, μ_a is the equivalent of α_a but in the presence of ions, and μ is the equivalent of α but in the presence of ions

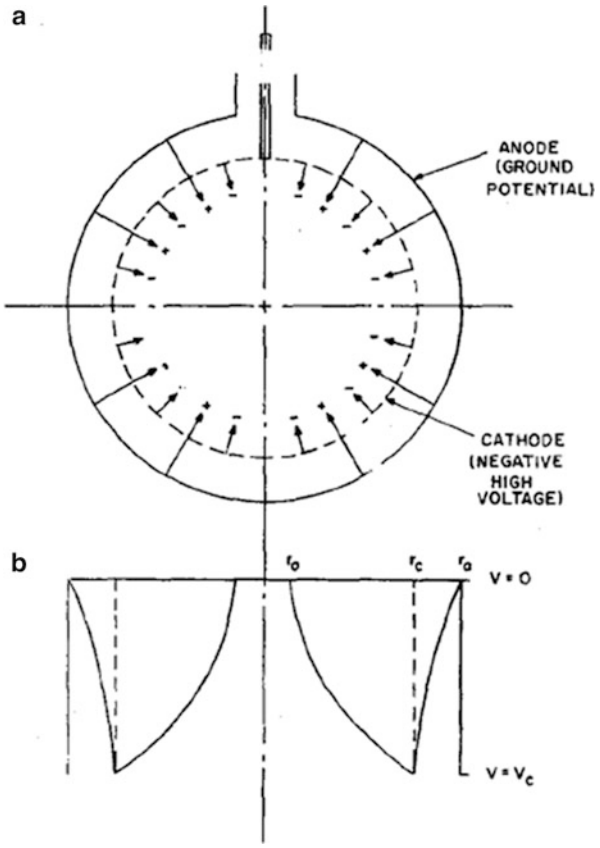

Fig. 2.7 The general arrangement and the potential distributions when ions only are present as assumed by Hirsch [5]

Subsequently, Farnsworth hired Robert Hirsch to work on IEC experiments at the Farnsworth International Telephone and Telegraph laboratory in Fort Wayne, Indiana. Following Farnsworth's work, Hirsch developed a unique six ion gun-based IEC device and published a paper [5, 10] in 1968 reporting the observation of copious number of neutrons. Hirsh considered a spherical cathode and anode (Fig. 2.7a). The cathode is assumed to be ion permeable, electron emissive on its interior surface only, and impermeable to electron flow into the interelectrode space. The anode is assumed to be uniformly ion emissive, and all ions are emitted with zero kinetic energy. Assume that all particle motions are radial, i.e., neglect angular moment and scattering.

For the case of finite ion current and zero electron current, an ion space charge will develop within the cathode. They will form a deep well potential which will be maintained by circulating ions. The associated potential distribution was calculated from a Langmuir–Blodgett-type [11] analysis shown in Fig. 2.7b. The potential at shell, at r_o, represents a virtual anode, i.e., it is a charge-saturated region from which ions are reflected in an outward direction.

For D+ ions at voltages and currents of thermonuclear interest, Hirsch estimates that for a reasonable cathode-to-virtual-anode radius ratio of 10 to 10^2, very high

ion currents of the order of 5 A would be needed. However, he pointed out that with high grid transparency, ion recirculation in the trap between r_c and r_o could exceed 10 round trips, so a more reasonable external current of only 0.5 A would be required. However, if this ion model could be realized experimentally, it would have a negligible fusion rate, since the ion density is low where the ion energy is high near the cathode. The situation changes if electrons are permitted to flow from the cathode. They would be accelerated by the virtual anode toward the center of the device. Once inside the virtual anode, they would be decelerated by their own space charge, and they would form a virtual cathode at $r_{vc} < r_o$. This negative space charge will cause ions from the virtual anode to be accelerated toward the center while also decreasing the radius of the virtual anode. In this manner a series of virtual electrodes would form, creating successively denser regions of high ion kinetic energies.

Hirsch's analysis of this situation [5] starts from Poisson's equation:

$$\left(\frac{1}{r^2}\right)\left(\frac{d}{dr^2}\right)\left[r^2\left(\frac{dV}{dr}\right)\right] = 4\pi(|p_e| - p_i). \tag{2.52}$$

Where the potential at the virtual anode is set to zero, conservation of energy becomes

$$\frac{1}{2}m_i^2 = |eV(r)|, \tag{2.53}$$

$$\frac{1}{2}m_e^2 = e(V - V_0), \tag{2.54}$$

where $V_0 =$ the cathode potential. Conservation of charge becomes

$$I_{e,i} = 4\pi r^2 \rho_{e,i} v_{e,i}. \tag{2.55}$$

Next the radius and the potential are normalized,

$$\phi(r) = \frac{V(r)}{V_0}, \tag{2.56}$$

$$R = \frac{r}{r_a}, \tag{2.57}$$

where $r_a =$ the radius of the virtual anode (note that $\phi(r_a) = 0$). Equation 2.52 then takes the form

$$\frac{d^2\phi}{dR^2} + \frac{2}{R}\frac{d\phi}{dR} = \frac{K_+}{R^2}\left\{\phi^{-\frac{1}{2}} - \lambda_+(1-\phi)^{-\frac{1}{2}}\right\}, \tag{2.58}$$

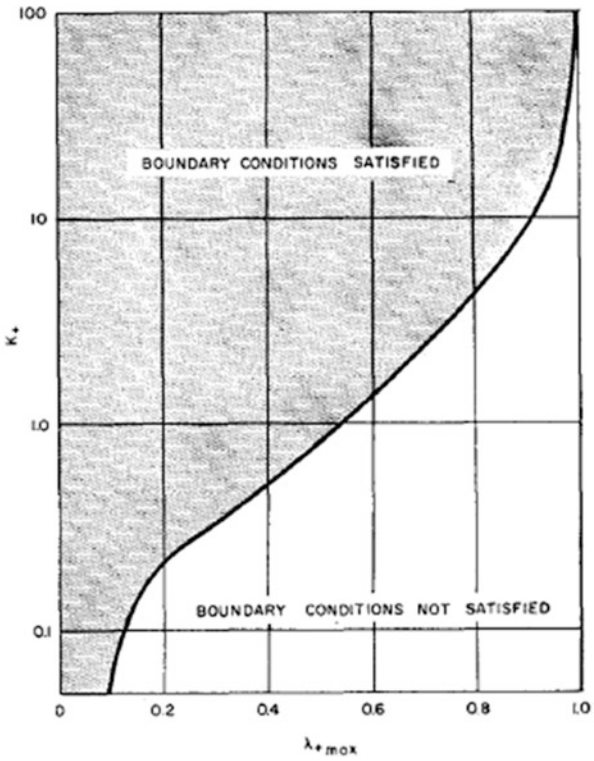

Fig. 2.8 Locus of $\lambda_{+\max}$ as a function of K_+, showing the region in which the boundary conditions are satisfied [5]

where

$$K_+ = \frac{I_i}{|V_0|^{\frac{3}{2}}}\left(\frac{m_i}{2e}\right)^{\frac{1}{2}} = \frac{4\pi r^2 p_i \phi^{\frac{1}{2}}}{|V_0|}, \tag{2.59}$$

$$\lambda_+ = \frac{1}{G_0} = \left(\frac{I_e}{I_i}\right)\left(\frac{m_e}{m_i}\right)^{\frac{1}{2}}. \tag{2.60}$$

Equation 2.60 relates λ_+ used by Hirsch to G_0 defined in Eq. 2.6b. The λ_+ in Poisson's Eq. 2.58 is a key parameter. If $\lambda_+ = 0$, Eq. 2.58 reduces to a form similar to that of Langmuir–Blodgett [10]. To solve Eq. 2.58, Hirsch shows that λ_+ and K_+ must be restricted to meet the boundary conditions. The solution must be carried out in the various regions between the virtual electrodes where the solution is non-determinate due to division by zero (Fig. 2.8).

In the region between the real cathode and the virtual anode, any combination of K_+ and λ_+ to the left of the $\lambda_{+\max}$ curve in Fig. 2.9 will satisfy Eq. 2.58 and the boundary conditions. However, in the region between the first virtual anode and the

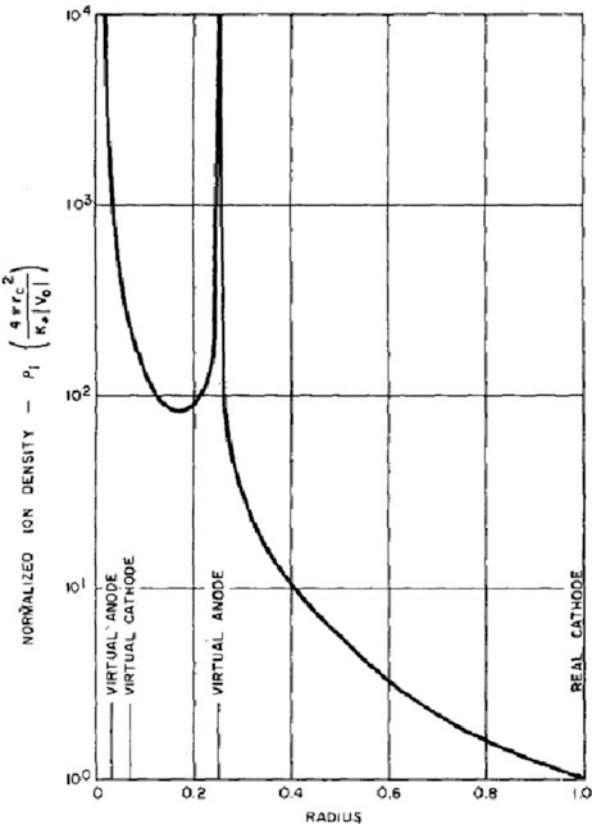

Fig. 2.9 Normalized ion density as a function of radius for $K_+ = 0.7$, $\lambda_+ = \lambda_{+\max} = 0.45$ [10]

inner virtual cathode, both currents are space charge-limited, i.e., they satisfy a K_+, $\lambda_{+\max}$ condition. This condition coupled with the continuity of electron current between the regions is sufficient to determine the ion current in this adjacent region.

A numerical solution using these conditions was shown earlier in Fig. 1.3 in Chap. 1 for $K_+ = 0.7$, $\lambda_+ = \lambda_{+\max} = 0.45$. For convenience this figure is repeated here in Fig. 2.9. Hirsch noted that as expected for this "Poissor" solution, the ion density is more than two orders of magnitude larger at the $R = 0.065$ virtual cathode [10].

Hirsch also addresses the associated issue of pressure balance and the related issue of how the virtual theorem is satisfied. He notes that with purely radial flow, a force balance exists at steady state because the inward and the outward currents of both particles are everywhere equal. In a plane electrostatic system, $E^2/8\pi$ balances the total particle pressure. In spherical geometry such a simple balance does not occur due to the effect of radial focusing [9]. In this simplified analysis the particle pressure is

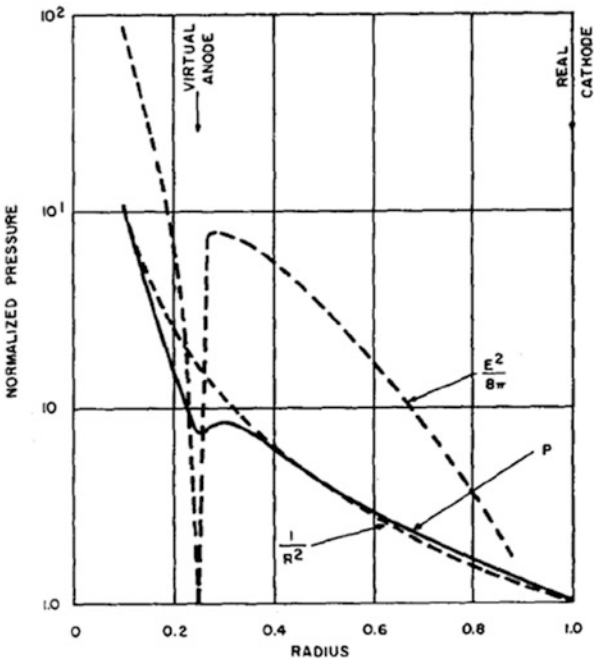

Fig. 2.10 Particle and electric field pressure versus radius for $K_+ = 0.7$, $\lambda_+ = \lambda_{+\max} = 0.45$ [10]

$$P = n_e m_e^2 + n_i m_i^2. \tag{2.61}$$

From Eqs. 2.53, 2.54, 2.55, and 2.59, we obtain

$$P = \left[\frac{(K_+ V_0^2)}{2\pi r_e^2}\right]\left(\frac{1}{R^2}\right)\left\{\lambda_+(1-\phi)^{\frac{1}{2}} + \phi\right\}. \tag{2.62}$$

From again using $K_+ = 0.7$ and $\lambda_{+\max} = 0.45$, Hirsch calculated the particle pressure from Eq. 2.61. It is plotted in Fig. 2.10 along with $E^2/8\pi$. The particle pressure generally follows a $1/R^2$ dependence with the largest deviation occurring at the virtual anode. The electrostatic pressure increases drastically with decreasing radius, but falls to zero at each virtual electrode. In this manner, very high particle and electrostatic pressures are realized near the center of the sphere. It is this dense, high-pressure central region which is of interest to fusion physics. In effect, this analysis shows that this device is not limited by the virial theorem [12]. Two other independent analyses of the generalized electrostatic system have also shown that no such limitation occurs [10]. From a practical point of view, the plasma pressure force in the IEC is ultimately taken up by the grid where the voltage is applied. This is analogous to magnetic confinement fusion where the plasma pressure force must be taken up by the magnetic coil structure.

Hirsch also employs the important features of this model, along with some reasonable assumptions, to determine the general characteristics of an electrostatic fusion reactor. He considers a small uniform, high-density region at the center of a Poissor-like structure. The ion density in this region is n_0, while its radius is r_0. If the reactivity (or power output) is evaluated at a temperature corresponding to the maximum cross section of the D–T reaction, the power output of this small region would be

$$P_0 \cong 10^{-26} n_0^2 r_0^2. \tag{2.63}$$

Assume that the center density is related to an ion current, I_0, at r_0 by

$$n_0 = \frac{I_0}{4\pi r_0^2 v_0 e}. \tag{2.64}$$

Then the fusion power output becomes

$$P_0 \cong 2 \times 10^{-8} \frac{I_0^2}{r_0} \text{W}, \tag{2.65}$$

where I_0 is in amperes. Equation 2.65 emphasizes the fact that the "active" volume in an electrostatic machine would be a small, high-density region rather than a large, moderate-density region, as in most magnetic devices. In a one-meter radius device, a central-region size of $r_0 = 0.1$ cm seems reasonable. At that size, Eq. 2.65 indicates a total ion current of 2×10^5 A at $P_0 = 10$ kW.

2.4 The Polywell: A Spherically Convergent Ion Focus Concept

The electron-injected spherical IEC devices proposed by Elmore, Tuck, and Watson and by Farnsworth in his early patents discussed here have several drawbacks. Grid wires are required to set up the potential trap for electrons, introducing collisional loses and posing materials damage issues in a fusion reactor. Also, as indicated in the analysis by Elmore and colleagues [1], the electron trap may not be adequate to confine the desired ion density needed for an attractive fusion reactor. To circumvent these problems, R. W. Bussard proposed adding a quasi-spherical magnetic field to confine the electrons which in turn electrostatically confines ions [13–15]. His concept was named the Polywell concept (illustrated in Fig. 2.11). Bussard described this as a magnetic version of a spherically convergent ion focus (SCIF) device. In this section we discuss the basic physics involved, largely following the original analysis presented by Krall [16].

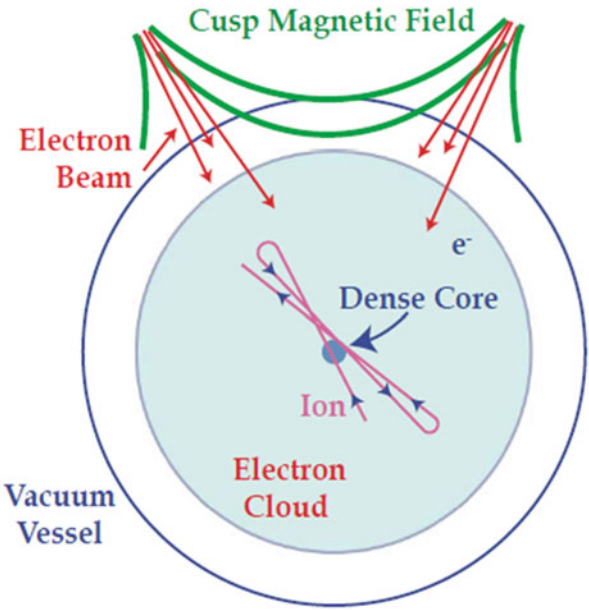

Fig. 2.11 Polywell SCIF schematic [15]

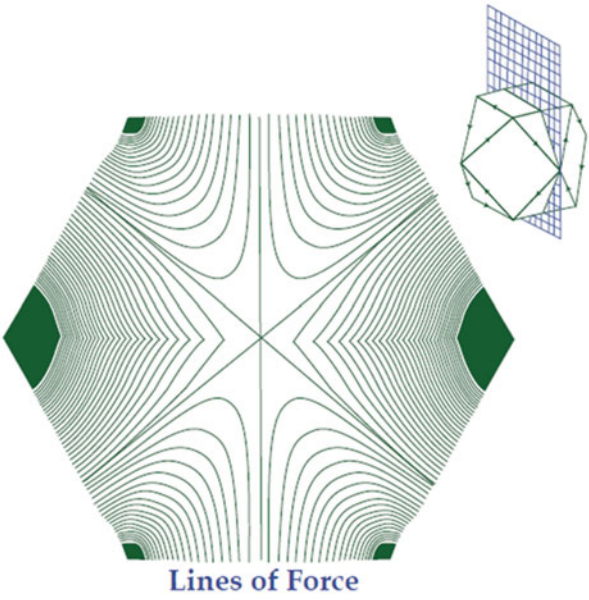

Fig. 2.12 Polywell magnetic geometry showing the magnitude of the *B*-field [15]

The objective is to inject high-energy electrons into a quasi-spherical cusp magnetic field, such as illustrated in Fig. 2.12. Then the electrons, confined by the cusp-like magnetic field, create a well potential of sufficient depth to accelerate ions from low energy at the periphery to fusion energies within a focus at the center of the sphere. Injection of electrons keeps the system electrically non-neutral, so that the well potential, which accelerates the ions, is maintained at a value sufficient to confine the ions within the device, where they circulate at high velocity through the central focus. To succeed, the cusp field needs to confine the electrons long enough so that the power required to maintain the electron "cloud" is less than the fusion power produced by the convergent ion beams. Further, the ions must maintain their radial flow with a nonthermal velocity distribution long enough to produce a high fusion rate in the dense focus at the center of the sphere, as shown in Fig. 2.11.

The power balance in the Polywell device includes the following elements:

1. Energy is largely lost by collisions that scatter the loss cone in the cusp field.
2. Energy is also lost in the magnetic coils that confine the electrons depending on the strength of the magnetic field needed.
3. Energy is produced by fusion in the dense center. The fusion rate there depends on the depth of the well potential (i.e., ion velocity in the center core) plus the degree of spherical focus in the ion flow (i.e., ion density in the center core).

The magnetic geometry is magnetohydrodynamically (MHD) stable by the nature of using cusp fields. Still, as in all IECs, the plasma in this device must be far from thermal equilibrium, and the ion velocity distribution should be far from Maxwellian. For magnetic confinement of electrons, their orbits in the magnetic field must be small compared with the size of the device. By contrast, the ion orbits can be comparable to the size of the device, consistent with the idea that electrostatic effects dominate the ion orbits. However, the orbits of the MeV fusion products (e.g., the 3.5-MeV alpha particle from D–T fusion, the 14.7-MeV proton from D–^{3}He, or the ~ 4-MeV alpha particles from p–B^{11}) will be much larger than the size of the device because they are much more energetic than the fuel ions. Thus, direct conversion of energy to electricity of these fusion products becomes an appealing possibility. Any neutrons created will, however, escape, and their energy must be recovered as heat in a "blanket" region such as envisioned for magnetic confinement fusion.

The basic magnetic geometry that confines electrons in the Polywell device is illustrated in Fig. 2.12. The magnetic field lines are shown on a plane through the center of the device. In the third dimension, the magnetic field continues to be a set of point cusps arranged in an alternating pattern in a generally spherical geometry. This quasi-spherical field arrangement is the basis of the Polywell concept but can correspond to various orders of polyhedra. The lines shown correspond to an $m = 3$ configuration, called a truncated cube, with $B = B_o(r/R)^m$ fairly near the center of the configuration, where R is the radius of the device.

Electrons are injected into this geometry from electron guns at high energy because the maximum depth of the well potential created will be approximately equal to the incoming electron energy. The current from the gun must be chosen to

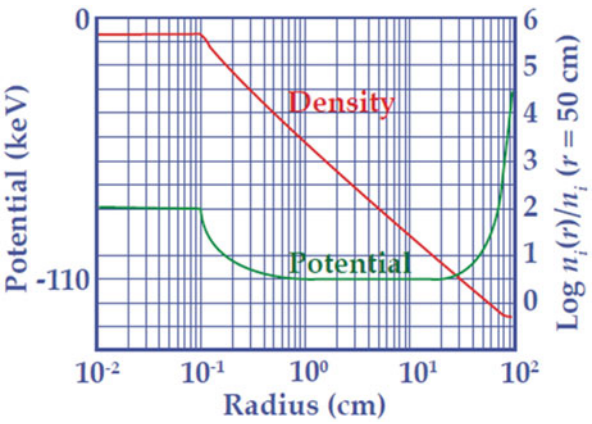

Fig. 2.13 Typical well potential profile [15]

balance the electron losses, which are twofold. First, losses directly through the cusps are inversely proportional to the strength of the magnetic field. The "standard" expression for the single point cusp confinement time t_c is [15]:

$$t_c = t_{transit} \frac{R^2}{a_0^2}, \tag{2.66}$$

where a_0 is the electron gyroradius and the gyration time is $t_{transit}$. The second loss mechanism comes from transport across the magnetic field, either due to collisions or to fluctuating electric and magnetic fields created by plasma instabilities. Estimates are that the cross field losses are relatively low, but more study is required to confirm this.

Another energy loss q_{br} associated with electrons is radiation, including synchrotron and Bremsstrahlung radiation, which is given by [14]:

$$q_{br} = 7 \times 10^{-38} {n_e}^2 T_e r_e \ \mathrm{W/m^3}, \tag{2.67}$$

where r_e is the radius (meters) over which the electrons have density n_e in electrons/m^3 and temperature T_e in eV. This loss is predominantly from the dense core region due to the ${n_e}^2$ dependence.

The effect of radiation losses on the power balance is complicated because the electron temperature must be determined consistently with the other physics of the system. As already stated, for successful operation, $T_e \ll T_i$.

In the Polywell, the ions are electrostatically confined in the device as a whole but are not confined in the dense center of the device. A potential of the sort shown in Fig. 2.13 will be produced because of the excess of electrons in the plasma, enforced by injection of energetic electrons from the guns. As shown, the well potential is formed, in this case with a depth of -110 keV. The ion density is shown

peaking in the center of the device due to the spherical convergence of the accelerated ions. The increased ion density in this "core" region causes the well potential to decrease in depth there to about −80 keV. The ion orbits will consist of large-scale radial excursions from + R to −R passing through the center of the well potential on each pass. Thus, the ions in the center of the device are transitory and highly non-Maxwellian. In summary, according to the calculations shown in Fig. 2.13, the ion orbits are indeed large scale, i.e., they do not gyrate in the cusp magnetic field but instead oscillate from boundary to boundary. Further, this oscillation produces a high-density region in the center of the device.

Next we consider the ion orbits. Assume that an ion is born with a low energy E_0 of a few electron volts at a location r_o and with comparable radial and azimuthal velocities v_r and v_i. Now assume that the ion enters an electrostatic potential $\phi(r)$ and magnetic field $B = B_o(r/R)^m$. To estimate whether the ion will reach $r = 0$ or instead be reflected by the magnetic field, for simplicity we consider a one-dimensional slab-like model [(x, z) coordinates].

$$v_0 = v_{x0}\hat{x}\,, \phi = \phi(x), B = B_0(x/R)^m\hat{z}\,. \tag{2.68}$$

Then the ion orbits can be written in terms of their $\hat{x}$ velocity. Krall [16] shows that integration from the ion birth point x_o to an interior point x gives (setting $v_{yo} = 0$)

$$v_x^2 = v_{x0}^2 - 2e\left[\frac{\phi(x) - \phi(x_0)}{m_i}\right] - \frac{\omega_{ci}^2}{(m+1)^2 R^{2m}}\left(x^{m+1} - x_0^{m+1}\right)^2. \tag{2.69}$$

Here ϕ_0 is presumed to decrease as x decreases, and $\omega_{ci} \equiv eB_o/m_i$. Also, $m = 0$, 1, 2, ... defines the curvature [16]. By examination of Eq. 2.69, the ions will reach $x = 0$ without reflection if

$$\frac{eB_0}{m_i}\left(\frac{x_0}{R}\right)^m \frac{x_0}{m+1} < \sqrt{\frac{2e\phi_0}{m_i}}, \tag{2.70a}$$

where ϕ_0 is the maximum depth of the well potential produced by the electron cloud. This means that the maximum birth velocity and local cyclotron frequency must satisfy

$$\frac{v_{\max}}{\omega_{c,\max}} > \left(\frac{x_0}{R}\right)^{m+1} \frac{R}{m+1}, \tag{2.70b}$$

if the ions are to have orbits as large as x_0.

This result (Fig. 2.14) shows that an ion born in a strong electrostatic potential will transit the entire geometry of size R, even when the gyroradius calculated from the velocity and magnetic field at the ion birth point is much smaller than R. We can

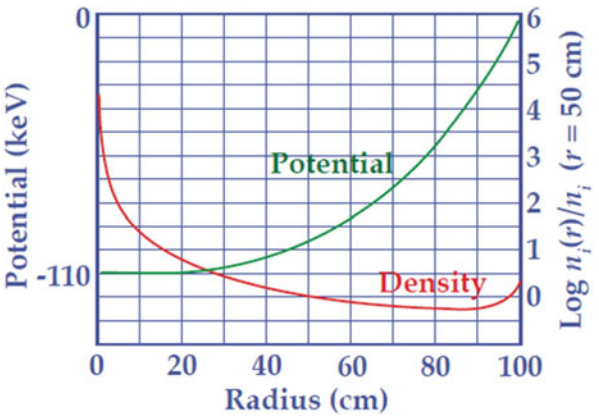

Fig. 2.14 Typical ion density profile [15]

also estimate the perpendicular deflection of the ion by the magnetic field during its transit through the core region of the well potential as

$$\frac{\Delta V}{V} = \frac{\omega_{ci}^2}{(m+1)^2}\left(\frac{x_0}{R}\right)^{2m}\frac{x_0^2}{\left(\frac{2e\phi_0}{m_i}\right)}, \tag{2.71a}$$

where

$$\Delta v_y \simeq \sqrt{v_x^2 - v_{x0}^2 + \frac{2e[\phi(x) - \phi(x_0)]}{m_i}}. \tag{2.71b}$$

This result shows that the maximum magnetic field allowed at the ion birth point in order for the ion to converge to a spot δr is

$$\delta r = R\left(\frac{\Delta V}{V}\right). \tag{2.72}$$

We next estimate the ion density in the Polywell due to spherical convergence. Assume that at birth the ion distribution function is uniform in energy up to some small energy E_0, and uniform in angular momentum up to some small azimuthal velocity $v_\perp$, and take the potential at the birth point to be $\phi = 0$. This distribution can be described in terms of the constants of the motion $\left[E = \left(\frac{1}{2}\right)m_i\left(v_r^2 + v_\perp^2\right) - e\phi, rv_\perp\right]$ by the function:

$$F = \begin{cases} 3\left(\frac{m_i}{E}\right)^{\frac{3}{2}} n_{edge}, 0 < E < E_0, 0 < rv_\perp < r_0 v_{\perp 0} \\ 0, \ otherwise \end{cases}. \tag{2.73}$$

The Vlasov equation for steady state is $F(E, rv_\perp) = \text{constant}$, so the density everywhere is determined by the potential and the value of F at the ion birth point. Integrating F over velocity determines the density. There are three distinct density regions. For a very small distance from the birth point, the potential is negligible, and the density is given by $n = n_{edge}$. Because the maximum well depth is in the keV range, compared with ion birth energies in the few eV range, a little way toward the center $E_0 \ll 2e\phi$ and $m_i {v_{\perp 0}}^2 (R/r)^2 < 2e\phi$. In that range, the electron density n_e is given by integrating Eq. 2.73 over $v_\perp dv_\perp dv_r$ with the result:

$$n_e = \frac{3}{4}\sqrt{\frac{E_0}{e\phi}}\left(\frac{R^2}{r^2}\right) n_{edge}. \tag{2.74}$$

Assuming that the potential reaches its full value at a moderately large distance from $r = 0$, we see that the electron density throughout the bulk of the device will be of the order (set $r = R/2$ in Eq. 2.74):

$$n_e = n_0 = 3n_{edge}\sqrt{\frac{E_0}{e\phi_{\max}}}. \tag{2.75}$$

Moving inward, the $(R/r)^2$ factor eventually becomes substantial, so that the density becomes much larger than n_0. Eventually, the radius is so small that $M {v_{\perp 0}}^2 (R/r)^2 > 2e\phi_{\max}$. Inside that radius, the density changes fairly slowly, on the scale of the changing potential. This defines the radius of the dense core r_c as the radius at which $2e\phi = m_i {v_{\perp 0}}^2 (R/r)^2$ because $n \sim 1/r^2$ outside that radius, while inside that radius n is nearly constant, with the value

$$n_e = \sqrt{\frac{m_e v_{\perp 0}^2}{2e\phi_{\max}}} R. \tag{2.76}$$

Thus, the ion orbits are seen to be of the size of the device, and the ion density at the center is large, $n_i \sim (R^2/{r_c}^2) n_0$. The size of the core and the central density are seen to depend on the angular momentum at the outer turning points of the ion motion. A typical ion density profile based on these assumptions was shown in Fig. 2.13.

If the performance follows these estimates, the Polywell configuration offers a number of advantages as a fusion reactor. It offers a high-beta geometry with no complex auxiliary heating or confinement systems; in practice, this means that the scheme can be tested with a fairly modest budget and with a fairly short development path. The trade-off, of course, is that the physics of the device is not simple at all, encompassing a highly nonequilibrium system with widely varying parameters at different radial points in the device.

It is clear from the assumption made in this analysis that there are a number of critical physics issues. One of the most important pertains to electron physics.

Electron losses will be a major energy drain on the system. Favorable energy balance will depend on the electron confinement time not being too much shorter than classical. Yet cusp losses are not a particularly well-established concept. If the single particle lifetime in a cusp field is calculated, the confinement time will resemble mirror confinement, with the effective collision time being comparable with a particle transit time. This is because in a single pass the particles lose track of their magnetic moment when they pass through the low-field region. Numerical calculations of single particle orbits in a cusp confirm this picture. Mirror losses with transit time collisions are not acceptable. However, when a plasma fills the cusp, magnetic field is excluded, and the $\beta = 1$ surface becomes a mod-β = constant surface. The transport picture is then expected to revert to the cusp picture, with a much longer confinement time. The ability to establish this high-beta plasma, which Krall [16] termed the "wiffle ball" mode, in order to reduce electron loss is a central issue for the Polywell scheme. The "wiffle ball" mode greatly reduces electron losses through the cusp loss cones if it can be achieved. One potential problem for experiments is that very high electron injection rates may be required to reach the high β "wiffle ball" mode. This is due to the fast loss rates through the cusps that occur before the favorable "wiffle ball" confinement mode is achieved. Once that occurs, the injection rate can be reduced, but this injection rate "barrier" must be met and sets the rating needed for electron gun injection.

2.5 Summary

This chapter has focused on well potential formation and fully ionized spherical IECs. Other geometries have also been studied to see whether such wells could be formed. One example is a gridded cylindrical device that can be viewed as a two-dimensional version of the spherical IEC. However, a spherical geometry has generally been favored due to the three-dimensional convergence of the ion beam in the central core. Such convergence has been viewed as important due to the reaction rate dependence on the density square. In order to eliminate the background neutral pressure, the ions must be generated externally and "injected" into the device. As stressed, this presents a problem because the desire is to have the ions born at an energy slightly below that of the outside anode or chamber wall.

The picture is similar but the voltages are reversed in an electron-injected type IEC. An analytical solution to space charge effects and well potential formation is difficult and requires a number of simplifying assumptions. Typically these include no background neutrals; monoenergetic/no angular momentum; nearly 100 % transparent grid; and symmetry of potential surfaces, including the high-voltage stalk area.

We have reviewed the early study by Elmore, Tuck, and Watson which assumed electron injection. For illustration we obtained a first order solution ($G_0 = 0$) given by Eq. 2.10. This result, however, restricts the fusion core volume such that high fusion powers do not appear feasible. It might be noted, however, that such a device

would be small and relatively inexpensive but still demonstrate fusion breakeven. When the restriction $G_0 = 0$ is relaxed, larger core volumes are possible but thermalization effects are found to require extremely large ion currents of the order of 10^{14} A. Even though this is a simplified solution, it errs on the optimistic side. In view of these disappointing results, various modifications to the basic IEC device have been proposed by other researchers. For example, the Polywell concept proposed by R. W. Bussard (described in Chap. 1) employs a magnetic field to confine the electrons, thus simplifying the problem of obtaining a larger trap region and, hence, fusion volume. While Philo Farnsworth initially studied several modified electron-injected devices, he and Robert Hirsch ended up studying an ion-injected IEC both theoretically and experimentally. The theory for this led to the multiple potential trap profile shown in Fig. 1.4, where the ion density and, hence, fusion rate increase in each potential trap going toward the center line of the device. It is difficult to take advantage of this effect, however, because as already stated only a single potential trap seems possible in practice. In that case, the reaction volume is again small, presenting a problem. The volume can be increased by adding angular momentum to the injected ions, but in doing that the required ion currents become progressively larger. These issues related to the practicality of fusion power devices are discussed further in a later chapter.

References

1. Elmore WC, Tuck JL, Watson KM (1959) On the inertial electrostatic confinement of a plasma. Phys Fluids 2(5):239
2. Yibin G, Miley GH (2000) Experimental study of potential structure in a spherical IEC fusion device. IEEE Trans Plasma Sci 28(1):331–346
3. Tzonev IV, Miley GH, Nebel RA (1995) A computational study of the convergence of large angular momentum, high current ion beams in an inertial electrostatic confinement (IEC) device. In: International conference phenomena in ionized gases XXII, vol 4, pp 197–198
4. Farnsworth PT (1966) Electric discharge device for producing interaction between nuclei. US Patent 3,258,402
5. Hirsch RL (1967) Inertial electrostatic confinement of ionized fusion gases. J Appl Phys 38(11):4522–4534
6. Farnsworth PT (1966) US Patent 3,258,402
7. Edwards BE (1979) Ion dynamics in a spherical reflex diode. Ph.D. thesis, University of Illinois at Urbana–Champaign
8. Nebel RA, Barnes DC (1998) The periodically oscillating plasma sphere. Fusion Technol 34(1):28–45
9. Langmuir I (1929) The interaction of electron and positive ion space charges in cathode sheaths. Phys Rev 33(6):954
10. Hirsch RL (1968) Experimental studies of a deep, negative, electrostatic well potential in spherical geometry. Phys Fluids 11(11):2486
11. Langmuir I (1913) Phys Rev 2:450; Physik Z (1914) 15:348; Langmuir I, Blodgett KB (1923) Phys Rev 22:347; 23, 49 (1924)
12. Clausius RJE (1870) On a mechanical theorem applicable to heat. Philos Mag Ser 4(40):122–127

13. Bussard RW Method and apparatus for controlling charged particles. US Patent 4,826,626, 2 May 1989
14. Bussard RW et al. (1988) Preliminary research studies of a new method for control of charged particle interactions. Report 1899, Pacific Sierra Research, 30 Nov 1988
15. Bussard RW (1991) Some physics considerations of magnetic inertia electrostatic confinement: a new concept for spherical converging flow fusion. Fusion Technol 19:273
16. Krall N (1992) The Polywell: a spherically convergent ion focus concept. Fusion Technol 22:42–49

Chapter 3
Gas Discharges in Gridded IECs

3.1 Introduction

Many experimental IEC devices employ a gas discharge between the grid and vacuum vessel wall (or outer grounded grid) as an ion source. To operate in this mode, the background neutral pressure must be large enough to sustain the gas discharge that serves as the ion source. As a consequence, the fusion reactions produced are predominantly due to collisions between the accelerated ions and background neutrals. This is not suitable for a power producing reactor that requires ion beam–beam fusion reactions, and in turn needs an extremely low neutral pressure, requiring an external ion source. However, the internal gas discharge approach provides a relatively simple method for many near-term IEC fusion device applications, such as neutron sources for neutron activation analysis (NAA). Thus, in this chapter we examine some of the basic physics of such discharges and the resulting voltage–current characteristics in the IEC.

3.2 Types of Gas Discharges

A gas discharge can be viewed as conduction of electricity through gas, due to movement of ions and electrons produced by collisions between the charges and the neutrals. Gaseous discharges have a number of important applications ranging from materials processing to lasers. Thus, they have been studied for many years as discussed in references [1–4]. Such a gaseous plasma discharge may be classified into self-sustaining and non-self-sustaining types. A discharge becomes self-sustaining if the discharge continues on its own even when the initiating source is removed. However, a power source is still required to keep the discharge going. On the other hand, the non-self-sustaining discharges will extinguish as soon as the initiating source is removed. To further understand this classification, consider the linear two-electrode device shown in Fig. 3.1. The extension to the three-dimensional IEC device is discussed later in this chapter.

G.H. Miley and S.K. Murali, *Inertial Electrostatic Confinement (IEC) Fusion: Fundamentals and Applications*, DOI 10.1007/978-1-4614-9338-9_3,

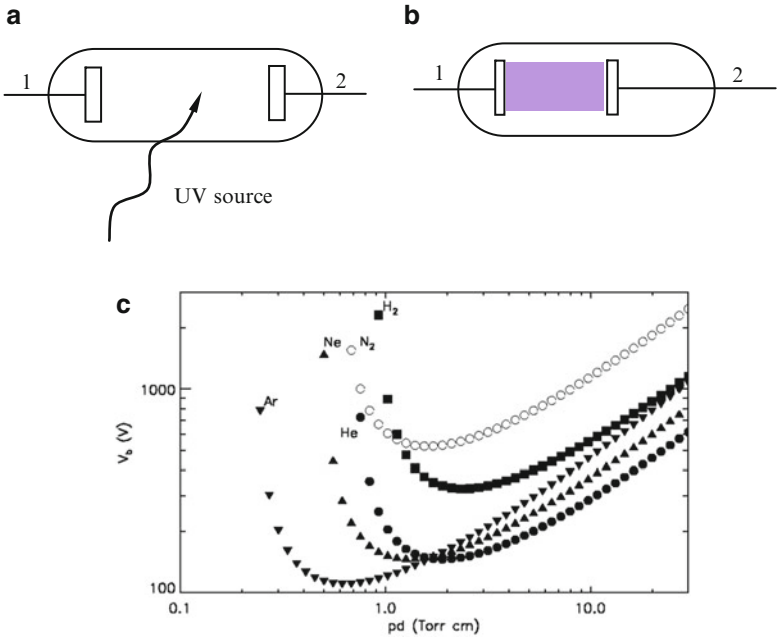

Fig. 3.1 (**a**) Non-self-sustaining DC discharge with UV-initiating source. (**b**) Self-sustaining DC discharge with smaller electrode gap. (**c**) Paschen curve for various gas species [1]

In Fig. 3.1a, a UV source is used to disassociate some of the neutrals forming ion–electron pairs to initiate the discharge. A voltage difference is maintained using a power supply connected to electrodes. The electrons and ions move in opposite directions toward the appropriate electrode depending on the sign (positive or negative) of the applied voltage. However, when the initiating UV source is turned off, the current will cease to flow between the electrodes unless the applied voltage and gas pressure are above a breakdown voltage defined by the Paschen breakdown criteria (see Fig. 3.1c) [2]. This criterion defines the breakdown voltage as a function of the gas pressure p multiplied by the distance d between electrodes. If the current flow does stop, this is a non-self-sustaining discharge. To achieve a self-sustaining discharge, either the voltage must be increased or the pressure and distance decreased. The latter is done in Fig. 3.1b, where the electrode spacing is decreased. In that case, the discharge feeds on the energy supplied by the power source and self-sustains even after the initiating UV source is turned off.

In any discharge the electrons, rather than ions, are the main current carriers. Their mass is smaller and their mobility is correspondingly much higher than that of ions. Electrons are either produced by ionization of the gas itself or originate from ion bombardment and field emission at the electrodes. Gas ionization can be accomplished in several ways, including electron impact ionization, photoionization, and associative ionization. Bombardment by photons, energetic ions or electrons, and excited neutral particles can also cause secondary emission from the electrodes.

A high-energy-per-unit electrode surface area can induce either thermionic or field emission of electrons, and sometimes one phenomenon is enhanced by the other. For instance, field emission could prematurely begin if the temperature of the electrode is raised. Alternately, the work function could be affected when the field is applied in a way that causes premature thermionic emission. Each of these means of producing electrons leads to a different response of the gas discharge.

IEC devices have been operated in both self-sustaining and non-self-sustaining modes. To obtain self-sustaining operation, a relatively higher chamber pressure is required. For non-self-sustaining operation, several different kinds of initiating sources have been employed – for example, filament electron sources, RF discharges, magnetron discharges, ion guns, and electron guns.

3.3 Direct Current Glow Discharge Mechanism

When a sufficiently high potential difference is applied between the two electrodes in the linear geometry of Fig. 3.1b, initiation can occur due to field emission at the negative electrode. These electrodes are accelerated by the electric field between the electrodes and rapidly cause a cascade of electron–ion pairs due to ionization of neutrals. This gives rise to a gas discharge. The resulting inelastic collisions lead to excitation and ionization. The excitation collisions, followed by de-excitations with the emission of radiation, are responsible for the characteristic name of the "glow" discharge. The ionization collisions create new electrons and ions ("pairs"). The ions are accelerated by the electric field toward the cathode, where they release new electrons by ion-induced secondary electron emission. The electrons give rise to new ionization collisions, creating new ions and electrons. These processes of electron emission at the cathode and ionization in the plasma create a self-sustaining glow discharge where the source plasma rate for creating electrons balances losses. Another important process in the glow discharge is the phenomenon of sputtering, which occurs at sufficiently high voltages. When the ions and fast atoms from the plasma bombard the cathode, they not only release secondary electrons, but given sufficient energy they also release atoms of the cathode material, which is called sputtering. This phenomenon causes the cathode grid material from the IEC device to be deposited on the high-voltage (HV) stalk. That can in time cause premature breakdown at the stalk, thus lowering the effective standoff voltage of the HV stalk.

A schematic picture of the elementary glow discharge processes that have been described is presented in Fig. 3.2. When a constant potential difference is applied between the cathode and anode, a continuous current will flow through the discharge, giving rise to a direct current (DC) glow discharge. It should be mentioned here that in a DC glow discharge the electrodes play an essential role for sustaining the plasma by secondary electron emission as already described.

All discharge regions shown in Fig. 3.2 occur in an IEC, but because it is three-dimensional (spherical), we cannot easily see the different regions. Because it

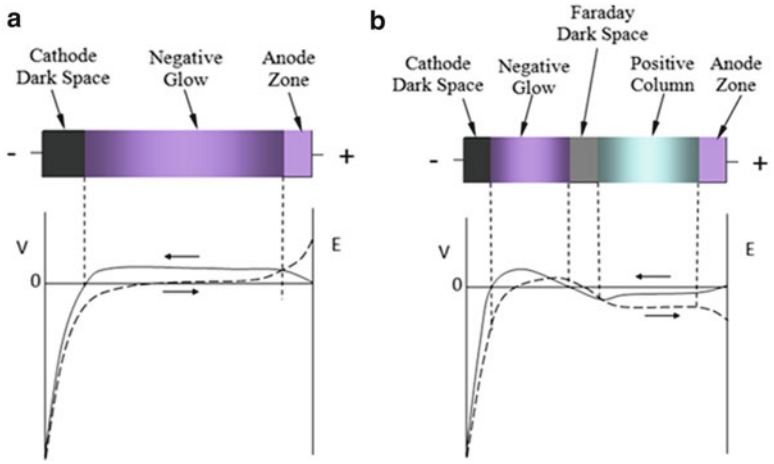

Fig. 3.2 Schematic diagram of the spatial regions present in DC glow discharges: (**a**) at short cathode–anode distance and/or low pressure; (**b**) at larger inter-electrode distance and/or higher pressure. The cathode (**a**) has a negative potential, whereas the anode (**b**) is grounded. The solid line (*left axis*) represents the potential distribution, whereas the dashed line (*right axis*) denotes the electric field distribution [3]

depends on the pressure, and because an IEC operates in multiple pressure regimes, the lack of clear visibility combined with the three-dimensional geometry obscures the discharge regimes.

When a time-varying potential difference is applied, as in a capacitively coupled radio-frequency (RF) discharge, the role of the electrodes becomes less important. In this case, electrons can oscillate in the time-varying electric field in between the two electrodes. Eventually, the role of the electrodes becomes negligible, giving rise to electrodeless discharges, as in the case of the inductively coupled plasma (ICP).

A DC glow discharge can operate over a wide range of discharge conditions. The pressure can vary from below 1 Pa to atmospheric pressure. It should, however, be realized that the product of pressure and distance between the electrodes (pd) is a better parameter to characterize the discharge. For instance, at lower pressure, the distance between cathode and anode should be longer to create a discharge with properties comparable to those of high pressure with small distance. The voltage is mostly in the range between 300 and 1500 V, but for certain applications it can increase to several kV. The current is generally in the mA range. The discharge can operate in a rare gas or in a reactive gas, as well as in a mixture of these gases [3].

The potential difference applied between the two electrodes is generally not equally distributed between cathode and anode, but it drops almost completely in the first few millimeters in front of the cathode (see Fig. 3.2). This region is adjacent to the cathode and is characterized by a strong electric field called the cathode dark space (CDS), or sheath. In the largest part of the discharge, the so-called negative glow (NG), the potential is nearly constant and slightly positive (which is called the

plasma potential). There the electric field is very small. When the distance between cathode and anode is relatively large (e.g., a few cm, at 100 Pa Argon, 400 V, and 0.87 mA), two more regions can be present, such as the Faraday dark space and the positive column (see Fig. 3.2b). They are characterized by a slightly negative electric field that conducts the electrons toward the anode. These two regions are often present in glow discharges used as lasers (positive column lasers) and as fluorescence lamps. However, for most of the other applications of DC glow discharges (sputtering, deposition, chemical etching, analytical chemistry, etc.), the distance between cathode and anode is relatively short. Then typically only a short anode zone (AZ) is present beside CDS and NG, where the slightly positive plasma potential returns back to zero at the anode (see Fig. 3.2a).

3.4 DC Discharges in Linear Two Electrode Geometries at Low Pressure

The geometry in Fig. 3.1b has been used by various investigators with a low pressure in the chamber for studying the voltage–current (V–I) characteristics. When the voltage applied to the electrodes is varied while the current flowing through the discharge is measured, the trace generated is typically highly nonlinear (as shown in Fig. 3.3). The mean free path in this glow discharge regime is relatively low, but comparable to the chamber dimensions. Further explanation of each of the regimes shown in Fig. 3.3 is given next.

We begin with very low voltages where only the background ionization persists, mostly because of the background radiation (cosmic rays and ionizing background radiation). Increasing the voltage in this regime increases the fraction of ions and electrons captured from the background ionization.

In the saturation regime, all the background radiation-ionized species (ions and electrons) are collected and no further ionization by either the electrons or ions occurs. This is because the energy of ions and electrons is relatively low in this regime.

The next regime is the Townsend regime (shown between points 3 and 5 in Fig. 3.3). The electrons in the discharge volume acquire sufficient energy from the electric field that they ionize some of the neutral background gas, leading to a very rapid, almost exponentially increasing current as a function of voltage.

In the Townsend discharge zone, the circuit resistance is so high that only a very small amount of current flows. The densities of electrons and ions are negligible, and the space charge is so small that the external field is not distorted. Thus if the distance L between the planar electrodes is small in comparison with the transverse size of the electrodes, then the field is the same as if there were no ionization, i.e., $E(x) \cong$ constant. This discharge is self-sustained by the striking or ignition voltage applied to the electrodes. This voltage ensures the sustained production of electrons ejected from the cathode and accelerated toward the anode. In this regime the V–I is almost constant. This self-sustaining discharge mode is called the Townsend (dark) discharge, wherein the ionization is so small that the gas emits little visible light and the current itself must be measured using high-sensitivity instruments.

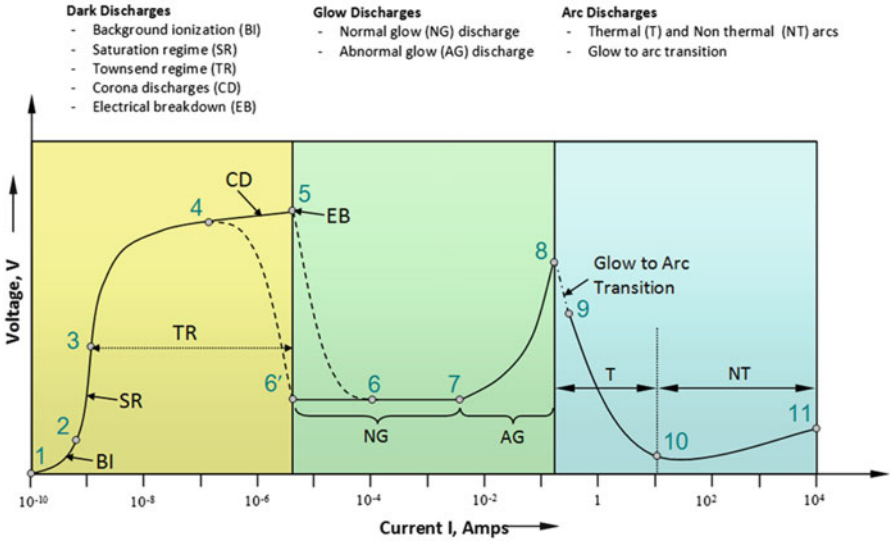

Fig. 3.3 Voltage–current characteristics of the DC discharge at low pressure [4]

In Fig. 3.3, the unipolar corona discharges occur in the region extending from points 4 to 5. Sharp edges or asperities occur as a result of local field enhancements due to sharp points. These strong local electric fields exceed the breakdown strength of the surrounding neutral gas.

The electric breakdown (EB) sets in as the voltage is further increased to the breakdown value. The region shown between points 1 and 5 in Fig. 3.3 is termed dark discharges, as these discharges are invisible to the eye and only a few sparks from corona discharge are sometimes visible.

Once the electric breakdown occurs, the discharge transitions into the glow discharge regime and is now visible. The current in this regime is high enough that the background neutral gas is highly excited.

After another nonlinear transition from points 5 to 6 in Fig. 3.3, the current enters the normal glow regime of the V–I characteristic, in which the voltage across the discharge is almost independent of the current over several orders of magnitude in current. Beginning at point 6 up to 7, the fraction of the cathode occupied by the plasma increases until the plasma covers the entire cathode surface at the point 7. Beyond this point, the current enters the abnormal glow regime until point 8 is reached. At this point the current is sufficiently high that the cathode begins to glow under the heat load. This then triggers the glow-to-arc transition. After this transition, the discharge settles down at some random point between 8 and 11, depending on the internal resistance of the DC power supply. In the regime between points 9 and 11, the discharge voltage decreases as the current increases, until large currents are achieved at point 10. Beyond this point the voltage once again increases slowly with increasing current. In this regime the plasma is close to local thermodynamic equilibrium where the temperature of all the species is approximately equal.

If we were to start at point 8 and retrace the path, a hysteresis effect occurs; wherein instead of retracing the path from 8 to 5, the discharge maintains itself in the normal glow regime up to point 6 (which is at considerably lower currents and current densities than 5). Only then does it make the transition back to the Townsend regime.

An IEC device typically operates in glow discharge mode, and in this mode the chamber pressure is such that the discharge is sustained.

In summary, our brief review of plasma discharges provides insight into the basics of such discharges. These various discharge regimes occur in the IEC but are almost impossible to identify visually. In addition, in the internal source-type IEC, some new phenomena show up and are discussed next.

3.4.1 Discharge Characteristics in the IEC

As stressed in Chaps. 1 and 2, a number of IEC devices built to date have used such discharges to provide an ion source in the region between the grid and wall. That provides a simple device design that has been exploited for applications such as a low-level neutron source for neutron activation analysis (NAA). However, to move toward an IEC power unit, as discussed in Chap. 2, it appears to be necessary to generate ions externally in an "ion gun" or equivalent. Then the main reacting chamber can be pumped to extremely low pressures to avoid neutral charge exchange and scattering effects. An alternate way to achieve high fusion rate would be to accelerate the charged particles generated within the IEC device to high energies within a single mean free path. Such operation would allow high reaction rates even at relatively high pressures. This requires extremely high applied voltage, however, necessitating a novel split-stalk design such as the Murali design briefly discussed in Chap. 4.

3.5 Discharges in the Spherical Geometry Used in an IEC Device

The plasma discharge in the IEC is unique, using a spherical grid in a spherical vacuum vessel with the discharge formed between the grid and the vessel wall, while the cathode grid also serves to extract high-energy ions. Two key features of the IEC discharge are [5]:

1. Breakdown voltage characteristics as a function of pressure–grid/wall distance (pd)
2. Formation of ion "microchannels" that carry the main ion flow through grid openings

However, compared to the linear DC discharge just discussed, the concentric spherical electrode in an IEC is more complicated, while the plasma discharge mode is difficult to observe. This is because we cannot view the electrodes in

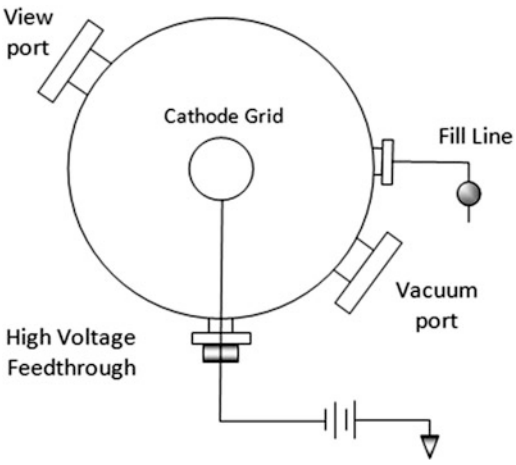

Fig. 3.4 Configuration for the single-grid IEC device used for studies summarized in Table 3.1 [5]

isolation, and the cathode is always surrounded by plasma. Any dark regions are invisible to observation. Abel inversion can be applied to visible light measurements to obtain a radial profile of light emission, but the discharge process is still difficult to decipher. In an attempt to understand the V–I characteristics in the operating regime, Miley and colleagues have conducted experiments using various grid dimensions and geometries [5].

3.5.1 Spherical Geometry Studies

Unlike the two-electrode linear cylindrical system, plasma discharges in spherical geometry of the IEC have not been studied in great detail to date. Discharge voltages that have been studied are in the operating regime and begin at several kV and end at several tens of kV with current in the range of few milliamps. One study [5] that reported V–I characteristics in the operating regime used two spherical vacuum chambers of different diameters – IEC-A (30 cm) and IEC-B (61 cm).

These two devices had the common geometry shown in Fig. 3.4. They consisted of a spherical cathode grid mounted concentrically within a grounded spherical vacuum vessel, which serves as the anode. The main difference in the two was the diameter of the cathode grid. The system is maintained at a constant pressure of 5–15 mTorr by bleeding gas into the chamber through a leak valve, with the vacuum pump running. The plasma discharge is then initiated by increasing the cathode voltage until breakdown occurs, typically at 5–50 kV. This is different from the DC discharge in a cylindrical geometry of Fig. 3.1b, where a small current flows even when the voltages are low as shown in Fig. 3.3. Careful measurements of currents shown in the IEC illustrated in Fig. 3.4 down to microamps were performed, but any current flow was too small to record accurately. The grid-type cathodes employed in the two IEC devices were constructed of 0.8 mm-diameter

Table 3.1 Spherical cathodes used in the IEC experiment for study of V–I characteristics

Device/grid	Diameter (cm)	Construction type/geometric transparency
IEC-A1	3.7	Wire grid/85 %
IEC-A2	7.5	Wire grid/90 %
IEC-B1	15.0	Wire grid/89 %
IEC-B2	15.0	Hollow sphere/0 %

stainless steel wire that was spot-welded into open spherical grids having 85–90 % geometric transparencies. Various sizes and types of cathode grids were used in these experiments, as indicated in Table 3.1. Among the grids used, B2 is a solid stainless steel sphere and was included in the experiments for comparison with data from other "conventional" solid-cathode discharge devices reported in the literature. A 0–100-kV, 0–25-mA DC power supply was used to power the IEC. However, due to voltage limitations on the cathode feedthroughs, the maximum voltage was limited to approximately 40 kV in these experiments.

3.5.2 *Breakdown Voltage Characteristics*

Unlike a cylindrical geometry where the electrodes can be easily moved to change the distance between the two electrodes, the spherical geometry is rather difficult to work with. The inter-electrode spacing is fixed, and the only way one could change this spacing is to replace the cathode grid, or by changing out the vacuum vessel.

We are now ready to discuss experiments carried out to understand the V–I characteristics of the IEC device using the various grids listed in Table 3.1. The mode of experimentation and the corresponding results are included to make it easier to understand the behavior of the system.

The current–voltage and pressure–voltage characteristics of the single-grid-type IEC were studied experimentally. These characteristics are shown to differ from those of equivalent "conventional" solid-cathode discharges that operate in this (pressure)–(electrode separation distance) product (pd), range [6, 7]. This difference is attributed to the fact that the transparent IEC grid cathode allows ion flow on a cord that connects the opposite sides of the spherical grid by passing through the center of the device.

3.5.3 *Voltage Versus (*pd*) Measurements in an IEC*

In order to determine how the applied voltage V depends on (pd) and current I, two types of measurements were performed: I versus V at various values of (pd) and the striking (or "breakdown") voltage V_s versus pd. The latter plot corresponds to the traditional "Paschen curve" V–I breakdown plot. However, note that in the IEC

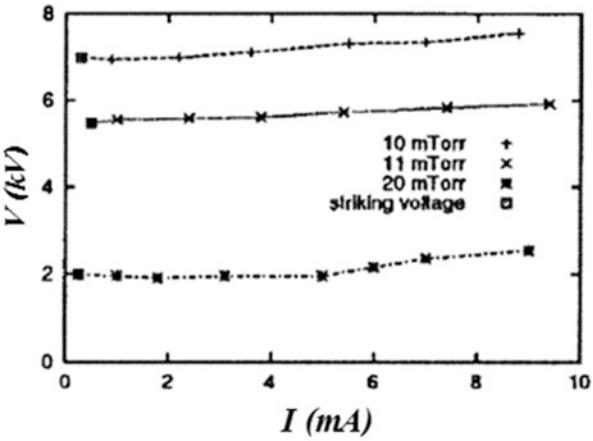

Fig. 3.5 V–I in IEC-A using grid A1 and hydrogen fill gas. As noted, the striking and operating voltages nearly coincide [5]

geometry, d refers to the radial distance from the grid to the vacuum chamber wall. Some groups have chosen to define this distance as equivalent to the diameter of the chamber itself in single-grid devices [8]. The V–I characteristics of these devices are shown in Fig. 3.5. The current essentially remains zero as it is increased until the discharge is initiated at V_s, after which, to a first order approximation, the voltage remains constant as the current is further increased. Similar behavior is observed for the solid-cathode discharge in this pressure range, but the actual voltage values are quite different.

The typical operating pressure inside an internal source IEC device is around 2 mTorr. The striking voltage is relatively low at the relatively high pressure of 20 mTorr, because the mean free path is lower at this pressure. The ion mean free path at 2 mTorr is ~7 cm, while at 20 mTorr it is around 0.7 cm. With such a low mean free path the initial energy of the ion is quickly distributed to the surrounding neutrals, and an avalanche of electrons and ions is created. This results in an early breakdown of the neutral gas at relatively low voltages for relatively high pressures inside the chamber. As the pressure decreases, the mean free path of the ions increases. As a result, these ions find it increasingly difficult to ionize the surrounding ions to create an avalanche effect. Hence the striking voltage increases with decreasing pressure.

A plot of V_s versus (pd) is shown in Fig. 3.6 for a hydrogen discharge in IEC-A with various grids, including results for a solid spherical cathode plus a curve for a "conventional" hydrogen discharge with a plate-type solid cathode [7]. Although the latter is for a plane-parallel discharge, it matches the data from solid-cathode B2 relatively well. For fixed V_s, the value of (pd) is seen to be about three times higher for both the spherical and the planar solid-cathode discharges than for the transparent grid-type cathode discharges. As discussed later in connection to cases where holes are drilled in the solid cathode, this difference is attributed to the flow of ion current through the transparent grid cathode versus the solid sphere which prevents directed flow on a chord passing through the center of the device.

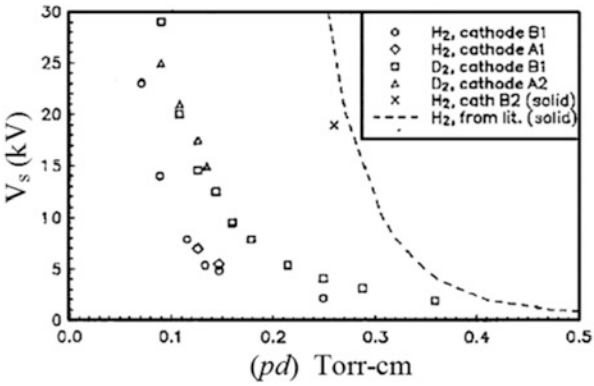

Fig. 3.6 Striking voltage V_s versus (pd) for various grid-type cathodes versus solid cathodes [5]

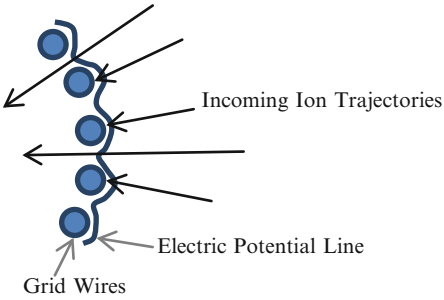

Fig. 3.7 Grid geometric transparency

Below ~ 0.5 Torr-cm, the discharge consists of current-carrying microchannels, which appear as spokes emanating from the holes in the cathode grid as shown in Fig. 3.7 [9]. This discharge phenomenon was first studied in detail at the University of Illinois and is termed the "Star" discharge mode. These microchannels radiate both outward from the cathode to the anode and inward to the center of the sphere where they form a bright central plasma "core." This implies that the intense microchannel discharge occurs between the anode and the local plasma volume encompassed by *holes* in the cathode (i.e., microchannels seek the regions of highest grid transparency). Thus, the discharge characteristics should depend on an "effective" grid transparency, t, as opposed to the geometric transparency. That is, t accounts for the higher transmission probability of ions in the microchannels versus a uniform "sheet"-like flow. Microchannel losses are determined by the frequency with which ions scatter out of the microchannel and onto a path that leads them into a grid wire. At high voltage, the scattering of energetic ions is relatively infrequent. Thus, t is significantly larger than the geometric transparency. Essentially, ions in the microchannels are "guided" through the grid, minimizing interception of the grid wires. The reason for this effect is illustrated by Figs. 3.7 and 3.8. As shown, the microchannels are created through a geometric "self-selection" process. In a grid with tight spacing such as shown in Fig. 3.7, the ions that pass

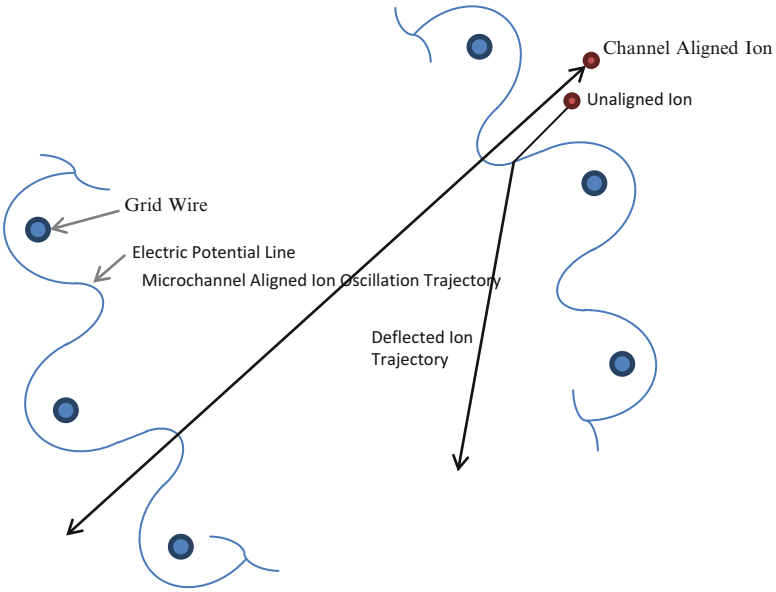

Fig. 3.8 A highly effective transparency occurs with microchannels

through the grid openings suffer little deflection. But many ions hit the grid wires, and the fraction passing through is given by the geometric transparency – namely, the fraction area of the grid openings mapped onto a spherical surface passing through the grid wires. It is hard to make grids that are sufficiency rigid with a transparency greater than 95 %. Also, the grid will create deflect trajectories if it is not extremely spherical. In contrast a grid with larger openings such as shown in Fig. 3.8 is less sensitive to overall sphericity and can achieve very high effective transparencies approaching 100 %. This may seem counterintuitive in the view that as seen from Fig. 3.7, the potential surfaces in the grid openings are defocusing for an ion entering from outside of the grid. However, ions born with trajectories hitting grids or passing through on a trajectory near the grid wires are quickly eliminated (i.e., lost by hitting the grid by deflection). Those passing repeatedly through or very near to the near center of the grid wire openings survive, leading to increased ionization ("births") along these favored trajectories. This then forms the "microchannels" that are visually observed in the "Star" mode shown in Fig. 3.9.

In order to test the effective transparency hypothesis for microchannels (as shown in Fig. 3.10), cathode A1 (see Table 3.1) was covered with aluminum foil, except for two 2-cm-diameter holes located 180 ° apart. Spokes now emanated from both holes, and, as shown in Fig. 3.10, the discharge characteristics for this configuration were similar to those of an uncovered cathode, despite the very low geometric transparency of the two-hole cathode. The foil was then replaced, and two new holes were cut 90 ° apart. While the *geometric* transparencies of these two cathodes are equal, due to the formation of microchannels, the *effective*

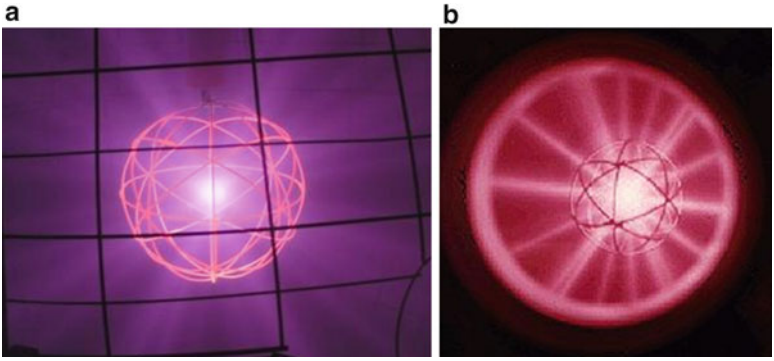

Fig. 3.9 "Star" mode operation of the IEC device. Microchannels emanating from the core of the cathode can be seen in the form of white spokes. Photo (**a**) displays the aluminum foil covered grid with holes; (**b**) is the traditional "Star" mode grid featuring large openings between the grid wires, resulting in strong microchannels [5]

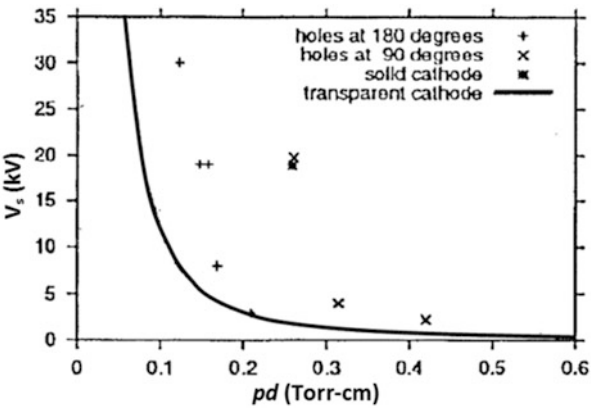

Fig. 3.10 Striking voltage V_s versus *pd* for solid cathodes, including cases with holes at various orientations. A curve for transparent wire grids is included [5]

transparency of the first grid is high, while that of the second is essentially zero. Although the striking voltages (V_s) for this second configuration were well defined, once initiated, the discharges were unstable and appeared qualitatively different from discharges using transparent cathodes. As shown in Fig. 3.10, the values of V_s for the 180 ° hole cathode fall close to that for a solid electrode, considerably higher than for the 90 ° hole case.

In summary, the discharges using a cathode with high effective transparency, such as the 180 ° hole-type cathode, behave much like transparent-type wire-cathode discharges, even if the geometric transparencies differ greatly. In sharp contrast, the discharges using the cathode with low effective transparency behave as solid-cathode discharges. Thus, the discharge characteristics are primarily a function of the effective, rather than the geometric transparency of the cathode.

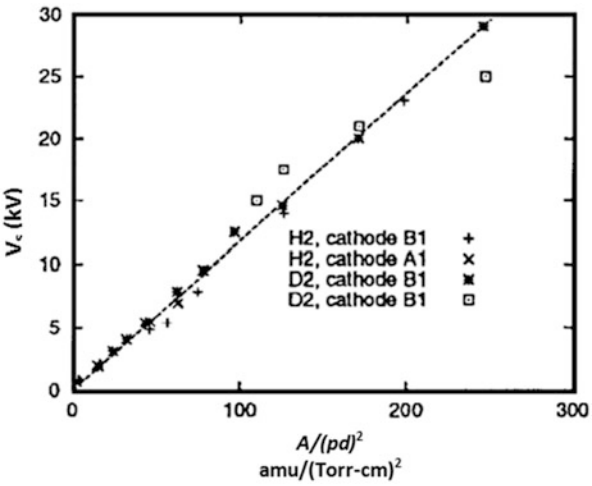

Fig. 3.11 Plot of the striking voltage V_s versus $A/(pd)^2$ for two different gases and various grids [5]

3.5.4 Scaling Laws

An empirical scaling law has been derived [10] by Hockberg, noting that a straight line is obtained if the striking voltage data from Fig. 3.8 are plotted versus the parameter $A/(pd)^2$, as shown in Fig. 3.11. Here, A, the atomic mass of the gas species, accounts for the use of various gases. This results in a simple scaling law for these IEC discharges, given by

$$V_s \approx \frac{0.118A}{(pd)^2} \quad \text{kV} \times (\text{Torr} \times \text{cm})^2/\mu\text{m}. \tag{3.1}$$

Equation 3.1 also provides a good estimate of the operating voltage as well as the breakdown value because of the operating voltage, $V \sim V$s, shown earlier in Fig. 3.5. Note that Eq. 3.1 also predicts the behavior of the discharge using cathode A1 reasonably well, even though the radius of this cathode is half that of the other grids. Thus, the discharge characteristics are at most a weak function of R, so the radius was not included as a parameter in the above Eq. 3.1 [10].

3.6 Cylindrical IECs

As discussed in a later chapter, most cylindrical IEC configurations can be viewed as a two-dimensional form of the spherical IEC. Consequently, the gas discharges in these devices generally follow the same description as described here for spherical devices. One exception is the "C-Device," which is cylindrical but uses a hollow electrode-type discharge [11]. The IEC C-Device is an electrostatic

confinement system which ionizes the background neutral gas through electron and ion impact ionization and then accelerates ions axially to a central core inside a hollow cylindrical cathode that exists between two hollow cylindrical anodes. Ions recirculate back and forth through the cathode between the anodes, while electrons recirculate back and forth through the anodes and between the end plates (reflectors) and the central cathode. Both ions and electrons continue to recirculate until they are lost to the electrodes or the vacuum chamber wall due to CX and scattering collisions. The anodes create an electrostatic radial focusing of ions, while the central cathode creates an electrostatic radial focusing of electrons. The combined axial acceleration and radial focusing causes the formation of a plasma beam in the C-Device. Fusion reactions are maximized in the hollow cathode region where fusion fuel ions are at their peak energy and density.

3.7 Summary

From a practical point of view, the experimenter operating an internal source gridded IEC often begins by selecting an operation of pressure for the IEC based on past experience. Once that is done, the cathode voltage must be increased to a point where plasma breakdown occurs and a plasma discharge is created between the cathode and the anode (the wall in the spherical chamber-type device or the grid in spherical grid devices located in a cylindrical vacuum chamber). This breakdown voltage will follow the Paschen rules discussed in this chapter. Once the breakdown occurs, the operation relaxes into a slightly lower voltage due to the high conductivity of the plasma discharge. Depending on what pressure was chosen to begin with, the operation may be in any of the various plasma discharge modes discussed here. The experimenter at this point may wish to optimize the operating pressure to achieve the purpose of the experiment, for example, to optimize neutron or proton production. The optimum pressure is a complex trade-off between the increased ion source created at higher pressures and changes in collision mechanisms (e.g., changes in charge exchange rates). Such optimization is best done experimentally because these factors are strongly dependent on the particular geometry employed, selection of grid materials, grid construction, stalk design, etc., However, the material in this chapter can help identify a starting range for pressures, so that the search can be rapidly narrowed down.

In addition to “conventional” discharge operation discussed here, Chap. 1 also introduced a high-pressure regime proposed by Murali [12]. In that case, fusion reactions can occur over a range of pressures with appropriate voltage. This is done by accelerating the ions to high energy within one mean free path so that every collision can potentially lead to fusion. Because it is relatively easier to raise the voltage using a small power supply rather than raising the ion currents, it is possible to achieve high fusion rates at high pressures using fast pulsed, ultrahigh voltage.

References

1. Lieberman MA, Lichtenberg AJ Principles of plasma discharges and materials processing, 2nd edn. Wiley-Blackwell, 13 May 2005, ISBN 0-471-72001-1, Table 14.1, p 545
2. Paschen F (1889) Ueber die zum Funkenübergang in Luft, Wasserstoff und Kohlensäure bei verschiedenen Drucken erforderliche Potentialdifferenz. Annalen der Physik 273(5):69–75
3. Bogaerts A, Neyts E, Gijbels R, Van der Mullen J (2002) Gas discharge plasmas and their applications. Spectrochimica Acta Part B 57:609–658
4. Glow Discharge dot Com. Discharge regimes. http://www.glow-discharge.com/?Physical_background:Glow_Discharges:Discharge_Regimes. Accessed 5 June 2013
5. Miley GH et al (1997) Discharge characteristics of the spherical inertial electrostatic confinement (IEC) device. Trans Plasma Sci 25(4):733–739
6. Von Engel A (1983) Electric plasmas: their nature and uses. Taylor and Francis, London, p 125
7. Brown S (1966) Introduction to electrical discharges in gases. Wiley, New York
8. Nadler J (1992) Ph.D. thesis, University of Illinois, Urbana-Champaign
9. Miley GH, Javedani J, Nebel R, Nadler J, Gu Y, Satsangi A, Heck P (1994) Inertial-electrostatic confinement neutron/proton source. In: Proceedings of the 3rd international conference dense Z-Pinches, AIP Press, New York, pp 675–689
10. Hochberg TA (1992) Characterization and modeling of the gas discharge in a SFID neutron generator. M.S. thesis, Department of Nuclear Engineering, University of Illinois at Urbana-Champaign
11. Bromley B, Chacón L, Miley G (1998) Approximate modeling of cylindrical inertial electrostatic confinement (IEC) fusion neutron generator. In: Proceedings of the 16th international conference on numerical simulation of plasmas, Santa Barbara, pp 191–192
12. Krupakar Murali S (2013) Systems and methods for accelerating particles. Patent application number: PCT/IB2012/054717

Chapter 4
High-Voltage Stalk Design for IECs

4.1 Introduction

Stalk design is crucial for successful internal source IEC device operation. This is particularly true for applications where very high voltages are desired. The basic issue is that the high-voltage "stalk" introduces an asymmetry that limits the spherical IEC operation. Extraneous fields that emanate from the stalk perturb the equipotential electric fields within the vacuum chamber. This can result in ion bombardment of the stalk, causing premature breakdown. Ohnishi and colleagues [1] pioneered studies of the energetic ion bombardment on the insulator surface voltages. In order to achieve maximum applied voltages in an IEC device, the breakdown between the conductor rod and the insulator surface must be suppressed through careful design of the insulator surface shape. That generally involves a scheme to lengthen possible leakage pathways, thus preventing leakage currents at lower voltage. Simultaneously, the outer shape of the insulator must also be modified to reduce the ion bombardment. To understand the magnitude of the problem, Figs. 4.1 [1] and 4.2 [2] show plots of calculated electric field distributions and corresponding ion trajectories. Possible stalk designs employed to accomplish these two goals (minimize surface leakage and reduce ion bombardment) are discussed next.

4.2 Various Stalk Designs and Design Considerations

In this section we will briefly review some stalk designs used in various laboratories, including Kyoto University, Idaho National Environmental Laboratory, University of Illinois, and University of Wisconsin. This chapter is focused on the lessons learned from these designs. Based on that, the various design considerations are illustrated in recent stalk designs at the University of Wisconsin used to achieve voltages over 150 kV.

G.H. Miley and S.K. Murali, *Inertial Electrostatic Confinement (IEC) Fusion: Fundamentals and Applications*, DOI 10.1007/978-1-4614-9338-9_4,

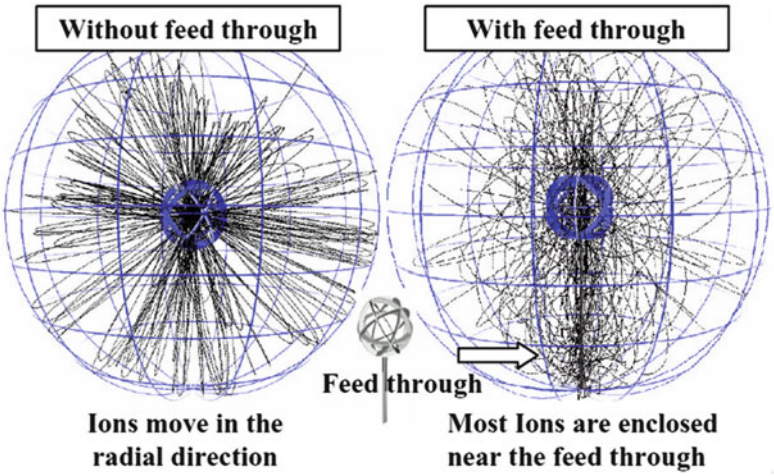

Fig. 4.1 Ion trajectories with and without the feedthrough show that many ions hit the feedthrough [2]

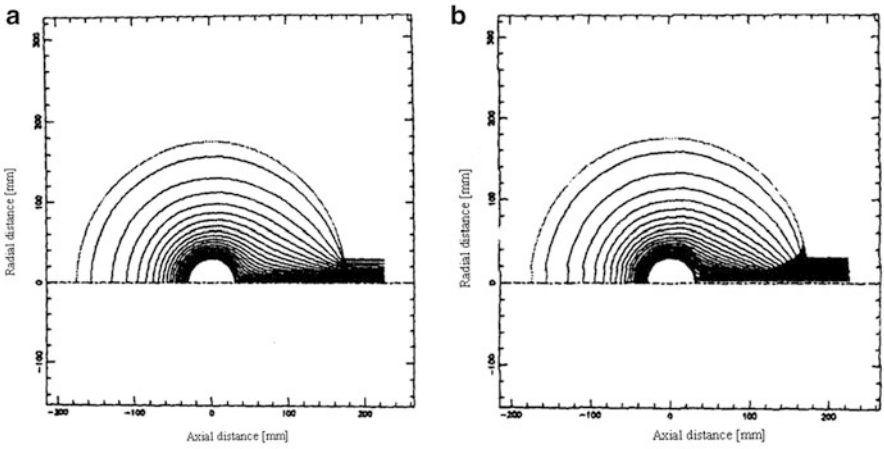

Fig. 4.2 Equipotential profiles within the vacuum chamber (**a**) without an insulator and (**b**) with an insulator shown by a shadow [1]

Many of the "lessons learned" are also taken from studies at the University of Wisconsin, because their experiments had the goal of these extremely high-voltage stalks for experiments requiring such voltages for D–^{3}He and ^{3}He–^{3}He reactions. Most studies at other laboratories have not required operation above 100 kV, often settling for ~ 80 kV for D–D neutron production and other physics experiments.

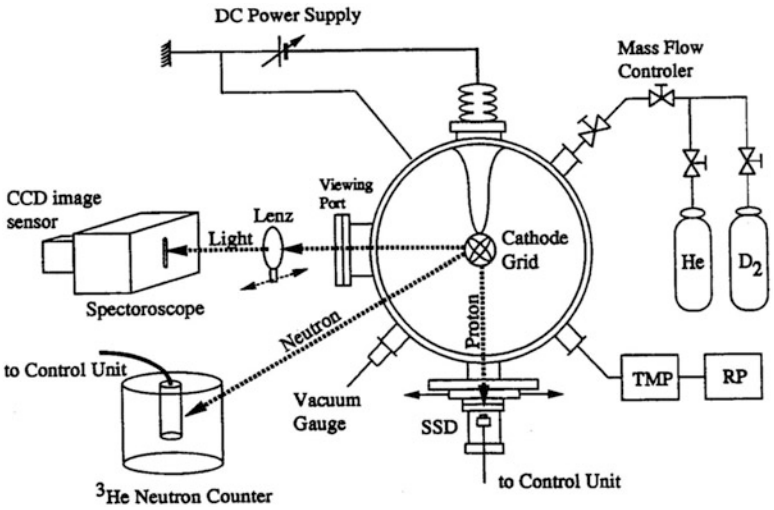

Fig. 4.3 Schematic view of an IEC device and measurement system [1]. The detector systems are generally nonintrusive, but the high-voltage stalk causes a major perturbation to the potential surfaces

4.2.1 Institute of Advanced Energy, Kyoto University, Japan Design

Figure 4.3 shows the stalk installed in the spherical IEC chamber used in Kyoto University along with various diagnostics used. The stalk occupies a non-negligible volume inside the chamber, and judging by the fields needed, the spherical equipotential structure desired within the chamber is obviously significantly perturbed.

It was observed that the potential profiles were concentric spheres except for the region near the feedthrough port, where profiles are very distorted near the conductor. If the equipotential surface lies parallel to the surface of the insulator, the ion density hitting normal to the insulator will be increased, eventually leading to breakdown as bombardment creates pinhole defect formation. On the other hand, if the surface shape of an insulator is designed to avoid ion bombardment normal to the surface, the ion density may be expected to decrease and subsequently reduce pinhole formation, delaying voltage breakdown. The outer surface profile of the stalk shown in Fig. 4.3 was designed accordingly with this intent. Subsequent experiments with this design confirmed the concept [1].

From Figs. 4.1 and 4.2, it is apparent that the spherical symmetry is lost due to the presence of a high-voltage stalk. Armed with this understanding, the research team at Kansai University [3] took up a theoretical study to understand the effect of electrode shapes on the ion recirculation in the presence of a perturbing high-voltage stalk. The theoretical calculations showed that over 50 % of the ions were

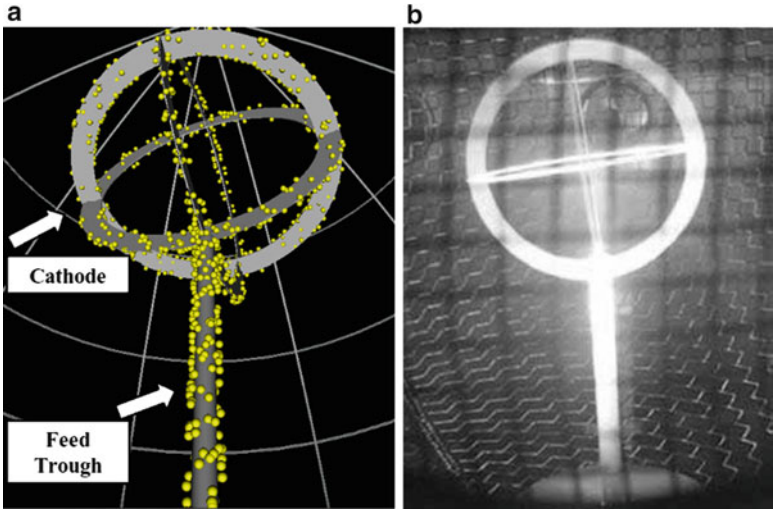

Fig. 4.4 (**a**) The highlighted spots on the cathode and feedthrough show the areas of ion bombardment. Over 50 % of the particles were lost to the feedthrough, while the remaining were lost by hitting the cathode. (**b**) The grid and feedthrough are shown in operation [2, 6]

bombarding the high-voltage stalk and thus degraded the performance of the device (see Fig. 4.4). Hence optimal shapes for both cathode and anode were investigated by numerically tracking the ion trajectories in this configuration. Results revealed that the lifetime of the fast ions was doubled by deforming a hemisphere of the anode pierced by the feedthrough into an ellipsoid. The shape of the cathode was found to exert less influence on the ion lifetime. The deformed anode was found to theoretically raise the neutron production rate by as much as 20 % compared with a spherical anode. A similar study carried out by Murali and colleagues at University of Wisconsin, Madison, using displaced grids revealed that offsetting the grids along the vertical axis caused new microchannels to appear in the region below the cathode, when it was displaced toward the anode at the bottom [4, 5]. Larger displacements caused premature breakdown and hence grid deformations would have to be done carefully, taking the breakdown issue into consideration.

As shown in Fig. 4.4, if ~ 50 % of the ions hit the feedthrough, then the chances of breakdown of the feedthrough significantly increase. Hence researchers in Japan have used bare feedthrough without any insulating material. They claim that this helps reduce the footprint of the feedthrough while simultaneously extending the life of the high-voltage stalk/feedthrough (as there is no insulating material that could breakdown). However, some insulation is used around the region where the feedthrough enters the vacuum chamber. This insulation isolates the feedthrough from the chamber. Possible surface leakage currents there can limit the voltage, but overall this arrangement appears to be quite advantageous.

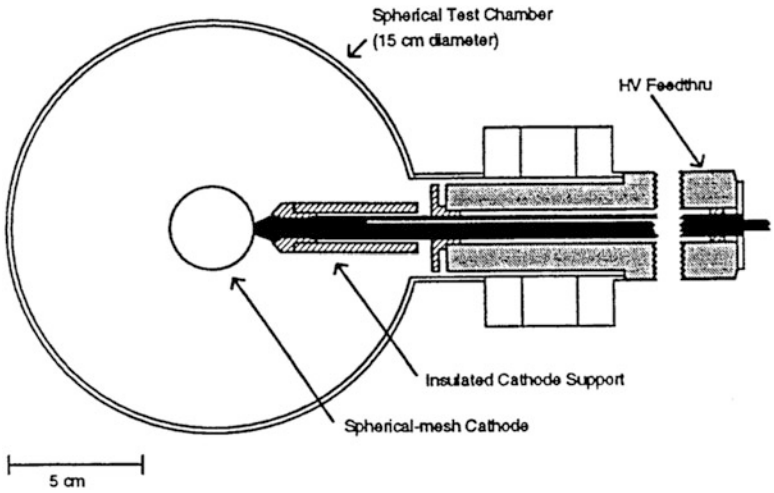

Fig. 4.5 Insulated cathode support structure for the 15-cm-diameter IEC device [7]

4.2.2 Idaho National Environmental Laboratory (INEL) Design

A unique shadow-shielded, cathode insulator support (shown in Fig. 4.5) was used at INEL to position the wire-mesh cathode configuration for the small IEC device [7]. The spherical-mesh cathode is attached to a stainless steel extension that is screwed onto the feedthrough electrode. The electrode is surrounded by a coaxial aluminum tube, which in turn is shadowed by a coaxial large diameter, aluminum tube. Cathode diameters were ~1/4 the test chamber diameter for most testing.

4.2.3 University of Illinois at Urbana–Champaign (UIUC) Designs

A high-voltage stalk frequently used by the group at UIUC is illustrated in Fig. 4.6. The stalk is a conical-shaped insulator facing toward the cathode grid that is expected to block the ions passing through the cathode grid. This stalk is made from "Lavite" (a machineable silicate). The corrugated surface is intended to lengthen surface current path lengths, preventing premature surface breakdown. Because this stalk occupies a non-negligible volume of the chamber, it will affect the reaction rate but allows higher voltages.

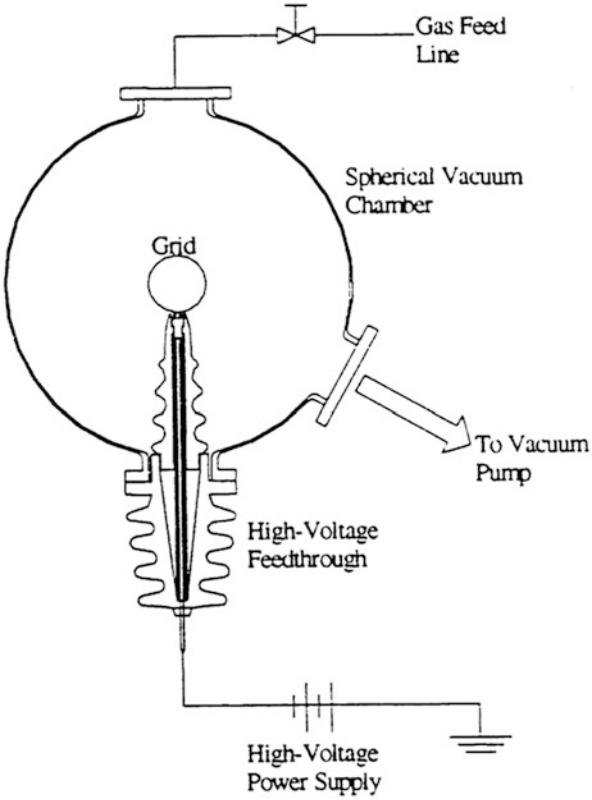

Fig. 4.6 Stalk installed in a spherical chamber at UIUC [8]

4.2.4 University of Wisconsin (UW), Madison Designs

At the University of Wisconsin, Madison, the construction of the inner-grid stalk support was done to ensure the structural integrity and minimize the electrostatic stresses that are imparted to the stalk. Figure 4.7 shows the schematic of the side view of the high-voltage stalk assembly [9]. Concentric tubes of aluminum and quartz were selected for the bulk stalk materials based on their rigidity and high-voltage insulation properties. The ceramics are cut to size from the stalk using a diamond-bladed saw, and they are sealed together using ceramic cement and Torr-seal vacuum epoxy. The vacuum end of the stalk is also rounded using diamond files in order to minimize the electric stresses in that region. The inner grids are tack-welded to rounded screws that then thread into the end of the stainless steel center tube.

The inner spherical grid hangs from a special ceramic stalk structure that is held in place by a ½" Cajon fitting atop a 100-kV isolation feedthrough [3]. This independent attachment allows the inner cathode to be raised, lowered, and rotated

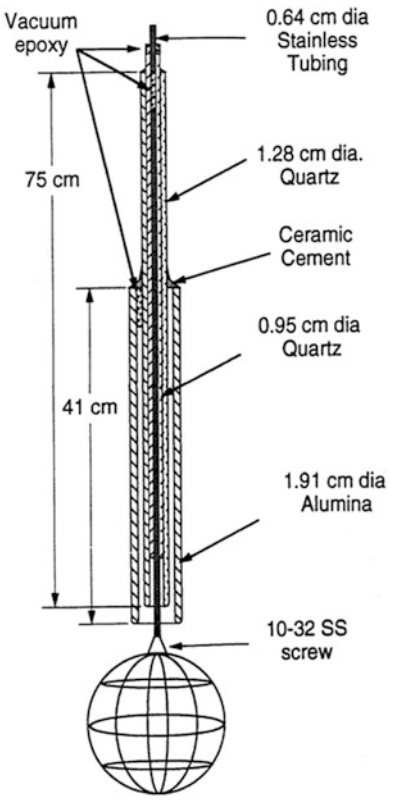

Fig. 4.7 Cross section of the complete stalk, along with the inner cathode grid, previously used at University of Wisconsin (UW), Madison [9]

with respect to the fixed outer grids and chamber walls. This arrangement provides external alignment of the cathode and further experimental flexibility (even under vacuum).

Another design used at UW Madison included additional insulation to reduce the arcing around the stalk's upper section. This section is positioned closer to the outer grids that are at a much lower potential, close to ground. Figure 4.8 shows the top view and the side view of this stalk.

In order to reduce the stalk volume, a third design, shown in Fig. 4.9, was used. Interestingly, the central conductor that carries the high voltage to the inner grid is only a wire. In this respect, this design is similar to those developed at Kyoto University. This design, in contrast to the larger inner stalk section used in other designs, helps reduce the volume of the stalk leading to the inner grid. However, this stalk failed at relatively low voltage because the thickness of the material used at the chamber entrance did not give sufficient standoff.

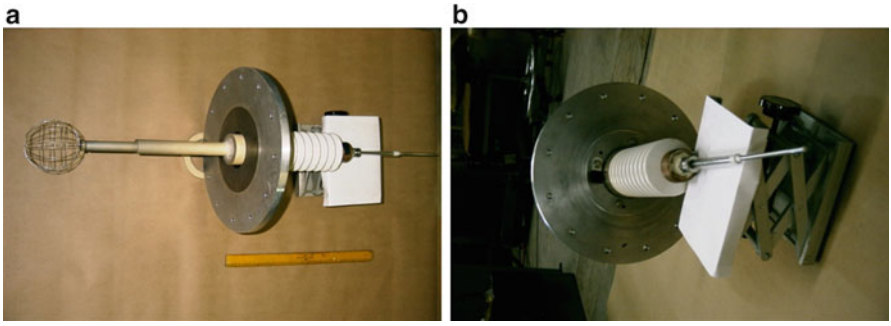

Fig. 4.8 Top view (**a**) and side view (**b**) of the stalk assembly [3]

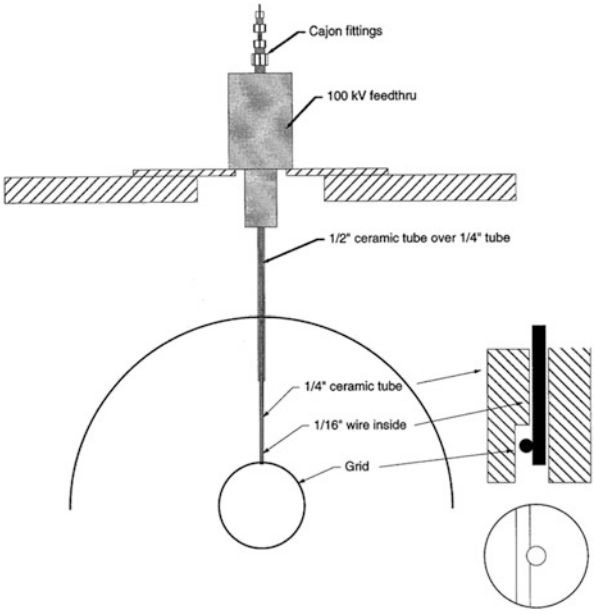

Fig. 4.9 An alternate reduced volume stalk design used at UW Madison (Ashley RP, 1999, University of Wisconsin, Madison, private communication)

4.3 A Stalk Design Using "Lessons Learned" from Prior Ones

The "ideal" stalk design should cope with the following problems:

1. Increase the life of the stalk to withstand the intense ion bombardment
2. Minimize the E-field stresses
3. Reduce the stalk size to minimize perturbation to ion recirculation
4. Allow easy fabrication
5. Employ economical materials

Fig. 4.10 A damaged inner quartz tube

Above all, these objectives must be realized without compromising the advantages of a stalk that can easily be raised, lowered, or rotated as desired for alignment and experimentation. This is a challenging task. However, a careful examination of the performance of the previously designed stalks and their failing patterns gives good insight into the various problems. Thus as a first step toward a design, we begin by discussing various types of damage incurred in the previously designed high-voltage stalks at the University of Wisconsin, Madison.

4.3.1 Various Types of Damage Caused to High-Voltage Stalks

Figure 4.10 shows a damaged inner quartz tube; the black coating inside and around the tube was formed due to extensive ion bombardment of the region. These ions were sputtered off of the grid and were directed toward the inner surface of the quartz tube. This is a design flaw, because no provision was made to stop the ions from bombarding the interior of the quartz tube. The composition of the coating material constitutes mostly of sputtered material from the grids (tungsten and iron) and chamber wall (aluminum). These metallic species are liberated when energetic ions bombard grids and the chamber walls. One way to avoid this is to stop or reduce the sputtering. But that is not completely possible, so one must design the stalk in such a manner as to minimize the free flow of ions to the interior of the chamber.

Once a stalk is heavily coated with splattered metallic species, it becomes useless, allowing frequent sparkover to the chamber and/or outer grids. This resulted in quenching of the plasma, causing frequent shutdowns of the device. The only way to restart the machine then is to remove the stalk and clean it. This can be done either with a diamond file or a sandblaster.

In some cases, ions are focused by the potential surfaces to bombard a discrete spot. In cases where that happens, the hole created by the ions as they chew through the stalk is quite visible to the eye. Interestingly, in tests at the University of Wisconsin, a major hole was formed at the point around 3.7 cm above the stalk's closest portion to the inner grid. There was another hole close to the upper portion of the stalk where the ceramic tube was merged with the quartz tube using epoxy.

Other types of breakdown that a designer should be concerned with include surface breakdown and electric breakdown. Neither electric nor surface breakdowns involve ion bombardment per se, though surface damage by ion bombardment can affect the surface breakdown voltage. Electric breakdown is a volumetric effect specific to the material capabilities. Surface breakdown is likely to occur first, so is explained in more detail next.

4.3.2 Surface Breakdown

Surface breakdown can be of two types: tracking and surface flashover. Tracking consists of the formation of a conducting path on the surface of the materials (i.e., a degradation of the solid material) due, for example, to prior discharges. Surface flashover is due to breakdown of the surrounding gas. This occurs when the stalk surface distorts the field so that the electric strength of the gas is exceeded.

4.3.3 Flashover Across Solid Insulators

If the electrodes in a vacuum gap are separated by solid insulating material in the form of a rod, breakdown over the surface of the rod takes place at a lower voltage than in a straightforward vacuum gap [10]. The operation of high-vacuum, high-voltage equipment such as the IEC device necessitates either constructing the vacuum chamber itself of an insulating material (which is not feasible for steady-state operation) or insulating the high-voltage conductor as it passes through the wall of a metallic vacuum chamber. In addition, there is often the problem of supporting the high-voltage conductor within the vacuum chamber.

4.3.4 Prebreakdown Conduction Mechanism

Usually the prebreakdown conduction mechanism across vacuum gaps is classified in two ways: field emission of electrons or regenerative exchange of positive and negative ions [11]. The first mechanism postulates either small dielectric inclusions giving rise to high local fields (and emission) or a macroscopic field causing the formation of whiskers on the metal cathode. The whiskers cause a local field

intensification and the resulting field emission from the whisker tips. That emission is traditionally represented by the Fowler–Nordheim equation, which can be written approximately as

$$j \propto E_l^2 \ \exp\left(-6.43 \times 10^9 \frac{\phi^{\frac{3}{2}}}{E_l}\right). \tag{4.1}$$

Here j is the current density in amperes per square meter, E_l is the local field in volts per meter, and ϕ is the work function of the material in electron volts [12]. For typical work functions, it appears from Eq. 4.1 that a large increase in current occurs only as the local field approaches 10^{10} V per meter. The local field can be given for a half ellipsoid of revolution on a flat plate by [13]

$$E_l = \beta E \tag{4.2}$$

$$\text{where } \beta = \frac{\lambda^2}{\ln \lambda}. \tag{4.3}$$

In the above equations, E is the macroscopic field, β is the field intensification, and λ is the ratio of the semimajor axis of the ellipsoid to its semiminor axis (with this ratio assumed large).

The second mechanism postulates an organic contaminant coating on the electrodes created by vapors from the associated pumping system. This coating is a source of hydrogen ions, which, upon the application of a large enough voltage, can be exchanged from cathode to anode and anode to cathode in a regenerative process [14]. In an IEC device, the fuel used is deuterium, so both mechanisms described above can play significant roles in governing the prebreakdown phenomena.

4.3.5 Characteristics of Gap Prebreakdown Currents

In an attempt to study the prebreakdown current in gaps, several experiments were conducted by K. F. Koral [11] using cylindrical electrodes (shown in Fig. 4.11). The original threshold voltage (before conditioning) current flow consisted of 5 micropulses of a frequency about 1 pulse per second (Fig. 4.12a). As the voltage was increased above the threshold, the frequency of the micropulses increased while their amplitude decreased. As shown in Fig. 4.12b, at 0.4 kV above threshold, the frequency was 26 pulses per second and the amplitude was about 30 microamperes. As the voltage was increased further, a steady current occurred with very low amplitude pulsing superimposed on the steady current. At 13 kV, the steady current was about 20 microamperes, and the pulse frequency was about 50 pulses per second. Apparently, the pulsing rate above the threshold voltage depends upon the difference between the applied and threshold voltages. As this difference increases,

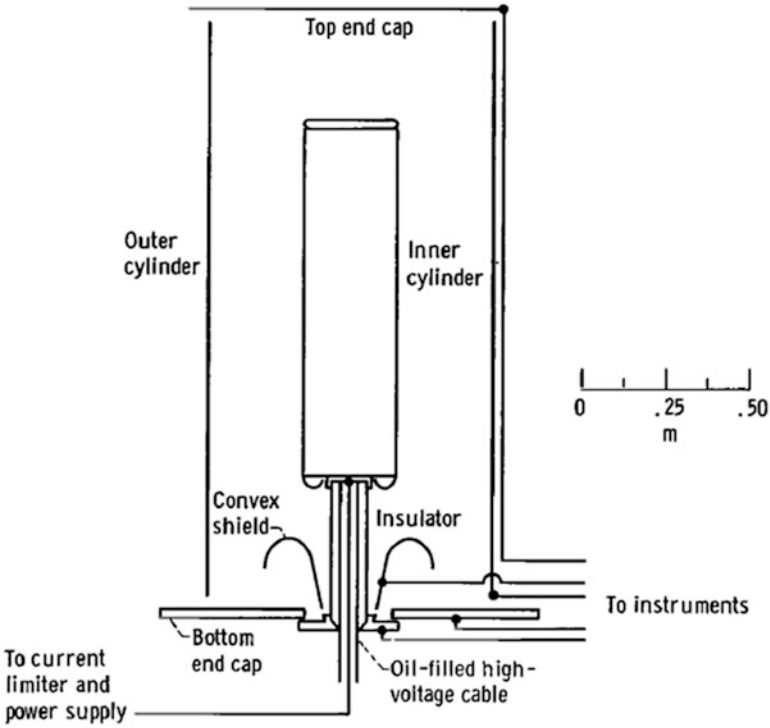

Fig. 4.11 Cross section of the test configuration used by K. F. Koral [11]

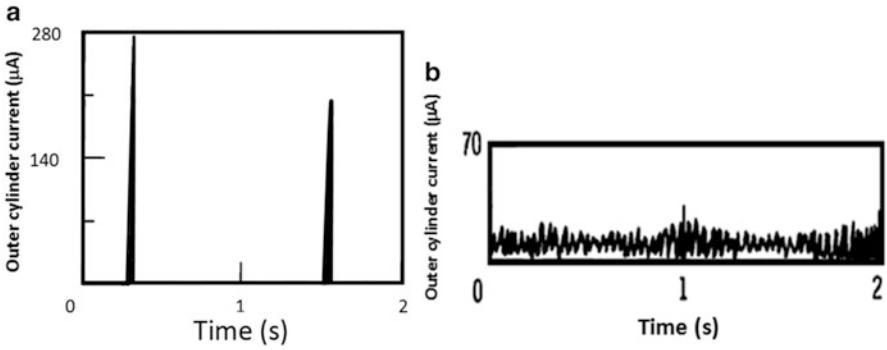

Fig. 4.12 Outer cylinder current versus time plot at the average applied voltage of (**a**) 65 kV and (**b**) 65.4 kV [15]

the pulses occur at a higher frequency. This is in agreement with what would be expected from simple resistance–capacitance circuit analysis. As the voltage is raised, the steady current becomes a larger fraction of the total time-averaged current. The appearance of a steady current is in agreement with the observations on prebreakdown currents for millimeter gaps in reference [15].

When the voltage is raised above the original threshold to a given value and kept at that voltage for a period of time, the magnitude of current that is flowing slowly decreases. After several minutes of current flow at the constant voltage, a remeasurement of the threshold voltage shows that it has increased. The current can be returned to its former value only by applying a higher voltage. This phenomenon is called conditioning. Conditioning can be attributed to the elimination of the sharpest of the cathode whiskers according to the field emission model or to the reduction or modification of the contaminant coating according to the particle exchange model.

4.3.6 Review of Breakdown Basics

Having reviewed various voltage breakdown problems encountered by prior stalk designs, we next discuss some of the basic physics studied that is relevant to these problems. One of the first comprehensive studies of the breakdown across insulators in a vacuum was reported by Gleichauf [16, 17]. The insulators he used were in the form of rods or cylinders and were made of fused quartz or Pyrex glass. Gleichauf found that variations in the pressure between 5×10^{-3} and 10^{-7} Torr had no effect on the breakdown voltage and that there was no critical prebreakdown current. During the prebreakdown stage current bursts (micro-discharges) that did not develop into breakdown also occurred. Pinhole camera x-ray pictures revealed that practically all the radiation in the gap originated from an area on the anode at a distance away from the insulator, with weak radiation coming from a ring immediately adjacent to the insulator.

Interestingly, Gleichauf also found that the phenomenon of conditioning took place for breakdowns across insulators, wherein, over a period of time and after repeated voltage applications, the insulator's behavior was more consistent with conditioning (the phenomenon of conditioning is explained in the subsequent section). He found that part of the conditioning was permanent. The non-permanent part was dependent on the state of the test sample prior to conditioning. This was shown by the fact that if the voltage was removed for 24 h, or the electrodes were exposed to the atmosphere, the next breakdown voltage would be much lower than the last one of the previous series. However, this voltage was still higher than the voltage at which the first breakdown had taken place, and the conditioning process then took place at a more rapid rate than in the previous series. Gleichauf also found that the breakdown voltage was strongly dependent on the material of the insulator but independent of the material of the electrodes (see Table 4.1).

It was observed that a stainless steel electrode with a Pyrex glass insulator gave the highest breakdown voltage, and the second highest was for a combination of copper–polystyrene. As in ordinary vacuum gaps, the breakdown voltage increased in a linear manner for the smaller gaps, while the stress decreased with the longer gaps. Roughening the surface of the insulator in a region adjacent to the cathode increased the breakdown voltage by about 40 %. Roughening the surface adjacent to the anode had little effect.

Table 4.1 Breakdown voltages for different electrode and insulator materials (after Gleichauf) with uniform field electrodes and insulators constructed of 2.2-cm-long cylinders with butt joint at electrodes [16, 17]

Electrode material	Insulator material	Breakdown voltage (kV)
Stainless steel	Pyrex glass	100
Copper	Pyrex glass	44.5
Magnesium	Pyrex glass	37
Aluminum	Pyrex glass	39
Copper	Soda-lime glass	40
Copper	Steatite	50
Copper	Rulite	40
Copper	Zirconium dioxide	40
Copper	Polystyrene	75
Copper	Teflon	50

Working in the same laboratory as Gleichauf, Kofoid [18, 19] thoroughly investigated the phenomena arising at the metal-dielectric junctions of solid insulators. He showed that electrons and negative ions were produced at the negative junction between the cathode and insulator. Kofoid suggested that these negative particles impacted on the solid insulator or anode surface and in doing so released x-rays which in turn released further electrons from the cathode and the solid dielectric. He concluded that the breakdown mechanism in this case was initially due to the production of negative particles by a field emission process at or near the negative junction. The importance of ensuring an intimate contact between the cathode and the insulator by coating the end of the insulator with a conducting film has been emphasized by many investigators.

Fryszman and colleagues [20] have postulated the following mechanism for breakdown across ceramic rod insulators in high vacuum. Free electrons emitted at the cathode–insulator junction bombard the anode, or insulator near the anode, and release secondary electrons. Thus the surface of the insulator near the anode becomes positively charged to a potential approaching that of the anode. The charged area gradually moves closer to the cathode so that the stress at the cathode eventually increases to a value sufficient to cause breakdown. Once the arc is formed, the insulator surface discharges, the field strength decreases, the arc is extinguished, and the cycle is repeated. Fryszman and colleagues found that by screening the section of the insulation surface near the cathode or covering this section with a semiconducting layer, the breakdown voltage was raised by a factor of approximately 2.5. Hence an attempt has to be made to incorporate this into the design of the cone section of the high-voltage stalk.

Hamisch [21] and Boersch and colleagues [22] varied the angle of inclination between an insulator surface and the cathode and measured the corresponding surface charge density. They found that at a critical angle of 31.5 °, the surface charge was zero; this angle was independent of the applied voltage. The surface charges were positive at smaller angles, but negative at larger ones. They recommended that in practice an insulator surface which is in contact with a negative electrode must be at

such an angle that only negative charging or no charging occurs. This information has been used in the University of Wisconsin IEC stalk design to decide the solid angle of the cone section of the stalk. Because the rest of the stalk also has a zero charge, 31.5 ° was selected to be the best angle.

4.4 High-Voltage Bushing Design

With this background information in mind, we now venture into the design of a high-voltage bushing. We begin by defining some of the commonly used terms. *Busbar* is when a conductive material passes through a space or barrier without earthed material close enough to influence the charge accumulation and flow in the device. *Bushing* is when a conductive material is insulated and passes through an earthed enclosure. As seen in the next section, bushings are useful for incorporating voltage grading in the stalk design.

Due to the significant operational differences between a busbar and the bushing, the design of a bushing requires a keen understanding of the electric field strength produced in the insulation, especially when earthed material is present in its vicinity. This is usually the case of IEC devices where the bushings are surrounded by the earthed vacuum chambers. As the strength of the electric field increases, the field stresses maximize between the conductor and the earthed material, and, if sufficient voltage is present, leakage paths would be initiated within the insulation. If the energy of the leakage path overcomes the dielectric strength of the insulation, it may puncture the insulation and allow the electric energy to conduct to the nearest grounded material, causing burning and arcing. Furthermore, if a plasma is present, the ions bombarding the cathode will deposit energy preferentially in areas where the fields concentrate, and the damage progresses exponentially. Once the surface is sputtered and pitting begins, the thickness of the material insulating the plasma (E-fields) from the inner conductor would decrease, and hence the possibility of dielectric breakdown increases. It is therefore very important to homogenize the E-fields and strictly avoid any field enhancements or focusing anywhere in or around the dielectric.

A typical bushing design has a conductor, (usually of copper or aluminum, occasionally of other conductive materials), surrounded by insulation, except for the terminal ends. In the case of a busbar, the conductor terminals will support the busbar in its location. In the case of a bushing, a fixing device will also be attached to the insulation to hold it in its location. Usually, the fixing point is integral or surrounds the insulation over part of the insulated surface. The insulated material between the fixing point and the conductor is the most highly stressed area.

The design of any electric bushing must ensure that the electric strength of the insulated material is able to withstand the penetrating electric energy passing through the conductor, via any highly stressed areas. It must also be capable of enduring occasional and exceptional transient high-voltage pulses as well as the normal continual service voltage, as it is the voltage that directs and controls the development of leakage paths and not the current.

4.5 Use of Bushing for Stalk Design

The concept of voltage grading to provide a uniform field has been applied by Denholm and colleagues [23]. This is used to reduce the length of high-voltage bushings in a vacuum. Their insulator consisted of a series of Pyrex glass rings interspersed with thin aluminum rings, and a cylinder of urethane was used as a potential grading resistor on the high-pressure side of the bushing to prevent localized accumulation of charge on the vacuum–glass interface. It was possible to hold 10^6 V across a 30-cm-long bushing of this type compared with 6×10^5 V across a 90-cm-long conventional porcelain bushing. The problem of taking high voltage across the coaxial stalk can be tackled using a bushing design such as this.

Bushings have provided electric insulation of the conductor for the working voltage and for the various overvoltages that occur in an IEC and also provide the mechanical support against various mechanical forces. Bushing techniques may be classified into two broad categories: non-condenser bushing and condenser bushing.

4.5.1 Non-condenser Bushing

In its simplest form, a bushing would be a simple cylinder of insulating material (such as aluminum or porcelain as shown in Fig. 4.13). This bushing would have a radial clearance and an axial clearance to suit the electric strengths of the insulating material and the surrounding media. These clearances will depend on the voltage distribution shown in Fig. 4.13b. However, in this design, the voltage is not evenly distributed through the wall thickness t or along the length of the insulation l. Then as voltages increase, the dimensions required become so large that really high-voltage bushings of this form are not a practicable proposition.

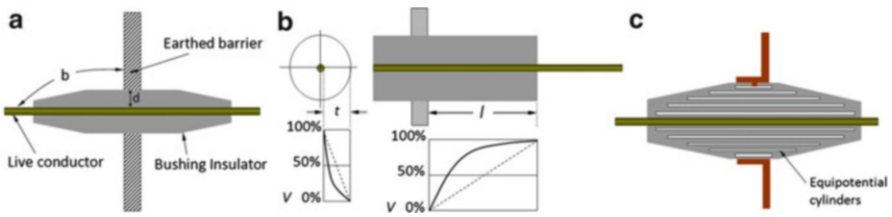

Fig. 4.13 (**a**) Simple bushing. (**b**) Voltage distribution in a simple bushing. (**c**) Bushing with capacitive gradings [10]

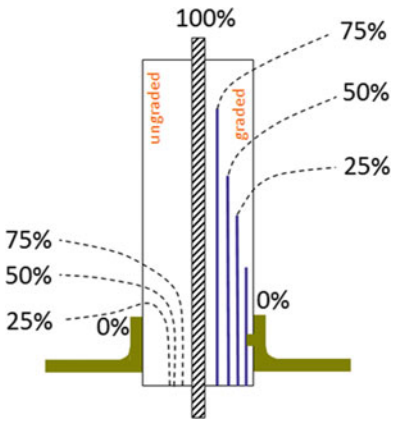

Fig. 4.14 Voltage distribution with (*left side*) and without (*right side*) capacitive grading [10]

4.5.2 Condenser Bushings

The previously mentioned difficulty with non-condenser bushings is overcome by the condenser bushing principle (illustrated in Fig. 4.13c), in which the wall thickness is divided up into a number of capacitors by concentric conducting cylinders. The comparative voltage distributions in condenser and non-condenser constructions are shown in Fig. 4.14. The condenser construction gives a compact design, and a laminated construction is usually most suitable.

4.6 Stress Control in Stalks

With concentric cylinders such as shown in Fig. 4.15, the stress on the inner cylinder is greater at points such as X, well inside the outer cylinder rather than near the edge of the outer cylinder (e.g., at Y). This phenomenon occurs because the stress on the outer cylinder is intensified near its edge at Z. Consequently the field is more symmetric near the edge than inside the outer cylinder.

In order to keep stress at Z below that at X in Fig. 4.15, the radius of curvature at Z should not be less than the radius of the inner cylinder. This concept can be incorporated into the stalk design as shown in Fig. 4.16. The radius of curvature of the outer cylinder (R_o) indicated by the arrows should be greater than the radius of curvature of the central cylinder (R_i).

4.6.1 Dielectric Materials

A dielectric is an insulator, playing an inert role in the electric circuit. The prime property for an insulator is its dielectric "strength," k, which has the units of V/mm. The designer can use this value in finding a design to avoid an electric

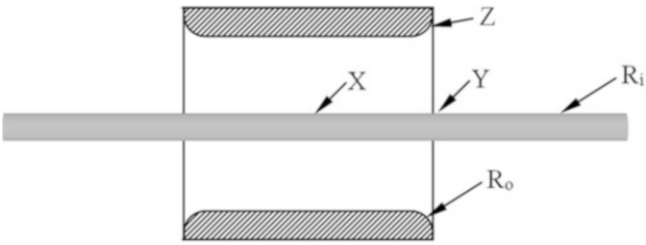

Fig. 4.15 Concentric cylinders. X, Y, and Z identify points where maximum stress occurs [10]

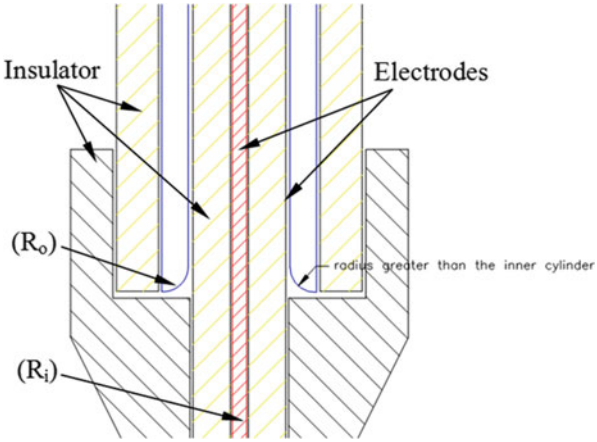

Fig. 4.16 Outer coaxial conductor is rounded off at the edges such that the $R_o > R_i$

breakdown. One of the geometric design parameters that an engineer needs to keep in mind is that effect of reduced electric breakdown at the interface of two different insulation materials. The interface is highly stressed in field regions which should be normal to the field lines. This is discussed in more detail in reference [24].

Further, if the angle between the interface and the electrode in the corner is $< 90\ ^\circ$, the field intensity becomes theoretically infinite [25, 26]. This phenomenon corresponds to the case when a solid dielectric is only partly attached to the electrode, leaving a void filled with dielectric materials of adequate breakdown strength.

It is now worthwhile to look at the law of refraction of the E-field intensities. In the situation where the electric displacement vector D meets the interface between two media of different permittivities at an angle other than $90\ ^\circ$, the direction of this vector will change in the second dielectric. This situation is analyzed in detail in reference [24] for the case where no free charges are present at the interface and only dipolar polarization charges define the boundary conditions.

In practical systems stressed under DC voltages, the accumulation of free surface charges at the interface will take place. This is caused by the differing conductivities of the materials also known as the interfacial polarization. Note the analysis in reference [24] for free charge voltages.

Though dielectrics do not conduct electricity, they are not completely inert to an electric field. The electrons and the proton-containing atomic nuclei will shift their positions in response to the field, a phenomena known as polarization. Dielectric polarization is the result of a relative shift of positive and negative charges in the matter. This shift is produced by an electric field, provoking either "induced polarization" of individual atoms and/or ions, an orientation of any permanent dipoles, the buildup of charges at interfaces between quite different dielectrics, or the creation of dipoles at localized "hopping" sites, as discussed in references [27, 28]. During all of these processes, the electric field is therefore not able to force the charges to escape, leading to electric breakdown (conduction).

4.7 Mixed Dielectrics

Consider two or more dielectrics in series, with an electric field (stress) applied across them. Then the voltage gradient across each individual dielectric is inversely proportional to its permittivity. This is particularly important when air spaces exist in solid and liquid dielectrics, as the permittivity of these dielectrics is always higher than that of air. Thus the air will have the higher stress, possibly causing sparkover through the air space [29]. Hence it is very important to carefully fill any gaps in a stalk between the central conductor and the surrounding dielectric with a compatible material. Furthermore, even when only solid dielectrics are involved, the stress is increased in medium of lower dielectric constant k. To illustrate these effects, we evaluate the stalk containing an air gap shown in Fig. 4.17, using a resistive analogy. Conductivity is proportional to the dielectric constant, and consequently the voltage V_a across the air gap is

$$V_a = \frac{Vxk}{\{d + x(k-1)\}}. \tag{4.4}$$

This gives a stress, V_a/x, in the air gap, given by

$$\frac{Vk}{\{d + x(k-1)\}}. \tag{4.5}$$

This tends to Vk/d if $x << d$. The stress in the air gap can thus be k times that in the solid. Such stress intensification can occur at electrode.

One method of overcoming this is to increase the inner electrode diameter, so that the surface of the solid is perpendicular to the equipotentials. Then the field is not distorted by the solid under these circumstances. Unfortunately, this approach increases the size of the assembly; furthermore, stress intensification may still result due to irregularities in the shape of the cylinder. Still, stress problems can be significantly reduced with this design. Subsequent sections explain how to optimize the radius of the central electrode to minimize the electric field stresses.

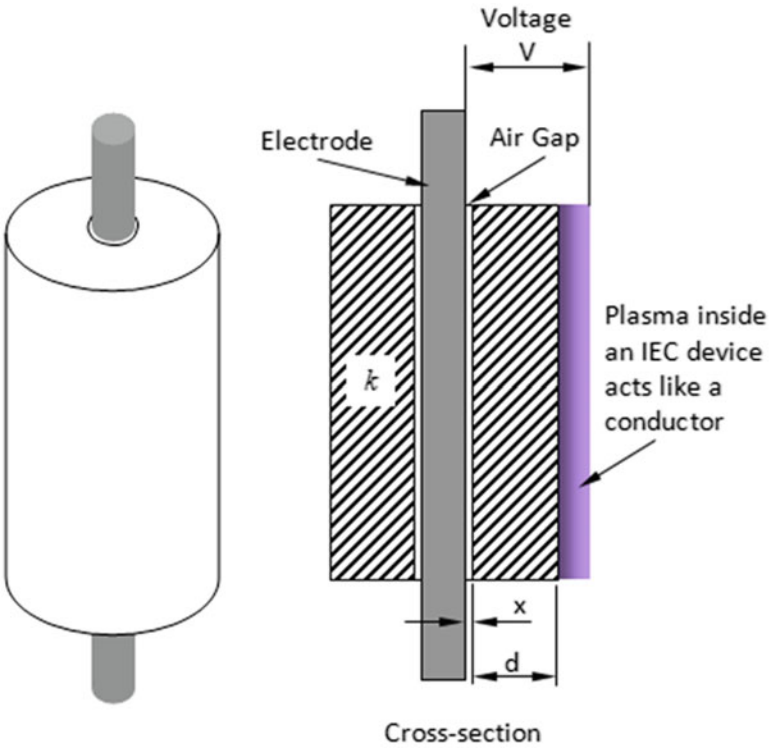

Fig. 4.17 Stress intensification in an air gap

4.7.1 Polarization

The polarizability of a dielectric is an intrinsic property that depends on its molecular composition. The dielectric constant or the relative permittivity depends on the polarization phenomena that take place inside the material under the influence of an external electric field. Most dielectrics may be modeled as chemical compounds with positive and negative ions that migrate toward the electrodes under the influence of external electric fields [30]. This polarization induces bound charges on the electrodes (as illustrated in Fig. 4.18).

The electric flux density D is related to the field strength E as follows:

$$D = \varepsilon E = \varepsilon_0 \varepsilon_r E, \tag{4.6}$$

where ε_0 and ε are, respectively, the permittivities of free space and of the dielectric. The relative permittivity (i.e., the dielectric constant) of the material $\varepsilon_r = \varepsilon/\varepsilon_0$. Hence,

$$D = \varepsilon E + P, \tag{4.7}$$

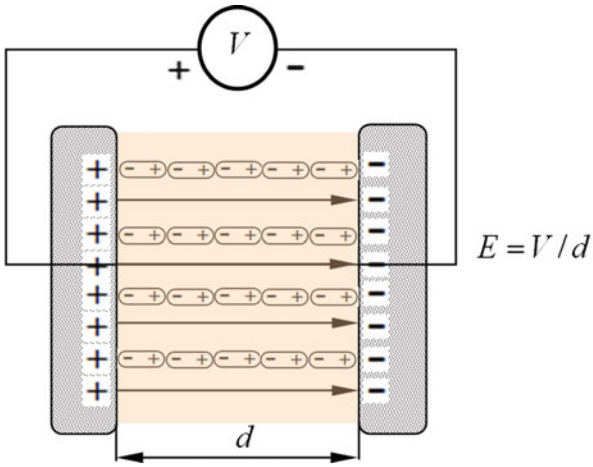

Fig. 4.18 Polarization of a dielectric material under the influence of an external electric field

where P is the partial charge density on the dielectric surface resulting from its polarization. P is also defined as the dipole moment per unit volume of the dielectric.

From Eqs. 4.6 and 4.7 we obtain,

$$\varepsilon_r = 1 + \frac{P}{\varepsilon_0 E} = 1 + \chi, \tag{4.8}$$

where χ is the susceptibility of the dielectric. It is noteworthy that when the dielectric is charged, the energy stored per unit volume is $\frac{1}{2}\varepsilon_0\varepsilon_r E^2$. Therefore, dielectrics with lower permittivities are to be favored for stalk design.

It is very difficult to achieve homogeneous fields within a finite volume of insulating material. Using parallel metal plates of limited dimensions creates the problem of a proper stress control at the edges of the plates. The situation is no different if a cylindrical arrangement of electrodes is used for building the high-voltage stalk. Furthermore, though a rotational symmetry exists when parallel plates are circular disks, the problem turns into a three-dimensional design. Depending on the material used for building the high-voltage stalk, the breakdown strength may be very sensitive to local high fields within the whole electrode arrangement. Therefore, the stalk design should be such that the highest stress is present in the homogeneous field region, where the electrode surfaces are parallel.

4.7.2 E-Field Profiles

A curvature profile of electrodes appears to be necessary outside the plane region to maintain small dimensions. Still the field strength at the curved edges should never exceed the value $E = V/d$. Here V is the applied voltage and d is the distance between the parallel plates. Prinz discussed Rogowski's [31] search for electrode

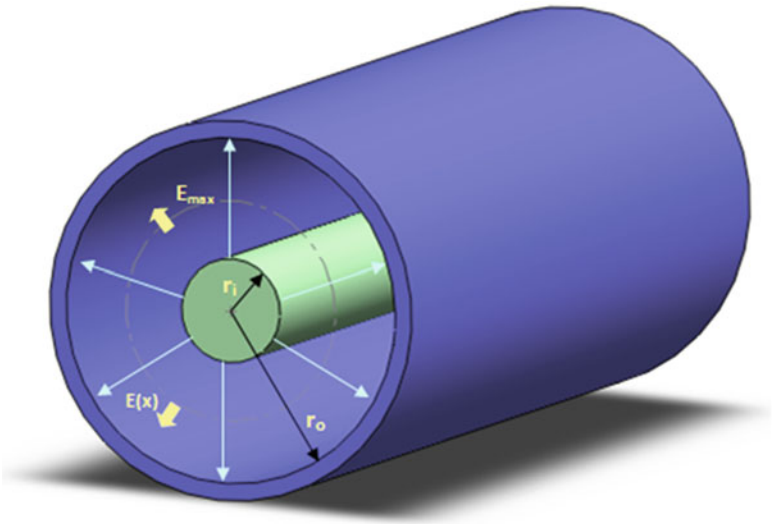

Fig. 4.19 Coaxial cylindrical electrode arrangement with the E-field distribution identified

profiles with uniform fields for axially symmetric systems. He suggested profiles that follow a "Rogowski profile," derived and discussed in detail in reference [31].

The decrease of field intensity at the outer curvature of the Rogowski profile could be prevented in IEC stalk design by using a smaller radius of curvature, providing smaller dimensions or diameters of the disk electrodes. Profiles approaching constant field intensities at the electrode surface with magnitudes *V*/*d* also outside of the uniform field regions can be obtained, for instance, by Bruce's profile [32] and Borda's profile [31]. Borda's profiles give a completely constant field intensity along the electrode surface, but as they are also based on a two-dimensional calculation, the uniformity will disappear if this profile is applied to an axisymmetric electrode. Improvements can be made by very accurate numerical, computer-aided field calculations, taking the actual surroundings as additional boundary conditions into account. For Borda's profile, such an optimization has already been performed by Okubo and colleagues [33].

4.7.3 Coaxial Cylindrical Fields

Field stress control is very important in the high-voltage stalk to avoid the various breakdowns normally observed in these components. Though a high-voltage stalk is not a coaxial arrangement throughout, it does offer a coaxial arrangement when it is surrounded by the conducting chamber material supporting the insulation around the central conductor. Further, the plasma surrounding the stalk is a conducting media so it can be considered a conductor for high-voltage stalk design purposes.

Figure 4.19 illustrates a single coaxial cylindrical electrode arrangement. The electric field distribution is symmetric with reference to the center of the cylinder

axis, the lines of force are radial, and the field strength E is only a function of the distance x from the center. The cylinders are charged with charge per unit length Q/l, where Q is the charge accumulated when a voltage V is applied to the electrodes of length l. Using Gauss's law, the field strength at x in Fig. 4.19 is given by

$$E(x) = \frac{\frac{Q}{l}}{2\pi\varepsilon} \times \frac{1}{x} = \frac{V}{\ln\left(\frac{r_o}{r_i}\right)} \times \frac{1}{x}. \tag{4.10}$$

Here r_o is the inner radius of the outer cylinder, and r_i is the outer radius of the inner cylinder. The maximum value of Eq. 4.10 is obtained when $x = r_1$, hence

$$E_{\max} = \frac{V}{r_i \ln\left(\frac{r_o}{r_i}\right)}. \tag{4.11}$$

4.8 Computation of the Optimum Radius Ratio for Cylindrical Geometry

If we now normalize the V (voltage) and r_o to 1, Eq. 4.11 becomes

$$V = 1, \frac{r_i}{r_o} \equiv r. \tag{4.12}$$

We now substitute Eq. 4.12 in 4.11 and differentiate Eq. 4.11 with regard to setting $dv/dr = 0$, giving the optimum ratio as

$$r = \frac{r_i}{r_o} = \frac{1}{e} \tag{4.13}$$

This optimum ratio minimizes the stresses within the coaxial electrode arrangement, independent of the material of the dielectric used. Thus this result is a very useful concept for stalk design.

4.8.1 Spherical Electric Fields

A simple concentric spherical electrode and its E-field are illustrated in Fig. 4.20. Here the electric field distribution is symmetric with reference to the center of the spherical axis, the lines of force are radial and the field strength E is only a function of the distance x from the center. The spheres are charged with charge per unit length Q/l, where Q is the charge accumulated when a voltage V is applied to the

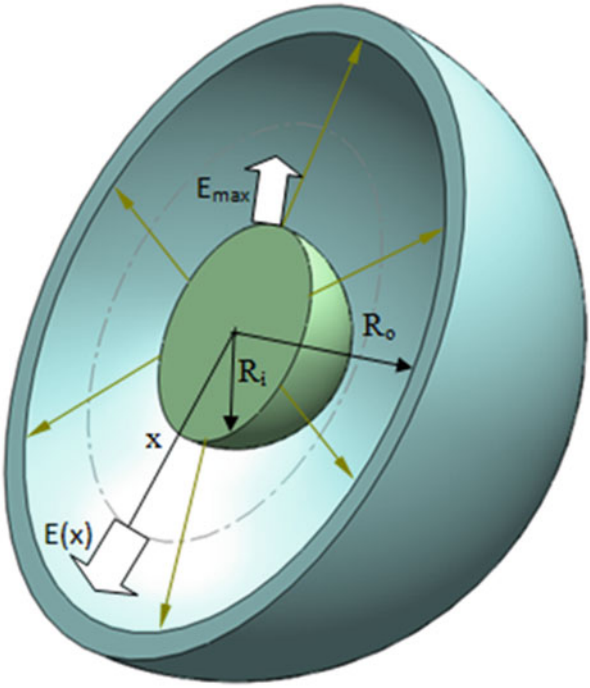

Fig. 4.20 Cross section of the concentric spherical electrode arrangement with the E-field distribution

electrodes. Using Gauss's law, the field strength for concentric spheres at x (see Fig. 4.20) is given by

$$E(x) = \frac{Q}{4\pi\varepsilon}\frac{1}{x^2} = \frac{V}{\frac{(R_o - R_i)}{R_i R_o}} \times \frac{1}{x^2}. \tag{4.14}$$

Here R_i and R_o are defined in Fig. 4.20. Once again, the maximum value of $E(x)$ is obtained for $x = R_i$, hence

$$E_{\max} = \frac{V}{R_i\left(1 - \frac{R_i}{R_o}\right)}. \tag{4.15}$$

It may be observed from Eqs. 4.10 and 4.14 that the electric field in a spherical geometry decreases much faster than in the cylindrical geometry. This is also evident through comparison of the denominators of Eqs. 4.11 and 4.15.

Following the steps taken earlier to compute the optimum radius ratio of cylindrical geometry, the optimum radius ratio for the spherical geometry is found to be 2. While this ratio minimizes stress, the corresponding voltage profile provides a first approximation for achieving maximum acceleration of ions born near the outer surface at R_o, hence given high fusion rates. In this analogy we view the electrodes as grids rather than in an electric insulator. Along this line,

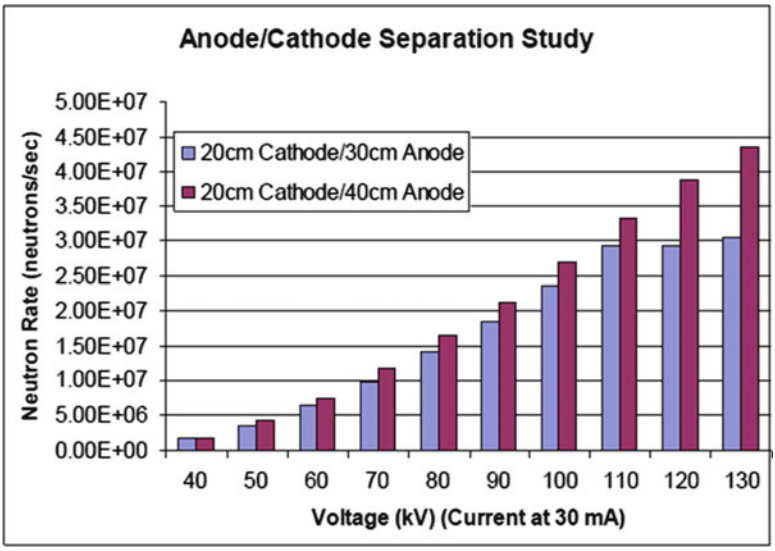

Fig. 4.21 Comparison between 20-cm cathode/30-cm anode and 20-cm cathode/40-cm anode configurations [34]

experiments conducted at UW Madison using various grid ratios suggest that the fusion rates tend to increase with the increasing cathode radius [34]. One of the reasons this occurs is because the E-field available to accelerate the ions is at an optimum value when the radius ratio approaches the optimum value of 2.0. This is further confirmed by the experiments conducted by Donovan [34], as shown in Fig. 4.21. Note that the 20-cm cathode/40-cm anode with the ratio of 2 consistently offered high neutron rates as the voltage was increased at constant current.

However, Donovan concluded that the absolute distance between the anode and the cathode is more important than the radius ratio for higher fusion rates. Thus a 20-cm cathode and 50-cm anode arrangement (not plotted here) produced the highest neutron rate. This illustrates the fact that a number of factors determine the optimum fusion rate in an IEC device. Other factors that influence the fusion rate include the grid transparency, grid and stalk materials, high-voltage stalk design, and secondary electron emission of the device. Other groups have also studied the grid radius effects on neutron production rates as discussed further in a later chapter.

4.9 Mechanical Stress Due to Electrostatic Charge

It is convenient to consider the dielectric stresses as being analogous to elastic stresses in other bodies. This hypothesis will explain all the mechanical effects noted in dielectrics, residual charge, electric expansion, and dielectric "elastic limit." The first mechanical effect noticed is the breakdown of the dielectric when a capacitor is overcharged. The attraction of the charges on the opposite

sides of the dielectric strains is so severe that it results in a breakdown, analogous to a drumhead that ruptures under too heavy a pressure. Similarly, when a hole is pierced through a dielectric by the charges, there is an analogous mechanical energy expended in the phenomenon.

In the absence of plasma, this kind of mechanical stress would cause the eventual breakdown of the stalk. Because all the previous designs had plasma in contact with the stalk's outer surface, the mechanical stresses were not considered to be a major contribution to the breakdown. The thought was that ion bombardment would degrade the stalk far too easily compared to other possible causes. One way to reduce this kind of damage to the stalk is to optimize the inner-to-outer radii ratio in the coaxial stalk design as explained earlier.

4.9.1 Multistage Stalk Design

Several other stalk designs have evolved in the recent times. One of the simpler designs addressed the high-voltage standoff and also created a radial electric field that directs the ions toward the central cathode rather than the stalk. Such a multistage stalk, first suggested by Ralph Moir at LLNL, is discussed in reference [35].

Figure 4.22 shows the distribution of the E-fields around this multistage stalk. The fields around the cathode are much more radial in comparison to those in Fig. 4.23. The voltage is applied at multiple points, and hence the controllability of the field strength is much easier. However, the footprint of the stalk is large, so the ions moving in the bottom-up direction will cause maximum bombardment. To improve the situation, Kai Masuda and colleagues [35] have chosen to make the multistage stalk relatively transparent using a mesh-like structure (instead of solid tubes) as shown in Fig. 4.24.

The radial distribution of the E-fields is designed to have a favorable effect on the recirculation of the ions. As evident from the simulation results of the configuration shown in Fig. 4.25, the average number of recirculation of ions injected is three times as larger when compared to regular single stage high-voltage stalk (see Fig. 4.25) [36]. However, the disadvantages of this design are that it is much more complex (has many more components) so it could undergo premature breakdown between the stages if the spacing is not right. Also, any sharp edges that might be created during the manufacturing can worsen the situation. These aspects have to be taken into consideration while manufacturing a multistage feedthrough.

4.9.2 Hollow Stalk Design

Traditional stalk designs at UW Madison as explained earlier in this chapter involved boring of boron nitride rod and inserting the central conductor. The

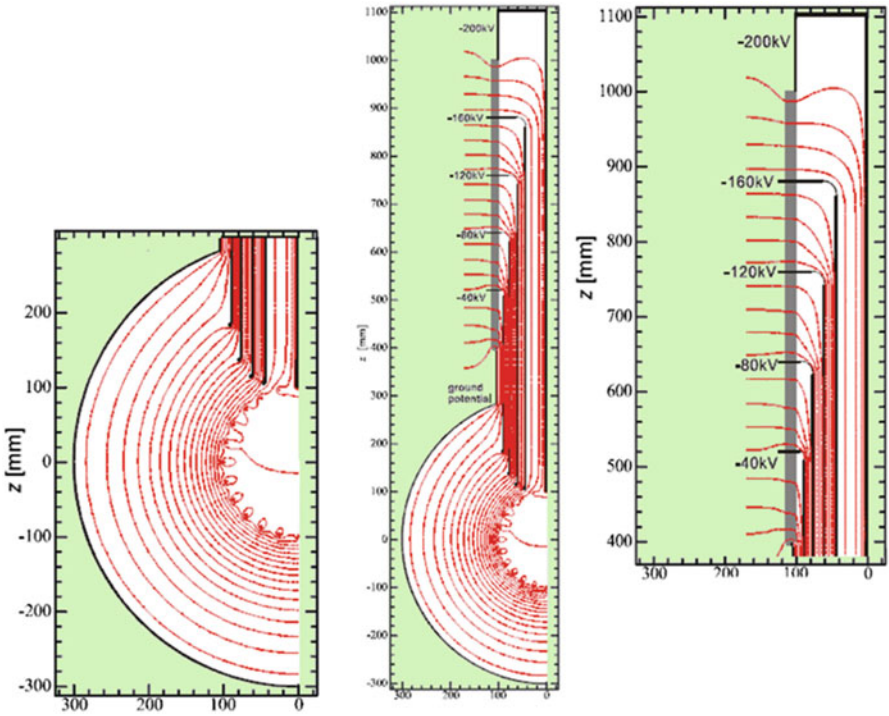

Fig. 4.22 Electric field distribution around the 5-stage stalk [36]

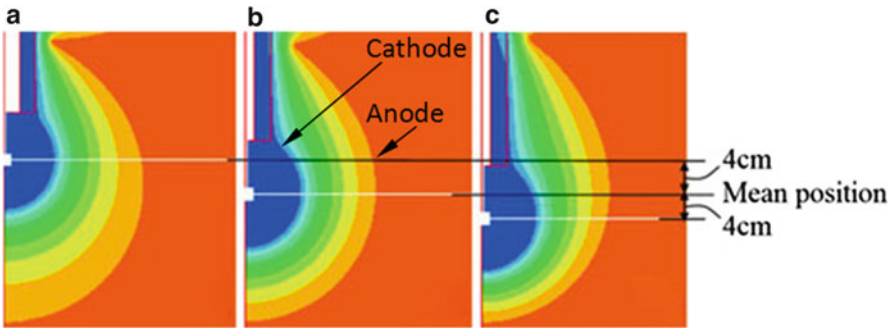

Fig. 4.23 The two-dimensional simulation of the E-fields in an IEC device with smaller 10-cm-diameter cathode about the (**a**) mean position, (**b**) offset cathode in the upward direction, and (**c**) offset cathode in the downward direction. The anode is at ground potential and the cathode is at −50 kV; every shade is ~5 kV [36]

intermediate gap was filled with liquid ceramic that prevents the formation of plasma close to the conductor. This allows the achievement of voltages well in excess of 130 kV, but could not achieve higher voltages desired for some D–^{3}He and ^{3}He–^{3}He fusion experiments. Improvements were made by placing a hollow

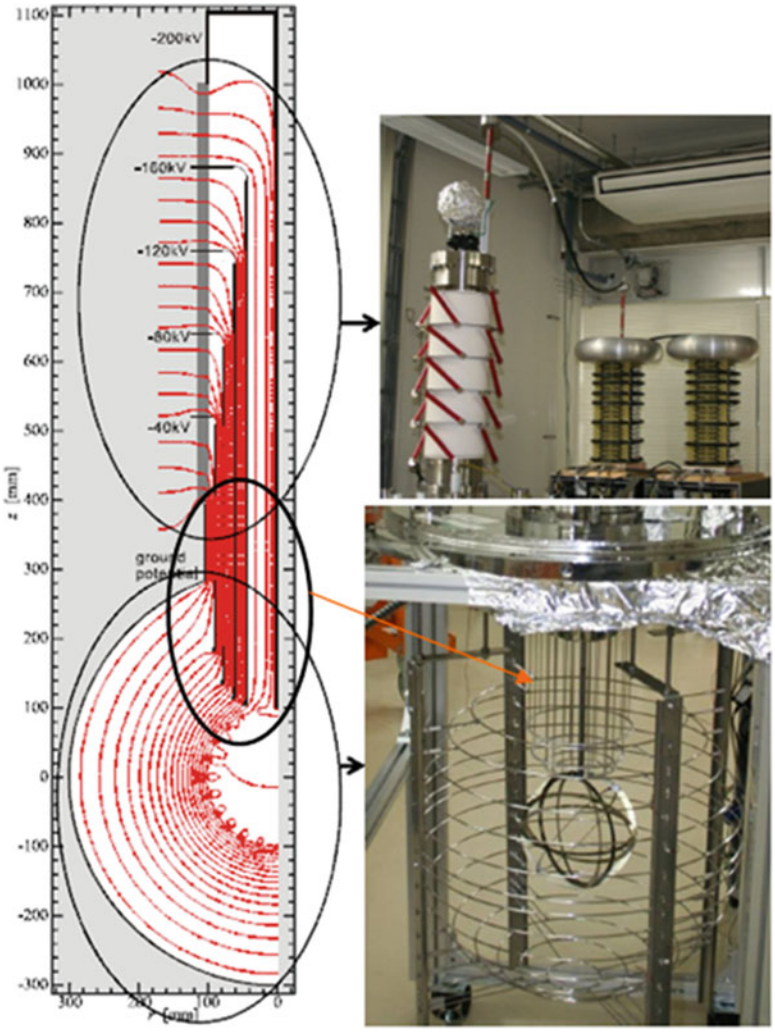

Fig. 4.24 Various segments of the mesh-like multistage stalk developed by Masuda and colleagues, along with a photo of the corresponding sections [36]

region around the central conductor that had the region evacuated. Hence even in the presence of high voltage, a plasma was not formed in this hollow region as the Paschen criteria could not be met there. This improved the voltage levels achieved, and 160 kV was achieved with this new design (shown in Fig. 4.26) [5].

One of the problems faced at the UW Madison was that the boron nitride (BN) material, though ideal for the stalk application, was porous, allowing the oil to seep through. The oil had been added to the tank to prevent any gases from leaking into the vacuum chamber and providing the required standoff for high-voltage connection between the power supply and the cathode, outside the chamber. To prevent this

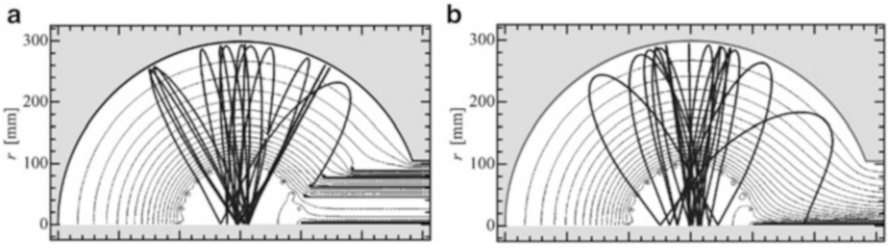

Fig. 4.25 Average ion recirculation in (**a**) 5-stage high-voltage stalk and (**b**) in a regular single stage high-voltage stalk [36]. The 5-stage design has less stray ions going to the outer surface of the stalk

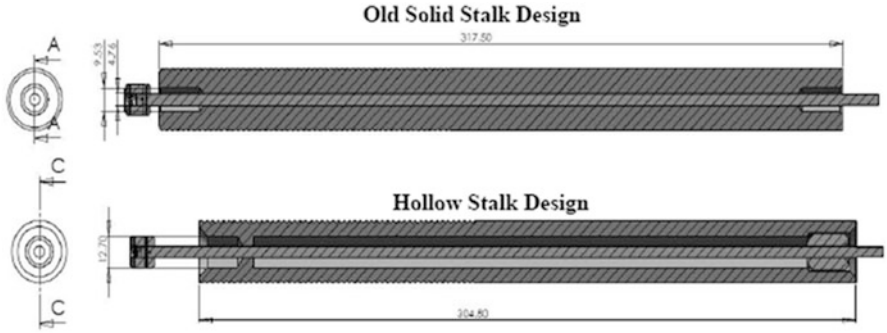

Fig. 4.26 Comparison of the older stalk design at University of Wisconsin, Madison, with the new hollow design (units in mm) [5]

oil from seeping through the stalk, a coating was provided on the surface of the BN stalk. One coating that was successfully used for this purpose was the PYRO-ML®. This coating provided a vacuum seal barrier that is impenetrable to most fluids and also has very high heat capacity. Several layers of the coating were baked on to the surface of stalk before it was used as the feedthrough. This coating completely solved the issue of oil leakage.

4.9.3 Nonconductive Isolated Stalk Design

The Swagelok fittings originally used at the University of Wisconsin to secure the feedthrough bring the ground potential close to the central conductor in the high-voltage stalk. Thus this was the region where breakdowns commonly occurred. In order to move the high E-field away from the Swagelok region, a ceramic plate was inserted that enabled the Swagelok fitting to float [5]. However, the insulator

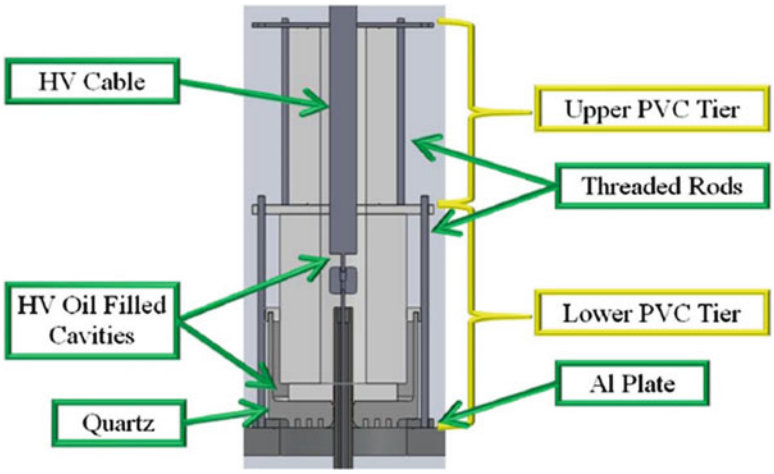

Fig. 4.27 High-voltage feedthrough with quartz base [5]

plate cracked due to thermal stress, and this design was abandoned for the more robust design shown in Fig. 4.27.

This feedthrough design completely eliminates the Swagelok fitting and uses an O-ring instead to seal and secure the central stalk. Because the stalk itself is completely isolated from the ground potential of the surrounding chamber through the efficient use of a quartz base, the standoff voltage obtained by this design is much higher than the "traditional" design employing Swagelok fittings. This design has allowed very high-voltage (~ 160 kV) experiments.

4.10 Summary

This chapter has reviewed various stalk designs employed in recent IEC experiments. From this and various failure mechanisms observed, the requirements for an "ideal" stalk design were listed. Persons undertaking stalk design are encouraged to consider these requirements carefully. However, many details must be considered in the design in order to prevent premature arcing, ion bombardment, or surface leakage currents. The basic concepts involved in prevention of these failure mechanisms have been discussed for possible incorporation into new designs. The design remains strongly dependent on the other aspects of the IEC system and on its desired application. For example, for a neutron source operating at modest voltages $\leq$ 80 kV, a relatively simple stalk design such as shown in Figs. 4.5, 4.6, and 4.7 would suffice. However, for high voltages such as ~ 160 kV, more complex features such as voltage grading and reducing stress intensification such as shown in Fig. 4.24–4.26 are necessary.

References

1. Ohnishi M, Yoshikawa K, Yamamoto Y, Toku H, Hasegawa M, Hoshino C, Koyama T, Taruya K (1998) Studies of inertial electrostatic confinement fusion neutron source. In: 13th ANS topical meeting on technology of fusion energy, Nashville, 7–11 June
2. Osawa H, Miyagi A, Tanaka R, Kiritani J, Sadahiro T, Tabata T (2002) Effects of cathode structure on neutron production in IEC device. In: US-Japan workshop, 9–10 Oct
3. Tanaka R, Osawa H, Tabata T, Ishibashi T, Ohnishi M (2003) Optimal shape of electrodes for high performance of inertial electrostatic confinement fusion. In: 20th IEEE/NPSS symposium on fusion engineering, pp 320–323
4. Krupakar Murali S (2004) Diagnostic study of steady state advanced fuel (D–D and D–^{3}He) fusion in an IEC device. Ph.D. dissertation, University of Wisconsin, Madison
5. Krupakar Murali S, Santarius JF, Kulcinski GL (2010) Effects of displaced grids on the fusion reactivity of an inertial electrostatic confinement device. J Fusion Energy 29:256–260
6. Yoshikawa K et al (2005) Research and development of landmine detection system by a compact fusion neutron source. Fusion Sci Technol 47:1224–1228
7. Anderl RA, Hartwell JK, Nadler JH, Demora JM, Stubbers RA, Miley GH (1995) Development of an IEC neutron source for NDE. In: 16th IEEE/NPSS symposium, vol 2
8. Miley GH (1999) A portable neutron/tunable X-ray source based on inertial electrostatic confinement. Nucl Instrum Methods Phys Res A 422:16–20
9. Thorson TA (1995) Ph.D. dissertation, University of Wisconsin, Madison
10. Alston LL (ed) (1968) High-voltage technology. Oxford University Press, London
11. Koral KF (1967) High voltage characteristics of a large-gap coaxial-cylinder electrode. Lewis Research Center, Washington, DC, NASA TN D-3949
12. Charbonnier FM (1964) High current density field emission and the transition to vacuum breakdown. In: Proceedings of the first international symposium on the insulation of high voltages in vacuum, Massachusetts Institute of Technology, pp 23–24
13. Germain C, Rohrbach F (1963) Mechanism of breakdown in a vacuum. AEC-Tr-6341
14. Mansfield WK, Fortescue RL (1957) Pre-breakdown conduction between electrodes in continuously-pumped vacuum systems. Br J Appl Phys 8:73–78
15. Pivovar LI, Gordienko VI (1958) Micro-discharges and pre-discharge currents between metal electrodes in high vacuum. Soviet Phys Tech Phys 3(10):2101–2105
16. Gleichauf PH (1951) Electrical breakdown over insulators in high vacuum. J Appl Phys 22:535
17. Gleichauf PH (1951) J Appl Phys 22:766
18. Kofoid MJ (1960) Effect of metal-dialectric junction phenomena on high-voltage breakdown over insulators in vacuum. Trans Am Inst Elect Eng Part 3 79:991
19. Kofoid MJ (1960) Effect of metal-dialectric junction phenomena on high-voltage breakdown over insulators in vacuum. Trans Am Inst Elect Eng Part 3 79:999
20. Fryszman A, Strazyz T, Wasinski M (1960) On a mechanism of breakdown in high vacuum. Bull Acad Pol Sci Ser Sci Tech 8:379
21. Hamisch H (1962) Oberflachenentladunger uber isolatoren im vakuum. Fifth international congress for electron microscopy D-13
22. Boersch H, Hamisch H, Ehrlich W (1963) Surface discharges across insulators in vaccum. Z Angew Phys 15:518
23. Britton RB, Arnold KW, Denholm AS (1960) Ability of a voltage-graded surface to support a high voltage in vacuum and in a pressurized gas. Rev Scient Instrum 34:185
24. Kuffel E, Zaengl WS, Kuffel J (2000) High voltage engineering – fundamentals, Second edn, Newnes, p 227
25. Takuma T, Kouno T, Matsuba H (1978) Field behavior near singular points in composite dielectric arrangements. In: Trans IEEE, vol EI 13, pp 426–435
26. Weiss P (1979) Fictious peaks and edges in electric fields. In: 3rd international symposium on high voltage engineering, Milan, Report 11.21
27. Popovic BD (1971) Introductory engineering electromagnetics. Addison-Wesley, Reading

28. Moon P, Spencer DE Field theory for engineers. D. Van Nostrand, 1961; Field theory handbook. Springer, 1961
29. Laughton MA, Warne DF (2003) Electrical engineer's reference book, 16th edn. Newnes, p 7
30. Seely S, Poularikas A (1979) Electromagnetics-classical and modern theory and applications. Marcel Dekker, New York
31. Prinz H (1969) Hochspannungsfelder. Oldenburg, Munich
32. Bruce FM (1947) Calibration of uniform field spark gaps for high voltage measurements at power frequencies. In: Proceedings of the IEE 94, Part II, p 138
33. Okubo H, Amemiya T, Honda M (1979) Borda's profile and electrical field optimization by using charge simulation method. In: 3rd international symposium on high voltage engineering, Milan, Report 11.16
34. Donovan DC (2011) Spatial profiling using a time of flight diagnostic and applications of deuterium–deuterium fusion in inertial electrostatic confinement fusion devices. Ph.D. dissertation, University of Wisconsin, Madison
35. Kai Masuda Y, Yamagaki TK, Kipritidis J (2011) Numerical study of ion recirculation in an improved spherical inertial electrostatic confinement fusion scheme by use of a multistage high voltage feedthrough. Fusion Sci Technol 60:625
36. Yamagaki Yu, Masuda K, Hashimoto G, Kamiya Y, Nagasaki K (2011) Experimental results from an IEC device employing a 5-stage high voltage feedthrough. In: 13th US-Japan workshop on ICF

Chapter 5
IEC Grid Materials and Construction

5.1 Introduction

Grid design and construction are a vital part of the IEC. In this chapter we concentrate on grids for spherical IEC systems. Similar considerations carry over to other geometries, e.g., cylindrical IECs. There are several factors that must be taken into consideration in doing this. First, the wire used for the construction of the cathode has to be a suitable material to supply the strength needed, have a high melting temperature, and control electron emission. Second, from the earlier discussion we know that the effective transparency is more important than the physical transparency of a cathode. Thus, ideally the cathode grid should be constructed in such a way that the openings in the cathode radially face each other with good symmetry and with openings of sufficient size to support formation of ion microchannels. Third, the overall size and shape of the cathode grid plays a significant role in the performance of the device and should be taken into consideration while designing a grid. This chapter concentrates on selection of grid materials and construction. Effects of grid design and geometry are covered in more detail in Chap. 6.

5.2 Grid Material Selection

The selection of grid material strongly depends on its strength under a high heat load plus its characteristics for electron emission under the influence of heat, electric fields, and ion bombardment. The heat load on the grid can melt, deform, and enhance thermionic emission and that in turn limits the power load (ion current) that can be handled. The electric fields applied to the material can change the work function of the material, enhancing thermionic emission. Moreover, the persistence of any sharp edges remnant from the manufacturing process can promote unwanted electron field emission.

G.H. Miley and S.K. Murali, *Inertial Electrostatic Confinement (IEC) Fusion: Fundamentals and Applications*, DOI 10.1007/978-1-4614-9338-9_5,

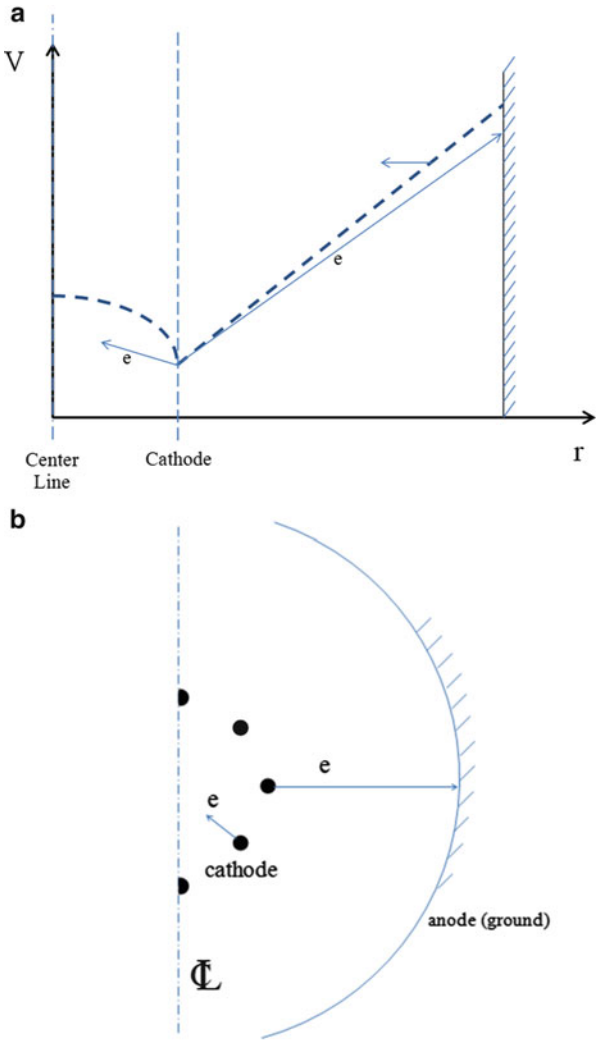

Fig. 5.1 (**a**) Potential diagram. Electrons "born" on the outer side (*anode side*) stream to the ground potential at the anode. Those born on the opposite (*inner surface*) stream inward toward the higher potential created by convergent ions. (**b**) Cross-sectional view showing motion of electrons born on the cathode inner/outer side

Because electron emission from grid wires is an important consideration in grid design, some basic concepts are important to keep in mind. The emission of electrons from the cathode grid is illustrated in Fig. 5.1. Most emission occurs on the outer side (facing the anode) due to ion bombardment plus thermionic emission. These electrons create desirable ion–electron pairs from collisions with neutrals and also simply stream to the anode where they are lost. Emission on the inner surface streams inward and, depending on conditions, serves to control ion space charge buildup and also serves (along with plasma electrons created inside the grid) to form the "double potential well" as discussed in Chap. 2.

It is also important to understand the external electric circuit and the role of the internal electron/ion currents. The external power supply that creates the cathode grid potential supplies an electric current that is a sum of ions hitting the grid plus electrons leaving, i.e.,

$$\begin{aligned} P_{ext} &= (i_i + i_e)V \\ i_e &= i_{eo} + i_e. \end{aligned} \tag{5.1}$$

Here P_{ext} is the power (V × I) supplied to the grid, i_i is the ion current, and i_e is the total electron current composed of the emission i_{eo} on the outer surface and i_{ei} from the inner surface. In general, excessive electron emission is undesirable, because for a fixed P_{ext}, the desirable ion current is reduced if the electron current increases. Ideally there would be a way to control inward and outer space electron emission separately, but no grid designs to date have accomplished this. There has, however, been some discussion of using a thermionic emission material on the inside surface of the cathode to enable controlled electron emission to aid virtual electrode formation. Using a wire across the diameter of the grid has however adversely affected the performance of the grid as this wire turned into a source of excessive secondary emission and thermionic emission as explained later in this chapter.

The selection of the grid material for an IEC device operating without double well formation (typical of most present neutron source-type devices) usually performs better with the reduction of electron emission. This is done because, as just discussed, a power supply cannot differentiate between an ion reaching the cathode grid and an electron leaving it (they both appear as positive current on the ammeter). Excessive electron emission then requires a reduced ion current (i.e., reaction rate), e.g., the neutron production rate, for a fixed power delivered by the power supply. Thus, a designer needs to use an understanding of electron emission processes and try to decrease emission. Various electron emission modes are thermionic emission, secondary electron emission, photo emission, and field emission [1]. Each of these processes is nonlinear and can increase quickly as conditions change. Next, we will briefly comment on each process, beginning with the thermionic emission.

5.3 Effect of Thermionic Electrons on the Performance of the IEC Device

In order to study the thermionic emission from the cathode, it is preferable to isolate the thermionic portion of the current from the rest of the cathode current. This is a difficult feat to accomplish because, as stated earlier, the power supply's ammeter does not differentiate between various electron currents. However, it is possible to increase the contribution of a particular kind of electron current selectively and study its effects on the performance of the device. The effect of grid material on the performance of the device has been studied by Murali and colleagues at the University of Wisconsin, Madison [2]. In that study, the thermionic electron current

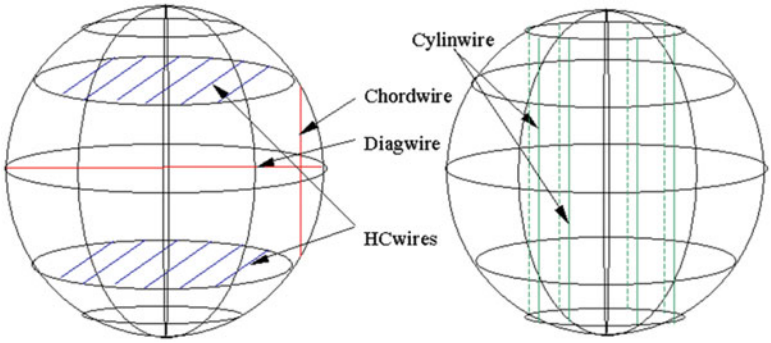

Fig. 5.2 Various configurations of chordwires used in the study of thermionic emission. All chordwires were constructed from thoriated tungsten wires to enhance their thermionic emission [2]

was artificially increased in two different ways. First, a simple diagnostic called the chordwire (see Fig. 5.2) was used that increased the temperature of a small segment of the wire placed inside the cathode. Second, the temperature of the cathode itself was increased by increasing the ion flux to the cathode [3]. The ion flux to the cathode could not be directly increased beyond the capabilities of the power supply, and the cathode was replaced by a single loop grid. What this accomplished was an increase in the ion flux to the reduced surface area of a single loop grid (by almost tenfold) when compared to the multi-loop spherical grid. Increasing the ion flux to the grid increased its temperature and caused thermionic emission to increase.

Several configurations were used to intercept the ions flowing across the cathode as shown in Fig. 5.2. The neutron rate was measured while the configurations shown were tested. As already explained, an increase in the electron current would decrease the ion current, because the total power supply current was held constant. The decrease in ion current results in a decrease in the neutron rate observed from the device as well. Thus, measuring the neutron rate with different carefully selected configurations allows study of the influence of the increased electron current on IEC operation.

5.4 Chordwire Diagnostic for Electron Current Studies

As the name suggests, the chordwire diagnostic consists of a metallic wire placed across the cathode grid of an IEC device (see Fig. 5.2). The wire itself is at the same potential as the cathode. Because the diagnostic is placed inside the cathode, the chordwire does not change the field distribution between the two electrodes. This chordwire intercepts some of the ions passing through the cathode and is heated as a result. A pyrometer placed outside the chamber was used to monitor the temperature of the wire. This pyrometer picked up the maximum temperature in its focus.

Several chordwires can also be placed inside the cathode for simultaneous data acquisition. However, the total number of wires must be limited, as too many can adversely affect the grid transparency.

Several different configurations of chordwire arrangements within the cathode grid (shown in Fig. 5.2) were used to determine the ion flux around the cathode and the effect of thermionic electron emission. The wire temperature should be high to cause significant thermionic emission. The chordwire placed in the region of maximum ion flux, termed a diagwire (i.e., a diametrically placed wire), has a corresponding higher temperature. In the diagwire configuration shown in Fig. 5.2, the chordwire runs across the spherical cathode along the diameter of a grid wire loop. This wire intercepts the most ions and was observed to reach the highest temperature when compared to any other configuration employed.

The cylinwires (cylindrical arrangement of chordwires) configuration has wires running from the topmost latitude to the bottommost latitude. These wires are symmetric about the vertical axis, so the electrons liberated from them populate the central region along the vertical axis. The temperatures of wires in this configuration were usually similar and symmetric. The addition of two sets of wires placed horizontally (horizontal as relative to floor) across either of the two latitudes shown in Fig. 5.2 produces the horizontal configuration (HC). Each of the previously mentioned configurations was studied separately and required that the central grid be removed from the chamber to change the configurations. After replacement, several conditioning runs were performed before acquiring data in order to reduce any impurity concentration.

5.4.1 Studies of Thermionic Emission Effects on the Neutron Production Rate

Due to its low work function (2.5 eV), thoriated tungsten wires were used for the chordwires to study the influence of thermionic emission on the total fusion neutron production rate. As illustrated in Fig. 5.3, the diagwire configuration showed the lowest neutron production rate, at 50 kV, 30 mA. This is because the diagwire became extremely hot ($\geq$ 1,170 °C), causing excessive electron thermionic emission, even forming concentrated jets of electrons. With a fixed input power, an increase in electron current correspondingly lowers the ion current to the cathode, as a consequence of which the neutron rate decreases.

The electron jets generated by the diagwire configuration were highly concentrated, and during one incident the jet hit the port view window and cracked the view window (shown in Fig. 5.4). Similar electron jets were observed in other configurations but were not intense enough to crack the window. Furthermore, permanent magnets placed close to the window deflected the beam, confirming that the jets were primarily constituted of electrons.

As previously stressed, the ammeter (in the power supply) cannot differentiate between the electrons leaving the cathode or the electrons lost due to ions reaching

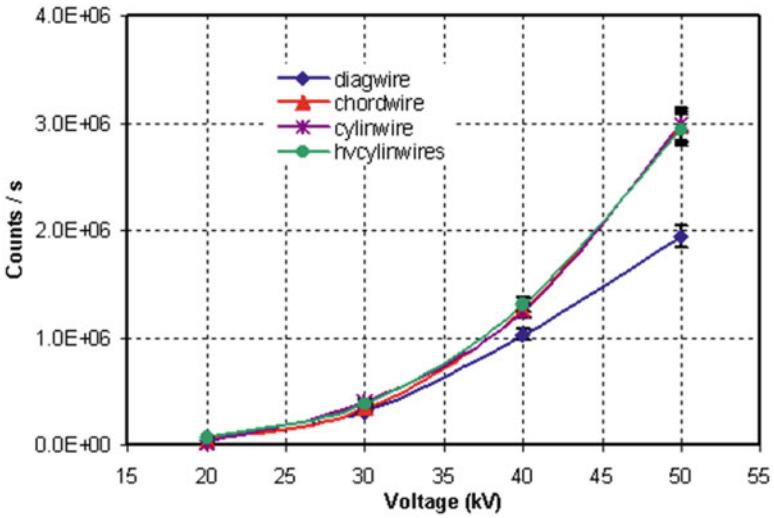

Fig. 5.3 D–D neutron production rate (NPR) versus voltage plot for a fixed power input from the power supply. The lowest number of neutrons was produced with diagwire configuration where the thermionic emission was a maximum [2]

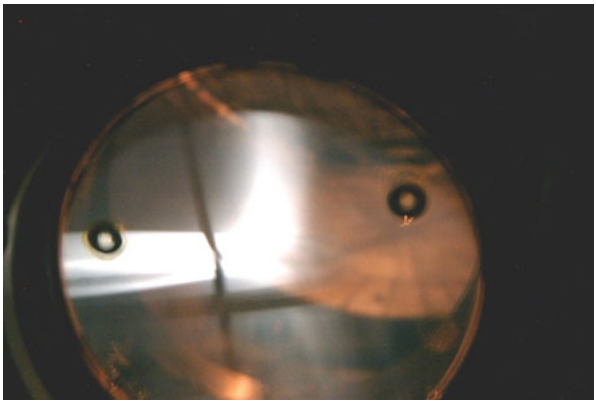

Fig. 5.4 The damaged glass window looking into the IEC chamber. Intense electron jets from the diagwire configuration increased the local heat load on the window, cracking it as shown [2]

the cathode (recombination at the cathode surface). Thus for a constant power supply current, if the electron current increases, the resulting decrease in ion current causes a lower fusion rate. Therefore, in general thermionic emission should be minimized to achieve higher fusion rates in internal source gridded IEC operation (versus low-pressure external ion source IECs where, as shown in Fig. 5.1, an inward flowing electron current is desirable for virtual electrode formation).

To study electron emission effects further, a general equation for the ion recirculation current derived by Thorson and colleagues [4] was modified by Murali and colleagues to account for thermionic emission as follows [2]:

$$I = \frac{\eta[I_{meas} - I_{th}]}{(1-\eta^2)(1+\delta)}, \tag{5.2}$$

$$\text{where } I_{th} = \Lambda \times A \times T^2 \times e^{-e\phi/kT}. \tag{5.3}$$

Equation 5.3 is known as the Richardson–Dushman equation for thermionic emission [5, 6], with T temperature in K, where k is the Boltzmann constant. For illustration, Eq. 5.2 can be applied to the diagwire experiments associated with Fig. 5.2. There A is the surface area of the heated diagwire monitored by the pyrometer ($\sim 0.06\ \text{cm}^2$), Λ is a constant ($\sim 120\ A \times \text{cm}^{-2} \times K^{-2}$), I_{meas} is the (measured) power supply current (20 mA), η is the geometric transparency of the grid ($\sim 92\ \%$), ϕ is the work function of the wire (2.5 eV), and δ is the secondary electron emission coefficient, which is assumed to be ~ 1 [4]. All other effects are assumed to be negligible so the average ion energy roughly stays constant. Thus, secondary electron emission and the number of ion passes through the core remain unaltered in this example.

From Fig. 5.3 we note that the neutron rate for the diagwire configuration at 50 kV is $\sim 30\ \%$ lower than for the other configurations. At 50 kV, 20 mA, the temperature of the diagwire configuration was the highest (1,170 °C), causing a high thermionic electron current, decreasing in the ion current, which in turn lowered the neutron rate.

The decrease in the recirculating ion current due to the increase in electron current is accounted for in Eq. 5.2. Using Eq. 5.3 the thermionic current (I_{th}) is found to be 6.3 mA with the diagwire temperature $T = 1{,}170$ °C and a work function $\phi = 2.5$ MeV. However, this is ~ 1 mA less than needed (7.4 mA) for the reaction rate in the diagwire configuration to match the neutron rate of the other configurations. There are many possible reasons for such a discrepancy, e.g., that the area surrounding the region monitored by the pyrometer could also be hot enough to contribute additional electron current.

Thermionic emission can be important when the grid is modestly hot (even before reaching the melting temperature) if uneven grid heating occurs. Such electron emission can become significant even at low input powers (< 10 kW) if asymmetric heating exists, as explained in the next section.

5.5 Study of Effects of Asymmetric Heating of the Cathode Grid

The asymmetric heating phenomenon first observed by Murali and colleagues at the University of Wisconsin, Madison [1], can occur as a consequence of uneven distribution of the ionization source that causes localized heating of the grid as illustrated in Fig. 5.5. Then ions from the asymmetric source bombard the grid, depositing energy unevenly around it.

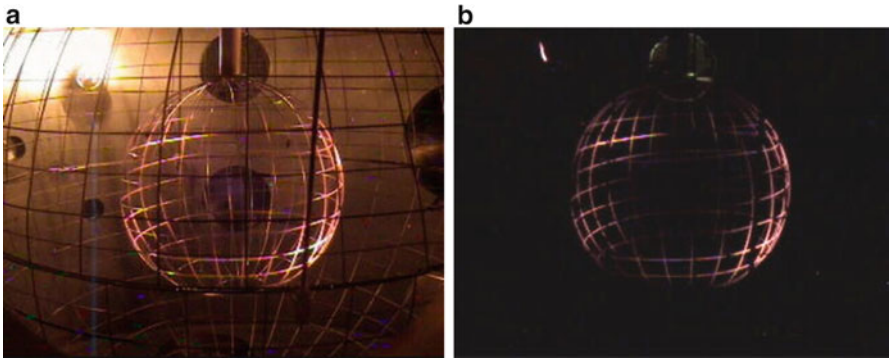

Fig. 5.5 (**a**) A large 20-cm-diameter central cathode grid during operation. (**b**) Picture taken soon after the shutdown showing the residual heat distribution around the grid [2]

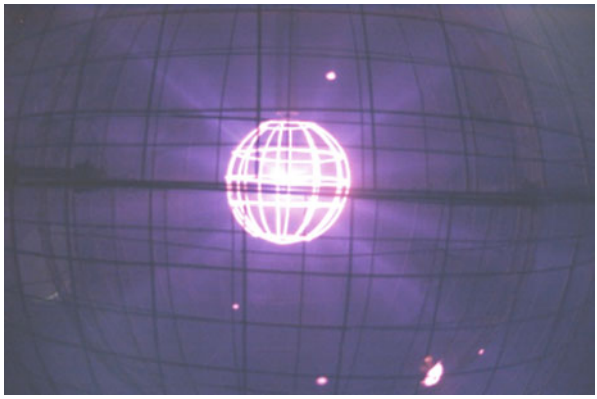

Fig. 5.6 Electron jets detected on the wire mesh placed around the intermediate grid (20 kV, 25 mA, 7-mTorr chamber pressure) [2]

In the experiment illustrated in Fig. 5.6, an intermediate grid (35 cm diameter) with fine mesh around it (~ 1 mm spacing) was used to intercept outgoing electrons. In this case, a concentration of electrons formed a "jet" or beam of electrons that show up in the picture as a hotspot on the fine mesh.

In the "jet" experiment, the IEC device was operated in a Paschen breakdown regime at a high chamber pressure (~ 7 mTorr). The plasma was sustained by impact ionization by both electrons and ions without the aid of an external ionization source. Under identical conditions the jets and hotspots diminished when an RF ionization source was turned on (see Fig. 5.7). In this case, the RF source was applied to the intermediate and outer grids simultaneously, as shown in configuration C in Fig. 5.8. Several other modes of operation are also illustrated in Fig. 5.8, and a summary of the operational stability for these modes is given in Table 5.1.

As series of experiments using added RF power were run to further examine these effects. Each of the modes in Fig. 5.8 had varying degrees of ionization uniformity around the grid. Such variation allowed varying degrees of control on

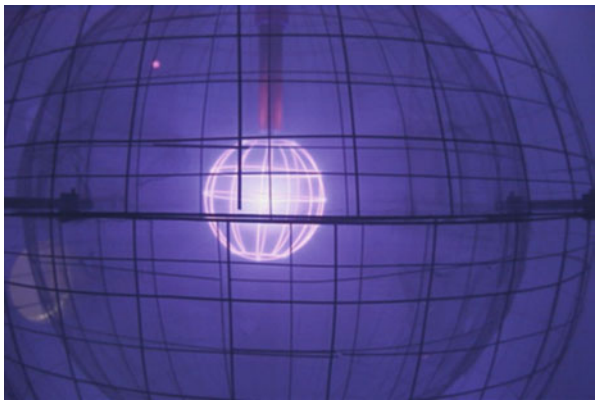

Fig. 5.7 Fewer electron jets are observed when a RF ionization source was used at 20 kV, 25 mA, 7 mTorr. This photo can be compared to Fig. 5.6 [2]

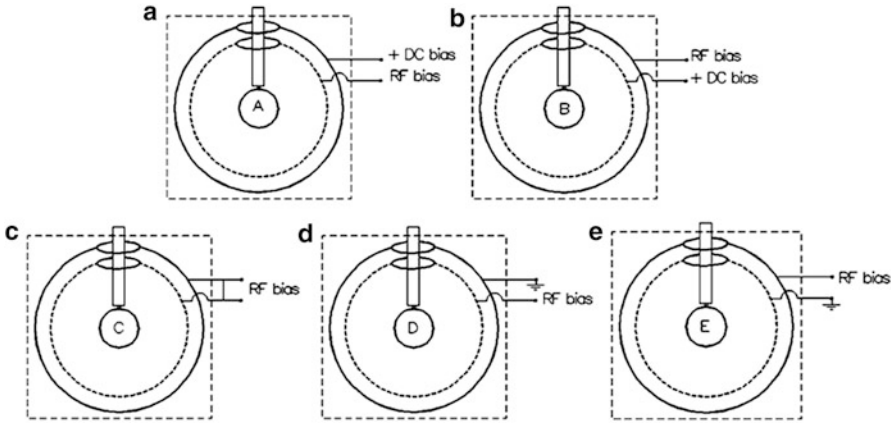

Fig. 5.8 Various bias configurations tested at University of Wisconsin, Madison. The cylindrical chamber wall is always maintained at ground potential [7]

the ion current going to the cathode. This result demonstrates how an uneven ion source distribution can cause preferential high ion/electron current channels that can be homogenized using a uniform ionization source. The uneven distribution of electrons leaving the grid and recirculating ions can cause asymmetric heating of the cathode. Use of a uniform ionization source is especially important at lower pressures where jet heating can be most severe.

In one experiment, when an RF ionization source was used at 2-mTorr chamber pressure, for reasons presently not understood, asymmetric heating caused the top and bottom halves to heat, while the central region of the cathode remained relatively cold. Furthermore, experiments were conducted by operating two of the three electron filaments in the IEC device at a given time. The temperature of the spot B (see Fig. 5.9a) on the central grid varied significantly as the electron sources were switched (on/off), as shown in Fig. 5.9b.

Table 5.1 Stability of plasma with various (intermediate and central) grid bias configurations [7]

Configuration	Intermediate grid	Outer grid	Stability of plasma at ~ 2 mTorr, 35 kV, 40 mA
A	RF signal	+DC bias	Stable
B	+DC bias	RF signal	Unstable
C	RF signal	RF signal	Stable
D	RF signal	Ground	Unstable
E	Ground	RF signal	Stable but requires higher RF power

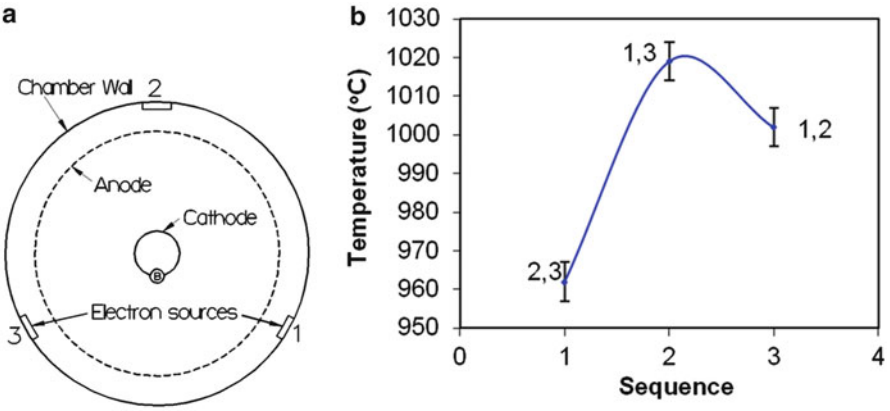

Fig. 5.9 (**a**) Top view of the IEC cross section showing the arrangement of filament electron sources. (**b**) Three experiments conducted in a sequence by switching the electron sources 1, 2, and 3 (shown in **a**) showed a significant temperature variation of a given spot on the grid [2]

The variation in temperature in this experiment was caused by higher ionization rates in the regions close to the electron sources. This can be explained as follows. An ion microchannel forms and provides the ion recirculation pathway around the cathode. The ion microchannels that form in the close vicinity of an electron source have higher concentrations of recirculating ions relative to other microchannels. This is because the electron impact ionization occurs more often in this region due to the availability of surplus electrons. Some of these ions hit the grid and deposit their energy on the portions of the grid wires in their pathway, thus resulting in localized grid heating, such as observed in Figs. 5.5 and 5.10. The temperature distribution of such an asymmetrically heated grid is shown in Fig. 5.10. Sometimes asymmetric heating was observed even when all three filaments were turned on.

The selective heating of certain regions of the central grid can cause the temperature difference between the different zones to be as high as ~300 °C (see Fig. 5.9). The outcome of such asymmetric heating could cause thermionic electron emission from the hotter regions even at low input power operation. This is especially important when a low work function material, such as stainless steel, is used in the construction of the cathode grid. Then very large thermionic electron emission rates can occur in elevated temperature regions.

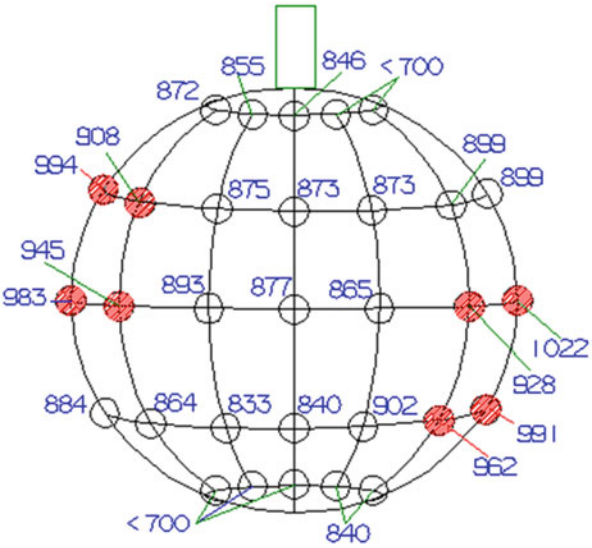

Fig. 5.10 Asymmetric temperature distribution as measured on the central grid at 25 kV and 15 mA, 2 mTorr. Temperatures are shown in °C. Red circles are the hottest portions of the grid [1]

5.5.1 *Treatment of Uneven Temperature in Emission Equations*

If the fraction of the grid surface f where the temperature is high enough to cause thermionic emission is known, the effect must be included in Eq. 5.1. Such measurements are tedious with a single pyrometer and are best done with a scanning pyrometer that can simultaneously measure the temperature of the entire grid and digitally map the readings.

The equation for thermionic emission from the cathode, corrected for the fractional surface with hot zones, now becomes

$$I_{th} = \sum_i f_i \times \Lambda \times \alpha \times T_i^2 \times e^{-e\phi/kT_i}. \tag{5.4}$$

Here f_i is the fraction of the grid surface area at a temperature T_i. This summation approximates the continuous temperature distribution by a set of discrete values.

With asymmetric heating, the thermionic emission can become significant even before grid meltdown or deformation occurs. This effect must be accounted for in any recirculating ion current calculations, especially for higher input powers (e.g., $>$ 10 kW for a 10-cm-diameter spherical cathode grid). However, thermionic emission also has a negative feedback effect – the increased electron emission causes decreased ion current and hence a decreased heat load. This automatically decreases the grid temperature, so that thermionic emission decreases. The net effect is that the recirculating ion current to the grid does not increase linearly with the power supply's meter current if the temperature of the grid or portions of it is so high that the thermionic emission becomes significant (e.g., $T >$ 1,100 °C for stainless steel and >1,600 °C for W-25 %Re).

5.6 Grid Wire Material Selection

A cathode grid material should have a high melting point, low sputter yield, and high work function and must be economical.

If the sputter yield of the material is high, the high-voltage stalk can be coated with sputtered material. For instance, stainless steel sputters profusely even at low voltages and often deposits on the high-voltage stalk (as shown in Fig. 5.11).

Measurement of the surface resistance along a stalk like the one shown in Fig. 5.11, used with a stainless steel cathode, is shown in Fig. 5.12. Measurements were done between equally spaced consecutive points.

A material with high work function will emit fewer electrons at high input power (i.e., at higher grid temperature). Hence with this material selection, a higher ion current fraction can be achieved for the same power supply current.

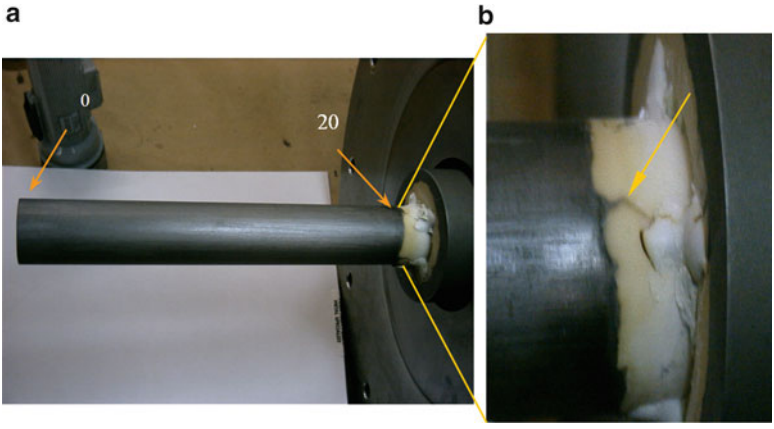

Fig. 5.11 (**a**) A high-voltage stalk coated with sputtered stainless steel material from the grid. (**b**) The resulting electric breakdown path from the stalk to the chamber walls [2]

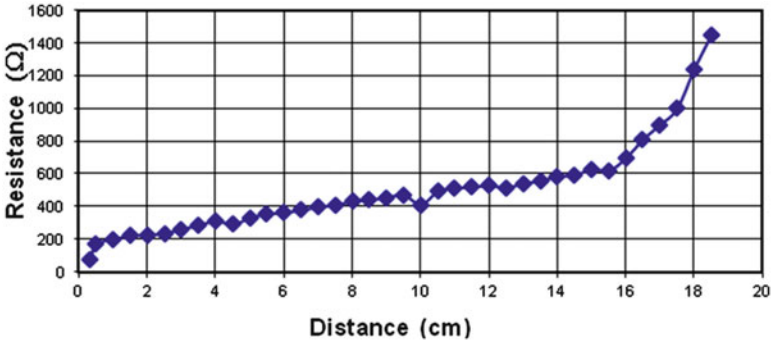

Fig. 5.12 Sputter-coated stalk resistance variation with distance. The resistance was measured in small increments of distance along a straight line [2]

The maximum current a grid can handle depends on the rate at which it can radiate the power (otherwise it will overheat, deform, and/or melt). This maximum current before melting or deforming can be calculated by assuming that all the energy of the bombarding ions is deposited into the grid wires. Then an estimate of the maximum "safe" operating temperature is needed. For example, for stainless steel the melting point is ~ 1,800 °K, but the deformation of the grid via sagging begins much earlier. Assuming that sagging occurs at ~ 1,500 °K and equating the black body radiation rate to the input power (cathode voltage V multiplied by the power supply current I in Amperes), the maximum current corresponding to the selected "safe" temperature is given as

$$I = A\varepsilon\sigma T^4/V. \tag{5.5}$$

Here A is the surface area (e.g., ~ 76 cm^2 for a 10-cm grid made of 0.08 cm diameter with 5 latitudes and 12 longitudes), ε is the emissivity of the material (~ 0.15 for stainless), σ is the Stefan-Boltzmann constant (5.67×10^{-8} W × m^{-2} × K^{-4}), and T is the temperature of the grid (set at ~1,500 °K for "safety"). This gives 9.5 mA of ion current at 200 kV, whereas the power supply can produce 75 mA at 200 kV. Hence, in this case, stainless steel does not allow full use of the available power supply. (This calculation presumes that the whole grid was uniformly heated to 1,500 °K; if asymmetric heating were to occur, the grid would be limited to much less input power due to the high thermionic emission in hot zones.)

Selection of a grid wire material with a higher "sagging" temperature would seem to be desirable. Still, many experimental devices in various labs have used stainless steel grids with success. The reason for selecting stainless steel is that it is easily obtained and easily formed into a grid. These grids have generally not been run at very high input powers such as assumed here.

In addition to seeking a higher sagging temperature, reduced thermionic emission is desirable. Though platinum seems to be the best material to reduce emission, as seen in Fig. 5.13, rhenium is generally preferred to reduce material costs. To further lower the cost, an alloy of W-25 %Re has been identified by the University of Wisconsin, Madison, researchers as an attractive material. Other materials may be selected for various reasons. As already noted, even stainless steel is a reasonable choice if operation at modest power levels is satisfactory. Indeed, it may be preferred due to its low cost and ease of construction.

Various materials shown in Fig. 5.13, pure-Re, W, Mo, Ta, and Ti, plus alloys such as W-5 %Re, W-25 %Re, and Mo-25 %Re were considered in some detail [2] at the University of Wisconsin, Madison. The W-25 %Re alloy was found to be very attractive for a 10 cm cathode grid in a device running below 130 kV. This grid has now been run to much higher voltages (~ 180 kV) and has shown satisfactory performance. It is relatively cheap, has a high melting point (2,800 °K), a low sputter yield, and is easy to manufacture by spot welding. To test this material, the 10-cm grid was run at various voltages in the range of 30–130 kV and with the current range of 30–180 mA for over 1,000 h [2]. In this test, all sharp

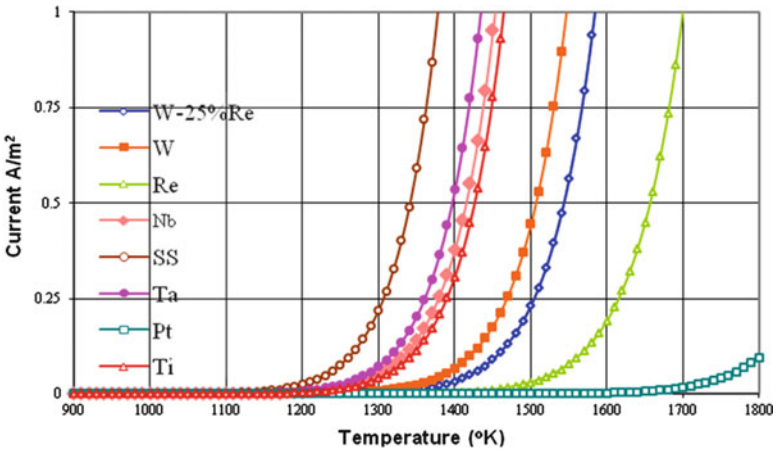

Fig. 5.13 Thermionic emission from Eq. 5.2 for various materials versus temperature

edges created during the manufacture were removed to avoid high local field emission. Very low sputtering was confirmed over the extended run time, adding to the attractiveness of this alloy.

5.7 Construction of Grids

Prior to standardized grid manufacturing, most groups resorted to manual grid construction. Wires were typically made of stainless steel or tantalum. These wires were turned into loops using a spot welder prior to arranging them in the form of a grid and securing these loops together, once again using a spot welder. A "mold" cut from wood or other material was often used to hold wires in place while spot welding them. It was realized early on that despite its low cost and ease of use, stainless steel is not ideal, as it sputters profusely and melts at a relatively low temperature. Thus, a variety of other materials have been used in some IECs. Though tungsten was a preferable alternative, it was not widely used due to the lack of accessible welding techniques. Attempts were made to use intermediate materials like nickel foil, placed between the two tungsten wires that needed spot welding. The nickel melted and secured the tungsten wires [8]. However, these grids were fundamentally limited by the melting point of the nickel so the advantages of tungsten wires could not be fully exploited. As previously discussed, the University of Wisconsin group selected W-25 %Re for grid construction and testing [2]. Experience with this alloy has been very encouraging. For example, the stainless steel wires previously used by Murali [2] lasted for under a week depending on the power load. In contrast, with the W-25 %Re alloy, the grid lasted for over 2 years. It was eventually replaced when a cleaning attempt (using a sand blaster) unfortunately turned the smooth surface texture into a rough surface, rendering the grid useless (Ashley RP, 2002, University of Wisconsin, Madison, private communication). Otherwise the grid could have continued in use for some time.

5.7.1 Rapid Prototyping for Grid Construction

In an attempt to standardize the grid construction, Chris Dobson and Ivana Hrbud at NASA's Marshall Space Flight Center (MSFC) adopted some rapid-prototyping technologies to construct a composite grid with a metal coating [9]. This technology allows the entire grid to be one composed of a single piece of material versus overlapping loops with spot welding. These grids were used in several experiments at NASA's MSFC, but few details are available. Their plan was to eventually produce hollow-looped stainless steel grids using aluminum templates. This design would allow internal cooling. However, that design was not implemented in practice.

Subsequently a very successful rapid prototyping technique was developed at the University of Wisconsin, Madison [10]. The technique is illustrated in Table 5.2 along with the description of the grid construction procedure. This procedure produces a reproducible, uniform grid, but unlike the NASA work, it still requires spot welding.

Another commonly used design for the cathode grid uses a series of plates/disks (such as shown in Fig. 5.14). The idea of using such disks for the construction of cathode grids was first suggested by P. T. Farnsworth in his original patents [12, 13]. The major advantage of using such grids is that while the grid transparency is maintained constant, the surface area for radiating the heat away from the grid increases. These disks are cut using lasers, though powerful water jets can also be used.

One of the principal considerations while building a grid is to improve the grid transparency. As we explained earlier, operation in the "Star" mode (microchannels) depends more on the "effective" transparency versus the geometric transparency. However, operation in other modes is very dependent on the geometric value, so improvements in the geometric transparency are very desirable. One such technique that was developed by Murali and colleagues at Los Alamos National lab for this purpose used a combination of several wires with different diameters to accomplish the desired grid transparency [14]. Thicker wires were used to construct a strong skeleton structure, while thinner gauge wires were used to fill in the gaps to obtain the desired spacing. The grid constructed in this way is shown in Fig. 5.15. The geometric transparency achieved with this technique was 95 %. With the large openings in these grids, microchannels form, providing an even higher effective transparency. Still, many ions eventually scatter out of the microchannels and hit grid wires. That factor in turn depends on the geometric transparency. The high geometric transparency is valuable in the sense of reducing those collisions, increasing ion recirculation times.

5.7.2 Using Carbon Nanotubes to Construct Grids

Carbon nanotubes (CNTs) are known for their robustness and excellent physical characteristics that make them an ideal material for grid construction. The CNTs have a minimal footprint and are capable of not only carrying maximum current but

Table 5.2 Standardized grid construction procedures developed at the University of Wisconsin, Madison [10]

	Figure	Procedure
1.		Plastic model created using rapid prototyping
2.		Rubber mold created using the plastic template
3.		Wax is poured into the rubber mold and is left there until it solidifies
4.		A wax template is created using the rubber mold
5.		The wax template is used to keep the wires positioned until it is spot-welded
6.		After spot welding the wires, the wax template is melted away using a hot air gun. The wax can then be reused
7.	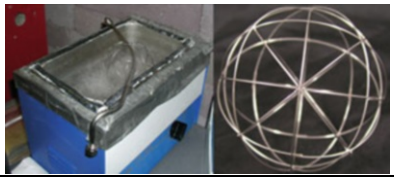	The grid is cleaned in an ultrasonic cleaner to remove any residual wax from the grid surface. The grid is now ready for use

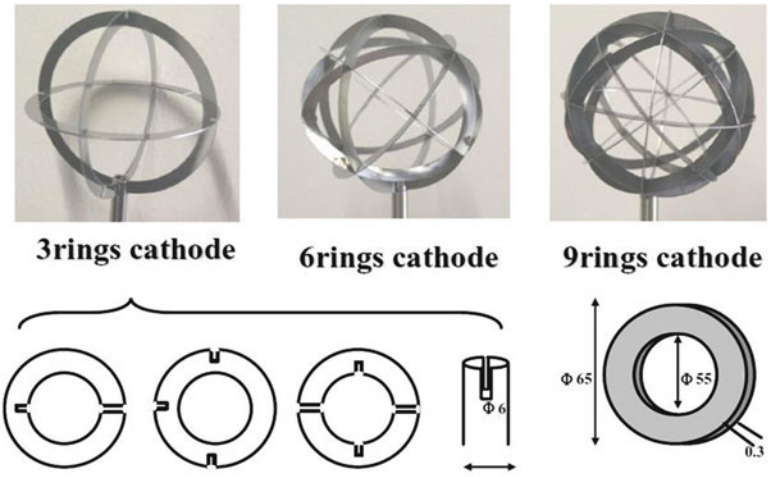

Fig. 5.14 Grid construction technique using disks. Several different types of cathodes (3, 6, and 9 rings) can be constructed using these precut disks [11]

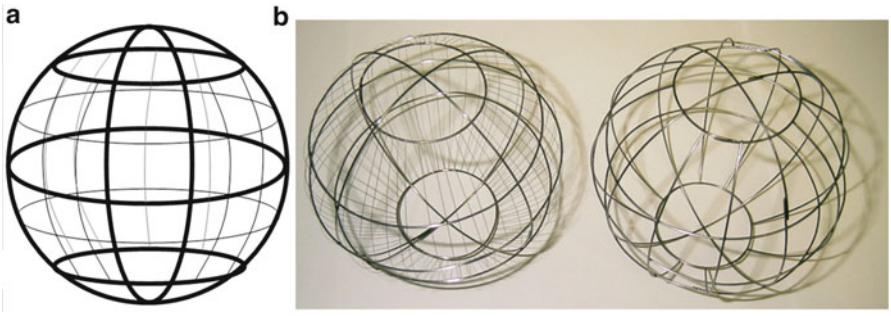

Fig. 5.15 (**a**) Grid constructed with wires that have a combination of gauges. (**b**) Two different designs using the combination of wires. The two grids shown here have equivalent geometric transparency [2]

also withstanding very high temperatures. Murali and colleagues were the first to suggest that CNTs could be used for the grid construction [15]. A running grid technology was suggested, wherein grid wires would be continuously replaced by constantly moving them across a dual stalk design as shown in Fig. 5.16.

The major advantage of the grid design shown in Fig. 5.16 is that the grids could be operated indefinitely. As pointed out by Murali and colleagues, the transparency of this grid could be very high (as much as 99.9999 %), and such transparencies make this grid suitable for the IEC Periodically Oscillating Plasma Sphere (POPS) concept [15]. The spherical shape of the cathode is achieved by maintaining a differential stress on the grid wires as they move across the two high-voltage stalks. Furthermore, these two stalks also offer a symmetric distribution of electric fields within the IEC

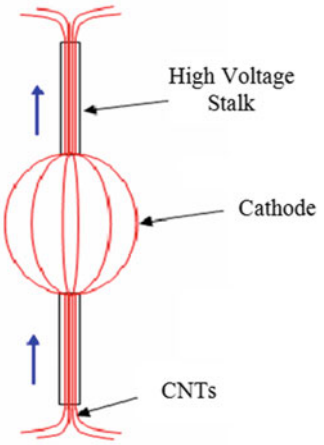

Fig. 5.16 Running grid design of a CNT-based grid [15]

device. Though very long CNTs are not yet available, carbon fibers or simple CNT wires could be used, and such materials also offer very high geometric transparency when used in cathode construction.

5.7.3 Multi-grid Design and Fabrication

The improvement of charged particle confinement in IEC systems is of paramount interest for higher intensity neutron sources and possible IEC fusion power plants. Sedwick and McGuire proposed a method of improving ion confinement times by electrostatically focusing ion beams to keep them away from cathode grid wires [16]. The practical implementation of this concept requires the use of three or more independently biased, concentric spherical grids (multi-grids). The potentials on these grids would be set so as to provide the desired confining electrostatic field. By minimizing the rate of ion–grid impact, the electron current is also reduced because the majority of streaming electrons are emitted as secondary electrons when ions collide with the cathode. Following theoretical studies of this configuration, an experiment was set up.

However, multi-grid construction poses a challenge. A decision was made to construct the multi-grid portion of the experiment with five concentric spherical wire grids. This required development of a standard method for constructing the grids. After considering many different options for grid wire materials, 1-mm-diameter 304 stainless steel wire was chosen for all grids so the structures would have sufficient rigidity to survive normal handling, and so that conventional spot-welding techniques could be implemented with ease. As discussed in the previous section, stainless steel is not ideal. However, it provides the operation with reasonable ease of construction, a paramount factor in this multi-grid design. A jig to hold the 304 stainless wire in place at the

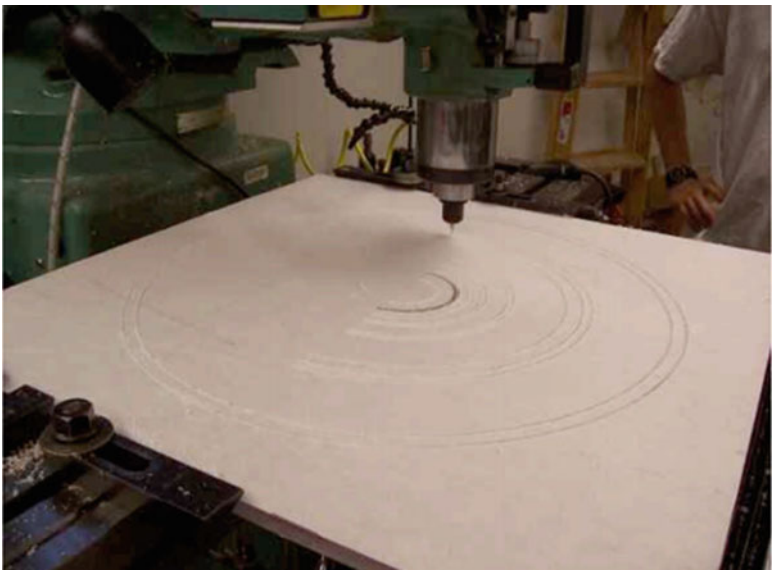

Fig. 5.17 Fabrication of a grid wire jig [17]

proper curvature for spot welding was machined from a piece of polycarbonate as shown in Fig. 5.17.

The wire was laid in the trough and spot-welded to the desired diameters. It was then removed from the jig. The wires that were to become longitude lines were then annealed to remove residual bending stress so they could be cut and still maintain the desired radius of curvature. After some limited experimentation, it was discovered that running a current of 35 A through the hoops for 1 min would give the desired effect. When less current was used for less time, the wire would show some residual "springback," but if more current was used longer, the wire would tend to deform significantly under its own weight and the forces applied by the alligator clips used to supply the current.

Figure 5.18 shows the atmospheric annealing of one of the grid wires. Once the annealing of the longitude lines was complete, they could be cut in sections and maintain the desired radius of curvature. The latitude lines were not annealed because they did not need to be cut during the assembly process. In order to attach the longitude wires to the polar feedthrough, special stainless steel rings were fabricated from 1/16" plate using a water-jet cutter. These rings provided structural support and an electric connection for the grids. The eight longitude wires were then spot-welded to the support rings. The support rings were designed to fit onto custom machined aluminum parts that were held onto the alumina feedthrough stalk at the appropriate radius by a setscrew. After the longitude lines were welded to the retainer rings, the latitude lines were spot-welded onto the outside of the longitude lines at the appropriate position. A simple wire spacer was used to locate the hoops

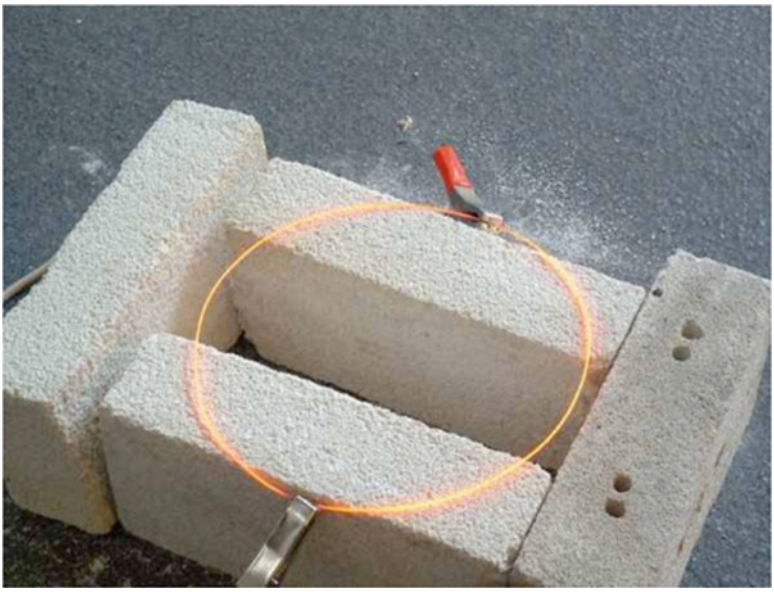

Fig. 5.18 Atmospheric annealing of longitudinal wires to remove residual bending stress [17]

concentrically around the poles. Errors in the actual location of the longitude lines were of concern because this could result in a perturbation of the latitude line position. In general, this construction variability was measured to be less than 5 %.

Figure 5.19 shows all of the completed wire grids. Slight asymmetries in the grid wires are visible to the naked eye, but position errors of the latitude line locations were all measured to be less than 8 % of the respective radius. Longitude line errors were significantly less than that.

In order to install the grids in the final multi-grid system, the grids had to nest one inside the other. This was accomplished by again cutting the longitude lines near the equator. The cut was made actually just "south" of the equator, above the southern "tropic" latitude line. This asymmetric cut was used to improve the ease of reassembly. It was desired to have one well-located, stiff wire end and one more easily manipulated, less well-located wire end that would be moved to align with the stiff end. This was assumed to be easier than lining up two wire ends of moderate stiffness.

The resulting "half-grids" resembled a flower blossom (as shown in Fig. 5.20) and a radar dish or directed listening device (as shown in Fig. 5.21). When the grids are assembled in the chamber, 1" sections of 1/16" diameter stainless steel tubing are crimped on the longitude wire ends on the "radar" half, which allow the insertion and perfect alignment of the longitude lines on the upper, "blossom" half. Figure 5.22 shows the completed multi-grid IEC assembly inside the vacuum chamber. Experiments using these multi-grids are discussed later in Chap. 8.

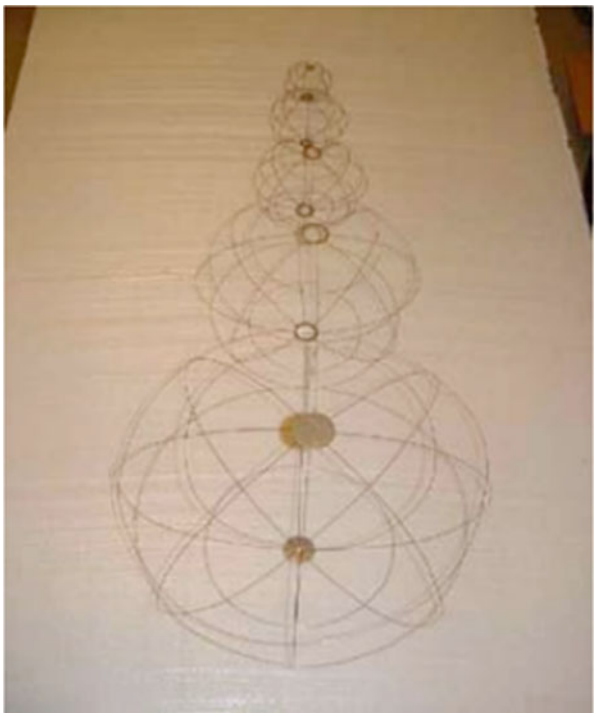

Fig. 5.19 A series of finished grids that are then combined to create the multi-grids [17]

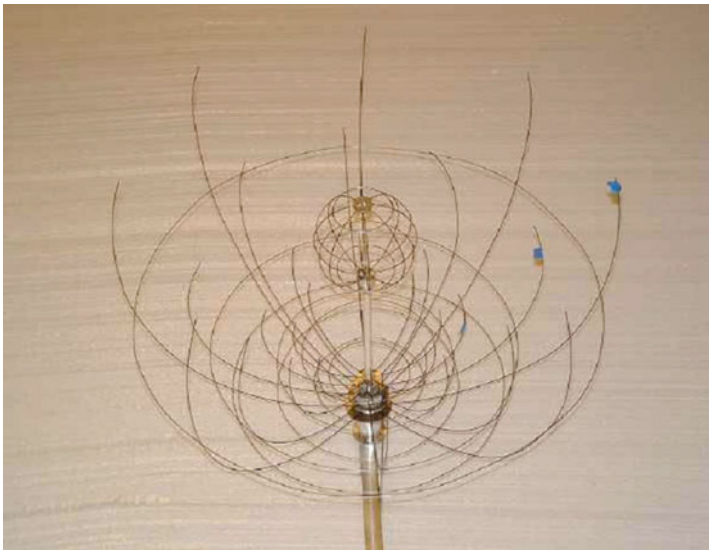

Fig. 5.20 The "awesome blossom" half-grid [17]

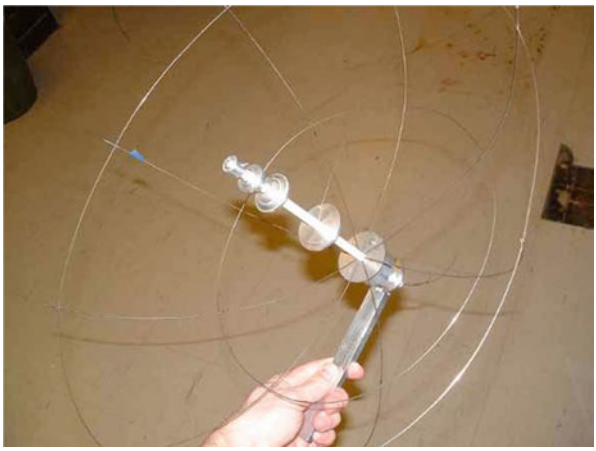

Fig. 5.21 The "radar" with alumina feedthrough and aluminum supports [17]

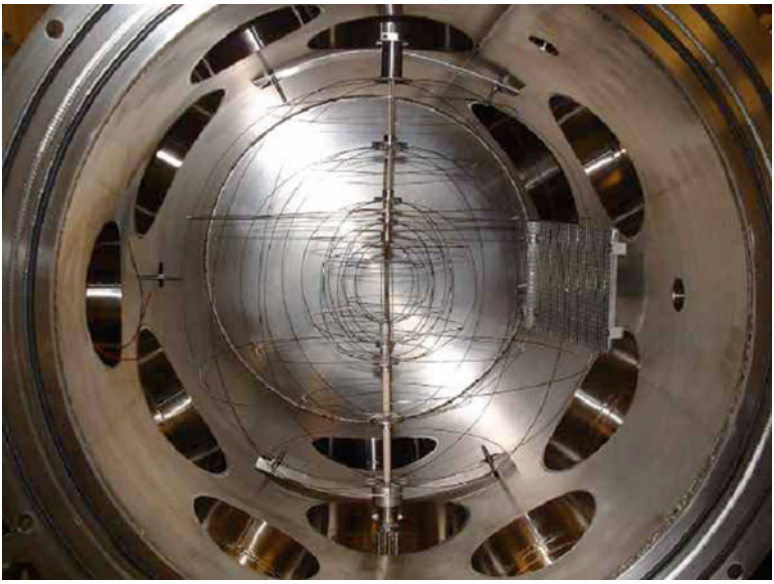

Fig. 5.22 The multi-grid IEC in the vacuum chamber [17]

5.8 Summary

In conclusion, the construction of the IEC grid is complex in that a number of factors contribute to grid performance relative to key issues such as neutron production and ion confinement times. In this chapter we have discussed issues that affect the selection of the grid materials and methods for assembling a grid. In Chap. 6, related issues of grid geometry are discussed. Another closely related aspect of the IEC is the

design of the grid stalk, discussed previously in Chap. 4. Connection of the stalk to the grid is an important consideration in the design. The connection must provide good structural support and also blend into the stalk design in order to prevent local bombardment and high-voltage breakdown. Thus, in order to optimize IEC operation, care must be taken in the design and treatment of all three of these factors – stalk, grid materials, and geometry. In addition, the application that the IEC is intended for may dictate the fuel (D, D–D, D–^{3}He, etc.) hence selection of the voltage and pressure range for operation. Most grids currently used employ a fairly simple construction method where the grid wires are spot-welded after wrapping the wires around a form that provides the spherical shape desired. However, in some cases where the power loading on the grid is extremely high, coolant-carrying tubes may be used instead of wires for the construction, but this increases the grid wire size and hence decreases the grid transparency, thus adversely affecting the device performance. Carbon nanotubes (CNTs) offer an attractive alternative to this complex grid construction, because the wires made from CNTs can be used to carry large currents while simultaneously conducting heat away from the grid. The large currents in such wires also deflect oncoming ions and hence reduce the heat load on grid wires. However, experiments are yet to be conducted to confirm this concept.

For many IEC operations, a long grid lifetime is desirable, and this implies minimizing grid sputtering, not only by material selection but with choice of plasma operational modes such as using Star mode to minimize ion bombardment. Electrons play a strong role in the IEC plasma, but often the source rate of electrons, particularly for the core plasma, is a complex function of grid temperature, thermionic emission rates for the material selected, and ion bombardment rates. In addition to this "passive" control, some experimentalists have added additional sources of electrons, such as thermionic emitters, near the wall which produce electrons that spiral around an added grid in that location. This technique provides an enhanced ion source near the wall which is desirable to maximize the ion acceleration by the cathode. The electrons in the core region are more difficult to control because the bulk of them come from emission on the inner surfaces of the cathode grid. Some researchers have discussed including thermionic emitters in the cathode grid region to provide a controlled source of electrons in the core region for formation of the desired double potential well. However, experimental data for such operation is not available, so that remains a research issue.

References

1. Krupakar Murali S, Santarius JF, Kulcinski GL (2010) Study of thermionic electrons in an IEC device. Plasma Sources Sci Technol 19:045029
2. Krupakar Murali S (2004) Diagnostic study of steady-state advanced fuel (D–D and D–^{3}He) fusion in an IEC device. Ph.D. dissertation, University of Wisconsin, Madison
3. Krupakar Murali S, Santarius JF, Kulcinski GL (2009) Ion flux mapping in an inertial electrostatic confinement device using a chordwire diagnostic. Phys Plasmas 16:103301

4. Thorson TA, Durst RD, Fonck RJ, Wainwright LP (1997) Convergence, electrostatic potential, and density measurements in a spherically convergent ion focus. Phys Plasmas 4(1):4
5. Richardson OW, Young AFA (1925) The thermionic work-functions and photoelectric thresholds of the alkali metals. Proc R Soc Lond A 107:377–379
6. Herring C, Nichols MH (1949) Thermionic emission. Rev Mod Phys 21:185
7. Krupakar Murali S, Santarius JF, Kulcinski GL (2010) Study of various modes of operation of an IEC device. J Fusion Energy 29(2):141–145
8. Thorson TA (1996) Ion flow and fusion reactivity characterization of a spherically convergent ion focus. Ph.D. dissertation, University of Wisconsin-Madison
9. Dobson C (2000) IEC research at MSFC. CDDF report FY2000, Marshall Space Flight Center
10. Radel RF (2007) Detection of highly enriched uranium and tungsten surface damage studies using a pulsed inertial electrostatic confinement fusion device. Ph.D. thesis, Department of Engineering Physics, University of Wisconsin, Madison
11. Osawa H, Miyagi A, Tanaka R, Kiritani J, Sadahiro T, Tabata T, Ohnishi M (2002) Effects of cathode structure on neutron production in IEC device. In: Fifth US-Japan workshop on inertial electrostatic confinement fusion, University of Wisconsin, Madison
12. Farnsworth PT (1966) Electric discharge device for producing interaction between nuclei. US Patent 3,258,402
13. Farnsworth PT (1968) Method and apparatus for producing nuclear fusion reactions. US Patent 3,386,883
14. Park J, Nebel RA, Stange S, Krupakar Murali S (2005) Periodically oscillating plasma sphere. Phys Plasmas 12:056315
15. Murali K, Nebel R, Park J (2006) Carbon nanotubes in IEC fusion reactors. In: ANS 2006 annual meeting, Reno, 4–8 June
16. McGuire TJ, Sedwick RJ (2005) Improved confinement in inertial electrostatic confinement for fusion space power reactors. AIAA J Prop Power 21:697
17. Dietrich CC (2007) Improving particle confinement in inertial electrostatic fusion for spacecraft power and propulsion. Ph.D. dissertation, MIT Press

Chapter 6
Effect of Grid Geometry on IEC Performance

6.1 Introduction

Grid geometry plays an important role in the performance of a gridded spherical IEC device because the ion recirculation, and hence the reaction rate, is strongly affected by the orientation and size of openings in the cathode in grid design. In Chap. 3 we learned that cathodes with reasonably large openings face each other so that an ion could easily recirculate via ion microchannels (corresponding to a high effective transparency) and perform much better than either a solid cathode or a cathode with holes that do not point directly at each other (i.e., causing a low effetive transparency). Aside from these major features, various researchers have investigated the effect of a variety of grid opening geometries [1]. However, these experiments have been generally inconclusive, because they operated in the grid performance "saturation" regime, wherein the maximum symmetry is already achieved and any further increase in symmetry through addition of more wires does not cause significant improvement in the observed reaction rate. For example, the experiments conducted using the two entirely different grid geometries shown in Fig. 6.1 demonstrated such saturation.

Figure 6.2 shows neutron production rates (NPR) for experiments using the grids in Fig. 6.1. There was no strong difference in the fusion rate with either geometry. Subsequently, Murali and colleagues undertook a systematic study to better understand this issue [2].

A set of experiments were conducted by gradually building an entire grid with 12 longitudes and 5 latitudes (see Fig. 6.3), starting from a single loop [3]. This process uniquely allows the observer to monitor the performance of the device with improving symmetry.

While studying the effect of grid symmetry on IEC device performance, it is important to keep the system isolated from consistent variations. Such variations might be caused by a drifting power supply voltage or current, the chamber pressure,

G.H. Miley and S.K. Murali, *Inertial Electrostatic Confinement (IEC) Fusion: Fundamentals and Applications*, DOI 10.1007/978-1-4614-9338-9_6,

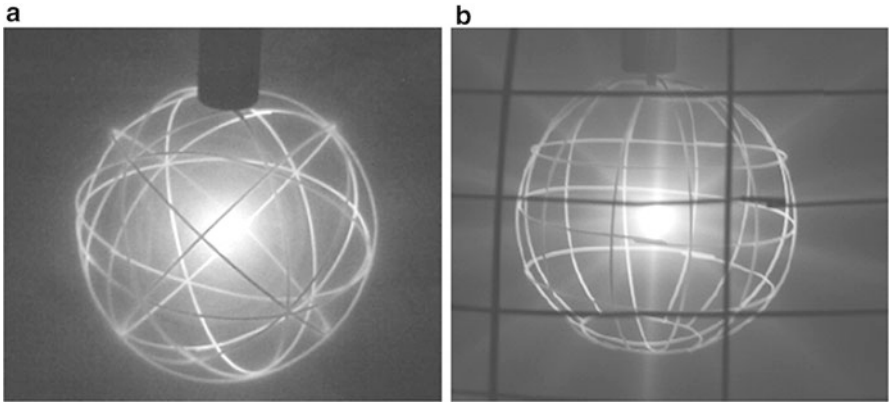

Fig. 6.1 (**a**) Geodesic (*symmetric*) design grid with uniform openings (*triangular*) between all the wires. (**b**) Globe grid (with latitudes and longitudes) with nonuniform openings between the wires. Both grids have the same diameter of 10 cm

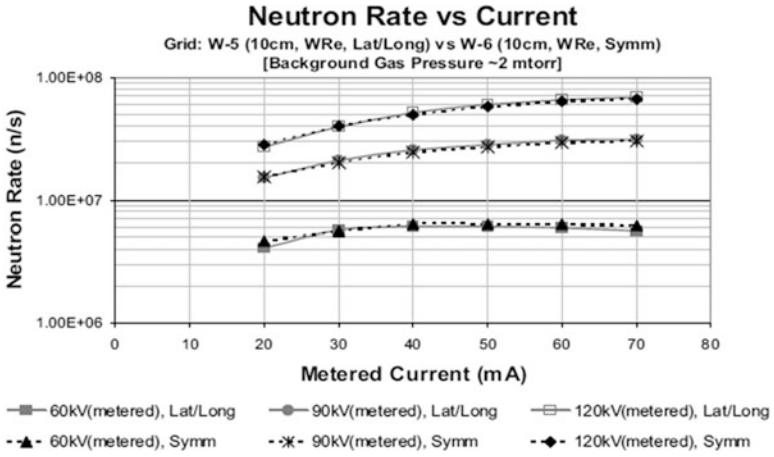

Fig. 6.2 Neutron production rate (NPR) observed at various voltages using the two different geometry grids of Fig. 6.1

or buildup of contamination. An effort was made to minimize each of these variations by closely monitoring the power supply, chamber pressure, and contamination concentration using various diagnostics. Another interesting feature of D–D reactions is that these reactions have a 50/50 branching ratio, as shown in Fig. 6.4.

Thus neutrons and proton reaction products are generated with equal probability. However, only a proton detector can be placed in a port inside the chamber (protons do not penetrate the chamber wall), so it is sensitive to location (spatial distribution)

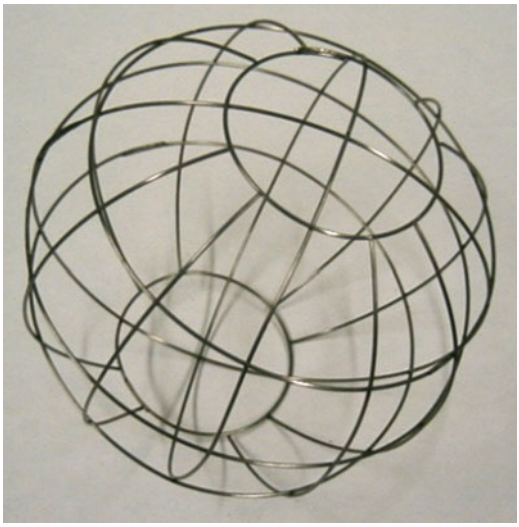

Fig. 6.3 Cathode grid with 12 longitudes and 5 latitudes [2]

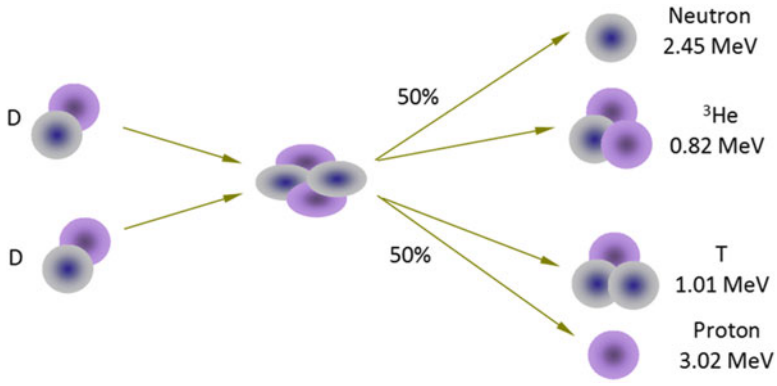

Fig. 6.4 D–D fusion reaction branching products

of the fusion reaction. In contrast, the typical ^{3}He neutron detector is placed outside the chamber and is surrounded by a plastic or paraffin wrapping, used to thermalize the neutrons. Such neutrons have a larger cross section for reactions with ^{3}He in the detector (see Chap. 11 for more on neutron detectors). Consequently the neutrons detected carry little information about spatial properties of the neutron source. The combination of placing the proton detector in close vicinity to the source and its detection of protons without thermalizing them gives the observer a unique capability to monitor the spatial distribution of the D–D reactions.

Figure 6.5a shows the two microchannels emanating from the single loop cathode, while Fig. 6.5b shows four such microchannels. Similarly more loops were added

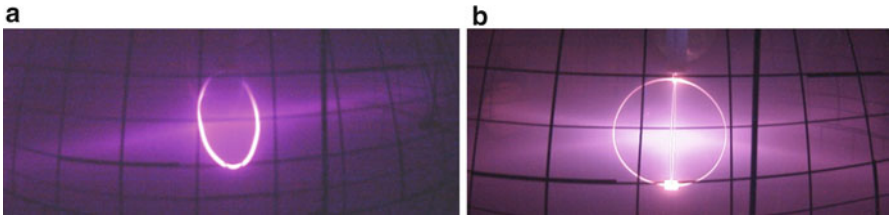

Fig. 6.5 (**a**) Single loop cathode grid in operation. (**b**) Double loop cathode grid in operation under identical conditions (Note: The variation in color is due to camera exposure) [2]

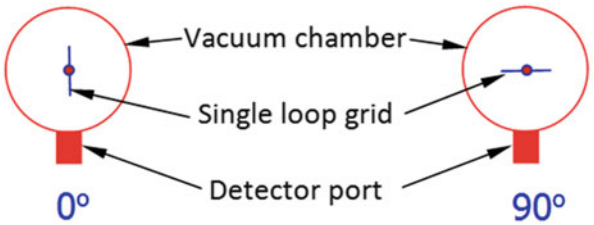

Fig. 6.6 Top view of the two orientations of the grid face-off (edge-on), 0°, and face-on, 90°, with respect to the proton detector. This detector was located inside a port to provide directionality and for protection from the plasma discharge [2]

Fig. 6.7 Various geometries used in the study, the numbers to the right of the name represent the number of loops, the letter C denotes the complete grid (also shown in Fig. 6.3) [2]

until the entire grid (shown in Fig. 6.3) was built. The proton detector measured the incident protons in two grid orientations, 90° and 0°, as shown in Fig. 6.6.

Figure 6.7 shows various geometries used in the study, and in Fig. 6.8, neutrons show the expected trend with increasing symmetry. However, the protons for XWLoopRe-1 by far produce the largest number of protons in the 90° orientation, contrary to one's expectations. This is because the proton detector sees a line source pointed face-on in the 90° orientation. When this happens, the volume of the source regime visible to the proton detector increases, and as a consequence the number of protons detected by the proton detector also goes up. Although the proton rate is high with the single loop configuration, the neutron rate is relatively low, because all spatial information is lost, owing to the detector placement and neutron moderation.

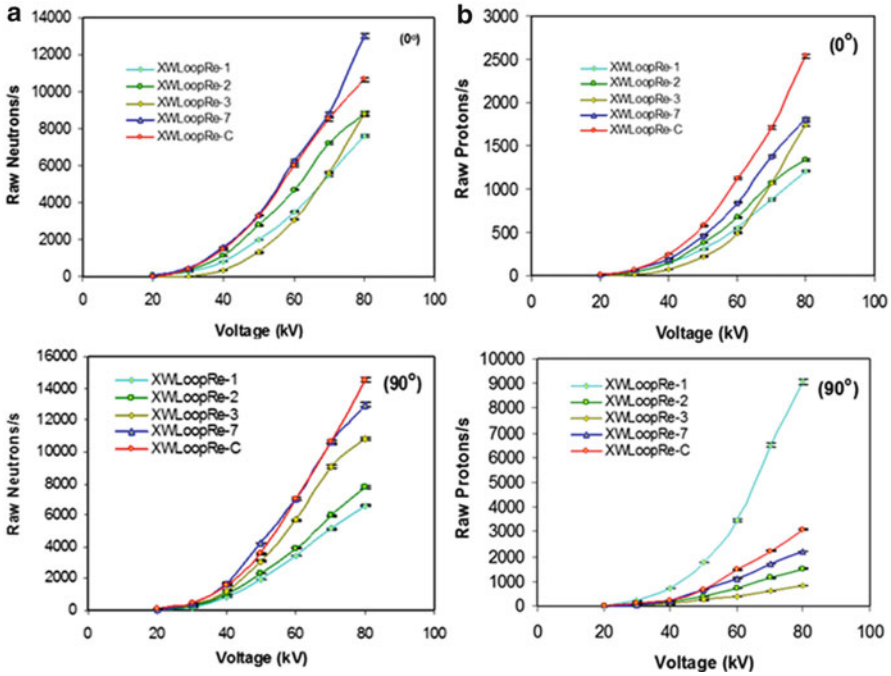

Fig. 6.8 Plot of voltage scans of (**a**) the neutrons/s and (**b**) the protons/s at 10 mA, 2 mTorr for various grid configurations in the two orientations (0° and 90°). The numbers at the end of XWLoopRe follow from Fig. 6.7 [2]

A similar trend is observed with the current scan of the grids, shown in Fig. 6.9. However, contrary to expectation, the fusion rate decreases with increasing current. The presence of a resistor in the high-voltage circuit caused this behavior. A high-voltage resistor was used to prevent the transient current signal from reaching the power supply that would otherwise shut down the device. As the current increases the voltage drop across this resistor increases such that the voltage on the cathode decreases, causing the overall fusion rate to decrease [2].

6.2 Transformation of Line Source into a Volume Source

The proton and neutron rates for various configurations are plotted for three voltages (40, 60, and 80 kV) in Fig. 6.10. The transformation of the single loop grid that is a line source (cylindrical) to a spherical grid (a volume source) is evident from Fig. 6.10a, where the proton rate is the highest when the line source is facing the detector. This proton rate decreases and then eventually increases once again. The neutron rate in Fig. 6.10b further supports this argument, because the neutron rate increases with symmetry irrespective of the orientation of the grid.

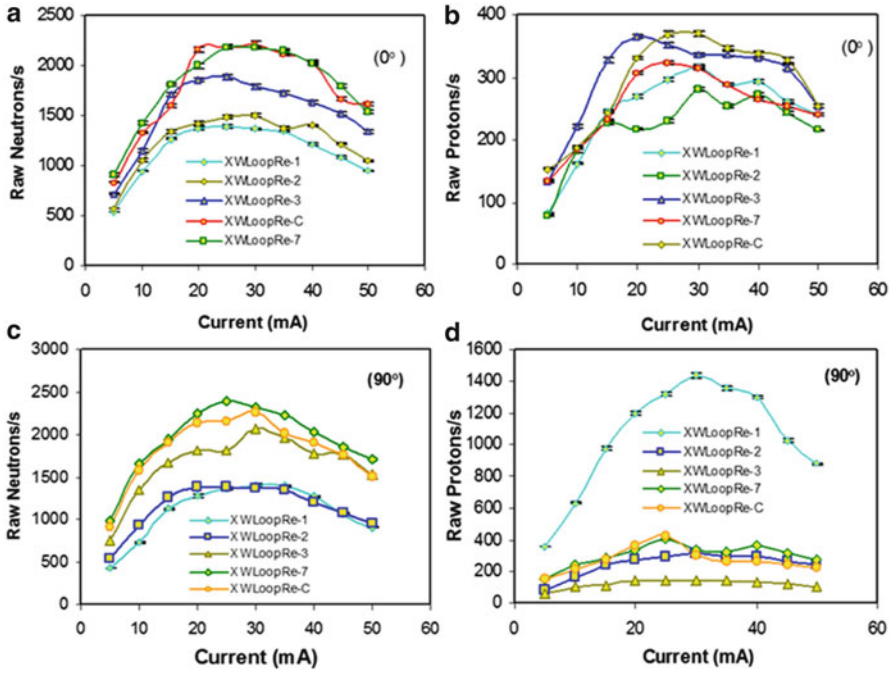

Fig. 6.9 Plot of current scans of the neutrons/s (**a**) and (**c**) and the protons/s (**b**) and (**d**), at 10 mA, 2 mTorr for various grid configurations in both the 90° and the 0° orientation [2]

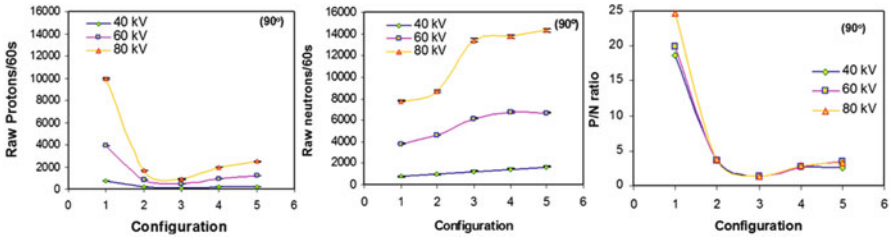

Fig. 6.10 Comparison of the proton and neutron counts with various grid configurations designated as 1→XWLoopRe-1, 2→XWLoopRe-2, 3→XWLoopRe-3, 4→XWLoopRe-7, 5→XWLoopRe-C. The chordwires were oriented face-on (90°) with respect to the detector [2]

6.3 Proton/Neutron (P/N) Ratio

The proton/neutron (P/N) ratio is defined as the ratio of protons produced over the neutrons produced in the same device. Raw counts are sufficient for the P/N ratio because the inclusion of the calibration factors of the two detectors does not affect the trend of the ratio. From Fig. 6.4 it is evident that for all practical purposes, the P/N ratio should be 1 (because the branching ratio is 50/50). There are two ways in which

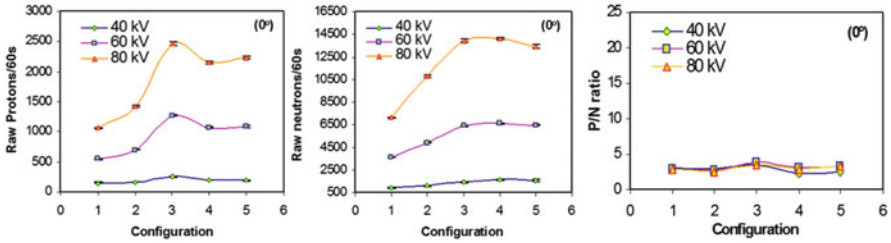

Fig. 6.11 Comparison of the proton and neutron counts with various grid configurations without the eclipse disk blocking the proton detector's view of the cathode. The chordwires are oriented face-off (0°) with respect to the detector. The P/N ratios follow the proton counts and are much smaller than the corresponding values in Fig. 6.9 [2]

the P/N ratio can deviate from unity. For example, if the fuel is polarized, the branching ratio for the D–D reaction can be shifted away from the normal 50/50 %. In fact, fuel polarization has been proposed to mitigate the unwanted reactions and promote the desired aneutronic reactions [3, 4]. When this is done, the D–D fusion reactions can be forced to become neutron lean. Then, the branching ratio does not remain 50/50; hence, the P/N ratio is not constant. Second, and most common, the measured P/N ratio deviates from unity due to detector capabilities. The proton detector is sensitive to direct line of sight, while a neutron detector is not. Thus the measured proton rate can also drift and change with the grid orientation, while the overall fusion rate (i.e., both proton and neutron rates) can drift with impurity levels, chamber pressure, power supply current, voltage, etc. Under these circumstances, it becomes difficult to understand variations using neutron measurements alone. However, if both the neutron and proton rates are followed simultaneously and the P/N ratio is plotted, a good indication of the source regime variation with the experimental parameters is provided – if the proton rate drifts, the neutron rate will also. Hence the P/N ratio will remain constant. Therefore, reporting the observation in the form of a P/N ratio is preferable to reporting proton or neutron rates separately, particularly when monitoring the source regime illustrated in Figs. 6.10 and 6.11 or when studying potential wells using deuterium as the fuel gas.

The neutron production rate (NPR) saturation is more prominent at higher voltages, and there is no significant increase beyond the XWLoopRe-7 configuration (4). Hence we may conclude that beyond a certain point the symmetry of the grid is not an issue (for spherical geometries) and huge gains in the fusion rate may not be expected with improved symmetry for relatively high-pressure operation, where volume source reactions dominate. However, if too many wires were added, the fusion rate can decrease due to the decrease in geometric transparency and the resulting decreased ion recirculation. Also, at some point, with many grid wires the openings to sustain microchannels ultimately become too small, causing a transition to the internal plasma "glow" mode and a corresponding decrease in ion recirculation, hence resulting in a decrease in NPR.

6.4 Fusion Regimes Inside an IEC Device

It was originally assumed that the IEC device is an isotropic source of fusion reactions. Unfortunately, this is not true, because the fusion reactions vary around the chamber and are heavily governed by the grid wire dimensions and grid spacing. In this section, we describe each of these cases as a "fusion regime." This expands the meaning of fusion regime beyond the glow, halo, jet, and Star modes discussed in earlier chapters. The distinction here is that the regimes of interest refer to where the fusion reactions (fusion source) are occurring. This distinction can be different depending on IEC geometry, pressure, etc., thus different locations within the various discharge modes (glow, halo, star, and jet).

Murali and colleagues studied the various fusion regimes using a unique diagnostic called the "eclipse disk" [5, 6]. As the name suggests, a metal disk is used to eclipse the protons coming from a fixed region in space in front of the proton detector, illustrated in Fig. 6.12. The fusion rate from the eclipsed region can be studied by comparing it with the fusion rate without the eclipse disk.

In one experiment, an eclipse disk comprised of three different radii was used. The first was large enough to cover the entire cathode (4.0 cm diameter), the second was an intermediate disk (2.4 cm diameter), and the third was the smallest disk (1.1 cm diameter), as shown in Fig. 6.13.

Several experiments were performed using the eclipse disk diagnostic. The results of experiments performed with a D–^{3}He fuel mixture are shown in Fig. 6.14.

When D–^{3}He fuel is used in an IEC device, parasitic D–D reactions occur along with D–^{3}He reactions. This aspect has been exploited in the present set of experiments to isolate and understand the contributions of the volume, embedded, and converged core regions. Figure 6.14 shows the approximate volume

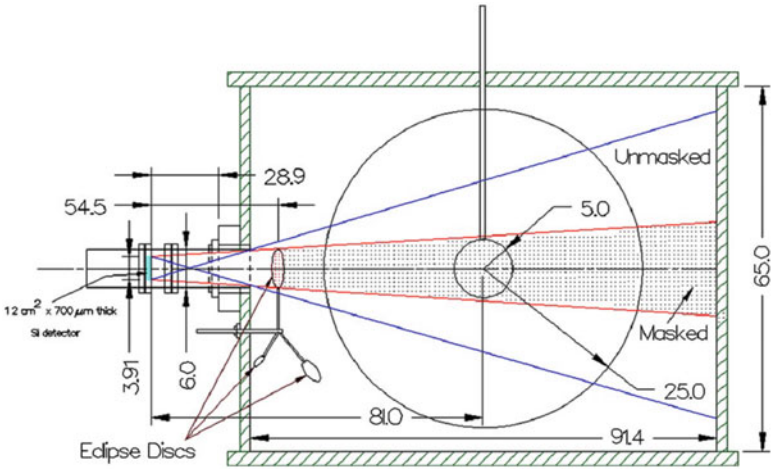

Fig. 6.12 Schematic of an eclipse disk diagnostic mounted on an IEC chamber port [6]

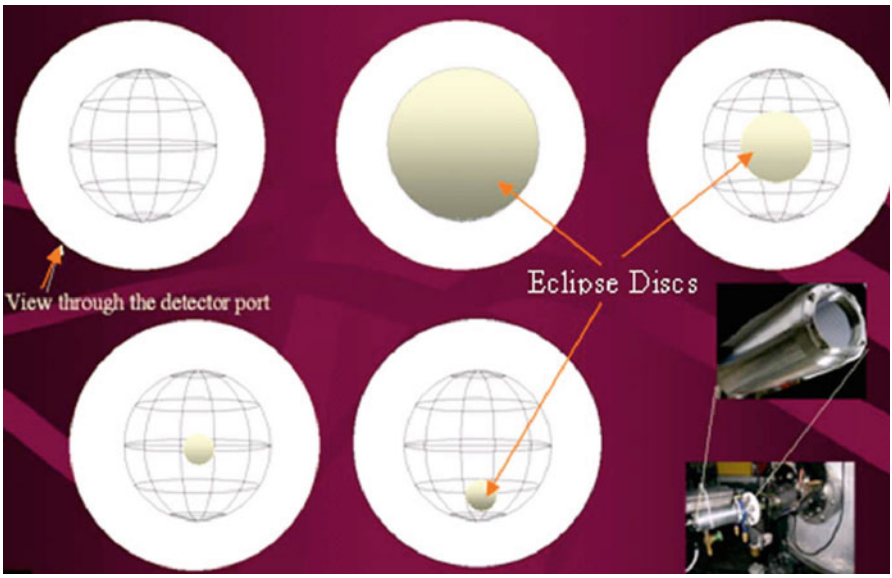

Fig. 6.13 (1) Unobstructed view through the detector port. (2) Large disk eclipsing the entire cathode. (3) Intermediate disk eclipsing the cathode. (4) Small disk eclipsing the core of the central grid. (5) Offset small disk eclipsing an arbitrary region of the cathode. (6) The proton detector mounted on the side wall of the IEC device, along with the enlarged view of the proton detector [6]

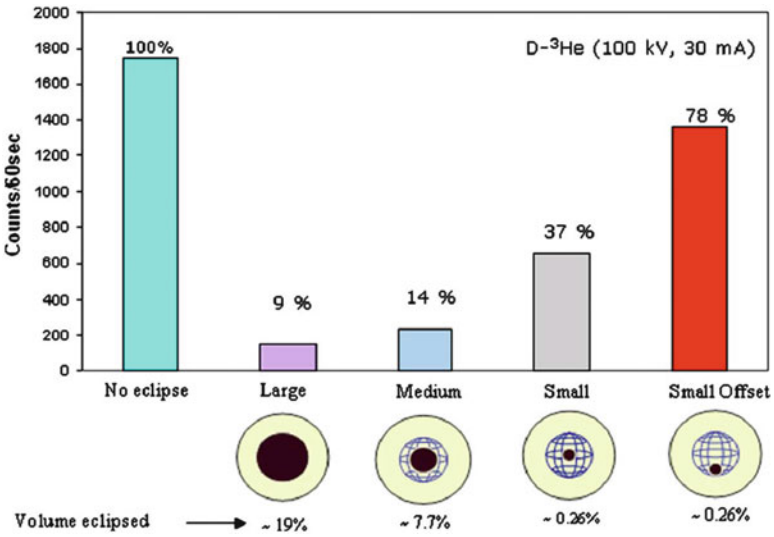

Fig. 6.14 Typical D–D proton counts integrating overall energies with eclipse disks in an IEC device with D–^{3}He fuel at 100 kV, 30 mA [5, 6]

Table 6.1 Fusion source regime contributions to the overall proton rate detected by the Si detector. The error in these contributions is ±2 % [5, 6]

Fusion source regime	D–D	D–^{3}He
Converged core	20–22 %	5–7 %
Embedded	5–8 %	93–96 %
Volume	67–70 %	Negligible
Wall surface	Negligible	Negligible

eclipsed by each of the disks. The no eclipse case is normalized to 100 %, and all the other counts are reported relative to this value. When the large eclipse disk is used, ~ 19 % of the volume visible to the proton detector is eclipsed. As a result, over 90 % of the D–D protons are blocked. With the intermediate disk that eclipses 7.7 % of the volume, 86 % of the D–D protons are blocked, so 14 % show up at the detector. With the small disk that eclipses just 0.26 % of the volume, about 63 % of the D–D protons are blocked and 37 % show up; this indicates that D–D reactions are predominant in the core region of the IEC device. The offset disk data that still eclipses 0.26 % of the volume further supports this observation. It blocked only 22 % of the D–D reactions and hence 78 % show up on the detector.

The fusion reactions occurring in each of the source regimes are tabulated in Table 6.1. For example, the 20–24 % D–D proton counts from the converged core mean that this source regime contributes that fraction of the total 3.02-MeV protons detected by the Si detector.

In order to understand the D–^{3}He reaction contributions, a comparative study was performed. As shown in Fig. 6.15, a comparison of the D–D reactions with D–^{3}He reactions shows several new features. The large disk blocks most of the D–D reactions and almost all of the D–^{3}He protons. The D–^{3}He protons that get through the eclipse disk show up as a shifted peak (see Fig. 6.16). However, some D–^{3}He protons are lost as they are scattered by the eclipse disk. These results suggest that most of the D–^{3}He reactions are contributions of either the converged core or the embedded reactions.

Experiments with the small eclipse disk resolved the two contributions (converged core and the embedded source) for the D–^{3}He reactions. The intermediate disk blocks 55 % of the D–^{3}He protons, and approximately 48 % show up as the shifted proton peak. With the small eclipse disk, only 10 % of the D–^{3}He protons are blocked, and even with the offset disk, only 8 % of the protons are blocked. Hence the D–^{3}He reactions are dominated by "embedded" reactions. This is the first confirmed evidence that D–^{3}He reactions in this IEC experiment (and possibly in others) are predominantly embedded reactions. Though the fraction of ^{3}He ions is small (due to the Penning ionization effect) in the D–^{3}He mixture, those ions that survive quickly embed themselves on the surface of the cathode grid wires, forming stationary targets for the oncoming deuterium ions [7]. Unlike ^{3}He, D can become embedded on the grid surface, but it easily diffuses out of the grid wires owing to its smaller size. Another independent experiment performed using solid targets provided

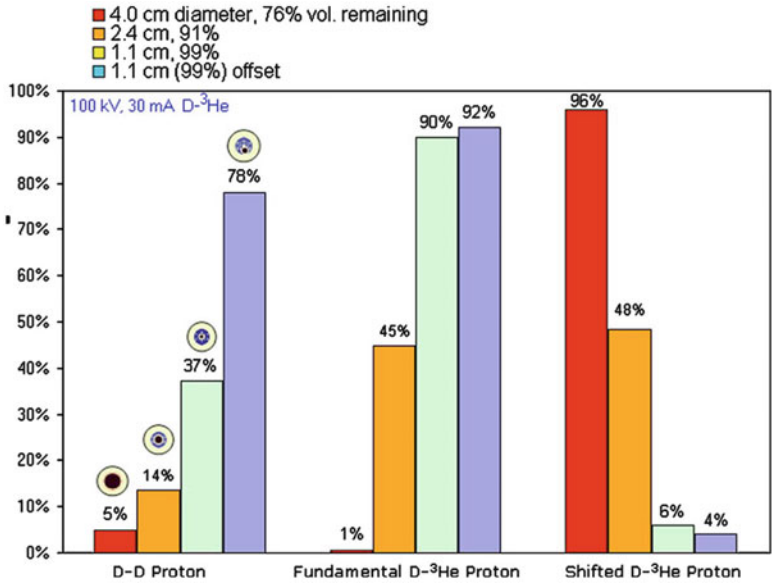

Fig. 6.15 The percent of protons detected by the detector corresponding to each of the eclipse disks [5, 6]

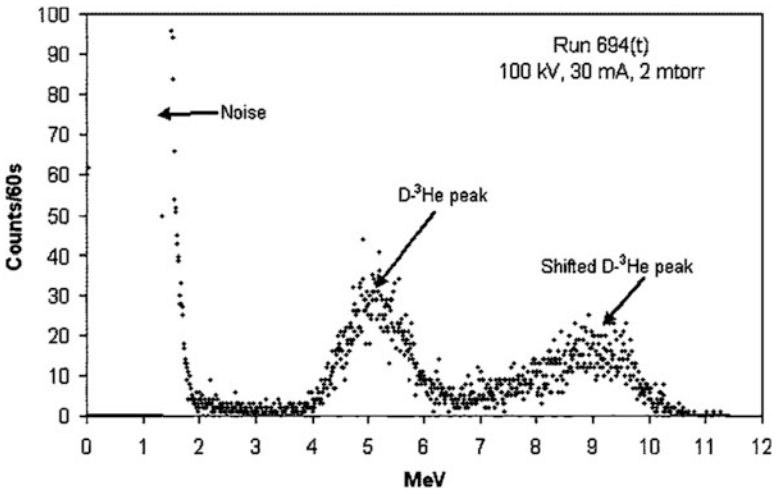

Fig. 6.16 A double peak is observed when D–^{3}He fuel is used in conjunction with an intermediate eclipse disk. The energy referred to in the Si detector measurements is the energy deposited into the detector, not the actual particle energy [6]

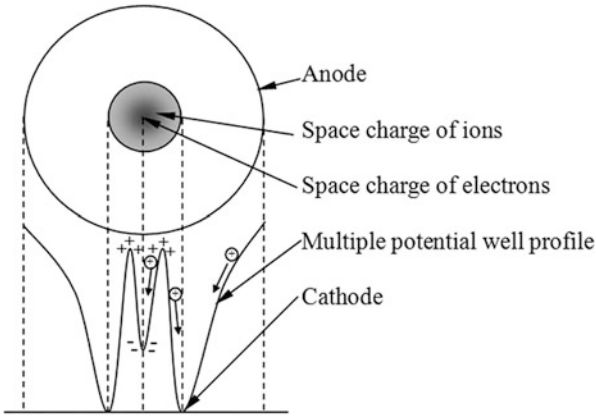

Fig. 6.17 Predicted multiple potential well (Poissor) structure within an IEC chamber [11, 12]

further evidence that the D–^{3}He reactions are often from the embedded regime (beam–target reactions) [8].

Now that we have explained the various fusion regimes within this IEC device and how they vary with the kind of fuel used, we move on to explain the effect of cathode grid wire dimensions and spacing on the fusion rate observed.

6.4.1 Grid Rotation Experiments for Potential Well Studies

Grid rotation experiments can be used for study of the Poissor structure (multiple electrostatic potential wells) in the radial direction of an IEC device. Such structures were first proposed by Farnsworth [9] as explained in Chap. 1 of this book. Theoretical work [10] has shown that a Poissor structure may be possible with IEC devices, though the analysis assumes purely radial motion. Under the conditions of that analysis, potential structures are predicted to form within the cathode due to alternate positive and negative space charge buildup (see Fig. 6.17). With higher ion current at higher voltages, multiple potential wells are believed to form. The interest in Poissor structures is that their formation can enhance the fusion rate, making the device more efficient, reducing the need for grids to create the potential well needed in the IEC. As stressed earlier, these features with beam–beam fusion appear to be essential if the IEC is to be extended to a power reactor.

Experimentally, several virtual anode measurements have been made in IEC devices by Nadler [13], Thorson et al. [14, 15], and Khachan [16]. The quantitative potential well depth estimates by Nadler are perhaps questionable due to their reliance on one-dimensional orbital model predictions and because they were performed with a relatively small potential. The detection of a virtual anode by Khachan [14], in essentially "Star" mode operation, differs from Thorson et al. [12], who observed a flat potential profile in "Star" mode. However, Khachan's [14] cathode consisted of two parallel conducting rings separated by

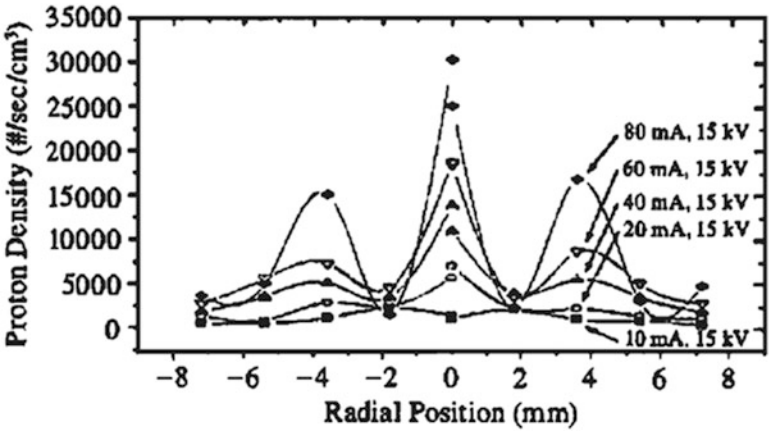

Fig. 6.18 Measurement of the potential well structure using a collimated proton detector [19]

only 2 cm, so space charge could escape radially. Yoshikawa et al. [17] observed negligible electric fields within the core region of a "Star" mode device. Several indications of double potential well structures have been reported [10, 18–20]. Gu and Miley [21] have reported double potential wells of substantial depth (~ 30 %) in "Star" mode based on spatial variation in the radial fusion profile (see Fig. 6.18). However, alternative explanations for the observation of this variation in the spatial profile of the fusion output have been proposed [22]. If it is assumed that fuel ions are confined, keeping the total energy and angular momentum almost constant, the double radial peak in the neutron production rate could appear (numerically) without the creation of the deep double potential well. Yet another explanation could be that the grid wires casted shadows for the protons on the detector surface and thus artificially decreased the fusion rate at these points [23]. This does not mean that the data points in Fig. 6.18 are false, only that more confirmational work is needed to put an end to the debate on the existence of multiple potential wells. Gu and colleagues were aware of the grid shadowing issue and addressed how to avoid it [21].

Next we will explain how observations similar to those observed in Fig. 6.18 can occur through the shadowing effect of the grid wires and how researchers doing proton detection measurements of this type must carefully guard against this phenomenon.

In an attempt to study the effect of grid "shadowing" on the fusion reactions, Murali and colleagues rotated the grid about the central axis (passing along the high-voltage stalk) while simultaneously monitoring the protons coming from the cathode region using a proton detector [23]. A typical grid has latitudes and longitudes as shown in Fig. 6.19. When this grid is rotated about the z-axis, a longitudinal plane sweeps a constant volume in the azimuthal direction about the central axis as shown in Fig. 6.19. Hence it blocks a constant volume along the line of sight of the detector aligned with the converged core irrespective of its orientation about the z-axis [23].

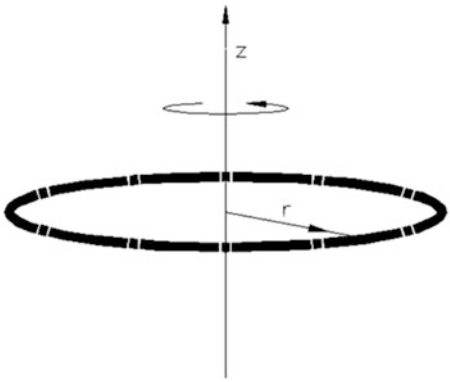

Fig. 6.19 Rotation of a longitudinal plane about the z-axis sweeps constant volume along the azimuthal direction [11]

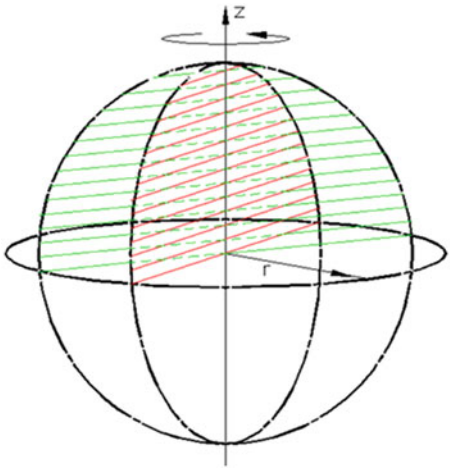

Fig. 6.20 Rotation of the longitude along the z-axis sweeps variable areas with respect to a stationary detector along the line of sight in the radial direction [11]

However, as the grid is rotated about the central axis, the longitudes sweep different volumes with respect to the line of sight of the detector because, unlike the latitude, the longitude rotates about the diameter (as shown in Fig. 6.20). The longitudes are spaced at equal intervals of 30°, and hence with the rotation of every 30°, the grid returns to the initial orientation, assuming the grid is symmetric. The use of this technique in an experiment is discussed next.

6.4.2 Grid Rotation Experimental Setup

To study the effect of grid wires (eclipsing) on the proton rate from the converged core, it is important that the grid be rotated in small increments of angle. In the present case the angular step sizes adopted were 7.5° ± 0.5° and 2.5 ± 0.3° as shown in Fig. 6.21 [11]. All the other parameters were maintained constant,

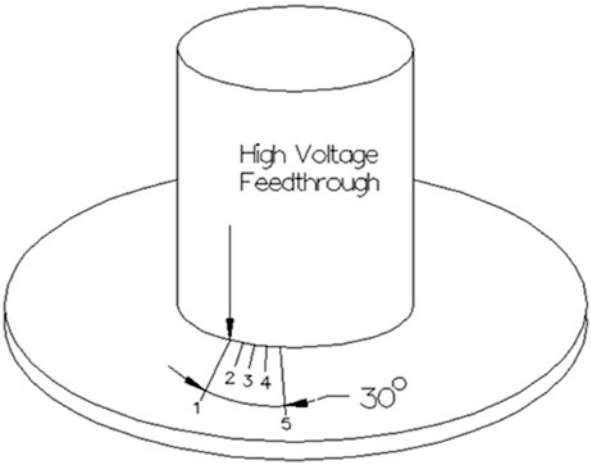

Fig. 6.21 The high-voltage feedthrough rotated in intervals of 7.5° up to 30° [2, 11]

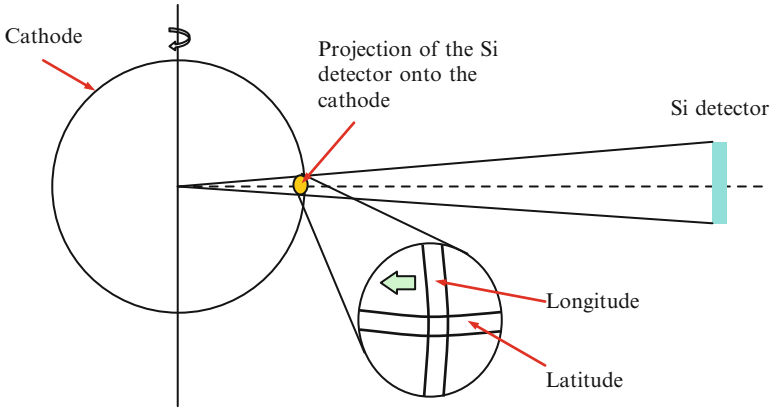

Fig. 6.22 The projection of the Si detector onto the cathode is approximately a circle. Assuming a perfect point source, the difference between the projected area and that blocked by the two wires is ~ 56 %. Without the longitude in the view, the difference is ~ 26 % [11, 25]

including impurities. Because the high-voltage feedthrough could be rotated under vacuum (without venting), the impurity levels in the chamber could be maintained constant during the entire experiment.

If a converged core exists in the center of the IEC device and if this core's dimension is very small (approximately point source), the grid wires can play a major role in masking the proton counts from such a converged region. The cross wires (one latitude and one longitude) would block approximately 56 % of the proton counts (see Fig. 6.22). Because the latitude constantly masks half (28 %) of the counts, the longitude alone should mask 28 % of the counts when it falls in the line of sight of the proton detector. Hence the maximum variation in the P/N ratio should not exceed 28 %. To verify this aspect, a set of experiments were performed where the

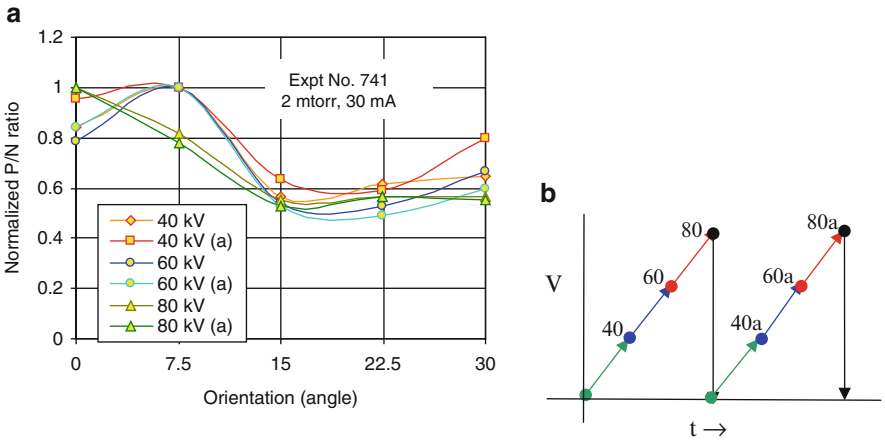

Fig. 6.23 (**a**) Variation of the P/N ratio with grid orientation. (**b**) Two voltage scans performed in a sequence (40–60–80 kV) [11, 25]

grid was rotated in small angular increments. This involved rotating the high-voltage feedthrough in angular increments of 7.5° ± 0.5°. Results are shown in Fig. 6.21. Protons were recorded by a fixed proton detector simultaneously with the NPR for each position at various voltages at each orientation as shown in Fig. 6.23a. Two voltage scans were performed at every orientation using the voltage sweeps as shown in Fig. 6.23b.

The P/N ratio (normalized to the maximum value in a particular scan) measured at each position revealed an average of 40 % variation between its maximum and minimum values. This variation can be the source of significant error in experiments with a fixed grid/detector orientation, because the proton detector could detect fewer protons than the maximum value if an "improper" (i.e., unoptimized, see Fig. 6.23) orientation is used. This error occurs in addition to the statistical errors (square root of the counts) in the proton counts.

To verify the above observation, another experiment was performed where the grid was rotated in steps of 2.5° ± 0.3°, through a total of 42°. The results of this experiment are plotted in Fig. 6.24. It is observed that the P/N ratio value repeats itself at an interval of 30°. This is expected because, as mentioned earlier, the cathode grid has longitudes separated by 30° and hence a rotation by 30° would reproduce the original configuration. The value of the P/N ratio in Fig. 6.24 varies by about 35–40 %. The small variation in the data is caused by misalignments during rotation. Hence the grid orientation could affect the proton counts by as much as 40 % if the appropriate orientation is not used.

Because the variation in the P/N ratio is greater than the expected 28 % for a converged core, it is unlikely that a truly converged core (approaching a point source) existed. Another factor affecting the P/N ratio was that the microchannel extending toward the proton detector from the cathode should cause the P/N ratio to increase due to the $1/r^2$ falloff of the fusion rate in such a microchannel [25].

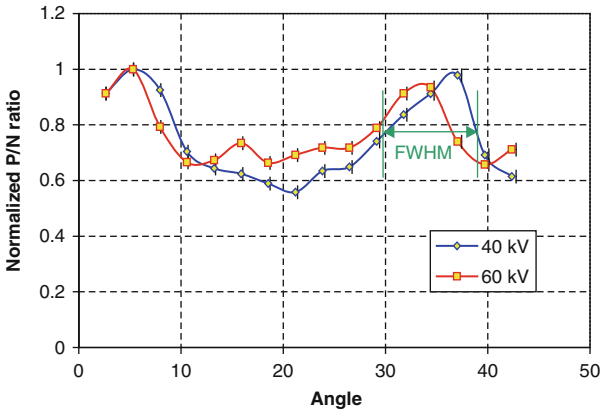

Fig. 6.24 Plot of the normalized P/N ratio scan with the angular orientation of the cathode grid is periodic every 30° [11]

These experiments were further confirmed using another proton diagnostic that was much more sensitive than the original collimated proton detector. The experiments were repeated with two different cathode grids. Both of these grids were of the latitude/longitude configuration. The first grid consisted of 11 latitudinal and 24 longitudinal wires, while the second one had 6 and 16; the latter grid did not have an equatorial latitude. This new diagnostic, termed the Fusion Ion Doppler (FIDO) diagnostic (explained in a later chapter), was used to repeat the grid rotation experiments [24]. The results of these experiments confirmed that the on-wire view accounted for approximately 45 % of the proton count rate when the diagnostic was directed at the on-hole view. This experiment further confirmed the fact that microchannels are regions of higher fusion event concentrations directed normally to the surface of the cathode sphere and passing through to the holes in the cathode. Next we will calculate the fusion reaction rate from a single microchannel generated by a single loop grid. This will lay the foundation for calculating the calibration factor for the proton detector in the subsequent sections. For this purpose, the data from an eclipse disk scan is used.

6.5 Calculation of Fusion Rate Using a Single Loop Grid

At the background pressure in these experiments, the fusion rate is almost constant in the volume outside of the converged core. Fusion reactions in that volume are mostly charge-exchanged neutral reactions.

Assuming that all reactions occur along the path that the ions recirculate, the total fusion proton rate (F_t) detected by the Si detector shown in Fig. 6.25 for 0° orientation can be easily derived giving

$$F_t = \frac{A\eta}{4\pi}\left(\int_{-\delta}^{\delta} \frac{\pi \times {r_{cy}}^2 \times f_v}{{r_i}^2} dl + \frac{f_c - f_v}{r^2} \times V_c\right), \tag{6.1}$$

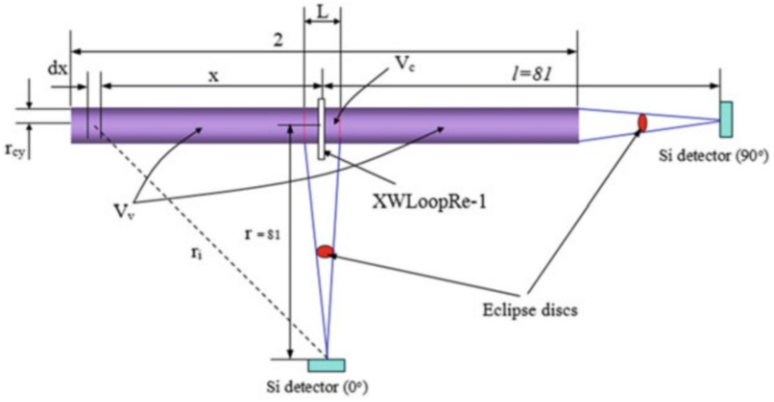

Fig. 6.25 Schematic of the line (*cylindrical*) source from the XWLoopRe-1 single loop grid configuration in two orientations (0° and 90°) (Note: Figure not to scale; all dimensions are in cm [2, 27])

where f_c is the fusion rate (protons × $\sec^{-1}$ × cm^{-3}) in the core of the chamber (close to the center of the XWLoopRe-1), assuming homogeneity, f_v is the fusion rate (protons × $\sec^{-1}$ × cm^{-3}) in the volume excluding the core, η is the detector efficiency, r_i, is the radial distance from the differential volume to the detector (see Fig. 6.25), A is the surface area of the detector (12 cm^2, in the present case where all of the detector's surface area is visible to the microchannel), and r_{cy} is the radius of the differential volume. The term $V_c \times f_v/r^2$ is subtracted from the second term on the right-hand side of the Eq. 6.1, to avoid counting the core volume twice (already included in $V_c \times f_c/r^2$).

From Table 6.2 we observe that the number of protons blocked by the disk in the central position (0° orientation at 60 kV) is 70 (in 60 s) ~ 1.17/s, while the total counts (without eclipse) registered by the proton detector are (150 in 60 s) ⇒ F_t ~2.5/s. The intersection of the cone projected from the detector to cylindrical source that passes through the LoopRe-1 is L ~1.5 cm wide.

Assuming that a cylinder with a diameter of 10 cm and a length of 2 cm for the volume of the core region (with uniform fusion rate) is used, a differential volume of length dx and radius r_{cy} ~ 5 cm is also assumed (as shown in Fig. 6.26) to calculate the contribution of the line source formed by the single loop grid. It is calculated using the following equation:

$$F_t = \frac{A\eta}{4\pi}\left(\int_{-\beta}^{\beta} \frac{\pi {r_{cy}}^2 f_v}{(r^2+x^2)}dx + \frac{f_c - f_v}{r^2} \times V_c\right), \tag{6.2}$$

where $r = 81$ cm and β is half the length of the volume source visible to the detector = 9.4 cm (see Fig. 6.26).

Table 6.2 Protons measured from experiments using LoopRe-1 in two orientations. Eclipsing was performed using the small disk (1.1 cm diameter). The difference with and without eclipsing gives the protons produced in the core [27]

Expt. no.	Orientation	Voltage (current at 10 mA)	Protons without the eclipse in the center (60 s)	Protons with eclipse in the center (60 s)	Protons produced in the core
982	0°	40 kV	50	13	37
		60 kV	150	80	70
986	90°	40 kV	410	372	NA
		60 kV	3,604	1,632	NA

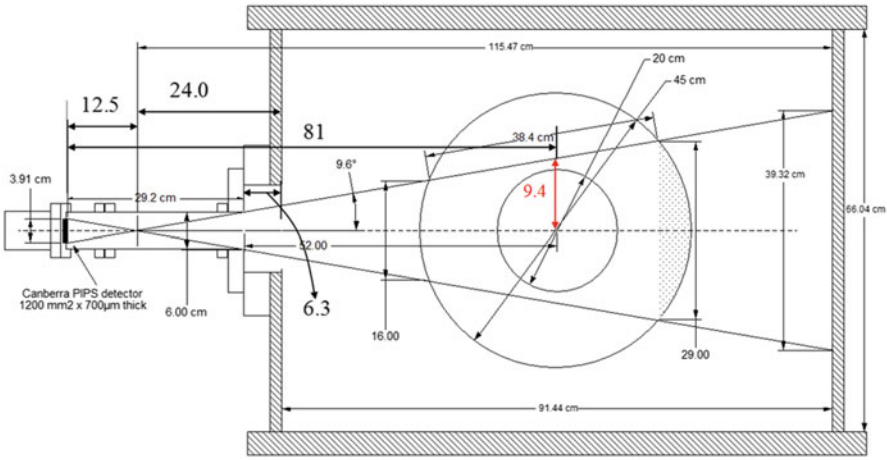

Fig. 6.26 Schematic of the IEC device showing the intersection of the line source with the cone of view of the Si detector [25]

A simplifying assumption is made here – the volume where the reactions occur is assumed to be a cylinder of ~ 10 cm diameter that has a uniform density over its volume. Hence the volume of the core where additional reactions occur is given by

$$V_c = L \times \pi \times d^2/4 = 117.8 \text{ cm}^3, \tag{6.3}$$

where $d \sim 10$ cm and $L \sim 1.5$ cm (a projection of the 1-cm eclipse disk at the center of the cathode). Hence the second term on the right-hand side of Eq. 6.2 is given by

$$\frac{A \times \eta \times (f_c - f_v)}{4\pi r^2} \times V_c = 1.33 \Rightarrow (f_c - f_v) \sim 71.8 \text{ protons/sec/cm}^3 \tag{6.4}$$

$$2.5 = \frac{A \times \eta}{4} \int_{-\beta}^{\beta} \frac{r_{cy}{}^2 f_v}{(r^2 + x^2)} dx + 1.17 \Rightarrow \frac{2A \times \eta}{4} \int_{0}^{\beta} \frac{r_{cy}{}^2 f_v}{(r^2 + x^2)} dx = 1.33$$
$$\Rightarrow f_v \sim 6.54 \text{ protons} \times \text{sec}^{-1} \times \text{cm}^{-3} \tag{6.5}$$

Inserting Eq. 6.5 into Eq. 6.4, we get

$$\therefore f_c \sim 65.3 \text{ protons} \times \sec^{-1} \times \text{cm}^{-3}. \tag{6.6}$$

Thus a large number of reactions still occur very close to the cathode even for a single loop grid. This is expected, because ions have maximum energy close to the cathode (higher reaction cross section), causing a higher fusion rate in the vicinity of the cathode.

While in the 90° orientation, the total counts are (at 60 kV) $(F_t)_{90} \sim 60$/s, and those registered when the eclipse disk blocked the cathode is ~ 27/s. This information cannot be used to characterize the contributions of the core volume segment (as was done earlier), because other volume segments' contributions are also eclipsed in this configuration.

The total fusion rate for the 90° orientation is given by

$$(F_t)_{90} = \frac{A\eta}{4\pi}\left(\int_{-\delta}^{45.7} \frac{\pi \times {r_{cy}}^2 f_v}{(l+x)^2}dx + \frac{f_c - f_v}{l^2} \times V_c\right), \tag{6.7}$$

where $l = 81$ cm (see Fig. 6.13) is the distance from the center of the core volume V_c to the Si detector. The upper limit of the integral is limited by the chamber walls 45.7 cm away from the center of the cathode. Next we have to determine the lower limit of δ. The total length of the line source would then be $(\delta + 45.7)$ cm. Substituting the values obtained above for f_v and f_c, plus $(F_t)_{90}$ in Eq. 6.7, and solving for δ iteratively, we obtain $\delta \sim 78.5$ cm. Hence the length of the line source is $L \sim 124$ cm (extending beyond the outer grid, coming close to the detector).

The above calculations does not account for the variation in the source strength close to the core volume segment where the beam background reactions may be significant (although the CX reaction rate would remain fairly constant). For that purpose, Eqs. 6.1 and 6.2 should be modified in future work. However, if we limit the volume source to the confines of the chamber in Eq. 6.6, a discrepancy between the measurements in the two orientations and those predicted by Eqs. 6.1 and 6.2 arises. This suggests that we have a directed source of protons, which is contrary to our understanding of this device's operation. This discrepancy can be resolved if we assume that the length of the line source is ~ 124 cm.

In summary, we may also conclude that a single loop grid generates a line (cylindrical) source of protons. The high-energy ions recirculate along the center of the line source. With improving grid symmetry (added wires), the fusion rate increases but eventually saturates for a given voltage (up until ~ 80 kV in the present case). The gradual transformation of a line source to a volume source is observed with the increasing symmetry obtained by the addition of more loops to the grid. However, once this saturation occurs, further improvement or variation in grid symmetry does not improve the device performance.

The presence of the grid wires seems to affect the fusion rate more drastically than previously thought. This can be attributed to an increase in the number of ion microchannels up to a point where the regime switches to a glow type discharge.

Fig. 6.27 Fine wires are introduced on the surface of the grid to intercept the ions leaving the cathode. The dimension of the jet is ~1 cm in diameter [25]

6.5.1 *Extension of Study to Entire Grid and Microchannel Effects*

We now extend this discussion to the entire spherical grid and calculate the calibration factor. Several fine wires were introduced on the surface of the central grid to find the microchannel's dimensions as it emerges from the cathode. Although the fine wires themselves affect the local E-fields, this gives us the first order measure of the microchannel dimension. Alternately, the microchannel dimensions can also be determined directly at relatively high-pressure operation in the halo mode, as shown in Fig. 6.28. The dimension of the single microchannel that emerges from the grid as shown in Figs. 6.27 and 6.28 is determined visually to be ~ 1 cm.

The microchannel that emerges from the cathode diverges, causing a diverging cone. The dimension of the base of this cone is determined from Fig. 6.24, where the solid angle subtended by the FWHM angular peak width is $\theta \sim 9^\circ$ at the core of the cathode. The length of the base of the triangle in Fig. 6.29 is the radius of the cone (microchannel) extending from the core of the cathode to the detector ~ 13.7 cm away. Though assuming the microchannel to be cone shaped would give better results, it is approximated here by a cylinder (since the divergence is small) for simplifying the calculations. The volume of this assumed cylinder (Fig. 6.30b) is equivalent to the volume of the microchannel (Fig. 6.30a).

It is assumed that the diameter of the converged core is the same as that of the cylinder. The volume of the microchannel in Fig. 6.30a is given by

$$V_m = \frac{2}{3}\pi h\left(r_c{}^2 + r_c r + r^2\right) + \pi r^2 d, \tag{6.8}$$

where h is the height of the cone $(l–d)/2$, r_c (~ 3.6 cm) is the radius of the cone's base, r (~ 0.5 cm) is the radius of the cylinder inside the grid, r_{cy} is the radius of the equivalent cylinder in Fig. 6.30b, and d is the diameter of the cathode grid.

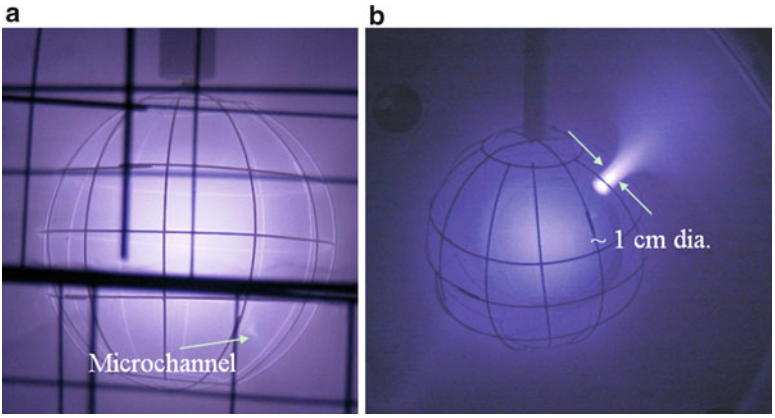

Fig. 6.28 Operation of the IEC device in "halo" mode allows easy measurement of the microchannel's dimensions. (**a**) High-pressure operation of the grid in "Star" mode shows the location of the microchannel to be ~ 2/3 arc distance between the two latitudes (from the lower latitude). (**b**) The microchannel's diameter is ~ 1 cm and diverges upon exiting the cathode in a spherical chamber at high pressure (~8 mTorr) [25]

Fig. 6.29 The base of the cone calculated from the FWHM in Fig. 6.28

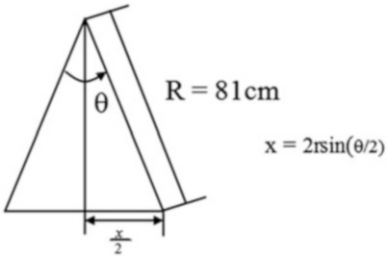

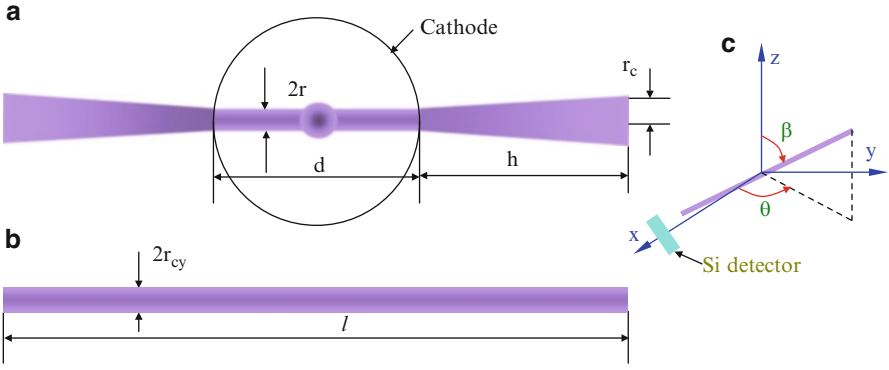

Fig. 6.30 (**a**) Approximate representation of a single microchannel. (**b**) Cylinder of equivalent volume (and hence equivalent number of reactions) of the microchannel. (**c**) Various angles that the microchannel makes with the axis [25]

Each set of microchannels that forms between any two consecutive latitudes has the same length l (as shown in Fig. 6.30b). Neglecting the variations at the intersections of the cone with the cylinder and chamber, the volume of the equivalent cylinder in Fig. 6.30b can be evaluated as follows:

$$\frac{2}{3}\pi h\left({r_c}^2 + r_c r + r^2\right) + \pi r^2 d = \pi \times {r_{cy}}^2 l, \tag{6.9}$$

where l is determined from the orientation β of the microchannel, as shown in Fig. 6.30b.

Then the value of l is given by

$$l = \frac{L}{\sin(\beta)}, \tag{6.10}$$

where L is the chamber height = 65 cm. However, for the set of microchannels that fall between the latitudes 2 and 3 in Fig. 6.31, we need to take the diameter of the cylinder into account; hence

$$l = \frac{L'}{\cos(\beta)} \tag{6.11}$$

where L' is the diameter of the chamber (anode) = 91.4 cm.

The lengths of the microchannels are $l = 66.7$ cm for the microchannel a, $l = 107.5$ cm for the microchannel b (evaluated using Eq. 6.10), and $l = 93.4$ cm for the microchannel c (evaluated using Eq. 6.11). Hence the values of r_{cy} for the microchannels a, b, and c in Fig. 6.31 (evaluated using Eq. 6.9) are 2.07, 2.14, and 2.12 cm, respectively.

Assuming that the fusion rate within the differential volume is constant, F_t becomes

$$F_t = \frac{A\eta}{4\pi}\left(f_v \int_{-\delta}^{\lambda} \frac{\pi \times {r_{cy}}^2 \cos^2\left(\beta'\right)}{\left[r^2 + x^2 + 2rx\cos(\theta)\right]} dx + \frac{f_c - f_v}{r^2} \times V_c\right), \tag{6.12}$$

where θ and β, β' = (90–β) (see Fig. 6.31) are the angles of inclination of the microchannel with y- and z-axis, respectively, as shown in Fig. 6.30c. Note also that δ and λ are the lower and upper limits of the cylindrical source, respectively. This source is generally limited by the chamber dimensions and/or the proton detector's view cone (see Fig. 6.32).

Though Eq. 6.12 gives an accurate estimate of F_t, it is easier to neglect the second term on the right side and account for it later after all calculations are completed. This simplifying technique is explained further later (see Eq. 6.13).

The length of a microchannel is specific for each orientation. However, using symmetry, the length of only half the number of microchannels, i.e., 13 in all,

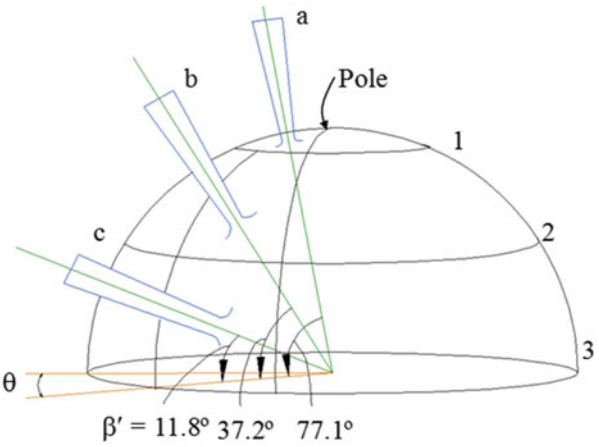

Fig. 6.31 Cathode grid showing some latitudes and longitudes along with the microchannels and the corresponding angles of orientation with respect to the core. The latitudes are numbered 1, 2, and 3, while a, b, and c are microchannels [25]

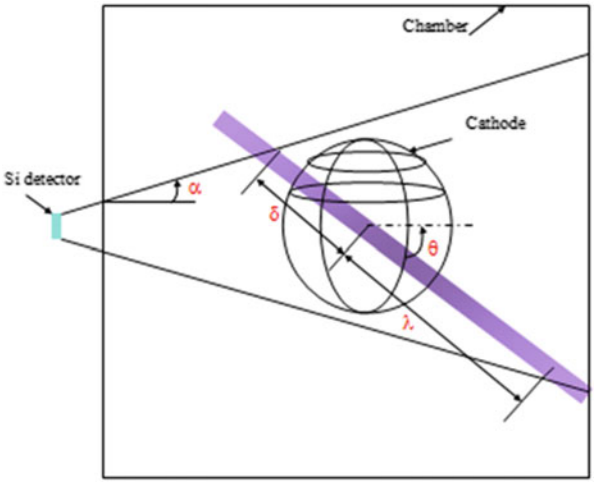

Fig. 6.32 The view of the single microchannel is limited by the view cone of the detector [25]

(which is ~ one quarter of the number of holes in the cathode), has to be evaluated because the other half has the same value.

The microchannels tend to form in a region where the electrostatic potentials between the wires are less negative and hence are removed from regions where the wires converge, as in the case of the latitudes 1 and 2 illustrated in Fig. 6.33. The angles that the axes of the microchannels make at the core of the cathode while passing through each of the holes shown in Fig. 6.31 are $\beta' = (90-\beta) = 11.8°, 37.2°$, and 77.1°.

The various lengths from Fig. 6.33 are listed below in terms of known quantities:

$$h_1 = r\frac{\sin\alpha\sin\theta}{\sin(\alpha+\theta)} = \frac{r}{\cot\alpha + \cot\theta}, \tag{6.13}$$

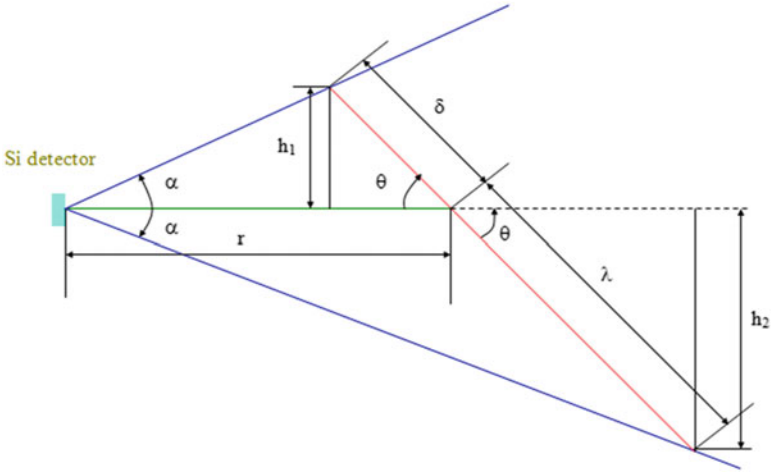

Fig. 6.33 Geometry of the detector and the microchannel orientations where $\theta = (15 + n \times 30)$, with $n = 0, 1, \ldots 5$, and $\alpha = 5.86°$ [25]

$$h_2 = r\frac{\sin\alpha\sin\theta}{\sin(\theta-\alpha)} = \frac{r}{\cot\alpha - \cot\theta}, \tag{6.14}$$

$$\delta = \frac{h_1}{\sin\theta}, \tag{6.15}$$

$$\lambda = \frac{h_2}{\sin\theta}. \tag{6.16}$$

The total length of the line source $L = \delta + \lambda$ is given by

$$L = \frac{h_1 + h_2}{\sin\theta} = \frac{2r \times \cot\alpha}{\sin\theta \times (\cot^2\alpha - \cot^2\theta)}. \tag{6.17}$$

The number of segments between latitude 1 and the pole of the grid in Fig. 6.33 (also see Fig. 6.19) is only four; hence, there are only two orientations of the microchannel a that we need to account for in the calibration. All the other microchannels that form between any two consecutive latitudes are 12 in number and 56 in total. Because the area of each of the openings is generally constant, we assume that the diameter of the microchannel remains constant (~ 1 cm).

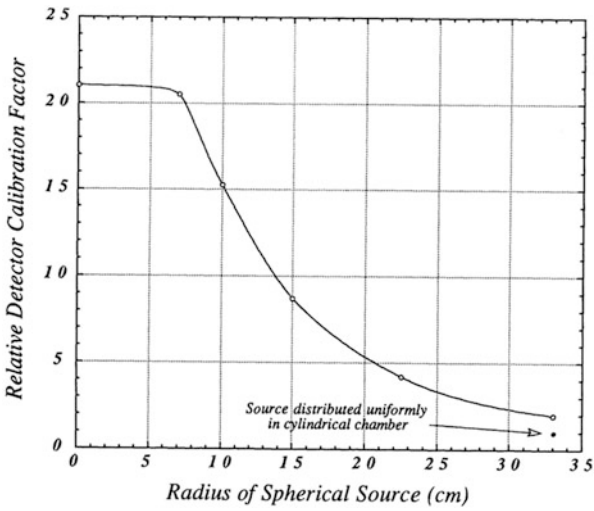

Fig. 6.34 Plot of a detector calibration factor relative to various spherical sources of different radii versus the radius of spherical source. For the point source the detector calibration factor is 1, but for a complete volume source, the factor is 21 (Sawan ME, 2000, University of Wisconsin, Madison, private communication)

6.5.2 *Detector Calibration Factors for Various Source Regimes*

In the following calculations we combine experimental data and geometric factors to determine the effective proton production rate corresponding to the count rate recorded by the detector. This provides a "calibration factor" for a particular orientation of the detector. Calibration factors are determined for each of the source regimes, i.e., volume source predominately in microchannels, embedded source due to collisions with absorbed fuel on the grids, and converged core due to intersection of the microchannels. These three separate contributions (calibration factors) are then multiplied by the percentage of the total volume associated with each and added to obtain the total proton source rate. The results presented are specific to the experiment at the University of Wisconsin, Madison. However, the general technique illustrated can be extended to other experiments of interest to the reader.

The volume source calibration factor calculated using MCNP (Monte Carlo N-Particle) code gave an approximate calibration factor of the form [23]

$$\frac{4\pi r^2}{A}\left(\frac{21}{\eta_d}\right), \tag{6.18}$$

where the factor 21 was found using MCNP computation. Figure 6.34 shows a plot of the relative detector calibration factor versus the spherical source radius. This includes the extrapolation from the solid angle of the detector to the entire chamber volume.

6.5.3 Calibration Factor for a Converged Core Created by Microchannel Intersection

The converged core source can be approximated to be a point source (as seen by the detector) and can be modeled using the following equation modified from Cipiti's work [24]:

$$F_c = \frac{4\pi r^2}{A}\left(\frac{1}{\eta_c \eta_d \eta_a}\right) \sim 7,818. \tag{6.19}$$

Here A is the surface area of the detector $= 12$ cm^2 (because the entire detector is visible to the protons born in this region), r is the distance of the proton detector from the center of the chamber ~ 81 cm, η_c is the transparency of the cathode ~ 0.925, and η_d is the detector efficiency ~ 0.95. The transparency of the anode η_a is taken as 1 because a hole was introduced into the anode in front of the detector so as not to block protons. Thus, as show, the calibration factor for the converged core as calculated from Eq. 6.19 is ~7,818.

6.5.4 Calibration Factor for Embedded Source

The embedded source can also be approximated by a point source with an additional factor of 2 because protons born on the far side of a grid wire are blocked by the wire and are given by [24]:

$$F_i = \frac{4\pi r^2}{A}\left(\frac{1}{\eta_d}\right) \times 2 \sim 14,550 \tag{6.20}$$

where $A = 12$ cm^2 (because the entire detector is visible to the protons born in this region).

In the present setup, $r \sim 81$ cm, $A = 12$ cm^2, and $\eta_d = 0.95$, which gives a calibration factor of ~ 164,192 (=151,878 if the anode transparency factor $\eta_d \sim 1.0$ for the case where a hole is introduced in front of the detector). This calibration factor (164,192) was used for all the earlier purposes, and in the calculation of this factor, the formation of microchannels was neglected; instead a uniform volume source was assumed [26]. In what follows, a new calibration factor is calculated after breaking down the various fusion contributions into volume (microchannel), embedded, and converged core source contributions.

6.5.5 Calibration Factor for a Volume Source Dominated by Microchannels

Because the contributions of the volume source alone are difficult to determine, the data from the large eclipse experiment is used. This disk masks 100 % of the central grid, and hence any protons detected by the Si detector come from the volume source. However, the exact volume of the microchannel is difficult to calculate. The cylinder of the microchannel's equivalent volume is used for the purpose. The length of this cylinder is calculated in two stages. The length of the microchannel when there is no disk is calculated first. Next, the length of the microchannel blocked by the eclipse disk is calculated. The difference in the two lengths gives the length of the microchannel visible to the detector and is tabulated in Table 6.3 (also, see Fig. 6.35 where $\Delta x_1 = \delta_1 - \delta_2$, $\Delta x_2 = \lambda_1 - \lambda_2$, $T_{i,j} = F_i/f_v = G_j/f_v$, and F_i, and G_j are shown).

If f_v is the source strength of the volume source in protons/s/cm^3 and if N is the total number of protons detected by the detector when the large eclipse disk is in position, then from Table 6.3 the relation between f_v and N is given by

$$\begin{aligned} &\underbrace{\left(4\left[\Sigma T_i(\mathrm{a,b}) + \Sigma T_j(\mathrm{a,b})\right]\right.}_{(4 \times 0.091365 +} + \underbrace{2\left[\Sigma T_i(\mathrm{c}) + \Sigma T_j(\mathrm{c})\right]\Big)}_{2 \times 0.018902)} \times f_v = N \\ &\qquad\qquad f_v \sim 0.403 f_v = N \end{aligned} \tag{6.21}$$

$$\therefore\ f_v \sim 2.48 \times (N)\ \text{protons} \times \sec^{-1} \times \text{cm}^{-3}. \tag{6.22}$$

The total fusion rate in the volume of the chamber is given by

$$T_f = f_v \times V_s. \tag{6.23}$$

Here V_s is the total volume of all the microchannels given by

$$V_s = 12\pi\left[{r_{cy1}}^2 l_1 + {r_{cy2}}^2 l_2\right] + 4\pi\left[{r^2}_{cy3} l_3\right] - 26\left(4/3\pi c r^3\right) \sim 36,903\ \text{cm}^3. \tag{6.24}$$

Here all the parameters are defined in Table 6.3, and r_{cv} is the core radius (~2.1 cm, region where the equivalent cylindrical microchannels overlap) and the factor of 26 arises from the fact that there are 26 microchannels in this grid configuration. Hence the volume source calibration factor is

$$F_i \sim 91,520. \tag{6.25a}$$

The total contribution of the microchannel (volume) source is given by

$$T_f = 91,520 N', \tag{6.25b}$$

where N' is the total number of protons detected by the Si detector.

Table 6.3 Various values used in the calculation of the volume source calibration factors using data from the large eclipse scan experiment [25]

i	α_1	α_2	θ°	β°	l	δ_1	λ_1	δ_2	λ_2	r_{cy}	Δx_1	Δx_2	T_i	T_j
1a	5.86	4.20	15	11.8	93.4	23.2	52.1	18.0	31.6	2.120	5.2	20.5	0.01576	0.01581
2a	5.86	4.20	45	11.8	93.4	10.7	13.1	7.8	9.1	2.120	2.9	4.0	0.00591	0.00573
3a	5.86	4.20	75	11.8	93.4	8.37	8.85	6.04	6.28	2.120	2.33	2.57	0.000420	0.004219
1b	5.86	4.20	15	37.2	107.5	23.2	52.1	18.0	31.6	2.136	5.17	20.45	0.01214	0.01218
2b	5.86	4.20	45	37.2	107.5	10.7	13.1	7.84	9.08	2.136	2.86	4.02	0.00449	0.004434
3b	5.86	4.20	75	37.2	107.5	8.37	8.85	6.04	6.28	2.136	2.33	2.57	0.00324	0.00325
1c	5.86	4.20	45	77.1	66.7	10.7	13.1	7.84	9.08	2.071	2.86	4.02	0.00559	0.00552
2c	5.86	4.20	90	77.1	66.7	8.31	8.31	5.95	5.95	2.071	2.36	2.36	0.00390	0.003896

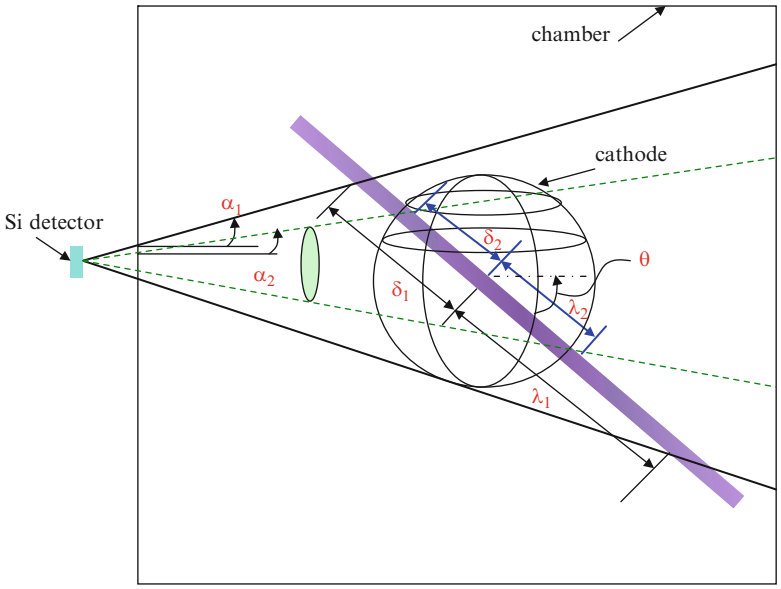

Fig. 6.35 Schematic representation of various parameter from Table 6.3, where $\alpha_1 = 5.86°$, $\alpha_2 = 4.20°$ [25]

6.5.6 Total Calibration Factor

The total calibration factor for the D–D fusion is given by a weighted sum of the three F_i values given in Eqs. 6.19, 6.20, and 6.25a. Thus the total proton source strength T_p is given by

$$T_p \sim \frac{7,818\ (\mathrm{x}) + 14,550\ (\mathrm{y}) + 91,520\ (\mathrm{z})}{\eta_{\mathrm{mag}}}, \tag{6.25c}$$

where x, y, and z are the percentage contributions of each of the source regimes to the overall fusion rate (converged core, embedded, and volume sources), and η_{mag} is the detector channel efficiency (Eq. 6.16) in the presence of the electron deflector magnetic field employed to protect the detector from damage by steaming electrons. The B-field distribution inside the proton detector view port (see Fig. 6.35) is not known accurately; hence, empirical data is used to determine η_{mag}. The proton rate is measured before and after the B-field is used at relatively low cathode voltage (−20 kV), which gives an indication of the influence of the B-field. Such an experiment was performed at low cathode voltage to avoid any energetic electron jets from damaging the proton detector. This also kept the noise generated by the e-beam from overwhelming the proton signal. From this measurement, it was observed that the proton rate changed by an average of 50 % and hence $\eta_{\mathrm{mag}} \sim 0.5$. Thus using the various source distribution data [25] (x = 0.21, y = 0.065 and

z = 0.725) in Eq. 6.25c, we obtain a calibration factor of ~137,879. The present calculations are unique and are for illustrative purposes only. New measurements and calculations are required for new grid geometries and dimensions even within the same IEC device, not to mention about other devices. Though a tedious process, unless the proton detector is calibrated properly, only neutron counts are used to determine the true fusion rate within the device.

6.6 Grid Geometry for Jet Mode Operation

Another aspect of grid design and geometry pertains to the jet mode of operation. This mode is of great interest for propulsion applications. Recent studies by Akshata Krishnamurthy [27] have explored the jet mode in some detail and will be briefly reviewed here. The "jet (halo)" mode is initiated in the same manner as "Star" mode (see Chap. 1) but at higher pressures and resulting lower cathode voltages. It can also be excited by introducing an asymmetry into the grid – for example, by enlarging one of the cathode grid openings in order to define the direction of jet propagation and to use a lower background gas pressure. For these propulsion experiments, argon has typically been employed. When operating a symmetric grid, the jet mode begins at a background pressure slightly higher than for "Star" mode, typically around 15 mTorr. However, when using an asymmetric grid, the "Star" mode is never excited, and the jet mode begins to form at less than 1.0 mTorr. At lower pressures, the intensity of the jet is very high due to its compact nature which avoids spreading of the escaping jet caused by collisions with background neutral gas. This is called the "tight jet" mode. It has been proposed that the jet mode creates a virtual cathode resulting from the formation of a double potential well. At higher pressures, mean free path decreases, causing the jet to fan out like a spray formation. This is called "spray jet" mode. Figure 6.36 shows photographs of the tight jet mode and spray jet mode in operation. The tight jet

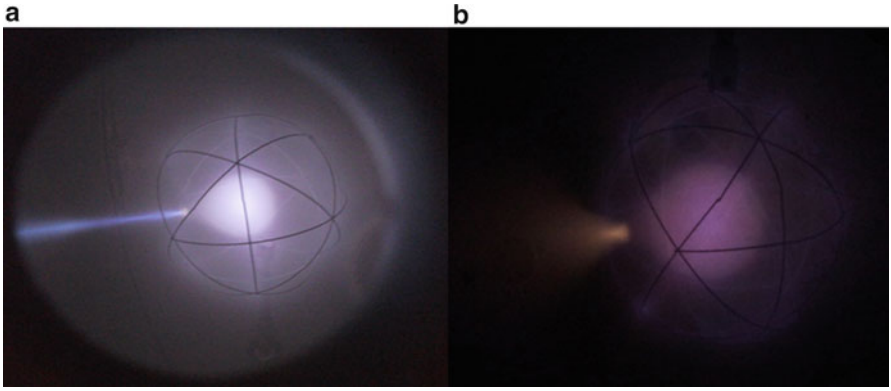

Fig. 6.36 Jet modes of operation using argon gas. (**a**) Tight jet mode and (**b**) spray jet mode

mode, due to its high intensity and plasma density, is of particular interest in the design of an electric propulsion system.

6.6.1 Characteristics of the Jet Mode Regime

In an IEC glow discharge, the electric field imposed between the central cathode grid and the anode chamber wall breaks down the gas glow discharge, similar to a Townsend discharge (see Chap. 3). The key characteristics of the jet mode regime have several deviations from traditional DC glow discharges. The IEC jet mode regime is weakly collisional, non-Maxwellian, and sheathlike and has a hollow cathode configuration with a capability of producing a double potential well.

Because the traditional DC discharges operate at several Torr of pressure, the plasma discharge is collisional with smaller Debye lengths and collisional mean free paths. The IEC device operates in the mTorr range and larger Debye lengths and mean free paths, setting up a weakly collisional system. The IEC device-operating voltage is hugely dependent on the background pressure due to the exponential nature of dependence on collisional ionization processes. The nature of the plasma production makes simulation of this device a challenge because it departs from traditional discharge characteristics.

Due to the weakly collisional nature of the IEC device, particles do not lose sufficient energy during their translation across the system, resulting in nonequilibrium thermal plasma with ions and electrons at different temperatures. Thus, the particle energy distribution function depends on the particle's initial birth region in the system and also on its current location. Standard collisional fluid approximations and diffusion models do not hold for this type of particle transport. Hence, it deviates from the traditional DC discharge; the IEC discharge is characterized as non-Maxwellian.

6.6.2 Jet Mode Discharge Characteristics

Jet mode operation for space propulsion generally employs a heavier gas such as argon versus traditional IEC experiments with deuterium. The breakdown characteristics are quite different. In order to determine how the applied voltage depends on the pressure, p, and distance between the anode (grounded vacuum chamber) and the cathode (asymmetric central IEC grid), d, Paschen curve experiments were conducted using grids of different sizes and at different pressures [28].

The system was maintained at a constant pressure in the range of 1.0–45.0 mTorr for this experiment by injecting gas into the chamber through the inlet quartz tube, with the vacuum pumps running. In these experiments aimed at space propulsion, argon gas was employed. The plasma discharge is initiated by increasing the cathode voltage until breakdown occurs. The current essentially remains zero as the applied voltage is increased until the discharge is initiated at V_b, the breakdown

Table 6.4 Cathode grids of different sizes and geometric transparencies

Radius of the cathode grid (mm)	Geometric transparency (%)	Number of grid wires
110	97.45	7
125	98.32	7
140	98.0	7
165	95.75	14

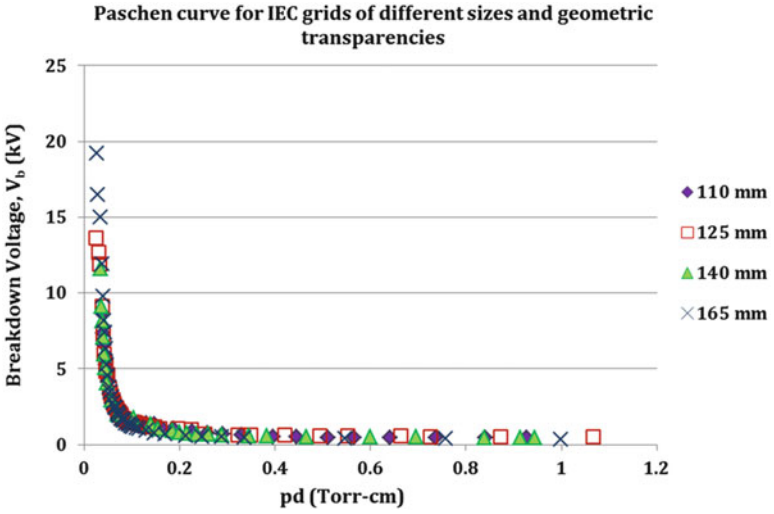

Fig. 6.37 Paschen curve for IEC grids of different sizes and transparencies using argon gas

voltage. The striking voltage is generally much higher compared to the operating voltage. The maximum breakdown voltage in this experiment was limited to 20 kV due to voltage limitations on the cathode feedthrough. Asymmetric cathode grids of different sizes and geometric transparencies were used as tabulated in Table 6.4.

Breakdown voltage V_b versus pd (pressure times the radial distance between the cathode grid and the vacuum chamber wall) measurements that correspond to the traditional Paschen curve plot were taken. The plot of V_b versus pd is shown in Fig. 6.37 for argon gas discharge with various grids. For a fixed value of pd, the breakdown voltage is seen to be the same for all the grids irrespective of their radius and geometric transparencies. As pressure decreases (or the diameter of the IEC grid increases), the breakdown voltage increases. Conversely, as pressure increases (or the diameter of the IEC grid decreases), the breakdown voltage decreases. Depending on the capacity and size of the power supply required for the mission, the respective operating pressure regime and IEC grid can be designed. This Paschen curve data gives valuable information required in scaling the IEC device.

Figure 6.38 shows a single current-carrying microchannel emanating from the larger openings of the asymmetric grids. Figure 6.38a shows the tight jet mode in

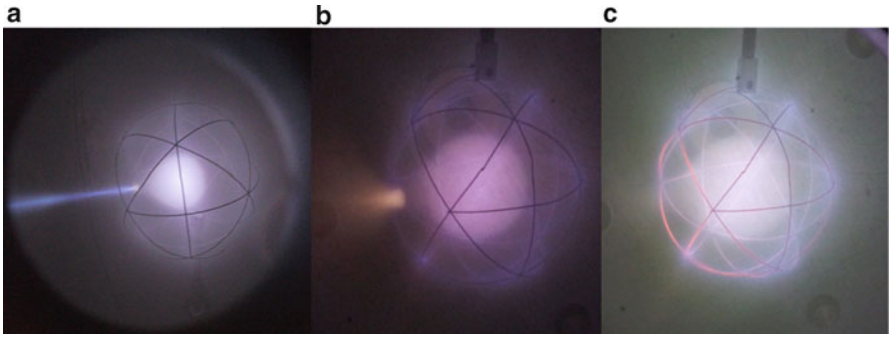

Fig. 6.38 (**a**) Tight jet mode. (**b**) Spray jet mode. (**c**) Glow

which the plasma jet is of 1 cm diameter and occurs below a *pd* value of about 0.05 Torr-cm. As the *pd* value increases above 0.05 Torr-cm, the jet turns into a spray as shown in Fig. 6.38b. Above the *pd* value of about 0.1 Torr-cm, it reduces to just the central dense core (Fig. 6.38c) with no microchannels emanating from the larger grid opening.

The microchannel is created through a geometric "self-selection" process [13]. Ions born with trajectories hitting the grids during the first few passes are quickly eliminated, while those passing repeatedly through the grid holes survive. The ions that make it through the larger grid opening cause increased ionization along the trajectory forming a bright microchannel or plasma jet. The spray jet and tight jet modes are highly pressure dependent. At higher pressures, due to increased collisions with background gas, a fan-shaped spray jet of lesser intensity is obtained.

6.6.3 *Size Scaling for IEC Jet Mode*

The jet mode of the IEC is of utmost relevance for application as a thruster due to its high intensity and energy. An empirical scaling law has been derived [29] by noting the linear variation of the breakdown voltage with the parameter $A/(pd)^2$, as shown in Fig. 6.39. Here A is the atomic mass of the gas species and accounts for the use of different gases, and the $A/(pd)^2$ values used in this figure correspond to the jet mode, i.e., *pd* values ranging up to 0.1 Torr-cm. The discharge characteristics of an IEC system are strongly dependent on the pressure and distance between the anode and cathode.

From the linear approximation shown in Fig. 6.39, a simple size scaling law for IEC jet mode in the present device can be obtained and is given by

$$V_b \approx \frac{\left(3 \times 10^{-4}\right)A}{(pd)^2} \text{ kV}. \tag{6.26}$$

Equation 6.26 represents the behavior of the discharge reasonably well and the discharge characteristics are at most a weak function of the radius of the

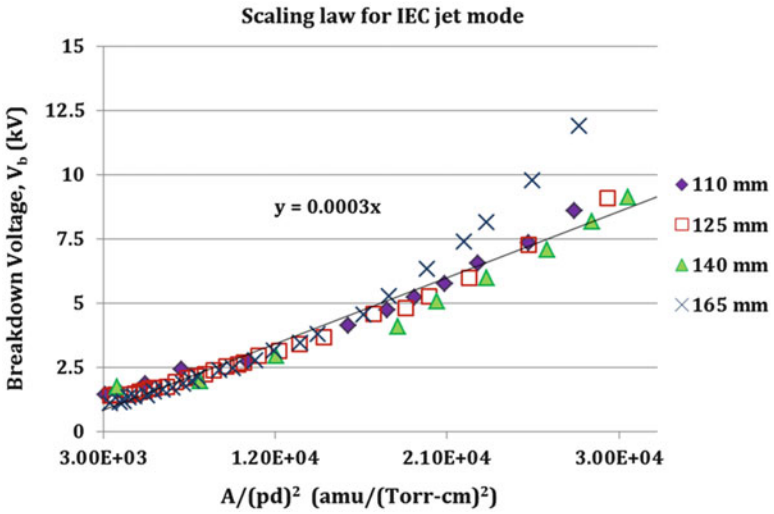

Fig. 6.39 Size scaling for IEC jet mode

cathode grid. Depending on the accuracy and range of input voltage of the IEC power supply, an appropriate jet mode pressure regime and hence the radius of the grid can be determined. The grid with the least geometric transparency seems to deviate slightly from this scaling law. The geometric transparencies appear to be of less relevance in the Paschen curve plot but require further studies to confirm their effect on the discharge characteristics.

6.7 Development of a Compact IEC Device

A recent study [30] at Kansai University, Japan investigated use of a small anode to allow high gas pressure operation where, theoretically, the neutron production rate (NPR) increases in proportion to gas pressure. This is opposite to operation at low gas pressure with a large anode where the NPR is not proportional to gas pressure. In addition to numerical studies of the discharge characteristics with a small anode, fabrication of such a compact IEC device was done to allow experiments for comparison to numerical studies as described in reference [31]. Here we provide some highlights of this study.

A three-dimensional Monte Carlo particle-in-cell code, termed K-PIC, that included the atomic processes was used for the numerical studies. The full three-dimensional potential was included to represent the potential effect of the feedthrough and the spatial structure of the cathode. The finite difference method with a 1-mm spatial mesh was used. Deuterium ions (D^+, D_2^+, D_3^+), fast neutrals

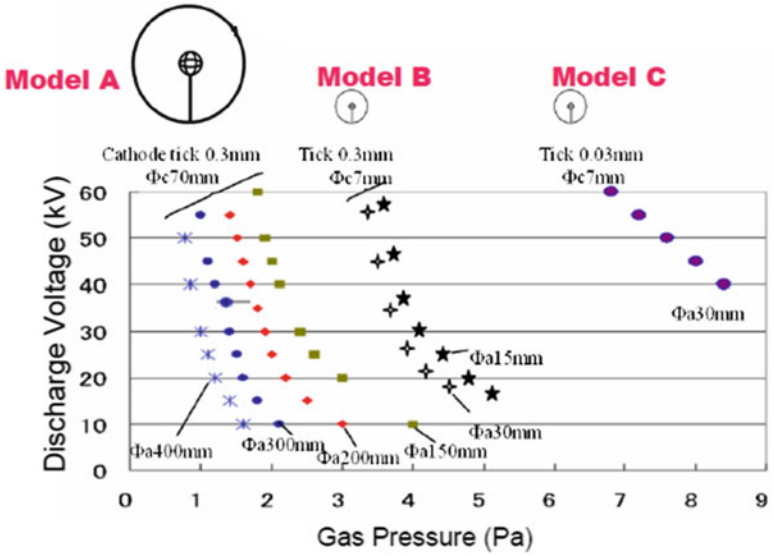

Fig. 6.40 Voltage–pressure curves for various cathode and anode diameters (Φ_c and Φ_A, respectively) [31]

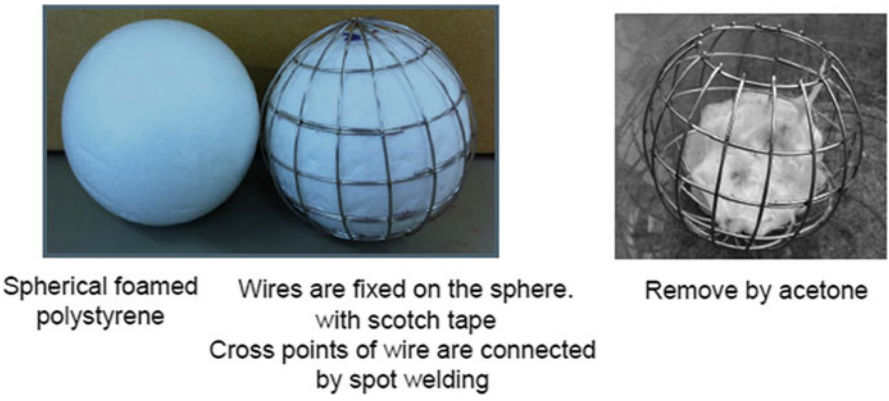

Fig. 6.41 Fabrication techniques for anodes [31]

(D^0, $D_2{}^0$), and electrons (e^-) were included as tracking particles. Results from these K-PIC calculations are shown in Fig. 6.40.

As seen from these curves, operation on the left side of the Paschen curve is predicted such that the discharge voltage rapidly increases with gas pressure Pa. Also for models A and B, the breakdown voltage increases for a fixed pressure as the diameter of the anode Φ_A is increased.

Correspondingly, the breakdown curve is shifted to the left. Fabrications of the compact anode used the techniques shown in Fig. 6.41. The cathode diameter, Φ_c, is

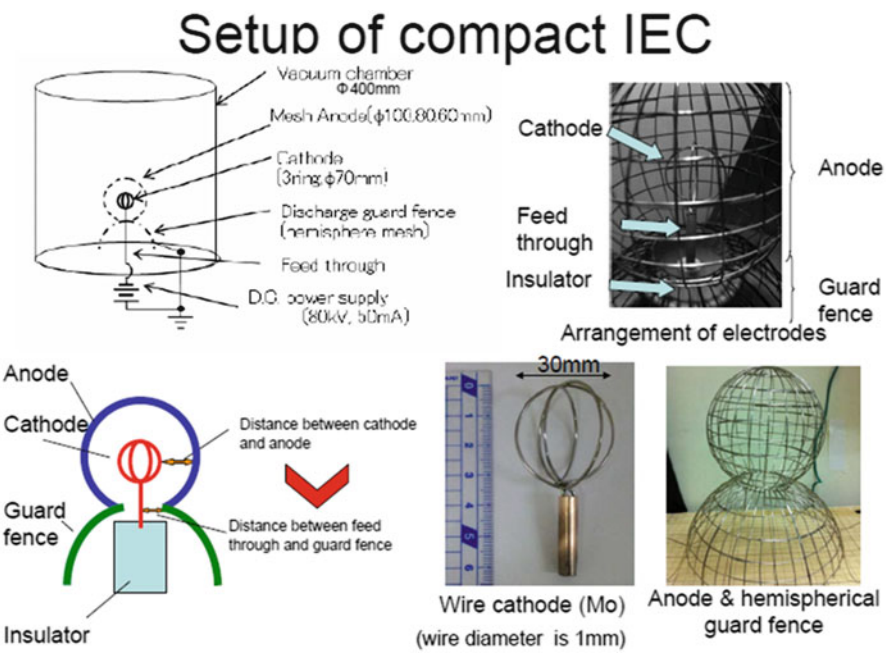

Fig. 6.42 Kansai compact IEC setup [31]

increased. These calculated behaviors are consistent with what would be expected for operation on the left of the Paschen curve. Also, as expected the crucial parameter is the pressure times the anode cathode spacing, i.e., pd where $d = \Phi_c - \Phi_A$. To verify these numerical evaluations, a technique to construct experiments with various sized small anodes was developed and is briefly reviewed here.

These grids were then employed in the experimental setup of the Kansai compact IEC as shown in Fig. 6.42, and results from the compact IEC experiment are shown in Fig. 6.43.

As seen from the plots to the right in Fig. 6.43, at lower pressures, the cathode runs at very high temperature. As a result, secondary electronic emission is strong, assisting significantly in the discharge formation through electron–neutron production of ion–electron pairs. This was not fully handled in the K-PIC code simulation, so it is thought to account for the discrepancy between these results and the V–P curves of Fig. 6.40. Most significantly, the breakdown voltage measured in Fig. 6.43 is significantly lower than predicted in the numerical studies of Fig. 6.40. This is attributed to the added ion–electron pair production from the streaming electrons.

The results from this new device were also compared to an earlier experiment, where the anode was varied from (Φ_A 150–300 mm). In this case, the cathode used six rings of thin (0.3-mm thick) Mo wire. With this design the cathode was not heated so much, reducing secondary electron emission, thus the P–V curve was shifted to the

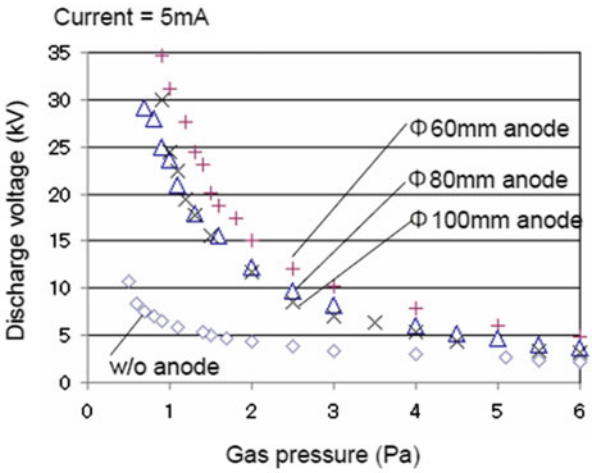

Fig. 6.43 Measuring units of voltage–pressure with varying anode diameters [31]

right corresponding to higher gas pressures, in better agreement with the numerical predictions of Fig. 6.18. These results provide important insight into the thermal-induced secondary electron emission (also see chapter 8) and the complicated inter-relations between the various effects that ultimately affect the NPR in a given device. This has caused confusion when the NPR for various IEC device designs has been compared. Such comparisons are not valid unless careful control is maintained over all factors, extending to grid design, temperature, and materials.

6.8 Summary

This chapter discussed several aspects of the effect of grid design on IEC operational performance. The IEC can operate with an amazing number of different grid designs ranging from a few isolated grid wires to a very dense, closely spaced wire construction. It is difficult to present a prescription for the "ideal" grid due to the many factors that affect the performance, such as the grid construction materials, symmetry, method of assembly at grid wire crossings, and pressure and voltage regimes. However, for common operation, it is recommended that the grid be designed with fairly large openings between grid wires so that microchannels, such as those that appear in the "Star" mode, are formed. This provides minimum interception of ions by the grid, because the microchannels guide the majority of ions through the center of the grid openings. In addition, once the microchannel mode is achieved so that the effective transmission ratio is large, the diameter of the cathode and anode plus operating pressure range and voltage begin to play an important role. Thus it is recommended that the grid parameters and operational parameters be studied experimentally to optimize performance for the application intended. Measuring the performance, though, presents additional challenges,

particularly where the majority of fusion occurs due to ion–neutral collisions, which are spread out over the volume of the IEC chamber. However, as discussed in this chapter, complications brought about due to charge exchange collisions and associated effects may make accounting for the entire source volume. For example, some reactions may occur due to ion or fast charge exchange neutral collisions with embedded gas in the grids, chamber wall, or parts of the high-voltage stalk. Indeed, the stalk design should be tailored to conform to the grid design.

Proton detector calibration is more complicated than a neutron detector calibration as a proton detector is capable of observing the variations in the source regimes. Grid wires play a major role in determining the observed proton rates, and depending on the presence of grid wires in the view of the detector, the proton rate could vary by as much as 40 % or higher. A thorough understanding of the source regime distribution is necessary for proton detector calibration. Dedicated eclipse disk diagnostics were used to determine the source regime contributions and discussions on how to use such measurements in the calculation of the calibration factors presented. The shadowing effects of the grid wires on the proton measurements are very significant and cannot be ignored during the direct proton-based multiple well observations. Sufficient care has to be taken to avoid the presence of the grid wires in the direct view of the proton detector during such measurements. The preferred orientation of the grid is to have the microchannels point away from the detector.

The jet mode size scaling law represents the behavior of the discharge reasonably well, and the discharge characteristics are at most a weak function of the radius of the cathode grid. Depending on the required specific impulse and range of input voltage of the IEC power supply, an appropriate jet mode pressure regime and hence the radius of the grid can be determined. Experiments have shown that the grid with the least geometric transparency deviates slightly from this scaling law, while the grid with the highest geometric transparency destabilized the power supply. These results require more study to fully evaluate, but the rough trends seem well illustrated.

References

1. Wehmeyer AL, Radel RF, Kulcinski GL (2005) Optimizing neutron production rates from D–D fusion in an inertial electrostatic confinement device. Fusion Sci Technol 47:1260
2. Krupakar Murali S, Kulcinski GL, Santarius JF (2008) Study of ion flow dynamics in an inertial electrostatic confinement device through sequential grid construction. Phys Plasmas 15:122702
3. Kulsrud RM, Furth HP, Valso EV, Goldhaber M (1982) Fusion reactor plasmas with polarized nuclei. Phys Rev Lett 49:1248
4. Tamor S, Shuy GW, Liu KF (1982) Fusion reactions of polarized deuterons. Bull Am Phys Soc 27:922
5. Ashley RP, Kulcinski GL, Santarius JF, Krupakar Murali S, Piefer G, Cipiti BB, Radel R (2003) Recent progress in steady state fusion using D–^{3}He. Fusion Sci Technol 44:559

6. Krupakar Murali S, Cipiti BB, Santarius JF, Kulcinski GL (2006) Study of fusion regimes in an inertial electrostatic confinement device using the new eclipse disk diagnostic. Phys Plasmas 13:053111
7. Penning FM (1936) Die glimmentladung bei niedrigem druck zwischen koaxialen zylindern in einem axialen magnetfeld. Physica (The Hague) 3:873
8. Cipiti BB (2004) Ph.D. thesis. Department of Engineering Physics, University of Wisconsin, Madison
9. Farnsworth PJ (1966) Electric discharge device for producing interaction between nuclei. US Patent 3,258,402
10. Hirsch RL (1967) Inertial-electrostatic confinement of ionized fusion gases. J Appl Phys 38(11):4522–4534
11. Krupakar Murali S, Santarius JF, Kulcinski GL (2012) Effects of the cathode grid wires on fusion proton measurements in inertial electrostatic confinement devices. IEEE Trans Plasma Sci 39(2):749–755
12. Miley GH, Sved J (2000) The IEC star-mode fusion neutron source for NAA status and next step designs. Appl Radiat Isot 53:779–783
13. Nadler JH (1992) Space-charge dynamics and neutron generation in an inertial-electrostatic confinement device. Ph.D. dissertation, University of Illinois at Urbana-Champaign
14. Thorson TA, Durst RD, Fonck RJ, Wainwright LP (1997) Convergence, electrostatic potential, and density measurements in a spherically convergent ion focus. Phys Plasmas 4(1):4–15
15. Thorson TA (1996) Ion flow and fusion reactivity characterization of a spherically convergent ion focus. Ph.D. dissertation, University of Wisconsin, Madison
16. Khachan J (2003) Spatial distribution of ion energies in an inertial electrostatic confinement device. Phys Plasmas 10(3):596–599
17. Yoshikawa K, Takiyama K, Koyama T, Taruya K, Masuda K, Yamamoto Y, Toku T, Kii T, Hashimoto H, Inoue N, Ohnishi M, Horiike H (2001) Measurement of strongly localized potential well profiles in an inertial-electrostatic fusion neutron source. Nucl Fusion 41 (6):717–720
18. Swanson DA, Cherrington BE, Verdeyen JT (1973) Potential well structure in an inertial electrostatic plasma confinement device. Phys Fluids 16(11):1939–1945
19. Meeker DJ, Verdeyen JT, Cherrington BE (1973) Measurement of electron density in a cylindrical inertial electrostatic plasma confinement device. J Appl Phys 44(12):5347–5355
20. Satsangi AJ (1996) Light intensity measurements of an inertial electrostatic confinement fusion plasma. M.S. thesis, Department of Nuclear, Plasma and Radiological Engineering, University of Illinois at Urbana-Champaign
21. Gu Y, Miley GH (2000) Experimental study of potential structure in a spherical IEC fusion device. IEEE Trans Plasma Sci 28(1):331–346
22. Matsuura H, Takaki T, Nakao Y, Kudo K (2001) Ion distribution function and radial profile of neutron production rate in spherical inertial electrostatic confinement plasmas. Fusion Technol 39:1167
23. Krupakar Murali S, Santarius JF, Kulcinski GL (2011) Effects of the cathode grid wires on fusion proton measurements in inertial-electrostatic confinement devices. IEEE Trans Plasma Sci 39(2):749–755
24. Donovan DC (2011) Spatial profiling using a time of flight diagnostic and applications of deuterium–deuterium fusion in inertial electrostatic confinement fusion devices. Ph.D. thesis, Department of Engineering Physics, University of Wisconsin, Madison
25. Krupakar Murali S, Santarius JF, Kulcinski GL (2010) Proton detector calibration in a gridded inertial electrostatic confinement device. IEEE Trans Plasma Sci 38(11):3116–3127
26. Cipiti BB (2004) Ph.D. thesis, Department of Engineering Physics, University of Wisconsin
27. Krishnamurthy A (2012) Development and characterization of an inertial electrostatic confinement thruster. M.S. thesis, Department of Nuclear, Plasma and Radiological Engineering, University of Illinois at Urbana-Champaign
28. Paschen F (1889) Ueber die zum Funkenübergang in Luft, Wasserstoff und Kohlensäure bei verschiedenen Drucken erforderliche Potentialdifferenz. Ann Phys 273(5):69–75

29. Hochberg TA (1992) Characterization and modeling of the gas discharge in a SFID neutron generator. M.S. thesis, Department of Nuclear, Plasma and Radiological Engineering, University of Illinois at Urbana-Champaign
30. Osawa H, Makino K, Nakagawa Y, Ohnishi M (2012) Development of compact inertial electrostatic confinement fusion device. In: 14th US-Japan workshop on IEC, University of Maryland
31. Osawa H, Tabata T, Ohnishi M (2005) Numerical study on glow discharge of IEC fusion. Fusion Sci Technol 47(4)

Chapter 7
Space Charge-Limited Flow

7.1 Introduction

Chapter 2 discussed solutions to Poisson's equation for the case of very high currents in spherical geometry. The emphasis was on the buildup of a large space charge of either ions or electrons in the center of the device followed by the formation of one or more virtual electrodes. This then creates a trap for ions which could lead to very large fusion rates. The formation of this trap requires a very high vacuum to avoid ion–neutral fusion reactions or charge exchange with neutrals. This then requires external generation of ions with differential pumping to prevent inflow of neutral gas from the source region. However, as stated in Chap. 2, current experimental devices aimed at near-term applications such as neutron sources do not meet these conditions. Still, quite high currents can be created in these devices. Then their operation, particularly the radial profile for neutron production, requires the use of classical space charge-limited flow analysis, i.e., does not involve formation of multiple virtual electrodes or the so-called double potential well. However, some experiments with gridded IECs that have examined space charge-limited flow show the practical consequences involved in the formation of the converged high-density core plasma.

In this chapter, for simplicity, we begin by considering a parallel plate vacuum diode to illustrate the space charge-limited flow. Conceptually, if the IEC has high ion currents, convergence at the center region creates an especially high space charge there. If the ion current is increased further, the center space charge may cause the ions to turn without passing through the center (see Fig. 2.2b). In that case they do not gain as high velocity as those circulating through the center core region, and this in turn reduces the fusion rate in the core. In that case, the fusion rate ceases to be a linear function of the ion current, and the spatial distribution of fusion reactions is shifted away from the center. This effect corresponds to the situation shown in Fig. 2.2b, although the fusion rate spatial profile will not necessarily follow the same trends as discussed in Chap. 2 due to the effect on the reactions taking place with background neutrals, which maintain an essentially uniform density.

G.H. Miley and S.K. Murali, *Inertial Electrostatic Confinement (IEC) Fusion: Fundamentals and Applications*, DOI 10.1007/978-1-4614-9338-9_7,

7.2 Space Charge-Limited Flow in a Parallel Plate Vacuum Diode

Consider the vacuum diode shown schematically in Fig. 7.1a. In this example, the current only consists of electrons. As a voltage is applied across the electrodes, electrons are emitted from the cathode surface due to the electric field created at the surface. The potential gradient creating this electric field is initially linear. As the electron current increases, the electrons flowing between the electrodes create a space charge that causes an opposing electric field as illustrated in Fig. 7.1a, b. As the electron current increases, this opposing field gradually reduces electron emission from the cathode, and if the net electric field at the surface is nulled out, the emission stops all together. This effect, illustrated in Fig. 7.1, is termed space charge-limited emission. In other words, the current produced by the diode is not limited by its capability for field emission of electrodes but by the canceling effect that the current has on the net electric field at the cathode surface.

In Fig. 7.1, the vacuum potential is linear. As the current increases, the space charge created by electrons in the space between the diode's electrodes increases until a potential profile is created that is perpendicular to the cathode plate. Thus, the electric field,

$$E = \frac{dV}{dX} = 0. \tag{7.1}$$

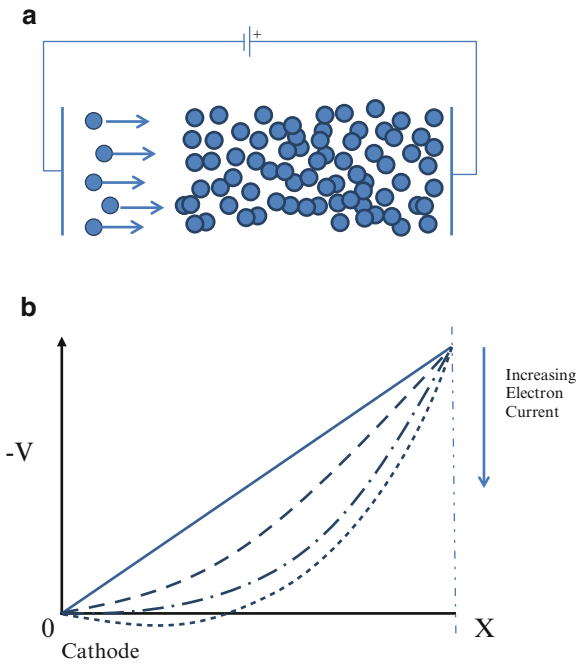

Fig. 7.1 (**a**) Illustration of electron emission from the cathode and buildup of density as seen from the cathode. (**b**) Plot of the potential, V, in a diode where electrons are emitted from the cathode

Then, the electron emission there stops, corresponding to the limiting current. If the current were to increase further, the potential would form a potential minimum in front of the cathode, creating a change in the direction of the electric field, trapping any electrons emitted (assuming electrons are emitted with zero velocity).

7.3 Child–Langmuir Law for Space Charge-Limited Emission

7.3.1 Geometry of a Parallel Infinite Plate Vacuum Diode

The derivation of space charge-limited emission is a cornerstone of diode physics. The first form of the well-known Child–Langmuir law was published in 1911 [1]. Beginning with Poisson's equation and the one-dimensional boundary conditions of a parallel infinite plate diode, the maximum current density at which the cathode surface electric field is nulled out can be found.

The geometry of the parallel infinite plate diode (shown in Fig. 7.2) consists of an infinite grounded cathode and an anode held at some potential, V_o. Any edge effects are ignored for simplicity, i.e., $R \rightarrow \infty$. The two plates of the diode are some distance, D, apart. Current is then allowed to flow across the vacuum gap. When the space charge-limited condition is met at the emission surface, the electric field produced by the current in the gap will balance the electric field produced by the potential difference of the two plates.

Though this case is not directly applicable to the spherical geometry of the IEC devices where current convergence occurs toward the center region, it is useful to illustrate the physics involved.

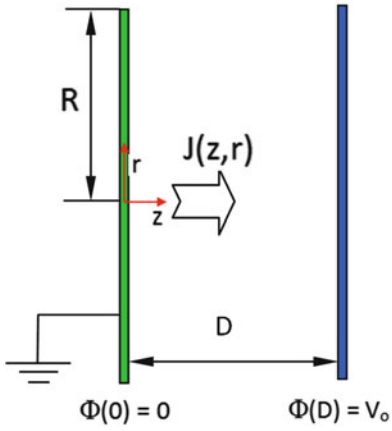

Fig. 7.2 Infinite parallel plate diode geometry

7.3.2 Derivation of the Child–Langmuir Law

The derivation of the Child–Langmuir law was carried out by Christopher G. Carr [2]. The unknown quantity is the maximum current density, $J(z,r)$, that can flow in such a diode. We begin with the Poisson's equation:

$$\nabla^2\Phi(z,r) = -\frac{\rho(z,r)}{\varepsilon_o}, \tag{7.2}$$

where Φ is the electric potential and ρ is the charge density. Also, ε_0 is the permittivity of free space, with a value of 8.854×10^{-12} farads per meter.

For the one-dimensional case, the potential does not vary in the radial direction and hence the Laplacian in Eq. 7.2 reduces to

$$\frac{\partial^2\Phi(z)}{\partial z^2} = -\frac{\rho(z,r)}{\varepsilon_o}. \tag{7.3}$$

By conservation of charge, we may obtain the current charge density as follows:

$$J(z) = \rho(z) \times \nu(z). \tag{7.4}$$

Similarly, the conservation of energy gives us the following relation:

$$PE(0) + KE(0) = PE(z) + KE(z). \tag{7.5}$$

We now assume that the charge is emitted at the cathode with zero velocity and hence $KE(0) = 0$; similarly, the potential at the cathode surface is also assumed to be zero. Hence, Eq. 7.5 becomes

$$0 = -e \times \Phi(z) + \frac{1}{2} m_e v(z)^2. \tag{7.6}$$

Then, the parametric representation of the velocity becomes

$$v(z) = \sqrt{\frac{2e \times \Phi(z)}{m_e}}. \tag{7.7}$$

Substitution of Eqs. 7.4 and 7.7 into the Poisson's equation results in an expression relating the potential and the current density. The expression is a second-order nonlinear differential equation.

$$\frac{\partial^2\Phi(z)}{\partial z^2} = -\frac{J(z)}{\varepsilon_o}\sqrt{\frac{m_e}{2e}} \times \frac{1}{\Phi(z)}. \tag{7.8}$$

The boundary conditions that lead to the space charge-limited solution are the potentials at the anode and the cathode (see Fig. 7.2), and the condition that the electric field at the cathode be zero.

$$\Phi(0) = 0 \tag{7.9a}$$

$$\Phi(D) = V_o \tag{7.9b}$$

$$\frac{\partial \Phi(0)}{\partial z} = 0 \tag{7.9c}$$

The last boundary condition is imposed because we are solving for the space charge-limited emission case.

If we now apply the boundary conditions and solve for J, we obtain the space charge-limited current emission density as follows:

$$J_{scl} = \frac{4}{9}\varepsilon_o \sqrt{\frac{2e}{m_e}} \times \frac{V_o^{3/2}}{D^2}. \tag{7.10}$$

This is the maximum current density that can flow in a collisionless parallel infinite plate diode, given a potential difference, V_o, and spacing, D. Given this current density, substitution yields solutions to the following useful quantities:

$$\text{Potential:} \quad \Phi(z) = V_o \times \left(\frac{z}{D}\right)^{4/3}. \tag{7.11}$$

$$\text{Electric Field:} \quad |E| = \frac{4}{3} \times \frac{V_o}{D} \times \left(\frac{z}{D}\right)^{1/3}. \tag{7.12}$$

$$\text{Charge Density:} \quad \rho(z) = \frac{4}{9}\varepsilon_o \frac{V_o}{D} \times \left(\frac{z}{D}\right)^{-2/3}. \tag{7.13}$$

7.3.3 Limitations of the Child–Langmuir Derivation

The Child–Langmuir approach gives us the space charge limit, but it is only valid for the one-dimensional case. It has been generalized to infinite cylindrical and spherical geometries, but it has not been solved for a finite emission area. Relative to the practical case of a gridded IEC, the transparency of the cathode (or anode) grid plus spherical geometry provides a considerable challenge for analysis. Instead of approaching the problem from the Poisson's equation, which generates a nonlinear differential equation, the integral form of Coulomb's law can be used.

Then the space charge limit can be developed by integration. For that reason, it is useful to consider this approach as well. We will continue with the idealized parallel plate geometry in this illustration. It may also be shown that the Coulomb's law and Poisson's equation are two different, but equally valid, forms of Gauss's law [2]. The results obtained by applying either equation to the conditions of the space charge-limited diode would be equivalent.

7.4 Langmuir Spherical Geometry Problem

In this section we will discuss an analytical solution to the Langmuir spherical problem for monoenergetic electrons with an initial velocity [3, 4]. The Langmuir spherical problem is expressed by a differential equation and the solutions were presented in Table 2.1 in Chap. 2. However, analytical solutions (see reference [5]) are more desirable and will be presented in this section.

The spherical vacuum diode is a system of two concentric spherical metal electrodes. The inner electrode, with a radius of r_k, acts as the cathode of the diode, and the outer electrode with a radius of r_a acts as the anode (see Fig. 7.3). There is a high vacuum in the volume between the two spheres (absolute permittivity of vacuum is ε_o); hence there is no source of ions or electrons between the electrodes in this model.

The cathode is assumed to emit electrons with a mass, m, an electric charge, q ($q < 0$), and an initial velocity, v_o, outward in the radial direction. The current density of the emitted electrons on the cathode surface is equal. Thus, the emitted electrons (their flow) create a current, I_0. Both metal electrodes are below the potential difference of $U = \phi_a - \phi_k$, where ϕ_k represents the cathode electric potential while ϕ_a stands for the anode potential.

The electron flow and the parameters of the electric field will be described using a spherical coordinate system with an origin lying at the center of the spheres $\vec{r} = (r, \theta, \phi)$. Due to the spherical symmetry of the problem, all scalars depend only on the coordinate r. All vectors of the values are radial and depend on the coordinate r.

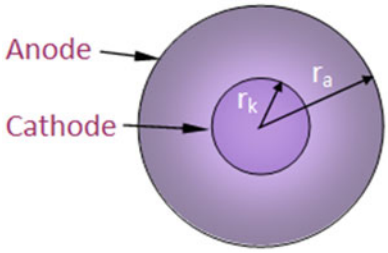

Fig. 7.3 Spherical vacuum diode arrangement

The electric potential $\phi(r)$ in the volume closed by the two spherical electrodes as a function of the potential is as follows:

$$\phi(r = r_k) = \phi_k, \tag{7.14}$$

$$\phi(r = r_a) = \phi_a. \tag{7.15}$$

The electric field potential is formed by the volume density of the electron charge of k (also represented by qn_e) and is expressed by the Poisson's equation. Due to spherical symmetry, the latter takes the form

$$\frac{1}{r^2} \times \frac{d}{dr}\left(r^2 \frac{d\phi}{dr}\right) = -\frac{k}{\varepsilon_o}. \tag{7.16}$$

The emitted cathode electrons flow into the volume of the two electrodes and move at a velocity of v_r. Due to the conservative electric field, which acts on the electrons, the law of conservation of energy is valid for the electrons. To calculate the velocity, the law of conservation of energy is applied for the cathode surface as well as for an arbitrary point in the volume at a distance of r from the origin of the coordinate system.

$$\frac{m \times {v_r}^2}{2} + q \times \phi(r) = \frac{m \times {v_0}^2}{2} + q \times \phi_k. \tag{7.17}$$

From Eq. 7.43 we obtain

$$v_r = \sqrt{{v_0}^2 + \frac{2q}{m}(\phi_k - \phi(r))}. \tag{7.18}$$

The charged particles move and create current with a density of j_r. For the current density, we have

$$\begin{aligned} j_r &= qn_e v, \\ &\equiv k v_r, \end{aligned} \tag{7.19}$$

where qn_e is the density. From the law of conservation of charge for the stationary case, we obtain

$$\frac{1}{r^2}\frac{d}{dr}\left(r^2 \times j_r\right) = 0. \tag{7.20}$$

In respect with Eq. 7.46, the product in the derivative is a constant quantity. Thus, the current density j_r can be written as

$$j_r = -\frac{I_0}{4\pi r^2}. \tag{7.21}$$

Equation 7.19 regarding Eqs. 7.18 and 7.21 gives

$$k = \frac{j_r}{V_r} = -\frac{I_0}{4\pi r^2 \sqrt{{V_0}^2 + \frac{2q}{m}(\phi_k - \phi(r))}}. \tag{7.22}$$

So far, the volume density of the electric charge (qn_e) k has been expressed by the current flowing along the diode, I_0, and the electron velocity, v_r. Inserting Eq. 7.48 into Eq. 7.42, we obtain

$$r^2 \frac{d^2\phi}{dr^2} + 2r\frac{d\phi}{dr} = \frac{I_0}{4\pi\varepsilon_o \sqrt{{v_o}^2 + \frac{2q}{m}(\phi_k - \phi(r))}}. \tag{7.23}$$

The result is a second-order ordinary differential equation for the electric field potential $\phi(r)$ in the volume of a spherical vacuum diode. Considering the fact that the equation is nonlinear, its solution is difficult. To simplify the process of finding the solution, we now make these equations dimensionless. The initial electron kinetic energy E_0 will be taken as a scale of energy [3]:

$$E_0 = \frac{m{v_0}^2}{2}. \tag{7.24}$$

Defining the dimensionless potential, we have [3]

$$\Phi = \frac{q(\phi_k - \phi(r))}{E_0}. \tag{7.25}$$

Inserting Eq. 7.51 in Eq. 7.49, we obtain

$$r^2 \frac{d^2\Phi}{dr^2} + 2r\frac{d\Phi}{dr} = -\frac{q}{v_0 E_0} \times \frac{I_0}{4\pi\varepsilon_o \sqrt{1+\Phi}} = \frac{i_0}{\sqrt{1+\Phi}}. \tag{7.26}$$

Here, the dimensionless current i_0 is given by

$$i_0 = \frac{-q}{v_0 E_0}\frac{I_0}{4\pi\varepsilon_o} = \frac{-2q}{m}\frac{1}{{v_0}^3}\frac{I_0}{4\pi\varepsilon_o}. \tag{7.27}$$

The classic Eq. 7.52 was first solved numerically by Langmuir [3] in 1924, and the results were originally presented in a tabular form (see Table 2.1 in Chap. 2).

7.4.1 Langmuir's Numerical Solution

In an alternate approach, Langmuir [2] used the logarithm from the relation between the radius and the emitter (cathode) radius as a space parameter. Assuming

the electric field intensity on the emitter is zero, this radius corresponds to the radius of the minimum electric potential r_m. We now define a quantity η as follows:

$$\eta = \ln\left(\frac{r}{r_m}\right). \tag{7.28}$$

Substituting Eq. 7.54 into Eq. 7.52, we obtain

$$\sqrt{1+\Phi}\left(\frac{d^2\Phi}{d\eta^2} + \frac{d\Phi}{d\eta}\right) = i_0. \tag{7.29}$$

The dimensionless potential $\Phi(\eta)$ is expressed as a function by the dimensionless function $\alpha(\eta)$ as follows [2]:

$$(1+\Phi)^{3/2} = \frac{9}{4} i_0 \alpha^2. \tag{7.30}$$

Then, the potential is expressed as

$$(1+\Phi) = \left(\frac{9}{4} i_0\right)^{2/3} \alpha^{4/3}. \tag{7.31}$$

Substituting Eq. 7.29 in Eq. 7.27, we obtain

$$3\alpha\alpha'' + \alpha'^2 + 3\alpha\alpha' = 1. \tag{7.32}$$

Here the prime represents a derivative with respect to the function's argument.

Thereby, we obtain the second-order nonlinear differential equation for $\alpha(\eta)$. An analytical solution has not been presented for this equation. Therefore, it has traditionally been represented in the form of Taylor infinite series. The first terms of the series give [2]

$$\alpha^2 = \eta^2 - 0.6\eta^3 + 0.24\eta^4 - 0.074\eta^5 + \ldots \tag{7.33}$$

Langmuir evaluated Eq. 7.33 numerically and presented $\alpha(\eta)$ as shown in Table 7.1.

7.4.2 *Effect of Grid Radius*

We now consider the saturated ion current calculated by solving Eq. 7.52. The maximum ion current equation is given by [3]

$$\mathrm{I}_{\max} = \frac{16\pi\varepsilon_0}{9}\sqrt{\frac{2q}{m}}\frac{V_0^{3/2}}{\alpha^2}. \tag{7.34}$$

Table 7.1 Values of $\alpha^2(r)$ (the solution of Eq. 7.33)

r/r_m	$\alpha^2(r)$	r_m/r	$\alpha^2(r)$
1.0	0.0000	1.0	0.0000
1.1	0.0086	1.1	0.0096
1.2	0.0299	1.2	0.0372
1.5	0.1302	1.5	0.2118
2.0	0.3260	2.0	0.7500
5.0	1.1410	5.0	7.9760
10.0	1.7770	10.0	29.1900
20.0	2.3780	20.0	93.2400
50.0	3.1200	50.0	395.3000
100.0	3.6520	100.0	1141.0000
200.0	4.1660	200.0	3270.0000
500.0	4.8290	500.0	13015.0000

From Eq. 7.34 it is apparent that the ion current that can be drawn from an emitter electrode is inversely proportional to the square of α, which is a function of radius ratio [$\alpha \sim \ln(r_c/r_a)$], where r_c is the cathode radius and r_a is the anode radius. Moreover, the current is independent of the actual sizes of the spheres because the radii appear only in a ratio. It is apparent from Eq. 7.78 that the ion current increases as the radius ratio decreases, meaning that the larger ion currents can be drawn from the system if the emitter cathode radius is increased. This trend would seem to apply to IEC grids, but the full behavior is not treated by Eq. 7.12 due to the many assumptions made in the derivation that are not applicable to the IEC (e.g., the IEC has electron–ion source production between the electrodes, electron emission due to ion bombardment, and the cathode is "transparent").

We now introduce the analytical solution of space charge-limited current for various geometries as developed by Oksuz [6].

7.4.3 Analytical Solution of Space Charge-Limited Current

The following section introduces a technique to generate analytical solutions without boundary conditions [8]. Such solutions are applicable to plasmas with single charged particle species and high bias voltage boundaries. In this technique, the velocities of electrons or ions are assumed to be low enough that the electric field at the sheath edge can redirect them toward the boundaries. These assumptions are valid in low-pressure, low-temperature, and weakly collisional plasmas as in the case of most IEC devices.

The general form of the ordinary nonlinear differential equation in Cartesian coordinates can be written as

$$x^a \frac{d}{dx}\left(x^b \frac{dy}{dx}\right) = y^c, \tag{7.35}$$

Table 7.2 Values of a and b in various coordinate systems

	Coordinate system	a	b
1	Cartesian	0	0
2	Cylindrical	−1	1
3	Spherical	−2	2

where a, b, and c are real numbers, and $a + b \neq 2$ and $c \neq 1$. As shown in Table 7.2, the values of a and b take different values for different coordinate systems.

Checking the scaling of the differential Eq. 7.35 gives

$$x^{a+b-2} \propto y^{c-1}. \tag{7.36}$$

The general solution in Cartesian coordinates for Eq. 7.35 can be written as

$$y = A[Bx + C]^{(2-a-b)/(1-c)}, \tag{7.37}$$

where the constants A, B, and C can be determined by substituting the solution into Eq. 7.35 and/or by using the boundary conditions. However, it is convenient to observe that C takes a value of zero for cylindrical and spherical systems. We continue our derivation with the continuity equation, energy conservation equations, and the Poisson's equation:

$$\varepsilon \frac{d^2\phi}{dx^2} = q(n_e - n_i), \tag{7.38}$$

where ε is the plasma permittivity, q is the electron charge, ϕ is the plasma potential, and n_e and n_i are the electron and ion densities, respectively. Inside the ion sheath there are no electrons, so $n_e = 0$, and using energy conservation and flux conservation, Poisson's equation can be written as [7]

$$\frac{d^2\phi}{dx^2} = \frac{j}{\varepsilon}\left(\frac{2q}{m}\right)^{-\frac{1}{2}} \phi^{-\frac{1}{2}}, \tag{7.39}$$

where $j = qnv$ current density. The general solution method is given in reference [10]. This equation can easily be solved for ϕ using the solution method given in Eq. 7.37 for the same boundary conditions, and the same results can be obtained:

$$\phi = \left(\frac{3}{2}\right)^{4/3} j^{2/3} \left(\frac{2\varepsilon^2 q}{m}\right)^{-1/3} x^{4/3}. \tag{7.40}$$

Pulling out the current density gives

$$j = \frac{4\varepsilon}{9}\left(\frac{2q}{m}\right)^{\frac{1}{2}} \frac{\phi^{\frac{3}{2}}}{x^2}. \tag{7.41}$$

When $x = 0$ the electric field is zero for planar sheaths. It is also clear that $\phi = 0$ at $x = 0$ for the special case with B = 0. This is similar to the Child–Langmuir space charge-limited current for planar sheaths. However, for the general solution, one would need two boundary conditions – one at $x = 0$ and the other at $\phi = \phi_s$ at $x = s$.

The first boundary condition gives us

$$\frac{d\phi}{dx} = E_0 \text{ and } \frac{d^2\phi}{dx^2} = \underbrace{\frac{j}{\varepsilon}\left(\frac{2q}{m}\right)^{-\frac{1}{2}}}_{D}\phi^{-\frac{1}{2}}.$$

Inserting the general solution into the differential equation gives

$$D = \frac{4}{9}B^2, \tag{7.42}$$

$$\text{where } B = \frac{3}{2}\left[\frac{j}{\varepsilon}\left(\frac{2q}{m}\right)^{-\frac{1}{2}}\right]^{\frac{1}{2}}. \tag{7.43}$$

The first boundary condition gives

$$C = \left(\frac{3E_0}{4B}\right)^3 = \left\{\frac{E_0}{2\left[\frac{j}{\varepsilon}\left(\frac{2q}{m}\right)^{-\frac{1}{2}}\right]^{\frac{1}{2}}}\right\}^3, \tag{7.44}$$

$$\phi = \left\{\frac{3}{2}\left[\frac{j}{\varepsilon}\left(\frac{2q}{m}\right)^{-\frac{1}{2}}\right]^{\frac{1}{2}}x + \frac{{E_0}^3}{8\left[\frac{j}{\varepsilon}\left(\frac{2q}{m}\right)^{-\frac{1}{2}}\right]^{\frac{3}{2}}}\right\}^{4/3}. \tag{7.45}$$

As stated earlier, by applying the second boundary condition that the potential $\phi = \phi_s$ at $x = s$, we obtain

$$\phi = \left\{\frac{3}{2}\left[\frac{j}{\varepsilon}\left(\frac{2q}{m}\right)^{-\frac{1}{2}}\right]^{\frac{1}{2}}(x-s) + \phi_s^{3/4}\right\}^{4/3}. \tag{7.46}$$

The current density can be found as

$$j = \left(\frac{2q}{m}\right)^{1/2}\varepsilon\left[\frac{2\left(\phi^{3/4} - \phi_s^{3/4}\right)}{3(x-s)}\right]^2. \tag{7.47}$$

This result is similar to the general form of the Child–Langmuir sheath solution in the Cartesian coordinates for a constant current density and constant flux case.

7.4.4 Cylindrical System

The Poisson's equation in the cylindrical system is given by

$$\frac{d}{rdr}\left(\frac{rd\phi}{dr}\right) = \frac{j}{\varepsilon}\left(\frac{2q}{m}\right)^{-1/2}\phi^{-1/2}. \tag{7.48}$$

The nonlinear ordinary differential equation can be solved directly using the given method, and we obtain

$$\phi = \left(\frac{3}{4}\right)^{4/3} j^{2/3}\left(\frac{2\varepsilon^2 q}{m}\right)^{-1/3} r^{4/3}, \tag{7.49}$$

and the current density is given by

$$j = \frac{16\varepsilon}{9}\left(\frac{2q}{m}\right)^{1/2}\frac{\phi^{3/2}}{r^2}. \tag{7.50}$$

7.4.5 Spherical System

For this system the Poisson's equation can be written for constant current density as

$$\frac{d}{r^2 dr}\left(\frac{r^2 d\phi}{dr}\right) = \frac{j}{\varepsilon}\left(\frac{2q}{m}\right)^{-1/2}\phi^{-1/2}. \tag{7.51}$$

Once again using the above method, we may integrate this equation directly. The solution thus obtained gives

$$\phi = \left(\frac{3}{2\sqrt{7}}\right)^{4/3} j^{2/3}\left(\frac{2\varepsilon^2 q}{m}\right)^{-1/3} r^{4/3}, \tag{7.52}$$

and the current density can be found for spherical geometry as follows:

$$j = \frac{28\varepsilon}{9}\left(\frac{2q}{m}\right)^{1/2}\frac{\phi^{3/2}}{r^2}. \tag{7.53}$$

There is no real application of the constant current density for spherical and cylindrical geometries unless there is ionization or loss inside the sheath. The

current to the electrode depends on the geometry. For planar geometry, sheath expansion has no effect on the collection area if the expansion is one dimensional, with exception to edge effects [8]. The current to a double-sided planar geometry in bulk plasma can be written as

$$I = jA = \frac{4A\varepsilon}{9}\left(\frac{2q}{m}\right)^{1/2}\frac{\phi^{3/2}}{x^2}. \tag{7.54}$$

Here, A is the area of the planar solid electrode and also the cross-sectional area of the sheath and pre-sheath. Similarly, for cylindrical geometry, the current can be found by multiplying the current density by the electrode area:

$$I = jA = 2\pi rlj = \frac{32\pi l\varepsilon}{9}\left(\frac{2q}{m}\right)^{1/2}\frac{\phi^{3/2}}{r}. \tag{7.55}$$

For space charge-limited current, the nonlinear Poisson's equation needs to be reorganized before solving for each of the geometries. We begin with the planar geometry, for which the solution is the same as that for constant current density. For this geometry, the Poisson's equation can be rearranged as

$$\frac{d}{dr}\left(\frac{rd\phi}{dr}\right) = \frac{2\pi rlj}{2\pi l\varepsilon}\left(\frac{2q}{m}\right)^{-1/2}\phi^{-1/2}, \tag{7.56}$$

where l is the length of the cylinder. The equation can be written as

$$\frac{d}{dr}\left(\frac{rd\phi}{dr}\right) = \frac{I}{2\pi l\varepsilon}\left(\frac{2q}{m}\right)^{-1/2}\phi^{-1/2}, \tag{7.57}$$

where I is the space charge-limited current. Thus, the solution is

$$\phi = \left(\frac{9}{4}\right)^{2/3}\left(\frac{I}{2\pi l\varepsilon}\right)^{2/3}\left(\frac{2q}{m}\right)^{-1/3}r^{2/3}, \tag{7.58}$$

and the current is given by

$$I = \frac{8\pi l\varepsilon}{9}\left(\frac{2q}{m}\right)^{1/2}\frac{\phi^{3/2}}{r}. \tag{7.59}$$

For two coaxial cylinders, the space charge-limited current is given by

$$I = \frac{8\pi l\varepsilon}{9}\left(\frac{2q}{m}\right)^{1/2}\frac{\phi^{3/2} - \phi_s^{3/2}}{r - r_s}. \tag{7.60}$$

This result is similar to the Langmuir–Blodgett's results [3] for space charge-limited current, but they introduced additional terms to solve the problem in terms of a series expansion.

Similarly, for spherical geometry, the current for constant current density is given by

$$I = j4\pi r^2 = \frac{112\pi\varepsilon}{9}\left(\frac{2q}{m}\right)^{1/2}\phi^{3/2}. \tag{7.61}$$

Though the Poisson's equation can be rearranged to represent a constant current case, the present method is not applicable because the constant A turns out to be zero in Eq. 7.37 and thus the solution becomes independent of r. Equation 7.60 is similar to the Langmuir–Blodgett equation given in reference [3] with $\beta = 1$ for cylindrical geometry. Equation 7.61 has a similar scaling to the Langmuir–Blodgett equations given in reference [3] for spherical geometry but with a different multiplication constant and $\alpha = 1$. The derivations are valid for electrons or ions without regard to the direction of the electric fields.

7.5 Experimental Observations of Space Charge-Limited Flow in Current IECs

Better models of system behavior and extrapolations of reactivity for higher voltages and currents can be developed by observing the effects of neutral pressure, asymmetries, injected current, and applied voltage on the ion velocity and density distributions. Hence, the experiments discussed in this section concentrate on convergence scaling and measurements of the potential and density distributions throughout the ion flow, initially at relatively low energies where probe technology can be deployed. First, we will introduce the logic behind the set of experiments conducted, followed by a detailed explanation of the experimental results observed.

Thorson and colleagues [9] have experimentally observed that the radial plasma potential distribution agrees with a collisionless, recirculating, space charge-limited current model. Flow convergence was observed to increase with voltage and neutral pressure, while the same decreased with cathode grid wire spacing and current. Using a high-voltage electrostatic probe, the first direct measurements of the central ion density, radial electrostatic potential profile, and accelerating potential symmetries were performed at relatively low pressures (< 53 mPa). To justify the collisionless assumption, a comparison of the various ion collision rates was studied. For the ion densities and neutral pressures studied in the Homer device at the University of Wisconsin, Madison, the ion–neutral collision rate ($\sim 10^5$/s) is lower than the effective ion–cathode collision rate ($\sim 2 \times 10^5$/s) [10]. The ion–ion collision rate is $\sim 10^{-3}$/s for the counterflowing ions and $\sim 10^4$/s for the

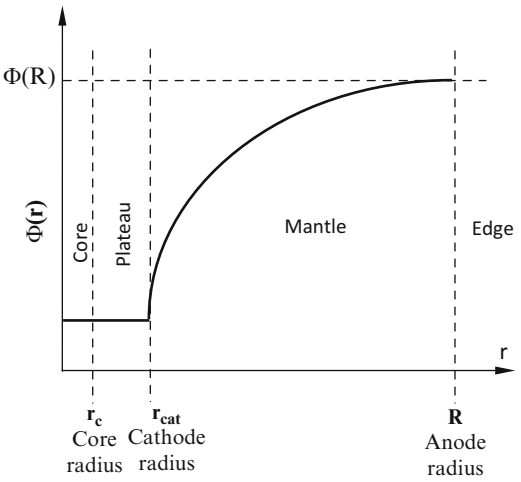

Fig. 7.4 The four regions of interest in a typical gridded IEC device [12]

co-propagating ions, and they are therefore less significant than the ion–cathode and ion–neutral collision [11]. Because the ion lifetime is limited mainly by the transparency of the cathode, the ions essentially appear as a collisionless species until termination at the cathode.

The ion flow characteristics change throughout the IEC device and are distinguished as illustrated in Fig. 7.4. In Fig. 7.4, the edge region is defined as $r > R$, the mantle is defined as $r_{cat} < r \leq R$, the plateau as $r_c < r \leq r_{cat}$, and finally the core is defined as $r \leq r_c$. Here R is the anode radius, r_{cat} is the cathode radius, and r_c is the core radius.

Figure 7.5 illustrates the idealized background ion distributions for the zones. For low-pressure discharges, cold plasma was generated at the edge, and any ions moving toward the cathode are accelerated to full energy in the mantle region. The plateau zone ideally contains monoenergetic ions inside the cathode, and the core distribution consists of a thin, spherical shell in velocity space at a radius of the core velocity.

Angular momentum of the ions at the edge, due to their perpendicular thermal velocity, $v_\perp(R)$, will keep the flow from perfectly converging to $r = 0$, but to the lowest order, one can assume the flow is converging to a radius r_c, defined as the core radius. All ions are assumed to be noninteracting and flow through the core with a velocity $v_c = \sqrt{2q\Phi_c/M}$ where Φ_c is the electric potential in the core [for $\Phi(R) = 0$], q is the ion charge, and M is the ion mass. By setting the average angular momentum of the ions at the edge equal to that of the ions passing through the core, $M\langle v_\perp\rangle R \approx (2/3)Mv_c r_c$, the core radius is then given by

$$r_c = \frac{3R\langle v_\perp\rangle}{2v_c} \approx \frac{3}{2}R\sqrt{\frac{kT_{\perp i}(R)}{q\Phi_c}}. \tag{7.62}$$

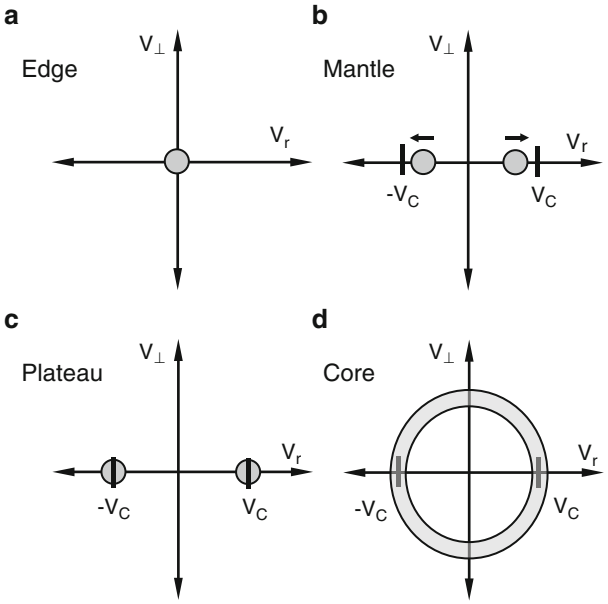

Fig. 7.5 Qualitative behavior of the ideal background ion velocity distributions in the lab frame for the different regions of interest (not to scale). (**a**) Edge: cold, thermal at $\langle v \rangle = 0$. (**b**) Mantle: low T_i, $v_r < v_c$. (**c**) Plateau: $v_r = \pm v_c$. (**d**) Core: isotropic shell $|v_r| = v_c$. In all cases, $T_i << \Phi_c$

Assuming no sources or sinks of particles, total current conservation demands that

$$n_i(r)v(r)r^2 = const \quad \text{for all } r, \tag{7.63}$$

where $n_i(r)$ is the local ion density. The steady-state radial profile is then given by

$$n_i(r) = n_i(R)\left(\frac{R}{r}\right)^2 \frac{v(R)}{v(r)} = n_i(R)\left(\frac{R}{r}\right)^2 \sqrt{\frac{E_{||}(R)}{q\Phi(r)}}. \tag{7.64}$$

Here, $E_{||}(R)$ is the radial energy of the ions at the edge.

Angular momentum conservation also prevents the ion density from diverging at $r = 0$, and a constant density is invoked in the core to provide a lowest-order estimate. Because the effective core area is a circle of radius r_c, the core density estimate becomes

$$n_{ic} = 4n_i(R)\left(\frac{R}{r_c}\right)^2 \frac{v(R)}{v_c} = 4n_i(R)\left(\frac{R}{r_c}\right)^2 \sqrt{\frac{E_{||}(R)}{q\Phi_c}}. \tag{7.65}$$

This model conserves average angular momentum and total particle flux, and while it fails to keep the density continuous at r_c, Eq. 7.65 should provide reasonable scaling estimates for comparisons with experimental results.

Substituting for r_c from Eq. 7.62 into Eq. 7.65, an estimate for the convergence factor (ratio of core to edge density) is found as follows:

$$\frac{n_{ic}}{n_i(R)} = \frac{16\sqrt{E_{||}(R)}}{9kT_{\perp i}(R)}\sqrt{q\Phi_c}. \tag{7.66}$$

From this equation we may conclude that the core density should optimally scale as the square root of the core potential for given edge plasma conditions.

The core density and system reactivity will ultimately depend on how much recirculating ion current can be sustained, and the resulting ion space charge limits the magnitude of this current for steady-state systems. The ideal space charge-limited ion current between concentric spheres (mantle region) is given by Eq. 7.34. Assuming no sources or sinks of particles between the electrodes (consistent at low pressure and density), Eq. 7.34 can be solved for the voltage as follows:

$$V(r) = \left[\frac{9I_{max}\alpha^2(r)}{16\pi\varepsilon_0}\sqrt{\frac{M}{2q}}\right]^{2/3}, \tag{7.67}$$

where α determines the radial dependence ($\alpha \rightarrow 0$ as $r \rightarrow R$). Although this equation was originally derived for solid electrodes, it also holds for semitransparent grids with counter-streaming ion flows if I_{man} represents the total recirculating ion current between the spheres.

For a gridded system, the amount of recirculating current is mainly limited by the effective cathode transparency. Assuming that the ions are equally likely to be lost at each pass through the cathode, the recirculation density enhancement factor, ξ, is given by [12]

$$\xi = \frac{I_{max}}{I_{cat}} = \frac{1}{(1-\eta^2)}, \tag{7.68}$$

where I_{cat} is the ion current collected by the cathode and η is the geometric grid transparency given by

$$\eta = \frac{(OpenArea)}{4\pi r_{cat}^2}. \tag{7.69}$$

We now assume that the grids are relatively cold (no thermionic emission), that there are no sharp points (no field emission), and that there are no photo emission electrons. Because the secondary emission cannot be ignored and is based on number of ions impacting the cathode and the measured ion grid current (I_{meas}) is

$(1+\delta)I_{cat}$, where δ is the secondary electron emission coefficient, the recirculation factor relates to the measured grid current by

$$\xi = \frac{I_{max}(1+\delta)}{I_{meas}}. \tag{7.70}$$

By comparing the measured radial electrostatic potential distribution, $V(r)$, with Eq. 7.67, the total recirculating current between the spheres, I_{max}, can be determined, and then an estimate for ξ is given by Eq. 7.70 using the measured grid current.

Thorson and colleagues used electrostatic probes to characterize the plasma and ion flow in different regions of the device. A standard Langmuir probe provides the edge plasma density and electron temperature, and double or emissive probes mounted on alumina-Pyrex probe shaft for 30-kV isolation allowed measurements inside the flow and core regions [9]. Observations of the core plasma potential and density are limited to ion flows with energies ≤ 5 kV to avoid thermal destruction of the probes by the energetic ions. Though the perturbation of the ion flow is a concern using the invasive diagnostic technique, no appreciable change in the discharge characteristics (i.e., cathode voltage, current, or visible core size) was observed during the measurements. Furthermore, in order to minimize the disturbance of the ion flow, the probe tips only intercept ≤ 10 % of the core surface area.

7.6 Experimental Observations of Some Effects of Space Charge-Limited Flow

If the ion flow is sufficiently collisionless, then a space charge-limited flow into the high-voltage cathode would be expected. Indeed, measurements by Thorson and colleagues of the cathode current versus voltage shown in Fig. 7.6 feature the $V^{3/2}$ scaling consistent with Eq. 7.34 for voltages above 3 kV in a variety of low-pressure cases [9]. The increase observed in I_{cat} with higher pressures is indicative of the increased edge plasma density with pressure while the plasma source biases were held constant.

The measured radial plasma potential distributions show detailed agreement with the space charge potential model in the mantle region (Eq. 7.67) along with a number of other phenomena within the central cathode grid. Figure 7.7 shows the plots of the plasma potential measured via an emissive probe using the inflection method [13] and the probe floating potential as a function of radius for a typical low-pressure case ($P = 13$ mPa H_2, $V_{cat} = 5.0$ kV, $I_{cat} = 40$ mA). For these detailed probe scans, ion flows with energies up to 5.0 kV in either 13 or 27 mPa of hydrogen fill pressure were studied, and the collected cathode currents at these conditions were either 20 or 40 mA.

A fit of Eq. 7.67 normalized to the observed voltage at $r = 5.0$ cm and using an anode radius of 9.0 cm shows good agreement with the measured plasma potential

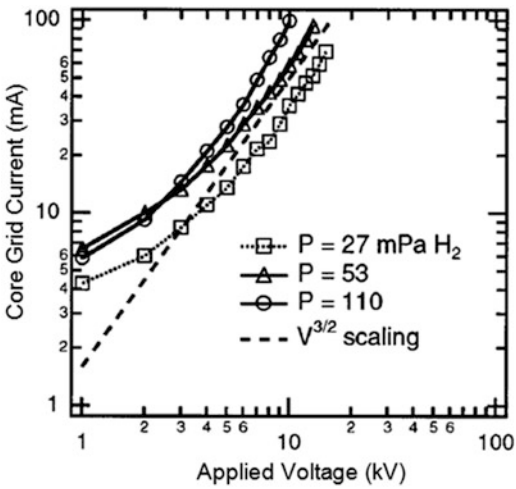

Fig. 7.6 Cathode current versus applied voltage for different converged core discharges showing a $V^{3/2}$ dependence above 3 kV for each pressure range [12]

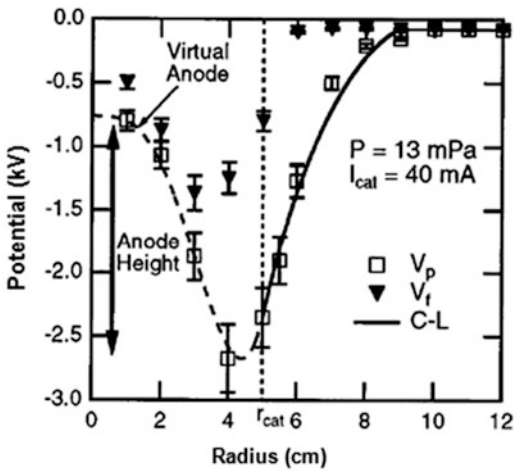

Fig. 7.7 Radial profile of the floating (V_f) and plasma (V_p) potentials for a 13-mPa, 5.0-kV, 40-mA case. Also included (*solid line*) is a normalized fit of the Child–Langmuir (C–L) potential distribution as expected from Eq. 7.77 (for $r > r_{cat}$) [12]

profile, as seen in Fig. 7.7. The theoretical current limit for the included best-fit graph in Fig. 7.7 is 150 mA, which is 7.5 times greater than the collected ion current of 20 mA (assuming $\delta = 1$) [14]. This roughly agrees with the geometric recirculation factor of 8.6 calculated from Eq. 7.68 for the grid used (with $\eta = 0.94$).

Figure 7.8 shows the comparisons of the radial potential profile against different currents and pressures. It may be observed that the space charge-limited model fits the measured data well in the mantle region. The amount of recirculating current determined as above also remains fairly constant for the three different cases studied by Thorson and colleagues (see Table 7.3) [9]. The effective source radius and the voltage at $r = 5.0$ cm appear to self-consistently adjust to provide the required space charge-limited current density.

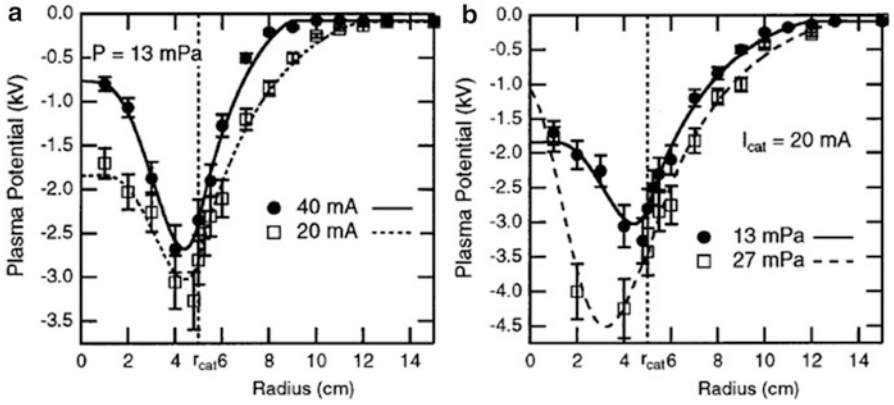

Fig. 7.8 Plasma potential measurements for different (**a**) cathode currents and (**b**) neutral background pressures. The normalized Child–Langmuir potential distributions for $r > r_{cat}$ and spline fits through the data for $r < r_{cat}$ are also included in the illustration [12]

Table 7.3 Theoretical currents from Eq. 7.34 and the estimated recirculation factor for the three cases shown in Fig. 7.8 (applied cathode voltage = −5 kV) [9]

Pressure (mPa)	Cathode grid current (mA)	Eff. source radius (cm)	Eff. cathode voltage (V)	Theoretical current (mA)	Estimated recirculation factor
13	20	12.0	−2,700	74	7.1
13	40	9.0	−2,300	150	7.5
27	20	13.5	−3,400	71	7.1

The observed potential at 5.0 cm is not equal to the applied 5.0 kV due to Debye shielding of the grid wires (λ_D is typically estimated to be ~0.05 cm) and to asymmetries in the potential because of the finite wire spacing. The measurements shown in Fig. 7.7 are from between cathode wires, where the plasma potential is weakest. The applied voltage is observed to differ from the observed potential between the grids by a factor of 2.

For neutral Maxwellian plasmas, the floating potential (V_f) of a probe is normally biased negative with respect to the plasma potential due to the higher mobility of electrons to reach the probe surface ($I_i = I_e$ at V_f). A comparison of the measured floating and plasma (V_p) potentials in the mantle and plateau regions of a low-pressure IEC device (see Fig. 7.7) indicates that the probe assumes the floating potential ($V_f > V_p$) to reflect the direct ion flow and collect the local electron saturation current. This signifies a deficiency of electron current in the ion flow, and hence $I_i > I_e$ for these low-pressure conditions. The difference between V_f and V_p is not as pronounced in the central core region, especially for higher pressure cases, which suggests a higher electron density or temperature in the core.

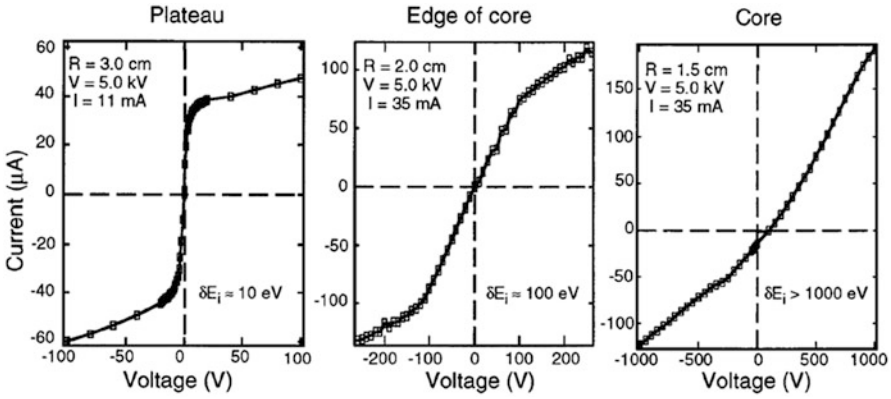

Fig. 7.9 Double-probe *I–V* characteristics for different radii near and inside the converged core region [9]

7.6.1 Converged Core Condition with Space Charge-Limited Flow

Figures 7.7 and 7.8 also show a virtual anode (i.e., potential hill) in the converged core region where the ion charge density increases due to radial convergence. A complete virtual anode [$V(r \approx 0) = 0$] would be expected for the case of a perfectly converging ion flow with no electrons. Under all conditions studied, the core virtual anode is a simple monotonically decreasing potential hill as r increases from 0 to r_{cat}. This structure agrees qualitatively with past experimental findings [15] and particle-in-cell (PIC) simulations that account for perpendicular flow velocities from a finite velocity spread in the edge region (Nebel R, 1994, Los Alamos National Lab, private communication).

However, the simple, purely radial flow model breaks down near the origin as the impact of perpendicular velocities becomes significant, and the ion velocity distribution approaches a spherical shell in velocity space in the core region (as illustrated in Fig. 7.5d). This effect is seen experimentally with double-probe *I–V* characteristics from the plateau and core regions. Because $I_i > I_e$ in the ion flow, the double probe actually samples the energetic ion beam distribution instead of the electron distribution as in normal, nonflowing Maxwellian plasmas. The slope of the *I–V* trace near $V = 0$ is then related to the spread of the ion energy distribution, where a beam-like distribution leads to a large slope at $V = 0$. Figure 7.9 includes three *I–V* characteristics taken in the plateau and core regions, and it can be seen that the slope decreases as the probe enters the core region. The sharp slope seen in the plateau region is indicative of a low-temperature or beam-like distribution, which is similar to the ideal distribution expected in that region (see Fig. 7.5c). Similarly, the broader slope in the core region is consistent with a

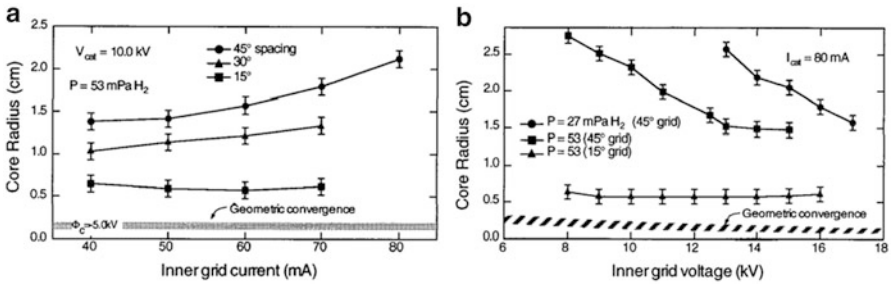

Fig. 7.10 Core size measurements for 45°, 30°, and 15° poloidal spacing grids as derived from the HWHM of the visible (H_α) core emission for variations of (**a**) cathode current and (**b**) cathode voltage. Included is the estimated geometric convergence estimate from Eq. 7.62

broad energy or isotropic distribution, which resembles the ideal spherical-shell distribution expected in the core region and illustrated in Fig. 7.5d. The detailed structure of the ion energy distribution in the core region cannot be well determined using this measurement technique, but an obvious change in the character of the ion distribution is seen between the plateau and the core regions.

7.6.2 Flow Convergence Measurement

The reactivity of a beam–beam-dominated IEC device is inversely proportional to the convergence radius of the ion flow [16]. Thus, it is important to understand and characterize any system parameters, i.e., accelerating well symmetry, applied voltage, injected current, and neutral pressure, that may limit the flow convergence. For example, beam–beam reactivity is expected to scale with the injected current squared, but if the core size also gets larger with current, the reaction rate will then not increase quadratically. Several measurements indicate that the converged ion core size reduces, and hence the flow convergence is improved, as the overall current is lowered, the neutral pressure is raised or the accelerating voltage is increased [9]. These results are seen in Figs. 7.8 and 7.10, which show the potential structures in the core region (Fig. 7.8) and the half-width at half maximum (HWHM) radius of the core intensity profiles from the CCD images in Fig. 7.10. Figure 7.8a indicates the core anode height increasing with I_{cat}, while Fig. 7.10a shows an increase in HWHM with I_{cat}. Figures 7.8b and 7.10b indicate a strong decrease of the core size with neutral gas pressure (P), and Fig. 7.10b also indicates a decrease of the core size with applied voltage V_{cat}.

Figure 7.10a shows the ideal geometric limit along with the core size measurements. In all cases, the observed core size is larger than the ideal limit, but the tightest cores of 0.6-cm radius are within a factor of 4–5 of the limit for those conditions ($V_{cat} = 10$ kV, $\Phi_c \sim 5$ kV, $T_{i\perp} \sim 0.1$ eV, $R = 20$ cm) [17].

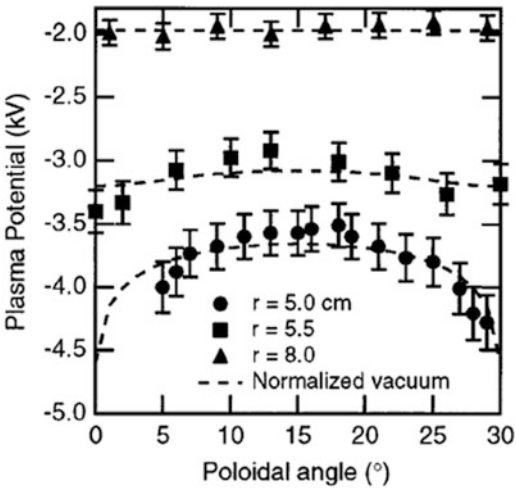

Fig. 7.11 Plasma potential measurements versus poloidal angle for a 5.0-kV, 20-mA, and 53-mPa ion flow at radii of 5.0, 5.5, and 8.0 cm. Grid wires were spaced at 0° and 30° for this cathode

The decrease observed in r_c with V_{cat} is much faster than the inverse square root scaling expected from Eq. 7.62. The most likely cause of this nonideal convergence behavior is asymmetries in the electrostatic potential due to the finite grid wires of the cathode. The potential near the cathode grid wires is more negative than its value between grid wires, and this results in a significant perpendicular force on the ions toward the wires. In addition, the region of highest acceleration for the flow is at radii nearest the cathode, where these large irregularities in the potential are also found. The magnitude of these potential variations decreases as the grid wire spacing decreases, and therefore finely spaced grids (e.g., 15° poloidal spacing) would be expected to yield smaller core sizes than more coarsely spaced (45° spacing) grids.

The observed core sizes decrease with decreasing grid spacing, and Fig. 7.10 includes comparisons of the core size scalings for differently spaced grids. Intensity profiles through the core region for the 45° and 15° poloidal spacing grids are shown in Fig. 7.10, which illustrates the dependence of core size on potential well asymmetries. Here, a factor of 2.5 reduction in core size results from tripling the density of grid wires on the cathode and holding all other parameters fixed. Note that by increasing the grid wire density, the grid transparency, and hence the amount of recirculating current, decreases. The measured HWHM tends to decrease with decreasing current, but this effect is not strong enough to account for the factor of 2.5 observed. Therefore, the observed enhancement of convergence is mainly due to the improved symmetry of the accelerating potential well.

By rotating the cathode globe past a fixed emissive probe, the poloidal variations in the plasma potential were measured. This is similar to the grid rotation experiments described in Chap. 6. Figure 7.11 shows the angular variation of the plasma potential for data taken at $r = 5.0$, 5.5, and 8.0 cm at 53 mPa, and $I_{meas} = 20$ mA. For comparison, the expected vacuum field variations due to the longitudinal

gridloops are included using superposition of the potential distribution of a single loop, given by [18]

$$\Phi(r,\theta) = q\sum_{l=0}^{\infty}\left(\frac{r_<^l}{r_>^{l+1}}\right)P_l(0)P_l(\cos\theta), \tag{7.71}$$

where P_l is the Legendre polynomial and $r_<$ and $r_>$ are the lesser/greater of the field and loop radii. The corresponding vacuum potential calculations from Eq. 7.71 are also indicated using the value of q that best fits the data for each of the three different radii. These normalized vacuum and measured plasma potentials match very well for the conditions shown in Fig. 7.11, which is generally true for all cases investigated.

The discrepancy near the wires is due to local Debye shielding which is not accounted for in Eq. 7.71 above. The data at $r = 5.0$ cm hence indicates a shielding of ≈ 400 V, and the amount of shielding appears to strongly depend on the grid current and background neutral density. This is shown in Table 7.1 through the dependence of the effective cathode voltage (V_{eff}) on pressure and current (less negative V_{eff} represents larger shielding). Qualitatively, a larger amount of shielding near the wires results in poorer flow convergence, for ions will have less energy entering the core region and the larger potential gradients near the wires will scatter the ions further. This effect therefore contributes to and may account for the observed core size scalings with pressure and current.

7.6.3 Core Density Measurements

Thorson and colleagues employed a scannable floating double probe for measurements of the core density [9]. However, shadowing of the recirculating ion flow by the radial alumina probe shaft leads to an underestimation of the ion density, and the measured electron saturation current, i_{sat}, is therefore corrected by the recirculation factor, ξ (from Eq. 7.68), to account for the shadowing effect and provide an upper limit for the ion density from these measurements (in this case, $\eta \approx 0.91$ and $\xi = 5.8$). Because $V_f \sim V_p$ in the core, the ion current ($I_i = en_iv_iA_p$) approximately equals i_{sat}, and the ion density is then given by

$$n_i = \frac{\xi i_{sat}}{eA_p}\sqrt{\frac{M}{2q\Phi_p}}, \tag{7.72}$$

where A_p is the probe area ($= 5.9 \times 10^{-6}$ m^2). For the core in Fig. 7.9, $i_{sat} > 150$ μA and $\Phi_p = 2{,}500$ V, giving the ion density calculated from Eq. 7.72 to be $\geq 1.33 \times 10^{15}$ m^{-3}.

Another approximation of the core density is given by the measured current collected at the cathode grid. For a gridded system, the effective cathode

transparency (η) leads to a fractional loss of the current between the mantle (I_{man}) and core (I_c) regions, and hence, $I_c = \eta I_{man}$. Using the definition of the recirculation factor ξ (Eqs. 7.68 and 7.70), I_c can be related to the measured grid current (I_{meas}) by

$$I_c = \eta I_{man} = \frac{\eta \xi I_{meas}}{(1+\delta)} = \frac{\eta I_{meas}}{(1-\eta^2)(1+\delta)}. \tag{7.73}$$

This result is also be related to the core density since $I_c = e n_{ic} v_c \pi {r_c}^2$. Therefore, the expected core density for a particular grid current is

$$n_{ic} = \frac{\eta I_{meas}}{(1-\eta^2)(1+\delta)} \left(\frac{1}{e v_c \pi {r_c}^2} \right). \tag{7.74}$$

Again, assuming $\delta \approx 1$ and $\Phi_c \approx 2{,}500$ V for these conditions ($r_c = 1.6$ cm for this 5 kV, 35 mA discharge), Eq. 7.74 gives a core density of 1.0×10^{15} m^{-3}. Equation 7.74 can be further refined, taking various electron current contributions such as thermionic emission, field emission, photo emission, and temperature dependence, as discussed in Chap. 8.

The core density can also be estimated in several other ways, such as the pyrometric estimate and the simple flow model given in Eq. 7.64 [9]. All of these estimates of the core density agree reasonably well with each other; hence, the ion density appears to follow classical expectations at the conditions studied.

7.7 Summary

This chapter has presented some classical studies explaining the limiting current in a planar electron vacuum diode as well as for a spherical diode. After many assumptions, the results show the functional performance for parallel plates follows Eqs. 7.15, 7.16, 7.17, and 7.18. Most important, the limiting electron current varies as the square root of the applied voltage V_o and inversely with the square plate separation D. For spherical geometry, the solution is even more complicated, but results in the behavior given in Eq. 7.68. Now the current depends on the voltage to the 3/2 power. The radii of the two spherical electrodes enter as ratios, such that the current increases as the ratio is decreased, favoring a larger emitter cathode radius. While the early derivations assumed electron currents, the solution for ion currents has the same form. However, the case of both ions and electrons of interest for practical IECs was not considered until the pioneering work of Elmore, Tuck and Watson, Farnsworth, and Hirsch, discussed in Chap. 2.

Still, the analysis presented in this chapter is of interest for several reasons. First, these analyses are historic in providing initial insight into space charge effects in diodes carrying large currents. Second, they illustrate techniques originally employed to solve the equations involved. Third, to some extent, the limiting current prediction as a function of applied voltage and anode–cathode spacing

roughly apply to the IEC behavior prior to the point where, with combined ion–electron currents, virtual electrodes are formed. Conceptually, the behavior predicted can be applied to neutron production that, in internal source IECs, depends strongly on the applied voltage, anode–cathode spacing, and absolute radii. However, the neutron production rate depends strongly on the ion velocity in the central region of the IEC. Thus, strong nonlinear behavior occurs because the space charge not only affects the ion current but also the ion velocity. This can in turn shift the neutron source rate from the central region where the ion velocity is reduced by the space charge effect. Thus, as discussed in Chap. 2, the total neutron rate can initially increase with increasing ion current, but at some point begins decreasing due to these space charge effects. However, for an internal source-type IEC, reactions of ions with neutrals plus charge exchange can drastically affect the neutron production rates beyond space charge predictions. In contrast, extremely low-pressure external source IECs follow the space charge effect predictions more closely.

These features have been studied experimentally by Thorson and colleagues, who developed a reasonable semiempirical model. This mode is suitable for many present IEC devices that have not gone into a Poissor type mode as discussed in Chap. 2. The plasma potential measurements for the low-pressure ion flows discussed above are consistent with a collisionless, space charge-limited flow model in the mantle region. In addition, both the effective source radius (R_{eff}) and cathode voltage (V_{eff}) adjust accordingly to provide the required current density for the edge conditions. Table 7.3 shows that, as expected from the space charge model, R_{eff} decreases (through α) as I_{cat} increases (at constant V_{cat} and P), but note that V_{eff} also decreases. This is attributed to enhanced shielding of the cathode grid wires by the increased local plasma density at higher currents. The increase in V_{eff} and R_{eff} for increased pressure (at constant V_{cat} and I_{cat}) is also consistent with the space charge model, for R_{eff} increases to offset the increased edge plasma density and V_{eff} observed at higher pressure.

The symmetry and depth of the accelerating potential well improve with increasing cathode voltage and pressure and with decreasing current and grid wire spacing, which results in improved ion flow convergence. It is the combination of the improved well symmetry with decreasing grid spacing and the reduced recirculation factor from the decreased grid transparency that accounts for the observed dependence of the flow convergence with the cathode geometry. Measurements of the electrostatic potential distribution throughout the IEC device show detailed agreement with a recirculating space charge-limited flow model and indicate the ions dominate the system at these low pressures (~53 mPa). A virtual anode structure forms in the converged core due to the enhanced ion density in that region, but no evidence of multiple potential well structures is seen for the conditions involved in these studies. Camera imaging and plasma potential measurements in the core region show that flow convergence improves with increasing voltage, pressure, potential well symmetry, and decreased current. Core density measurements have shown a factor of ~10 increase in ion density in the core region, which agrees with a simple flow conservation model.

References

1. Child CD (1911) Discharge from Hot CaO. Phys Rev 32(5):492–511
2. Carr CG (2004) Space charge limited emission studies using Coulomb's Law. M.S. thesis, Naval Post Graduate School, Monterey
3. Langmuir I, Blodgett KB (1924) Current limited by space charge between concentric spheres. Phys Rev 23:49
4. Stoyanov DG (2006) Planar vacuum diode with monoenergetic electrons. J Appl Electromagn 8(1–2):35–48
5. Stoyanov DG (2010) Analytical solution to the Langmuir spherical problem. arXiv:1008.4935v1 [physics.gen-ph]
6. Oksuz L (2006) Analytical solution of space charge limited current for spherical and cylindrical objects. Appl Phys Lett 88:181502
7. Liebermann MA, Lichtenberg AJ (1994) Principles of plasma discharges and material processing. Wiley, New York, p 165
8. Amemiya H, Annaratone BM, Allen JE (1999) The collection of positive ions by spherical and cylindrical probes in an electronegative plasma. Plasma Sources Sci Technol 8:179
9. Thorson TA, Durst RD, Fonck RJ, Wainwright LP (1997) Convergence, electrostatic potential, and density measurements in a spherically convergent ion focus. Phys Plasmas 4(1):4–15
10. Janev RK, Langer WD, Evans K Jr, Post DE Jr (1987) Elementary processes in hydrogen–helium plasmas. Springer, Berlin
11. Anders A (1990) A formulary for plasma physics. Akademie, Berlin
12. Hirsch RL (1968) Experimental studies of a deep, negative, electrostatic potential well in spherical geometry. Phys Fluids 11:2486
13. Hershkowitz N (1989) In: Auciello O, Flamm DL (eds) Plasma diagnostics. Academic, Boston, p 176
14. Oak Ridge National Laboratory Report No. ORNL-6088 (unpublished, 1985)
15. Nadler JH, Miley GH, Gu Y, Hochberg T (1991) Inertial electrostatic confinement: an approach to burning advanced fuels. Fusion Technol 20:850
16. Krall NA (1992) The Polywell: a spherically convergent Ion focus concept. Fusion Technol 22:42
17. Chapman B (1980) Glow discharge processes. Wiley, New York, p 52
18. Jackson JD (1978) Classical electrodynamics. Wiley, New York, p 93

Chapter 8
Ion and Electron Current Scaling Issues

8.1 Introduction

Studies to scale an IEC device for higher neutron yields or breakeven fusion operation require the prediction of scaling laws that relate the device performance to the ion and electron current. Ion currents contribute to the fusion reaction rate, while a major energy loss channel occurs through electron currents. Early studies focused on ion beam reactions in the compressed central core region. However, due to high background pressures and modest ion currents in early experiments, it soon became apparent that ion beam–background neutral interactions along with charge exchange reactions and ion interactions with absorbed gas on grid wires were dominant factors. These interactions produce nonlinearities that make the development of scaling laws for internal ion source IECs much more complicated than originally recognized. In addition, breakeven calculations for fusion power concepts involve low-pressure potential well physics, so completely different scaling laws come in. Some approximate reaction rate scaling laws based on the ion density, n_1, in the ion beams illustrate how these conditions radically affect operation. Assuming a deuterium gas filling of the IEC, the volumetric reaction rate, $r_{1,2}$ (units of m^{-3} s^{-1}), arising from monoenergetic populations 1 and 2 of colliding deuterons is given by

$$r_{1,2} = n_1 n_2 \sigma(v_{12}) v_{12}, \tag{8.1}$$

where n_1 and n_2 are the respective population densities and v_{12} is the magnitude of the collision velocity in the rest frame of either particle (assuming head-on collisions). The subscripts 1 and 2 may refer to either beam deuterons, gas molecules, or those embedded in a solid target. For a fixed grid voltage, we expect the density of beam deuterons to be proportional to the grid current I_{grid}. Thus for beam–beam reactions, we expect to observe

$$r_{1,2} \propto I_{grid}^2, \tag{8.2}$$

G.H. Miley and S.K. Murali, *Inertial Electrostatic Confinement (IEC) Fusion: Fundamentals and Applications*, DOI 10.1007/978-1-4614-9338-9_8,

whereas for beam–gas reactions, we expect

$$r_{1,2} \propto I_{grid}. \tag{8.3}$$

The equations assume that the current I_{grid} has been corrected to subtract out electron currents as previously stressed.

8.2 Reaction Regime Issues

For high rate neutron sources and for eventual reactor operation, the beam–beam reaction regime is essential for efficient operation. McGuire and Sedwick have studied the issues related to operation in these two regions (beam–background and beam–beam) in some detail [1, 2]. Thus, we summarize some of their findings here.

McGuire and Sedwick show that two significant factors that set the ion lifetime in a gridded IEC system are charge exchange with background gas and ion impact with grids. That, combined with the defocusing effect of the cathode grid and of the support stalks, typically limits the ions to about 10 passes through the system – far fewer than needed for a significant fusion rate to develop. Note that the ion lifetime is a measure of the confinement time in the IEC. The confinement time is given by the product of the number of passes an ion makes times the grid diameter divided by the average ion velocity. Based on these considerations, McGuire and Sedwick proposed that if a mechanism could be found to mitigate this ion defocusing effect, operation in a high vacuum IEC would drastically decrease charge exchange and increase the ion lifetime by orders of magnitude. Assuming that well-defined beams of ions are created and intersect at the inner core, the contribution to the total fusion rate versus background pressure for beam–beam and beam–background interactions for "confinement limited" and "background limited" conditions is shown in Fig. 8.1a, b, respectively. *Confinement limited* corresponds to the case where grid optics defocusing losses dominates, while *background limited* corresponds to the case where charge exchange and scattering losses dominate. As shown, in confinement limited (with a single cathode) operation, the fusion rate will increase with background pressure over a limited range. Eventually the mean free path becomes too short for ions to gain sufficient energy to fuse, and the rate levels off. With good confinement, as the pressure is reduced, the recirculating current continues to grow, potentially increasing the core density, causing the fusion rate to increase. Thus, as shown in Fig. 8.1a, for the "typical" IEC, beam–beam fusion dominates below a background pressure for 10^{-9} Torr. Above that, beam–background gradually takes over. In the case shown, the maximum beam–beam fusion rate (i.e., neutron production rate for deuterium fueled devices) is about two orders of magnitude lower than the maximum beam–background value. This illustrates the fact that the ion current must be increased in order to effectively operate in the regime. Fortunately the favorable scaling (Eq. 8.2) makes this somewhat easier assuming

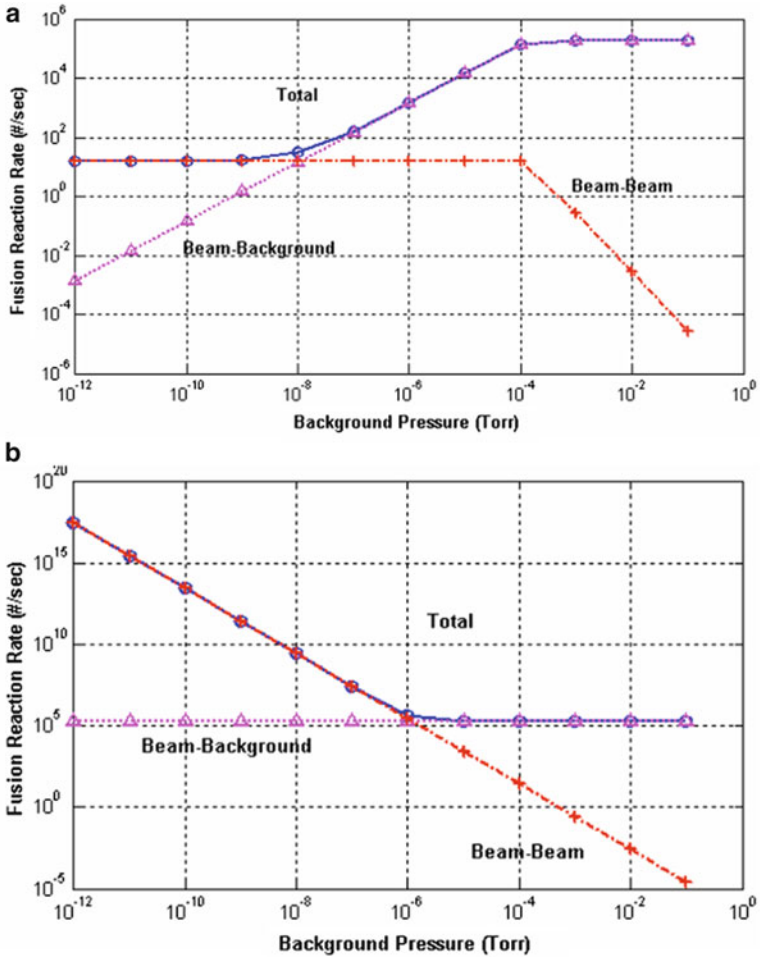

Fig. 8.1 Fusion reaction rates for beam–beam and beam–background contributions. Results shown are for confinement limited (**a**) and charge exchange limited (**b**) operations as a function of background pressure [2]

a high-current external ion source is used. In the charge exchange limited regime (sub-case of "background limited" where scattering can be neglected) of Fig. 8.1b, the crossover pressure for dominance is about 10^{-6} Torr, somewhat higher than for confinement time limited operation. However, in this regime, much higher beam–beam fusion rates are obtained due to the increased ion lifetime. The issue remains of how to obtain a long lifetime.

The view is that the single-grid cathode presents a highly defocusing acceleration of the ions into the core. Then ions that are slightly "off-axis" rapidly assume a chaotic path, impacting the grid after approximately 10 passes. Operation in "Star" mode develops less defocusing, but still the number of passes is limited, and

formation of this mode requires sufficient background pressure for ion source production in the discharge plasma. One possible solution is to use extremely well-focused external ion sources, such as employed by the original Hirsch six-gun experiment discussed in Chap. 1. However, Sedwick and colleagues propose an interesting multi-grid approach that further explains some of the issues involved. Thus, we discuss this approach next.

8.2.1 Multi-grid IEC Concept

To get around the restrictions for beam–beam operation, Sedwick and colleagues [1] have proposed the use of multiple concentric grids (each in the "shadow" of the one inside it as seen from the core). This is a very interesting approach that provides insight into key issues for power operation. However, with the assumptions made for Fig. 8.1, there is only a small "window" at very low pressure ($\leq 10^{-9}$ Torr) for the beam–beam reaction needed for a power reactor. Operation at interesting reaction rate levels for neutron source operation is possible over a larger range including the beam–background regime. With multiple grids, ion beams can be focused, increasing ion lifetimes by many orders of magnitude. Shadowing the grids in this way maintains the same level of transparency, which is important for allowing the fusion products to escape the system. The effect of additional grids on particle confinement is illustrated in Fig. 8.2 [3].

However, once improved ion confinement is obtained, the desired non-Maxwellian ion beam region can be lost due to thermalization. The dominant cause of thermalization is due to small-angle scattering collisions. In a non-gridded or single-grid IEC, these occur throughout the volume, resulting in deflection of ions away from the desired radial trajectories that take them to the core of the device. As the angular momentum of the ions (relative to the core) increases, their radial energy is converted to azimuthal energy, and eventually the system settles to a Maxwellian distribution over the entire volume, with low-energy ions filling the core. However, there are mitigating effects. Rosenberg and Krall [4] have argued that the residence time of the ions at the outer turning points is so much longer than in both the "bulk" and the core of the device that the ions will tend to thermalize into a Maxwellian distribution at the periphery and due to the reacceleration still be reasonably monoenergetic (i.e., highly non-Maxwellian) in the core. As discussed in a later chapter, Nevins [5] presented an alternate view with an analysis (using different simplifying assumptions) demonstrating that the thermalization in the bulk would be just as significant as that at the periphery, resulting in global thermalization (see Chap. 12). Subsequent studies by Chacon and colleagues, also discussed in Chap. 2, show that the assumption made in both of these analyses strongly affects the conclusions. Elimination of these assumptions showed a narrow window of opportunity for at least partially avoiding thermalization.

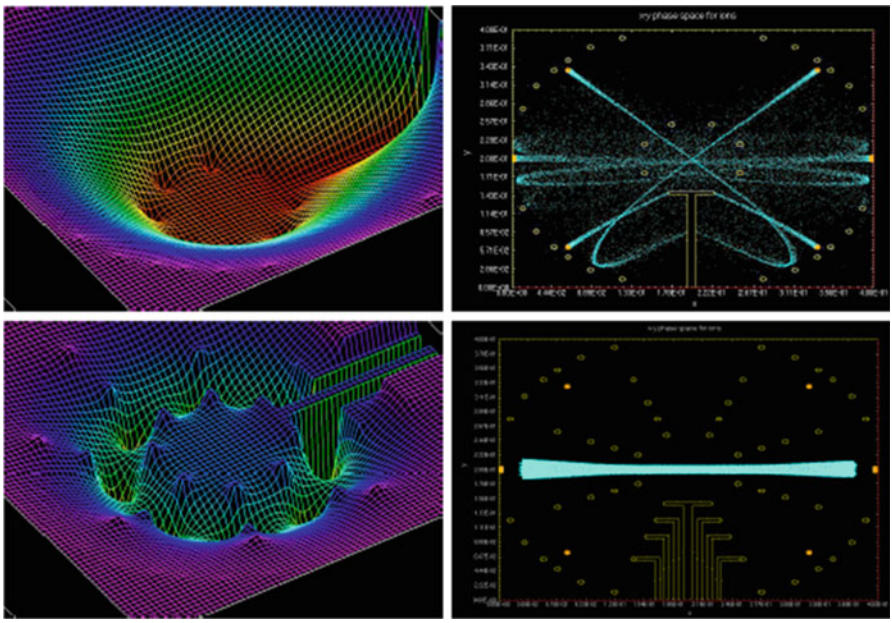

Fig. 8.2 Single cathode grid and stalk produce a highly defocusing beam line (*top left*) resulting in chaotic ion paths terminating on the grid (*top right*). Additional grids shield this effect (*bottom left*) and greatly extend ion lifetime (*bottom right*). These particle simulations used a commercial particle-in-cell (PIC) code [2]

In their studies, McGuire and Sedwick have shown numerically [3] and verified experimentally [6] that in the multi-grid IEC design, the well-confined ion beams quickly destabilize radially to form ion "packets" as a result of the classical counter-streaming ion instability. However, they find that these packets are stable (long lived) as a result of the IEC potential trap kinematics [7]. In addition, the packets become synchronized such that they simultaneously meet in the core of the device.

The formation of synchronized packets in the multi-grid system results in inter-packet collisions occurring only in the core of the device where the packets meet. Here, small-angle deflections will only deflect ions onto other nearby radial (or nearly radial) paths, lying within the same beam line. In addition, the packets will spend the majority of their time at the outer perimeter where they tend to thermalize locally into a low-energy Maxwellian distribution that due to reacceleration by the inner grids again forms monoenergetic ion beams as envisioned by Rosenberg and Krall [4]. As a result, the average angular momentum of the packets relative to the core remains zero, and the mean energy of the packets will not decrease over time. Thus, McGuire and Sedwick conclude that the packet kinetics provide a possible way of circumventing the defocusing effects and thermalization of the ions in the multi-grid IEC.

Based on these studies, it appears that "packet" kinetics allows a possible approach to the non-Maxwellian ion time scale needed for breakeven fusion.

High-angle scattering could still become a problem, because there are now many grids with which ions can collide if they are scattered at larger angles in the core. That issue requires more study. In addition to D–D and D–T fusion, McGuire and Sedwick considered p–B^{11} fusion. The peak fusion cross section for p–B^{11} at the 170 keV resonance is 0.1 b. The integrated scattering cross section for a particle to be taken out of its beam line at this energy is ~ 65 b based on the grid geometry discussed later. However, grids can be constructed to be greater than 90 % transparent. At 95 % transparency, 95 % of the high-angle scatters result in the ion pair simply ending up on another beam line, rather than impacting the grid. The grid "loss" cross section is then effectively only 3.3 b – closer to the fusion cross section. This may be an overoptimistic scenario. However, loss of an ion pair is only a loss of 100 keV of input energy, whereas a fusion reaction with p–B^{11} produces 8.7 MeV in the form of alpha particles. Assuming the alpha particle energy is recovered, this is a gain factor of 2.6 (3.3 MeV of ion loss per 8.7 MeV of fusion gain), providing a tight but nonzero margin to achieve net power output.

Another issue for this concept is that the presence of the grids will result in a fraction of the fusion product energy being lost (5 %) as some alpha particles will impact the innermost grid. In addition to the energy loss, sputtering of this grid by the alpha particles must be considered. A benefit of the high-angle scattering is that fuel may only need to be introduced into one or two beam lines (e.g., one each for p and B^{11}), and the others should fill as a result of the scattering.

To make best use of the p–B^{11} reaction, a method to directly convert the charged alpha product energy into electricity is desirable. Two options need evaluation. One method is to surround the IEC with high-voltage direct collection plates. Otherwise, a magnetic collimator can be added to direct the alphas into the direct energy conversion section, e.g., a Venetian blind-type arrangement or alternately a traveling wave direct energy convertor (TWDEC) [8, 9].

A second major problem addressed by McGuire and Sedwick is that obtaining high densities in the core is not possible if only ions are present in this region. Space charge will not allow for sufficient ion density. To mitigate this problem, electrons can be introduced into the core, provided they are not allowed to freely stream out to the anode. There are several possible approaches to this problem in the multi-grid geometry. First, the innermost grid can be biased positively relative to the "true" cathode that is then located at a slightly larger radial distance. This helps to electrostatically confine electrons to the core, even as ions are allowed to recirculate through this region.

An alternate, more aggressive method is to confine the electrons with an appropriately shaped magnetic field. Such a field has been implemented by Bussard [10] in his Polywell "cusped" field configuration, where the fields are generated electromagnetically (see the Polywell discussions in Chaps. 1 and 2). In contrast to the multi-grid approach, the Polywell does away with grids and uses the magnetically confined electrons to electrostatically confine ions. Thus, the electrons form a deep potential well to achieve this ion confinement. As an alternative to the Polywell, Sedwick proposed a grid constructed of rare earth magnetic material (shown conceptually in Fig. 8.3).

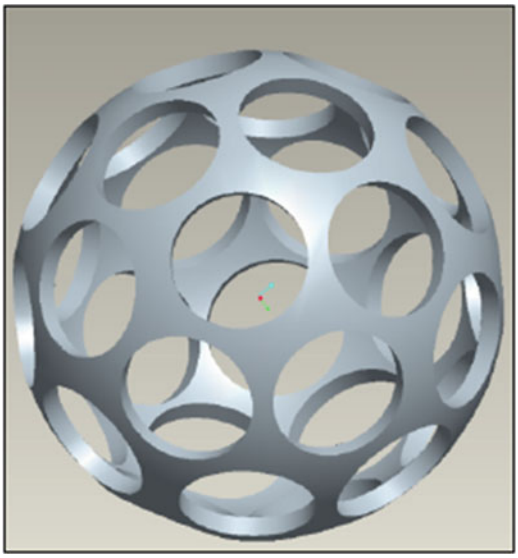

Fig. 8.3 Permanent magnet grid concept. Distribution of holes is based on a truncated icosahedron. The grid is constructed from neodymium or samarium–cobalt and is radially magnetized. Field lines start at the outer surface and curve back through the openings to terminate on inner surface, forming magnetic "plugs" [2]

The presence of the high-voltage stalks connected to the multi-grids introduces a high degree of asymmetry to the potential in between the grids. High-voltage stalk design discussions in Chap. 4 were generally directed at two grid (anode and cathode) IEC devices versus the present multi-grid concept. With multi-grids, if the stalks are assumed to be confined to a single axis of the system (e.g., the polar axis). Then "equatorial" and "low latitude" beam lines are relatively unaffected. However, beam lines that are directly adjacent to the polar axis suffer from a high degree of destabilizing asymmetries. To avoid this problem, a single high-voltage stalk (at the most negative potential relative to ground) can be embedded in a conical volume. This high-voltage stalk connects to the innermost (or most negative, if not the innermost) grid, as well as to the narrow end of each cone. The surface of the cone can be constructed from highly resistive material, where the resistance is tailored to vary in a continuous manner as a function of radial distance from the core. With proper design, a constant current flowing radially along the conical walls will experience a potential drop that essentially mimics the radial variation in potential if the high-voltage stalk were not present. This effectively shields the recirculating ions from the field of the high-voltage stalk, making the surrounding field appear as if the high-voltage stalk was not present. Other grids are then connected to the outer surface of the cone, biasing them at the appropriate potential. A single high-voltage stalk therefore supplies the appropriate bias for all the grids, while ideally its effects are completely shielded from the recirculating ions.

The high-voltage stalk and all of the grids would be initially biased by an external voltage source that might consist of a Cockroft–Walton generator or perhaps a pyroelectric crystal, such as lithium tantalate. A continuous current is not necessary, because once fusion begins, the anode–cathode bias is automatically maintained. To achieve this, neutral gas particles pass down feed tubes inside the

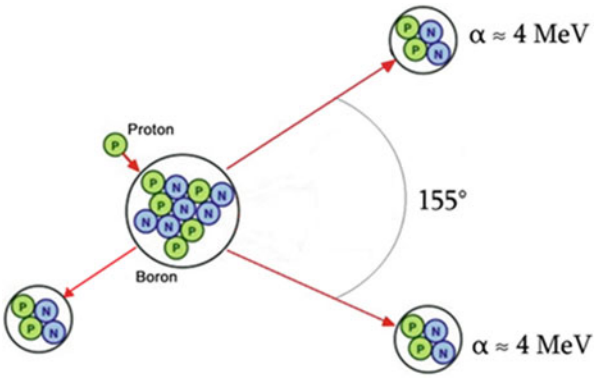

Fig. 8.4 p–B^{11} fusion results in charged fusion products (three alphas at 8.7–9 MeV total)

conical structure and are ionized at the appropriate potential relative to the core, giving both the appropriate center-of-mass energy, as well as zero relative momentum. For the p–B^{11} reaction, this results in two of the three alpha particles leaving the core at approximately the same energy. The third alpha carries only a fraction of the total energy (shown schematically in Fig. 8.4).

If the cathode is biased at −4.3 MV relative to the chamber, the alphas will be decelerated to rest at the chamber wall, where they can be neutralized. Each fusion event therefore deposits two electrons at (or near) the cathode and removes two electrons from the anode, effectively "pumping" two electrons down to the cathode from the anode, and increasing the voltage between the two. Some of this excess charge is leaked down the surface of the conical structures to maintain the other grid potentials (and to shield the stalk), but the majority of it is converted to a low-voltage, high-current source through the use of a capacitor charge pump. This output is supplied to the "customer." Conversion efficiencies to electricity with such an approach could in principle exceed 80–90 %.

Radiation losses from the core region can be a major issue for p–B^{11} operation. The presence of the neutralized electrons in the core will result in Bremsstrahlung radiation as the ions pass through this region. Unless the electron "temperature" is kept much lower than the average ion energy, such losses can easily exceed the fusion power output for fuels such as p–B^{11} [8, 11]. The power lost to Bremsstrahlung for D–T fusion would typically be ~ 0.7 % of the fusion energy (assuming thermal equilibrium), so this is not a major detriment in that case. Even D–^{3}He would only suffer 19 % loss by this mechanism. However, due to the high Z of boron, the electron "temperature" must be kept to ~ 1/3–1/6 of the ion temperature in order to achieve net gain [8]. This highly nonequilibrium case may be possible with the beam-like ions versus the background electrons in the core region. However, this physics issue requires more study to ensure that this is possible.

In summary, the multi-grid apparatus proposed by McGuire and Sedwick offers a very interesting approach to a power reactor. However, it is complicated, so the practicality needs to be evaluated. It is presented here to illustrate many of the physics issues involved in attempting to achieve IEC fusion power plants. It and some other possible approaches are briefly discussed in Chap. 12.

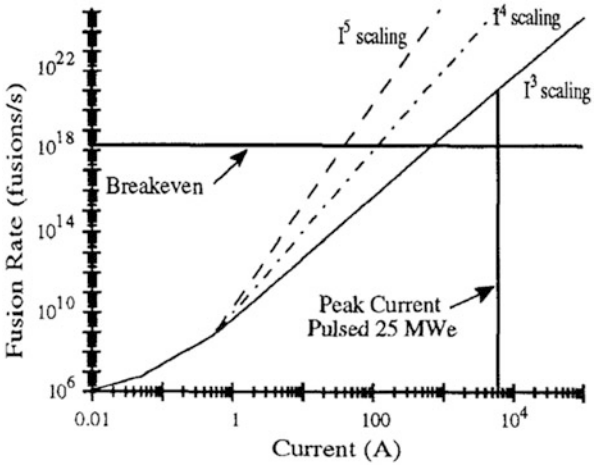

Fig. 8.5 Predictions incorporating the possibility of a highly nonlinear fusion rate scaling at higher ion currents. Aggressive I^n ($n > 2$) assumes standing wave compression of the core. If achieved, that would enable much lower injection currents [13]

8.2.2 Low-Pressure Experiments

Instead of using multi-grids, beam–beam scaling (Eq. 8.2) may be achieved with an external ion source combined with strong differential pumping (between the chamber and the ion source region) to obtain very low background pressure in the IEC chamber. The objective is to achieve a chamber pressure so low that the mean free path of the ions is much larger than the chamber diameter. Indeed it may be possible to obtain an even more favorable scaling than that of Eq. 8.2 owing to greater compression associated with standing wave formation [12]. This scaling could potentially reach I^n where $n = 3$, 4, or 5 as shown in Fig. 8.4. Because a physical grid would melt under such intense heat load from the ions, an actively cooled grid in a pulsed system has been proposed in one conceptual design [13]. However, with present devices, pumping to sufficiently low pressures while simultaneously injecting large ion currents has not been done experimentally, limiting IEC experiments to linear or less-than-linear beam–background reaction scaling. The injected ion current required for breakeven is quite achievable. For example, for the IEC plant design shown in Fig. 8.5, a kA ion current would be required with I^2 scaling, though the wave compression effect could possibly reduce that [10, 13].

A variation to the external ion source approach has been studied by Masuda and colleagues [14], who attempted to achieve this condition by using the unique ring-shaped magnetron ion source (RS-MIS) operating at low chamber pressures (5–100 mPa). See Chap. 1 for details about this device.

The experiments conducted by Masuda and colleagues with and without the RS-MIS showed a marked difference at lower ion current (< 1 mA) as shown in Fig. 8.6. The RS-MIS seemed to outperform a conventional glow discharge-type IEC device. However, repeated experiments showed that this was only an initial effect and could not be repeated over multiple experiments. Thus, despite the

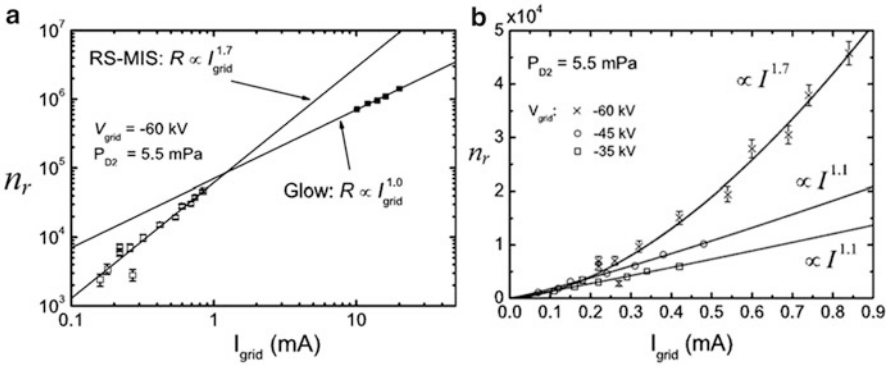

Fig. 8.6 (**a**) Comparison of n_r (neutron rate) versus I_{grid} between glow discharge mode and RS-MIS-driven IEC devices at $V_{grid} = -60$ kV. (**b**) Scaling of the n_r with grid current at various voltages [14]

lower pressure, the RS-MIS generally provided a neutron production rate that was approximately proportional to the grid current [14]. While this result is disappointing, improvements in the RS-MIS or other types of external ion sources should be able to move into the beam–beam reaction regime. This will be an important milestone for studying the physics of non-Maxwellian fusion with the IEC.

Much of their difficulty in getting into nonlinear beam–beam scaling is due to the low ion current obtained in most experiments to date. Indeed, that has been a common problem in most external ion source experiments. The experimental focus and funding to date has largely been on neutron sources and related applications where larger ion currents have not been needed. Still, it is important at this point to consider some issues related to moving to fusion power experiments. Formation of adequate deep potential traps has already been discussed in Chap. 2 and remains a formidable challenge. Reducing both electron and Bremsstrahlung energy loss channels represents another difficult challenge.

Reduction of electron current energy losses also deserves more consideration. Electrons are spontaneously emitted from the cathode whenever an ion collides with it. Moreover, photoemission, field emission, and also thermionic emission contribute to the total electron current. This phenomenon can be important for both high- and low-pressure IECs. All these effects are nonlinear and increase with the applied voltage. Furthermore, the electrons emitted from the cathode gain almost full potential of the applied voltage prior to exiting the system after reaching the anode (chamber walls). To further complicate this issue, as stressed in Chap. 5 (see Eq. 5.1 and its associated discussion), the power supply current meter does not differentiate between the electrons leaving the cathode or an ion hitting it and recombining on the surface. Hence it is necessary to increase the input power due to the increasing electron current in order to maintain the ion current.

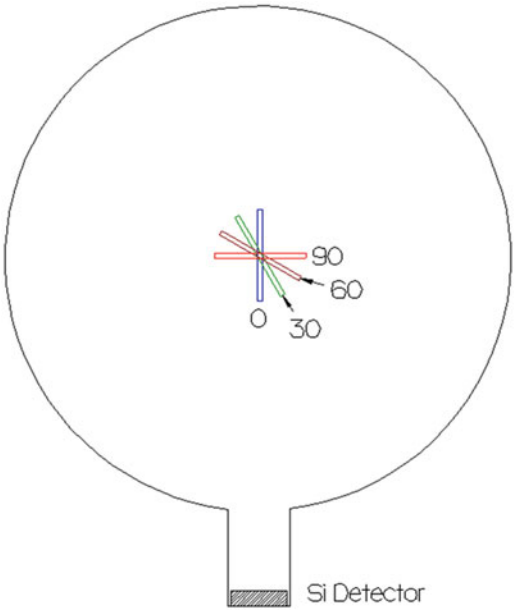

Fig. 8.7 Top view of the single loop grid rotation with respect to the Si detector [15]. Various rotation angles in degrees are shown

8.2.3 Studies of Energy Loss Mechanisms

Some basic experiments to better understand the various energy loss mechanisms involved in an IEC device have been carried out by S. K. Murali and colleagues at the University of Wisconsin, Madison [15]. To begin, the spherical cathode was replaced by a single loop grid. As a consequence the heat load per unit surface area of the cathode was significantly increased. The corresponding grid temperature increased to very high values, so that thermionic emission became significant. The single loop grid also helped in consistent grid orientation. The resulting single loop grid's fusion regimes were studied and calculated, as discussed in Chap. 6 [15]. The single loop grid was rotated about the axis using the high-voltage stalk as a pivot axis (shown in Fig. 8.7). The corresponding proton and neutron data were recorded simultaneously and are plotted in Fig. 8.8. The proton-to-neutron (P/N) ratio (see Chap. 6) is seen to increase as the grid orientation is increased from 0 ° to 90 °. This occurs in large part because the proton detector sees more of the volume source with incremental rotation toward 90 °.

From Fig. 8.8 it is observed that in a single loop grid configuration, the highest number of fusion reactions is observed by the proton detector when it looks face-on at the loop (see Fig. 8.9a). In this configuration, the maximum volume of the cylindrical source is covered by the line of sight. This indicates that the single loop geometry creates a line source. Such a line source cannot be detected by the neutron detector, as it still only sees an effective point source (owing to the distance between the source and the detector).

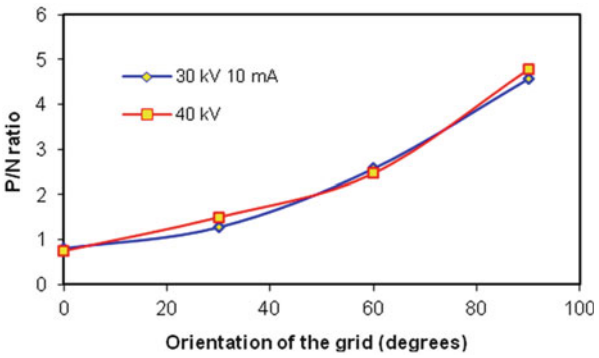

Fig. 8.8 The P/N ratio increases as the grid is rotated from 0° to 90° showing that a single loop grid behaves like a line source [15]

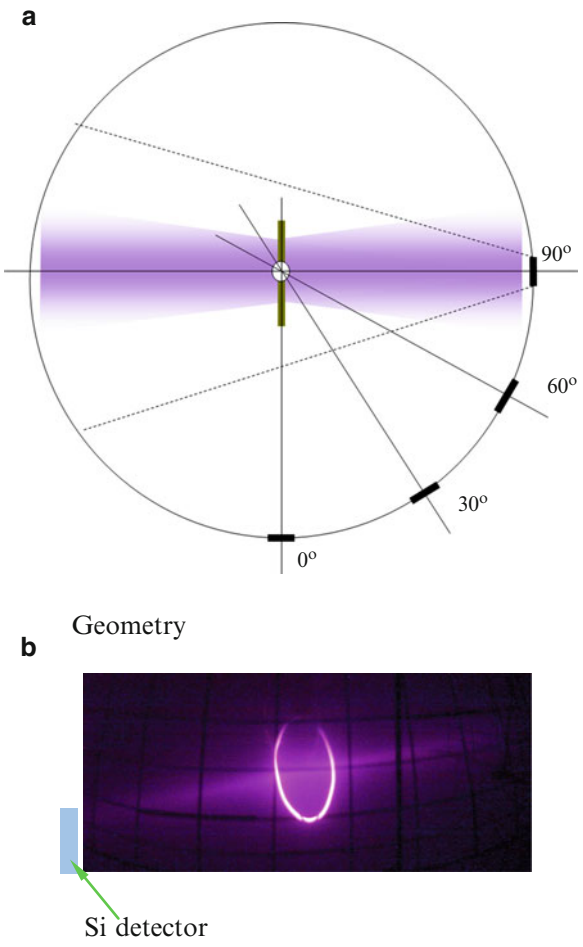

Fig. 8.9 (**a**) In this geometry the loop grid is fixed and the detector is rotated (though physically it is the other way around). The view of the detector is a cone that encompasses greater volume of the line (*cylindrical*) source as it is rotated from 0° to 90°. (**b**) Picture of the plasma in the single loop grid configuration at 7.35 mTorr, 10 kV taken from the viewport oriented at 90° to the axis of the detector port [15]

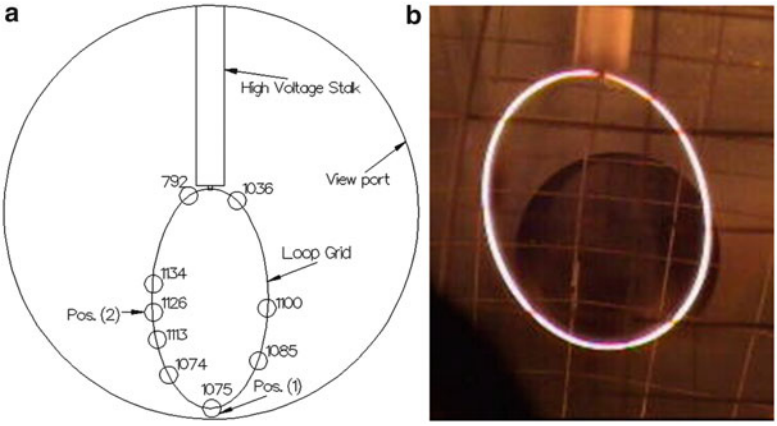

Fig. 8.10 (**a**) Temperature measurement (in °C) at various locations on the loop, as seen from a viewport. (**b**) Picture of the loop as seen from the viewport at 25 kV and 10 mA [15]

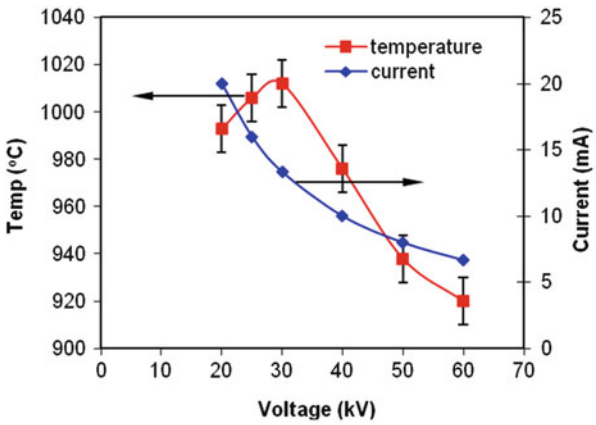

Fig. 8.11 Voltage versus temperature and current at constant power (400 W) for LoopW [15]

The temperature of the grid at various points along the loop was measured at 25 kV and 20 mA (as shown in Fig. 8.10a). The wire showed a gradual variation in temperature indicating an uneven distribution of ion flux reaching the loop grid. A similar temperature variation was observed with a pure Re wire loop grid (LoopRe) [15].

The temperatures at one spot (shown in Fig. 8.11) for LoopW and two different spots (shown in Fig. 8.12) for LoopRe were measured. The input power was fixed at 400 W. The voltage and current were varied during this experiment. The temperature variation is shown in Figs. 8.11 and 8.12. Interestingly, it is observed that at higher input voltage and correspondingly low input current (used in maintaining the power constant), the temperature of the grid remained low; on the other hand, at low input voltage and high current, the temperature of the grid was relatively high.

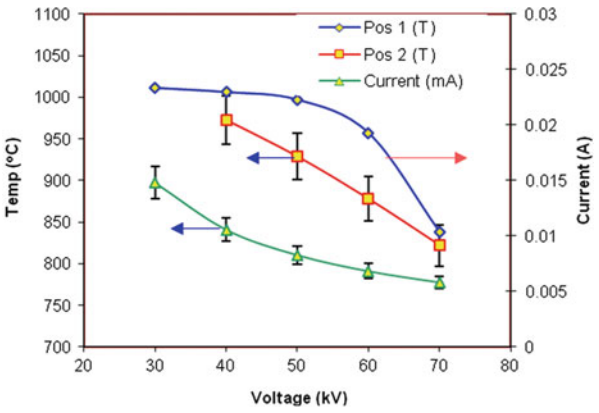

Fig. 8.12 Voltage versus temperature and current at constant power (400 W) at two spots for LoopRe [15]

Though one may expect that the temperatures would remain constant for a constant input power, this was not the case (either with W-25%Re Loop, Fig. 8.11, or with Re Loop, Fig. 8.12). This is postulated to be due to an increase in the electron current emitted from the cathode with a voltage increase, resulting in a corresponding decrease in the ion current. Thus, the energy deposited on the grid will decrease as well. Because the thermionic emission at the measured temperatures is negligible, that contribution is ignored. The effect is consistent with an increase in the secondary electron emission (SEE) coefficient with voltage. That would produce a higher electron emission at higher voltages. As a consequence, the ion current would decrease, reducing the energy deposition on the grid. Though experimental measurements of the SEE coefficient are not available for W-25%Re alloy and the Re at the desired voltages, their trends should be similar to that for Mo [16, 17] (shown in Fig. 8.13). This analogy seems reasonable because the SEE coefficient varies slowly with Z (as shown in Fig. 8.14).

As already discussed, SEE from the chamber wall side of the grid wires appears in the grid power supply reading, I_{meas}, as an ion current. Thus, this must be accounted for in the actual current, I. Without having detailed emission coefficients, a reasonable first estimate is possible, as done by Thorson and colleagues [21]. They assumed a constant secondary electron emission coefficient $\gamma \approx 1$ in the following expression (assuming randomized orbits of the recirculating ions [21]) for the true ion current I:

$$I = \frac{\eta[I_{meas}]}{(1-\eta^2)(1+\gamma)}, \tag{8.4}$$

where I_{meas} is the (measured) power supply current, η is the geometric transparency of the grid, and γ is the SEE coefficient.

Further information about these effects was obtained from the neutron rate measurements in the two loop experiments. The neutron rate of the two loops under identical conditions showed significant differences. The average fusion rate with Re was ~ 27 % higher than with W-25%Re loop grid, as shown in Fig. 8.15 for 90 ° orientation (face-on with the detector, see Fig. 8.9b).

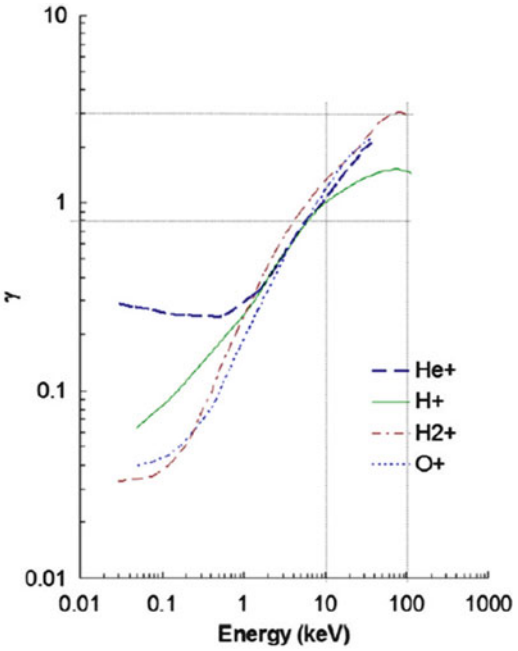

Fig. 8.13 Variation of γ with ion energy (keV) for various species (H^+, $H_2{}^+$, He^+, O^+) on Mo [15]

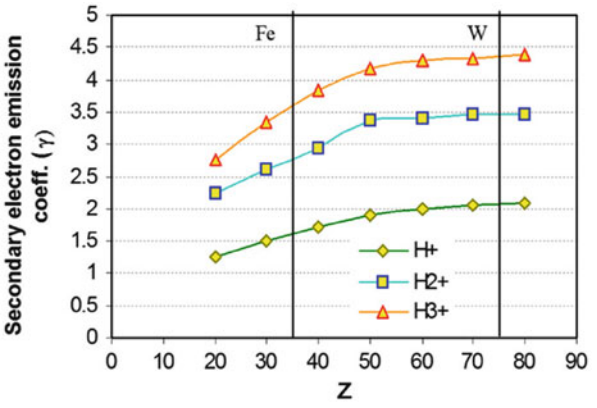

Fig. 8.14 Variation of the secondary electron emission versus the atomic number for various H^+, $H_2{}^+$, and $H_3{}^+$ ion impacts at 100 keV $\gamma(H^+) < \gamma(H_2^+) < \gamma(H_3^+)$ irrespective of the material used. Variation of γ with Z is small from 74 (W) to 79 (Au) and hence the data for Au can be used for W without adding large errors to the final results [18–20]

This is in contrast with the nearly constant neutron rate observed by A. Wehmeyer and colleagues [22] who conducted experiments with complete grids instead of single loops. The full grids did not get very hot, and hence the effects of thermionic emission were not significant at the power levels used. In contrast, the single loop temperature did rise to significant temperature levels relative to thermionic emission.

The difference in the measured proton/neutron fusion rates of the two loops occurs because the neutron detector effectively sees a point source, whereas the proton rate is subjected to the line source effect described earlier. In Fig. 8.16, the

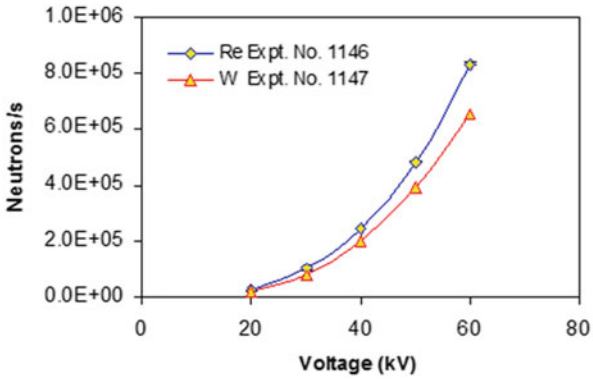

Fig. 8.15 The neutron rate versus voltage for the two Loops (W and Re) at 90° orientation [15]

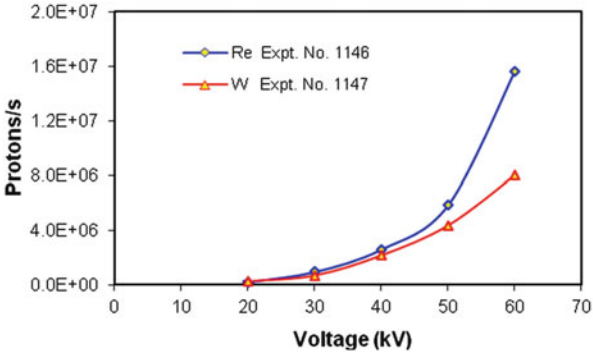

Fig. 8.16 The proton rate versus voltage for the two Loops (W and Re) at 90° orientation [15]

proton count increases with voltage at a faster rate than the neutrons do (as shown in Fig. 8.15), because the increased ion current causes a higher ion recirculation, resulting in a higher fusion rate along the axis of the loops.

If we were to include the variation of γ with voltage in the ion current Eq. 8.1, its value would change according to Fig. 8.17. This aspect is evident in the constant power scans wherein the temperature of the loop increased at low voltage and decreased correspondingly at high voltage at a constant input power 400 W (see Figs. 8.11 and 8.12). From Fig. 8.17, the variation in $1/(1+\gamma)$ is as high as ~ 40 % when γ changes from 1 to 2. Hence it appears that at higher voltage, the additional current is from secondary electrons. If these electrons were reduced, the fusion rate could be further increased.

8.2.4 Secondary Electron Emission

As seen in the previous section, secondary electron emission (SEE) can be important in IEC operation. Thus, we review SEE in more detail next. SEE is caused by inelastic interaction of the atoms or ions entering the uppermost layers of a solid surface. There are two mechanisms contributing to SEE [23], termed "potential"

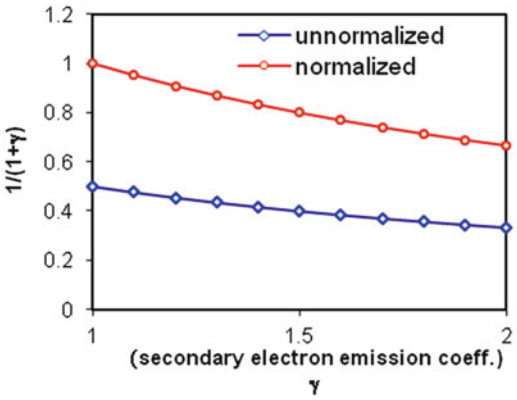

Fig. 8.17 The effect on the coefficient $1/(1+\gamma)$ in Eq. 8.4 by the variation in γ [15]

Table 8.1 Values of Λ for various materials [26]

k	$\Lambda(H^+ \rightarrow k)$
Ag	0.13
Al	0.11
Au	0.1
Cu	0.09
W	0.07

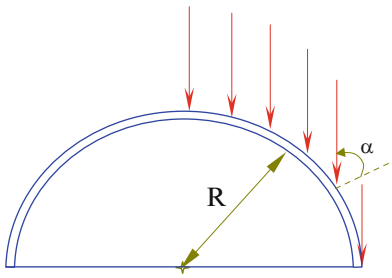

Fig. 8.18 Sketch of incidence of ions on a grid wire/loop wire of radius R. The angle of incidence of the ions, α, varies from $-90°$ to $+90°$ with a singularity at $90°$ [15]

and "kinetic" emission. In the case of potential emission, the yield γ of secondary electrons is proportional to the potential energy of the incident ion. This energy is assumed to be mainly relaxed via the Auger process. On the other hand, in the case of kinetic emission, γ is assumed to be proportional to the stopping power for the impinging ion [24, 25].

An empirical formula to relate the SEE coefficient γ with the stopping power $(dE/dx)_e$ is given by [13, 17, 23, 25]:

$$\gamma(H^+) = \frac{\Lambda}{\cos(\alpha)} \left(\frac{dE}{dx}\right)_e, \tag{8.5}$$

where Λ is listed in Table 8.1. For example, Λ for H^+ on tungsten is 0.07 (which is also assumed valid for W-25%Re). For the case of ions converging toward the central core, the angle of incidence α can be taken as $\sim 0°$ (see Fig. 8.18).

The stopping power dE/dx to be used in Eq. 8.5 is given by [27]:

$$-\frac{dE}{dx} = \frac{4\pi e^4 z^2}{m_o v^2} NB, \tag{8.6}$$

$$\text{with } B \equiv Z\left[\ln\left(\frac{2m_o v^2}{\phi}\right) - \ln\left(1 - \frac{v^2}{c^2}\right) - \frac{v^2}{c^2}\right]. \tag{8.7}$$

Here N is the number density of the absorber atoms of atomic number Z, m_o is the electron rest mass, e is the electronic charge, and c is the speed of light. The parameter ϕ represents the average excitation and ionization potential of the absorber and is normally treated as an experimentally determined parameter for each element. For a nonrelativistic case of present intent, $v \ll c$, hence only the first term in the expression for B is significant. This gives

$$B \equiv Z \ln\left(\frac{2m_o v^2}{\phi}\right). \tag{8.8}$$

Researchers have also known that the SEE depends on the temperature of the substrate [28–30]. Such temperature variations can be estimated using the following expression [12]:

$$\frac{\gamma(T_1)}{\gamma(T_2)} = \frac{1 + \beta T_2}{1 + \beta T_1}, \tag{8.9}$$

where β is approximately the temperature coefficient of resistivity and T_1 and T_2 are in °K.

8.2.5 *Molecular Effects on the Secondary Electron Emission*

It is observed that [15]:

1. The Z dependence of the yields for hydrogen and helium projectiles is very similar.
2. The yields for H^+ and D^+ show the same energy dependence as that of the electronic stopping powers.
3. Isotope effects are negligible in the energy range 2–50 keV.

These observations are adapted here and are assumed to be approximately valid for energies up to 150 keV. An important associated observation for IEC operation is that molecular ions generally give lower yields per atom than atomic ions.

It has been suggested that the observed lower secondary emission yield with H^o than H^+ [$\gamma(H^o) \approx 0.85\gamma(H^+)$] for Au is related to electron liberation within the solid.

Liberation is less effective for shielded protons as a consequence of lower stopping power in the first monolayers before the equilibrium projectile charge is reached. Bombardment with molecular ions H_2^+ and H_3^+ should yield similar screening effects as for H^o due to accompanying electron(s). No distinction is possible about whether the H_n^+ molecules dissociate when penetrating the solid into $(n-1) \times H^o$ atoms and one proton or, alternately, the $(n-1)$ electrons from a negatively charged cloud screening the n protons. However, the secondary electron yield due to bombardment with molecular ions is generally given by adding the measured yields $(n-1) \times H^o$ atoms and one proton [31]. Then the SEE coefficient γ can be generalized as

$$\begin{aligned} \gamma\left(H_n^+\right) &= (n-1)\gamma(H^o) + \gamma(H^+) \\ &= ((n-1) \times x + 1)\gamma(H^+). \end{aligned} \tag{8.10}$$

Here x is typically around 15 % [31, 32], hence

$$\therefore \gamma\left(H_n^+\right) \approx [0.0595n + 0.0105] \times \left(\frac{dE}{dx}\right)_e. \tag{8.11}$$

Boris and colleagues [33] showed that in the "typical" University of Wisconsin IEC experiment, the relative concentration ratio of D^+:D^{2+}:D^{3+} was x:y:z::6:24:70 (at 2 mTorr, 100 kV, and 30 mA). Therefore, the SEE coefficient for that case is given by

$$\begin{aligned} \gamma &= x \times \gamma(D^+) + y \times \gamma\left(D_2^+\right) + z \times \gamma\left(D_3^+\right) \\ &= 0.06\gamma(D^+) + 0.24\gamma\left(D_2^+\right) + 0.7\gamma\left(D_3^+\right) \\ &= 1.246\gamma(D^+). \end{aligned} \tag{8.12}$$

Hence γ for a typical deuterium IEC plasma at 2 mTorr chamber pressure becomes

$$\gamma \approx \frac{1.246 \times \Lambda}{(\cos\alpha)^f} \times \left(\frac{dE}{dx}\right)_e. \tag{8.13}$$

If the effects of impurities were included, this coefficient would be even higher.

Considering all of these electron emission effects, a general equation for the recirculation ion current can be written as

$$I = \frac{\eta\left[I_{meas} - I_{th} - I_p - I_f\right]}{(1-\eta^2) \times \left\{1 + \frac{[x \times \gamma(D^+) + y \times \gamma(D_2{}^+) + z * \gamma(D_3{}^+)] \times \Lambda}{(\cos\alpha)^f} \times \left(\frac{dE}{dx}\right)_e\right\}}. \tag{8.14}$$

Here I_{meas} is the power supply (measured) current, and η is the geometric transparency of the grid. The term I_{th} is the thermionic emission current [34], I_p accounts for photoemission, and I_f is field emission (explained in subsequent sections). This expression can be corrected for temperature variations according to Eq. 8.9. Care must be taken because values vary with the device operational parameters.

One general observation from this equation is that there are a number of potential electron emission sources in an IEC device. Each of these sources varies nonlinearly and hence has to be carefully suppressed to increase the ion current, i.e., improve the device efficiency in terms of fusion reactions per unit power input.

8.3 Impurity Effects on SEE

It is a general observation that the fusion rate in IEC devices decreases in the presence of impurities. Some of this change can be traced to the effect on SEE. Impurity buildup occurs due to processes such as grid sputtering. Significant changes in fusion rates have been observed even when only trace amounts of impurities are present. This is because the SEE coefficients for most impurity ions are higher than the fuel gas (D^+; same as H^+ shown in Fig. 8.19).

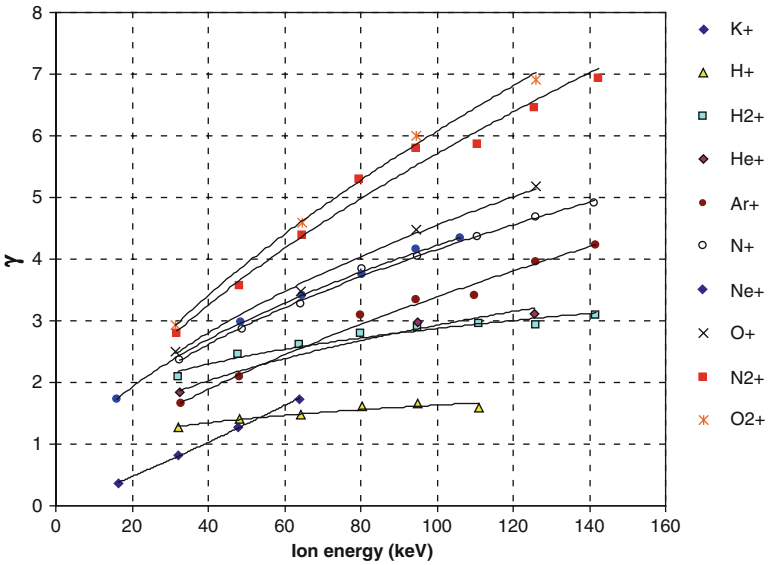

Fig. 8.19 SEE yield versus various incident ion energies on tungsten [35]. Various incident ions are listed to the right with corresponding symbols. Behavior of the SEE coefficients γ for other species with W metal surface would be similar to this graph (higher γ for higher ionization states) [36–42]

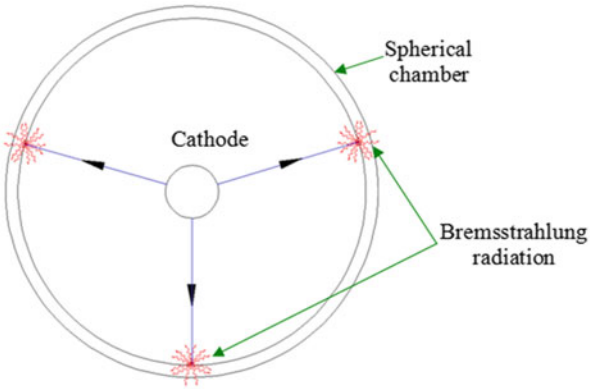

Fig. 8.20 The electrons released near the cathode accelerate and deposit their energy in the chamber walls, releasing Bremsstrahlung radiation [15]

Besides not contributing to the fusion rate, the impurity ions that are accelerated liberate many more secondary electrons than a single D^+ ion, thus reducing the ion current reaching the cathode for a constant power supply current. Moreover, in terms of SEE, even $D_2{}^+$ and $D_3{}^+$ are impurities in the sense that they generate more secondary electrons than D^+. Hence in a gridded IEC device, it is desirable to populate the deuterium plasma with the highest fraction of D^+ ions possible. To realize this, external ion guns generating high densities of D^+ ions offer more control than an internal plasma discharge.

8.3.1 Photoemission Electrons

The electrons liberated from the cathode accelerate to high energies before hitting the chamber walls where they deposit their energy, resulting in Bremsstrahlung radiation emission. Because these electrons are nonrelativistic, the Bremsstrahlung radiation is released isotropically in all directions [43]. Each electron is capable of releasing many photons through Bremsstrahlung radiation. Some of these photons impinge back onto the cathode as shown in Fig. 8.20. The resulting photo-absorption releases more electrons, further reducing the efficiency of the IEC device.

Electron emission occurs through the photoelectric effect. As illustrated in Fig. 8.21, some electrons acquire enough energy from the photons associated with incident electromagnetic radiation to overcome the work function, ϕ, of the substrate material. For this process to occur, the frequency υ of the incident radiation must be above the photoelectric threshold, $\upsilon_{\min}$, given by

$$\upsilon_{\min} = \frac{e\phi}{h}. \tag{8.15}$$

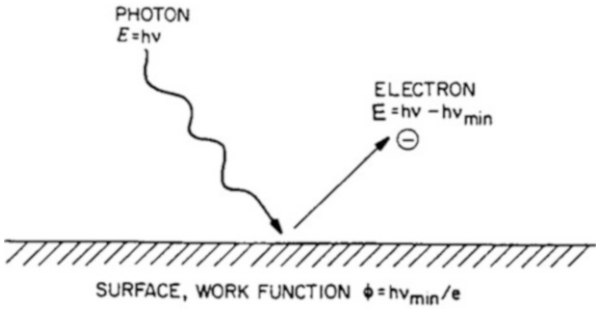

Fig. 8.21 Emission of a photoelectron from a surface with work function ϕ (for Al, ϕ = 4.28 eV) [44]

Here e is the electronic charge of an electron and h is Plank's constant.

For most metals and insulators, 4 eV $< e\phi <$ 5 eV, thus requiring intense sources of ultraviolet radiation in order to observe the photoelectric effect. However, in the present case, the soft Bremsstrahlung x-rays easily create photoelectrons.

The energy of electrons emitted from a surface is given by Einstein's photoelectric equation,

$$\varepsilon = h(\upsilon - \upsilon_{\min}). \tag{8.16}$$

Photoemission can result in producing several more electrons from the cathode. This effect is stronger with a chamber made of stainless steel, because heavy metals generate more Bremsstrahlung (proportional to Z^2) than light metals (such as aluminum).

The high-energy primary electrons created by Bremsstrahlung come from fairly deep beneath the metal surface, thus these electrons scatter before they escape, producing large numbers of secondary photoelectrons [45]. This effect can be described as follows. The mean free path of kilovolt x-rays in matter is several orders of magnitude greater than for the ejected photoelectrons (as shown in Fig. 8.22). The probability for photo-ejecting an electron from a given subshell per unit volume is given by [46]:

$$I_o = \sigma \times n_o \times \Gamma, \tag{8.17}$$

where σ is the photoelectron (photoionization) cross section for a given subshell of the element. Here Γ is the x-ray flux, and n_o is the density of the element in terms of atoms per unit volume. Figure 8.23 shows a sample of photoionization cross sections for Al and Fe in the energy range of 10 eV to 1 keV.

Though electrons may be liberated everywhere inside the cathode grid material, the photoelectron must emerge without significant energy loss due to an inelastic collision. Thus, the photoelectron intensity I is equal to

$$dI = I_o e^{-x/\lambda} dx, \tag{8.18}$$

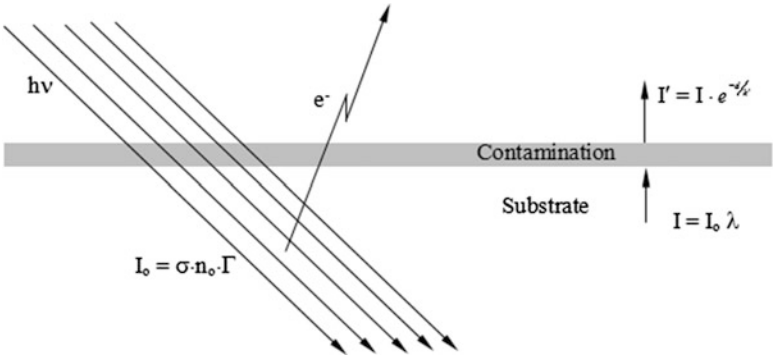

Fig. 8.22 Schematic representation of electron emission from a substrate with a contaminated surface layer [15]

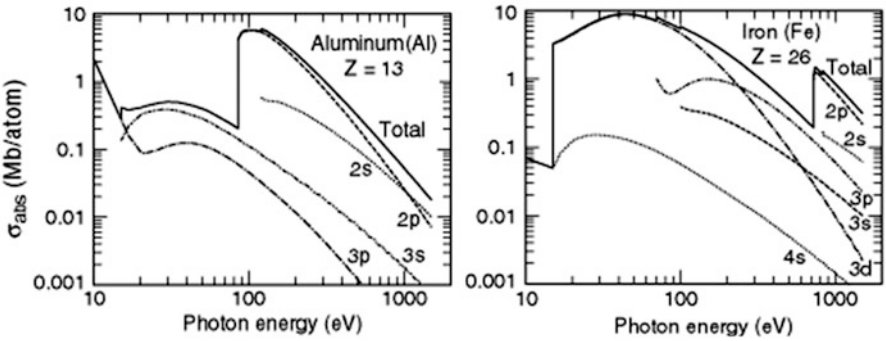

Fig. 8.23 The atomic subshell photoionization cross sections of Al and Fe for various energies [47–51]

where λ is the mean free path for inelastic scattering and x is the distance below the surface. The total photoelectron intensity I_p, found by integration from the surface to an infinite depth, gives

$$I_p = \int_0^\infty I_o \times e^{-x/\lambda} dx = I_o \times \lambda = \sigma \times n_o \times \Gamma \times \lambda. \tag{8.19}$$

In the case of monoenergetic electrons, related x-rays occur whenever electrons are rapidly accelerated across a high potential difference (e.g., electrons emitted near the cathode). The fraction of the energy in the electron beam that is converted into x-rays (f_x) is given by

$$f_x = 1.0 \times 10^{-7} \times Z \times E, \tag{8.20}$$

where E is the electron energy in keV and Z is the atomic number of the absorber.

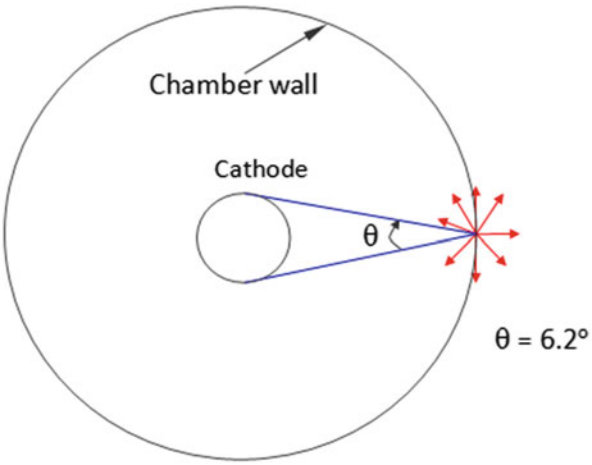

Fig. 8.24 Nonrelativistic electrons hitting the chamber wall release Bremsstrahlung radiation isotropically. Only a small fraction of this radiation (f_c) that for the geometry of the IEC shown subtends a solid angle of 6.2° converges on the cathode [15]

To reduce Bremsstrahlung production, the chamber wall of the IEC device should preferably be made of Aluminum, or at least be coated with Aluminum or other light materials such as graphite (however, contamination might be an issue with carbon).

It is suggested that Bremsstrahlung radiation is easier to measure than to calculate, and if such data are available, then we can calculate the flux of x-ray photons at the center of the chamber. Though the x-ray flux is usually measured outside the chamber, with necessary corrections for the attenuation in the chamber walls, we can estimate the initial flux generated inside the chamber. Only a fraction of this radiation converges on the cathode grid (f_c). One can then estimate the photoemission electrons (I_p) from Eq. 8.19 using a measured distribution for n_o and Γ.

The fraction of the Bremsstrahlung radiation that converges on a solid spherical cathode (as shown in Fig. 8.24) is given by

$$f_c = 6.2/360 = 0.017. \tag{8.21}$$

Because the grid has 92 % geometric transparency, the fraction of the radiation that reaches the cathode grid is given by

$$f_c{}' = 0.08 \times 0.017 = 1.38 \times 10^{-3}. \tag{8.22}$$

Though this is a small number, given that each electron impinging on the chamber wall produces many x-ray photons (e.g., ~ 1,000 photons per electron at 50 keV), there are also many electrons (e.g., 20 mA of electron current = 1.25 $\times$ 10^{17} electrons per second) hitting the chamber wall. Thus, the number of x-ray photons reaching the cathode grid could become a significant number (~ 1.72 $\times$ 10^{14} per second). Furthermore, depending on their energy, each of the x-ray photons could release multiple numbers of electrons from the cathode.

This phenomenon could be especially significant in pulsed devices due to large currents during a pulse [52]. At 50 kV, 20 mA cathode current, the photoelectron current is only 0.03 mA, but this can be significant. In the absence of measured data for W-Re alloy, a study of the behavior of other similar high-Z materials reveals that the total electron yield per x-ray photon could be as high as 50 [53]. This can bring the photoelectron emission from the cathode to significant levels (~1.2 mA). Though this photoelectron current seems to be a small fraction of the total power supply current (20 mA), it does significantly reduce the ion current by an estimated 14 %.

While an exact estimate of the photoelectron emission in an IEC device is difficult, these values are presented to illustrate its possible importance. Though these photoelectrons cannot be avoided, the knowledge of their influence on the performance of the device could be useful during the design phase of the experiment and aid in the material selection of the chamber and other structures. For instance, the IEC chamber "Homer" at the University of Wisconsin, Madison, is made of aluminum, instead of stainless steel. Note that simply lining the chamber walls with a thick aluminum foil can improve the performance of an existing stainless steel chamber. Furthermore, the cathode grid can be designed in such a way that the electrons are preferentially released in a particular direction. If the target for these impinging electrons is made of low-Z material, the overall photoelectron emission from the cathode will be further reduced.

8.3.2 *Field Emission*

There is one other source of electrons, field emission, that can become significant if care is not taken during the manufacture of the grids.

Sharp projections can result in a strong local electric field that can release electrons from a substrate due to the Schottky effect [54]. This effect corresponds to a reduction of the work function barrier ϕ_w by an amount given by [55]:

$$\Delta\phi_w = -(eE)^{1/2}. \tag{8.23}$$

Here E is the applied electric field, and e is the electronic charge. This change in ϕ_w not only causes electron field emission but also increases thermionic and photo emission currents that depend on ϕ_w of the substrate material.

When the applied electric field is above ~ 10^7 V/cm, strong electron field emission can occur. However, in IEC devices such high fields mainly occur at sharp edges on the cathode grid (because the applied voltage itself does not generally exceed 200 kV). As an example, this effect was observed in the University of Wisconsin Homer IEC device when the grid wire (Fig. 8.25a) was sandblasted in an attempt to clean the surface, introducing sharp microstructures (Fig. 8.25b). After that, the grid could no longer be operated at over 80 kV. Above that limit, the current would quickly increase nonlinearly and the power supply would shut down.

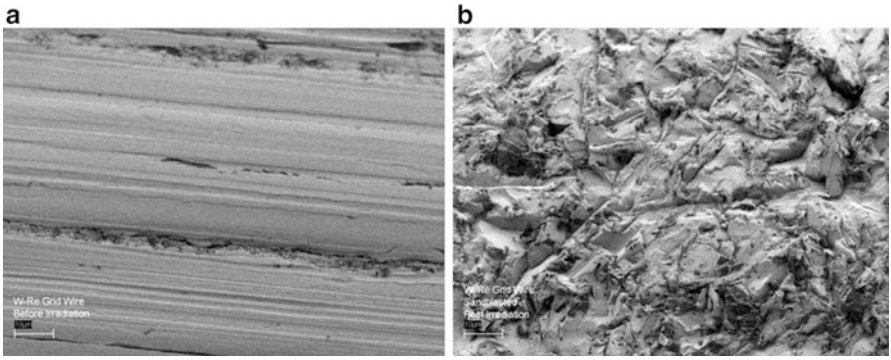

Fig. 8.25 (**a**) W-25%Re grid wire before sandblasting. (**b**) The same wire after sandblasting [56]

The sharp edge effect on the electric field can be estimated as a function of the radius of curvature (of the sharp edge of a projection) and is given by [57, 58]:

$$E = \frac{2V}{r\ln(R/r)}. \tag{8.24}$$

Here V is the applied voltage, R is the distance from the tip of a projection to the anode, and r is the radius of curvature of the projection tip.

This effect can show up when the grid is not manufactured carefully or is damaged by heat, bombardment of ions, or use of cleaning such as sandblasting. Sharp points appear whenever two wires are spot-welded. The electrode tends to melt (unevenly) at the surfaces of contact (electrode–wire, wire–wire, and wire–electrode contacts). Such sharp points and those of the wire used in grid construction should be ground off and polished carefully. Once this is done, the field emission effect can usually be ignored.

8.3.3 Tests of Grid Materials

A simple way to test the material properties suitable for building the cathode grid is to use single loop grids built of different materials, instead of whole grids. A single loop grid produces a (~line) cylindrical fusion source, and higher proton rates are observed when this grid is oriented face-on with the proton detector. Hence in a cylindrical IEC device, the proton count rate observed would be higher along the two faces of the cylinder [56]. At higher input voltages, the ions tend to continue recirculation, causing a higher fusion rate along the line of sight of the detector in the face-on orientation (90 °) with the single loop grid. Electron emission from the cathode increases nonlinearly. As a result, the ion current increases in a less than linear fashion with the power supply current. Hence simply increasing the power supply current by pulsing or other means would not increase the fusion rate unless

a fundamentally different mode of operation, such as converged core, is obtained. In addition, a simultaneous effort to decrease the electron current is recommended.

When selecting grid materials, ones with a lower SEE coefficient γ are desirable, e.g., rhenium seems to be a good choice for this reason. The γ is also affected by the composition of the plasma (D^+:D^{2+}:D^{3+}) even in a chamber with few impurities. Thus, as noted earlier, it is desirable to increase the D^+ concentration using external ion guns. The variation of γ with voltage has to be accounted for in the ion circulation current equation.

In conclusion, one design criterion for an IEC chamber design is to minimize the electron emission from the chamber wall and from the outer cathode surface. This is complex, however, due to many different sources of electrons (illustrated by Eq. 8.14). Most processes are nonlinear by nature and, if allowed to increase, lead to a decrease in the ion current. This explains why researchers have not easily obtained I^2 beam–beam reaction rate scaling even when pulsed to higher currents.

8.4 Summary

This chapter has discussed the issues related as to how the fusion rate scales with the ion current in the ion-injected-type IEC. Because most present IECs use internal plasma discharge ion sources, they operate at a fairly high background pressure. Consequently, the fusion rate roughly scales as a product of the ion current and the neutral background density. Still, a number of related effects enter. For example, charge exchange leads to energetic neutral ions that can also react with background neutrals; ions and energetic neutrals can bombard and react with absorbed gas on the grid wires or other components in the chamber; and electron currents generated at the cathode, which stream to the anode, represent an energy loss and complicate evaluation of the actual ion current. Due to these complexities, the fusion rate typically turns out to deviate from the ideal linear scaling with the ion current. Still, for a variety of applications involving neutron, proton, and x-ray production, the beam–background scaling trend provides a good "rule of thumb" guide for operation.

Research to move the field toward a very high yield neutron–proton source, or to achieve a fusion reactor, requires a very low background pressure, such that the fusion rate scales at least with the current squared, i.e., representing beam–beam fusion. Figure 8.1 provides a good guide for the operating parameters needed to achieve this type of scaling. However, this representation assumes rather ideal conditions. The variety of effects such as secondary electron emission remain, while a number of new issues such as prevention of ion thermalization in the core region and maintenance of a low electron temperature in the core become crucial. Instabilities, too, may play a role in this regime, including two-stream, Wiebel, and beam–wave instabilities. Most instabilities would have a negative effect on IEC operation, but as noted earlier, Bussard and colleagues postulate that the plasma wave effect can increase the core density by compression. To date, resources have

prevented IEC researchers from building experiments with adequate ion source power supplies to access this regime. The closest to doing this appears to be the recent six-gun experiment at the University of Wisconsin, designed to duplicate Hirsch's original results with six external ion guns. As a result, much more theoretical and experimental work is necessary to fully understand operation in the beam–beam and related regimes.

References

1. McGuire TJ, Sedwick RJ (2005) Improved confinement in inertial electrostatic confinement for fusion space power reactors. AIAA J Propuls Power 21:4
2. Sedwick RJ (2012) Magnetic core multi-grid inertial electrostatic confinement concept using p-^{11}B. In: Nuclear and emerging technologies for space. The Woodlands, 21–23 Mar
3. McGuire TJ, Sedwick RJ (2008) Numerical predictions of enhanced ion confinement in a multi-grid IEC device. In: AIAA-2008-4675, 44th AIAA/ASME/SAE/ASEE JPC, Hartford, 21–23 July
4. Rosenberg M, Krall NA (1992) The effect of collisions in maintaining a non-Maxwellian plasma distribution in a spherically convergent ion focus. Phys Fluids B 4:1788
5. Nevins WM (1995) Can inertial electrostatic confinement work beyond the ion–ion collisional time scale? Phys Plasmas 2:3804
6. Dietrich CC, Eurice LJ, Sedwick RJ (2008) Experimental verification of enhanced confinement in a multi-grid IEC device. In: AIAA-2008-4760, 44th AIAA/ASME/SAE/ASEE JPC, Hartford21–23 July
7. Zajfman D et al (2005) Self-bunching effect in an ion-trap resonator. J Opt Soc Am B 20:1028
8. Miley GH (1976) Fusion energy conversion. American Nuclear Society, LaGrange
9. Ishikawa M, Kudo T, Hayashi S, Yamane T, Tomita Y, Momota H (1998) Basic numerical simulation of TWDEC for a D–^{3}He fusion reactor. Fusion Eng Des 41(1):541–546
10. Bussard RW (1991) Some physics considerations of magnetic inertial-electrostatic confinement: a new concept for spherical converging-flow fusion. Fusion Technol 19:273
11. Rider TH (1995) A general critique of inertial-electrostatic confinement fusion systems. Phys Plasmas 2:1853
12. Bussard RW, Jameson LW, King KE (1992) Ion-acoustic waves and ion wave group trapping in IEC systems. Bull Am Phys Soc 37(6):1582
13. Miley GH, Satsangi AJ, Yamamoto Y, Javedani JB (1993) Conceptual design for a D–^{3}He IEC pilot plant. In: IEEE/NPSS 15th symposium on fusion engineering, IEEE No. 93CH3348-0, 1, pp 161–164
14. Masuda K et al (2010) Cathode grid current dependence of D(d, n)3He reaction rates in an inertial electrostatic confinement device driven by a ring-shaped magnetron ion source. Plasma Phys Control Fusion 52:095010
15. Krupakar Murali S, Santarius JF, Kulcinski GL (2010) Consolidated electron effects in an IEC device. Plasma Sources Sci Technol 19:045029
16. Oak Ridge National Laboratory (1985) Atomic data for fusion, vol 3. http://www-cfadc.phy.ornl.gov/redbooks/three/c/3c13.html
17. Hasselkamp D, Lang KG, Scharmann A, Stiller N (1981) Ion induced electron emission from metal surfaces. Nucl Inst Meth 180:349–356
18. Arifov UA, Rakhimov RR (1960) Secondary emission in the bombardment of molybdenum by neutral atoms and argon ions. Bull Acad Sci USSR Phys Ser 24:266 [Mo, Ta, and W]
19. Magnuson GD, Carlston CE (1963) Electron ejection from metals due to 1- to 10-keV noble gas ion bombardment. I. Polycrystalline materials. Phys Rev 129:2403 [Al, Ni, Cu, Zr, Mo, and Ti]

20. Large LN, Whitlock WS (1962) Secondary electron emission from clean metal surfaces bombarded by fast hydrogen ions. Proc Phys Soc (Lond) 79:148 [Ti, Ni, Cu, Zr, Mo, Ag, Au & Pt]
21. Thorson TA, Durst RD, Fonck RJ, Wainwright LP (1997) Convergence, electrostatic potential, and density measurements in a spherically convergent ion focus. Phys Plasmas 4:4
22. Wehmeyer AL, Radel RF, Kulcinski GL (2005) Optimizing neutron production rates from D–D fusion in an inertial confinement device. Fusion Sci Technol 47:1260
23. Sternglass EJ (1957) Theory of secondary electron emission by high-speed ions. Phys Rev 108:1
24. Parilis ES, Kishinevskii LM (1960) Kinetic secondary electron ejection from molybdenum by cesium ions. Sov Phys-Solid State 3:885
25. Schou J (1980) Transport theory for kinetic emission of secondary electrons from solids. Phys Rev B 22:2141
26. Baragiola RA, Alonso EV, Oliva Florio A (1979) Electron emission from clean metal surfaces induced by low-energy light ions. Phys Rev B 19:121–129
27. Knoll GF (2000) Radiation detection and measurement, 3rd edn. Wiley, New York, p 31
28. Dekker AJ (1954) Energy and temperature dependence of the secondary emission of MgO. Phys Rev 94:5
29. Linford LH (1935) The emission of electrons by swiftly moving mercury ions. Phys Rev 47:279
30. Allen JS (1939) The emission of secondary electrons from metals bombarded with protons. Phys Rev 55:336
31. Lakits G, Winter H (1990) Electron emission from metal surfaces bombarded by slow neutral and ionized particles. Nucl Instrum Methods B48:597–603
32. Khachan J, Collis S (2001) Measurements of ion energy distributions by Doppler shift spectroscopy in an inertial-electrostatic confinement device. Phys Plasmas 8(4):1299–1304
33. Boris DR, Emmert G (2008) Composition of the source region plasma in inertial electrostatic confinement devices. Phys Plasmas 15:083502
34. Murali K, Santarius JF, Kulcinski GL (2010) Study of thermionic electrons in an inertial electrostatic confinement (IEC) device using a novel 'chordwire' diagnostic. Fusion Sci Technol 57(3):281–291
35. Large LN (1963) Secondary electron emission from a clean tungsten surface bombarded by various positive ions. Proc Phys Soc 81(6):1101
36. Arifov UA, Rakhimov RR, Khozinskii OV (1962) Bull Acad Sci USSR-Phys Ser 26:1422
37. Ferron J, Alonso EV, Baragiola RA, Oliva-Florio A (1981) Dependence of ion-electron emission from clean metals on the incidence angle of the projectile. J Phys D 14:1707
38. Hagstrum HD (1956) Auger ejection of electrons from molybdenum by noble gas ions. Phys Rev 104(3):672
39. Losch WHP (1970) Angular distribution of secondary electrons from ion bombardments. Phys Stat Sol (A) 2:123
40. Mahadevan P, Magnuson GD, Layton JK, Carlston CE (1965) Secondary-electron emission from molybdenum due to positive and negative ions of atmospheric gases. Phys Rev 140:A1407
41. Perdrix M, Paletto S, Goutte R, Guillaud C (1969) Emission électronique secondaire d'une cible de molybdène bombardée par des ions positifs et négatifs d'un même element. J Phys D Appl Phys 2(3):441
42. Vance DW (1968) Auger electron emission from clean Mo Bombarded by positive ions. II. Effect of angle of incidence. Phys Rev 169(2):252
43. Jackson JD (2002) Classical electrodynamics, 3rd edn. Wiley, New York/London
44. Michaelson HB (1977) The work function of the elements and its periodicity. J Appl Phys 48 (11):4729
45. Cardona M, Ley L (eds) (1978) Photoemission in solids I. Springer, Berlin/Heidelberg/ New York, p 28

46. Carter WJ, Schweitzer GK (1974) Experimental evaluation of a simple model for quantitative analysis in X-ray photoelectron spectroscopy. J Electron Spectrosc 5:827–835
47. Yeh J-J, Lindau I (1985) Atomic subshell photoionization cross sections and asymmetry parameters: $1 < Z < 103$. At Data Nucl Data Tables 32:1
48. Yeh J-J (1993) Atomic calculations of photoionization cross sections and asymmetry parameters. Gordon and Breach, Langhorne
49. Cooper JW (1962) Photoionization from outer atomic subshells. A model study. Phys Rev 128:681
50. Manson ST, Cooper JW (1968) Photo-ionization in the soft x-ray range: 1Z dependence in a central-potential model. Phys Rev 165:126
51. Manson ST (1976) Atomic photoelectron spectroscopy, part I. Adv Electron Electron Phys 41:73
52. Nadler JH, Miley GH, Momota H, Shaban Y, Nam Y, Coventry M (2001) Neutron production and ionization efficiency in a gridded IEC device at high currents. Fusion Technol 39(2):492–497
53. Ebel H, Svagera R, Ebel MF (2000) Quantitative surface analysis by X-ray induced electron emission. JCPDS-Int Cent Differ Data Adv X-ray Anal 43:519
54. Schottky W (1914) Über den Austritt von Elektronen aus Glühdrähten bei verzögernden Potentialen. Ann Physik 44:1011
55. Herring C, Nichols MH (1949) Work function measurements of contact materials for industrial use. Rev Mod Phys 21:185
56. Krupakar Murali S (2004) Diagnostic study of steady-state advanced fuel (D–D and D–^{3}He) fusion in an IEC Device. Ph.D. thesis, Department of Physics, University of Wisconsin, Madison
57. Cardona M, Ley L (eds) (1978) Photoemission in solids I–general principles. Springer, Berlin/Heidelberg/New York, p 21
58. Reece Roth J (1995) Industrial plasma physics: Vol. 1, principles. Institute of Physics Publishing, Bristol/Philadelphia, p 165

Chapter 9
Cylindrical and Other IEC Geometries

9.1 Introduction

Spherical geometry has been widely used following Farnsworth's original studies that stressed the possibility of three-dimensional compression of recirculating beams in the central core of this geometry. This becomes a very important feature if the goal is net power production. However, in many other applications, less compression (e.g., two-dimensional compression in a cylindrical geometry) may be adequate. Indeed, a unique feature of the IEC is that we can adapt its geometry to a number of important near-term applications short of power production. In this chapter, we consider cylindrical, jet extraction, dipole-assisted, and magnetically coupled IEC geometries. These provide unique capabilities for various near-term commercial applications. For example, a long, cylindrical IEC can operate as an extended "line-like" neutron source for scanning large areas quickly; the IEC jet provides an intense localized beam for space thrusting or other applications such as ion implantation. Other important configurations, which are quasi-spherical, include the magnetic-assisted HEPS (Polywell) configuration, the Penning trap IEC, and the POPS oscillating IEC. These concepts are discussed elsewhere in this book, so they will not be included here. Finally, we will briefly consider several variations involving a linearized beam–beam interaction mechanism proposed for power production.

9.2 Cylindrical IECs

Cylindrical is a prime alternate geometry that has been widely studied for IECs. Originally developed at the University of Illinois at Urbana–Champaign, the configuration has spread to other labs including the University of Wisconsin, Kyoto University, and the Tokyo Institute of Technology. The objective of this geometry is to obtain a dense core region extending along the axis of the cylinder.

G.H. Miley and S.K. Murali, *Inertial Electrostatic Confinement (IEC) Fusion: Fundamentals and Applications*, DOI 10.1007/978-1-4614-9338-9_9,

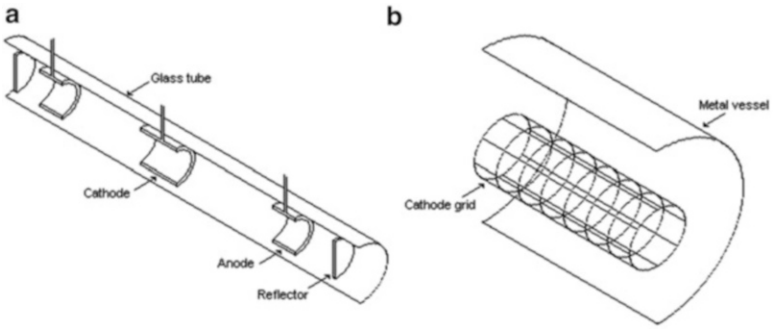

Fig. 9.1 Two types of cylindrical IECs. (**a**) The hollow cathode (often termed the C-Device). (**b**) The two-dimensional gridded version, called the cylindrical IEC [2]

This is especially interesting for neutron sources because it offers a very long source that can be used for broad area coverage of large objects such as container boxes. Conventional spherical neutron sources require multiple "ganged" sources to do the same. That configuration is also under study in several labs, though little has been published on it to date. A downside, however, for the cylindrical IEC is the high power input required for long configurations. Thus the advantage of source length must be weighed against the alternative of moving a smaller spherical (point) source that requires less input power over the surface of interest.

The cylinder geometry can be an alternative neutron, proton, etc., source, but does not seem suitable for scaling to a power reactor. It can be viewed as a two-dimensional version of the spherical unit. As such, the beam convergence (compression) is limited to lower values, hence lower core densities. A high core density is essential for beam–beam fusion desired for power reactors, but less so for beam–background reactions used in most current IEC neutron and proton sources.

Two types of cylindrical sources [1–5] have been studied (shown schematically in Fig. 9.1) – a gridded type which is essentially the spherical unit converted into a cylinder and a quite different hollow cathode design. The gridded design was a natural variation of the original Farnsworth device and was first studied experimentally in the 1970s by Tom Dolan at the University of Illinois at Urbana–Champaign. He used laser diagnostics with a noble gas discharge to study density–temperature and species profiles [6]. The hollow cathode design was later proposed by G. H. Miley as an attempt to retain the long axial reaction region without the grids (e.g., see studies [1] and [2]).

The hollow cathode C-Device of Fig. 9.1a has an insulated vacuum chamber with an alternating series of hollow cylindrical cathodes and anodes spaced along a common longitudinal axis. Biased end plates serve as charged particle reflectors. The anodes, cathodes, and end plates are biased to steady-state and/or pulsed voltages, depending on the operational mode. This configuration is used to initiate a plasma discharge, resulting in electrostatic confinement of fusion fuel ions in both the axial and radial directions. Typical operation produces about 10^7 2.45-MeV n/s (D–D) steady state, while pulsed output provides about 10^9 2.45 MeV n/s (D–D).

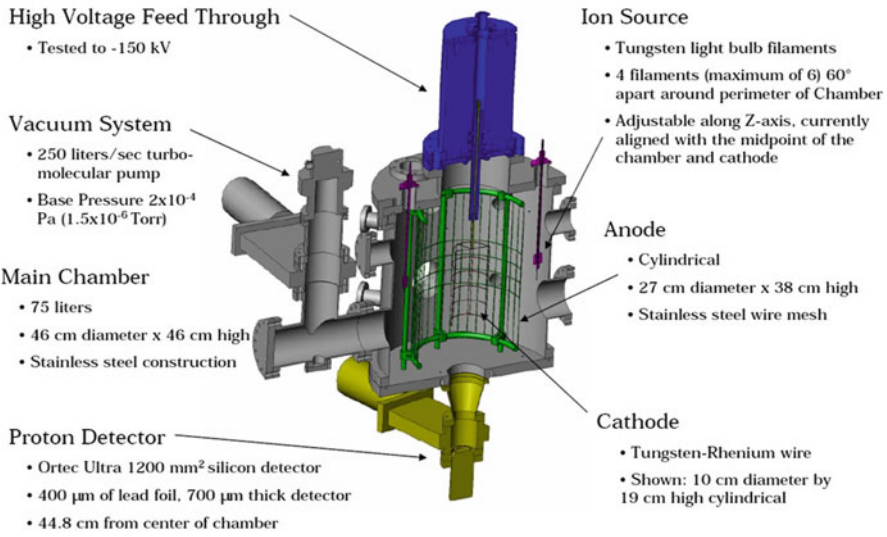

Fig. 9.2 Components and diagnostics of the ^{3}He Cylindrical Transmutation Reactor (^{3}HeCTRE) [8]

These values are adequate for a very attractive neutron or proton source application. Such devices are the first to be commercialized and are being used to replace ^{252}Cf sources [7].

In the cylindrical two-dimensional IEC (Fig. 9.1b), a cylindrical cathode grid is placed with its axis concentric with the axis of the surrounding vacuum vessel. This is then, in effect, a two-dimensional version of the spherical IEC. It operates by convergence of ions created between the grid and wall onto a small volume along the axis; hence it has sometimes been called the Radial Converging IEC (RC-IEC). While the first study of the cylinder IEC by T. Dolan was done in the 1970s, the concept lay dormant until revised and upgraded by UIUC researchers several decades later using improved grid designs for neutron production [1–5].

In 2006, researchers working with G. L. Kulcinski at the University of Wisconsin, Madison, undertook a detailed study to develop an attractive cylindrical device and to compare spherical and cylindrical IEC operation. Brian Egle and colleagues there constructed a cylindrical IEC of the design shown in Fig. 9.2 [8]. It was named the ^{3}He Cylindrical Transmutation Reactor (^{3}HeCTRE). The objectives were twofold: medical isotope production and investigation of performance differences between spherical and cylindrical geometries. D–D and D–^{3}He reactions were studied in the cylindrical IEC chamber with a D–D rate of 2.7×10^{7} n/s at 145 kv, 35 mA, 0.3 Pa, and the D–^{3}He rate of 2.0×10^{7} p/s at 130 kV, 30 mA, 0.3 Pa.

For comparison, two cathode configurations were used and are shown in Fig. 9.3 (spherical in (a) and cylindrical in (b)). These were compared to the two spherical devices also shown in Fig. 9.3. Results for operation of these configurations using D–D reactions are shown in Fig. 9.4 and for D–^{3}He reactions in Fig. 9.5.

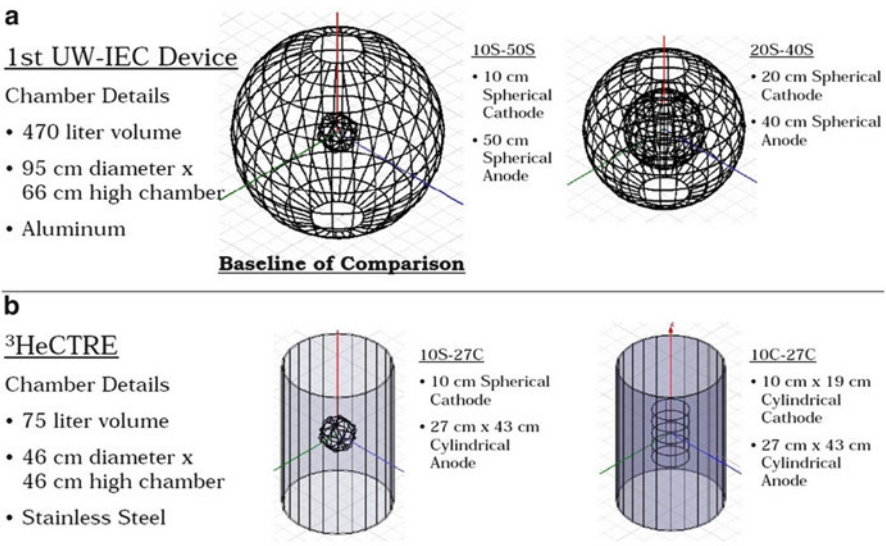

Fig. 9.3 Spherical geometries (**a**) and cylindrical geometries (**b**) used in D–D and D–^{3}He neutron reaction rate comparison studies at the University of Wisconsin [8]

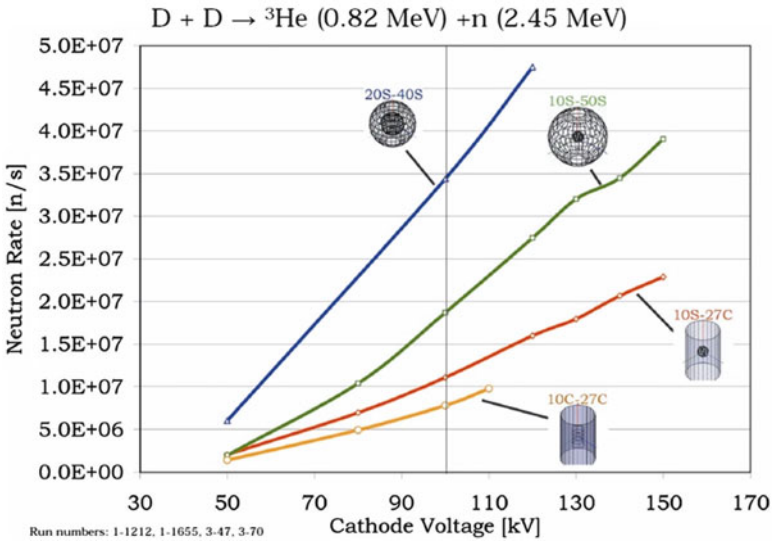

Fig. 9.4 Comparison of D–D neutron rates for the spherical and cylindrical IEC geometries shown in Fig. 9.3. Operations used 0.3 Pa of D gas and 30 mA meter current at steady state [8]

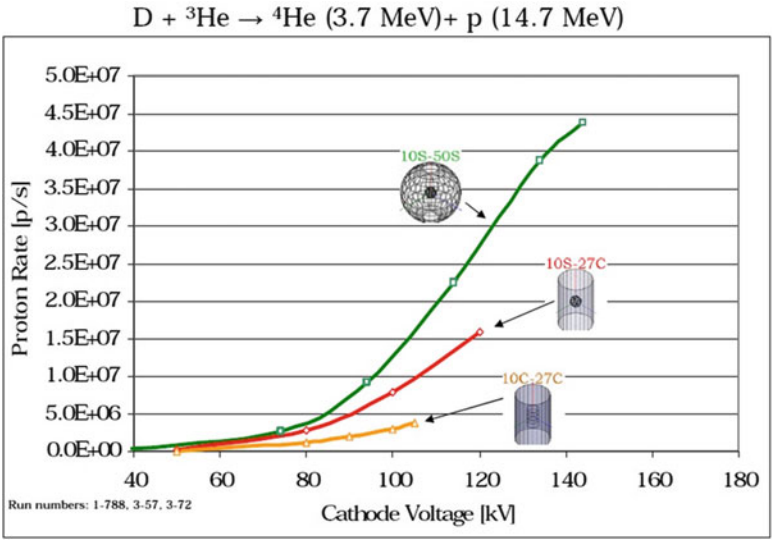

Fig. 9.5 Comparative D–^{3}He 14.7-MeV proton production rates for three different geometries using 0.3 Pa of D and ^{3}He gas mixture with 30 mA meter current at steady state [8]. The 14.7-MeV proton is of particular interest for medical isotope production

As seen from these figures, in both cases, the cylindrical configuration resulted in lower reaction rates as might be expected due to the two-dimensional versus a three-dimensional convergence. However, the comparisons were done with similar gas pressure and currents, so it is not clear whether separate optimization of conditions in each device would change the result. As stressed earlier, as long as the pressure is high enough that the background neutral density results in beam–neutral reactions, beam convergence is not so crucial. Consequently, rather than convergence, differences in reaction rate depend more on geometric factors such as anode–cathode radius ratio, device diameter, cylinder length, and microchannel formation. Thus the basis for a comparison becomes a complex issue. Such factors are difficult to quantify without performing detailed optimization of conditions for each geometry. While the D–D neutron and D–^{3}He proton curves in these two figures follow similar trends, there are marked differences in rates versus voltage; the D–D case provides much higher rates at low voltage. This difference is expected due to the differences in fusion cross sections for the two reactions.

As seen from these studies, the cylindrical geometry allows good performance and interesting shapes for near-term applications such as neutron sources or medical isotope production.

9.3 Electrically Driven IEC Jet Thruster

The use of an IEC design for space propulsion was originally proposed by Bussard [9]. His concept was for a high thrust scram jet device. This concept as well as Miley and colleagues' Spaceship I and II concepts discussed later in Chap. 12 are conceptual designs that envision that an IEC fusion reactor with a positive gain will be achieved. Later chapters address issues relative to achieving breakeven performance in an IEC fusion reactor. However, in this section, we discuss a near-term electrically driven IEC designed for space applications. In this case, electric power would come from a solar panel as is commonly done for current Hall thrusters employed for satellite station keeping.

For conventional "Star" mode operation, the IEC grid is designed to be highly symmetric so that the microchannel beams are also symmetric, providing good convergence. However, experiments have demonstrated that enlarging one of the grid openings distorts the potential surfaces. This results in the creation of a very intense, tightly coupled space charge-neutralized ion jet directed outward from the central core plasma region (see Fig. 9.6) [10], and it is this mode of operation ("Star" with jet) that would be employed for the proposed thruster.

The IEC jet thruster is intended as an ultra-maneuverable space thruster for satellite and small probe thrust operations. The IEC jet design potential offers a unique capability to cover a wide range of powers (few watts to kilowatts) with good efficiency while providing a plasma jet that can start with a large diameter but be narrowed directionally for maneuvering or to focus the intense beam on to a target, such as an asteroid, for diagnostic analysis. The IEC thruster uses the same spherical configuration with grids as employed for neutron production. For thrusting, however, a gas such as argon may be used rather than deuterium. Ions are generated and accelerated toward the center of the device as described earlier. However, in this case, a carefully designed enlarged opening in the cathode grid causes a locally distorted potential field that extracts the accelerated ions from the

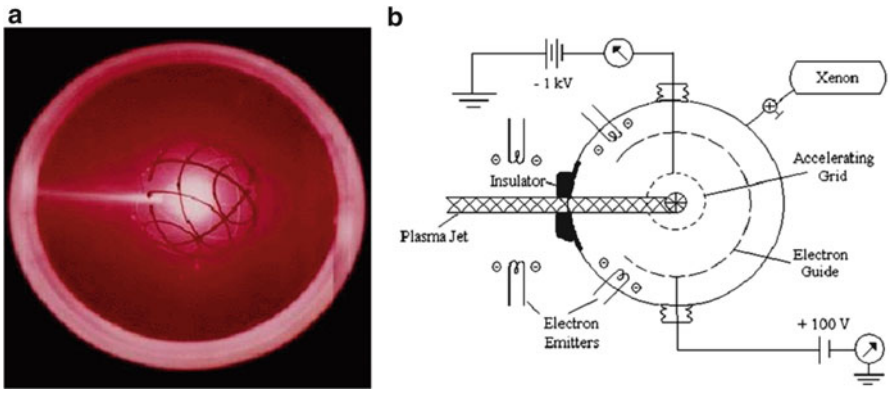

Fig. 9.6 (**a**) Jet operational mode in experimental IEC device. (**b**) Jet setup [10]

device, forming an intense quasi-neutral ion jet. The ability to use multi-kV potentials on the IEC grid provides much higher velocity ions than possible with other thrusters (e.g., Hall thrusters typically operate well below 1 kV). These ultrahigh velocity ions and the ability to use a variety of gases are distinguishing features of the IEC plasma jet. The simple structure, low gas leakage, and good heat removal make it possible to scale the design to either low powers or high powers, covering a range of interest for present small satellites on to future medium and large satellites. In addition to maneuverable thrusting, the jet channel extraction technique enables directing and focusing the plasma stream onto an asteroid or other object for interrogation of it. Analysis of the plasma emission spectra could provide an identification of the materials and surface features of the object. With further development the IEC system potentially offers a very attractive fusion power source for space propulsion. Another advantage of the IEC jet thruster is that it provides a step toward a future p-B^{11} IEC power source and/or thruster for satellite operations. This possibility is also briefly discussed next.

9.4 The Dipole-Assisted IEC (DaIEC)

The Dipole-assisted IEC (DaIEC) is an extension of the basic spherical IEC concept where a dipole magnet is located in the center of two hemispherical grids [11]. A schematic of the setup is shown in Fig. 9.7. The DaIEC was first proposed by G. H. Miley and has been investigated at the University of Illinois. This concept is closely related to the levitated dipole reactor [12] but is much simpler, being smaller and not requiring magnetic levitation. It also differs in the physics of the associated plasma confinement. Studies to date have assumed use of D–^{3}He fusion to minimize neutron damage to the magnets. Two ion sources would inject 40-keV

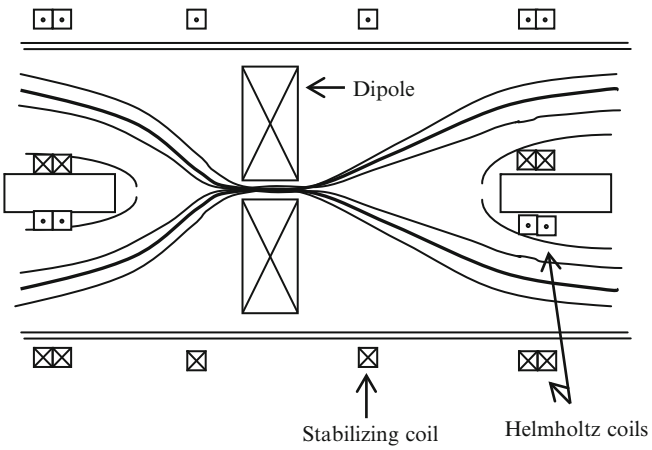

Fig. 9.7 Dipole reactor propulsion scheme [12]

D and ^{3}He ion beams toward the center of the dipole magnet (shown in Fig. 9.7). The magnetic field compresses the ion beams by trapping ions along the magnetic field lines, so that they fuse within the volume inside the dipole magnet. The products of D–^{3}He fusion reaction are 14.7-MeV protons and 4-MeV alpha particles. These can be used for direct charged particle propulsion or direct conversion to electricity for station keeping.

For propulsion applications, the ions that exit toward the right in Fig. 9.7 are trapped by the magnetic field produced by the stabilizing coil and are exhausted to produce thrust. This configuration of the magnetic field reduces the mechanical components. Because the magnetic field does not close at the nozzle but is open, it is not necessary to neutralize the reaction products (protons and alpha particles) because the reaction is charge neutral. Still, a neutralizer (such as electron injection into the exhaust) is required to avoid possible charging up of the system at the nozzle due to the non-neutral background plasma exhaust.

There are several advantages of the DaIEC. By applying the desired voltage to the cathode grid, high-energy ions are easily obtained; hence plasma heating is straightforward. Indeed, in this case, fusion is dominated by beam–beam (non-Maxwellian) reactions. Also, the dipole magnet at the center of the device produces field lines that trap ions and compresses them within the inner radius of the dipole. Thus, a very high ion beam density can be achieved, leading to high reaction rates via beam–beam fusion. Biasing the dipole magnet to the same potential as the cathode grid solves the problem of space charge buildup due to the high ion density at the center of DaIEC.

Technology issues of neutron damage to the magnet even with D–^{3}He appear challenging. Thus further reduction of neutrons with p–B^{11} may become a necessary fuel choice.

9.4.1 DaIEC Experiments

Preliminary experiments have been carried out at the University of Illinois to investigate the focusing effect of the dipole magnetic field [11, 13]. A schematic of the experimental setup is shown in Fig. 9.8. The primary goal was to measure the increase in plasma densities achieved by a DaIEC. Thus the configuration is somewhat different from the schematic in Fig. 9.7 that included added coils to direct the charged fusion products into a directed direction representing a "magnetic nozzle."

This experiment employed two split spherical grids as shown in Fig. 9.8. Ions are created in the discharge between these grids and the vessel wall. They are extracted and accelerated by the grid potential so they pass through the dipole field, as illustrated in Fig. 9.8a. The experiment had the goal of confirming that an order of magnitude plasma electron density increase (versus no dipole present) could be achieved in the center region. A double Langmuir probe was inserted at various positions throughout the center region to measure the electron density, n_e. Figure 9.9

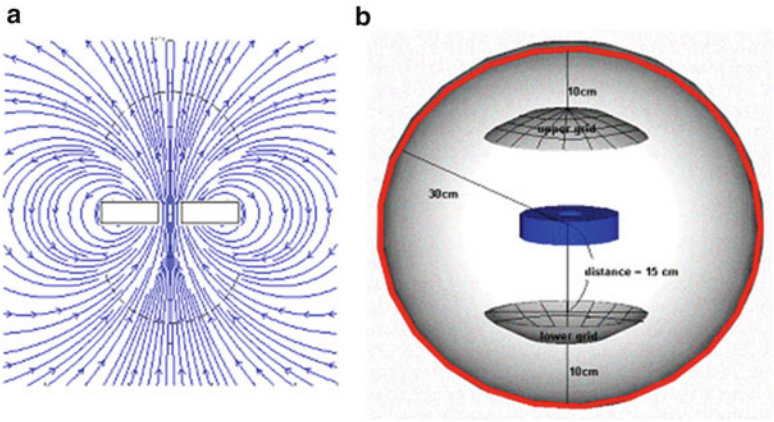

Fig. 9.8 (**a**) Dipole magnetic field. (**b**) Layout of the split cathode grid and magnet in the DaIEC experiment [11]

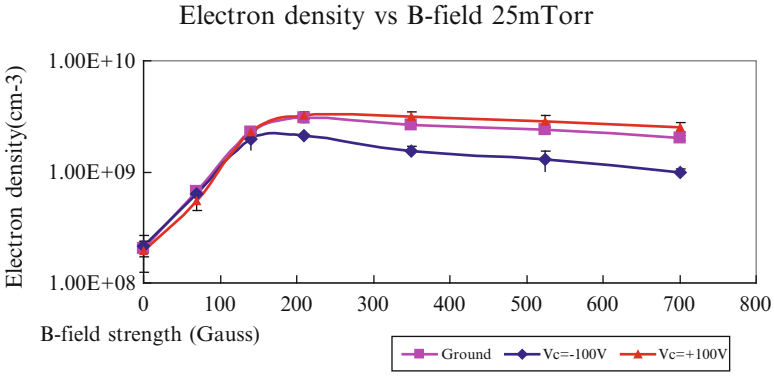

Fig. 9.9 Electron density versus dipole magnet field strength at 25 mTorr, 20 mA with various applied voltages on the dipole magnet [11]

shows changes in the electron density with increasing magnetic field measured at various coil electric potential biases. It was found that electron density increases about 17 times that of a nonmagnetic field IEC with this configuration, very close to theoretical estimations.

The use of a bias voltage on the dipole magnet structure to control space charge buildup was also studied. In an ion-injected IEC, partial space charge neutralization at the core region is essential to decrease the center potential and consequently allow incoming beam ions to penetrate into the core region (represents a space charge-limited flow per Chap. 7). In the DaIEC, it is possible to control the centerline potential by applying a bias voltage to the dipole coil. In the University of Illinois experiment, this was done by applying a voltage to a

small copper ring inserted in the core of the dipole magnet. This is obvious in Fig. 9.9 where the increase in the electron density with a small centerline bias applied was about 30 %, while the applied voltage to the dipole structure of −100 V was ~ 3 % of the discharge voltage. The setup prevented the use of larger applied voltages which should further improve neutralization, but these results still demonstrated the basic concept of dipole focusing with coil bias voltage control.

9.5 Microchannel Type IEC Thruster

The microchannel IEC thruster concept was originally proposed and studied in Joe Khachan's IEC laboratory at the University of Sydney. His group has also pioneered use of optical emission spectroscopy on gridded IEC devices. This work, among other things, had led to their "microchannel"-type thruster concept [14, 15]. Using Doppler spectroscopy of the hydrogen Hα line, they have shown that the microchannels in an IEC hydrogen gas discharge operating in the units at tens of mTorr pressure range (for voltages less than 30 kV) are mostly composed of molecular ions with approximately 20 % atomic hydrogen. They developed a spectroscopic model based on collisional radiative emission modeling to spectroscopically measure ion densities and electron energies and predict fusion rates. This latter achievement makes spectroscopic measurements simpler to carry out because hydrogen can be used to predict fusion rates in situations where use of fusionable fuels, such as deuterium, would result in a neutron radiation hazard if shielding in a laboratory is not available. In follow-up work, they simplified the modeling of charge exchange with an analytical approach based on Markov chain theory [15].

The flow of neutrals moving away from the cathode seen from the spectroscopic measurements was also confirmed by carrying out a dusty plasma measurement. This showed charged micron-sized insulating spheres (dust) experienced a force directed away from the cathode center [16]. The explanation of this was attributed to a local potential maximum established at the center of the cathode, which accelerates ions at that point away from the center. Due to charge exchange, these ions become neutrals and are able to leave along the microchannels out to the anode. The ion drag force on the dust in the "dusty plasma" moved the dust particles away from the center. Based on this observation, Khachan has studied the concept of using the collimated beam of neutrals exiting from the cathode to make a simple but effective electric propulsion thruster. In this design, illustrated in Fig. 9.10, a unidirectional microchannel emerges from a conical cathode [17]. Khachan concludes from these measurements that the specific impulse of this microchannel thruster and its efficiency greatly exceed that of existing electric propulsion thrusters. Note that this concept, while having some similarities, differs in important detail from Miley's jet thruster described earlier.

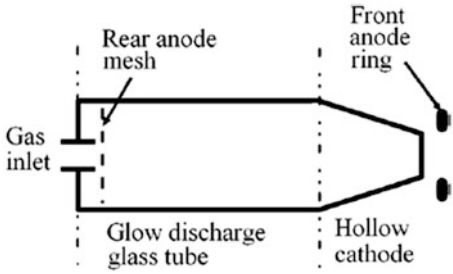

Fig. 9.10 The charge exchange thruster [17]

9.6 A Counter-Streaming Beam Linear IEC

The cylindrical IEC geometry with two-dimensional converging ion beams led to Momota and Miley's concept of a linear counter-streaming IEC [18]. This concept was conceived of to provide a broad area neutron source. The common feature it shares with the spherical and cylindrical IECs is that reactions occur through colliding beams. The linear design allows reactions over a longer distance, thus making it possible for neutrons to sweep a very large area. Such a design is illustrated in Fig. 9.11.

Neutrons are produced by reactions between energetic beam deuterium injected from both ends of cylindrical reaction chamber and trapped there. Ionization chambers produce deuterium ions by rf-electric fields and accelerate them by applied high electrostatic potential of ~ 30 kV. The ionization chambers are filled with neutral deuterium gas with a pressure of several 0.1 Pa. They are connected to the reaction chamber through two stages of differential pumping to maintain a neutral gas pressure below 0.001 Pa in the reaction chamber.

A thin column deuterium beam is essential to achieve a high reaction rate. This introduces, however, possibilities of various modes of instabilities in the beam column. Momota and Miley [18] analyzed beam stability issues to provide guiding data for designing the linear neutron generator. Their detailed analysis showed that a counter deuterium beam system with a thin column radius is unstable in general due to electrostatic two-stream modes and also magnetostatic filamentary Weibel's modes. However, they found that the application of a strong magnetic field parallel to the column stabilizes those instabilities. On the base of this analysis, a set of parameters for a stabilized deuterium counter-beam column were developed for a neutron source, as summarized in Table 9.1. This design would provide a long (~ 3 m) line-like neutron source for broad area neutron activation analysis (NAA) coverage. This linear counter-streaming beam device is, in a sense, representative of a single microchannel in the spherical IEC. The spherical IEC provides a means of bringing a number of these beams together such that they intersect in the center of the IEC device, resulting in extremely high ion densities there. Klein had this concept in mind when he designed the Multiple Ambipolar Recirculating Beam Line Experiment (MARBLE). That design stresses the intersecting beam principle and will be described next.

Fig. 9.11 A conceptual drawing of the counter-streaming linear IEC generator [18]

Table 9.1 A set of target parameters for the counter-streaming linear IEC device [18]

Column length (m)	Column radius (m)	Deuterium beam energy (keV)	Deuterium density	Magnetic field (Tesla)	Neutron yield
3	0.005	30	$10^{19}/m^3$	0.4	2.6×10^{11} n/s

9.7 Multiple Ambipolar Recirculating Beam Line Experiment (MARBLE)

The MARBLE proposed by Alexander Klein [19] was inspired by Daniel Zajfman's work on a Linear Electrostatic Ion Trap (LEIT) at the Weizmann Institute [20]. Klein points out that the LEIT community is interested in LEIT for ion storage, basic research, and for commercial gas composition detectors. Such ion storage requires very low pressure to achieve very long confinement times (now $>$ 5 min). The IEC community wants ions for fusion applications and needs high density along with good confinement. We first review some of the basic physics and ion optics behind the MARBLE concept. This provides added insight into spherical IEC scale-up issues as well as a background for MARBLE physics.

9.7.1 Ion Confinement in MARBLE

The confinement of ions in the MARBLE design is based on an analogy with an optical resonator (see Fig. 9.12).

A laser optical cavity for photons works on essentially the same principle as electrostatic confinement of ions, but with three major differences: photons have no charge, hence space charge effects are not a consideration; photons bounce on real (mechanical) surfaces, but charged particles are reflected at iso-potential surfaces in space; and the stability of ion orbits is a function of ion energy, because the turning-potential and focusing action are different for different ion energies.

Klein identifies a key issue with the ion-injected IEC that space charge electrostatic confinement necessitates Debye lengths greater than the beam dimensions, yet near the ion turning points, space charge limits occur due to the low ion velocity there. Such operation then requires low ion densities, resulting in low fusion rates.

This space charge problem sets limitations on the increase in beam density for electrostatic traps in the "conventional" IEC. One way to overcome this problem is

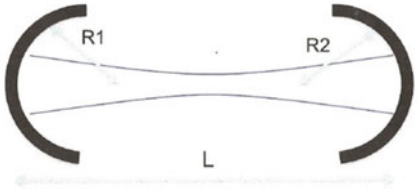

$$0 \le \left(1 - \frac{L}{R1}\right)\left(1 - \frac{L}{R2}\right) \le 1$$

Fig. 9.12 Stability criterion in a confocal cavity [19]

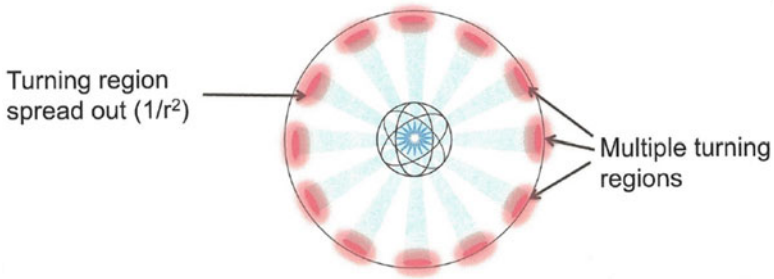

Fig. 9.13 Multiple turning regions and beam intersections are used in conventional IEC to increase beam density [19]

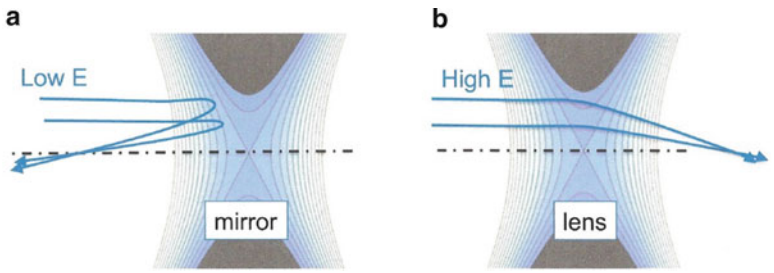

Fig. 9.14 (**a**) Accel–decel lensing and (**b**) alternating gradient (strong) focusing [19]

to increase the number of turning regions and simultaneously cross many beams in the core region, as shown in Fig. 9.13.

In contrast, Klein's MARBLE device addresses this issue using a design based on electrostatic optics. This builds on the recognition that the electrostatic field created by an electrode can serve either as a mirror or a lens, depending on particle beam energy. These two well-known methods for charged particle beam focusing are illustrated in Fig. 9.14.

These two concepts can be exploited to manipulate several distinct populations of charged particles in very different ways, using the same electrodes. To do that, simple conical electrodes are arranged with monotonically increasing potentials. This forms a series of mirror lenses which confine multiple beams on the same axis.

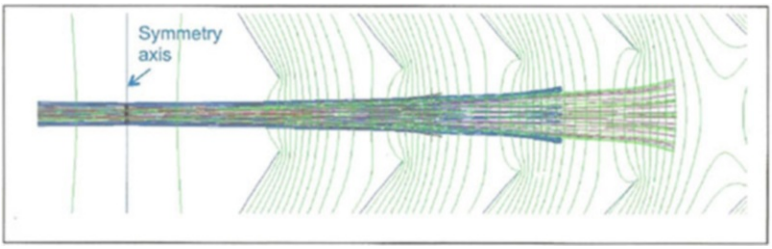

Fig. 9.15 Simulation of five cone-shaped, equi-spaced electrodes (angle 45 °, bias 100–500 V in 100 V increments). Four stably trapped beams with four turning surfaces are shown [19]

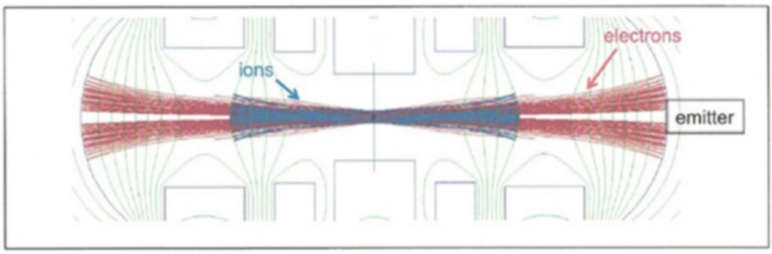

Fig. 9.16 Simulation of simple cylinders forming electrode configuration containing trapped ion and electron beams. Energy of both ion and electron beams in the core is 40 keV. Vertical lines are equi-spaced equipotentials [19]

Beam trajectories in this type of configuration based on a numerical simulation are illustrated in Fig. 9.15.

This configuration can be used for particle trapping or for simple "one-way" beam generation. Note that each beam is essentially independent of the others, with turning regions separated. For MARBLE, Klein proposed an extension of this concept that uses multiple conical electrodes, with monotonically increasing potentials. In that arrangement, a series of mirror lenses are formed that confine multiple beams on the same axis [19]. This arrangement has several advantages, namely, that if trapping, the small angle scattered ions (majority) may easily be deflected onto the next lower stage, so most of the ion energy is recovered, and that the beam is not monoenergetic. It can be pulsed to yield temporal compression (simultaneous exit of all particles). Then the trapped beams can be arranged so that all have the same period.

Accel–decel focusing to trap ions also works for electrons. Thus a configuration can be found which contains both energetic ions and electrons on the same axis and in stable orbits. Such a configuration is illustrated in Fig. 9.16. The electron emitters can produce large currents with a very narrow temperature spread. These electrons mitigate effects of ion space charge on beams, allowing the desired high ion currents needed for practical IEC power units.

In summary, the design in Fig. 9.16 went from a one-dimensional (LEIT) to a two-dimensional IEC fusor and then to a three-dimensional type of ion trap, increasing density limits by several orders of magnitude. Scattered ions are

collected at low energy on electrodes not too different from ion birth potential. To access very high-density regime, IEC devices must include electrons to neutralize ion space charge and drive virtual electrodes. In the multiple well hypothesis described in Chap. 2, virtual cathodes are formed due to the spherical geometry. In contrast, MARBLE is linear but drives virtual cathodes at chosen locations, with depths controlled by electron emitter voltages as shown in Fig. 9.16.

However, some important issues remain. Electrons tend to scatter and thermalize much faster than ions – thus intuitively, multiple ambipolar beams represent a very delicate state. Also, two polarities of high voltage are required, making voltage breakdown an important design issue. A source, e.g., ionization or injection of ions into the trap, is needed.

The "fix" for these issues used in MARBLE involves adding an axial magnetic field. This field confines electrons axially. At the same time, electrode voltages are simplified. The electrons may come from outside of trap, and the top of the potential hill with an axial B-field represents a Penning trap. This in turn provides excellent confinement of cool electrons.

These considerations led to the final design of the MARBLE device. However, several additional issues deserve mention:

- Adjustment of the negative electrodes – the ground potential can create virtual cathodes between ion birth regions. Virtual cathodes can be fed via a single external grounded emitter, while electrons are constrained radially by the B-field.
- At potential peaks, electrons ionize low-density background gas. Ions born outside of trapping regions are immediately lost. Those ions born within trapping phase space feed the recirculating ion beams.
- An external emitter can be used merely to "jump-start" ionization, as each ionization event creates a well-confined electron used in further ionizations.

Klein points out that the magnetic field in MARBLE requires only modest B-fields (~ 200 G) to be effective. One option for creating the axial fields is to use opposing fields on each side of symmetry axis-cusped field (giving $B = 0$ at the core). A cusped field allows crossing of many linear stages, e.g., a multipole. Other details of note from initial experiments are that lower E-fields allow use of lower B-fields to achieve "good" electron density throughout, only weak B-fields are required toward the core, and that it may be possible to use simple coils exterior to the vacuum system.

The resulting 5-beam experimental device shown in Fig. 9.17, termed MARBLE-1, was designed with the goal to achieve simple component shapes, robust trapping, and versatility. MARBLE-1 became operational in March 2011, but unfortunately the project was shutdown 2 months later when funding was stopped [19]. The preliminary results obtained within the short experimental period were that the Penning trapping was very effective. Ionization is spontaneous, given sufficient B-field, potentials on electrodes, and neutrals (gas). If the B-field is increased, a plasma is created which destroys ion trapping optics. Keeping $B < 200$ Gauss limits this effect. An "electron beam" mode is obtained by biasing the emitter and Faraday cup at both

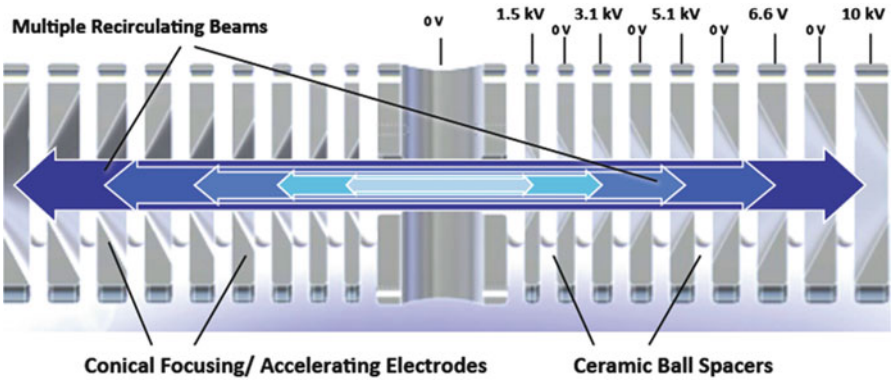

Fig. 9.17 The prototype MARBLE-1 [19]

ends negative. Then electrons bounce between ends (all other potentials ≥ 0). Under certain conditions, an electron emitter is not even required to get into this mode. With the solenoids forming a cusp, nearly all of the primary electron current (from the grounded external emitter) to innermost positive electrode occurs when this electrode is biased > 50 V. A high frequency instability is observed when the B-field is low (~ 100 G). The frequency appears to be proportional to B, and the potential represents a diocotron mode. The beam dump signal, a primary diagnostic, can change from strongly negative to strongly positive. Secondary electrons produced in the dump present a challenge to the signal interpretation.

These preliminary experimental results are encouraging for a design of this type. However, some basic MARBLE questions remain for study. Energy bands are separated by forbidden energies, reminiscent of quantum-mechanical systems. In view of this, it is not clear how much of the total phase space is available for trapping. Nor is it clear how the trapping fraction can be maximized. Likewise, ways to maximize the energy width of each stable energy band need study, and a related question is discovering what energy ratio can be achieved between beams. Smaller ratios are desirable to allow more beams. Another geometric concern is how close the electrodes should be packed. Closer packing gives a smaller device but also requires higher potential gradients, posing voltage breakdown problems.

As in all high ion beam density IEC-type devices, possible instabilities are important subjects to note. For example, MARBLE is candidate for electrostatic two-stream and magnetostatic Weibel instabilities. The 10-keV energy difference between beams in theory is stable up to ~ 3 A/beam (deuterium). Multiple beams at multiple energies have higher threshold for unstable density when the energy difference between beams is higher. The counter-streaming linear ion beam concept by Momota and Miley [18] discussed in the previous section involved some detailed stability analyses. Extrapolation of these to MARBLE suggests it is stable up to three magnitudes of higher densities due to the magnetic field used. In fact, Klein states that MARBLE has many similarities to the counter-beam linear device of Momota and Miley.

9.7.2 Potential Applications for MARBLE

It is not clear yet whether the MARBLE approach can be developed for a high-performance neutron generator or even a fusion power reactor. Still, as with all IEC devices, it offers a number of potential applications while operated in an electronically driven mode (e.g., see Chap. 12). However, there are other features of MARBLE that offer some unique uses. These features include an inventory of energetic particles to be rapidly switched out, producing very short pulses of these particles, and one-half of the geometry could be omitted entirely to produce a single-pass, high-current, and high-power particle beam consisting of multiple energies. With the MARBLE approach ("beams within beams"), beams could be produced from a small area footprint, with powers and currents perhaps substantially exceeding what can be done today.

In view of these attributes, Klein suggests specialized applications for MARBLE such as energy analyzers, ion propulsion engines, proton therapy machines, and ion implanters.

9.8 Shaban's Magnetic-Assisted IEC

Yasser Shaban has proposed the use of magnetic fields to assist gridded IEC operation with external ion injection [21]. However, few details have been published about this concept, so we will only briefly discuss it here. Shaban notes that the "conventional" IEC concept achieves confinement (or focusing) of the ions at the center due to an electrostatic potential well. The fusion reaction rate largely depends on the size of this core. However, the ratio of the volume of the dense core to the total volume of IEC is very small. In the magnetically assisted concept, the added B-field enables fusion reactions over much of the volume of the IEC instead of just in the core. This is achieved if the deuterium and helium-3 ions interact circularly in the opposite directions in the ion cyclotron orbits. This requires they have different kinetic energies and different ion cyclotron frequencies in order to increase the rate of intersection. To accomplish that, as shown in Fig. 9.18, two different primary ion beams are injected from two external ion sources with the IEC in a sub-breakdown IEC mode. The magnetic field is perpendicular to the IEC grid and its field line intensities cover part of the grid. Thus the ion beam (M^+ for ^3He and m^+ for D) trajectories lie inside the transparent grid.

Once the ions enter the magnetic field zone, they will bend with a curvature counterclockwise and perpendicular to the magnetic B-field, as shown in Fig. 9.19.

The orbital radii of these ions depend on the velocity and the mass of each particle as well as the intensity of the magnetic field. As shown, the larger orbital radius is for the heavier mass helium-3 and the smaller orbital radius is for the deuterium, such conditions being controlled by the ion source injection "gun" used for each. Secondary ions are created by interaction of the injected ions with

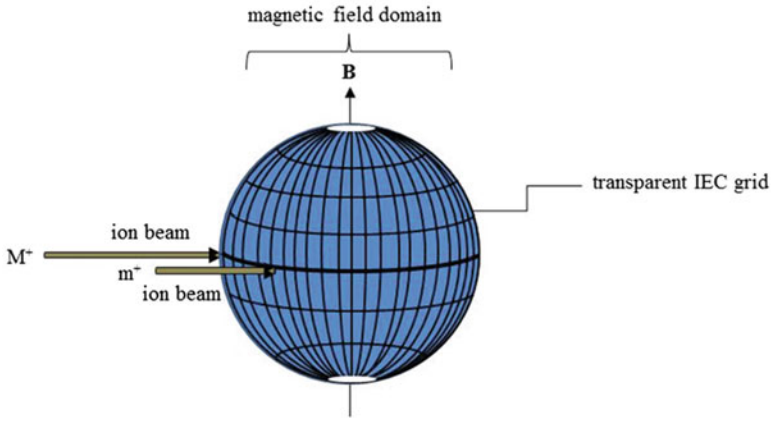

Fig. 9.18 Orientation of the magnetic field B and the ion beams with respect to the transparent IEC grid [21]

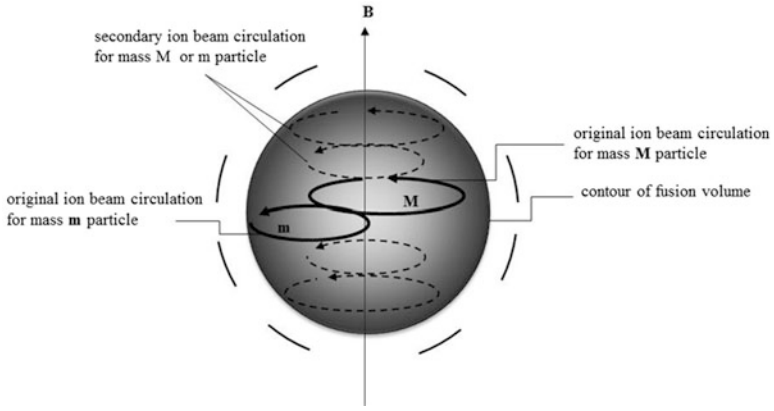

Fig. 9.19 Ions cyclotrons (positive ions) of masses m and M of different kinetic energies are circling in different orbital sizes counterclockwise inside IEC grid. These are secondary ion beams initially generated in a sub-breakdown due to external ion sources [21]

background neutrals in the sub-breakdown regime. They too undergo cyclotron motion inside the grid. Fusion reactions occur when kinetic energy of ^{3}He is greater than the kinetic energy of deuterium particle. Secondary ions also contribute.

The secondary ions move into circular orbits of various sizes depending on their birth location. The ions that are closer to the grid wires have maximum kinetic energy; consequently the ions with minimum kinetic energy are at the center of the device, out of the grid domain. The circles eventually intersect causing a (head-on) fusion reaction.

This concept has been implemented in the experimental arrangement shown in Fig. 9.20 [22]. The design shown was developed for fusion proton production of

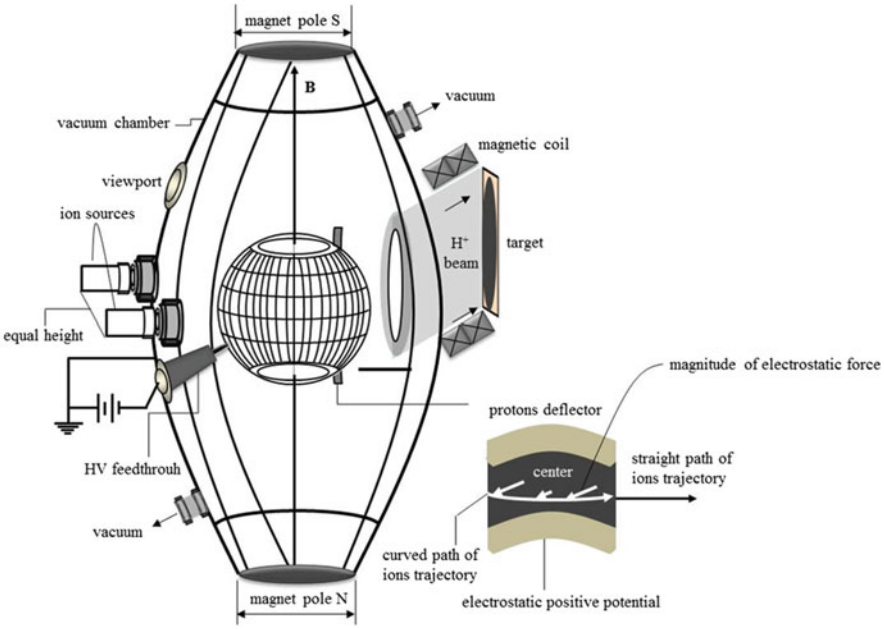

Fig. 9.20 A layout of the experiment with major components for the magnetic-assisted IEC fusion approach. The transparent grid at the center is biased with a negative potential. The wall of the chamber is connected to ground [22]

medical isotopes [23]. A jet-shaped chamber is connected to a vacuum system to ensure uniform pressure during operation. The experiments are carried out below the breakdown regime, and below the Paschen curve, for the given geometry (at about 1 mTorr). The IEC transparent grid is connected to a negative high voltage dc power supply. As shown in Fig. 9.20, permanent magnets enclose a major portion of the transparent grid such that the magnetic field lines do not affect the edges of the grid. The proton deflector, collimator, and target are shown in Fig. 9.20 in a side view with details shown in the insert. Most protons produced are given an angular momentum by the magnetic field, but some manage to escape through the transparent grid. Because the kinetic energies of the fusion product protons are much higher than the fusing ions, their angular momentum is also greater than the reactants. The curvature of their trajectories is counterclockwise and can be intercepted with the special concave deflector shown in Fig. 9.20. The deflector is connected to the wall of the chamber (positive) to intersect a sector of proton orbits. Because of the grid shape, the protons will be bent more strongly at the edges than at the center. A straight proton beam is directed outside the IEC chamber with the assistance of electromagnetic coils. The "target" from production of the desired radioisotopes is located at the end of this deflection channel.

Shaban also describes an alternate version that uses internal magnetic coils (lamellas) instead of wires for the grid of the electrode, as shown in Fig. 9.21.

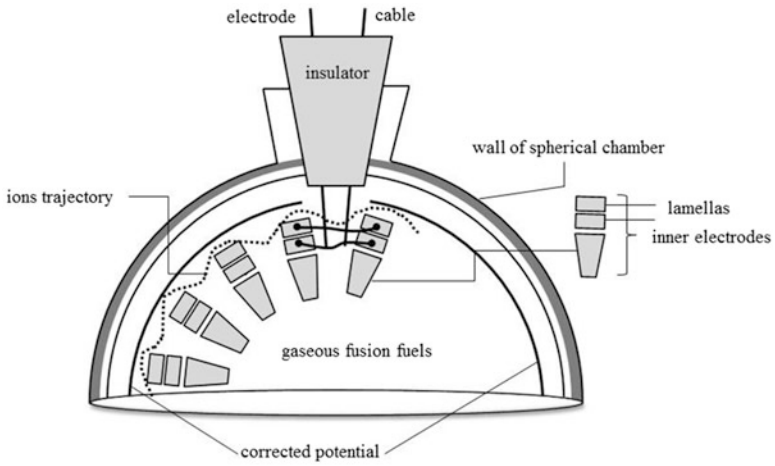

Fig. 9.21 A layout of a spherical IEC chamber with internal magnetic field created by lamellas [24]

He states that a significant increase of the reaction gain has been confirmed in experiments using this arrangement. A reevaluation of the design showed that a modification of the lamellas giving sections of separated parts of the lamellas with variable voltages will change the local variation in the equal-potential areas, giving a further increase of the efficiency. This field produces a dark discharge such that positive nuclei of helium-3 and deuterium are accelerated to the electrode. The monoenergetic ions move ballistically within the field-free electrode through the spherical center and on to the opposite side where they slow down and accelerated back in the reverse direction. This back-and-forth motion continues a number of times until the ions hit an electrode and their charge is conducted away as a loss current. As their motion passes through the center, the ions undergo fusion reactions. While experiments with this device are described, no quantitative results have yet been disclosed.

9.9 Summary

The primary focus of this chapter has been on nonspherical ("alternate") IEC geometries: cylindrical, jet, dipole, counter-streaming linear, and MARBLE-type IECs. This IEC technology is just now emerging, so its success in commercialization has yet to be established. More about such applications is discussed in Chap. 12.

The motivation for such geometries has largely been to provide specialized designs for specific applications, such as broad area neutron activation analysis, space thrusters, medical isotope production. Several alternate geometries, e.g.,

MARBLE as well as the HEPS and POPs discussed in previous chapters, also address some of the issues that need resolution if IEC power reactors are to be developed.

References

1. Bromley B, Chacon L, Miley G (1998) Approximate modeling of cylindrical inertial electrostatic confinement (IEC) fusion neutron generator. In: Proceedings of the 16th international conference on numerical simulation of plasmas, UCLA Department of Physics, Los Angeles/Santa Barbara, 10–12 Feb, pp 191–192
2. Miley G, Bauer T, Nadler J, Hora H (2000) Converging beam neutron source for driving a sub-critical fission reactor. In: Proceedings, ICONE 8, CD/Track 8, 8500, Baltimore, 2–6 Apr, pp 1–8
3. Stubbers RA, Kim HJ, Miley GH (2002) Two-dimensional modeling of a radically-convergent cylindrical inertial electrostatic confinement (IEC) fusion device. In: 5th US/Japan workshop, IEC fusion, Madison, 9–10 Oct
4. Miley GH, Stubbers RA, Momota H (2003) Advances in cylindrical IEC neutron source design for driven sub-critical operation. In: Proceedings of ICONE 11: 11th international conference on nuclear engineering, nuclear energy-dawn of a New Era, Tokyo, 20–23 Apr
5. Miley GH, Javedani J, Nebel R, Nadler J, Gu Y, Satsangi A, Heck P (1994) An inertial electrostatic confinement neutron/proton source. In: Third international conference on Dense Z pinches, AIP conference proceedings, vol 299, pp 675–689
6. Dolan TJ, Verdeyen JT, Meeker DJ, Cherrington BE (1972) Electrostatic-inertial plasma confinement. J Appl Phys 43(4):1590–1600
7. "NSD-GRADEL-FUSION" www.nsd-fusion.com. Accessed 6 Sept 2013
8. Egle BJ (2006) Comparison of spherical and cylindrical geometries in inertial electrostatic confinement devices. In: ANS 17th TOFE, 15 Nov
9. Bussard RW (1990) Fusion as electric propulsion. J Propuls 6(5):567–574
10. Gu Y, Nadler JH, Satsangi AJ, Javedani JB, Miley GH, Nebel RA, Barnes DC (1994) Physics and effects of grid-electric field perturbation on spherical electrostatic-inertial confinement fusion. In: 21st EPS conference on controlled fusion and plasma physics, Montpellier, vol 436
11. Miley GH, Momota H, Shrestha PJ, Thomas R, Takeyama Y (2006) Space propulsion based on dipole assisted IEC system. In: AIP conference proceedings, Albuquerque, STAIF, vol 813, pp 1240–1248
12. Hasegawa A, Chen L, Mauel ME (1990) A D–^{3}He fusion reactor based on a dipole magnetic field. Nucl Fusion 30:2405
13. Miley GH, Momota H, Thomas R, Takeyama Y (2005) Dipole assisted inertial electrostatic confinement. In: 7th US–Japan workshop on inertial electrostatic confinement fusion, Los Alamos, 14–16 Mar
14. Khachan J, Collis S (2001) Measurements of ion energy distributions by Doppler shift spectroscopy in an inertial electrostatic confinement device. Phys Plasmas 8(4):1299–1304
15. Shrier O, Khachan J, Bosi S, Fitzgerald M, Evans N (2006) Diverging ion motion in an inertial electrostatic confinement discharge. Phys Plasmas 13(1), Art No. 012703
16. Khachan J, Samarian A (2007) Dust diagnostics on an inertial electrostatic confinement discharge. Phys Lett A 363(4):297–301
17. Blackhall L, Khachan J (2007) A simple electric thruster based on ion charge exchange. J Phys 40(8):2491–2494
18. Momota H, Miley GH (2009) Neutron source based on a counter-deuterium beam linear IEC. J Fusion Energy 28:191–194

19. Klein A (2011) The multiple Ambipolar recirculating beam line experiment. In: 13th US–Japan IEC workshop, Sydney
20. Zajfman D, Heber O, Vejby-Christensen L, Ben-Itzhak I, Rappaport M, Fishman R, Dahan M (1997) Electrostatic bottle for long-time storage of fast ion beams. Phys Rev A 55(3):1577–1580
21. Shaban YR et al (2002) High perveance steady state deuterium ion beam extracted from floating plasma stream. Blt APS 47(9):25
22. Shaban YR et al. Methods, apparatus, and systems involving ion beam generation, US Patent 7,271,400, filed on 6 Aug 2004, and referenced on 18 Sept 2007
23. Shaban YR (2011) Radioisotope productions by inertial electrostatic confinement fusion unit for medical and industrial applications. Hochschule Deggendorf University, Bavaria, 11 Sept
24. Höpfl R, Hora H, Prelas MA, Shaban YR. German patent application 102011119997.0, 03 Dec 2011

Chapter 10
Various Other IEC Concepts and Experiments

10.1 Introduction

A number of IEC concepts have been proposed over the years. Here we have chosen a few experiments that have received attention and supplement discussions in Chaps. 1, 2, and 9. We begin with the early Hirsch gun injected IEC experiment, briefly mentioned in Chap. 1. This device is important both historically and from a physics perspective. Recent studies at the University of Wisconsin, Madison, using gun injectors designed to reproduce Hirsh's results are then described. This is followed by discussions of variations of "Star" mode experiments, including pulsed operation and getter pumping. Several experiments using alternate ion or plasma formation, including an internal magnetron discharge and Helicon plasma generation, are reviewed. Other experiments using electron injection, including the Penning trap and POPS concepts studied at Los Alamos National Laboratory (LANL), are briefly discussed.

10.2 Hirsch Ion Gun Injected Experiment

As noted in Chap. 1, Robert Hirsh [1] disclosed experimental results with very high D–T neutron rates from an ion-injected IEC shown in Fig. 10.1.

Note that six ion "guns" were used to create a low-energy ion beam that entered the chamber and was trapped via electrostatic fields to form the potential well structure desired for IEC operation. However, differential pumping was not used, so beam–background and charge exchange (CX) collisions must have still played a significant role in this experiment. Still, Hirsch obtained "record" neutron rates for D–T fusion, as shown in Fig. 10.2.

The key point about this remarkable result is that the neutron production rates are well above those predicted by simple beam–background fusion reactions, implying that a benefit was obtained from recirculation beam–beam reactions in a

G.H. Miley and S.K. Murali, *Inertial Electrostatic Confinement (IEC) Fusion: Fundamentals and Applications*, DOI 10.1007/978-1-4614-9338-9_10,

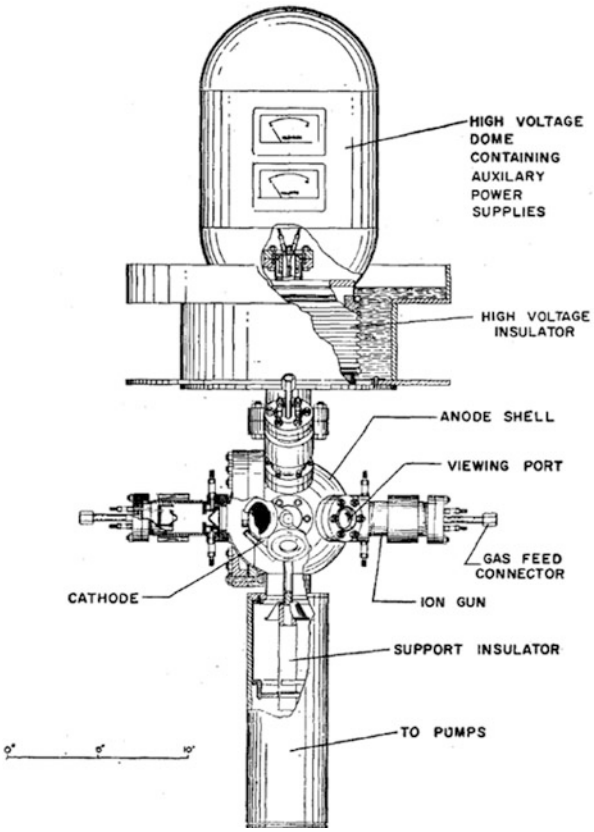

Fig. 10.1 Hirsh and Farnsworth's "historic" early IEC ion injection experiment [1]

potential well (but without multiple structures). Indeed, to further confirm the existence of a potential well, Hirsch did both collimated neutron and gamma measurements. Hirsch found a special structure for both that was consistent with double potential well formation (also discussed in Chaps. 1 and 2) [1]. However, without use of differential pumping, the chamber pressure seemed too high for this. One possible explanation is that the ion–electron densities obtained were high enough to "burn out" (completely ionize) the background neutrals in the potential well. There is no direct evidence to support this view, however.

These important results have never been fully explained. Attempts to reproduce his experiments were done by Gardner and colleagues at Brigham Young University [2] who borrowed the original device used by Hirsch. However, despite many months of effort, the neutron production they obtained was significantly lower than that reported by Hirsch. They attributed this problem to a failure to regain the gun alignment necessary to have a highly converged plasma "core" in the center of the device. A major hurdle to this appears to have been that no provision was made to allow precision alignment of the gun ions entering the device (though the

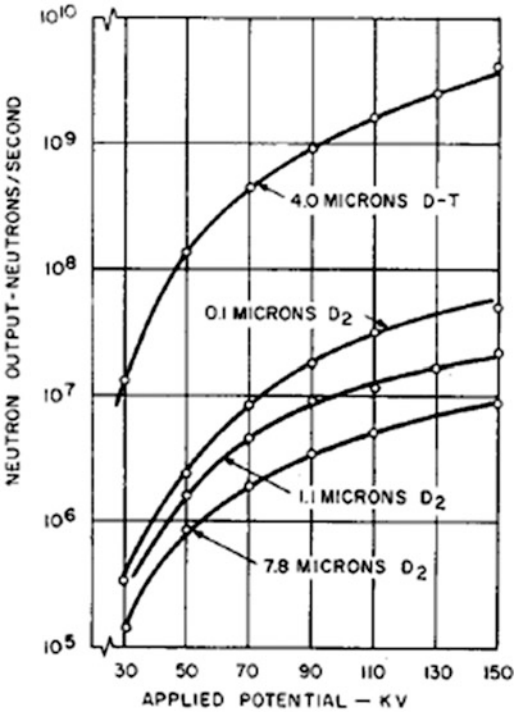

Fig. 10.2 Neutron production rates (NPRs) measured with the IEC of Fig. 10.1 exceeded 10^9 D–T n/s at 150 kV. For perspective, note that as discussed later, IEC gridded devices at the University of Illinois routinely produce 10^8 D–D n/s at ~ 80 kV. This NPR is slightly above Hirsch's result, but the device used higher ion currents [1]

investigators did not mention this explicitly). Later when Miley reinitiated gun experiments, his first gun design followed many of the design elements used by Hirsch but incorporated electrostatic beam steering [3]. This worked well, but the design was eventually discarded to move to RF guns with much higher beam currents [4]. In addition, the gun design uses a magnetic nozzle for reducing the exiting beam diameter and to allow strong differential pumping (not used in the prior Hirsch experiments).

It should be stressed again that the terms "injection" and "gun" are misleading. The objective is to simply "flow" low-energy ions into the device such that they are then accelerated to fusion energies by either the grid or the virtual electrode structure. Still, a loss of "excess" energy after injection is needed to trap the ion (i.e., prevent it from simply passing through the potential well and hitting the opposite wall). A biased reflector on the opposite wall can be introduced to help prevent this loss, but that only works well if the entering ions have little excess energy. To further understand this problem, the reader is advised to study the design of the Hirsch chamber, which uses an auxiliary biased grid ("reflector") near the wall. Indeed the issue of how to best introduce ions into the potential well so that their energy falls below that required to escape the well is key for proper design of the IEC. Later we will discuss designs to cause an initial ion energy loss to "drop" them into the potential well, as well as designs with ion source "imbedded" in the well such that ions are born trapped.

10.3 SIGFE Six-Gun Experiment at University of Wisconsin

To study the Hirsch-type gun experiment in more detail, G. L. Kulcinski's group at the University of Wisconsin constructed a six-gun IEC that is very similar to the one originally used by Hirsch [5]. This unit permitted a study to replicate and further explain Hirsch's results. Michalak and colleagues who constructed this experiment named it the Six Ion Gun Fusion Experiment (SIGFE). It is shown in Fig. 10.3, and a schematic of the opposing guns employed is shown in Fig. 10.4. These guns employ filament-driven plasma production along with a series of ion extraction lenses. Differentiated pumping provides a very low chamber pressure of ~10 mPa, enabling operation in a variety of modes as shown in Fig. 10.5. While many features of the Hirsch experiment were duplicated with SIGFE, the efficiency (neutrons per input power) Hirsch reported has not been matched to date. A major factor governing this is that D–D fuel has been used instead of the D–T used by Hirsch. The peak cross section alone is over 200 times larger. The present IEC devices would be able to exceed the fusion rates originally reported by Hirsch once the fuel is changed to D–T. However, operating with D–T fuel is expensive and requires special licenses and upgrades to the facilities.

If the guns are under-focused, the neutron yield for SIGFE decreases with pressure, a characteristic also observed by Hirsch. In contrast, IECs with an internal gas discharge ion source (such as the University of Wisconsin's gridded device) observe an increase in neutron rate with pressure due to the increase in source ions through collisional ionization in the neutral background gas.

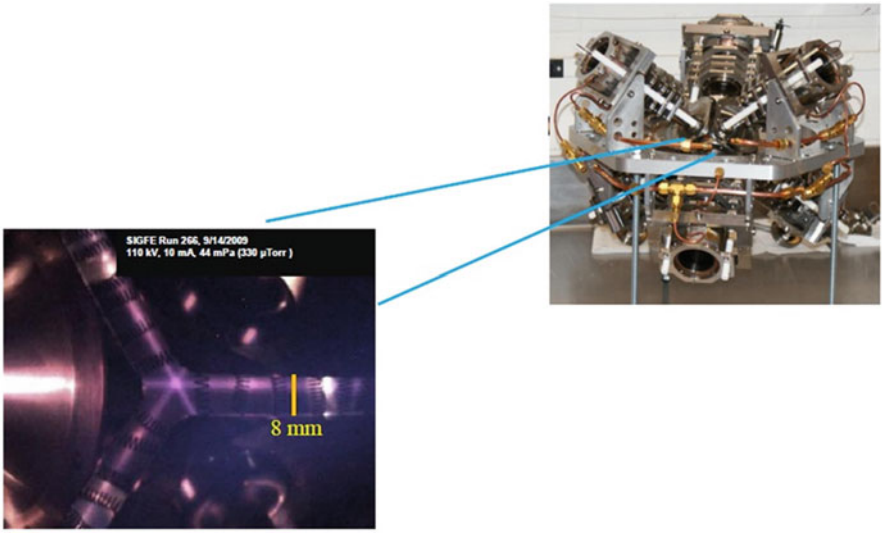

Fig. 10.3 The Six Ion Gun Fusion Experiment (SIGFE) device [5]

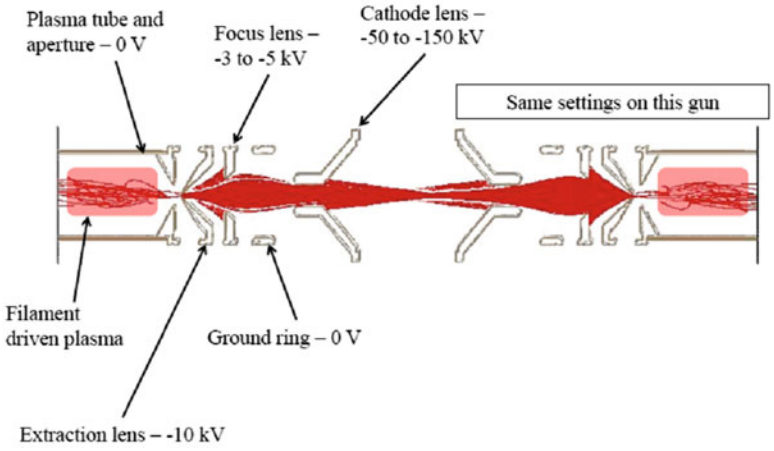

Fig. 10.4 Schematic of two opposing guns as arranged in the SIGFE device [5]

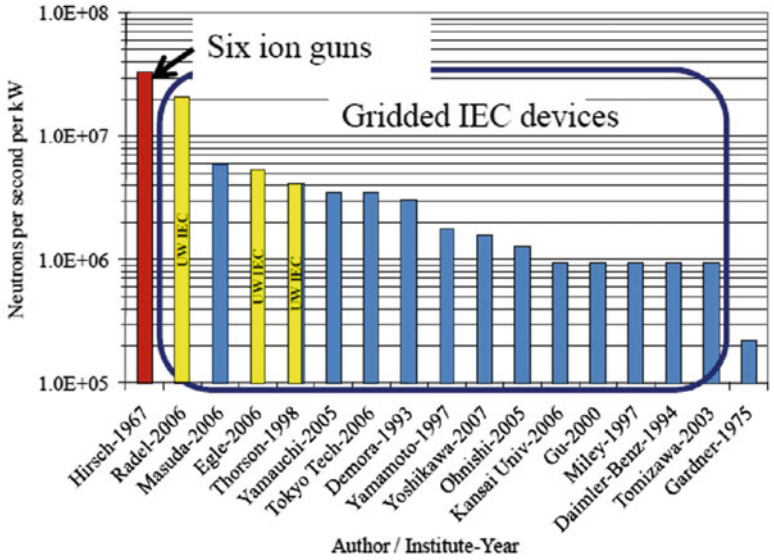

Fig. 10.5 Comparison of the SIGFE with the original Hirsch device [5]. SIGFE replicated some of the mechanical and electric features of Hirsch's experiment. However, the original Hirsch device remains the most efficient IEC for neutron production per kW input power

Hirsch's original experiment was known to be extremely sensitive to beam focus, and his setup made alignment adjustments difficult [5]. Thus the replication of his results using his unit at BYU failed to keep proper alignment. The defocused gun runs of SIGFE indicate that the dominant neutron source could

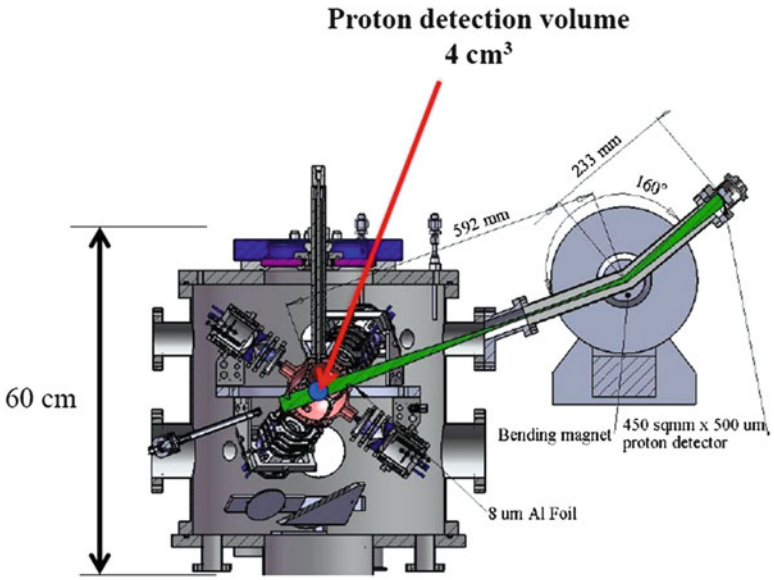

Fig. 10.6 The SIGFE with a bending magnet to reduce x-ray noise while studying the protons from D–D reaction at the cathode center [5]

be from beam reactions with surface-embedded deuterium. To study this, the setup shown in Fig. 10.6 was employed. A strong bending magnet diverted protons from the D–D reaction ~ 100 ° to a solid-state detector, greatly reducing x-ray noise. However, a comparison of the proton production rates with neutron production rates (these two rates should be equal due to 50/50 branching ratio for D–D) confirmed that most reactions were not occurring in the center volume that the proton detector probed.

Thus, despite similarities, these results are not fully consistent with Hirsch's 1967 study. His shielded collimation measurements of neutrons and γ-rays indicated fusion was occurring in the main plasma volume, presumably due to a formation of a "Poissor"-type potential well. Whether SIGFE can duplicate that finding remains an important open question. Subsequent work on SIGFE has demonstrated that its reaction rate performance can be improved by a factor of 2–3 with improved lens alignment plus better electron confinement in the cathode [5]. During that work, it was found that the beams from the guns are not yet fully matched. This is attributed to differences in the filaments and hence the plasmas produced in the guns. Work is underway to better balance these. In any case, SIGFE is a very important experiment for learning about the mechanics and physics of multiple gun ion source IEC operation for improved neutron production efficiency and as a step toward a power reactor.

10.4 “Star” Mode with Vane-Type Grids and with Pulsed Operation

The majority of IEC experiments done in the various laboratories involved have used an internal discharge to create the source ion. In 1997 Miley and his group published an IEEE paper that summarized their internal ion-injected grid experiments [6]. As noted earlier, “ion injected” has been used to define the species forming a potential well. It is not to be confused with external “gun” injection where ions form the potential well but are introduced from an external source. This paper discussed the discharge physics and plasma characteristics for various modes of operation, and it explained how the “Star” mode is created by the defocusing properties that concave inward (toward the center core) in open grid structures. Indeed the concept is somewhat anti-intuitive because one might hope for focusing “optics,” but this is not possible in these configurations. Indeed various multigrid approaches have been studied with the objective of improving beam optics for reflection of ions, hence recirculation (e.g., see reference [7]). When ions pass through the concave potential, all but those in the exact center of the curved surface are deflected and lost. The centered ions pass through to the opposite side and go through the grid opening and then are reflected and repeat this trajectory. Subsequently ionization events along this path cause a rapid increase in the recirculating current through the center of the grid openings. This then produces the beautiful “Star” mode discharge shown in Fig. 10.7.

Fig. 10.7 Photograph of a “Star” mode discharge. The “vane”-type grid shown is only one of a number of large opening grids designed and used for Star mode operation of the IEC. This particular design (but with variations) has been used by University of Illinois, Daimler-Chrysler, and Kyoto University in IECs intended for neutron production. It is rugged, shows little sputtering, and has proven very efficient for neutron production. Materials used vary from stainless steel to molybdenum

10.5 Pulsed Operation

The use of a pulsed power supply represents an important way to study the physics of high-current IECs without employing expensive, large power supplies. Pulsing also avoids the need for strong cooling to remove the waste heat. The key physics point is that the beam–beam fusion rate scales as the ion current squared. Most steady-state experiments employ 100s of mA, and peak values of many amps are possible while pulsing. By selecting the pulse width to match or exceed the ion confinement time, typically an order of ms in present devices, a quasi equilibrium is established during the pulse. This allows study of "equivalent" steady-state physics during the pulse. Miley's early pulsed IEC studies [8] used a Marx bank technology to provide peak currents of 10s of amps with ~0.1 sec width but with a low repetition rate (selected to minimize cooling requirements and also reduce bank recharging requirements).

The pulser circuit was designed to provide pulse currents up to 500 mA with a width of 10s of ms (providing a quasi-steady-state operation during the pulse). The pulse is initiated during low-level steady-state operation of the IEC; this is essential for maintaining an approximately constant discharge voltage during the pulse and for preventing arcing when the pulse is applied. This biasing scheme allows the cathode voltage to be set to a desired level to establish and maintain the desired steady-state glow discharge. The resistor R_{Shunt} allows a small (5–20 mA) steady-state current to flow into the cathode at all times to maintain the initial low-power glow discharge.

The device is then pulsed. The breakdown voltage at the device operation pressure is a few kV higher than the steady-state discharge voltage, which follows the traditional Paschen curve.

The capacitive discharge system of the circuit results in a current pulse with a typical RC exponential decay. The peak current occurs immediately upon triggering and then decays toward the steady-state value with a time constant set by the pulse capacitor and the total load impedance.

The ideal load for this type of pulse driver is one with a very low impedance. Though the IEC approaches this ideal load during glow discharge operation, the effective impedance increases during the pulse due to trapping of charge carriers in the potential structure. This limits the pulse current unless the shunt resistor is adjusted to match the current and effective impedance. However, this requires changing the resistor as the current is varied.

The pulse switch is a vital part of the design (see reference [8] for further details). It employed a thyratron designed to conduct high currents. Because pulse voltage and current decay exponentially during the pulse, they are integrated by a digital scope and averaged to a full width of 10 % maximum to obtain average values of the voltage and current in each pulse. Thus the values reported were the average values obtained in this manner.

One very encouraging result of these experiments was the stability of the discharge against arcing during pulses. Visual observation indicated that the entire

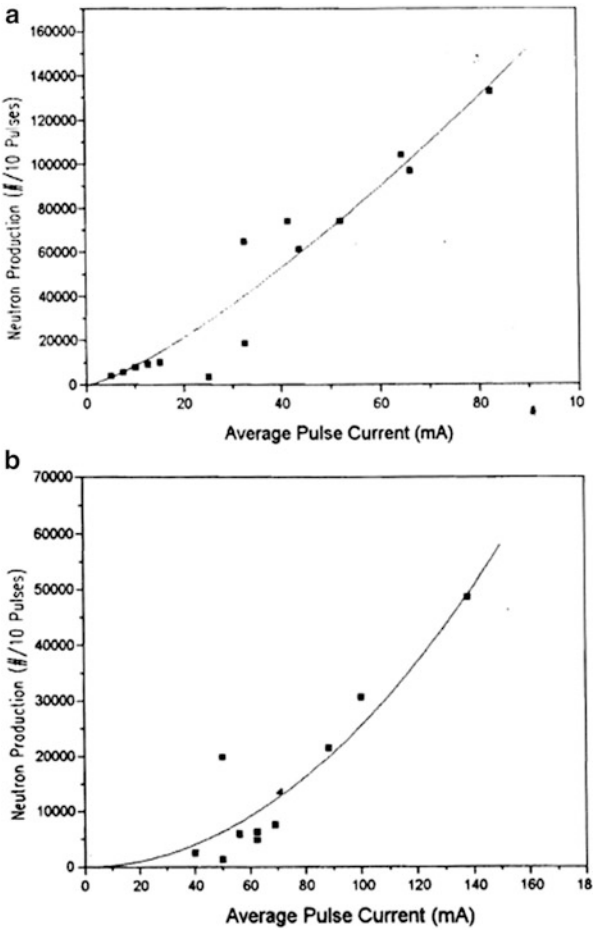

Fig. 10.8 (**a**) Neutron production versus average pulse current at $V_{cat} = 15$ kV shows $n = 1.3$ scaling. (**b**) Neutron yield versus pulse current at $V_{cat} = 10$ kV shows $n = 2.0$ scaling [8]

chamber volume becomes brighter during a pulse and then quickly relaxes back to the typical steady-state glow with a "Star" mode pattern [9]. Results from neutron yield scaling studies are described next.

While the current injection (< 150 mA) achieved with the RC pulse driver was modest, the neutron data obtained confirmed the theoretical I^2 scaling at higher currents. The neutron production results were analyzed along with the corresponding average pulse currents to produce Fig. 10.8 for runs at 15 and 10 kV, respectively. The uncertainty in the data points results mainly from variations in the pulsed voltage width and height over the duration of the ten pulses that the neutron yields are averaged over. The pulsed operation results show a neutron yield versus current, I, with a scaling of I^n where $n = 1.3$–2.0. Lower values of n occurred at higher voltages. This is expected because the slower moving ions at 10 kV have a longer residual time in the crucial central core region.

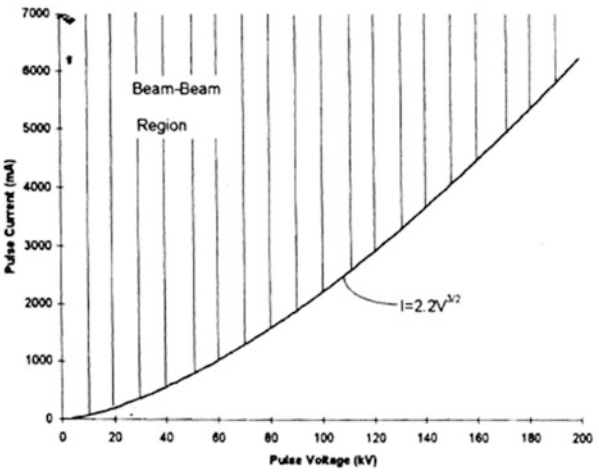

Fig. 10.9 The lined area shows the region where a double well structure forms for various values of V_{cat} in the IEC device [8]

In order to examine the effects of perveance on potential well structure, a correlation between neutron yield and pulse perveance ($I/V^{3/2}$) was considered. Perveance is selected as an appropriate parameter for this condition, because it provides a measure of space charge effects that in turn determine the potential structure in the core region. The neutron yields were plotted against the corresponding values of pulse perveance:

$$\frac{I(mA)}{V(kV)^{\frac{3}{2}}}.$$

The neutron production scaling exponent (n for I^n) falls into the range between 1.3 and 2.0 for all values of perveance below 2.2. Above a perveance value of 2.2, the vast majority of data points indicate I^2 neutron scaling, suggesting beam–beam reactions dominate. Therefore, the perveance value of ~ 2.2 $mA/kV^{3/2}$ represents a transition value between these two cases, indicating that a double well structure ($n \geq 2$) requires a perveance of at least 2.2 $mA/kV^{3/2}$ to form. More data for a variety of parameters (grid design, diameters, etc.) are needed to confirm the general applicability of this result. However, this threshold value provides a good first estimate for the present IEC device.

The preliminary perveance threshold condition (see Fig. 10.9) can be used to predict the current injection needed to achieve a beam–beam scaling in future IEC devices. Because the neutron yield increases rapidly with voltage, operation around 100 kV is desired for high yield. Then, according to Fig. 10.9, a pulsed current of ~ 2–3 A is required to achieve a double well, i.e., I^2 scaling. Such operation is a goal of future experiments, but a larger pulse driver will be necessary, along with a modification of the internal grid structure to prevent arcing at the higher voltages. Combining the I^2 scaling data with present steady-state operation, a peak neutron yield of ~10^{11} n/s is predicted during the pulse. With a 10 % duty factor, this would

give a 10^{10} D–D n/s source. (Use of D–T could provide a 10^{12} n/s source, the increased rate being due simply to respective cross-section ratio.)

Based on these results, it appears that the IEC used in these experiments could be operated with a 3-A, 100-kV pulse driver to produce neutron yields about four orders of magnitude greater than 10^6 n/s for steady-state operation. This assumes that a repetitive pulse rate with a 10 % duty factor is used.

10.6 Getter Pumping of an IEC Device

Another important technology regarding the IEC vessel pumping was developed in the mid-1990s by staff from Miley's group working at the Idaho National Environmental and Engineering Laboratory (INEEL) with Robert A. Anderl [10]. This work substituted a metallic hydride getter for the external pumping on the IEC chamber. With this arrangement, the deuterium is absorbed in the getter material while the vapor pressure, hence the chamber background pressure, is controlled by regulation of the getter temperature. With proper selection of the size and type of getter material, plus a good temperature feedback control, this arrangement was found to work exceedingly well. This allows a "sealed" IEC unit and removes the bulky pumps. Such an arrangement is essential for small mobile neutron sources. Daimler-Chrysler licensed the use of this IEC neutron technology through the UIUC and used this approach for their NAA quality control units at ore mines in Germany.

The general strategy employed by Daimler-Chrysler and others is to send sealed units into the field for NAA application. The impurity buildup in the chamber gas eventually causes the performance to deteriorate. At that point, the unit is returned to the originating "factory" or originating laboratory for refueling by pumping down and, if necessary, replacing the getter. As it occurred, Daimler-Chrysler uses such units in Germany for NAA inspection of ore composition on some of their ore delivery belts. In this role the IEC directly replaced ^{252}Cf neutron sources, allowing on–off operation, simpler licensing, and lower costs. The Daimler-Chrysler plan to distribute commercial units externally for sale did not materialize, due to company financial problems in the automobile industry at that time. However, this technology was bought and improved by John Sved and is now being marketed successfully [11].

10.7 Compact IEC Neutron Source for Landmine Detection at Kyoto University

An example of a compact IEC neutron source is the work on a landmine detection system at Kyoto University, Japan [12]. These investigators used a device which was designed for mounting on a crane (as shown in Fig. 10.10).

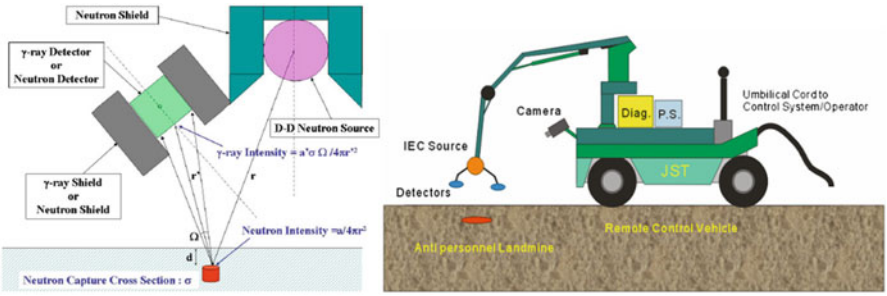

Fig. 10.10 IEC landmine detection project at Kyoto University [12]

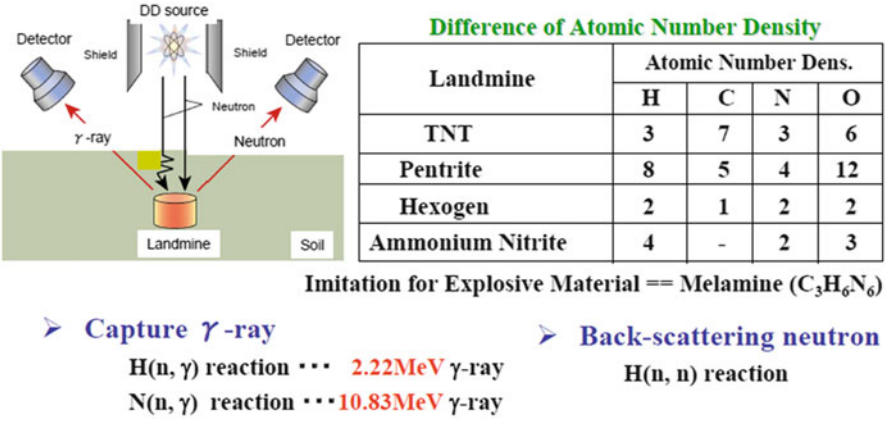

Fig. 10.11 Scheme for landmine detection using a magnetron source-type IEC neutron source [12]

The basic principle of this detection method, shown in Fig. 10.11, is common to many NAA applications, but now specialized for detecting the basic elements in the landmines. Key design considerations for NAA operation are the source strength required, the neutron energy desired (i.e., D–D versus D–T fusion), and the type and location of the neutron and x-ray detectors (if any) employed in the operation [12].

The IEC developed for this work used a magnetron ion generation technique to improve the neutron production efficiency [12]. A built-in magnetron discharge ion source such as the RS-MIS discussed in Chap. 1 was installed in the IEC (a schematic of an RS-MIS device was shown in Fig. 1.10). With the magnetron discharge, ions are produced in the vicinity of the vacuum chamber (anode) at negative electric potential. Therefore, the ions produced are expected to have nearly full energy corresponding to the applied voltage to the IEC cathode but slightly smaller energy than the anode potential. This prevents them from hitting the anode of the opposite side improving both fusion reaction rate and ion recirculation life. (Note that this approach is yet another way to address the problem of preventing

ions created externally from escaping after entering the potential well. Here the ions are produced at a potential level less than the height of the potential well.)

As pointed out in Chap. 1, in addition to an internal source, the magnetron can produce ample ion current to maintain the discharge under low-pressure conditions. Ions generated in the ion source are attracted by the IEC central cathode because of its high negative electric potential. Therefore, the Kyoto investigators expected that a higher applied voltage would increase the extraction current, giving a higher IEC cathode current. However, it was found that there is an optimum voltage in terms of a maximum IEC cathode current. Ions supplied by the magnetron ion source are essential to maintain the hybrid (glow and magnetron) discharge under low gas pressure conditions. The reason for this voltage limit is not clear. Unfortunately this effect limits the cathode voltage despite the need for high voltage for neutron production near the peak energy of the fusion cross section. Several methods to overcome this problem were planned. Still, the lower neutron yield was adequate for the initial demonstration of mine detection experiments. Unfortunately, the project was terminated prematurely due to financial constraints, so information on the possibility for higher neutron yield designs remains incomplete.

10.8 Helicon-Injected IEC for ^{3}He Experiments at University of Wisconsin

The design of the ion source also depends on the ion species being injected. Sources described thus far have focused on deuterium or, in some cases, on tritium. However, workers at the University of Wisconsin have had a great interest in studying ^{3}He reactions (both D–^{3}He and ^{3}He–^{3}He) for medical isotope production, so have developed a gun specialized to ^{3}He ion production [13]. To maximize the ion current, a Helicon source was selected because Helicons are well known for production of very high-density plasmas from which high ion currents can be extracted. This source is illustrated in Fig. 10.12 [14]. They state that this source has produced steady-state ion currents of 10 mA into IEC systems with background gas pressures as low as 200 μTorr. Though Helicon sources are known to produce high-density plasmas, it is still incumbent upon the scientists to prove that doubly ionized ^{3}He^{++} species are indeed produced in copious amounts from such ion sources. If the helium ions provided are singly ionized, ^{3}He–^{3}He reactions will not be favored, making observation of such reactions difficult and any such claims questionable.

Piefer originally constructed the Helicon in 2002 to provide helium ions for a converged core operation of an IEC using D–^{3}He [15]. One of the main purposes of that unit was to study proton-induced reactions for production of medical isotopes. More recently, Piefer and colleagues used this source to study the nuclear physics of the ^{3}He(^{3}He,2p)^{4}He reaction [16]. This reaction is of interest to nuclear physicists because it is poorly characterized at energies less than 200 keV. A long proposed resonance in the ^{3}He(^{3}He,2p)^{4}He fusion cross section could help explain a discrepancy between theoretical predictions and measurements of neutrino emations from

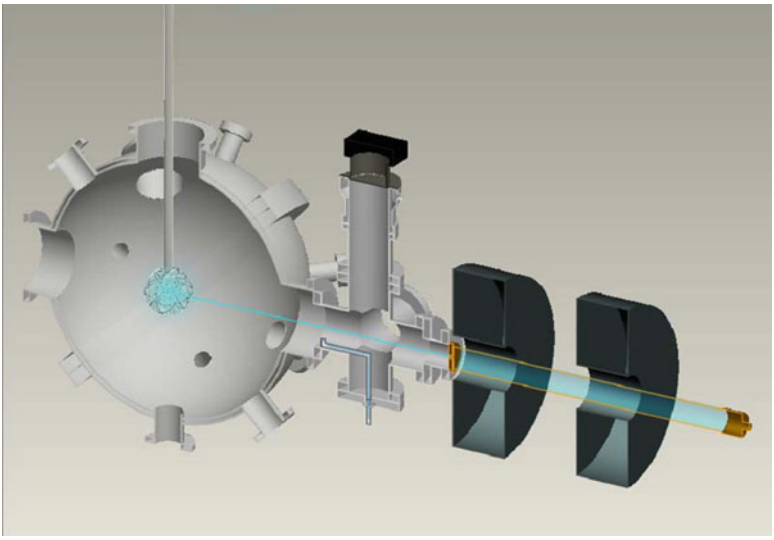

Fig. 10.12 ^{3}He ion source for use in ^{3}He–^{3}He fusion rate studies at the University of Wisconsin [13]

the sun. Use of the Helicon-injected IEC provides a way to achieve high-energy ion currents though recirculation of energies up to a few hundred keV. This allows measurements at lower energies compared to accelerator-target-type studies where the ion currents are much lower, limiting the reaction rate to the point where background noise hampers measurements. While using the Helicon for a helium ion source is very important for these applications, it in general provides an excellent external ion source which could play a role in achieving very low-pressure IEC systems that provide beam–beam fusion reactions necessary to move toward a power unit. Thus it is instructive to review the Wisconsin Helicon source.

10.8.1 University of Wisconsin Helicon Source

Helicon plasma sources have been widely used in recent years because the Helicon efficiently produces a low-temperature plasma which is nearly fully ionized. Helicon sources work by launching Helicon waves along an axial magnetic field. Helicon sources have been shown to produce ~ 10^{13} ions/cm^3 in helium [17]. The general layout for the Wisconsin Helicon uses steady-state magnetic fields up to 2 kG and steady-state RF power up to 1.4 kW. The objective of this setup is to extract an appropriate ion beam while using differential pumping to remove excess neutral gas that might enter the main IEC chamber. A schematic of the ion extraction system is shown in Fig. 10.13. An extraction/acceleration grid is used, and ions are extracted and accelerated to several keV, after which they are slowed

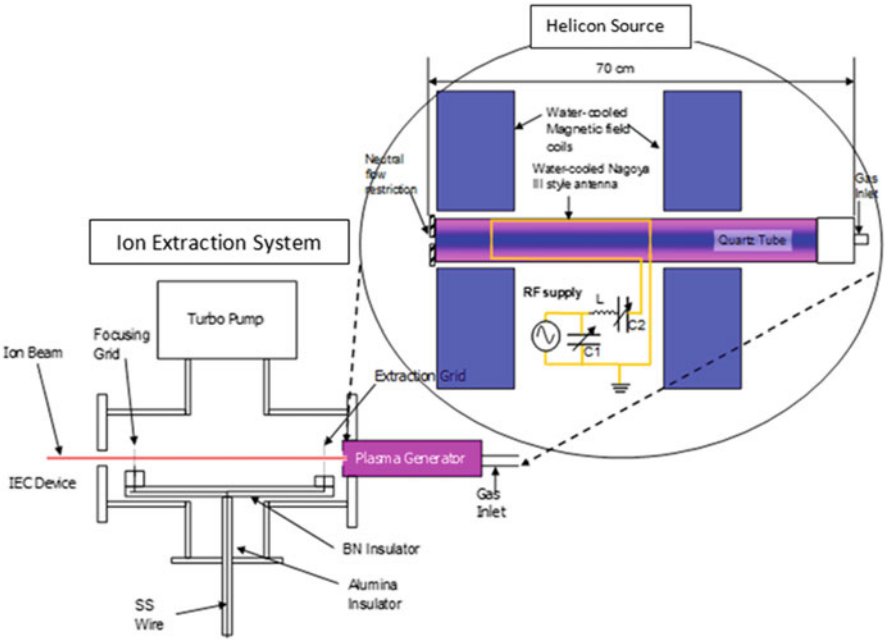

Fig. 10.13 Helicon source and the ion extractor system [18]

down as they approach the IEC wall. An axial magnetic field is used for beam confinement. Orifice plates with a small opening pass the beam but minimize neutral gas flow, which is pumped out from the extraction system by a turbo pump.

Figure 10.14 shows the ion source connected to the spherical IEC. This system has employed several different gases, including helium and argon. Figure 10.15 shows the helium beam as it is extracted and flows into the spherical IEC cathode grid operating at 35 keV, 2 mA.

In later studies for ^{3}He–^{3}He reactions, the Helicon provided high currents (~ 75 mA) at low pressures (30 mPa = 0.2 mTorr) in an IEC device [17]. However, further confirmation through observation of doubly ionized ^{3}He species from the Helicon source is awaited to confirm the true observation of ^{3}He–^{3}He reactions.

10.9 The University of Illinois Helicon-IEC Thruster, HIIPER

The Helicon-Injected Inertial Plasma Electrostatic Rocket (HIIPER) is a two-stage electric propulsion system that uses a Helicon plasma source for plasma production and an inertial electrostatic confinement (IEC) stage for plasma acceleration [19]. The Helicon stage uses low-frequency whistler waves to produce a plasma

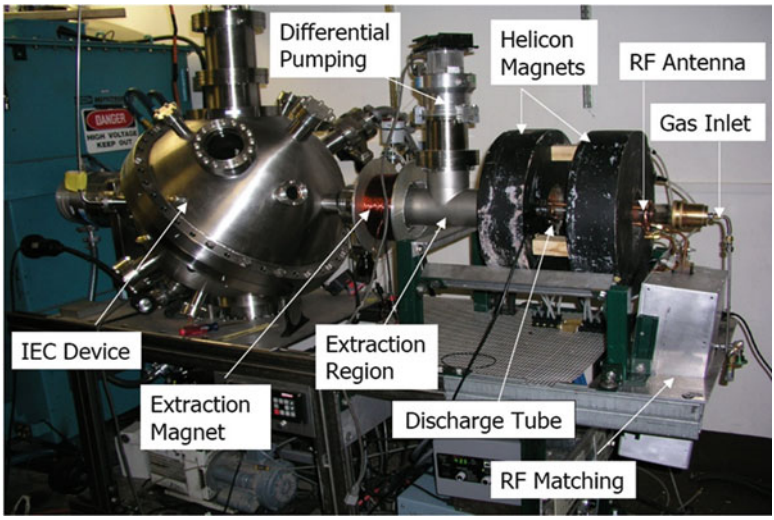

Fig. 10.14 Ion source mated to the University of Wisconsin, Madison, IEC [18]

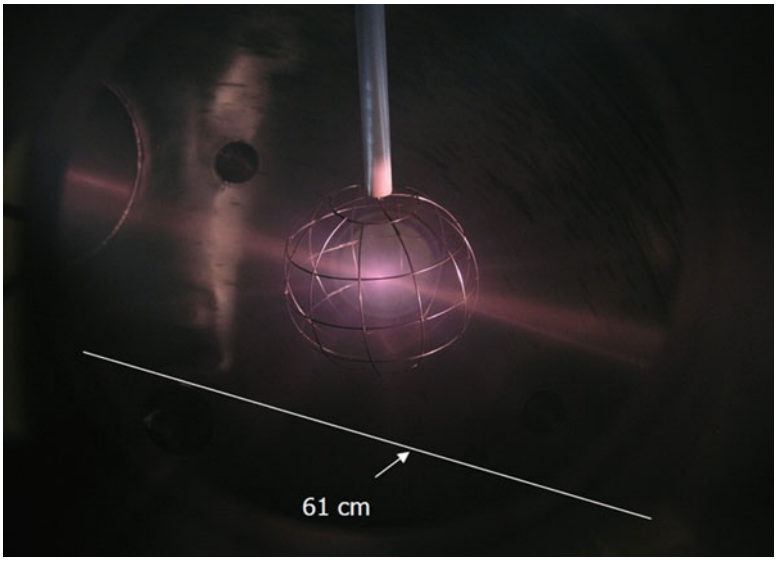

Fig. 10.15 Helium beam discharge into the University of Wisconsin, Madison, IEC (35 kV, 2 mA) [18]

discharge [20]. This plasma flows into the IEC stage that accelerates the ions to multi-keV energies in a spherical potential well. An axisymmetric opening in the IEC cathode grid causes a high-intensity jet less than 1 cm diameter that is ejected out of an enlarged grid opening producing thrust.

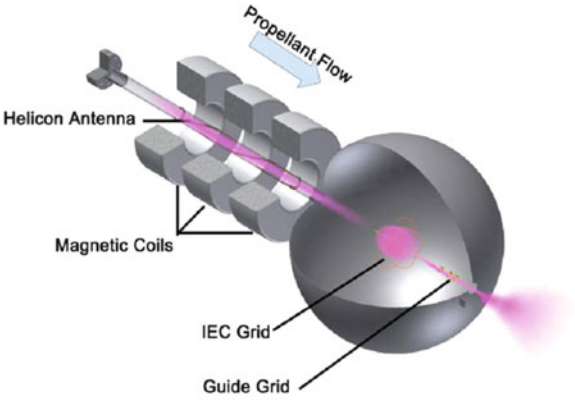

Fig. 10.16 Schematic of the HIIPER concept [21]

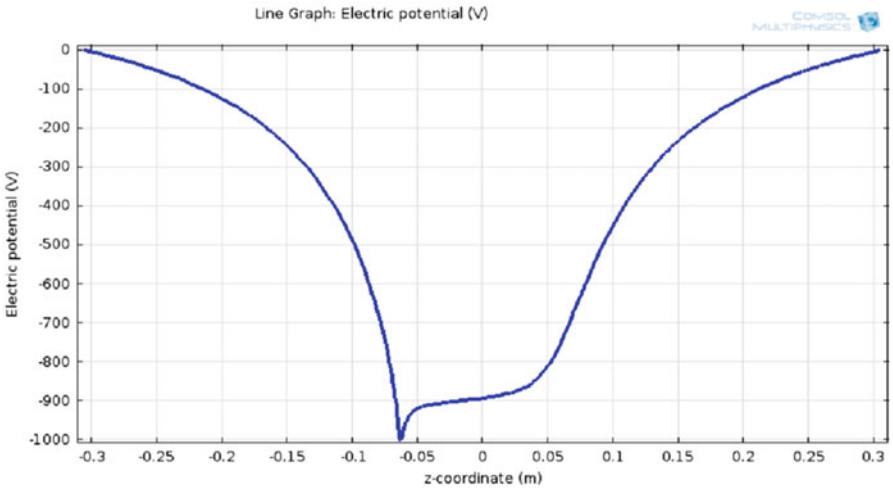

Fig. 10.17 The spherically asymmetric potential well with the x-axis representing the radial direction [21]

Figure 10.16 shows a schematic of the HIIPER concept [21]. The propellant (argon gas) flows through the quartz tube with a helical antenna and magnetic coils, where it is ionized. The plasma diffuses into the grounded IEC chamber (anode) that has an asymmetric stainless steel spherical grid (cathode). The cathode grid is biased with a high negative DC voltage on the order of −2,000 to −8,000 V with respect to the outer spherical chamber or grid. This forms a spherical potential well as shown in Fig. 10.17. The ions pass through the transparent grid, cross the center, and travel out of the other side of the grid, where they are once again attracted to the negatively biased inner grid and eventually fall back to the inner grid, and so forth. This essentially confines the ions into a dense core (shown in Fig. 10.18). A larger opening in the cathode grid is created to induce symmetry into the potential

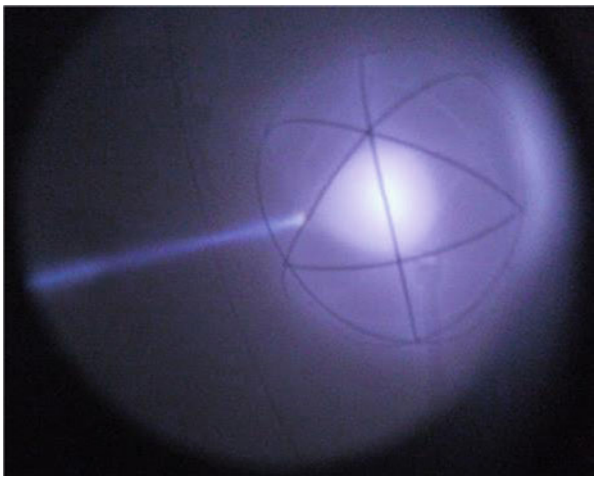

Fig. 10.18 High-intensity plasma jet exiting the asymmetry in the IEC acceleration stage [21]

structure, which creates a region of slightly higher potential (shown in Fig. 10.17), so that a thin plasma jet flows out from the larger grid opening. This jet is clearly visible in Fig. 10.18.

Characterization of the plasma jet is currently underway using experimental and computational tools, and proof-of-concept of this aforesaid thruster is currently being established [22]. A precision force sensor is used to measure the thrust, a Faraday cup for current and thermal power measurements, and a gridded energy analyzer to understand the energy spectrum and measure the ion and electron densities (see Chap. 11 for further discussion of these diagnostics). The design of the central IEC spherical grid with varying transparencies and sizes is under study to better understand the relation of key parameters like breaking potential, ion and electron densities, and velocities with varying size and transparency of the grids. Furthermore, an electrostatic nozzle (the guide grid is shown in Fig. 10.16) is currently under construction to aid better extraction of ions into the plasma jet.

10.9.1 Numerical Simulations for HIIPER

A COMSOL computer simulation was created to model the potential drop inside the dielectric cylinder attached to the IEC. The dielectric cylinder is a simplified representation of the Helicon plasma source, which is a dielectric tube concentric with annular electromagnets and a driving antenna. The simulation that contained no plasma (i.e., a first approximation) assumes the angle of the dielectric cylinder is parallel to the IEC plasma jet, but on the opposing side of the IEC.

This simulation showed that most of the voltage drop occurs between the IEC grid and the IEC chamber, with an approximately 20 V drop occurring within the dielectric tube representing the Helicon. Figure 10.19 shows the voltage as a function of position in the dielectric tube.

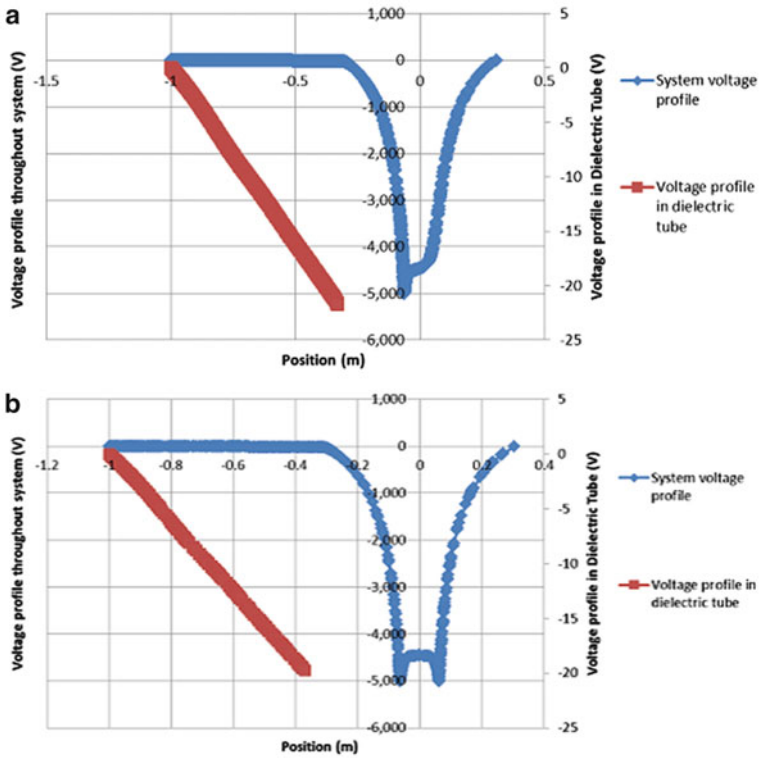

Fig. 10.19 (**a**) Voltage profile of the entire system along with a rescaled voltage profile of the dielectric tube parallel to the IEC plasma jet. (**b**) Voltage profile of the entire system along with a rescaled voltage profile of the dielectric tube perpendicular to the IEC plasma jet [19]

10.10 Electron-Injected IEC Concepts

Electron injection IEC concepts can provide an important approach to high-level neutron production and to future reactor operation. One of the best known, the Polywell, was discussed in Chaps. 1 and 2. Another important electron injection-type IEC proposed by Barnes and Nebel in 1998 is the Periodically Oscillating Plasma Sphere (POPS). Early on it was realized that a gridded system had many disadvantages – though promising for practical neutron source applications, the existing gridded IEC devices operate at modest fusion yields, with a low gain (output fusion energy/input electric energy $Q << 1$). In addition to ion losses to the grids, ion–ion Coulomb collisions can cause a rapid relaxation of the desired

beam-like ion distribution to a Maxwellian distribution. These collisions add angular momentum to the particles and result in defocusing of the potential well. Consequently, either the energy expense of maintaining the beam-like ion distribution exceeds the fusion energy gain or the fusion power density is reduced as the ion focus spreads [23, 24]. Solutions for these issues have been proposed with some degree of success. Gridless IEC devices such as a Penning trap [25] or a Polywell configuration [26] can form an effective potential well by combining electrostatic and magnetic fields without a physical grid. (See Chaps. 2 and 13 for detailed explanations and methods for handling such issues.)

The POPS concept was intended to circumvent these issues [27], and the occurrence of POPS resonance was also confirmed experimentally [28]. As noted earlier in Chap. 1, this concept uses electron injection into a spherical device to produce a virtual cathode with a harmonic oscillator potential. In spherical geometry, the harmonic oscillator potential is produced by a radially constant electron density. This concept requires uniform electron injection into the central region of a spherical device to produce harmonic oscillator potential. An ion cloud in such an environment will undergo harmonic oscillation with an oscillation frequency independent of amplitude. Tuning the external radio frequency (rf) electric fields to this naturally occurring mode allows the ion motions to be phaselocked. This simultaneously produces very high densities and temperatures during the collapse phase of the oscillation when all the ions converge into the center. Solutions to POPS oscillation have the remarkable property that they maintain equilibrium distribution of the ions at all time. This would eliminate any power loss due to Coulomb collisions and would greatly increase the neutron yield, making IEC devices attractive for potential applications.

10.10.1 Experimental Observation of POPS Oscillations

The POPS oscillation has been experimentally measured, confirming the scientific basis for a POPS-based fusion device [28]. The harmonic potential well is created by electron injection. Ions in the potential well undergo harmonic oscillation. By applying rf fluctuation to the grid voltage, researchers were able to phaselock the POPS oscillation and to measure the resonance behavior of the ions. Mathematically, ion dynamics during the driven POPS oscillation are equivalent to the driven harmonic oscillator as described by the Mathieu equations. The ions can gain a large amount of energy from a small external perturbation when the driving frequency is equal to the resonance frequency. The ion orbits become unstable, and ion loss from the potential well is enhanced. In an experimental setting, the enhanced ion loss compensates the background ionization and extends the lifetime of the potential well. On the other hand, rf fluctuation outside the POPS resonance frequency has little impact to the ion loss. This resonance behavior of ion dynamics is shown in Fig. 10.20, where the temporal variation of the plasma response is measured for various rf frequencies. Without the rf fluctuation, the lifetime of the potential well is very short, ~ 0.5 ms, due to significant background ionization. By applying small rf

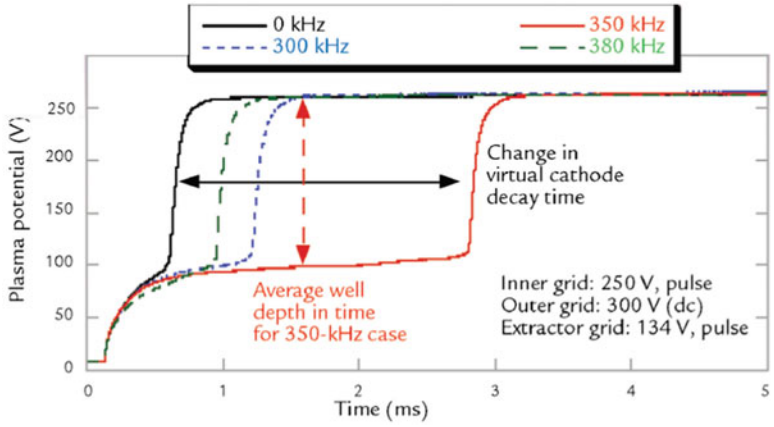

Fig. 10.20 Temporal evolution of plasma potential at the center. The potential well lifetime is extended by applying rf fluctuation to the inner-grid bias voltage at POPS frequency [28]

fluctuation (~ 4 V amplitude compared to a direct-current bias voltage of 250 V) at POPS frequency, the lifetime increases greatly to ~ 2.5 ms. In comparison, rf fluctuation outside the resonance frequency changes the lifetime only slightly.

The frequency at which the POPS oscillation is found scales as

$$f_{POPS} = \left(\sqrt{\frac{2}{\pi}}\right)\left(\frac{V_{well}}{r^2{}_{well} \times M_{ion}}\right)^{\frac{1}{2}}. \tag{10.1}$$

In using a harmonic oscillator analogy, the ion mass provides the inertia, whereas the curvature of the potential well is equal to the coefficient of the restoring force. Because this was the first time that the POPS oscillation had been experimentally observed, extensive efforts were made to verify the POPS frequency scaling as a function of the well depth and the ion mass. As shown in Fig. 10.21, excellent agreement was obtained between the experiments and the theory, confirming that the observed resonance is the ion mode associated with the POPS oscillation. The potential well depth was controlled by varying the dc component of the inner-grid bias, whereas the well radius is fixed by the inner-grid dimension. Note that the well radius was estimated as $r_{well} = r_{grid} + \lambda_{\text{Debye}}$, where λ_{Debye} is the effective Debye length to account for the Debye shielding. The fill gas was also varied, using three different ion species, $H_2{}^+$, He^+, and Ne^+, to investigate the POPS frequency scaling.

10.10.2 Particle Simulation of POPS Plasma Compression

One of the most significant issues facing a fusion device based on POPS is the plasma compression, which determines the achievable fusion rates. In the case of D–D fuel, a radial plasma compression of about 25 is sufficient for active nuclear

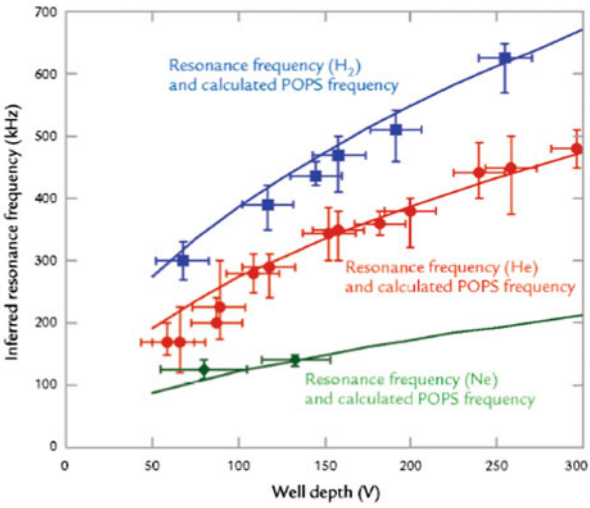

Fig. 10.21 Comparison between the experimentally measured resonance frequencies due to POPS oscillation (*points*) and the theoretical calculations (*lines*) as a function of potential well depth and ion mass [28]

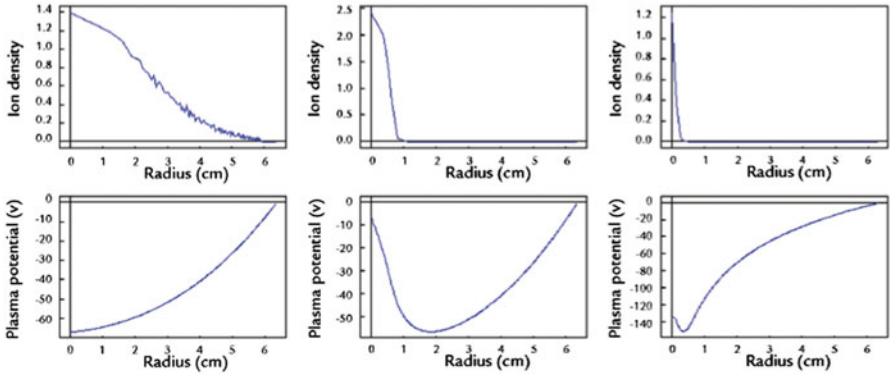

Fig. 10.22 Radial profile of ion density and plasma potential during POPS oscillation from the one-dimensional particle code. The profiles on the left (*top and bottom*) come from the expansion phase, whereas the profiles in the center (*top and bottom*) and on the right (*top and bottom*) come from the collapsed phase [29]

assay applications, whereas neutron tomography would require a compression of 100. In comparison, a practical fusion power plant would require a compression of 2,000 for D–D fuel but less than 100 for D–T fuel. One factor that greatly affects the compression ratio is the extent of space charge neutralization. Inadequate space charge neutralization can cause self-repulsion of the ion cloud during the collapse phase, limiting the compression. To investigate this, a gridless particle code with one dimension in space and two dimensions in velocity space was developed to study the space charge neutralization during POPS compression [29].

Figure 10.22 shows the radial profiles of ion density and plasma potential during POPS compression. The results on the left are from the expansion phase of POPS

oscillation. The ion-density profile is Gaussian in space, and the plasma potential profile matches the required harmonic oscillator potential for ions, produced by constant electron injection. In the middle, the ion density and the plasma potential during the collapsed phase of POPS oscillation are shown. A large distortion of plasma potential is due to the insufficient space charge neutralization and ion self-repulsion during the POPS compression. This has limited the radial plasma compression to only 6.3. In comparison, the results on the right come from the case where the initial velocity distribution of injected electrons is modulated as a function of time to improve the space charge neutralization. This simple remedy helped to improve the space charge neutralization in the core during the collapse phase. A radial plasma compression of 19 is computed, resulting in the ion-density enhancement of ~ 10,000 in the core as compared to the expansion phase.

A major hurdle for the achievement of breakeven performance with the POPS concept has been identified to be the cathode grid transparency [27]. It has been shown that no fusion reactions would be observed until the grid transparency is at least 99 %. For the device to achieve breakeven performance, a grid transparency of 99.9 % or better is required. Though magnetically insulated grids were proposed to solve this problem [27], such a concept is plagued by the fact that the electrons would be thermalized in the magnetic fields and this would be counterproductive for the POPS compressions. Because none of the conventional grids could achieve this, Murali and colleagues proposed that the grids be built from carbon nanotubes (CNTs) that would allow the achievement of grid transparency well in excess of 99.99 % and hence open up new avenues for improved performance of the POPS concept [30]. CNT grids are discussed further in Chap. 5. The major advantage of the CNT grids is that these grids possess the best combination of properties desirable for the grid construction such as high thermal conductivity, low resistance, high mechanical strength, and excellent flexibility. However, experimental demonstration of their capability has not yet been done.

10.10.3 Penning Trap Concept

In parallel to the POPS concept, the Penning trap concept was proposed [31]. This device does not have a central cathode and hence was believed to be ideally suited to observe the POPS compressions. However, this device has been plagued by high-voltage breakdowns. Thus achievement of high voltages necessary for the achievement of fusion has remained a challenge. Here we briefly review this concept and the experimental progress made with it.

The Penning fusion experiment (PFX) has been investigated to look into the possibility of raising the confined densities (through spatial nonuniformity) to levels of interest for thermonuclear fusion applications while retaining the excellent confinement of thermal non-neutral plasmas (see Fig. 10.23). Penning traps have exhibited remarkable confinement of non-neutral plasmas, when compared to quasi-neutral, magnetic confinement laboratory plasma devices. However, due to

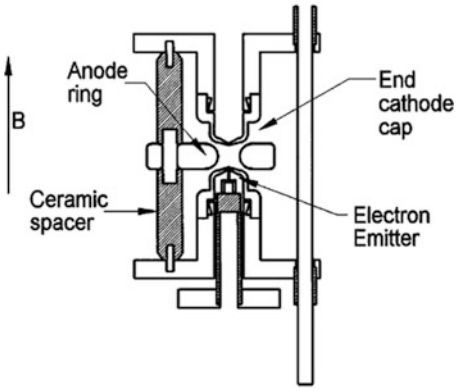

Fig. 10.23 The PFX hyperbolic trap. Three electrodes are suspended by three support rods and mechanically connected by ceramic spacers whose cathode ends are tailored to maximize voltage standoff. An emitter is placed near the injection hole in the lower cathode [31]

the charge non-neutrality of these plasmas, the uniform densities attainable in static traps are limited, the maximum value being the Brillouin limit given by [32]:

$$\bar{n} = \frac{B^2}{2\mu_0 mc^2}. \tag{10.2}$$

Here B is the magnetic field, μ_0 is the permeability of free space, m is the mass of confined particles, and c is the speed of light.

Barnes and colleagues suggested that the *local* density might exceed $\bar{n}$ in a strongly nonequilibrium plasma. This local concentration may occur either in space or time. The possibility of spatial concentration via spherical focusing was examined in reference [33]. The concept of spherical focusing of ions was studied by Hirsch in a system in which a grid provided ion confinement and acceleration [1]. Also explained in Chap. 1, Bussard introduced the concept of Spherically Convergent Ion Focus (SCIF) systems [26]. This work first introduced the important concept of using electrons confined by a combination of magnetic and electric fields to produce a large negative space charge field for the gridless acceleration and confinement of spherically convergent ions.

As shown in Fig. 10.23, in its simplest form, a Penning trap consists of three electrodes, the inner surfaces of which are hyperbolae of revolution [34]. Two end cathode caps and a central anode ring produce a rotationally symmetric electrostatic quadrupole field when a voltage V is applied to the anode. Charged particles are confined axially in the electrostatic well, while radial confinement is provided by a uniform magnetic field applied parallel to the trap axis. It has been established that the eccentricity of the resulting spheroidal well is tunable [31]. As the voltage V is increased at constant magnetic field B, the limiting equipotential of the trap changes from a prolate spheroid intersecting the end cathodes (preventing electrons from reaching the anode), to a sphere nearly intersecting both the cathodes and anode, to an oblate spheroid which intersects the end cathodes and a portion of the anode. A low-energy, zero canonical angular momentum electron in a spherical well will oscillate along the trap axis through the center of the well. Any scattering event

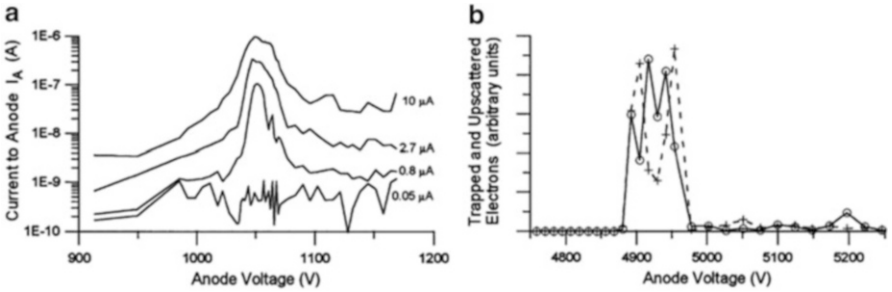

Fig. 10.24 Data showing coincident indication of an elastic scattering process occurring only near the spherical point. (**a**) Observed anode current versus anode voltage V near the spherical point for $B = 0.076$ T. As the injection current (*indicated*) is increased, a sharp resonance appears at $V = Vo$ and broadens slightly. (**b**) Observed upscattered (*solid curve*) and trapped/downscattered electrons (*dashed curve*) versus V near a second spherical point ($B = 0.164$ T). The double maxima of the dashed curve is an artifact caused by amplifier saturation [31]

which occurs at or near the center of the trap will deflect the electron away from the trap axis onto an orbit which will necessarily pass near the trap center again. In the absence of collective effects, a cloud of such electrons will result in a non-neutral plasma with an enhanced central density due to the spherical convergence of the single particle orbits. Such a density focus has been reported by Mitchell and colleagues [25].

A remarkable feature of the observations is the spontaneous appearance of a nearly spherically symmetric state. This occurs only when B and V are adjusted to produce a spherical well according to

$$V_0 = \frac{eB^2a^2}{8m_e}. \tag{10.3}$$

Here e and m_e are the electron charge and mass, and a the trap radius. Then if the ion current I_i exceeds a threshold value, a spherical state appears. Several indicators of this are shown in the experimental data of Fig. 10.24.

Spherical focusing has been observed over the range of PFX operation. Figure 10.24 shows a summary of the observation of three diagnostics over the range of B and V, compared to the theoretical relation of Eq. 10.3. As can be seen the agreement is excellent, with focusing indicated only for points within 1 % of the curve given by Eq. 10.3. These results, combined with a theoretical analysis, indicate that PFX has achieved the desired spherical focus over a range of well depths [25]. The indicators of this are a sharp resonance whose width (~1 %) is expected to be comparable to the ratio of the core radius to the trap radius; the sudden transition to large angle deflections of injected electrons, indicating the appearance of significant central space charge; expected scaling with B, V, and I_i; and sensitivity of the focus (resonance) to field and injection errors. It was therefore concluded that dense non-neutral plasma could be produced in a Penning trap. The demonstration that a density focus can be established in a pure electron plasma in a

Penning trap was led by the observation that the peak density exceeds the Brillouin limit over some small region of the trap [35].

In conclusion, studies of the physics underlying the Penning trap fusion concept have advanced to obtain improved insight into this concept. However, considerable work is needed to develop it as a suitable neutron source or fusion reactor.

10.11 Summary

The experiments selected for discussion in this chapter are far from exhaustive. The experiments were selected then to explain some issues and status relative to gridded devices for near-term applications such as neutron sources and also to address some issues such as ion injection related to future fusion power units. The latter issues revolve around how to create deep potential wells in the IEC and trap the reacting ions in the well while excluding neutral gas atoms. The use of external ion sources with differential pumping then becomes a key approach for production of ions while keeping ultralow background pressure in the reacting chamber. This is the approach used in the six-gun SIGFE and the ^{3}He Helicon source at the University of Wisconsin and in the HIIPER experiment at the University of Illinois. However, introduction of the source into the configuration such that the ions are born at potentials below the well depth is another possibility as shown by the hybrid magnetron source work in Japan. The POPS concept that operates with local thermodynamic equilibrium plasma at all times has been introduced to solve many of the problems faced by conventional IEC device. The experimental confirmation of the POPS oscillation and successful plasma compression in a particle simulation has provided a solid scientific foundation for further exploration of this promising fusion device concept that has the latent possibility to reach high fusion rates for near-term applications and a good future potential for the achievement of breakeven performance. The Penning trap experiment has shown some promise through the initial experiments; however the high-voltage breakdown issues and the stability of the plasmas still remain a challenge with this alternate concept.

References

1. Hirsch RL (1967) Inertial-electrostatic confinement of ionized fusion gases. J Appl Phys 38(11):4522–4534
2. Gardner AL (1974) Studies of charged-particle distributions in an electrostatic confinement system. In: U. S. atomic energy commission final report, N. C00-2180-7, Washington, DC
3. Burton R, Momota H, Richardson N, Coventry M, Shaban Y, Miley GH (2002) High performance manned interplanetary space vehicle using D–^{3}He intertial electrostatic fusion. In: AIP conference proceedings, Albuquerque, New Mexico, vol 608, p 819
4. Miley GH, Yang Y, Webber J, Shaban Y, Momota H (2005) RF ion source-driven IEC design and operation. In: TOFE meeting, Madison, Sept

5. Michalak MK, Kulcinski GL, Santarius JF (2012) Exploring non-uniformities in gun-to-gun performance on the Six Ion Gun Fusion Experiment (SIGFE). In: 14th U.S.-Japan IEC workshop, College Park, 14–16 Oct
6. Miley GH, Gu Y, DeMora JM, Stubbers RA, Hochberg TA, Nadler JH, Anderl RA (1997) Discharge characteristics of the spherical inertial electrostatic confinement (IEC) device. IEEE Trans Plasma Sci 24(4):733–739
7. McGuire TJ, Sedwick RJ (2005) Improving IEC particle confinement times using multiple grids. In: 7th US-Japan IEC workshop, Los Alamos National Laboratory, 14–16 Mar
8. Gu Y, Williams M, Stubbers R, Miley G (1996) Pulsed operation of spherical inertial-electrostatic confinement device. Fusion Technol 30(3):1342–1346
9. Miley GH et al (1994) Inertial electrostatic confinement neutron/proton source. In: AIP conference proceedings, London, United Kingdom vol 299, p 675
10. Anderl RA, Hartwell JK, Nadler JH, DeMora JM, Stubbers RA, Miley GH (1996) Development of an IEC neutron source for NDE. In: 16th symposium on fusion engineering, IEEE conference proceeding 95CH35852, Piscataway, pp 1482–1485
11. http://www.nsd-fusion.com. Accessed 9 Sept 2013
12. Takamatsu T, Kyunai T, Ogawa S, Masuda K, Toku H, Yoshikawa K (2005) A magnetron discharge ion source for an inertial electrostatic confinement fusion device. In: 7th U.S.-Japan IEC workshop, Los Alamos National Laboratory, 14–16 Mar
13. Piefer GR, Santarius JF, Ashley RP, Kulcinski GL (2005) Progress in the development of a 3He ion source for IEC fusion. In: 7th U.S.-Japan IEC workshop, Los Alamos National Laboratory, 14–16 Mar
14. Nevins WM (1995) Can inertial electrostatic confinement work beyond the ion–ion collisional time scale? Phys Plasmas 2:3804
15. Piefer G (2003) Helium ion source for D-^{3}He converged core operation. In: 6th U.S.-Japan IEC workshop, Tokyo Institute of Technology
16. Piefer GR, Santarius JF, Emmert GA, Ashley RP, Kulcinski GL (2006) Development of an experimental method to investigate ^{3}He-^{3}He fusion with inertial electrostatic confinement techniques. In: Division of plasma Physics meeting, Philadelphia
17. Jacobson VT (2002) Development of VASIMR Helicon source. In: 43rd annual meeting of the APS Division of Plasma Physics
18. Piefer G (2004) ^{3}He–^{3}He and converged core fusion in an inertial electrostatic confinement device. Preliminary examination report, Department of Nuclear Engineering-Engineering Physics, University of Wisconsin, Madison
19. Krishnamurthy A, Chen G, Ulmen BA, Miley GH (2012) Numerical and experimental measurements in a Helicon-IEC thruster. In: 48th AIAA/ASME/SAE/ASEE joint propulsion conference & exhibit, 10th annual international energy conversion engineering conference
20. Chen FF (1991) Plasma ionization by helicon waves. Plasma Phys Control Fusion 33(4):339–364
21. Krishnamurthy A, Ulmen BA, Keutelian P, Chen G, Miley GH (2012) Helicon-Injected Inertial Plasma Electrostatic Rocket (HIIPER): experimental proof of principle. In: 48th AIAA/ASME/SAE/ASEE joint propulsion conference & exhibit 10th annual international energy conversion engineering conference, Atlanta
22. Ulmen BA, Keutelian P, Chen G, Krishnamurthy A, Miley GH (2012) Investigation of plasma properties in Helicon-Injected Inertial Plasma Electrostatic Rocket (HIIPER). In: 48th AIAA/ASME/SAE/ASEE joint propulsion conference & exhibit 10th annual international energy conversion engineering conference, Atlanta
23. Chacon L, Miley GH, Barnes DC, Knoll DA (2000) Energy gain calculations in Penning fusion systems using a bounce-averaged Fokker-Planck model. Phys Plasmas 7(11):4547–4560
24. Rider TH (1995) A general critique of inertial-electrostatic confinement fusion systems. Phys Plasmas 2:1853
25. Mitchell TB, Schauer MM, Barnes DC (1997) Observation of spherical focus in an electron Penning trap. Phys Rev Lett 78:58

26. Bussard RW (1991) Some physics considerations of magnetic inertial-electrostatic confinement: a new concept for spherical converging-flow fusion. Fusion Technol 19(2):273–293
27. Barnes DC, Nebel RA (1998) Stable, thermal equilibrium, large-amplitude, spherical plasma oscillations in electrostatic confinement devices. Phys Plasmas 5(7):2498
28. Park J, Nebel RA, Stange S, Krupakar Murali S (2005) Experimental observation of a periodically oscillating plasma sphere in a gridded inertial electrostatic confinement device. Phys Rev Lett 95:015003
29. Nebel RA, Stange S, Park J, Taccetti JM, Krupakar Murali S, Garcia CE (2005) Theoretical and experimental studies of kinetic equilibrium and stability of the virtual cathode in an electron injected inertial electrostatic confinement device. Phys Plasmas 12:012701
30. Krupakar Murali S, Nebel R, Park J (2006) Carbon nanotubes in IEC fusion reactors. In: ANS annual meeting, Reno, 4–8 June
31. Barnes DC, Nebel RA, Turner L, Tiouririne TN (1993) Alternate fusion: continuous inertial confinement. Plasma Phys Control Fusion 35(8):929
32. Roberson CW, Driscoll CF (eds) (1988) Non-neutral plasma physics. American Institute of Physics, New York; Fajans J, Dubin DHE (eds) (1995) Non-neutral plasma physics II. American Institute of Physics, New York; Davidson RC (1990) Physics of nonneutral plasmas. Addison-Wesley, Redwood City
33. Barnes DC, Mitchell TB, Schauer MM (1997) Beyond the Brillouin limit with the Penning fusion experiment. Phys Plasmas 4(5):1745
34. Brown LS, Gabrielse G (1986) Geonium theory: physics of a single electron or ion in a Penning trap. Rev Mod Phys 58:233
35. Schauer MM, Mitchell TB, Holzscheiter MH, Barnes DC (1997) Electron Penning trap for the generation of high density non-neutral plasmas. Rev Sci Instrum 68(9):3340–3345

Chapter 11
IEC Diagnostics

11.1 Introduction

A wide variety of plasma diagnostics can be applied to an IEC. However, the specific diagnostics incorporated are usually selected based on the objective of the research or application involved. Groups doing research on the IEC device itself will employ a wide variety of diagnostics intended to understand the plasma characteristics, the spatial distribution of reactions, and the electrostatics of the device. By contrast, persons interested in using the IEC as a neutron source for practical applications such as neutron activation analysis (NAA) may settle for overall neutron rate measurements. Most IEC studies to date have been of a research nature involving use of a variety of diagnostics. The most common of these will be briefly discussed in this chapter.

11.2 Neutron Detectors

Neutron detectors are widely used to study IEC devices. They can be stationed outside the chamber, so are noninvasive. They readily provide information about the neutron production rate (NPR) in the IEC device.

Neutron detectors can be classified as active detectors and passive detectors. Active detectors use electronics to count the number of neutrons detected. Passive detectors, such as activation foils, integrate neutron production over a period of time. They generally do not employ any electronics, hence are not affected by the ambient electric noise.

A neutron detector relies on ionization reactions due to neutron scattering interaction or through neutron-induced nuclear reactions. Some examples of detectors based on one or the other of these processes will be discussed in the next section.

G.H. Miley and S.K. Murali, *Inertial Electrostatic Confinement (IEC) Fusion: Fundamentals and Applications*, DOI 10.1007/978-1-4614-9338-9_11,

11.2.1 Polyethylene-Moderated ^{3}He Gas Filled Neutron Detectors

^{3}He gas filled detectors rely on neutron reactions with ^{3}He. Because the neutron reaction cross section for ^{3}He is largest at a low neutron energy, a polyethylene moderator surrounding the detector is commonly used to thermalize the high-energy neutrons. The thermalized neutron (n*) then undergoes the reaction:

$$^3\mathrm{He} + n^* \rightarrow H + T + Q \ \ (764\ \mathrm{keV}). \tag{11.1}$$

The energy Q is released in the form of kinetic energy of the two reaction products. The average thermal neutron cross section for this reaction is 5,330 b, and it obeys an inverse relationship with neutron velocity up to around 0.2 MeV.

These detectors have a flat response to the neutrons in the energy range of few keV to several MeV. They have low γ-ray sensitivity and are simple and reliable. Owing to these beneficial features, ^{3}He detectors are highly desired for use in association with IEC devices.

11.2.2 BF_3 Neutron Detectors

BF_3 detectors use the neutron reactions with the isotopically pure Boron (B^{10}), where

$$B^{10} + n^1 \rightarrow Li^7 + \mathrm{alpha} + Q. \tag{11.2}$$

In about 97 % of the reactions, the energy is released from the nuclear reaction $Q = 2.31$ MeV, leaving the Lithium nuclide in the first excited state. The other 7 % of the reactions have $Q = 2.79$ MeV, with the Lithium nuclide in the ground state. The energy from the reaction with a thermal neutron is shared as kinetic energy of the daughter products. The reaction products are 0.84 and 1.47 MeV for the Lithium nuclide and alpha particle, respectively.

11.2.3 Typical Detector Electronic Arrangement

Figure 11.1 shows a schematic of the electronics employed in a typical gas filled neutron detector. The anode is usually a thin wire and the cathode is the chamber wall. The detector wall material is selected based on the detection efficiency; for example, aluminum absorbs around 0.5 % of the incoming neutron flux while stainless steel absorbs around 3 %; hence aluminum is preferred for chamber walls. Despite its higher neutron absorption cross section, steel tubes are preferred in low count rate applications (1 cpm) as the impurity levels are more controllable versus

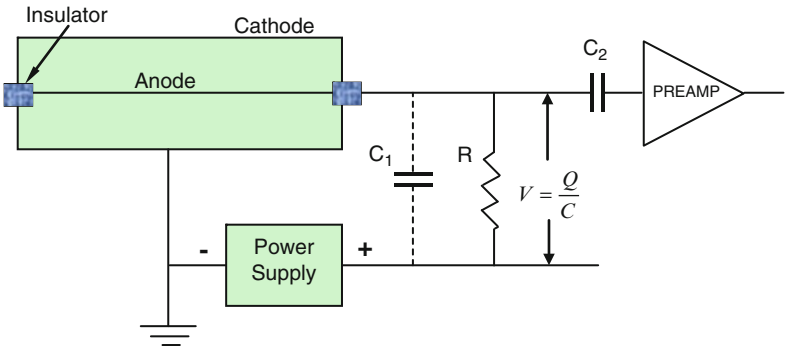

Fig. 11.1 Various components of a gas filled neutron detector [2]

aluminum, which often has some level of radium impurity [1]. The central wire is generally made of gold-plated tungsten wire. Gold provides the necessary conductivity and tungsten provides the necessary tensile strength. The insulators are usually made of a ceramic that maintains the vacuum seal. Furthermore, the inside wall of the chamber is coated with activated charcoal to absorb electronegative gases that build up during neutron irradiation. The chamber is typically filled either with BF_3 or ^{3}He gas. ^{3}He is still widely used despite the fact that it has become scarcer and more expensive.

The detection of neutrons involves the transfer of energy from the neutrons to charged particles (e.g., H and T in a ^{3}He filled detector per Eq. 11.1 or the Li^7 and alpha in the BF_3 detector per Eq. 11.2). The charged particles leave a trail of ionization and excitation events along their path as they slow down. In the ^{3}He detector, roughly 30 eV is required to create a single ionization pair. This represents the sum of energies going into ionization and excitation. As shown in Fig. 11.1, a bias voltage is applied to the detector chamber to separate and collect the electron–ion ionization pairs at the respective electrodes. The applied voltage, the geometry of the detector chamber, and the type of fill gas determine the output signal strength.

11.2.4 Operational Regions

The operational region, namely, the ionization region, the proportional region, or the applied voltage, determines the Geiger–Müeller region. These different regions are shown for a typical ^{3}He detector in Fig. 11.2.

Detectors operated in the ionization region are called ion chambers. In this region, some electrons recombine before reaching the electrode. When sufficient voltage is applied (Geiger–Müeller region), nearly all the electrons are collected before they recombine. Because the neutron rate from IEC devices is typically quite high (10^6 n/s and above), the ion chamber mode is generally employed to avoid current saturation effects. Uses of ^{3}He detectors for operation in the proportional or Geiger–Müeller regions are covered in reference [2].

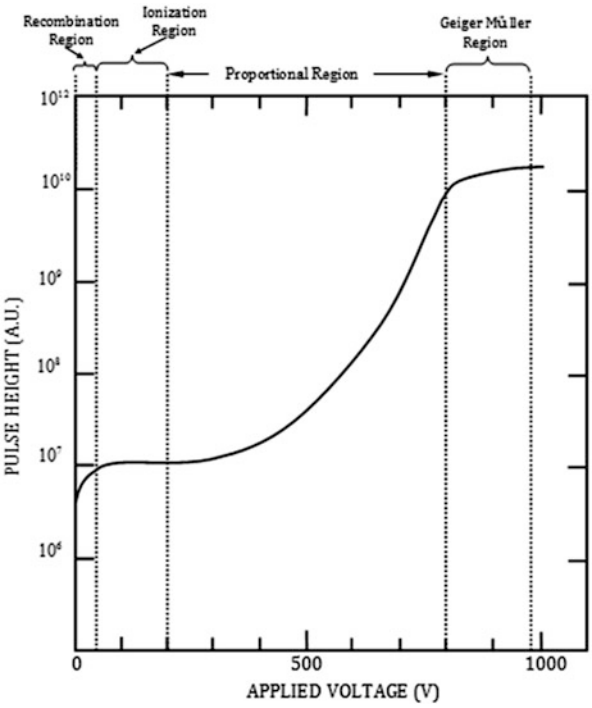

Fig. 11.2 Pulse height versus applied voltage curves illustrating ionization, proportional, and Geiger–Müeller regions of operation [2]

The γ-ray sensitivity of ^{3}He detectors becomes important in situations where the γ-ray flux is higher compared to the neutron flux. However, IEC devices generally have low levels of γ-ray emission. IEC devices do generate low-energy x-rays due to Bremsstrahlung emission from the electrons hitting the chamber walls and grids. The chamber walls effectively absorb these, preventing escape. Care must be taken to control leakage through glass ports and diagnostic openings (e.g., pressure gauge). Leaded glass is often employed in ports. If the applied voltage is raised above ~ 100 kV (for comparison, note that dental x-ray units typically run around 70 kV), higher energy x-rays can increase leakage. However, added shielding can easily be implemented if needed.

11.2.5 Comparison of Gas Filled Detectors

BF_3 neutron detectors typically contain enriched boron (>90 % B^{10}). The average thermal neutron cross section for B^{10} is 3,840 b while that of ^{3}He is 5,330 b. ^{3}He detectors are much more sensitive due to their higher cross sections. Further, the reaction energy of the ^{3}He reaction is only a quarter of that of the ^{10}B reaction utilized in BF_3 proportional counters. ^{3}He counters have been used as neutron spectrometers as well as neutron flux detectors. Though gas filled detectors are usually constructed in tubular form, they are also made in spherical form when an omnidirectional response is required.

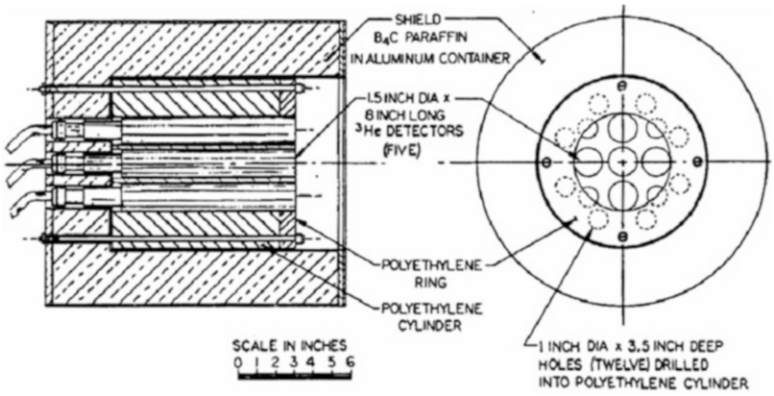

Fig. 11.3 Modified long counter used for IEC neutron detection at the University of Wisconsin [4]

Compared to ^{3}He detectors, BF_3 detectors function at much higher voltages, usually in the range of 2–2.5 kV. Leakage currents are minimized by using an insulator ring around the anode. BF_3 detectors have better γ rejection than ^{3}He due to higher deposition energy. A disadvantage of BF_3 detectors is the associated toxicity hazard.

11.2.6 Example of a ^{3}He Detector in an IEC Experiment

Many IEC experiments have used a single gas detector tube placed in a hole drilled in a thick plastic or paraffin tube. These detectors are adequate for flux measurements. More elaborate detector arrangements have been used to deal with a range of neutron energy spectra. The University of Wisconsin detector (shown in Fig. 11.3) is a modified long counter consisting of an aluminum cylinder filled with paraffin [3]. Five ^{3}He detectors are placed in holes drilled into the central region. In addition, an additional 12 smaller holes are strategically placed in the central region of the cylinder. These holes are used to produce a reasonably flat response to different energy neutrons. This is a particularly useful feature as the detector is calibrated with a plutonium–beryllium source, which emits a full spectrum of energies at ~4 MeV, while 2.45-MeV D–D fusion neutrons are of interest for deuterium-filled IECs.

11.2.7 Calibration of Neutron Detectors

The calibration of neutron detectors is typically performed using a neutron source with known intensity such as Am–Be or Pu–Be. Typically the source strength is ~10^6 n/s which is quite sufficient for calibration purposes. The source (with source strength T) is placed at the center of the IEC device. The external neutron detector records N neutrons; hence the calibration factor is given by the ratio T/N. This type

of calibration is reasonably accurate because a spherical device is an approximate point source when the detector is placed a meter or so away. However, for cylindrical sources the calibration process is more complex as there are no uniform line sources available in the market. Thus, an array of Am or Pu–Be sources placed in a line along the cylindrical chamber has been employed.

When IEC devices are used in a pulsed mode, several methods have been employed. Calibration techniques are different for active and passive detectors. Once the detector is calibrated using a steady-state source, the neutron rate during IEC pulsing can be calculated from the observed data and the time duration of the pulse [4, 5]. Another common technique is to use a silver activation detector and pulse the device in a controlled fashion until the silver activation saturates. Then measurement of the γ-ray emission from the activated silver can be used to calculate the neutron source strength. This method has the advantage of avoiding electronic noise generated by the device during the detection period.

11.2.8 Comments About Nonlinearity in Detection Rates

Various factors in IEC operation can cause nonlinear neutron source behavior which should not be confused with problems in neutron detectors. Some nonlinear effects are discussed next.

The neutron rate depends strongly on IEC operational pressure. The neutron production rate from an IEC device operating at ~2 mTorr closely follows the variation of averaged reactivity, "sigma vee," i.e., $<\sigma v>$, with the applied voltage. This is because the mean free path for deuterium ions is larger than the dimensions of the reaction chamber. However, if the mean deuterium ion-free path is smaller, as occurs at higher IEC chamber pressures, the variation of the neutron rate with voltage will deviate from the reactivity curve. This can be understood as follows: As the ions are accelerated by the electric field created by the cathode, they gain energy. However, if the ions collide with an ion or a neutral in the process, they lose part of their energy. With a higher collision rate, the energy gained by the ions is lower, reducing fusion reactions. This is also one of the reasons why a gridded IEC device has an optimum chamber pressure for maximum reaction rate. Even if energetic neutrals from CX reactions dominate, at high pressures these neutrals will have lower energies, thus reducing the fusion rate.

As explained in Chap. 8, beam–beam fusion should follow an I^2 scaling; however, this does not occur in higher pressure IEC operation where beam–background and beam–embedded gas reactions dominate. Indeed, several research groups have attempted to increase the reaction rate by simply increasing the grid current, but even increasing it to 17 kA from the usual 10s of mA only showed a marginal increase in reaction rates [6]. As explained in Chap. 6, this is due to space charge effects plus nonlinear energy losses, which are discussed in Chap. 8.

There are several other reasons involving the electric circuitry that can contribute to nonlinearity. An example is illustrated in Fig. 11.4, showing data from the

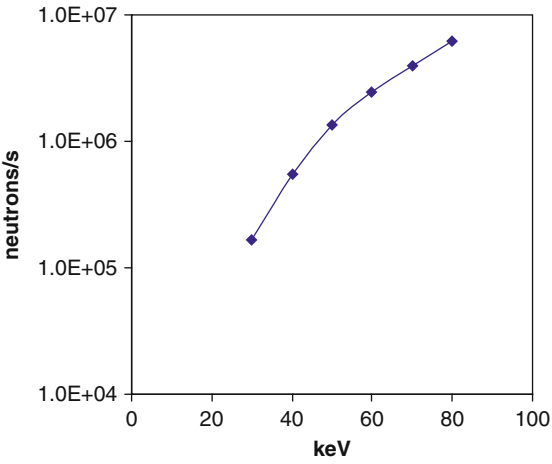

Fig. 11.4 Neutron rate variation with applied voltage from a typical reaction measurement performed on the UW IEC device (Homer). Measurements were performed with deuterium fuel and at 2 mTorr pressure and 30 mA power supply current (Ashley RP, 1999, University of Wisconsin, Madison, private communication)

Fig. 11.5 High-voltage buffer resistor used in UW Madison IEC device (Homer) [7]

"Homer" IEC device at the University of Wisconsin. A rollover in the neutron counts occurs at higher currents due to the use of an ~200-kΩ resistor in the high-voltage circuit. Such a buffer resistor (shown in Fig. 11.5) was introduced to suppress the transient high-voltage arcing (Ashley RP, 1999, University of Wisconsin, Madison, private communication). However, this caused a reduced voltage on the grid compared to the voltage recorded on the power supply. If the count plot is obtained by varying the voltage to compensate for the resistor (i.e., using $V \times I = I^2R + 400$ to determine V), the rollover effect is removed.

11.3 Bubble Detectors

Bubble detectors are classified as passive detectors because there are no electronics involved in the neutron flux measurement. These detectors are more accurate at low neutron flux rates because they time integrate counts and avoid electronic noise. Tiny droplets of superheated liquid are suspended in a polymerized gel matrix inside the detector [8, 9]. These droplet detectors consist of an emulsion of metastable superheated droplets of liquids (such as C_3F_8, C_4F_{10}, CF_3Br, or CCl_2F_2) at a temperature higher than their boiling point, dispersed in an aqueous solution, subsequently polymerized after dissolution of an appropriate concentration of a heavy salt (e.g., CsCl) in water to equalize densities of droplets and solution. By applying an adequate pressure, the boiling temperature can be raised allowing the emulsion to be kept in a liquid state. Under this external pressure, the detectors are insensitive to radiation [10].

By removing the external pressure, the liquid becomes superheated and sensitive to radiation. Bubble formation occurs through liquid-to-vapor phase transitions, triggered by the energy deposited by radiation. Bubble detectors are threshold detectors as they require a minimal energy deposition to induce a phase transition. Their sensitivity to various types of radiation strongly depends on the operating temperature and pressure. The signal measurement of the detectors is described in [11]. These detectors are reusable by recompressing the bubbles back to droplets.

When a neutron strikes a droplet, the droplet spontaneously vaporizes, forming a visible gas bubble trapped in the gel. The number of droplets provides a direct measurement of the tissue-equivalent neutron dose. Figure 11.6 shows bubble detectors with and without bubble formation, along with an automated bubble counter.

These detectors can be purchased precalibrated and are ideal for calibrating pulsed neutron sources. Their sensitivity can be adjusted by changing the temperature of the droplets.

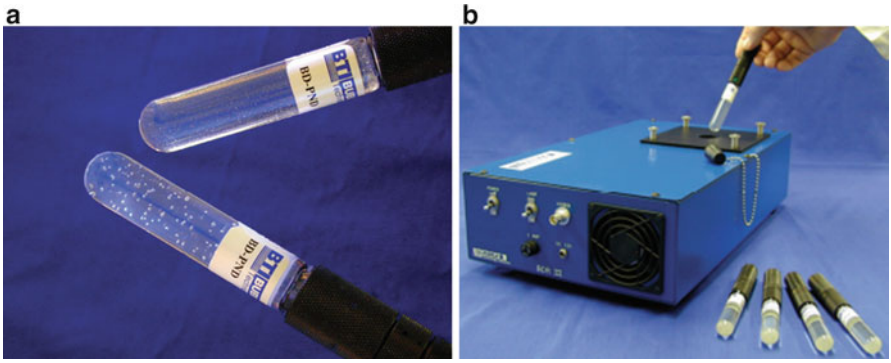

Fig. 11.6 (**a**) Bubble detectors, before and after neutron exposure. Bubbles form in the detector when exposed to neutrons. (**b**) Automation of bubble measurements is possible using commercial readers [12]

These detectors provide integrated neutron yields over a given run time or during a pulse. Due to the count integration, they are not useful for measurements such as the variation of the neutron flux as the voltage or current is varied. These detectors are particularly effective for use with cylindrical IECs where a series of bubble detectors can be located along the length of the cylinder. This then establishes the axial profile for neutron production.

11.4 Silver Activation Detectors

The integral neutron yield can also be measured with an activation detector consisting of a self-extinguishing Geiger–Müeller (GM) counter surrounded by a silver foil or simply a PMT-scintillator assembly with a silver foil in front of it. Silver possesses a high-activation cross section (σ) by thermal neutrons, making it very useful in these transducers.

Natural silver consists of two isotopes, Ag^{107} (51 %) and Ag^{109} (49 %), with corresponding activation cross sections of 45 and 113 b, respectively. When Ag nucleus captures a thermal neutron ($E_n \leq 0.25$ eV), two radioactive isotopes are produced: Ag^{108} with the half-life time of $T_{1/2} = 145$ s and Ag^{110} with the half-life time of $T_{1/2} = 24.4$ s. Energetic β-particles ($E_\beta > 1$ MeV) are produced through radioactive decay of both isotopes. These particles are detected with a GM counter. Because silver has a large activation cross section with thermal neutrons, the fast neutrons produced in a D–D or D–T reaction should be moderated in a medium with a high content of hydrogen such as paraffin wax or polyethylene surrounding the silver foil.

One configuration uses a GM counter with a cylindrical frame that is covered by a silver foil (0.1 mm thick) and placed within a polyethylene unit. The neutron detection element can be calibrated to find the total proportionality factor using a Pu(α,n)Be neutron source placed at the center of the IEC chamber.

In the next section we describe the charged particle solid-state detectors that are also important for an IEC device. These detectors provide information that a neutron detector cannot, such as the number of reactions, the energy spectrum, the kinds of reactions, the associated directionality, the source regime distribution, and information about x-ray noise levels.

11.5 Solid-State Detectors

Solid-state detectors are used to detect charged particles such as energetic protons or alpha particles produced in fusion reactions. The range of the charged reaction products is limited and they are entirely stopped by the chamber walls. Thus the detector must be located inside a port or in a port extension. However, the ambient light produced in the plasma can damage the detector and so can the

electrons that stream outward from the cathode. Hence a shield foil is usually placed in front of the detector to preferentially block light and electrons. Alternately a thin light shield combined with a magnetic field can be used to deflect the electrons away from the detector. Deflection of the electrons has the advantage of minimizing x-rays that would be produced in the shield foil and cause noise in the detection signal.

Charged particle detectors have been an important diagnostic tool in IEC research for nearly two decades. Nadler first used this diagnostic to measure the potential structures within an IEC device with a collimated proton detector [13]. Thorson used a similar technique to map the fusion reaction profile in the IEC device at the University of Wisconsin, Madison [14]. Thorson's work was the first to show that the vast majority of D–D fusion taking place in the University of Wisconsin device was the result of interactions between fast neutrals from charge exchange and background gas. Using an Abel inversion, Thorson was able to calculate that over 75 % of the fusion events are distributed over the volume of the IEC device rather than within the core. Murali used the proton detector to study the D–D and D–^{3}He fusion reactions at the University of Wisconsin, Madison, and explained the fusion proton spectrum and made preliminary attempt to use the Doppler broadening of the proton energy peak to predict the reacting ion energy [6]. This work was followed by Murali, Ashley, and Cipiti to diagnose the source regimes in an IEC device, as explained in Chap. 6 [15, 16]. Similar work was then performed by Masuda, Fujimoto, and Yoshikawa at Kyoto University in Japan [17, 18].

A solid-state proton (charged particle) detector is a reverse-biased, large surface area, silicon or germanium diode of the PN or PIN type. These diodes operate at prescribed temperatures; for instance, the silicon detector operates at ~ 300 °K (room temperature), while the germanium detectors operate at ~ 85 °K, requiring liquid nitrogen cooling. The barrier created at the junction at these prescribed temperatures reduces the leakage current to acceptably low values. Thus, when a reverse bias electric field is applied, it is sufficient to collect the charge carriers liberated by the ionizing radiation transiting through the detector. Further information on the topic is available in reference [19].

Charged particles such as protons lose energy in a solid-state detector by two processes: the Coulomb interaction with the electrons and the direct nuclei collisions. The energy expended in electron collisions results in the creation of electron–hole pairs, whereas the energy spent in nuclear collisions is largely lost to the detection process for the present light ions (versus heavy ions such as fission fragments). Though silicon detectors have been used to detect electrons, in IEC devices the electron flux is very high and could quickly damage the silicon detector. Therefore, we will focus on proton and alpha particle detection.

Most silicon detectors are ionization-type detectors without gain. The ionizing radiation creates electron–hole pairs in the device that without an external electric field creates a large DC current that must be removed. This is done through the application of reverse bias. The induced motion of the electron–hole pairs induces a current in the external circuit. The resulting signal can be amplified and detected.

Radiation damage can occur in semiconductor devices. The nuclear interactions displace silicon atoms from their lattice position, creating interstitials and vacancies. The corresponding energy states in the bandgap change accordingly. This results in an increase in the leakage current that can be easily observed. The bulk material behaves more P-type as more defects act as acceptors than as donors. The damage is partially reversible through temperature annealing. Though such radiation damage is not important when the neutron fluxes are low, it becomes significant when the detector is used for an extended duration of time. Hence, even in IECs operating with lower neutron fluxes, as time progresses it is important to periodically record the leakage currents to detect possible degradation of the detector.

11.5.1 Energy Required for the Creation of Electron–Hole Pair

Electron–hole pairs are created with the passage of ionizing radiation across the semiconductor detector. This process occurs in both direct and indirect ways. When the ionizing radiation generates secondary electrons, such electrons tend to be highly energetic and they create more electron–hole pairs as they travel through the device. The average energy ε necessary to create an electron–hole pair in a given semiconductor (at a given temperature) is called the "ionization energy." It has been experimentally observed that ε for semiconductors is roughly independent of the type and the energy of the ionizing radiation, contributing to the versatility and flexibility of semiconductor detectors. For instance, the values of ε are 3.62 eV in silicon at room temperature and 3.72 eV at 80 °K. In contrast, the average energy (E_{avg}) necessary to create an electron–ion pair in a gas is typically 15–30 eV.

The value of ε for silicon detectors is generally insensitive to the type of radiation. There is a measured discrepancy of about 2.2 % between the alpha particles and protons [2]. This can usually be ignored in IEC proton measurements due to the large statistical variation typically encountered with the low particle rates involved.

11.5.2 Energy Calibration of the Proton Spectrum

The energy level calibration of the proton spectrum is usually accomplished using an alpha particle source such as Americium with a known strength. A flat disk source can be placed directly over the solid-state proton detector's surface. The number of alphas detected is roughly equal to the number of protons that would be detected of same flux levels. Figure 11.7 shows a calibration signal generated using Americium-241 superimposed over the observed proton spectra for a D–^{3}He fueled IEC.

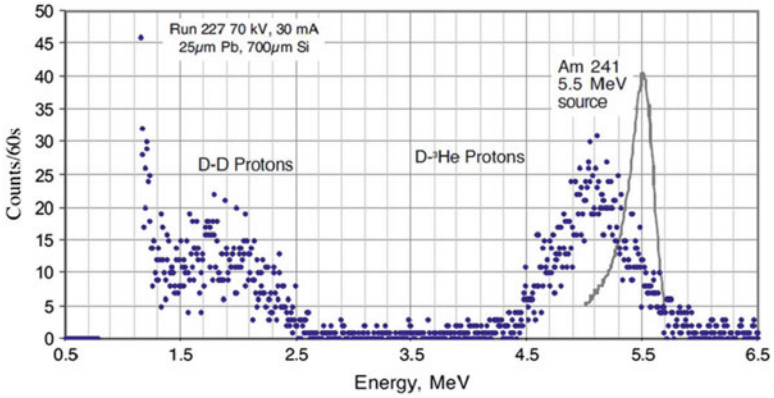

Fig. 11.7 Proton energy spectrum from an IEC device using D–^{3}He fuel measured with a 700-μm Si detector with a 25-μm Pb shielding foil. The energy spectrum (*solid line*) from Am-241 was used for energy calibration [20]

11.5.3 Understanding the Proton Energy Spectrum Recorded with Si Detectors

Silicon detectors are commonly used for 3.52-MeV proton spectra measurements of deuterium-fueled IECs [21, 22]. Such detectors have also been useful in detecting 14.7-MeV protons from D–^{3}He reactions. Figure 11.7 shows the proton spectrum observed in an IEC device fueled with D–^{3}He.

The 3.52 MeV D–D protons represent a relatively low energy. Hence most of their energy is deposited in the detector itself. As shown in Fig. 11.7 the D–D protons peak around 2 MeV. The lower energy recorded is due to energy loss in the shield foil used on the detector face. The more energetic protons from the D–^{3}He reactions (14.7 MeV) lose less energy in the shield foil, but do not completely slow down in a detector of common thickness (e.g., the 700-μm Si used for Fig. 11.7). This causes their peak to "shift" down to ~ 5–5.5 MeV in Fig. 11.7.

These fusion protons are monoenergetic but the peaks detected by the Si detector are broadened and shifted due to Doppler and collisional broadening, plus energy transferred to recoil nuclei. Recoil nuclei lose their energy in inelastic collisions with surrounding atoms but have too low an energy to form many additional electron–hole pairs. Large fluctuations of energy loss can occur because the loss is strongly influenced by a few relatively large recoil events [2]. Other contributions to peak broadening and energy shifting are the effects of incomplete charge collection and variations in the energy lost by the particle in dead layers at the detector surface [23].

Other effects are also possible. Collisional broadening depends on the initial energy of the proton, which in turn is governed by Doppler broadening. All the other sources of peak broadening are normally independent of each other; the square of each Full-Width Half-Maximum (FWHM) value that would theoretically be observed for each source separately can be summed together to give the overall FWHM.

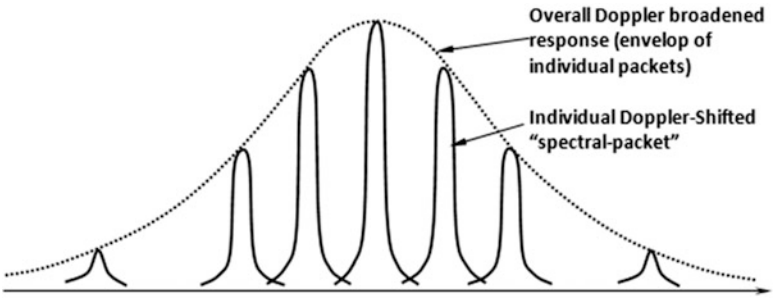

Fig. 11.8 The Doppler-broadened line shape is made up of the superposition of a large number of individual "energy packets," which are the contributions from different groups of atoms with different Doppler velocities [24]

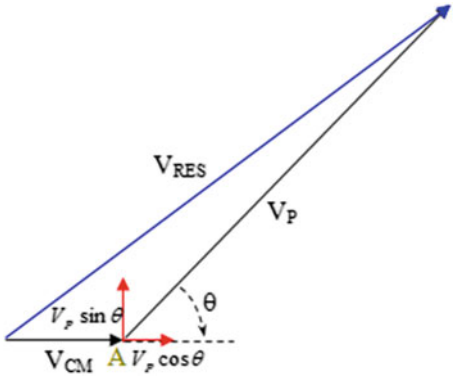

Fig. 11.9 The protons detected by the detector have Doppler-shifted velocities. A fusion event at the point A causes a proton to be generated at an angle θ to the direction of motion. Other products of fusion are not shown here

Doppler Broadening of the Proton Energy Spectra. Different deuterium (D^+, D_2^+, D_3^+) ions inside the IEC have different velocities in the direction of the observer owing to the spherical symmetry of the IEC device (assuming the concentration of D^+ dominates – in reality this is not completely true, but is assumed for the sake of discussion). The cumulative result of this velocity distribution is a smearing or broadening of the proton energy line shape. For computational convenience we will view the broadened line shape as being made up of a large number of "energy packets" centered at different velocities throughout the line shape (shown in Fig. 11.8). The individual energy packet at a particular velocity v is the contribution of that fraction of atoms whose Doppler-shifted resonance frequencies lie within a small range of frequencies about v. Many such packets added together produce the smooth Doppler-broadened line shape.

Initially, the neutral particle (D_2) is at rest in the lab frame and it senses a charged deuteron coming toward it with a velocity V_D. After the fusion reaction a proton leaves the rest frame of the reacting particles at an angle θ (as shown in Fig. 11.9). But the rest frame of the reacting particles is itself moving with respect to the lab frame with velocity V_{CM}.

The protons generated in the fusion reaction are now energy shifted with respect to the reactant velocities and it is this energy that the detector detects. A fusion product that enters a detector will possess the combined velocity of the fusion reaction (constant 3.02 MeV for D–D fusion) plus the center-of-mass velocity of the reacting ions.

Doppler-Shifted Energy Spectra Calculations. Assuming projectile–target mode with a stationary target and the center-of-mass velocity v_{cm}, the resulting fusion product's energy, E_{tot} (as sensed by the Si detector) is calculated as follows:

The velocity v_p of the proton in the rest frame is given by

$$v_p = \sqrt{\frac{2E_p}{m_p}}, \tag{11.3}$$

where E_p is the proton's energy (3.02 MeV for D–D) and m_p is the fusion product's mass.

For head-on collisions, both the reacting particles have energy (E_a and E_b) with $E_b = 0$ for a stationary target (a valid assumption for neutral background), and masses (m_a and m_b), and the center-of-mass (CM) velocity (v_{cm}) is given by

$$v_{cm} = \frac{\sqrt{2E_a m_a} + \sqrt{2E_b m_b}}{m_a + m_b}. \tag{11.4}$$

The number of fusion products with the respective energy weights the energy range. In the lab frame the resultant velocity (v_{RES}) of the proton due to the center-of-mass velocity effect (see Fig. 11.9) is given by

$$v_{RES}^2 = \left(v_p \cos\theta + v_{cm}\right)^2 + {v_p}^2 \sin^2\theta. \tag{11.5}$$

Hence the total energy of the proton that the detector senses is now given by

$$E_{tot} = \frac{1}{2} m_p {v_{RES}}^2 = \frac{m_p}{2}\left(\frac{2E_p}{m_p} + {v_{cm}}^2 + 2v_{cm}\sqrt{\frac{2E_p}{m_p}}\cos\theta\right), \tag{11.6}$$

where E_{tot} is the energy of the ion before going through the Pb foil or the detector and θ is the angle between the v_{cm} and the fusion product's velocity (directed toward each other = 0 °).

A code based on these equations developed by Santarius (Santarius JF, 2002, private communication) was used to calculate the resultant energy deposited into the detector (see Fig. 11.10). The collisional broadening of these energy peaks caused by the presence of the Pb foil in the front of the detector is not included by this code (the dead layers of SiO_2 on the detector also contribute to a small extent to this broadening).

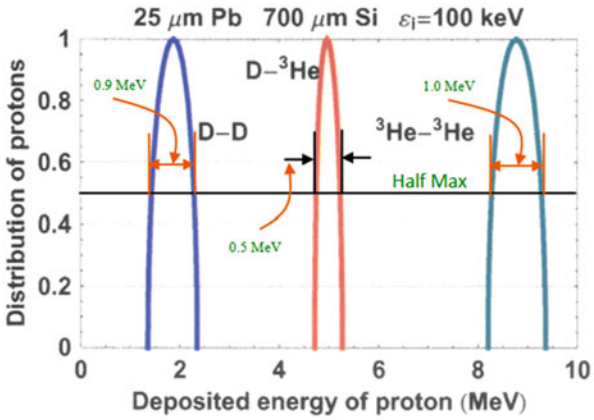

Fig. 11.10 The energy deposited by the protons into the 700-μm-thick Si detector is the total proton energy for the D–D and ^{3}He–^{3}He reactions and about one-third of the incident proton energy for the D–^{3}He reactions (Santarius JF, 2002, private communication)

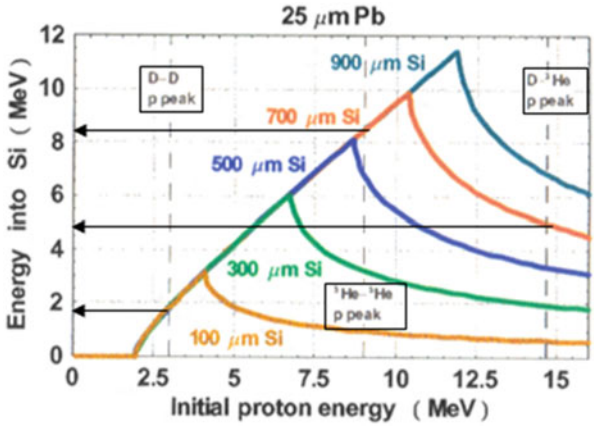

Fig. 11.11 The energy deposited into the Si detector of various thicknesses versus the initial proton energy. A 700-μm Si detector is a good choice for maximum separation of the three proton peaks coming from D–D, D–^{3}He, and ^{3}He–^{3}He reactions. However, if detection of all three is not the objective, a different thickness may offer advantages (Santarius JF, 2002, private communication)

As the protons enter the Pb foil, they are scattered and lose some energy to the foil before depositing their energy into the detector. The energies deposited into the Si detector vary according to the initial energies of the protons and the thickness of the detector. This energy variation for a typical case is shown in Fig. 11.10.

Depending on the thickness of the Si detector, the energetic protons can escape without depositing all their energy into the detector. This can cause the energy peaks to overlap. Hence, an appropriate Si detector thickness should be selected to isolate the contributions due to various fusion reactions. This is especially crucial for D–D and D–^{3}He reactions because both occur simultaneously when D–^{3}He fuel is used (in the present case, a suitable value is 700 μm). As shown in Fig. 11.11,

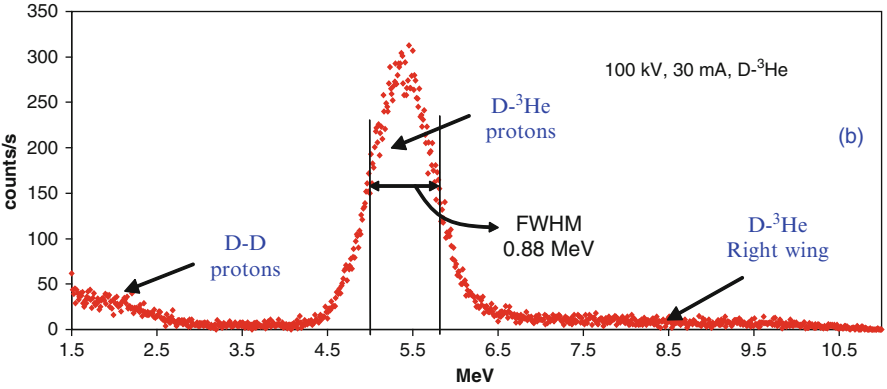

Fig. 11.12 D–^{3}He proton energy spectrum observed in a gridded IEC device [6]. The signal to the right of the peak is elevated above the noise levels and becomes more prominent as the data is acquired. Such a signal does not exist (or is minimal) to the left of the peak

a proton from the D–^{3}He reaction has an initial energy of 14.7 MeV but it deposits only ~5 MeV into the 700-μm thick Si detector, the rest of the energy being carried off by the kinetic energy of the proton as it escapes the detector.

A calculation of the energy deposited into the detector is shown in Fig. 11.12. The final responses (in the absence of collisional broadening) are Doppler-broadened functions. A comparison between this prediction (Fig. 11.11) and the experimental data in Figs. 11.7 and 11.12 show discrepancies (~0.87 MeV for D–D and ~0.47 MeV for D–^{3}He) in the FWHM values. This is because the predictions in Fig. 11.11 do not account for the broadening due to scattering collisions in the Pb foil and the Si detector.

The total collisional broadening has been computed for this case using the well-known Monte Carlo Stopping and Range of Ions in Matter (SRIM) code [25]. This is discussed next.

SRIM Prediction of Si Detector Proton Spectra. The SRIM code can be used to calculate the stopping and range of ions (10 eV to 2 GeV/amu) into matter using a full quantum mechanical treatment of ion–atom collisions [26]. Application to the present detector case is described in reference [6]. This computation employs the Doppler-broadened line shape "packet" approach shown in Fig. 11.8. The resulting prediction of the collisional broadened D–^{3}He proton energy peak for the present detector is shown in Fig. 11.13 [27].

The FWHM values of the SRIM results in Fig. 11.13 plus similar calculation for D–D protons are compared with the experimental data in Table 11.1. The error in the experimental data shown here is the inverse of square root of the number of particles detected.

As seen from Table 11.1, the SRIM predicted values are in reasonable agreement with the measured values.

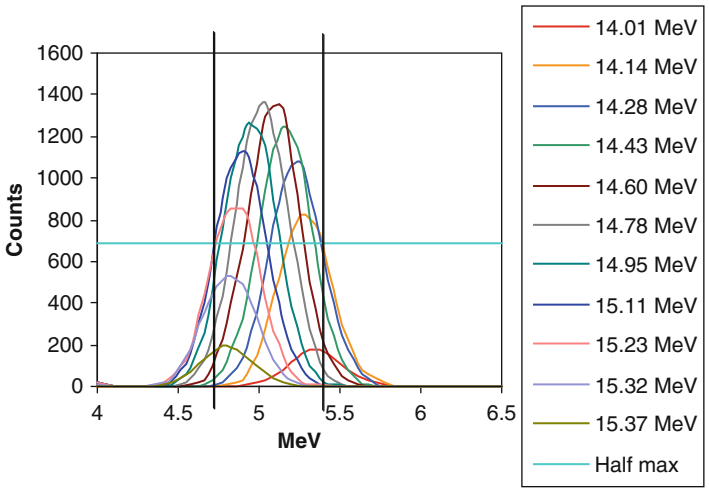

Fig. 11.13 SRIM prediction of Doppler and collision broadened D–^{3}He proton energy peak [26]

Table 11.1 Experimental and theoretical values [26]

Proton peak	Experimental value	SRIM predicted value
D–D	2 × FWHM ~ 1 MeV ± 0.1 MeV	0.95 MeV ± 0.01 MeV
D–^{3}He	FWHM ~ 0.8 MeV ± 0.1 MeV	0.7 MeV ± 0.01 MeV

11.5.4 Comments About D–^{3}He Fueled IEC Reactions

Figure 11.13 shows the first simultaneous measurement of D–D and D–^{3}He protons in an IEC device with D–^{3}He fuel at 100 kV, 30 mA. The D–D peak is weaker than the D–^{3}He peak, because only a small fraction of the D–^{3}He fuel (depending on fuel ratio, chamber pressure, etc.) undergoes D–D reactions. An interesting feature observed in almost all of the D–^{3}He proton spectra is the "right wing" shown in Fig. 11.12. This broadening of the D–^{3}He proton peak is above noise level and is observed to taper off beyond 10 MeV. This feature cannot be created by the ^{3}He–^{3}He reactions because the cross section values for ^{3}He–^{3}He reactions are small at the voltages used. This effect is attributed to grid effects discussed next.

Effects Due to Reactions by Bombardment of Absorbed Gas on Grids. D–^{3}He reactions caused by bombardment of ^{3}He absorbed on cathode grid wires play an important role in these experiments. The average range of ^{3}He atoms at 100 kV energy in the cathode grid wire is ~0.25 μm, while that of deuterium ions is ~0.5 μm. Hence, most D–^{3}He reactions due to deuterium bombardment occur in the first 0.25-μm thick surface layer of the cathode grid wire. The detections of the resulting protons must account for their passage through the grid wires.

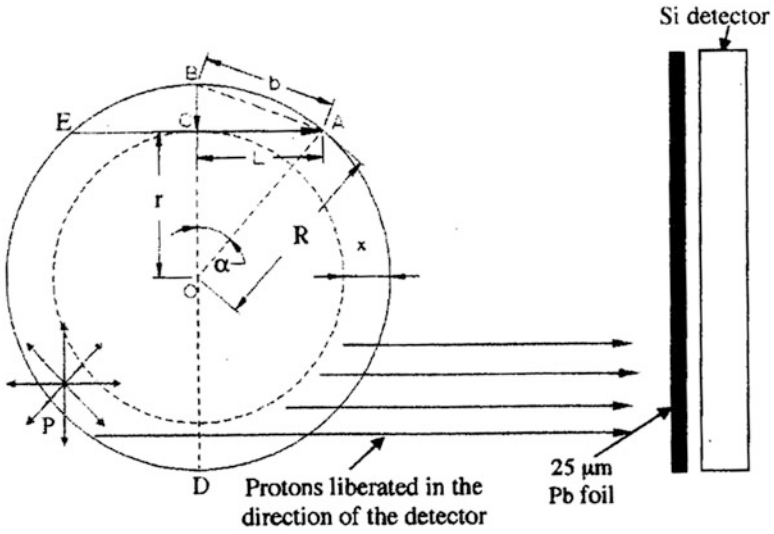

Fig. 11.14 Cross section of the W-25%Re wire. D–^{3}He protons are born isotropically on the surface of the grid wires as shown at the point C. Protons born behind the wire have to pass through greater thickness of material before reaching the detector [16, 27]

A proton from a D–^{3}He fusion event at any point C, as shown in Fig. 11.14, has equal probability of liberation in all directions. The protons liberated in the direction CA have to travel through the maximum thickness of the grid material before being detected by the Si detector. Any protons generated to the left of point C have to travel through even more material and hence lose relatively more energy to the grid wires.

Fusion occurs everywhere on the surface of the grid wire; hence they must travel through various thicknesses of the wire. The protons going through an effectively higher thickness of the grid wire are concentrated close to the two poles of the wire (top, B, and bottom, D, orientations with respect to the detector). These protons contribute to the right wing of the D–^{3}He peak (shown in Fig. 11.12). There are few proton counts beyond 10 MeV because of the Bragg peak response of the Si detector.

A D–^{3}He proton generated at the point C has to pass through the maximum effective wire thickness L before reaching the Pb foil in front of the detector. This thickness is given by

$$L^2 = R^2 - (R - x)^2 \Rightarrow L = \sqrt{2Rx - x^2}. \tag{11.7}$$

If $x = \delta$ (the range of $^3He^+$ ions in the W-25%Re grid wires), we can neglect the second-order (δ^2) term because $\delta \ll R$. Eq. 11.7 then reduces to

$$L \approx \sqrt{2R\delta}. \tag{11.8}$$

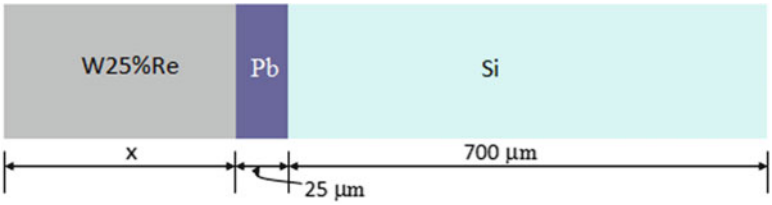

Fig. 11.15 The protons born on the surface of the grid wire travel through different thicknesses of the grid wire before reaching the Si detector [27]

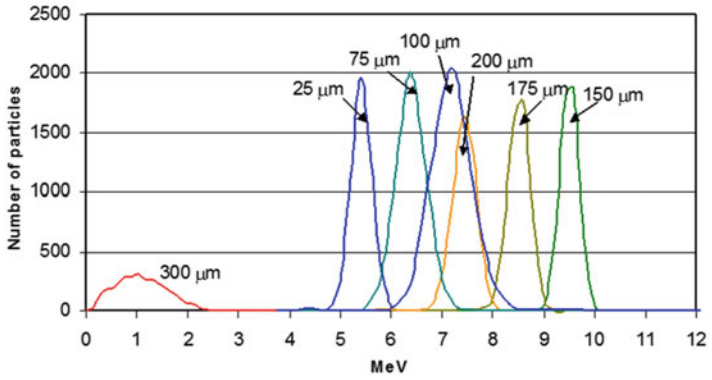

Fig. 11.16 As the thickness of the wire increases, the energy deposited into the proton detector increases up to a maximum of 10 MeV and then decreases [27]

We next calculate the energy deposited into the Si detector. With the geometry shown in Fig. 11.15 and the algorithm explained earlier for the D–^{3}He protons, the SRIM code can be used to compute the energy deposited into the Si detector. The peaks generated using 5,000 particles in the SRIM code for various values of x (i.e., 25, 100, 150, 175, 200 and 300 μm) are plotted in Fig. 11.16. It is observed that up until $x \sim 150$ μm, the energy deposited into the Si detector increases. Beyond that thickness the energy deposited decreases.

Assuming x in Fig. 11.15 is small, the maximum distance through which the D–^{3}He protons would have to traverse before reaching the detector 2L is around 300 μm (see Fig. 11.16). The protons born on the side facing the detector have little material to attenuate their energies and hence contribute to the main peak. But as shown in Fig. 11.14, those protons born behind the front face of the wire (with respect to the detector), including some of those born at an angle, must pass through more material than δ before exiting the wire. This effect is responsible for the counts that appear in the right wing of Fig. 11.12. Further insight into this can be obtained by using Eq. 11.7.

The angle θ in Fig. 11.14 is given by $\theta = \sin^{-1}(\frac{L}{R})$, where $L \approx \sqrt{2Rx - x^2}$ from Eq. 11.7. Substituting $L = 150$ μm and $R = 838$ μm, we get $\theta \gg 10.3$ °. Hence the right wing in the Fig. 11.12 mostly results from the two sections behind the front face of the detector spanning a total angle of 20.6 °. The total number of protons that come from the front face of the grid wire without any attenuation appear in the D–^{3}He peak at 5.5 MeV, while those protons born in the rear of the grid wire that are attenuated by the grid wire appear as the right wing in Fig. 11.12. The overall intensity of the right wing is low because the number of protons that make it to the detector from behind the grid wire is a small fraction of the total energy range which spreads from 0 to 10 MeV. The ratio of protons from the main peak to those from the right wing in Fig. 11.12 is ~ 10. Though the right wing is comprised of only 10 % of the total counts, this contribution is important for applications such as medical isotope production. An example of this is the use of the D–^{3}He protons to create positron emission tomography (PET) isotopes for medical treatment.

11.6 Noise Levels in Silicon Detectors

The noise level from the detector–preamplifier–amplifier combination is dominated by fluctuations in the detector leakage current, the inherent preamplifier noise, and the characteristics of the field effect transistor used in the input stage of the preamplifier.

One disadvantage of surface barriers in Si detectors is their sensitivity to light [2]. The thin entrance windows of the Si detector are optically transparent, and photons striking the detector surface can reach the active volume. The energy of visible light photons of 2–4 eV is greater than the bandgap energy of most semiconductors, so electron–hole pairs can be produced by photon interactions. Normal room lighting produces a very high noise level, but a 25-μm Pb foil "shielding" used in front of the Si detector acts as a barrier to suppress the visible light even though it is nearly transparent to x-rays (beyond 50 keV).

11.7 Natural Diamond Detectors

Natural diamond detectors (NDD) have proven to be the most temperature- and radiation-resistant devices (up to 200 °C and 10^{14} cm^{-2}, respectively) with a fast particle energy resolution of 1–5 % [28]. Diamond also has the highest bandgap energy (about 5.5 eV). This makes the device a preferred material of choice for a high-radiation environment. The reverse current or leakage current in diamond is near zero. While such detectors appear very useful for IEC diagnostics, they have not been used because suitable designs are not yet commercially available.

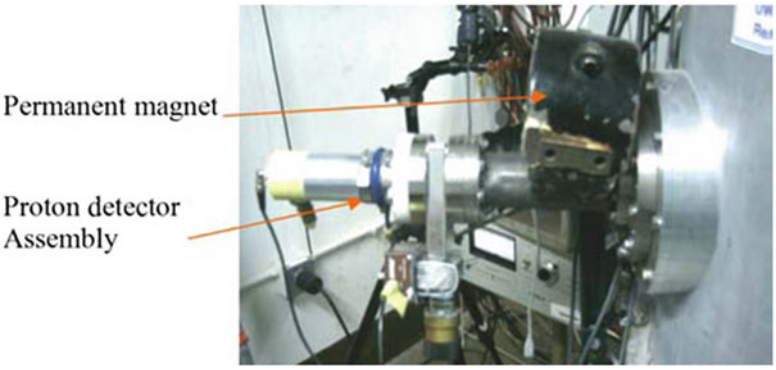

Fig. 11.17 A permanent horseshoe magnet is used on the detector channel to deflect the electrons away from the detector. In this case the detector is mounted in a short tube section that leads directly to a beam port on the IEC [6]

11.7.1 Electron Noise

Proton detectors also undergo bombardment by electrons accelerated toward the anode (chamber wall) associated with secondary electron emission from the grid (discussed in Chap. 5). The maximum energy that these electrons can have is equal to the cathode grid potential. This is well below the MeV energies of the protons. However, the electrons are copious in number and can produce significant background "noise" in the detector signal. If this noise level is too high, there are ways to reduce it. Because electrons are much lighter than the ions, they can be easily deflected using a magnetic field. Another approach is to increase the thickness of the Pb shielding foil on the detector face. A disadvantage is that this will also result in a reduction of the proton flux. Thus the shield foil thickness should be selected such that most protons make it to the detector, while the less energetic electrons are stopped.

One other way to reduce the electron noise is to deflect it away from the detector. Rutherford was the first to use magnetic fields to separate the three kinds of radiation emanating from the naturally radioactive materials. It is relatively easy to implement a magnetic field in the Si detector assembly. The magnetic field strength must be selected to avoid a significant effect on the proton trajectory while the electrons are deflected from hitting the detector face. Fields of the order of 0.1 T are adequate to deflect electrons without significantly affecting proton trajectories. Permanent magnets can provide field strengths of this magnitude. A permanent magnet was used to reduce the electron noise on the proton detector channel in the Homer experiments at the University of Wisconsin [29]. This setup is shown in Fig. 11.17.

One issue about using a magnetic field with a silicon detector is that the field may induce the Hall effect in the detector. This could lead to pulse pileup, causing a faulty measurement. However, in cases to date where permanent magnets have been used, the Hall effect has been too weak to present a problem.

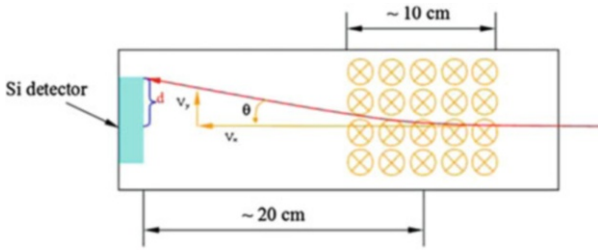

Fig. 11.18 Schematic of the approximate dimensions of the detector port with the magnetic field. Though the magnetic field typically has some fringing, it is reasonably constant over the 10-cm length of the horseshoe magnet shown in Fig. 11.17 [29]

11.7.2 Calculation of the Proton Deflection Inside the Detector Port

A schematic of the silicon detector setup in the port containing the magnetic field is shown in Fig. 11.18. The gyroradius of a 3-MeV D–D fusion proton in a 0.15-T B-field is 1.66 m, which is much longer than the length over which the magnetic field acts. Thus the proton deflection will be small and is assumed to be approximately a straight line in the perpendicular direction. The velocity of the particle (V_x) is assumed to be constant in the x direction and it is on the same order as the initial proton velocity V_p.

The proton accelerates in the y direction. Its velocity V_y is calculated as follows:

$$V_y = a_y \times t, \tag{11.9}$$

$$\text{where } a_y = \frac{F_y}{m_p} = \frac{qV_pB}{m_p}. \tag{11.10}$$

For the present case, $B = 0.15$ T, $m_p = 1.67 \times 10^{-7}$ kg, and $q = 1.6 \times 10^{-19}$ C. The electron path is assumed to be in the field of influence (10 cm). Hence a 3-MeV D–D fusion proton's speed is

$$V_x \sim V_p = \sqrt{\frac{3.0 \times 10^6 \times 1.6 \times 10^{-19}}{1.67 \times 10^{-27}}} = 1.7 \times 10^7 \text{m/s} \tag{11.11}$$

$$\Rightarrow \text{a}_\text{y} = 2.4 \times 10^{14} \text{m/s}^2. \tag{11.12}$$

Assuming that the proton is in the influence of the field for 10 cm as shown in Fig. 11.18, the time that the proton takes to traverse the field is given by

$$t \approx \frac{0.1m}{V_p} = 5.9 \times 10^{-9} \text{s}. \tag{11.13}$$

The angle of deflection θ in Fig. 11.18 after the proton traverses the 20-cm path from the midplane of the magnets to the detector is given by

$$\theta = \tan^{-1}\left(\frac{V_y}{V_x}\right) = 4.7^\circ, \tag{11.14}$$

$$\therefore\ \mathrm{d} = 20 \tan\theta = 1.64\ \mathrm{cm}. \tag{11.15}$$

The radius of the detector is only 1.96 cm, so a significant number of protons can miss the detector, especially those that arrive at an angle. However, if the proton detector is calibrated in place with the B-field, these losses are accounted for in the calibration.

11.7.3 Fusion Ion Doppler (FIDO) Diagnostic

The charged particle detector in the Fusion Ion Doppler (FIDO) diagnostic is a silicon detector. It builds on the fact that most unambiguous information about the fusion product energy is provided by the silicon detector. The preliminary observation of the manner in which the silicon detector isolates the parallel and antiparallel velocity shifts from the remainder of the possible fusion product velocities (as shown in Fig. 11.19) was performed by Murali using single loop grids [6]. This silicon detector allows us to isolate the parallel and antiparallel components of v_{cm}, and it is relatively straightforward to unfold the line-averaged velocity spectrum of the deuterium reactants that create the detected fusion products.

The x-ray noise in the detector is one major problem, because the noise almost entirely washes out the energy spectrum from heavier tritons from the fusion reactions and creeps into the spectrum of the protons (illustrated in Fig. 11.19). In order to reduce the x-ray noise and to protect the silicon detector, a thin Pb foil (25 μm) is generally used, but the presence of this foil skews the results further. Boris developed a FIDO diagnostic that handles this noise issue by moving the silicon detector completely out of the line of sight of the x-rays emanating from the device as shown in Fig. 11.20 [30].

Because the silicon detector in the FIDO no longer has a protective Pb foil, a complete noise suppression of visible light is necessary. To eliminate signal from visible light, a 300-nm thick reflective coating was added to the charged particle detectors used in the FIDO diagnostic. The thickness of the coating was chosen to eliminate penetration from optical wavelength photons, while not perturbing the energy spectra of the fusion products that must also traverse the light shield.

Though the 300-nm coating was effective at eliminating noise in the charged particle detector for low cathode voltages, it was not very effective at higher cathode voltages. The signals were essentially noise-free below 50-kV cathode potentials, and both tritons and protons could be detected. However, between 40 and 50 kV,

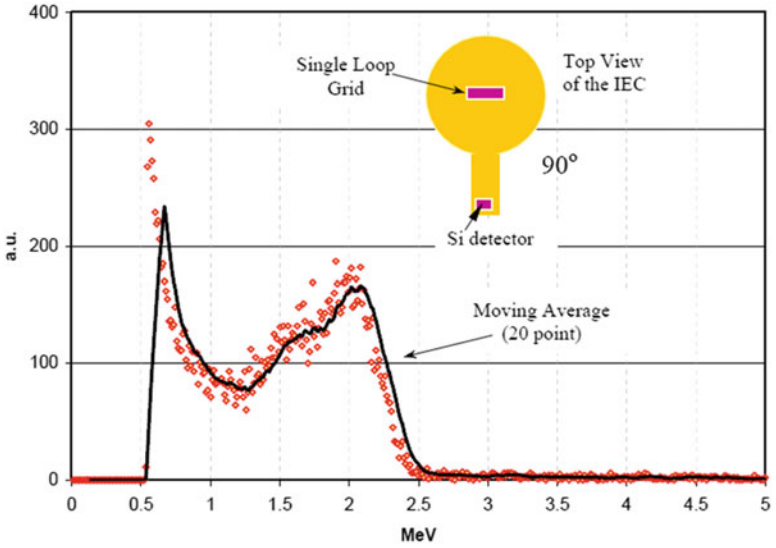

Fig. 11.19 A double peak is observed in the D–D proton data for 50-kV applied voltage when a single loop is used as the central grid with face-on orientation (90°). A 20-point moving average fit to the proton data shows a double peak feature at ~1.7 and ~2.0 MeV. The noise signal from the x-ray is large enough that it affects the left peak and somewhat skews the observations. Due to the presence of the Pb shield, the protons appear at different energy than their true energy

there was an abrupt 10^4 increase in the noise level. Previous work indicates that this transition stems from negative deuterium ions and fast neutrals created in the IEC device streaming outward due to acceleration by the cathode potential. The details of the negative-ion spectra can be found in work by Boris and colleagues [32]. The current density of negative ions in the bending arm was measured to be ~1 μA/cm^2 and the fast neutral flux is likely to be of even greater magnitude. Charged particle detectors are typically saturated when measuring signals that exceed 10^6 cps. A deuterium ion current density of ~10 μA/cm^2 is required to achieve saturation in the detectors used for this diagnostic. The deuterium anion energy spectra generally have a median energy of one-half the cathode voltages [30, 31]. The FIDO diagnostic has shown that the energy spectrum of energetic deuterons within the University of Wisconsin IEC device contains very few deuterons at or near the cathode energy, at least for background gas pressures between 0.25 and 4 mTorr. This work, in addition to theoretical calculations, indicates that charge exchange processes that dominate at energies of a few keV are largely responsible for this effect. From the observations of the results from FIDO diagnostic, it was concluded that a reduction in the background gas density will simply lead to lower fusion rate as the majority of the fusion reactions are between the fast ions and the slow background neutrals. In order to attain significant amounts of fusion while maintaining an energetic ion population with nearly the full cathode energy, the ion source region must be separated from the main IEC chamber and the IEC chamber must be differentially pumped with respect to the ion source.

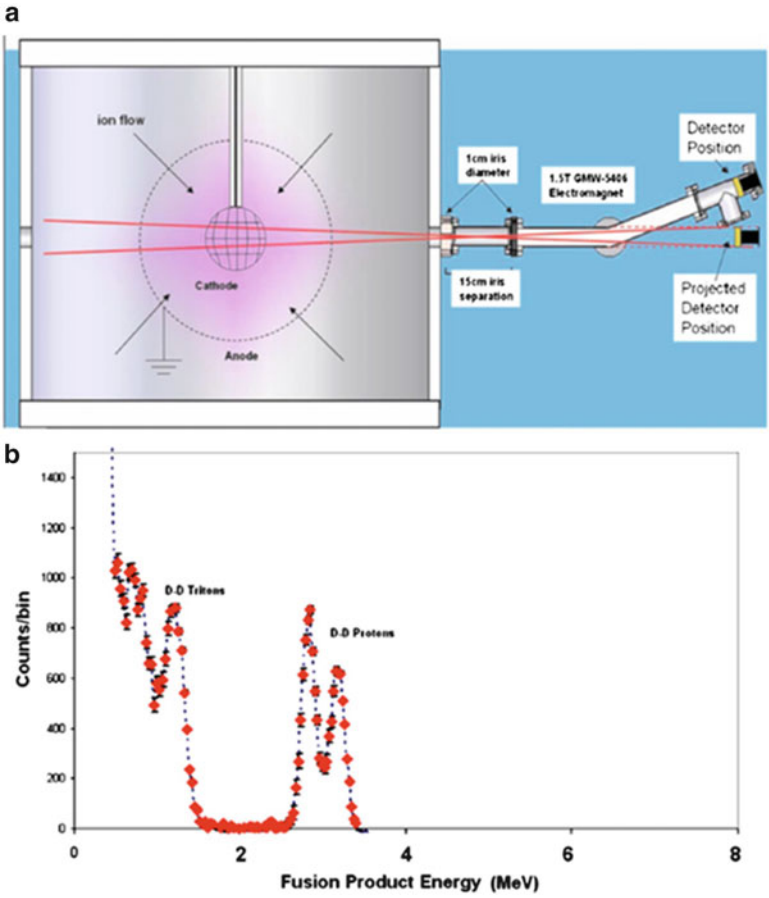

Fig. 11.20 (**a**) Schematic of the FIDO diagnostic illustrating how the silicon detector is moved out of the path of the x-rays. (**b**) Raw data taken at 70-kV cathode voltage, 30-mA cathode current, and 1.25-mTorr background pressure [31]

11.8 Scintillation Detectors

Scintillation detectors were one of the first detectors developed to detect radiation, because these detectors could be used with simple photographic film acting as a light sensor. However, with the arrangement shown in Fig. 11.21, the light sensor can be a photodiode or photomultiplier, as well as photographic film. The choice of the detector depends on the response time desired, the kind of radiation, and its intensity.

Scintillation detectors are of several types, classified according to their state – solid, liquid, or vapor – based on their chemical nature (organic or inorganic). The scintillation mechanism itself is dependent on the crystal lattice structure of the scintillator material. Such detectors have been used for the detection of positron

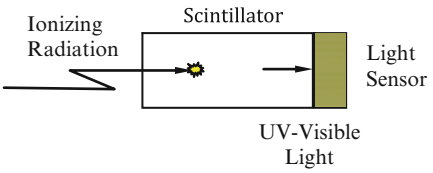

Fig. 11.21 Schematic of the operating principle of the scintillation detectors

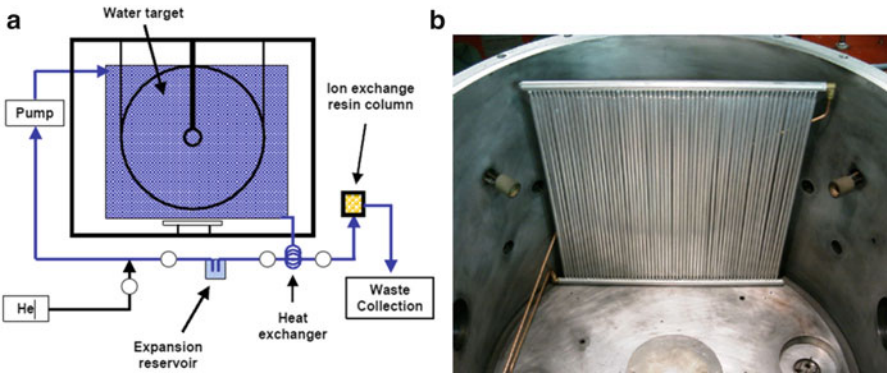

Fig. 11.22 (**a**) Schematic diagram of isotope production system. (**b**) A volume of water is continually circulated through a containment apparatus inside the IEC chamber [33]

emission tomography (PET) isotopes created in IEC devices [33]. An IEC device used for PET isotope production at the University of Wisconsin is shown in Fig. 11.22. The energetic protons (14.7 MeV) from the D–^{3}He reactions penetrated the thin-walled tubes shown in Fig. 11.22b and created short-lived medical isotopes.

As water circulated through the device, medical isotopes accumulated in the ion exchange resin column (shown in Fig. 11.22a). A NaI scintillation detector was used to measure the concentration of the PET isotopes generated in this column [34]. Further information on this application is given in Chap. 12.

11.8.1 Negative Ions in Gridded IEC Devices

The contribution by fast neutrals from charge exchange reactions in IEC devices has been investigated extensively by Emmert and Santarius [35] at the University of Wisconsin, Madison, as well as Khachan, Moore, and Bosi at the University of Sydney [36]. Important phenomena that have not been considered to date are electron attachment and charge-transfer reactions that create deuterium anions within IEC devices. Electron attachment involves the attachment of a thermal electron to a neutral deuterium gas molecule, in an excited vibrational state, thus producing a negatively charged deuterium molecule.

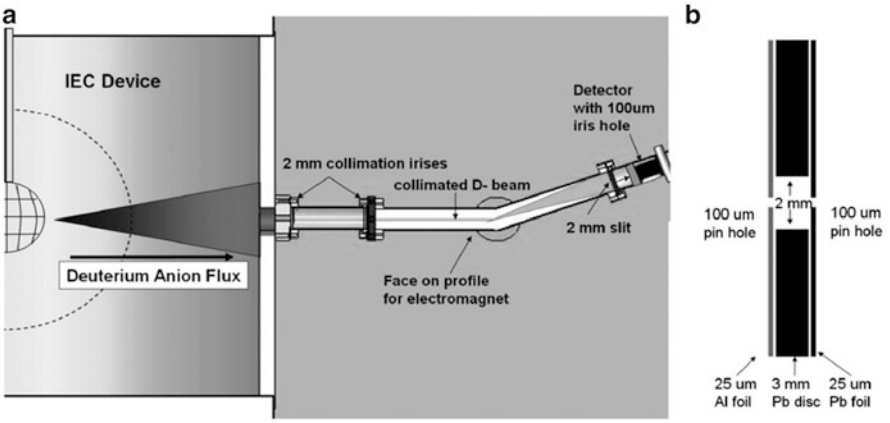

Fig. 11.23 (**a**) Schematic of the magnetic deflection-energy analyzer. (**b**) A close-up of the construction of the 100-μm iris hole (not to scale) used to both limit particle flux to the detector and narrow the energy resolution of the diagnostic. The 100-μm iris sits on the face of the detector

The detection of deuterium anions in the University of Wisconsin IEC device was accomplished with two separate diagnostics: a magnetic deflection experiment (illustrated in Fig. 11.23) in which a variable electromagnet was used to measure the energy of negative ions with a specific charge-to-mass ratio streaming from the center of the device and a current collection plate with secondary electron suppression (i.e., a Faraday trap, illustrated in Fig. 11.24) coupled with a weak permanent magnet tuned to deflect electrons emitted from the cathode but allow the detection of negative ions born within the anode.

11.8.2 Magnetic Deflection-Energy Analyzer

The magnetic deflection-energy analyzer diagnostic shown in Fig. 11.23 operates by first collimating the divergent flux of deuterium anions emanating from the IEC into a narrow beam with a pair of 2-mm-diameter lead irises. This beam of deuterium anions is then passed through a variable electromagnet, which causes the beam to deflect in a direction perpendicular to both the velocity of the beam and the applied magnetic field. The angle of the deflection of an incoming particle, with charge q and mass m, when passing through a constant magnetic field $\vec{B}$ is given by the following expression:

$$\sin(\theta_d) = \frac{at}{v}, \tag{11.16}$$

where $a = \left|\frac{q}{m}\left(\vec{v} \times \vec{B}\right)\right|$ is the magnitude of the acceleration due to the magnetic field, t is the time spent in the magnetic field, and ν is the velocity of the ion.

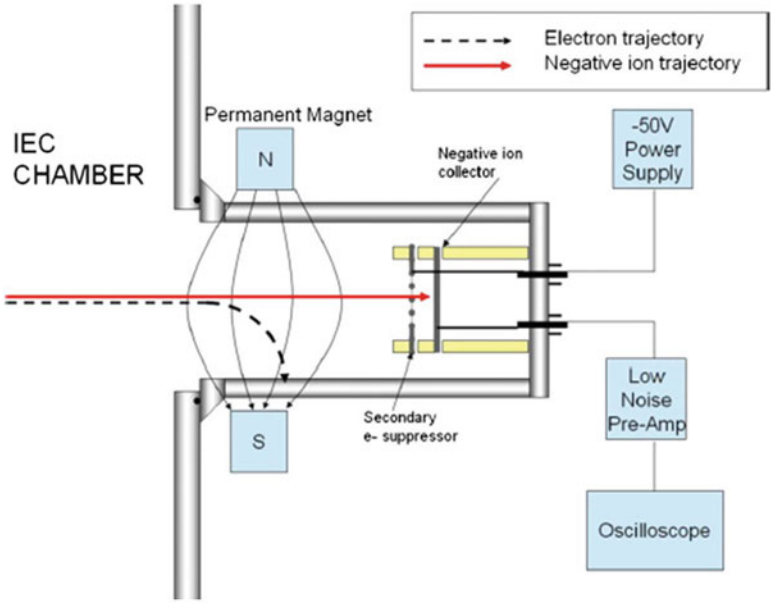

Fig. 11.24 Schematic of the Faraday cup diagnostic illustrating differing trajectories of negative ions and electrons. The negative-ion collector plate and secondary electron suppressor grid are isolated from the chamber and each other by ceramic standoffs. The magnetic field is 100 G, and its orientation has been rotated by 90° to show the spatial extent of the magnetic field [42]

The time t can be defined as $t = l/\nu$, where l is the path length of the particle in the region of significant and nearly constant magnetic field. The acceleration due to the constant magnetic field can be expressed as

$$a = \frac{qpB}{m^2}, \tag{11.17}$$

where p and B are the magnitudes of the ion momentum and magnetic field, respectively. Therefore Eq. 11.16 can be simplified as

$$\sin(\theta_d) = \frac{qlB}{p}. \tag{11.18}$$

Equation 11.17 indicates that the deflection angle θ_d is dependent on the charge-to-mass ratio, the spatial extent of the magnetic field, and magnitude of the magnetic field.

Once the anions have been deflected by the electromagnet, they will continue toward the detector until they encounter a smaller lead iris with a diameter of 100 μm. This iris samples a narrow portion of the resulting fan-shaped beam of anions, consequently, isolating a narrow band of the velocity spectrum of deuterium anions

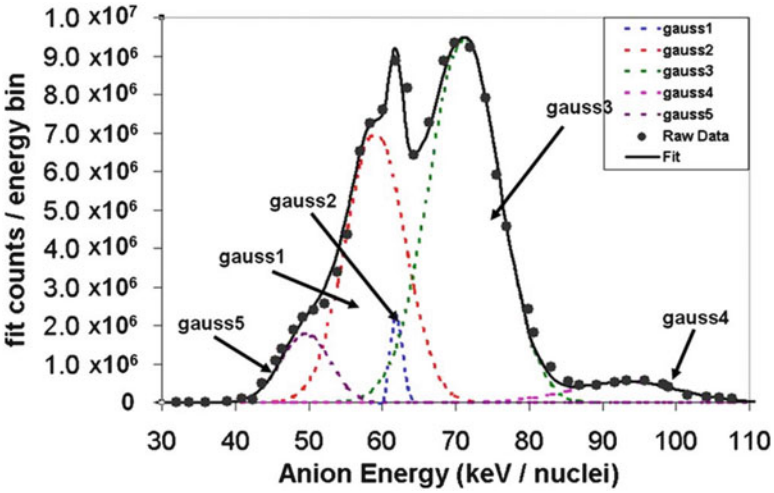

Fig. 11.25 Detailed view of the 100-kV, 30-mA, and 2-mTorr data set. It shows the five Gaussian "least-squares" fit used to accurately replicate the structure from the data set. The fits "gauss1," "gausss2," and "gausss3" account for deuterium anions produced through D_3^+/D^-, D_2^+/D^-, and D^+/D^- charge-transfer reactions, respectively. The "gauss 4" fit is accounted for by D^- formed at the cathode via thermal electron attachment to background neutral gas. The "gauss5" fit is accounted for by metastable D_2^- formed via thermal electron attachment at the cathode [32]

emanating from the IEC device. A silicon-charged particle detector is used to detect the portion of the beam passing through the lead iris. Counts from the silicon-charged particle detector are collected by a single-channel analyzer (SCA). The count rate in the SCA was recorded as a function of applied magnetic field from an electromagnet with a 76-mm-diameter cylindrical cross-section magnet pole. The magnetic field was measured using a Gauss meter with the transverse magnetic field probe mounted to the side of the bending section of the experiment. Spectra as a function of magnetic field were obtained using this setup. The SIMION-charged particle optics software package [37] was then used to model and predict deuterium anion trajectories in the magnetic field produced by the electromagnet. Thus, for the magnetic field settings applied during the experiments, the energy of anions directed into the charged particle detector could be calculated, yielding a measure of number of ions/(keV amu). The small iris allows the acquisition of high-resolution energy spectra of the deuterium anions. The resolution of the magnetic deflection-energy analyzer is dependent on the tenability of the electromagnet, the width of the final iris (100 μm in this case), and fidelity of the magnetic field simulations in SIMION. The magnetic field was measured to remain constant to within 50 G. Assuming an accurate simulation of the magnetic field structure energy resolution of ±1 keV/nuclei is achievable using this setup.

Figure 11.25 shows a typical voltage scan performed on the University of Wisconsin device with the cathode current and background pressure held constant at 30 mA and 2 mTorr, respectively. The spectra are shown offset from each other

on the y-axis to illustrate the manner in which the spectra evolve as the cathode voltage is changed.

While the magnetic deflection-energy analyzer was able to measure the energy spectra of negative ions to a resolution of ~1 keV, the Faraday cup was used as a means of confirming the presence of deuterium anions and to examine the manner in which the negative-ion current scales with the operation parameters. The Faraday cup will be discussed later in the section on Faraday diagnostics.

11.9 Laser-Induced Fluorescence of Well Profiles

As discussed in Chaps. 2 and 13, potential well profiles in an IEC fusion device play a key role in moving to future IEC beam–beam fusion devices. In an effort to resolve the issue of presence of multiple wells within the cathode of a present IEC device, Yoshikawa and colleagues [38] embarked on direct measurements of the electric fields within the cathode. To achieve this goal, they used Laser-Induced Fluorescence (LIF), measuring the electric fields directly and unambiguously using the Stark effect. Their initial examination of the application of the LIF method to an IEC device has revealed some important requirement that must be kept in mind: a wavelength resolution of about 0.4 nm is required, and a spatial resolution of 1 mm requires a $2^1{}_S$ He atom density of more than 10^{10} cm^{-3}.

Yoshikawa and colleagues used a Nd:YAG laser-pumped dye laser for the diagnostics of the potential well in their IEC device. Measurements showed a double well potential profile for the first time in a He plasma [39]. Later studies examined theoretical predictions of the effect of angular momentum on the spherically converging ion beams on the potential profiles [40].

Using LIF, Yoshikawa and colleagues first set out on measuring the potential profile in a "Star" mode configuration as the fusion rate is higher with this mode when compared to "central spot" mode.

For application of the LIF method, however, because the "Star" mode discharge appears for relatively high voltage of the IEC device, it is predicted that the beam-induced electric fields inside the hollow cathode would be small due to smaller beam perveances compared with the "center spot" mode. This calls for the LIF transition with more electric field-sensitive capability. To meet this requirement, the transition of HeI $n = 4$ (2^1s to 4^1D; 0.05–0.5 kV/cm) was chosen instead of the usual $n = 3$ (2^1s to 4^1D; 0.5–5 kV/cm), and the former is expected to be about one order of magnitude more sensitive to the electric fields, as is shown in Fig. 11.26.

As schematically shown in Fig. 11.26, the metastable helium atoms at the 2^1s state are excited to the n^1D state by the laser (397.3 nm for $n = 4$ and 504.2 nm for $n = 3$, respectively) with two different polarizations (e_{Lx}, e_{Lz}) through the forbidden transitions, i.e., the Stark-induced electric dipole moment and electric quadrupole moment (QDP) transitions [41]. The LIF (HeI; 492.2 nm for $n = 4$ and 667.8 nm for $n = 3$, respectively) is then observed through a lens (L2 in

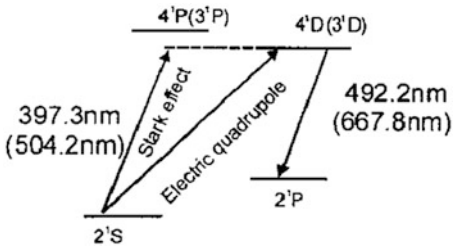

Fig. 11.26 Relevant energy diagram for the LIF transitions of HeI in electric fields [38]

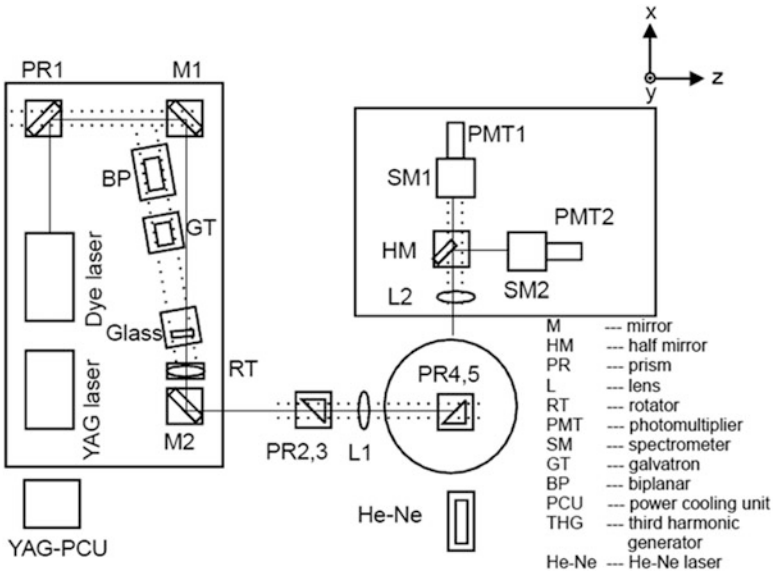

Fig. 11.27 Experimental setup for LIF diagnostics [39]

Fig. 11.27) along the x-axis. Both the polarized components are detected for both polarized ions of the injected laser, namely, $I_z(e_{Lx})$, $I_y(e_{Lx})$, $I_z(e_{Lz})$, and $I_y(e_{Lz})$. To measure the spatial profile of the electric field, both the lens L2 and the laser injection position are moved synchronously in the z-direction.

In order to gain the improved signal-to-noise ratio, the LIF method for $n = 4$ transition was examined instead of $n = 3$ used previously [42, 43]. The transition probability of the Stark excitation depends on the electric field strength, while in contrast that of QDP excitation does not. Therefore, for evaluating the electric field, the intensity ratio of the two components is evaluated. The polarization of fluorescence due to the Stark excitation is quite different from that due to the QDP excitation. Use of the difference thus makes it possible to derive the intensity ratio of the Stark to the QDP components.

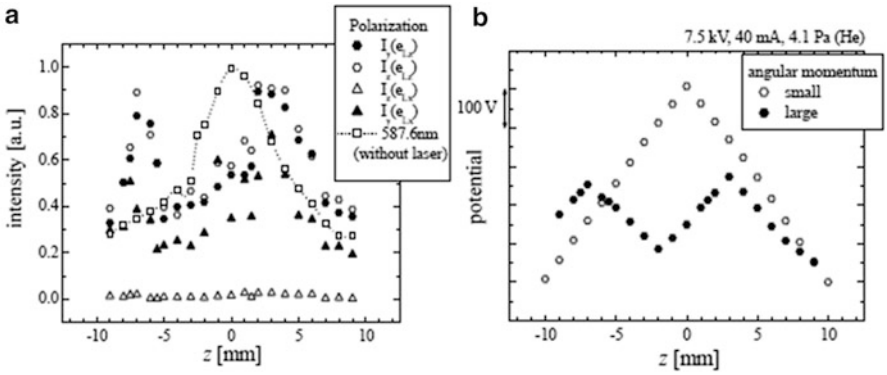

Fig. 11.28 (**a**) Profiles of four polarized components. (**b**) Potential profiles for ions with relatively larger (*solid circles*) angular momenta [39]

Using the degree of polarization P, defined by [38]

$$P = \frac{I_z(e_{Lx}) - I_y(e_{Lx})}{I_z(e_{Lx}) + I_y(e_{Lx})}, \tag{11.19}$$

the electric field E can be calculated by

$$E = C^x \sqrt{\frac{2(P+1)}{1-3P}}. \tag{11.20}$$

Here $C^x = 0.28$ kV/cm for $n = 4$, which is much smaller than $C^x = 1.96$ kV/cm for $n = 3$.

From the measured LIF intensities and derived electric fields, considering the error limits, preliminary results showed no noticeable potential or electric fields compared with the "center spot" mode discharge. This was thought to be due to much smaller perveance of the "Star" mode compared with the "center spot" mode.

However, later measurements of spatial profiles of LIF peak intensity are plotted in Fig. 11.28a for ions with enhanced angular momenta together with the intensity profile of the radiation at 587.6 nm, which corresponds to the visible image. The angular momentum was accidentally enhanced when a small chip of the high-voltage stalk broke off unintentionally. This incident led to added understanding of the measurement. Profiles of three polarization components, $I_z(e_{Lz})$, $I_y(e_{Lz})$, and $I_y(e_{Lx})$, are considered to approximate the profiles of collisionally excited He metastable atoms (2^1S), which are sensitive to electron temperature in the range $T_e \leq 20$ eV. The peaks are thus thought to correspond to the potential peaks where electrons with ample energies are expected to exist.

On the other hand, the intensity of $I_z(e_{Lx})$ is due to the Stark effect, with which electric fields can be evaluated together with $I_y(e_{Lx})$ on the basis of Eqs. 11.19 and 11.20. The potential profiles for the two cases thus obtained are shown in Fig. 11.28b. It is seen that a double well potential forms for ion beams with larger angular momenta, but that

for ions with smaller angular momenta, the potential has only one peak that is much steeper compared with the double well potential, consistent with theoretical predictions [40].

In conclusion, these LIF measurements demonstrate that this is a very powerful diagnostic for IEC potential profile studies. However, the equipment and the diagnostic setup are very demanding and require dedicated work.

11.10 Spectroscopic/Langmuir Probe Measurements of Ion Energies

Khachan and colleagues [44] using Doppler shift spectroscopy and a single-ended Langmuir probe to study the core plasma in an IEC device with modified cathode as shown in Fig. 11.29. They found a direct correlation between the ion energies and the spatial plasma potential. It was shown that the ion energy is a maximum at the point where the potential is the deepest, which occurs about halfway between the center and the cathode radius. The diagnostic techniques employed provide good insight into these measurement methods.

11.10.1 Langmuir Probe Measurements

The positive bias range of a typical current–voltage plot from the Langmuir probe is shown in Fig. 11.30a. The plasma potential was obtained from the intersection of the two straight line extrapolations [45], as shown Fig. 11.30a. A plot of the measured plasma potential at different radial positions is shown in Fig. 11.30b. The potential at the center is ~ −600 V but falls away to ~ −1,100 V at approximately 10-mm radial distance before starting to rise again. The potential in the center was observed to be ~30 % of the applied potential to the grid (−2,000 V), consistent with the previous results that show the ion energies are approximately at 20–25 % of the cathode grid potential for this grid size [46]. Figure 11.30b also shows the expected vacuum potential obtained using the commercial software SIMION, which was used to solve the Laplace equation for the present grid configuration. As a result, Khachan and colleagues concluded that the center potential cannot reach the applied potential of −2,000 V but is lower than that measured by the Langmuir probe. Furthermore, the measured increase in potential at the center implies a possible buildup of positive space charge thus producing a so-called virtual anode, such as that observed earlier through indirect measurements by Gu and Miley [47]. For these measurements the zero potential was taken to be at the outer grid.

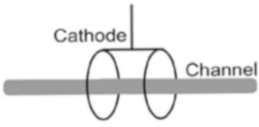

Fig. 11.29 Two-ring cathode to generate a one-dimensional IEC [44]

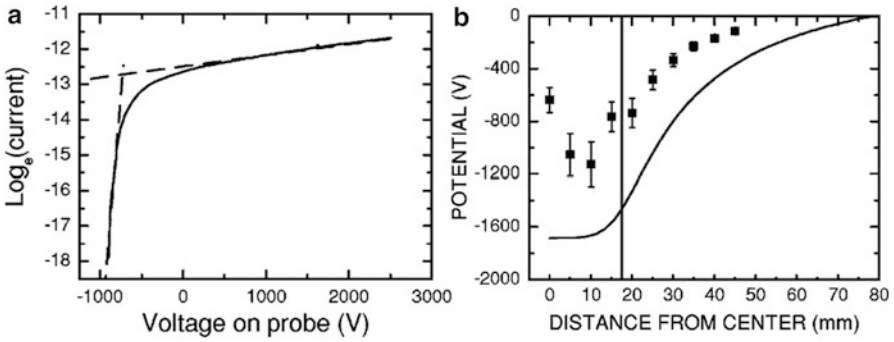

Fig. 11.30 (**a**) Typical current–voltage curve from a single-ended Langmuir probe. (**b**) Plasma potential as a function of the distance from the center at 5 mTorr and 22-kV cathode potential. The *solid line* is the calculated vacuum potential along a channel [44]

Though these results are in agreement with double-probe measurements on a similar device, one cannot be totally sure that the measured potentials were not due to a perturbation of the actual potentials due to the presence of the probe [48]. For this reason, the potentials were compared with noninvasive Doppler shift spectroscopy measurements.

11.10.2 Ion Energy Measurements

Doppler shift spectroscopy was used to determine the ion energies at different points along a channel. A typical Doppler-shifted spectrum taken along the axis of a channel (shown in Fig. 11.31) consists of a sharp central peak with a broadened base. Due to the symmetry of the spectrum, only one-half of the spectrum (the redshifted part) is shown. The central peak is the characteristic hydrogen Balmer H_α line and results largely from electron impact with atomic and molecular hydrogen. The broadened base is also due to electronic processes, explained elsewhere [49].

The three peaks highlighted by their Gaussian fits shown in Fig. 11.31 are of interest for ion energy measurements. It has been shown that these peaks are due to the following three charge exchange reactions [46]:

$$\begin{aligned} H^+ + H_2 &\rightarrow H^* + H_z^+ \\ {H_2}^+ + H_2 &\rightarrow H^* + H + H_z^+ \\ {H_3}^+ + H_2 &\rightarrow H^* + H_2 + H_z^+ . \end{aligned} \tag{11.21}$$

Here H_2 is the background gas, and H^* represents the resulting fast excited neutrals. These neutrals have trajectories that are in the same direction as the incident ions [48]. Beam spreading is between 1 ° and 2 °, depending on the energy of the incident beam. Moreover, the total energy of the resulting fragments from the reactions is approximately equal to the energy of the incident ion. Any energy

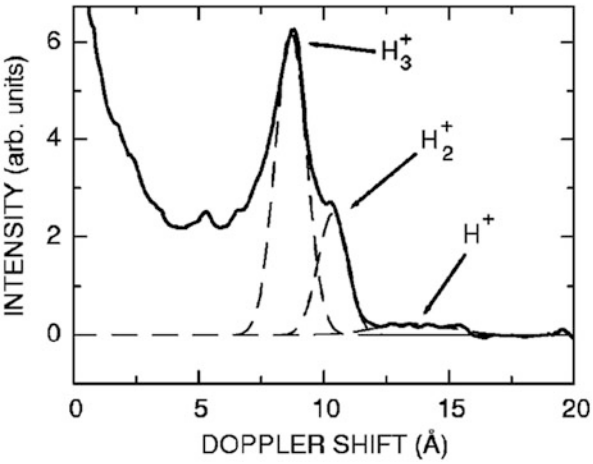

Fig. 11.31 Doppler-shifted spectrum along the axis of a channel at 5 mTorr and 210 kV cathode potential. The labels of H_3^+, H_2^+, and H^+ shown indicate the original particle that underwent a charge exchange collision leading to the Doppler-shifted H_α line. The *dashed lines* are Gaussian fits to the three Doppler-shifted peaks [44]

lost to electronic or vibrational excitation is only a few tens of eV and is considered negligible compared to the keV range of energies considered. It has also been shown that although the most intense Doppler-shifted peak is due to charge exchange of the H_3^+ ions, the most abundant species is H_2^+ forming about 60 % of the ion density in the present device [46]. The kinetic energy, K, of an excited atomic hydrogen is given by

$$K = \frac{m_H c^2 (\Delta\lambda)^2}{2\lambda_0^2 \cos^2\theta}, \tag{11.22}$$

where m_H is the mass of atomic hydrogen, θ is the angle between the observation direction and the axis of the channel, $\Delta\lambda$ is the Doppler-shifted wavelength of the Hα wavelength, λ_0 (= 656.3 nm), and c is the speed of light.

Any energy lost to electronic or vibrational excitation is only a few tens of eV and is considered negligible compared to the keV range of energies considered here. Furthermore, it has been shown that although the most intense Doppler-shifted peak is due to charge exchange of the H_3^+ ions, the most abundant species is H_2^+ forming about 60 % of the ion density [46]. These measurements appear to be definitive, but for some reason disagree in detail with the direct measurements made by Boris [30] using a Faraday cup diagnostic, wherein the D_3^+ concentration was >50 % for 2-mTorr chamber pressure; hence at higher pressures the concentration of D_3^+ (and not D_2^+) should be much higher. This discrepancy between the two measurements is due to the difference in the IEC devices used in these two analyses.

A typical Doppler-shifted spectrum recorded at 16 mTorr when the channel axis was at 30 ° with respect to the monochromator line of sight is shown in Fig. 11.32. In this figure, the H_2^+ and H_3^+ peaks are not resolved, and there is an additional low-energy peak. The 30 ° angle will naturally move the peaks closer together as a result of the cos θ dependence of the Doppler shift and therefore the merged H_2^+

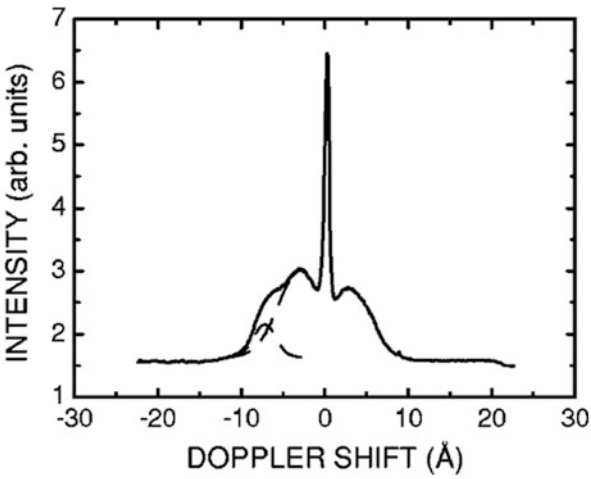

Fig. 11.32 Doppler-shifted spectrum taken at 30° with respect to the channel axis at 16 mTorr and 210 kV cathode potential. The *dashed lines* are Gaussian fits to the blue Doppler-shifted spectrum [44]

and H_3^+ peaks start to approximate a single Gaussian. Because this peak appears on one side of the spectrum, it implies that, at this pressure, most of the incident ions do not continue past the center of the potential well. That is contrary to what is usually assumed in discussions of IEC at similar lower pressures. However, it is consistent with the Langmuir probe results that show a virtual anode that is less than the height of the applied potential.

Because the three peaks originate from particles with the same energy, we need only consider the Doppler shift of the most prominent peak (due to the H_3^+ charge exchange reaction) in order to measure ion energies at different positions [46]. Since the intensity of the peak associated with H_3^+ is much larger than the other two peaks, the position of the one Gaussian fit to the merged peak in Fig. 11.33 can be shown to be very close to the position of H_3^+ peak, only differing by about 5 % and no more than 10 % from the true position.

The ion energy as a function of distance from the center of the cathode is shown in Fig. 11.33. The position of the ring in the cathode is indicated by a vertical line on the graph. Note that the maximum energy is approximately halfway between the ring and the center, reaching a local minimum at the center. There seems to be a direct correlation between the plasma potential spatial profile shown in Fig. 11.33 and the probe measurements in Fig. 11.29, even though different-sized cathodes were used [44]. This result further confirms the validity of the plasma potential measurements and the buildup of plasma potential at the center resulting in a reduction of ion energy at that point. Laser-Induced Fluorescence (LIF) has been used by Yoshikawa and colleagues (discussed earlier) to show a similar buildup of potential, but it has also shown a possible virtual cathode at the center [38]. These measurements do not exclude the existence of the virtual cathode, but if it exists its potential is below the resolution of the instruments used.

Alderson and colleagues reported their extension of the Doppler-shifted spectrometry to Charge Exchange Emission Spectroscopy [50]. The observed

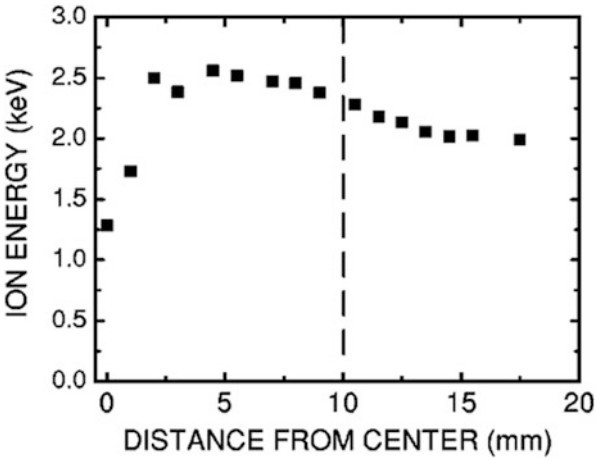

Fig. 11.33 Ion energy as a function of distance from the center at 16 mTorr and 210 kV cathode potential

wavelength of the photons emitted by excited atoms is Doppler shifted. Lighter species reach a higher velocity than the heavier species, allowing a measurement of relative accelerated molecular population as well as energy distribution information in a variety of IEC conditions. Initial studies on the IEC provided data on atomic and molecular species, spatially resolved species energy, and gas temperature. In the next step, experiments will be used to determine the molecular distribution in the IEC, to study ^{3}He behavior in the IEC, and to contrast ion and neutral behavior in the IEC. The technique is also being used to study plasma in the Helicon used for plasma injection into the IEC. The intensity of the Helicon plasma allows the measurement of molecular hydrogen lines. Theoretically, these lines can be used to measure gas temperature in the dense Helicon mode. Such spectroscopic analysis of the Helicon and IEC is possible in regimes that physical probes cannot survive.

In summary, Doppler shift spectroscopy was used to determine the spatial ion energy distribution in an IEC device. It was found that the maximum energy occurred halfway between the center and the cathode wire. This correlated with Langmuir probe measurements that showed that the minimum in the potential well also occurred at the same position as the maximum ion energy. These results suggest that there is a buildup of positive space charge in the center which can be interpreted as a virtual anode.

11.11 Diagnostics for an IEC Plasma Jet

Some specialized diagnostics have been employed by University of Illinois researchers to study the characteristics of the IEC space thruster HIIPER, described in Chap. 10. These include a gridded energy analyzer, Faraday diagnostics, and a force sensor. Each is described next.

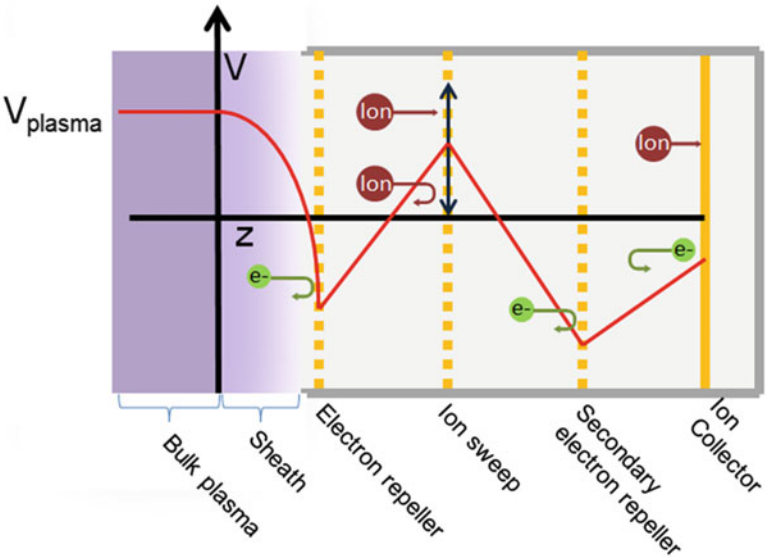

Fig. 11.34 Schematic showing the electrostatic potentials of the grids inside the gridded energy analyzer

11.11.1 Gridded Energy Analyzer

The major diagnostic employed to understand the HIIPER plasma jet ion–electron composition and particle energies is the gridded energy analyzer (GEA) [51–53]. The GEA, shown schematically in Fig. 11.34, consists of three electrically biased grids, one biased collection plate, and a floating aperture that limits the total current into the device. The first grid is called the electron repeller. It is negatively biased to repel all of the plasma electrons. The second grid, known as the ion sweep grid, is varied in potential from zero to a high positive value. Only ions with energy greater than the applied voltage will be collected as signal current. The third grid, called the secondary electron repeller, is slightly more negatively biased than the first grid to repel secondary electrons created from collisions with the ion collector plate or any of the other grids. The ion collector plate is also slightly negatively biased, though not as much as the second electron repeller, to give a slight energy boost to the ions for good signal collection.

As shown in Fig. 11.34, the electron repeller grid is connected directly to a high-voltage DC power supply. This power supply can supply the same voltage as the grid itself to make sure it can reject all electrons being accelerated away from the central cathode. A sawtooth function generator coupled to a 1-kW bipolar op-amp runs the ion sweep grid.

By changing the voltage of the ion sweep grid, the ion spectrum of the plasma jet can be obtained. The current collected is

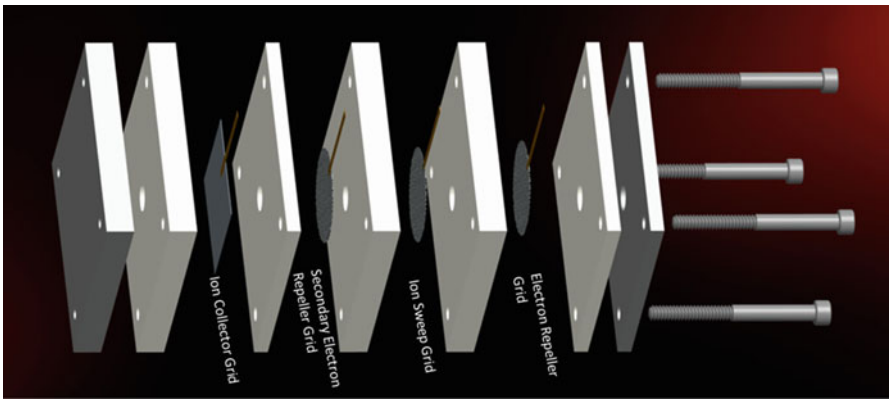

Fig. 11.35 Expanded three-dimensional model of gridded energy analyzer constructed to study HIIPER [55]

$$I(E)\alpha\int_{E_0}^{\infty} I(E)dE, \tag{11.23}$$

where E_0 is the minimum energy of an ion that can be collected. The GEA is a current integrated device, meaning that it collects all ion current above a threshold voltage. This device can give the spectrum, but in order to find the ion temperature, an assumption of the ion spectrum shape must be made. Typically a Boltzmann distribution of ion energies is assumed as a first approximation. It is also possible to obtain the ion spectrum using this diagnostic without making an assumption of its shape by introducing a small AC jitter signal on top of the sweep voltage. In that case, the peak-to-peak value of the current for each voltage jitter step allows a direct calculation of the spectrum [54].

A three-dimensional expanded model of the GEA is shown in Fig. 11.35. Macor insulation is used based on its high dielectric strength and machinability. The grid wires are 20 mesh stainless steel wire of 0.01-cm diameter. The wires are thin so they don't block too much of the jet and decrease the signal, but at the same time, they need to be robust enough not to melt under the heat load. For higher power settings, a tungsten wire grid of similar mesh and wire size can be used. The small aperture allows good radial spatial resolution as the GEA is moved across the plasma jet beam.

11.11.2 Faraday Cup Diagnostics

The Faraday cup diagnostic is operated by collecting negative ions on a 0.7-cm^2 aluminum current collection plate and suppressing the emission of secondary electrons from the plate with a transparent steel mesh biased to −50 V relative to the collection plate. With the University of Wisconsin IEC device, this configuration

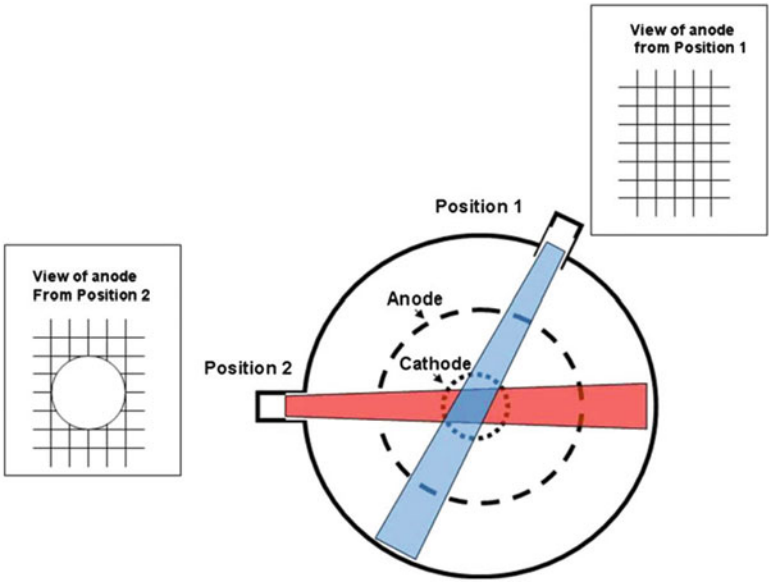

Fig. 11.36 The two positions and corresponding lines of sight on which the Faraday cup diagnostic was oriented

resulted in a negative current corresponding to the collection of electrons and negative ions diverging from the center of the device. A current collection diagnostic such as this must isolate the charged particle signal from negative ions streaming from the IEC and from the signal caused by secondary electrons born through fast positive ion impact at the device cathode. These secondary electrons are born as the cathode stream from the device with high kinetic energy, just as deuterium anions do. In order to isolate the negative ions from the high-energy electrons, a set of weak permanent magnets were used to create an ~100-G magnetic field transverse to the electron trajectory. This served to deflect the high-energy electrons away from the collection plate, while leaving the trajectory of the negative ions relatively unperturbed. This is illustrated in Fig. 11.36.

The secondary electron suppressor grid is isolated from the negative-ion collector plate by ceramic standoffs, and both of these metallic components are isolated from the chamber by additional standoffs. The negative-ion current collected by the Faraday cup is fed to a low-noise current preamplifier through isolated BNC feedthroughs. The preamplifier provides +5 V of bias to drive the negative-ion signal collection. The amplifier is able to measure negative-ion currents, a fraction of a nanoamp reliably on the 1 nA/V amplification setting. This signal is then fed to an oscilloscope. This allowed the total negative-ion current to be measured in addition to the spectral measurements made with the magnetic deflection-energy analyzer diagnostic. The Faraday cup diagnostic took measurements at two locations on the University of Wisconsin device. These are illustrated in Fig. 11.36.

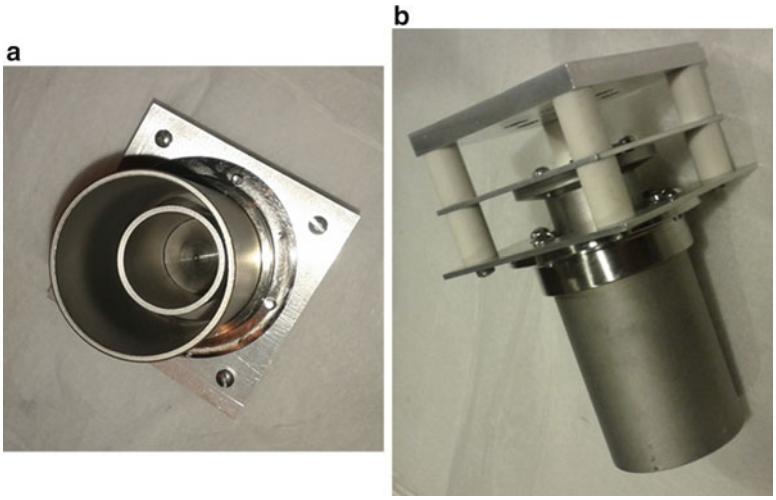

Fig. 11.37 The Faraday cup constructed to study HIIPER. (**a**) Top view with ground shield aperture removed to show conical insert at the base of the collection cup. (**b**) Side view showing the large spacing and electric isolation between collection cup and outer ground shield [55]

Negative ions observed in the device using a Faraday cup diagnostic consisted of a current collection plate with a secondary electron suppression grid, situated so as to collect the divergent negative-ion flux from the spherical potential well [56]. The Faraday cup diagnostic shown in Fig. 11.36 was used to corroborate the data from the magnetic deflection-energy analyzer and to make measurements of deuterium anion current at two positions around the device. This diagnostic indicated that the deuterium anion current was highly variable with angular position, indicating a strong dependence on device geometry. In addition, a total anion current of ~1 mA was calculated from the Faraday cup measurements.

Deuterium anion current densities as high as 8.5 μA/cm^2 have been measured at the wall of the University of Wisconsin IEC device, 40 cm from the surface of the device cathode with a detector assembly of admittance area 0.7 cm^2. This was the first time that such a current was reported from an IEC device. Energy spectra obtained using a magnetic deflection-energy analyzer diagnostic also indicated the presence of D_2^-, and D^- ions produced through thermal electron attachment near the device cathode, as well as D^- ions produced via charge-transfer processes in the region between the anode and cathode of the device.

The Faraday cup diagnostic (shown in Fig. 11.37) has been developed for the study and analysis of the jet mode plasma emanating from the cathode by Miley's group at the University of Illinois at Urbana–Champaign. It is used to measure the total charge flow of the HIIPER jet. While a Faraday cup is a common plasma diagnostic, this design employs special features due to the high jet power involved (this design builds on an earlier design). Several hundred watts of power can hit the Faraday cup with 10s

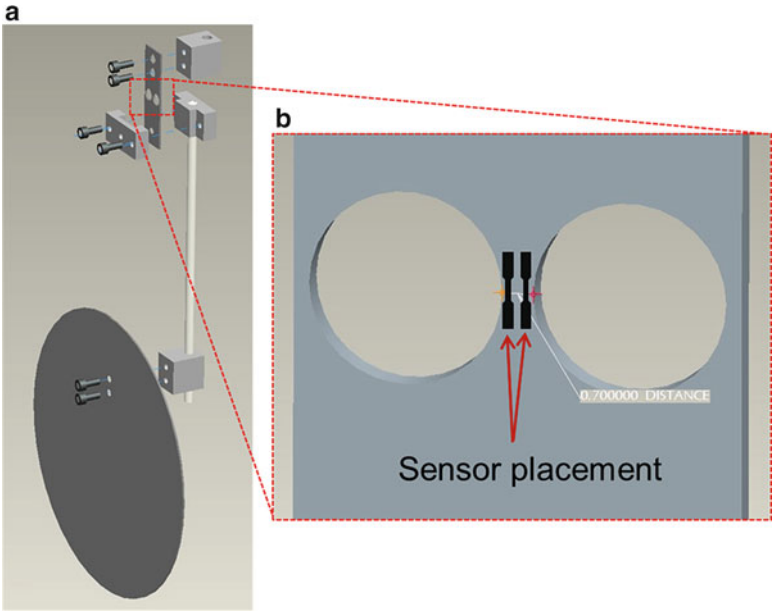

Fig. 11.38 (**a**) An exploded three-dimensional model of a piezoelectric force sensor. The round plate is 12 cm in diameter. (**b**) Two piezoelectric sensors on front, two on the back. The isthmus of stress concentrator is 0.70 mm wide

of mA currents while the voltage can be several thousand volts. Thus the Faraday cup was made large and robust to deal with the high current and voltages while the design is able to dissipate heat quickly to avoid damage to its structure. It is fabricated from alumina ceramic, stainless steel, and aluminum. An outer grounded sleeve around the inner cup minimizes plasma interaction with the outer sidewalls of the cup that may distort the measurement of the plasma jet current. It is mounted to a linear motion feedthrough that allows translation radially across the plasma jet.

11.11.3 Plasma Force Sensor

The plasma force sensor constructed for this work is very similar in design to that constructed by Chavers for use in testing the VASIMR electric thruster [57–59]. It consists of a cluster of piezoelectric sensors on a stress concentrator that measure the deflection of a lever arm connected to a titanium plate. When the plasma strikes the plate, the lever arm bends backward very slightly and this deflection is measured from the piezo sensors as a small change in voltage. Figure 11.38a shows a three-dimensional model of the force sensor showing how the sensors are placed. There are four sensors connected in a Wheatstone bridge configuration with temperature

compensation resistors. The sensor installation on the titanium stress concentrator was performed by a commercial vendor. Figure 11.38b shows a detail of the senor placement. Further explanation of this sensor including details on simulations and calibration is presented by Krishnamurthy and colleagues in reference [55].

11.12 Summary

Neutron and proton diagnostics are vital to the performance evaluation and optimization of the IEC devices. Several different passive and active detectors have been introduced in the chapter to familiarize the reader with the wide variety of such detectors. The advancement of new technical areas such as the IEC depends strongly on continual improvement of the diagnostics developed for their study. The diagnostics covered here do not represent new concepts per se, but their modification and adaptation to the unique IEC environment is "new."

Solid-state proton detectors are a good example of this. As described in this chapter, the Pb face shielding, detector thickness, and magnetic field noise reduction are features especially selected because of the IEC environment presented for measurement. Calibration and interpretation of the resulting proton measurements are also unique to the IEC. Neutron detectors in general are not sensitive to spatial distribution of fusion source in an IEC device, but proton detectors are. Hence much more information can be collected with a proton detector than is possible with a neutron detector. Proton detectors provide information such as the energy spectrum of the charged fusion particles, fusion rate, and energy of the reactants. However these detectors are plagued by the x-ray noise from the source. The FIDO diagnostic completely isolates the detector from the pathway of the x-rays, thus reducing the noise signal and enabling the detection of not only the protons but also the tritons.

Other kinds of charged particle detectors include the deuterium anion detectors such as the magnetic deflection-energy analyzer and the Faraday cup detector. These diagnostics have helped study and analyze the deuterium anions that were previously ignored, but are now known to be significant. These diagnostics can also be potentially used to map the dependence of the deuterium anion intensity and to determine the extent to which the IEC devices can produce molecular hydrogenic anions. Plasma jets have been relatively difficult to analyze, but unique diagnostics such as the gridded energy analyzer have helped perform this feat. In this detector the voltage of the ion sweep grid is varied to obtain the ion spectrum of the plasma jet. The plasma force sensor works by sensing the plasma striking the plate. The lever arm bends backward very slightly and this deflection is measured from the piezo sensors as a tiny change in voltage that can be measured.

The topics covered in this chapter do not include all of the diagnostics that may be employed in particular IEC experiments or applications. For example, plasma spectroscopy has been used very effectively by some researchers, but is not included here. The reader is encouraged to search for additional research for specific topics of interest.

References

1. Engineering Data Sheets 1.21 and 1.22 for BF_3 Proportional Counters (1979) Reuter Stokes, Cleveland
2. Knoll GF (2000) Radiation detection and measurement, 3rd edn. Wiley, New York
3. East LV, Walton RB (1969) Polyethylene moderated ^{3}He neutron detectors. Nucl Instrum Methods 72:161–166
4. Radel RF (2007) Detection of highly enriched uranium and tungsten surface damage studies using a pulsed inertial electrostatic confinement fusion device. Ph.D. thesis, Department of Engineering Physics, University of Wisconsin, Madison
5. Nadler JH, Miley GH, Coventry M, Williams M, Jurczyk B, Stubbers R, Nam Y (1999) High current pulsed operation of an Inertial Electrostatic Confinement (IEC) device. In: IEEE 18th symposium on fusion engineering
6. S. Krupakar Murali (2004) Diagnostic study of steady state advanced fuel (D–D and D–^{3}He) fusion in an IEC device. Department of Physics, University of Wisconsin, Madison
7. Piefer GR (2006) Performance of a low-pressure, helicon driven IEC ^{3}He fusion device. Ph.D. thesis, Department of Engineering Physics, University of Wisconsin, Madison
8. Apfel RE (1979) The superheated drop detector. Nucl Instrum Methods 162:603
9. Ing H, Noulty RA, McLean TD (1997) Bubble detectors: a maturing technology. Radiat Meas 27(1):1–11
10. Barnabe-Heider M et al (2003) Characterization of the response of superheated droplet (Bubble) detectors, arXiv:hep-ex/0311034v1
11. Gornea R (2002) Systéme d'acquisition des données et de controle du détecteur à gouttelettes surchauffées dans le cadre du projet PICASSO. M.Sc. thesis, University of Montreal
12. Bubble Technology Industries (2013) www.bubbletech.ca. Accessed 6 Sept 2013
13. Nadler JH, Gu YB, Miley GH (1992) Potential profile measurements using a collimated proton detector in spherical inertial-electrostatic plasma confinement. Rev Sci Instrum 63(10): 4810–4812
14. Thorson TA, Durst RD, Fonck RJ, Sontag AC (1998) Fusion reactivity characterization of a spherically convergent ion focus. Nucl Fusion 38(4):495
15. Ashley RP, Kulcinski GL, Santarius JF, Krupakar Murali S, Piefer G, Cipiti BB, Radel R (2003) Recent progress in steady state fusion using D-^{3}He. Fusion Sci Technol 44:559
16. Krupakar Murali S, Cipiti BB, Santarius JF, Kulcinski GL (2006) Study of fusion regimes in an inertial electrostatic confinement device using the new eclipse disk diagnostic. Phys Plasmas 13:053111
17. Masuda K, Yoshikawa K, Ohnishi T, Ogawa S, Zen H, Takamatsu T (2006) Spatial distribution of D–D/D–^{3}He advanced fuels fusion reactions in an inertial electrostatic confinement device. In: Proceedings of the 21st IAEA fusion energy conference, Chengdu, China
18. Fujimoto T, Oishi T, Zen H, Masuda K, Yoshikawa K (2007) Intensity distribution of D–^{3}He fusion reaction rate in an IEC device. Fusion Eng. In: IEEE 22nd symposium on fusion engineering, pp 1–4
19. Knoll GF (1989) Radiation detection and measurement, 2nd edn. Wiley, New York. In: Bertolini G, Coche A (eds) Semiconductor detectors. North Holland Publishing 1968 (distributed in the U.S. by American Elsevier Publishing Co.), New York City
20. Murali SK, Santarius JF, Kulcinski GL (2010) Proton detector calibration in a gridded inertial electrostatic confinement device. IEEE Trans Plasma Sci 38(11):3116–3127
21. Heidbrink WW, Strachan JD (1985) Tokamak ion temperature and poloidal field diagnostics using 3-MeV protons. Rev Sci Instrum 56:501
22. Bosch HS (1990) Diagnostics with charged fusion products in ASDEX. Rev Sci Instrum 61(6):1699–1707
23. Kis Z et al (1998) Comparison of efficiency functions for Ge gamma-ray detectors in a wide energy range. Nucl Instrum Methods Phys Res, Sect A 418(2):374–386

24. O'shea DC, Callen WR, Rhodes WT (1977) Introduction to lasers and their applications. Addison-Wesley, Reading, p 82
25. Ziegler JF (2004) The stopping and range of ions in matter. Instruction manual, Ver. 96.xx
26. Ziegler JF, Biersack JP, Littmark U (1996) The stopping and range of ions in solids. Pergamon Press, New York
27. Krupakar Murali S, Santarius JF, Kulcinski GL (2008) Advanced fuels (D–D and D–^{3}He) fusion proton energy distribution from an IEC device. Fusion Sci Technol 53(3):841–853
28. Canali C et al (1979) Electrical properties and performances of natural diamond nuclear radiation detectors. Nucl Instrum Methods 160(1):73–77
29. Murali SK, Santarius JF, Kulcinski GL (2010) Effects of B-fields in the proton detection channel of an IEC device. J Fusion Energy 29(2):124–129. doi:10.1007/s10894-009-9243-9
30. Boris DR (2009) Novel diagnostic approaches to characterize the performance of the Wisconsin inertial electrostatic confinement plasma. Ph.D. thesis, Department of Engineering Physics, University of Wisconsin, Madison
31. Boris DR, Kulcinski GL, Santarius JF, Donovan DC, Piefer GR (2010) Measuring D(d,p)T fusion reactant energy spectra with Doppler shifted fusion products. J Appl Phys 107:123305. doi:10.1063/1.3437629
32. Boris DR, Alderson E, Becerra G, Donovan DC, Egle B, Emmert GA, Garrison L, Kulcinski GL, Santarius JF, Schuff C, Zenobia SJ (2009) Deuterium anions in inertial electrostatic confinement devices. Phys Rev E 80:036408
33. Weidner JW, Kulcinski GL, Santarius JF, Ashley RP, Piefer G, Cipiti B, Radel R, Krupakar Murali S (2003) Production of 13N via inertial electrostatic confinement fusion. Fusion Sci Technol 44:539
34. Weidner JW (2003) The production of 13N from inertial electrostatic confinement fusion. Master's thesis, Department of Engineering Physics, University of Wisconsin, Madison
35. Emmert GA, Santarius JF (2010) Atomic and molecular effects on spherically convergent ion flow II: multiple molecular species. Phys Plasmas 17:013503
36. Khachan J, Moore D, Bosi S (2003) Spatial distribution of ion energies in an inertial electrostatic confinement device. Phys Plasmas 10:3
37. Computer code SIMION® Version 8 (Scientific Instrument Services, Inc)
38. Yoshikawa K, Takiyama K, Masuda K, Yamamoto Y, Toku H, Nagasaki K, Hashimoto H, Nagafuchi A, Mizutani T, Ohnishi M, Horike H (2002) Potential profile measurements by laser-induced fluorescence method in a helium discharge plasma. In: 19th symposium on fusion engineering, Atlantic City, New Jersey, pp 438–441
39. Yoshikawa K et al (2000) Fusion energy. In: Proceedings of the 18th symposium, Albuquerque, p 27
40. Matsuura H (2000) Ion distribution function and radial profile of neutron production rate in spherical inertial electrostatic confinement plasmas. In: U.S.–Japan workshop on IEC neutron sources
41. Takiyama K et al (1986) Measurement of intensity and polarization of He-I forbidden lines for diagnostics of electric field in a plasma. Jpn J Appl Phys 25:L455–L457
42. Yoshikawa K et al (2001) Strongly localized potential profile measurements through stark effects in the central core region of an inertial-electrostatic fusion device. Fusion Technol 39(3):1193–1201
43. Yoshikawa K et al (2001) Measurements of strongly localized potential well profiles in an inertial electrostatic fusion neutron source. Nucl Fusion 41(6):717–720
44. Khachan J, Moore D, Bosi S (2003) Spatial distribution of ion energies in an inertial electrostatic confinement device. Phys Plasmas 10:596
45. Ruzic DN (1994) Electric probes for low temperature plasmas. The American Vacuum Society Education Committee, New York
46. Khachan J, Collis S (2001) Measurements of ion energy distributions by Doppler shift spectroscopy in an inertial-electrostatic confinement device. Phys Plasmas 8(4):1299–1304

47. Gu Y, Miley GH (2000) Experimental study of potential structure in a spherical IEC fusion device. IEEE Trans Plasma Sci 28(1):331–346
48. Thorson TA, Durst RD, Fonck RJ, Wainwright LP (1997) Convergence, electrostatic potential, and density measurements in a spherically convergent ion focus. Phys Plasmas 4(4):4
49. Barbeau C, Jolly J (1990) Spectroscopic investigation of energetic atoms in a DC hydrogen glow discharge. J Phys D 23:1168
50. Alderson EC, Santarius JF, Boris DR, Piefer GR (2007) Spectroscopic diagnosis of plasma in the IEC. In: 9th annual U.S.–Japan IEC workshop, Argonne National Laboratory, Lemont, Illinois
51. Honzawa T, Sekizawa T, Miyauchi Y, Nagasawa T (1993) Effects of space charges in a gridded energy analyzer. Jpn J Appl Phys 32:5748–5753
52. Honzawa T (1997) Characteristics of gridded energy analyzers in relatively dense plasmas. Fusion Eng Des 34–35:551–554
53. Pitts RA et al (2003) Retarding field energy analyzer for the JET plasma boundary. Rev Sci Instrum 74(11):4644–4657
54. Simpson JA, Leder LB (1958) Improved electrical differentiation of retarding potential measurements. Rev Sci Instrum 29(7):571–574
55. Krishnamurthy A, Ulmen BA, Chen G, Keutelian P, Reilly MP, Miley GH (2012) Force measurements in a helicon injected inertial plasma electrostatic rocket (HIIPER) using a plasma momentum flux sensor. In: 48th AIAA/ASME/SAE/ASEE joint propulsion conference & exhibit 10th annual international energy conversion engineering conference, Atlanta
56. Boris DR, Alderson E, Becerra G, Donovan DC, Egle B, Emmert GA, Garrison L, Kulcinski GL, Santarius JF, Schuff C, Zenobia SJ (2009) Deuterium anions in inertial electrostatic confinement devices. Phys Rev 80:036408
57. Chavers DG, Chang-Diaz FR (2002) Momentum flux measuring instrument for neutral and charged particle flows. Rev Sci Instrum 73(10):3500–3507
58. Longmier BW, Bering III EA, Reid BM, Gallimore AD, Squire JP, Glover TW, Chang-Diaz FR, Brukardt M (2009) Hall thruster and VASIMR VX-100 force measurements using a plasma momentum flux sensor. In: 47th AIAA aerospace sciences meeting including the new horizons forum and aerospace exposition, AIAA-246, Orlando
59. Longmier BW, Reid BM, Gallimore ADG, Chang-Diaz FR, Squire JP, Glover TW, Chavers G, Bering EA III (2009) Validating a plasma momentum flux sensor to and inverted pendulum thrust stand. J Propuls Power 25(3):746–752

Chapter 12
Potential Applications

12.1 Introduction

The ability to use the IEC for practical applications with operation well below energy breakeven is a unique, attractive feature of this device. The basic reason this is possible is that the simple structure of IEC devices allows a modest construction cost. Also, operation with small fusion power levels is possible, so it becomes economical to purchase the electricity needed to drive the IEC. The use of IECs for a small portable neutron source for various neutron activation analysis (NAA) applications is an example. In this chapter we discuss some NAA applications, along with medical isotope production. With some increase in energy gain and power, an IEC neutron-driven subcritical fission assembly for student labs seems feasible. We discuss that use in this chapter, along with more demanding use in future fusion–fission hybrid reactors. IEC fusion space propulsion, another future application, is discussed to stress the potential for high power-to-weight systems using the IEC.

Figure 12.1 shows the various applications possible using an IEC device. As the fusion rate increases, the number of applications also increases. It is worthwhile to observe that as the fusion rate increases, not only do we get into newer applications of the device, but also the existing applications become more efficient due to increased flux. Though not exhaustive, we will discuss some of these applications in this chapter.

12.2 Neutron/Proton/X-ray Sources

The main application of the IEC to date has been as a small portable neutron source for neutron activation analysis (NAA) [1]. In addition, because both D–D and D–^{3}He reactions can be used for proton production, this route has been pursued for medial isotope and PET (positron emission tomography) scan isotope

G.H. Miley and S.K. Murali, *Inertial Electrostatic Confinement (IEC) Fusion: Fundamentals and Applications*, DOI 10.1007/978-1-4614-9338-9_12,

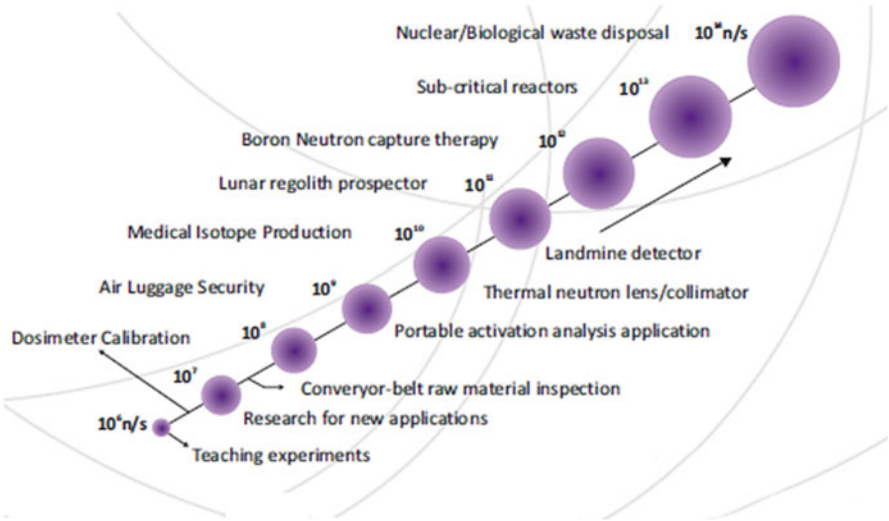

Fig. 12.1 Various applications of an IEC device with increasing fusion rate [1]

production discussed in a following section. However, due to the need for high source strengths to fully compete in the medical isotope area, this application is still undergoing research. Another novel application is the use of the IEC device to simulate implantation of D^+ and He^+ in candidate fusion first wall materials. Yet another novel use involves running the IEC with reverse polarity such that the trapped electrons produce soft x-rays that can be extracted through a special port (the port must have a thin low-Z window for transmission). This can be viewed as a small-scale soft source for individual laboratory studies such as done at various large-scale synchrotron "light sources" located at several national laboratories in the United States. In particular, cylindrical IEC devices have gained widespread acceptance and have been successfully used to replace ^{252}Cf sources for conveyor belt material analysis. Such devices are currently commercially available.

12.3 Production of Medical Isotopes

Several researchers have considered IECs to create radioisotopes for medical diagnostics. Both the D–D and advanced D–^{3}He fusion reactions can be considered. The D–^{3}He reaction is particularly interesting. The high-energy 14.7-MeV proton produced is energetic enough to be used to create radioisotopes. The advantage of isotope production using this method is that the IEC device is small and relatively inexpensive, so it may be developed into a semiportable device. Cipiti and Kulcinski utilized the beam–target D–^{3}He fusion regime in a converged core IEC to create medical isotopes in two different systems [2]. In the first design shown in Fig. 12.2,

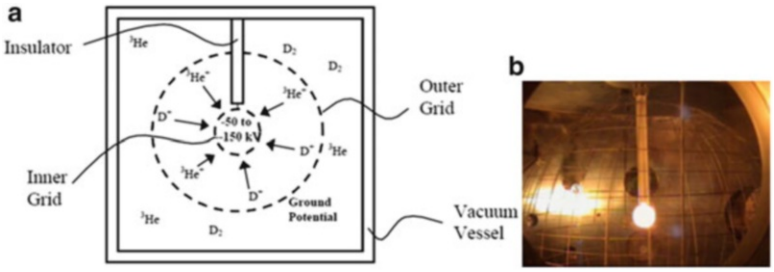

Fig. 12.2 (**a**) Solid target is used to replace the central grid in an IEC device to generate PET isotopes. (**b**) Picture of the white hot solid target after running for 15 m in the University of Wisconsin IEC device [2]

Table 12.1 PET isotopes [4]

PET isotope	Production	Half-life (min)
^{18}F	$^{18}O(p,n)^{18}F$	110
^{15}O	$^{15}N(p,n)^{15}O$	2
^{13}N	$^{16}O(p,\alpha)^{13}N$	10
	$^{13}C(p,n)^{13}N$	
^{11}C	$^{14}N(p,\alpha)^{11}C$	20
^{94m}Tc	$^{94}Mo(p,n)^{94m}Tc$	52

the deuterium ions focused on the cathode reacted with the ^{3}He ions that were embedded on the surface, forming the stationary targets to the oncoming deuterium ions and thus creating short-lived positron emission tomography (PET) isotopes.

Table 12.1 lists a few isotopes that can be used in PET. The first isotope created was ^{94m}Tc, a positron emitter with a 52-min half-life. In the first technique the PET isotopes were created in a solid molybdenum cathode [3]. Beam–target D–^{3}He reactions occurring in the outer layers of the molybdenum created high-energy protons to activate the surrounding material. Approximately 1.5 nCi of ^{94m}Tc were created using the $^{94}Mo(p,n)^{94m}Tc$ reaction.

In the second design, Cipiti built upon the design formulated by Weidner to produce ^{13}N. Weidner and colleagues produced medical isotopes using thin-walled stainless steel tubes [5]. The high-energy protons from the D–^{3}He reactions were used to create the positron emission tomography (PET) isotopes. Specifically, ^{13}N was produced via the $^{16}O(p,\alpha)^{13}N$ reaction by irradiating a water target enclosed in a thin-walled stainless steel tube. However, the concentration of the medical isotopes generated was very low and only at proof-of-principle levels. This marked the first confirmed production of medical isotopes in an IEC device. It was later realized that the diffused flux of protons reaching the target was insufficient to increase the medical isotope concentration. Hence, Cipiti argued that moving the target to the center of the device as illustrated in Fig. 12.2a would increase the ion flux to the surface of the thin-walled stainless steel tube, thus increasing the isotope production [6]. With this setup, the ions converged onto the steel tube placed at the center of the device, as shown in Fig. 12.3. The tube itself was protected by the

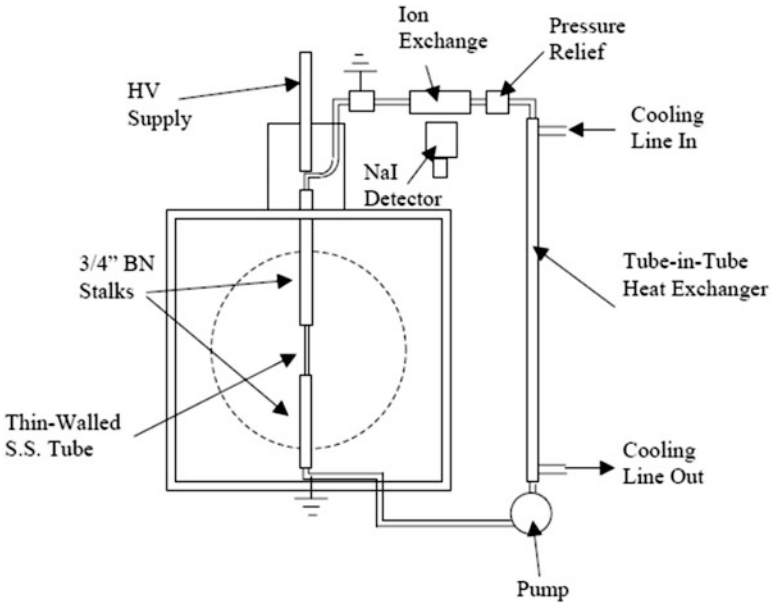

Fig. 12.3 Cooled water target design [6]

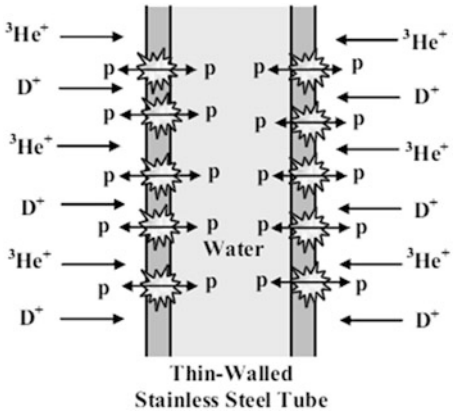

Fig. 12.4 Beam–target isotope production mechanism in an IEC device [6]

water circulating through it that also formed the target. Approximately 1.0 nCi of ^{13}N was created using this system.

As high voltage was applied to the tube in Fig. 12.4, both deuterium and helium ions impinged on its surface. Though the deuterium diffused out, the helium was retained by the tube. These recombined helium atoms formed targets to the oncoming deuterium ions that in turn caused fusion on the surface. Because the fusion products had equal probability of moving either into or out of the tube, 50 % of the protons were assumed to move inward. These high-energy protons then fused with the oxygen in the water and produced ^{13}N through the $^{16}O(p,\alpha)^{13}N$ reaction.

The PET radioisotope ^{13}N mentioned earlier is used to label ammonia (NH_3) in order to detect coronary artery disease. Because of its 10-min half-life, ^{13}N must be produced at or very near the location of the PET scan. This limits the availability of this procedure to those locations with accelerators or cyclotrons. However, if IEC devices managed to produce these isotopes at useful concentrations, the commercial application of IEC devices will increase tremendously. Again, the advantage of using the IEC is that these devices are small and hence economical to locate in numerous hospitals.

In summary, these experiments demonstrated the ability to use an IEC for production of medical isotopes. Before the practicality of this approach can be evaluated, commercial-scale units must be designed and tested to prove lifetime and production rates, and they must be shown to be economically attractive.

12.3.1 Chemical Explosives Detection Using an IEC Device

The 2.45-MeV neutrons from the D–D fusion reaction occurring in an IEC device can be used for detection of explosives. These neutrons activate the low-Z materials found in explosives, thus producing the characteristic gamma radiation that can in turn be detected. Specifically, the neutrons, once thermalized, will be captured by the ^{14}N nuclei with a thermal capture cross section of 11.3 mb, resulting in a characteristic gamma ray of 10.829 MeV [7].

A common technique for explosives detection utilizing thermal neutron activation analysis (NAA) uses neutrons produced from the radioactive decay of ^{252}Cf. However, this method of explosives detection poses a significant health because there is no way to stop the radioactive decay of ^{252}Cf, and protection from this radiation is a concern [8]. The health hazards are significantly reduced by using an IEC device as the neutron source. However, radiation emission is only a concern while the IEC device is operating, and the health hazard essentially disappears once the IEC device is turned off. Additionally, if an explosive device were detonated during inspection of a container using the IEC device, the fusion of D–D immediately ceases and no health hazard would arise due to dispersal of stable deuterium. The emission of 10.83-MeV gamma rays due to the (n,γ) reaction has been identified as the key reaction for the detection of explosives.

In order to accurately predict the energy spectrum that could be expected while activating the C-4 explosive, the ratio of C:H:N:O is required. Numerous publications indicated that C-4 is approximately 90 % RDX by weight and RDX is $C_3H_6N_6O_6$. Ignoring the remaining 10 %, the percentage of nitrogen in the sample is around 37.8 % [9]. The experimental setup shown in Fig. 12.5 was successfully used to demonstrate the C-4 detection through nitrogen activation using a NaI detector. The data acquisition was performed for 10 min, and the results of this experiment are shown in Fig. 12.6.

While the researchers in the United States have concentrated on making the source stronger, the Japanese group headed by K. Yoshikawa has taken a different

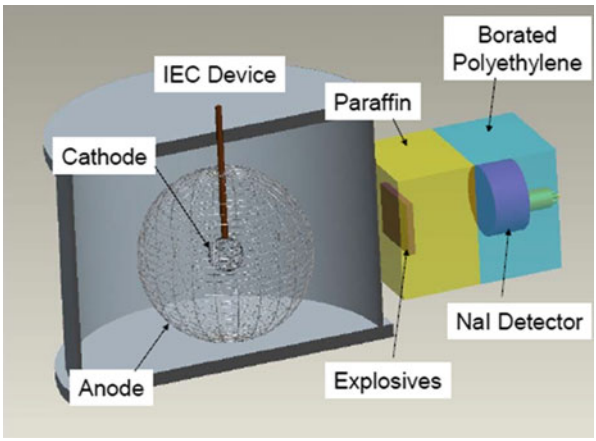

Fig. 12.5 Typical setup of the explosives detection experiment at University of Wisconsin, Madison [9]

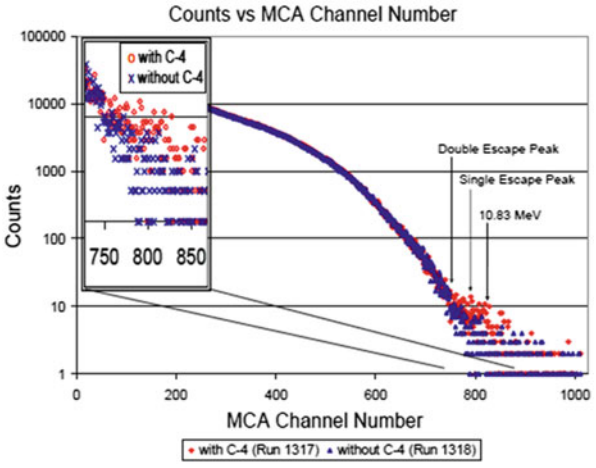

Fig. 12.6 Experimental results from the IEC device setup shown in Fig. 12.5, with and without C-4 in front of the detector

approach [10]. The sensitivity of the detector was increased. A relatively weak (collimated) source with a source strength of 10^7 n/s was used (shown in Fig. 12.7) but employed a highly sensitive BGO/NaI (TI) combined scintillator through anticoincidence method for a collimated γ detection (as shown in Fig. 12.8). Yoshikawa and colleagues successfully detected melamine (a simulated explosive), as shown in Fig. 12.9.

12.3.2 Detection of Highly Enriched Uranium (HEU)

The smuggling of illicit nuclear material has been an issue of serious concern for US officials since the early 1990s and has gained increased attention. In the past decade, there have been over 150 confirmed incidents of smuggling of nuclear

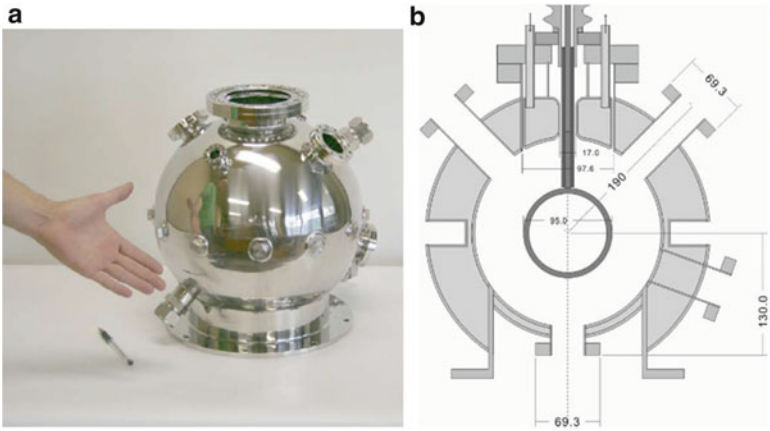

Fig. 12.7 (**a**) Photo of the water-jacketed IEC neutron source. (**b**) Schematic of the cross section of this device. The water jacket not only kept the device cooled during operation but also reflected some neutrons in the downward direction [10]

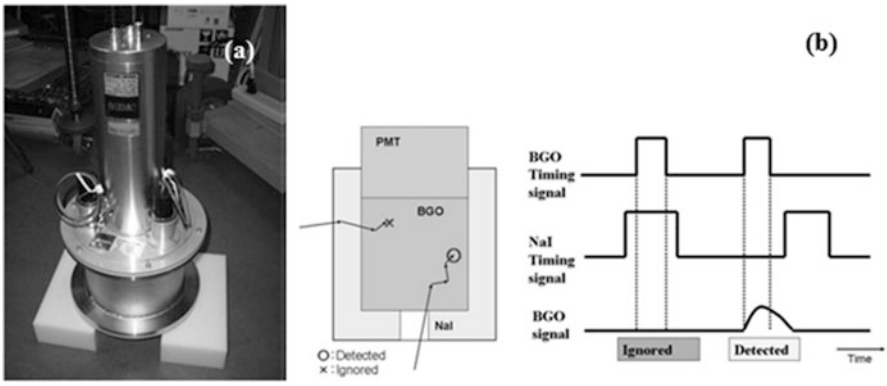

Fig. 12.8 (**a**) BGO/NaI (TI) combined scintillator for well-collimated γ-ray detection. (**b**) Schematic of the anticoincidence method by the BGO/NaI(TI) combined scintillator [10]

material in the International Atomic Energy Agency's (IAEA) Illicit Trafficking Database [11]. Of these, nearly half involved enriched uranium or plutonium. In the wrong hands, these materials could represent a serious threat to national security, and preventing this from occurring has become a high international priority. The development of a reliable, compact means to detect fissile and other nuclear materials will allow the port authorities to inspect cargo as it enters their borders.

A pulsed neutron HEU detection system has been developed at proof-of-principle levels at the University of Wisconsin, Madison [12]. The work performed to date has focused on achieving three specific goals. The first is the characterization of the steady-state IEC ion source to determine optimum conditions for pulsed

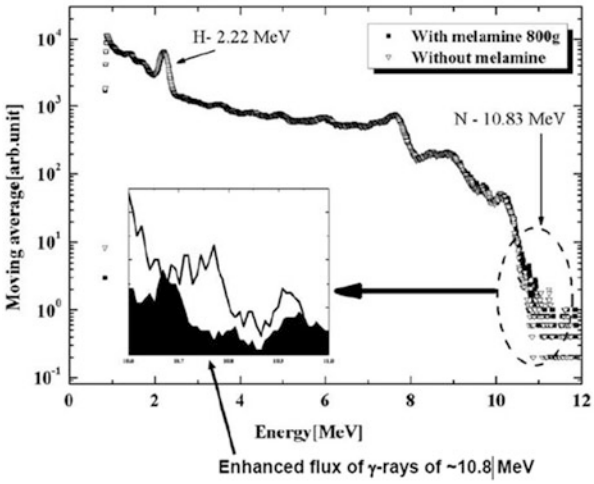

Fig. 12.9 Energy spectrum of γ-rays for the cases with and without 800 g melamine ($C_3H_6N_6$) and an expanded view around the 10.8-MeV region showing the signal of "with melamine" in black and "without melamine" in white [10]

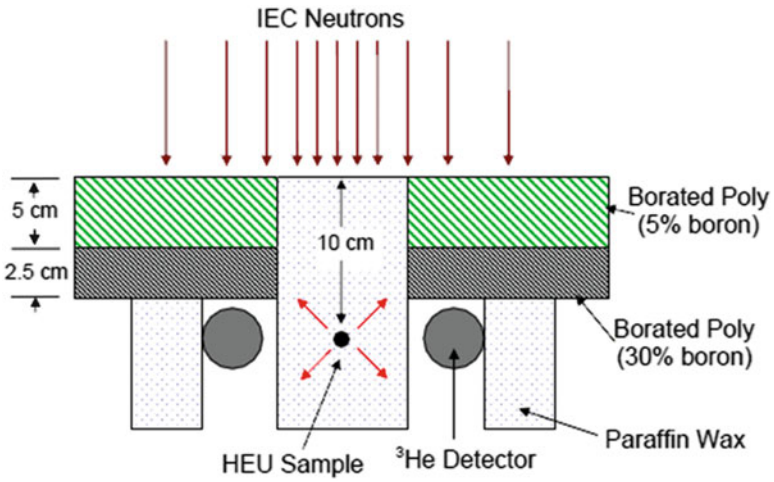

Fig. 12.10 Modified HEU detection module (not to scale) shields detectors while allowing neutrons into HEU sample

IEC operation. Initial experiments with steady-state neutron fluxes showed that the delayed neutron production increased as the neutron fluence increased. Through these initial experiments it was found that a steady-state fusion level existed between the pulses. The HEU detection hardware was then modified to lower the level of detected neutrons between pulses with no HEU present. A top-down view of this modification is shown in Fig. 12.10.

Using this detection apparatus, neutrons were measured during pulsed operation. Figure 12.11 shows neutron counts as a function of time during and between 10,000 0.5 ms IEC fusion pulses. While there is some scatter in the data, the delayed neutron population is clearly elevated above the background counts.

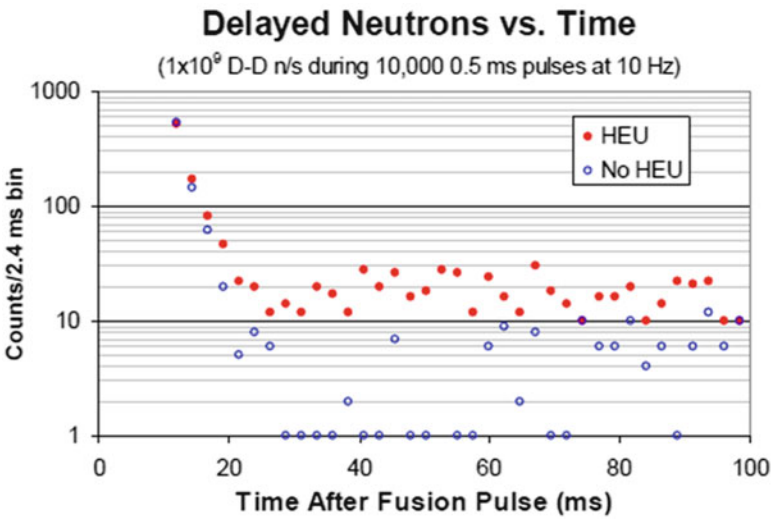

Fig. 12.11 Neutron counts versus time after fusion pulse (ms) shows increased levels of neutrons measured when HEU is present

12.4 Integrated Interrogation System

A design for an integrated interrogation system using cylindrical IECs has been proposed by Miley and colleagues [13]. It incorporates combined 2.5- and 14-MeV IEC neutron sources and an x-ray IEC source. While this system design assumes very aggressive IEC development, it does serve to provide some insight into the unique capabilities of IEC sources. Neutron sources have already been described in the previous chapters, but some comments about the x-ray source are also important to note. X-ray operation involves reversing electrode polarities and adding electron emitters along the vessel wall [14]. Hydrogen gas is substituted for D or T because in this configuration the main function of gas ions is to provide electron Bremsstrahlung emission. Intense emission is concentrated in a small volume surrounding the central axis due to the high electron density formed there. The resulting x-ray energy spectrum peaks at an energy about two-thirds of the applied voltage. In the present case, a voltage around 120 kV will be employed to obtain ~80 kV x-rays with some distribution of energies above and below this mean value. This unique x-ray energy spectrum, combined with x-ray production over a long line-like region in the IEC, provides broad area coverage for the x-ray imaging, consistent with the broad coverage neutron source. Consequently, the basic concept of the integrated inspection unit discussed here is to combine IEC neutron and x-ray sources into a single unit. This combination expands the range of elements that can be detected during a single scan and incorporates x-ray imaging with three-dimensional NAA to obtain improved identification of the shape and location

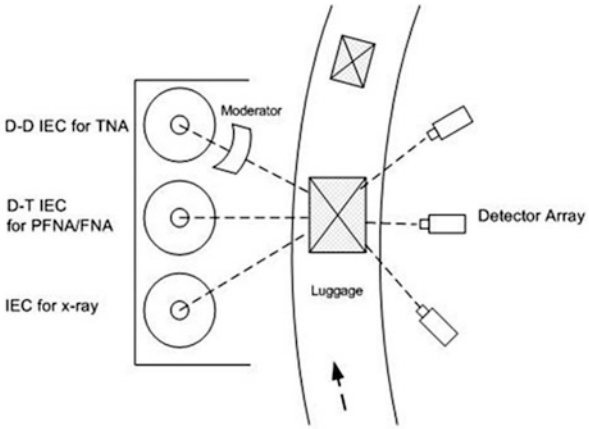

Fig. 12.12 Schematic (*view from top*) of a broad coverage IEC inspection system for luggage inspection [14]

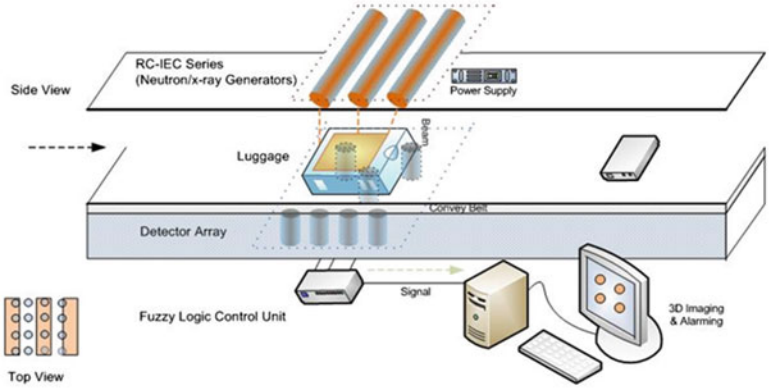

Fig. 12.13 The integrated system for airport luggage inspection. If desired, a second belt and detector array could be located above the IEC units to provide increased capacity [14]

of suspected objects in a container. In cases where the object is too large to allow good x-ray penetration, rough imaging is still obtained from the three-dimensional neutron detector array.

12.4.1 Design of a Total Integrated Interrogation System for Luggage Inspection

There are a number of inspection station applications possible, ranging from luggage to cargo ship container inspection. Each requires a specific design. To illustrate one case, a luggage inspection unit is discussed next. The proposed integrated system for luggage inspection is illustrated conceptually in Figs. 12.12 and 12.13.

This unit employs two broad area neutron sources to provide both 14.1-MeV and 2.45-MeV coverage. The IEC Bremsstrahlung source provides broad area 80 kV x-rays. An array of γ-ray and x-ray detectors are provided for simultaneous NAA and x-ray analysis using a fuzzy logic-type artificial intelligence system as described later. In the inspection station, typical of airport luggage inspection stations, objects being interrogated pass between the sources and detection array on a conveyor belt. For maximum efficiency a duplicate conveyor belt and detection array would be placed on the left-hand side of the IEC sources.

For other cases, such as unloading containers from a ship, the detector system might be suspended along the side of the vessel with containers as they are lowered from the upper decks to the waiting cargo train cars or trucks. The difficulty accounted by conventional detector system is that the unloading time is short and the containers are large and thick. Thus, rapid scans and good penetration into the containers are needed. The present integrated system with its multi-IEC broad coverage and fast fuzzy analysis technology is designed to overcome these deficiencies. Further, the size and cost of conventional accelerator type systems hamper their use in sea ports, but the increased accuracy and reduced cost of the integrated system should enable wide use. This would close a vital gap in our seaport/airport cargo security system that has been often cited by critics of the present handling of port security.

12.5 Integrated System Detection Methods

Most current inspection systems concentrate on x-ray imaging. This interrogation relies on the photoelectric effect or Compton scattering imaging (CSI). It provides good localization and some geometric information for higher-*Z* materials. The NAA technique, including both thermal neutron analysis (TNA) and fast neutron analysis (FNA), is a powerful method for detecting certain types of explosives. Basic elements such as oxygen, carbon, and chlorine present in the explosives can be identified through the (n, n′γ) reaction initiated by fast neutrons. The γ-rays produced in the reaction are characteristic of the element being interrogated. Nitrogen, another basic element in many explosives, is usually measured through (n, γ) reactions initiated by thermal neutrons. Either steady-state or pulsed sources can be employed for TNA. However, increased sensitivity can be obtained with pulsed FNA (PFNA). This method uses a pulsed high-energy neutron source and the time-of-flight (TOF) diagnostics to reduce the “noise” effect resulting from scattered neutrons and x-rays. These various techniques and their capabilities are summarized in Table 12.2. The three techniques shown in Table 12.2, thermal neutron analysis (TNA), fast neutron analysis (FNA), and x-ray analysis, have been used for various detection stations. However, each has always been used independently. The proposed integrated unit uses IEC source technology making use of all three methods simultaneously. Thus, the strengths and weaknesses of each come together to provide a consistent overall coverage of elements/objects.

Table 12.2 Three kinds of techniques used in explosives detection system

	TNA	FNA	X-ray
Element identification			Element density
Nitrogen	High	Medium	–
Carbon	Very low	Very high	–
Oxygen	N/A	High	–
Hydrogen	Very high	High	–
Chlorine	Very high	High	–
C/O ratio	N/A	High	–
Background noise	High	Low with FNA	N/A
Imaging: geometry and localization information	Limited	PFNA provides depth information	High resolution
Source availability	Need thermalization	Directly	Directly
Application	Small suitcase	Suitcase to cargo	Suitcase to cargo, not good for plastics objects
Configuration	Complicated	Complicated	Simple
Operation and maintenance cost	High	High	Low

The integrated system employs a combination of PFNA/TNA methods and conventional x-ray techniques to collect elemental information as well as three-dimensional imaging of any suspected objects. The 14.1-MeV neutrons that form the D–T reaction will be the primary source for TOF D FNA, while thermalized neutrons from a block of thermalizing plastic placed in front of the 2.45-MeV D–D IEC will be used for TNA. This combination will increase spatial resolution and significantly reduce the false alarm rate to a low level (compared to the conventional method, which employs single sources and is limited to yield due to lack of broad area sources).

12.5.1 Pulsed Power Supply for a Pulsed IEC Neutron Source

Detection methods are generally improved by the use of a pulsed neutron source. Pulsed operation for an IEC device was described in Chap. 10. The pulsed power supply proposed for the integrated system is a variation of that design. It and associated control circuits use advanced materials and methods to minimize weight and size. This pulsing capability is then an important feature of the IEC inspection station. This allows use of the unit in mobile platforms such as vans, law enforcement vehicles, or light military trucks. Figure 12.14 shows a block diagram of the power and power control circuits.

The power is taken from the platform power system and can be either 12–48 VDC or single phase 120 VAC. For use on small platforms or in the field, an

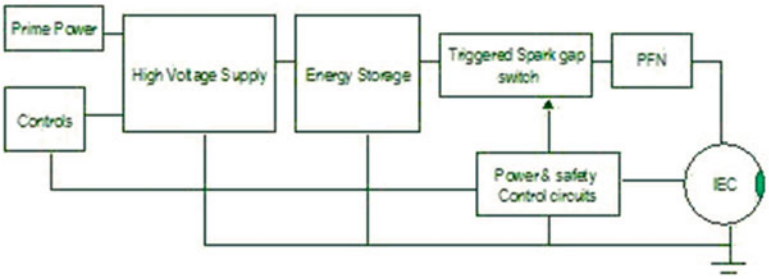

Fig. 12.14 Block diagram of a pulsed power system [14]

auxiliary generator or marine lead acid battery may be used. The high-voltage power supply is a solid-state switch-mode inverter followed by a voltage multiplier circuit that incrementally steps the voltage up a series of capacitors fed by high-voltage diodes**.** The energy storage unit is composed of high-voltage capacitor segments with a low series inductance and resistance. The capacitor bank is charged and discharged at the fundamental pulse repetition frequency (PRF) or the pulse repetition rate, which is determined by the power available from the switch-mode inverter circuits. The custom capacitor sections are engineered to withstand the mechanical stress caused by rapid charge/discharge cycling. The nominal capacitor bank voltage will be 120 kV at full pulse power output. A triggered spark gap is used to rapidly switch a high-energy pulse of current from the capacitor bank to pulse modulate the magnetron. The triggered gap is a compound three-element spark gap. When a high potential is suddenly switched to the trigger electrode, the gap arcs over, releasing photons and applying a high potential across the main gap, which in turn causes the main gap to arc over. The arc is sustained until the capacitor bank discharges. The pulse shaper is a tapped inductive line with each tap terminated by a discrete capacitance, commonly called a Pulse-Forming Network (PFN). Each tap performs a filtering function for a discrete Fourier function or band of frequencies, which results in a smoother, more uniform pulse rise and fall, and also provides more constant load impedance matching, as the IEC tube has high input impedance. This aids in the forward coupling of energy into the IEC by helping to minimize backward or reflected standing waves generated by the dynamic impedance discontinuity presented by the spark gap and the cathode to anode circuit path. The PFN, in effect, serves as a pulsed coupled transformer with a low input impedance and a high output impedance to drive the IEC tube. Components for the PFN are commercially available. The spark gap trigger is activated by an isolated gate bipolar transistor (IGBT) driven by the power control circuits.

A stable multivibrator timer circuit is reset each time the spark gap is fired by a fast phototransistor circuit that detects spark-generated photons. This is coupled by a light wave guide or optical fiber to provide high-voltage isolation between the solid-state control circuits and the high-voltage sections. This optically isolated signal can also be input to signal processing to give time-of-flight (TOF) measurements. A digital or manual potentiometer range selector controls the time delay by

increasing or decreasing the resistance in an RC network. When the capacitor in this network charges to a nominal voltage threshold, the timer circuit changes its logic state and drives the gate of the spark gap trigger IGBT on, which initiates the spark gap arc. This RC time period ramp is an analog of the energy storage capacitor charging ramp, which also begins after the main arc occurs and drains the energy store. The longer the charge time, the higher the charge in the energy storage capacitor bank and the higher the voltage is when the next pulse is initiated. The voltage applied to the IEC tube is thus varied over a nominal 40 % range. The peak output voltage can therefore be varied over a range of 50–120 kV.

12.5.2 Detector Array for the Integrated System

The final imaging quality is determined by neutron source yield integrated over the area of coverage, by the number of detectors, the detector configuration, the collimated beam size, the acquisition time, and other scan-related parameters. Scintillators such as NaI, CsI, and BGO as well as Plastic NaI (TI) are candidates for γ-ray and x-ray detectors. Due to their small size, they can be used in large numbers (array) along with TOF spectrometry to provide more detailed special information.

12.5.3 Fuzzy Logic Analysis System

With the combined sources, the detector array receives a vast amount of information in a short scan time. A fuzzy logic system is employed to most efficiently handle this flow of data. This system is patterned after a methodology developed for the diagnosis of abnormal situations in nuclear reactor safety analysis. The knowledge box employs a goal tree (i.e., an "and/or" tree) for representation. The detection array would employ many of the same concepts and elements.

This system will use learning-based rules that evolve from extensive simulation tests to provide training about the simultaneous occurrence of specific elements and embedded object shapes. It will also learn to differentiate between positive and negative data by creating rules from these test runs. The advantage of this system is twofold. The broad area scan analysis is optimized for fast throughput of objects while the multiple neutron/x-ray identification reduces the probability of false identification. The fuzzy logic system will be trained extensively to pass the item or sound the alert (if a suspicious object is found in the container) automatically without human interference. Humans will only be involved when an alert is sounded. An alert will be sounded for a range of reasons, from positive identification of material to suspected identification of a threat. The multiple source detector array concept is designed to minimize items that fall into the category of "in-between" positive identification and clearance.

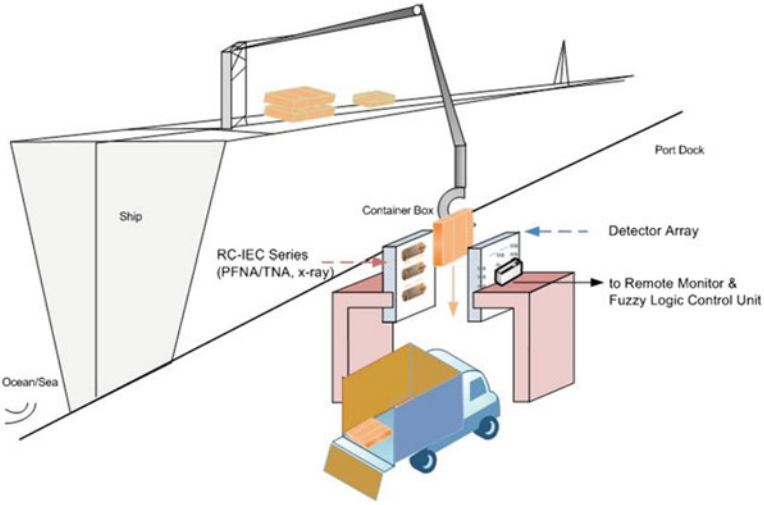

Fig. 12.15 The integrated system for ship container inspection [14]

12.5.4 Adaptation to Container Ships

Because the integrated system is modular, the basic components can easily be assembled in a variety of configurations for use at different facilities. An example is the extension to inspection of container ships being unloaded in port illustrated in Fig. 12.15.

A related application discussed in Chap. 10 (see Fig. 10.10) is for use in landmine detection. In that case, the IEC neutron source and the detector are mounted on long arms fixed to a mobile truck base. The design shown in Chap. 10 did not use an integrated-type system, but future versions might benefit from the added capability.

12.6 IEC Fusion Space Propulsion Design Studies

The IEC can be used for both near-term electrically driven low-power thrusters for satellite operations (using the jet mode) and fusion-powered deep space propulsion. Near-term electrically driven plasma propulsion with the IEC jet is discussed next section on "HIIPER." Here, we present some design studies that explore concepts and issues associated with the use of IECs for future fusion space propulsion. The very high power-to-weight ratio offered by IEC fusion devices (due to their simple, lightweight construction) makes them a leading candidate for space propulsion. That assumes, of course, that the physics issues related to moving to an IEC power reactor, discussed in Chap. 13, are resolved. At that time, terrestrial power plants will be attractive also. However, as Edward Teller and other have pointed out, some

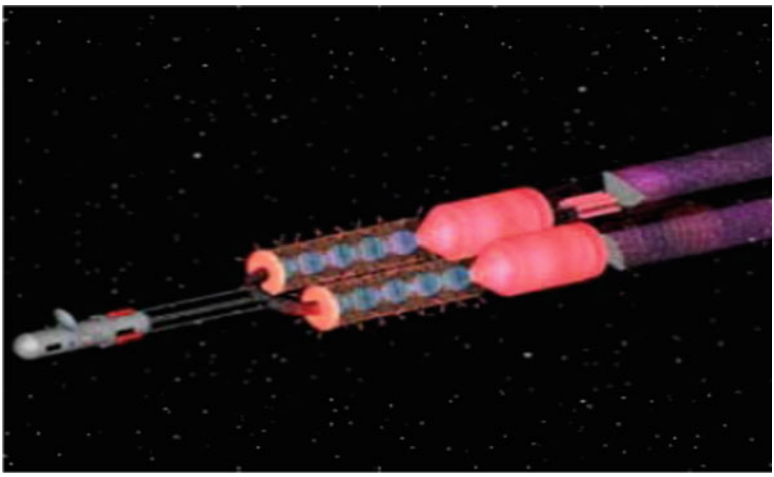

Fig. 12.16 The Fusion II Spaceship, a 750 MWe IEC fusion-powered manned spacecraft with ion thruster propulsion [16]

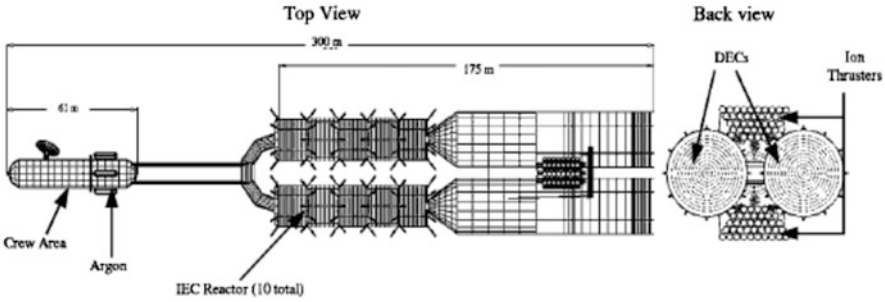

Fig. 12.17 Schematic of Fusion Ship II [16]

characteristics of space propulsion (such as the natural vacuum in space and the stress on conversion of the fusion energy to an exhaust jet versus using electricity, and the concentration on economics versus performance) could result in early development of fusion power for space [15]. In this section, we illustrate some concepts for IEC space propulsion from study [16], where a D–^{3}He reactor was utilized.

The conceptual design for IEC spaceship "Fusion Ship II" is shown in Figs. 12.16 and 12.17. The overall spaceship length is 300 m, and the initial mass at mission start is 500 metric tons. Crew and avionics/computer are located in the central compartment at the forward end of the vehicle. The crew compartment has a 12-m diameter and could contain a rotating centrifuge for sleep and exercise. A steerable antenna located on the side of this module provides communication. Twin 175-m-long assemblies, comprised of five D–^{3}He spherical IEC reactors and a

Table 12.3 Comparison of IEC design and magnetic fusion design

	Fusion ship I	Fusion ship II	Spherical tokamak
Overall mass (metric tons)	500	500	1,690
Overall length (m)	174	300	240
Number of crew	10	10	6–12
Thrust power (MW)	86	750	4,830
Reactor gain	4	9	73
Reactor power (MW)	296	2,178	7,895
Thrust system	Krypton ion	Argon ion	H_2 – magnetic nozzle
Specific impulse (sec)	16,000	35,000	35,435
Jupiter one-way trip (days)	400	210	118

Traveling Wave Direct Energy Converter (TWDEC) each, generate 1,394 MW of a 14.7-MeV proton flux and 469 MW of thermal components. These are converted to 1,197 MWe of RF electric power, 242 MW of which recirculates to run the reactors with 750 MWe used to drive the ion thrusters and the remainder being rejected as waste heat. A fusion fuel recirculation and separation system is operated continuously to remove the fusion product ^{4}He from the D–^{3}He reactants. The ion thrusters run on an argon propellant at a specific impulse of 35,000 s and an efficiency of 90 %. The thrust is 4,369 Newtons, which produces an initial acceleration of 0.0087 m/s^2. A typical trip time for an out-and-back mission to Jupiter is 210 days out and 153 days to return. This is comparable to or faster than that which prior fusion studies have achieved.

Of the initial 500 metric tons spaceship mass at mission start, 222 metric tons are argon propellant for a Jupiter round trip with ΔV of 220 km/s. The total mass of the IEC reactor, direct energy converters, and ion thrusters is 178 metric tons. The remaining 100 metric tons includes 20 metric tons for the crew areas, 15 metric tons for the electronics/computers, 20 metric tons for food and life support, 15 t for crew shielding, and 1.2 metric tons for the antenna. A contingent of 30 % added to the dry mass adds 60 metric tons and adds 30 days to the round trip flight time.

A design for Fusion Ship II, a manned IEC-powered spaceship with ion propulsion, has been presented. The spaceship is capable of roundtrips to planets with times that are on the order of 1 year, meeting a performance goal for fusion ships announced at the 2000 NASA-MSFC workshop on this subject. Human factors have not been fully evaluated in this design, but are thought to be acceptable for a "short" 1-year mission. Fusion Ship II would be one of the largest propelled vehicles ever built, though its mass would be one-fourth that of the space shuttle at lift-off. By far the most challenging technical aspect of the design is the development of a D–^{3}He IEC reactor with a gain of 9:1 or better. A second serious challenge requiring research and engineering development is that of the direct energy converters. More mundane but nevertheless challenging problems are those of the argon ion thrusters and of lightweight crew shielding for long missions.

Table 12.3 compares the present preliminary design using IEC reactor [16] and a design using magnetic fusion [17] based on an "advanced" Tokamak reactor

"scaled up" from the spherical Tokamak experiment at Princeton's Plasma Physics Laboratory.

Another version of the IEC space propulsion was developed that used a number of IEC power units coupled together but with magnetic guide channels. This was described by Miley and colleagues in study [18], which is briefly discussed next.

12.7 Magnetically Channeled Spherical IEC Array (MCSA) Concept

The IEC device represents a very attractive approach to fusion power due to its high power density combined with a simple lightweight structure. However, the need for an internal grid and a limited confinement time has prompted several researchers to seek an alternative configuration that combines the IEC and magnetic fields. Thus, Bussard proposed the hexapole field configuration to confine electrons while ions remain electrostatically confined [19]. However, large electron losses through the field cusps remain an issue for this concept. Barnes and Nebel proposed a Penning trap concept [20], but this approach is limited to the use of a large number of very small diameter devices due to the Brillouin density limit. University of Illinois researchers proposed the Magnetically Channeled SIEC Array (MCSA) concept for a hybrid magnetic-assisted SIEC configuration that addresses the issues faced in these earlier hybrid concepts [17]. The MCSA is illustrated conceptually in Fig. 12.18. The SIEC is confined in a hexapole field configuration, quite different from the hexapole field proposed by Bussard, that is in turn located in a field channel (β Z-field) created by a column of Helmholtz coils. The field strengths of these coil sets are adjusted such that the fields cancel in the center of the IEC, giving a larger field null region compared to that in a cusp confined field. The present configuration retains the advantage of stability due to good field curvature obtained in a cusp, plus it also effectively closes the "belt" loss cone, and leakage in that direction is led around the hexapole coils and back into the confinement region, termed as "recirculation." Losses, due to scattering into the spindle loss cone along the z-axis, including stochastic scattering due to the violation of adiabatic

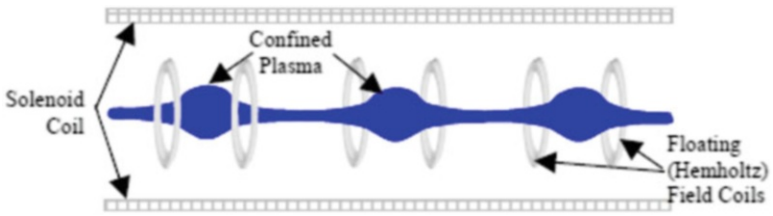

Fig. 12.18 Illustration of a three-unit MCSA device [18]

invariance in the field null region, still occur without the collisionallity required in "linked mirrors" configuration. However, with the present channel configuration, the axial losses from one IEC configuration enter a neighboring unit. Thus, as they pass through the field null region in that unit, stochastic scattering leads to "retrapping" of much of this flow. Experimental verification of this "retrapping" is then a second physics proof-of-principle objective. In this fashion, an array of multiple IECs increases the overall confinement time roughly in proportion to the number of units. In operation, electrons would be magnetically confined as described, providing electrostatic confinement of ions injected into the SIEC region. An additional benefit of this configuration is that in a reactor embodiment, both leaking fuel plasma and energetic charged fusion products (e.g., the 14-MeV proton from D–^{3}He) can be collimated and aimed into a direct energy converter such as a TWDEC [21]. This results in a high overall energy conversion efficiency. Alternately, for space propulsion, the proton beam, augmented by injection of heavy atoms, can be directly exhausted for thrust.

If the physics of this concept were found to be valid, a very attractive power plant would be possible. This was vividly demonstrated in the Space Ship II study where a D–^{3}He fueled MCSA was combined with a TWDEC and an ion gun to provide a propulsion unit for deep space missions [16]. This design provided the thrust and specific power needed for a manned round trip to Jupiter in about 1 year, a target set by NASA due to space radiation effect buildup on astronauts for longer trip times. While the added magnets add more complexity than for a "pure" SIEC, as shown in Table 12.3, their size and weight were still minimal compared to conventional magnetically confined fusion devices such as a Tokamak. While weight per se is not so crucial for land-based electric power plants, these aspects are reflected in reduced costs and easier maintenance. The combination of D–^{3}He fuel and TWDEC resulted in a high conversion efficiency (>60 %) and reduced weight (cost) for the energy conversion subsystem [16]. While the MCSA concept leads, in principle, to a very attractive power unit, several key new physics aspects of the concept (namely, recirculation and retrapping) need to be verified experimentally. These new physics concepts are briefly discussed next.

12.7.1 Recirculation of Radial Belt Cone Losses

Because the magnetic field lines that exit the cusp-like field reconnect to the confinement region within the coils, plasma particles that exit through the belt cusp loss cone will recirculate back into the confinement region. This recirculation significantly increases the confinement time versus that of a simple cusp devise, leading to a favorable concept. The linear scaling of an MCSA fusion device with plasma radius, as well as successful operations of multiple units in the array, is in large part controlled by this recirculation effect. Field configuration and a hypothetical particle trajectory through a belt cusp are shown in Fig. 12.19.

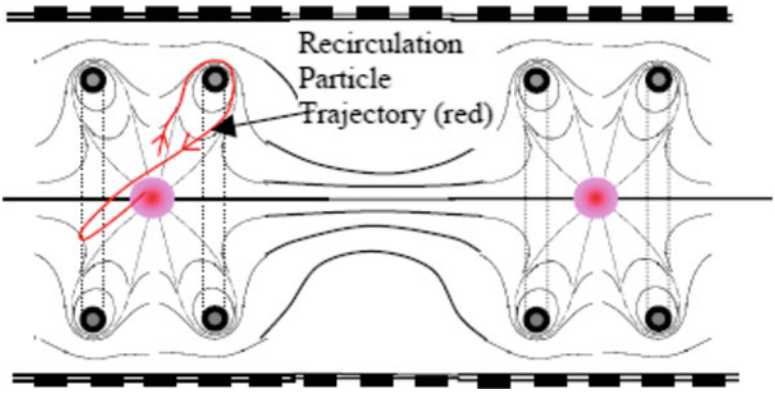

Fig. 12.19 Diagram of belt cusp fields and particle recirculation [18]

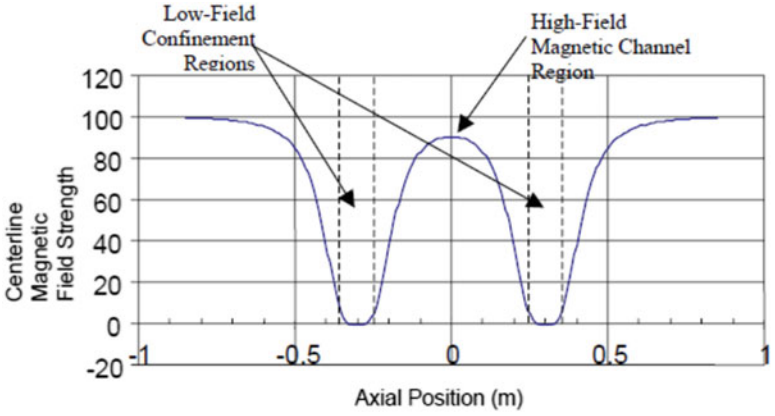

Fig. 12.20 Axial magnetic field strength along a two-unit MCSA centerline [18]

12.7.2 Retrapping of Axial-Loss Particles

Axial plasma particle loss escaping out through the end cone (spindle cone) of the first MCSA unit should be retrapped in the second unit because of the KAM effective scattering. This KAM scattering occurs as particles move into the null-field region within each SIEC unit. Figure 12.20 illustrates the axial magnetic field component along the centerline of the two-unit MCSA experiment. Particles escaping from the low-field region of an MCSA unit into its neighboring unit pass through the high magnetic field region between the two units. Upon entering the SIEC region, the direction of the particle is effectively randomized when it loses adiabatic invariance during passage through the field null region. Though those particles with high velocities parallel to the magnetic field (relative to their perpendicular velocity, v) will not experience as much effective scattering, many

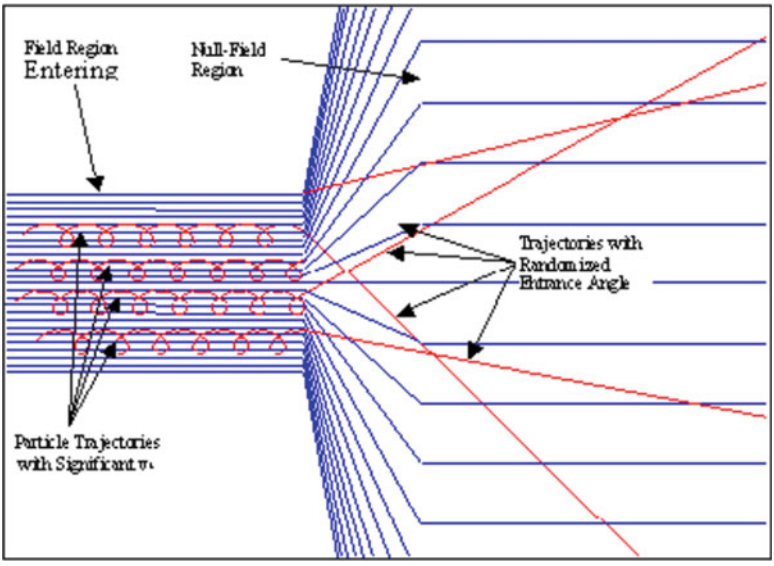

Fig. 12.21 Diagram of direction randomization (KAM effect) due to magnetic field null region in SIEC [18]

of the particles entering the null-field region should experience enough scattering to be retrapped.

Figure 12.21 illustrates this KAM scattering process conceptually. Before entering the null-field region, particles have a gyroradius that depends on their perpendicular velocity. If $v_{\perp}$ is large compared to v_{11}, the effective scattering angle will be large, resulting in retrapping in the case of the MCSA. While in the high-field region, the gyroradius of the particle is small. When the low-field region is reached, the particle moves in a straight-line path along the vector direction it has at the edge of the null region. Because the phase of the gyro motion of the particles is random at this point, the vector direction they assume is crossing the null is random. The result then can be viewed as a random, collisionless scattering process. Particles that stream along the axis and enter a neighboring SIEC scatter in this way and become confined in the neighboring SIEC (termed axial-loss retrapping). This retrapping greatly increases the confinement time of a MCSA fusion device. This process results in a linear scaling of confinement time with the number of units in the SIEC array.

In summary, if the physics principles are demonstrated successfully, the MCSA fusion power plant will offer numerous advantages for space propulsion. The non-Maxwellian plasma involved is well suited for operation with D–^{3}He fuel that provides much of the energy output in the form of very energetic 14-MeV protons. Proton energy can be employed for either direct conversion to electricity or directed thrust [18]. As demonstrated in the Fusion Ship II design study, the MCSA power plant is especially well suited for manned deep space missions. Though the

physical principles discussed here have not yet been demonstrated experimentally, initial tests could be done with a modest small experiment and stepped up in size to eventually demonstrate a full-scale prototype power unit.

12.8 IEC Electrically Driven Space Thruster, HIIPER

A new plasma thruster called HIIPER (Helicon-Injected Inertial Plasma Electrostatic Rocket) is being studied experimentally at the University of Illinois [22–24]. HIIPER space propulsion represents a radically new class of electric thruster with advanced capabilities necessary to perform deep space missions. HIIPER employs a very high-density Helicon plasma source for ion production and an IEC stage for plasma acceleration into thrust in the form of a plasma jet featuring a tight "pencil-like" beam. As with current electrically driven thrusters, such as Hall thrusters, the electric power required will be obtained from a solar power panel. Thus, HIIPER uses electric input power rather than fusion power.

Though the Helicon source and IEC have been studied separately for a variety of applications, this is the first time that these two devices have been coupled to solve electric thruster issues of longevity, scalability, and cost that have been a barrier in achieving more comprehensive deep space explorations (see Fig. 12.22). Aspects of using Helicon plasma injection for HIIPER were briefly discussed in Chap. 10. Here, we will discuss the concept and its space thruster operation in more detail.

The Helicon source generates high-density plasma with high efficiency using wave heating [25]. It is responsible for the primary ionization in HIIPER because it has a characteristic low energy cost per ion. In this experimental device, it consists

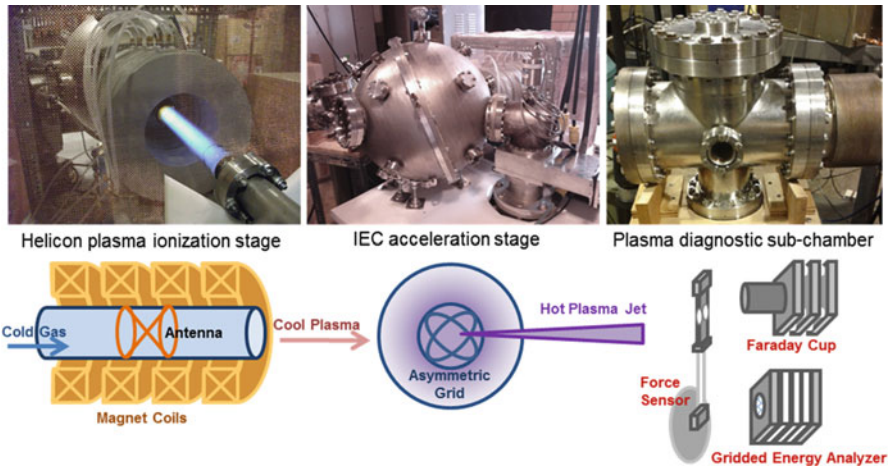

Fig. 12.22 The HIIPER concept couples a Helicon plasma ionization stage with an IEC acceleration stage to produce a hot, confined plasma jet. Three diagnostics can be mounted in a sub-chamber to measure the plasma properties [24]

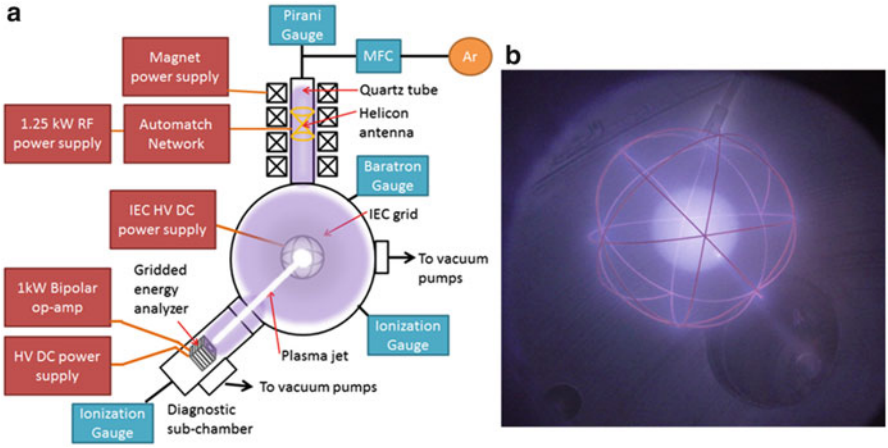

Fig. 12.23 (**a**) Diagram showing the general setup of HIIPER. (**b**) High-energy argon plasma jet exiting the asymmetry in the IEC acceleration stage (grid shown is ~ 126 mm in diameter) and hitting an early generation gridded energy analyzer (picture is from the 500-W proof-of-concept HIIPER lab experiment) [24]

of a quartz tube with a helical m = +1 copper strap antenna. It is surrounded by magnetic field coils capable of producing fields exceeding 1,200 Gauss. This plasma is fed into an asymmetric spherical IEC grid that accelerates the ions to produce thrust. The decoupling of plasma source and plasma acceleration through the two stages allows the ability to have variable specific impulse.

As described in this book, the IEC was originally devised as a plasma confinement technique for fusion plasmas. In the present implementation, it is constructed as a spherical plasma diode. The outer stainless steel wall of a vacuum chamber functions as a grounded anode. A strongly negatively biased cathode grid is placed at the center of the vacuum chamber. The ions circulate in the grid due to the potential well. An asymmetry in the grid, for example, from a snipped grid wire, changes the shape of the potential, and at the correct operating pressure, a plasma jet will form and propagate out through the asymmetry in the grid. The total coupled setup of the HIIPER concept is shown in Fig. 12.23.

As discussed earlier in Chap. 3, IEC in a spherical diode configuration has several modes of operation that depend on the number of grids present and the grid diameter as well as the operating pressure. These modes are known colloquially as central spot mode, “Star” mode, and jet mode. The third mode, jet mode, is of most interest to the present work on HIIPER [26]. This mode is most easily created by introducing an asymmetry into the central cathode grid typically by removing some of the grid wires. Under certain conditions, even in a symmetric grid, small jets are observed exiting some of the cathode grid openings. However, the direction of these jets is not controllable and may change several times per second. The asymmetry allows specific control of the jet direction to produce a defined thrust vector. The compactness of the plasma jet is dependent on the

operating pressure of the device. Under the correct operating pressure of a few mTorr, a pencil-like beam of plasma is formed. If the pressure is a little higher, the beam rapidly spreads due to collisions and a "spray" is formed. Unlike fusion studies with the IEC which use either D or D–T, the HIIPER uses heavy non-fusing gases like argon or xenon, which are suitable for thrusting.

In order to characterize HIIPER operation as a new electric propulsion concept, three key diagnostics have been constructed to study the jet: the gridded energy analyzer (GEA) (also called a retarding potential analyzer), the Faraday cup, and the piezoelectric force sensor. These were discussed further in Chap. 11, which covers diagnostics. The results will allow more accurate estimates of the space thruster relevant quantities such as specific impulse, total thrust, efficiency, and thrust-to-weight ratio.

12.8.1 Comments About Scale-Up to p–B^{11} IEC Space Power Unit/Thruster

The electrically driven IEC jet thruster provides an important database for a next step p–B^{11} IEC jet thruster. Jumping to p–B^{11} for this application may appear overly ambitious. However, neutronless fusion seems essential in a space application to avoid excessive weight from shielding and the need for tritium breeding/handling. Such operation is very demanding and its feasibility remains to be established. The issues and possible steps toward a p–B^{11} reactor are discussed further in Chap. 13. Assuming that is possible, a recent design study of such a system, termed VIPER, was undertaken. The objective was to achieve a deep space probe capable of high ISP for fast missions [27].

12.9 IEC-Driven Fusion–Fission Hybrids

One potential use of IEC neutron sources is for fusion–fission hybrid reactors [28]. This application takes advantage of the excellent neutron production capability of the IEC. The conditions required could be achieved with the IEC operating below energy breakeven such that the surrounding fission blanket produces the main net energy gain for the coupled hybrid reactor. This general situation has been generically described as "D–T fusion is neutron rich, while fission is energy rich." The IEC-driven hybrid is closely related to accelerator-driven hybrid concepts.

An accelerator-driven subcritical reactor potentially offers important safety advantages for future fission power systems [29–33]. A fast neutron spectrum subcritical reactor system with heavy metal coolant has received considerable attention in Europe, the United States, and Japan. Alternate versions, using intermediate or thermal spectrum neutronics with lighter moderators, are also possible.

Another attractive application of a driven reactor is for burning of plutonium isotopes, actinides, and select long-lived fission products. In addition to large power reactors, special low-power designs are candidates for student subcritical laboratory experiments and research reactors. The driven system is especially beneficial, because the enhanced safety allows a wider variety of experimental conditions, including dynamic studies.

The main approach considered for the driver to date has been an accelerator–-spallation-target system. While this concept appears feasible, the large size and cost of the accelerator system remain an issue. Also, the in-core target system poses significant design and engineering complications. Here, we consider the alternative of using unique IEC neutron sources that are small enough to fit within fuel element channels or in a central cavity region of the subcritical core assembly. Thus, the IEC replaces both the accelerator system and spallation target by either a central neutron source or by multiple modular sources configured as elements within the "standard" core assembly. This feature provides flexibility in design of the core and in flux profile control. Most importantly, these small units can be produced at a lower cost than the accelerator-target system.

Considerable research on the IEC concept has already been carried out on a laboratory scale as described in this book. However, a key remaining issue concerns the ability to achieve the high neutron rates required using the small volume units that are envisioned. Also, there are engineering issues such as the high-voltage stalks that will require improved technology to prevent unwanted arcing in the intense radiation fields encountered in the reactor core.

In addition to the spherical IEC units, a unique cylindrical version has also been developed as described in Chap. 9, and it provides an alternative geometry for subcritical-driven application. Present steady-state IEC units produce ~10^8 D–D n/s, while advanced pulsed versions extend to 10^{10} n/s, equivalent to 10^{12} n/s if D–T is used under similar conditions. This is in the range desired for use in small research reactors, but it is roughly four orders of magnitude lower than what is needed for driven power reactor applications. The concept of using an IEC to drive a subcritical reactor was originally proposed based on various gridded IEC concepts [34–38]. However, grid transparency issues might be avoided by the use of virtual electrode structure formed in a high-current ion-injected spherical IEC or, alternatively, in the hollow electrode cylindrical IEC design, improving the neutron production efficiency and allowing higher yields [39, 40]. The prototype cylindrical IEC version (see Fig. 9.1 in Chap. 9), called a C-Device, has a geometry that is particularly attractive for the driven subcritical application. It forms deuterium (or D–T) beams in a hollow cathode configuration such that fusion occurs along the extended colliding beam volume in the center of the device, giving a line-type neutron source. The prototype design uses hollow cylindrical anodes (held at ground potential) at either end of the unit, while a similar but longer hollow cylindrical cathode in the center of the device is biased to a high negative potential. Deuterium gas introduced at the end of the unit is ionized in the resulting discharge, creating an ion source. These ions are accelerated back and forth along the axis of the unit, where they collide and fuse.

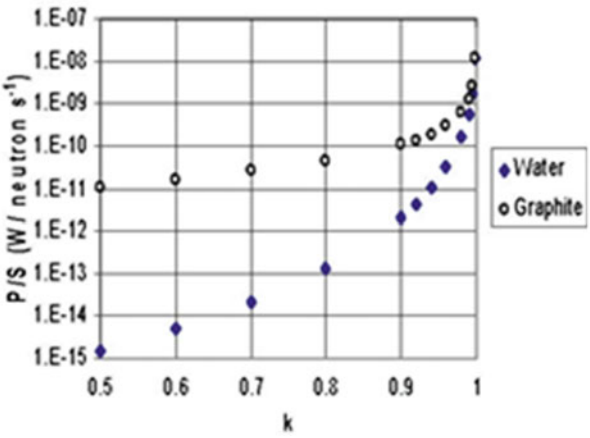

Fig. 12.24 Power level per unit source (P/S) as a function of k_∞ for two different moderators. Results for two different moderators, graphite and water, are presented [36]

Table 12.4 Parameters for a 1-kW graphite-moderated subcritical system [36]

Fuel	UO_2 (0.5 % U-235)
Moderator material	Graphite
Moderator volume fraction	95 %
Multiplication factor	0.99
Radius (cm); height (cm)	30; 50
Source strength (neutrons/s)	1×10^{12}
Power (kW)	1.2

12.9.1 Possible Initial Use in Low-Power Research Reactors

The first use of IEC-driven systems could well be for application to low-power research reactors. In this case, a lower source strength is required, and present experimental IEC devices are very close to meeting that goal. This concept is illustrated by some approximate calculations for a representative system.

The system is assumed to be a cylindrical homogeneous reactor fueled by uranium dioxide. The fuel enrichment is adjusted to give the desired value of k_∞, maintaining the fraction of core volume occupied by the fuel fixed at 5 %. From Fig. 12.24 it can be observed that the graphite-moderated system can deliver 1 kW of power with a source of 10^{12} n/s when the multiplication factor k_∞ of the reactor is 0.99, far from critical. Specifications for that system are summarized in Table 12.4.

While these calculations are quite approximate, this study provides a target reference design for a 1-kW IEC-driven graphite-moderated research reactor. Such a reactor appears to be quite attractive from a cost and safety point of view. Also, because existing experimental IEC devices have already achieved approximately 10^{11} D–T n/s equivalent, the improvement required in this technology to achieve the target of 10^{12} n/s to drive the system outlined in Table 12.4 appears to be feasible in the near term. This is consistent with the source levels used in existing research reactors such as Garching II, where subcritical operation is based on a Cf-252 neutron source with 4×10^9 n/s.

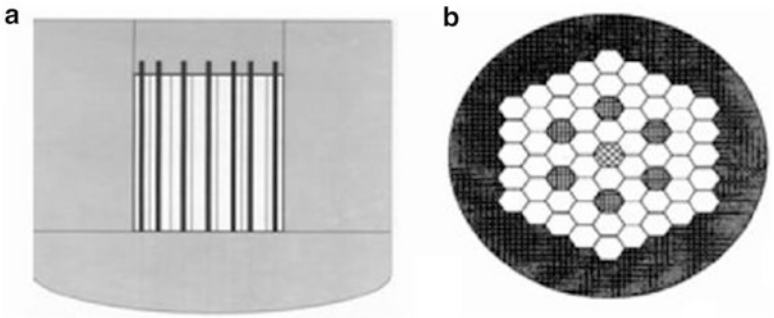

Fig. 12.25 (**a**) Vertical cross section of the core showing cylindrical IEC modules (dark vertical lines). (**b**) Cross-sectional view of the reactor core showing the IEC modules (crosshatched channels) [41]

12.9.2 IEC Configuration for the Subcritical Reactor Design

The higher power IEC driven-reactor system would be designed to ensure safety against criticality and loss-of-coolant accidents, as is done in the conventional accelerator-target designs. Some important differences exist, however, in the method used to safeguard against hypothetical beam power and reactivity increase accidents. In accelerator designs, a passive beam "shut off" device is incorporated using a combination of thermocouple readings and a melt-rupture disk in the side wall of the beam guide tube [41]. The IEC would use a simple temperature-sensitive fuse in the in-core electric circuit to shut down the high voltage needed to maintain neutron generation. A melt-rupture disk on the IEC wall could be added to spoil the IEC vacuum.

To illustrate the IEC system, a rough conceptual design for a 1,000-MWe plant has been developed. The reactor core employs distributed IEC units as shown in Fig. 12.25.

In this design, cylindrical IEC units occupy seven fuel channels and are stacked such that 15 units can be stacked in each channel. Though a variety of arrays are conceivable, this particular configuration was selected to optimize neutron profiles in both the radial and vertical directions across the core. This "distributed source" design is to be contrasted with an accelerator-driven reactor where the center of the core is allocated to the spallation target. In contrast, waste heat from the IEC is deposited on the large-area hollow electrodes and removed through the normal coolant flow around the fuel channels.

The conceptual 1,000-MWe reactor is designed with a $k_{eff}<0.99$ requiring $\sim 10^{15}$ n/s per IEC module. This source rate is to be compared to the present experimental values of $\sim 10^{11}$ D–T n/s from the pulsed C-Device (the D–T "equivalent" yield based on measured D–D rates). While the driven-reactor requirement is four orders of magnitude larger, there does not appear to be a fundamental block for

such a scale-up in source strength [39, 42]. Because IEC scaling involves velocity space scattering losses (versus cross-field diffusion as in other magnetic confinement devices), increasing the yield does not require a significant increase in unit size. Instead, higher beam currents and improved ion recirculation are the key physics issues. Other crucial issues involve technology concerns such as incorporation of other high-voltage stand-offs that are "radiation hardened" against the high nuclear radiation levels encountered in the nuclear core. Fortunately, many of these issues can be studied using a small unit, allowing a low-cost, time-effective research and development program.

In conclusion, IEC neutron sources that can be in a central location or distributed across a number of fuel channels could be employed as an alternative to the standard driven-reactor accelerator–spallation-target design. Such a modular design has distinct advantages in reduced driver costs, plus added flexibility in optimizing neutron flux profiles in the core. The basic physics for the IEC has been demonstrated in small-scale laboratory experiments, but a scale-up in source strength is required for ultimate power reactors. However, the IEC source strength is already near the level required for low-power research reactors or for student subcritical laboratory devices. This application would be advantageous because the safety advantages of these reactors should enable a next generation of research reactors to be constructed quickly, meeting educational and research needs during a rebirth of interest in nuclear power.

12.10 Summary

As pointed out earlier, the IEC is one of the few fusion confinement approaches that offers a number of practical applications now without waiting to improve the energy output Q value. Several of these, such as the low-level neutron source, have already been employed commercially in some limited applications. Exploratory experiments to study other near-term applications such as nuclear materials detection for Homeland Security and medical isotope production have been discussed. Other applications discussed here have been taken from design studies, such as future potential IEC fusion space propulsion and IEC-driven fusion–fission hybrids. In these cases, however, nearer-term development steps have been identified. For example, the electrically driven HIIPER plasma propulsion system is intended for near-term application to satellite station keeping where it competes with devices such as Hall plasma propulsion. The development of IEC-driven subcritical assemblies for use in student laboratories is within the neutron source strength range achievable for current advanced IEC sources. Once such a step is taken, and experience is gained with the laboratory-scale IEC technology, development of the more aggressive reactor designs discussed in this chapter could be undertaken.

References

1. Kulcinski GL (1997) Overview of neutron/proton source applications from IEC fusion devices. Trans Am Nucl Soc 77:507
2. Cipiti BB (2004) The fusion of advanced fuels to produce medical isotopes using inertial electrostatic confinement. Ph.D. thesis, University of Wisconsin–Madison
3. Cipiti BB, Kulcinski GL (2003) Embedded D-^{3}He fusion reactions and medical isotope production in an inertial electrostatic confinement device. Fusion Sci Technol 44:534–538
4. Firestone RB (1996) Table of isotopes, 8th edn. Wiley, New York
5. Weidner JW, Kulcinski GL, Santarius JF, Ashley RP, Piefer G, Cipiti B, Radel R, Krupakar Murali S (2003) Production of 13N via inertial electrostatic confinement fusion. Fusion Sci Technol 44:539–543
6. Cipiti BB, Kulcinski GL (2005) The production of ^{13}N using beam–target D–^{3}He fusion reactions. Fusion Sci Technol 47:1245–1249
7. Nuclear Data Services, International Atomic Energy Agency (2003) http://www-nds.iaea.or.at/pgaa/data/gamdoc.pdf
8. Committee on the Review of Existing and Potential Standoff Explosives Detection Techniques (2004) Existing and potential standoff explosives detection techniques. The National Academies Press, Washington, DC
9. Wehmeyer AL (2005) The detection of explosives using an inertial electrostatic confinement D–D fusion device. MS thesis, Department of Engineering Physics, University of Wisconsin, Madison
10. Yoshikawa K, Masuda K, Takamatsu T, Hotta E, Yamauchi K, Shiroya S, Misawa T, Takahashi Y, Ohnishi M, Osawa H (2007) Research and development on humanitarian landmine detection system by use of a compact D–D fusion neutron source. Fusion Sci Technol 52:1092–1095
11. Orlov VA (2004) Illicit nuclear trafficking and the new agenda. IAEA Bull 46(1):53–56
12. Radel RF (2007) Detection of highly enriched Uranium and Tungsten surface damage studies using a pulsed inertial electrostatic confinement fusion device. Ph.D. thesis, Department of Engineering Physics, University of Wisconsin, Madison
13. Miley GH, Wu L, Kim HJ (2005) Nuclear techniques in national security studies on contraband detections IEC-based neutron generator for security inspection system. J Radioanal Nucl Chem 263(1):159–164
14. Gu Y, Miley GH (2001) Spherical IEC device as a tunable X-ray source. Bull APS 11:185
15. Teller E, Glass AJ, Hasegawa A, Santarius JF (1992) Space propulsion by fusion in a magnetic dipole. Fusion Technol 22(1)
16. Burton R, Momota H, Richardson N, Shaban Y, Miley GH (2003) Fusion ship II—a fast manned interplanetary space vehicle using inertial electrostatic fusion. In: Space technology and applications international forum, STAIF 2003, AIP conference proceeding, vol 654. Albuquerque, pp 553–562
17. Neumeyer C et al (2001) Engineering design of the national spherical torus experiment. Fusion Eng Des 54(2):275–319
18. Miley GH, Stubbers R, Webber J, Momota H (2004) Magnetically-Channeled SIEC Array (MCSA) fusion device for interplanetary missions. In: Space Technology and Applications International Forum (STAIF 2004). American Institute of Physics
19. Bussard RW (1991) Some Physics considerations of magnetic inertial-electrostatic confinement: a new concept for spherical converging-flow fusion. Fusion Technol 19(2):273–293
20. Barnes DC, Nebel RA (1998) Stable, thermal equilibrium, large-amplitude, spherical plasma oscillations in electrostatic confinement devices. Phys Plasma 5:2498
21. Momota H, Miley GH, Nadler J (2000) Direct energy conversion for IEC propulsions. Report to National Institute for Fusion Science, NISF-641, ISSN 0915-633X
22. Krishnamurthy A, Chen G, Ulmen BA, Miley GH (2012) Numerical and experimental measurements in a helicon-IEC thruster. In: 48th AIAA/ASME/SAE/ASEE joint propulsion

conference & exhibit, 10th annual international energy conversion engineering conference, Atlanta
23. Krishnamurthy A, Ulmen BA, Keutelian P, Chen G, Miley GH (2012) Helicon-Injected Inertial Plasma Electrostatic Rocket (HIIPER): experimental proof of principle. In: 48th AIAA/ASME/SAE/ASEE joint propulsion conference & exhibit 10th annual international energy conversion engineering conference, Atlanta
24. Ulmen BA, Keutelian P, Chen G, Krishnamurthy, Miley GH (2012) Investigation of plasma properties in Helicon-Injected Inertial Plasma Electrostatic Rocket (HIIPER). In: 48th AIAA/ASME/SAE/ASEE joint propulsion conference & exhibit 10th annual international energy conversion engineering conference, Atlanta
25. Chen FF (1991) Plasma ionization by helicon waves. Plasma Phys Control Fusion 33(4):339–364
26. Nadler JH, Yoder ED, Hunsicker C, Miley GH (1998) Experimental investigation of unique plasma jets for use as ion thrusters. In: 29th plasmadynamics and lasers conference, AIAA-2570, Albuquerque, pp 1–5
27. Miley GH, Orcutt J (2012) A fusion space probe—viper, an ultra-high I_{SP} pulsed fusion rocket. In: Space Technology & Applications International Forum (STAIF II), Albuquerque
28. Miley GH, Thomas R, Takeyama Y, Wu L, Percel I, Momota H, Hora H, Li XZ, Shrestha PJ (2009) Driven subcritical fission research reactor using a cylindrical inertial electrostatic confinement neutron source. Report of the Research Needs Workshop (ReNeW), Research needs for fusion-fission hybrids, Gaithersburg
29. Dautray R (1993) Future development of energy resources. Position paper CEA, CHC/93-104
30. Rubbia C (1998) Harmless energy from nuclei: a quest worth pursuing? Workshop on innovative options in the field of nuclear fission energy, Centre de Physique des Houches
31. Carelli M, Green L, Paramonov DV (1999) A sub-critical reactor design for accelerator transmutation of waste. In: 3rd Int'l topical meeting on nuclear applications of accelerator tech, pp 359–366
32. Beller DE, Van Tuyle GJ, Venneri F (1999) Systems studies of ATW-coupled fuel cycles for the 21st century. In: 3rd internationa'l topical meeting on nuclear application of accelerator technology, pp 355–358
33. Wider HU, Karlsson J, Jones AV (1999) Safety advantages of heavy metal-cooled accelerator-driven systems. Joint Research Centre of the European Commission, Institute for Systems, Informatics and Safety (ISIS)
34. Miley GH, Momota H, Shaban Y, Hora H (2002) Progresses in development of a converging beam neutron source for driving a driving a sub-critical fission reactor. In: ICONE 10, Arlington, Virginia, pp 1–7
35. Miley GH, Stubbers RA, Momota H (2003) Advances in cylindrical IEC neutron source design for driven sub-critical operations. In: ICONE 11, Tokyo
36. Miley GH, Stubbers RA, Wu L, Momota H (2004) An IEC-driven sub-critical assembly for teaching laboratories offering a new generation of sub-critical experiments. In: 14th Pacific Basin nuclear conference, Honolulu, Hawaii
37. Hora H, Prelas MA, Miley GH (2003) Kernspaltreaktor mit unterkritischer Auslegung. German Patent 4327920 C2
38. Hora H, Miley GH (2001) Upgraded reactor for electrostatic confined nuclei. German Patent Appl. 10118 251.1
39. Bromley B, Chacón L, Miley GH (1998) Approximate modeling of cylindrical IEC fusion neutron generator. In: Proceedings of the 16th internationa'l conference on numerical simulation of plasmas, Santa Barbara, California, pp 191–192
40. Chacón L, Bromley B, Miley GH (1997) Prospects of the cylindrical IEC fusion device as a neutron source. In: Proceedings of the 17th IEEE/NPSS symposium fusion engineering, San Diego, California, vol 2, pp 858–861

41. Miley GH, Bromley B, Jurczyk B, Stubbers RM, DeMora JM, Chacón L, Gu Y (1998) Scaling of the inertial electrostatic confinement (IEC) for near-term thrusters and future fusion propulsion. STAIF-98, Part 3, pp 1373–1375
42. Chacón L, Miley GH, Barnes DC (1999) Energy gain studies of spherical IEC devices using the BAFP code. Bull APS 44(7):48

Chapter 13
Reactor Confinement Theory and IEC Reactor Visions

13.1 Introduction

Basic IEC theory was described earlier in Chaps. 1 and 2. We now turn to issues related to confinement theory for extension to a high flux neutron source or a power reactor. Work on reactor grade confinement for an IEC is closely tied to formation of a deep potential well and trapping of ions in that well sufficiently long enough (i.e., sufficient confinement time) to meet the Lawson Criteria. For D–T fuel, this is approximately given by $n_i\tau_i = 10^{14}$ s/cm^3 at about $T_i = 25$ keV (varies with fuel, e.g., about 10^{16} at $T_i \sim 150$ keV for p–B^{11}) [1, 2]. Here, n_i is the ion density, τ_i is the ion confinement time, and T_i is the average ion temperature, or, for a non-Maxwellian plasma, the average ion energy. This applies to both electron-injected and ion-injected IEC configurations. However, due to ion beam convergence in typical spherical geometry, the ion density peaks strongly in the center region making it difficult to estimate the appropriate average density, n. In addition, it is generally hoped that beam–beam fusion collisions will dominate rather than Maxwellian reactions or beam–background gas reactions. In view of these considerations, the Lawson Criteria, which assumed a Maxwellian-type plasma for reaction rates, must be revised for the IEC. For a rough order of magnitude, assume that the converged region average density is around 10^{16} cm^{-3}, then the confinement time needed is roughly 10^{-2} s. Radiation losses also need attention. The elimination of a magnetic field in the ion-injected case minimizes cyclotron radiation losses. Such losses are still encountered in "hybrid" magnetic trapping concepts such as the Polywell, but hopefully this radiation loss can be kept reasonably low with a relatively low magnetic field strength in the plasma trapping region.

Still, Bremsstrahlung losses remain very important for both ion- and electron-injected IECs. These losses depend on the electron temperature, which in turn depends on energy transfer rates between the energetic ions and the colder electrons. It has often been assumed that in the IEC the electrons remain at a much lower temperature than the average ion energy, reducing Bremsstrahlung losses. Due to the complexities invoked, detailed simulation computations are needed to

G.H. Miley and S.K. Murali, *Inertial Electrostatic Confinement (IEC) Fusion: Fundamentals and Applications*, DOI 10.1007/978-1-4614-9338-9_13,

study these issues in detail for a given configuration. Some done to date are reviewed in this chapter, but much more study is needed to fully resolve these issues and qualify the IEC for reactor operation with D–T fuel, or perhaps more importantly, with advanced fuels such as D–^{3}He or p–B^{11}.

The IEC has been frequently cited as one of the key approaches to using advanced fuels due to its non-Maxwellian beam–beam fusion ability and reduced radiation loss rates. In view of the very demanding physics requirements for burning fuels like p–B^{11}, much detailed study remains to verify the potential for the IEC to achieve that goal. An important factor to keep in mind, however, is that current experiments can achieve the ion energies needed for fusion of all of these fuels by simply applying the necessary voltage to the grid. Ions are generally accelerated to some 80 % or so of the applied voltage. Thus, IEC D–D neutron sources have been very successfully developed using voltages around 60–160 kV. However, p–B^{11} would require 170–200 kV. That is possible if care is taken to prevent arcing and other voltage holding issues addressed in Chap. 4. While the ion energy required may be obtained, the density and confinement time must be achieved simultaneously to achieve the Lawson Criteria. For the IEC, those parameters pose more of a challenge. In this chapter we summarize some of the computational studies that have examined these issues. In addition, we close with comments and speculation about considerations for the development of an IEC reactor.

13.2 Early Ion Thermalization and Energy Balance Studies of Potential Well-Trapped Plasma

Collisional degradation of the beam-like ion energy distribution function is a crucial issue in the assessment of the physical feasibility of IEC devices, because it may preclude adequate ion concentration at the spherical center. An early study of this problem by Nevins [3] has caused concern about the suitability of the IEC for a fusion power reactor. He did a semi-analytic analysis where the IEC systems are treated as a non-equilibrium ion distribution function trapped in an idealized square potential well. Nevins found that Coulomb collisions between ions cause this distribution to relax to a Maxwellian on the ion–ion collisional time scale. This analysis showed that the power required to prevent this relaxation and to maintain the IEC configuration for times beyond the ion–ion collision time scale is greater than the fusion power produced. Thus, Nevins concluded that IEC systems showed "little promise" as a basis for the development of commercial electric power plants but could leave the way open for driven neutron sources. More specifically, Nevins predicted that the Q-value (defined as fusion power over ion input power) for ion-injected IEC devices operating with a 50 % D–T mixture would be ~0.21 for a 50-kV deep square well.

Note, however, that a tightly focused monoenergetic ion beam is in fact quite a pessimistic scenario. That is because different co-moving ion species such as D and T with the same energy result in a finite speed difference, fostering ion–ion

collisions and the degradation of the ion distribution function. It would be more realistic to consider that, in a square well, friction between species would homogenize the speed within the ion beam after a short time, making the speed difference infinitesimal. This line of argument was pursued by Barnes and colleagues [4], who found $Q \sim 1.3$ for the same system as treated by Nevins. This result showed that more detailed analysis of the potential well-trapped plasma in the IEC is needed before a conclusion about reactor feasibility is possible. One such study was done by Chacon and colleagues, and its analysis is discussed in the next section.

Another aspect of potential well trapping is that ion up-scattering losses are caused by some ions picking up sufficient kinetic energy via Coulomb collisions to surmount the well and be lost from the system. According to study [5], the ion up-scattering time is about a thousandth of the fusion time, and thus it represents a power sink that must be evaluated for a specific configuration. Note, however, that this is different from the ion thermalization issue addressed by Nevins and by Barnes and colleagues.

13.3 Bounce-Averaged Fokker–Planck (BAFP) Analysis

Later, to further explore concerns raised by Nevins, Chacon revised this issue in his thesis work at the University of Illinois [6]. He elected to develop a bounce-averaged Fokker–Planck (BAFP) treatment for analysis of the IEC so that some of the assumptions used by Nevins could be relaxed. The computational code developed for this study was termed the BAFP code. In this study, Chacon specifically dealt with a Penning-type IEC due to interest at that time in the Penning trap experiment at Los Alamos National Laboratory (LANL) [4]. The experimental device at LANL, PFX-I, was discussed earlier in Chap. 10 and is illustrated in Fig. 13.1, while the reactor-like configuration model is shown in Fig. 13.2. It should be stressed, however, that the conclusions from this analysis still apply in principle to the ion-injected IEC, because the issues discussed involve “equivalent” potential well trapping. The Penning trap and ion-injected devices differ in the detail of how the well is formed and stabilized, but the physics of the trapped plasma confinement is the same.

Nevins addressed this issue by calculating the collisional relaxation rates from a beam-like, monoenergetic ion population, absolutely confined in an idealized square potential well [3]. From his analysis, Nevins concluded that the IEC system cannot work beyond the ion–ion collisional time scale, after which the system will thermalize and lose ion focusing before sufficient fusion events take place to provide a net energy gain.

In spherical Penning fusion devices, a spherical cloud of electrons confined in a Penning-like trap creates the ion-confining electrostatic well. In the early studies, fusion energy gains for these systems had been estimated in optimistic conditions (i.e., with a spherically uniform electrostatic well, no collisional ion–electron interactions, and a single ion species). In Chacon’s study [6], the BAFP code was

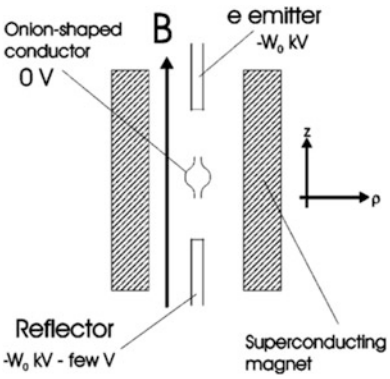

Fig. 13.1 Cross section of the experimental layout of the PFX-I experiment. The emitter electron source, onion-shaped anode, and reflector form an axial electrostatic well for electron axial confinement (radial confinement is provided by the axial magnetic field). The reflector is biased slightly more negative than the emitter to avoid electron losses to the reflector [6]

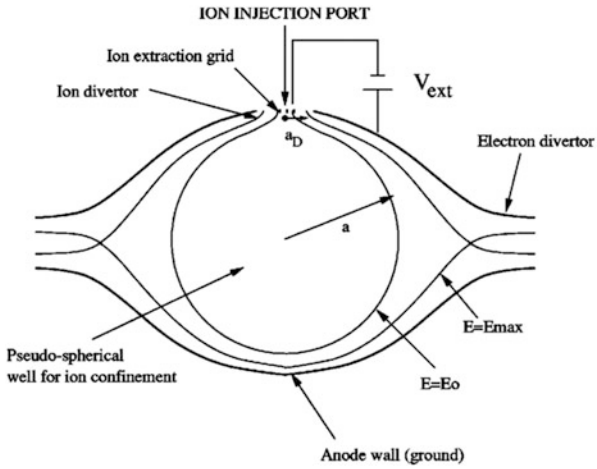

Fig. 13.2 Detail of the anode and the ion injection port in PFX-I. Ion and electron divertors are indicated, as well as the E_0 and E_{max} equipotential lines that define the ion confinement region. The E_0 contour line determines the region of absolute ion confinement [6]

employed to obtain steady-state solutions for the confined ion distribution function and to calculate associated fusion energy gains (Q-values). More details about the solution method used in the BAFP code are provided in references [7] and [8]. Chacon's study considered a variety of operating conditions in terms of the strength for the source and sink (i.e., energy loss channels), ion injection energies, well depths, and electrostatic potential shapes. Prior analyses of the Q-value of IEC devices such as Nevins [3] assumed that ions were confined in a square potential well, and that their distribution was tightly focused and monoenergetic. When these restrictive assumptions were relaxed using BAFP calculations, it was found that large energy gains ($Q \sim 10$) for beam-like solutions in square wells are possible in Penning IEC devices. These gains required that the electrostatic well is deep

Table 13.1 Comparison of analytical and numerical estimates of Q-values in a beam-dominated solution for a 50 kV square well

Analytical	Energy gain, Q (semi-analytic)	BAFP
With co-moving ions, Nevins [3]	~0.21	NA
Without co-moving ions, Barnes et al. [4]	~1.3	~1

enough ($E_0 \sim 100$ kV); the ion confinement time against up-scattering is long enough ($\theta \geq 0.01$); the ion source strength is moderate ($\hat{S}_{max} < 300$), while the ion injection energy is slightly below the potential well maximum. (Here, the ion confinement time θ and source strength $\hat{S}_{max}$ are normalized quantities defined in [9].) Further details about these results are provided next.

13.3.1 Comparison of Semi-analytic and BAFP Code Results

Calculated Q-values from the BAFP code in the beam-like cases are about five to ten times larger than those obtained in by Nevins's semi-analytic treatment [3]. This inconsistency was traced back to the different treatment of the D and T ion species in the two calculations. Thus, while BAFP treats both species as one with an average mass, Nevins treats both species separately but assumes they follow the same monoenergetic distribution function. This results in an "artificial" velocity difference between species that boosts collisionality, rendering smaller Q-values. This effect had been noticed and treated in the "revised" semi-analytic analysis by Barnes and colleagues [4] discussed earlier. As summarized in Table 13.1, the BAFP code results (that used a square well for comparison but did not assume co-moving ions) are in reasonable agreement with the Barnes and colleagues Q-value, which is about five times larger than the Nevins result.

The results in Table 13.1 assume an ion injection energy close to the top of the well. This restriction was removed in subsequent BAFP simulations. In those studies, novel, very efficient (Q; ~ 50) operating regimes were identified in deep square wells for weak ion sources ($\hat{S}_{max} \sim 30$) and moderately long ion confinement times ($\theta \sim 0.01$). In these cases a modified Maxwellian contribution becomes dominant over the beam contribution. These results indicate that efficient use of the electrostatic well is essential to achieve large fusion gains and demonstrate that a quasi-Maxwellian ion distribution – which has been neglected in previous analyses – might also be of interest. Another assumption in the earlier semi-analytic calculations, namely, an ideal square well, has been explored with BAFP [3]. Results also indicate that the square well assumption, used in previous analytical estimates by Nevins, gives a pessimistic result for Q. Thus, parabolic wells result in larger density peaks at the center, yielding Q-values three to five times larger (for $E_0 \sim 150$ kV) than those obtained with square wells.

Operating regimes with large Q-values of interest for power reactors have been identified as plotted in Fig. 13.3. In these calculations, the effect of electron losses

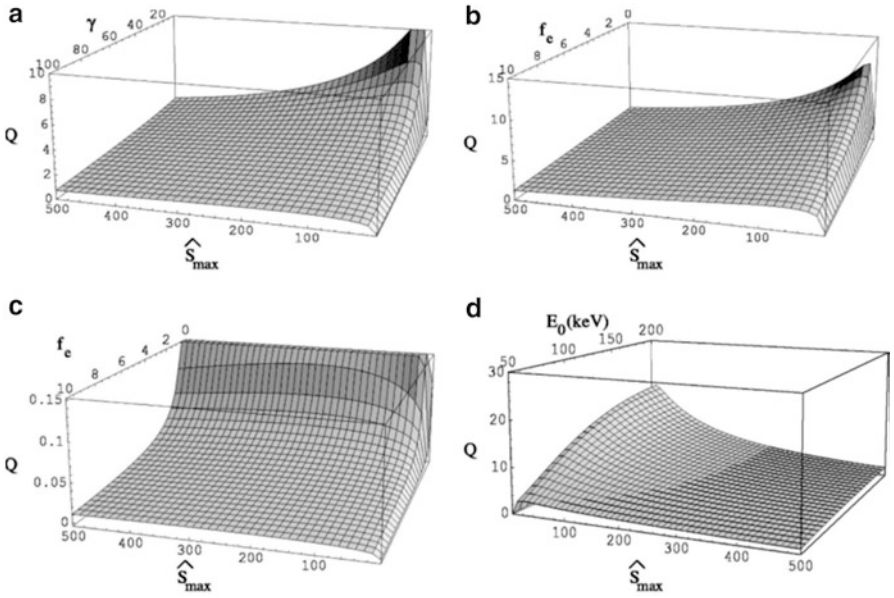

Fig. 13.3 Plot of the Q-value (including electron losses) as a function of (**a**) $\hat{S}_{max}$ and γ with $f_e = 10^{-3}$, (**b**) $\hat{S}_{max}$ and f_e with $\gamma = 5$, (**c**) $\hat{S}_{max}$ and f_e with $\gamma = 100$, and (**d**) $\hat{S}_{max}$ and E_0 with $\gamma = 5$ and $f_e = 10^{-3}$. These plots have been obtained for E_0 =100 keV [except (**d**)], $\theta_b = 0.01$, and $\hat{E}_s = 1.04$ [6]. All quantities are defined in reference [7]

on the Q-value has been addressed heuristically using a semi-analytic model, indicating that large Q-values are still possible provided that electron particle losses are kept small, and well depths are large with small electron to ion density ratios. The regions of large Q-values obtained in Fig. 13.3 can be explained as corresponding to an optimal ion source strength (small enough to allow a quasi-thermal solution, but large enough to provide sufficient fusion power density in the system to overcome electron power losses). Also, the electron particle losses are small ($0 < f_e < 1$) and well depths are large ($E_0 \geq 100$ kV). (The normalized electron loss function, f_e, and well depth E_0 for these plots are defined in reference [7].)

These results confirm that in addition to potential well shape, the source strength versus up-scattering losses play a crucial role in the IEC energy gain. More insight into this can be obtained from the conceptual distribution functions for trapped ions sketched in Fig. 13.4.

Two opposite limits corresponding to the ion energy distributions involved in the Q-value plots of Fig. 13.3 are depicted in Fig. 13.4. The realization of either of these limits depends on the equilibrium between two competing effects, namely, up-scattering of the Maxwellian ion population confined in the well (which increases as the Maxwellian temperature increases, and tends to empty the well) and down-scattering of the beam (which tends to fill it). The relative importance of these effects is directly related to the strength of the source in the problem characterized here by S_{max}. This is balanced against the ion replacement time, t_i,

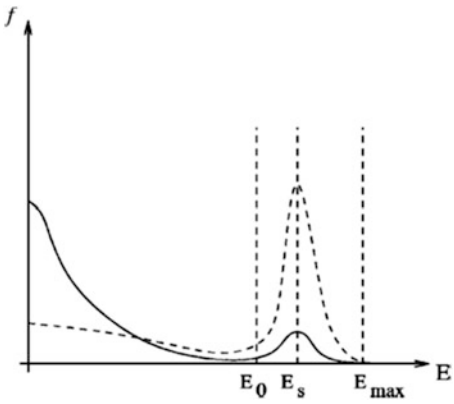

Fig. 13.4 Sketch of two opposite limits of the beam-Maxwellian equilibrium. The *solid line* corresponds to a case in which the Maxwellian population is dominant, and the *dashed line* corresponds to a case in which the beam contribution is dominant

which characterizes the sink term. Thus, weak sinks and strong sources will result in a large beam population, increasing the beam down-scattering rate. That in turn increases the Maxwellian temperature, resulting in the dotted line profile in Fig. 13.4. Conversely, weak sources and strong sinks will result in a small beam population, thus decreasing the beam down-scattering rate and resulting in smaller Maxwellian temperatures, leading to the solid line profile in Fig. 13.4. In steady state, particle sources and sinks must be matched, giving a distribution function lying between these two extremes.

In conclusion, these simulations of reactor grade plasmas in potential wells show how complex an accurate evaluation of the energy gain, Q, is. A combination of extensive computations and experiments is needed to fully explore this regime before definite conclusions are made.

13.3.2 Angular Momentum Effects on a Potential Well

The well-trapped plasma simulation by Chacon and colleagues is quite encouraging, but leaves open the issue of whether or not a sufficiently deep potential well can be created to access the regime of interest for a reactor. To pursue this issue further, Ivan Tzonev and colleagues considered well formation with emphasis on angular momentum [10]. While earlier studies had assumed that very low angular momentum (zero in the ideal case) is necessary to achieve a potential well structure capable of trapping energetic ions in the center of a spherical device. That presents a problem for ion-injected well formation, because the total volume of the core, hence the total power of the system, remains very low. Thus, to explore larger volume core formation, Tzonev and colleagues considered high-current ion beams having large-angular-momentum spread. The results found were positive. A small volume core requiring less energy input could be used to demonstrate energy breakeven. Following that using a larger momentum spread could extend studies to higher power reactors. Before discussing this work, some definitions for the potential well structure should be reviewed.

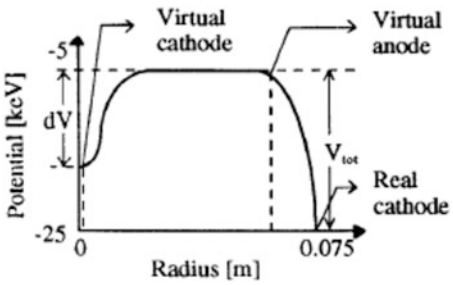

Fig. 13.5 The definition of the double well depth: namely, double well depth (%) $= \frac{dV}{V_{tot}} \times 100$ [10]. Here, the depth of the "inner" potential minimum (i.e., the double well depth) is defined as a percentage of the height of the "outer" potential maximum. For the case shown, the double well has a depth of ~ 60 %

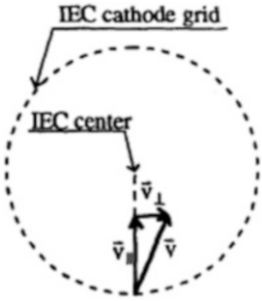

Fig. 13.6 The definition of the parallel $\vec{V}_n$ and perpendicular $\vec{V}_\perp$ velocities at the IEC cathode grid [10]

13.3.3 Potential Well Structure

The potential structures are called double potentials because two extremisms ("outer" and "inner" wells) are observed in the plots of electrostatic potential versus IEC radius, excluding the real cathode grid minimum at −25 keV. A schematic representation of a typical calculated potential for present work is shown in Fig. 13.5. These cases are different from Hirsch's ideal case described previously, where multiple potential wells with sharp peaks were observed. In Tzonev's study, spread-out potential extremisms are observed due to the high angular momentum spread. The virtual anode is defined as that position where the potential increases from its minimum value at the real cathode up to about 95 % of its maximum value. The virtual cathode is defined as the position where the potential is 95 % as deep as its minimum value in the center of the IEC device (see Fig. 13.5). The depth of the "inner" potential minimum, more frequently called the double well, is defined as a percentage of the height of the "outer" potential maximum (see Fig. 13.5). For the case shown, the double well has a depth of about 60 %. Also, the definition of angular momentum (i.e., the "perpendicular" velocity component) is shown in Fig. 13.6.

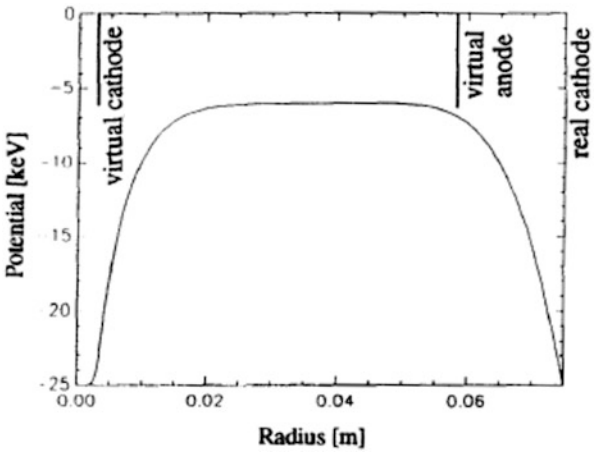

Fig. 13.7 An example of 100 % double well depth calculated with IXL code achieved at dE_{perp}, $i = 14$ keV, $I_i = 55$A, and $I_e = 59$ A [10]. In this case, the "inner" negative potential well has the same depth (dV) as the outer positive potential height (V_{tot})

13.3.4 Deep Well Studies

Simulations were done by Tzonev and colleagues using the IXL (ion accelerated code) – a one-dimensional electrostatic Poisson–Vlasov equation solver for use in spherical geometry [7]. IXL was developed by Mission Research Corp. for R. W. Bussard and his company, EMC^2. The primary purpose of the code is to determine an electrostatic potential consistent with the dynamics of the charged particles within that same potential and to determine the charged particle density distribution inside of the spherical cathode. While IXL neglects collisional effects, it still provides an important limiting case where space charge effects dominate. The boundary conditions for each particle population are characterized by four parameters: the injected beam current, the average injection energy, the energy spread associated with the velocity component in both parallel and perpendicular directions, and the number of recirculations through the core.

Tzonev and colleagues found that deep double electrostatic potential wells can occur at high ion and electron currents (30–60 A); high perpendicular ion energy spread (3–14 keV); low perpendicular electron energy spread (3 eV); and low radial ion energy spread (0.l–0.5 eV). An example is given in Fig. 13.7.

The corresponding ion density profile, shown in Fig. 13.8, has a high value $>$ 25 keV inside the virtual cathode (center core plasma) and also a peak in front of the grid (real cathode).

An important new insight obtained in the study revealed that these potential profiles create ion density distribution functions completely different from the ones observed when a single well electrostatic potential exists. Two ion density peaks were commonly observed – one in the central IEC core region and one near the cathode wire grid (shown in Fig. 13.8). In this manner, the single ion peak, created by the single well potential, is split into two peaks. The central ion peak has a much smaller radius than the original peak. This causes higher ion densities to occur in the central potential well, which is essential for the achievement of high fusion rates.

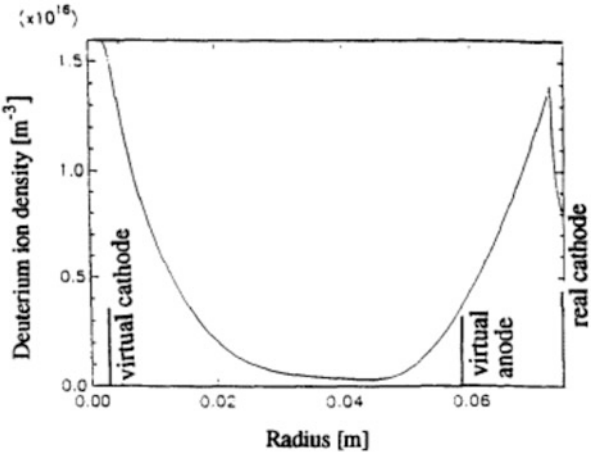

Fig. 13.8 Ion density profile for the potential well shown in Fig. 13.7

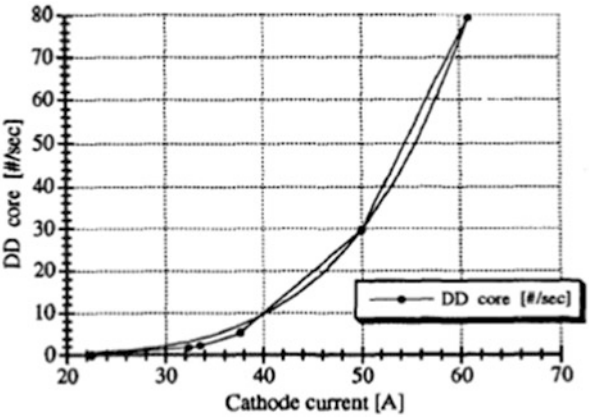

Fig. 13.9 The D–D fusion reaction rate versus cathode current for dE_{perp}, $i = 8$ keV [10]. Here, dE_{perp} is defined as the maximum injection energy of the ions. The reaction rate scales with the cathode current I_c as I_c^5. The cathode current is determined from the total ion and electron currents I_i and I_e, and the ion and electron recirculation factors

However, simultaneously, because the fusion core radius is very small – on the order of 0.4–0.9 cm – the total number of neutrons emitted per second is too low to create a useful fusion power (see Fig. 13.9).

A reduced angular momentum spread and higher injection energies would be required to correct this problem. Still, the D–D fusion rate exponential scaling approaching I^5 is encouraging. In addition, it is surprising that this large angular momentum spread achieves such distinct double well structures. As stated previously, the current scaling for beam–beam reactions is strictly I^2. However, as shown by Tzonev and colleagues, nonlinear changes in the potential well shape and ion density profile combine to create the higher power current scaling law such as in Fig. 13.9. It would be anticipated, however, that this effect would saturate at some current, ultimately trending back to the fundamental I^2 relation. Along these lines it should be noted that prior investigators also predicted scaling laws with exponents greater than two. Bussard first suggested this based on theoretical arguments

involving wave compression [11], and then later Ohnishi and colleagues [9] found an I^3 scaling from numerical simulations. The unanswered question is at what current level these effects occur and where they saturate. Future simulations should address this issue and also examine low angular momentum spread and higher ion injection energies.

13.4 Early Theoretical Studies of Potential Well Traps

Early theoretical studies of potential well structure for both ion- and electron-injected IECs necessarily included assumptions that prevented full insight into requirements and restrictions on the desired creation of non-Maxwellian reactor grade plasmas. Some of these studies were noted in Chap. 1. However, it is useful to review them again here in the context of supplementing the insights gained from the numerical simulations cited in prior sections.

One-dimensional (1-D) orbital modeling was used almost exclusively in early works [12–21]. The 1-D orbital model was primarily used to explore the relationship between the inner-electrode radial potential profile and the shapes of the distribution functions for the injected and trapped particles. Farnsworth hypothesized the formation of an infinite number of virtual electrodes based on a bipolar version of analytical work by Langmuir and Blodgett [22]. This potential well structure was later confirmed with a numerical solution by Hirsch [13]. Hu and Klevans showed that the placement of these virtual electrodes can be altered when spreads of a finite width in the radial energies of the injected and trapped particles are considered [18]. However, all of these investigations assumed pure radial focusing of the injected and trapped particles [4, 22, 23]. The potential structure consisting of an infinite number of alternating virtual electrodes disappears when spreads in energies and angular momentum of injected ions are included.

An extensive investigation of finite angular energy spreads is the result of the combined works of Dolan [14, 15], Swanson [16, 17], Black and Klevans [19], and Imel [20]. In particular, Dolan searched for solutions with large spreads in particle angular energy [15], while Imel [20] investigated small angular energy spreads. Mostly, the distribution functions were approximated with rectangular shapes, with the exception of Swanson [16, 17], who modeled the angular energy spreads with Maxwellian shapes. Meyer considered the detailed relationships between the control variables and fractional well depth for the structure in Fig. 13.10a, summed up in Table 13.2 from this early modeling [24]. Exceptions to the 1-D orbital modeling include two-dimensional dynamic modeling of unipolar and bipolar discharges by Hockney [25] and Barnes [26]. Hockney produced a result similar to the structure in Fig. 13.11 and found that it was stable [25]. Barnes's results indicated that the double well structure in Fig. 13.10b is only a transient phenomenon [26]. Barnes's work represents the only theoretical prediction of a double potential well during this early era.

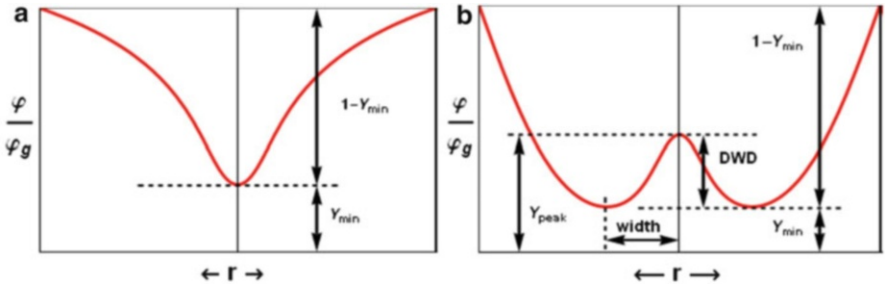

Fig. 13.10 (**a**) A single potential well structure. In this case, the minimum normalized potential, Y_{min}, coincides with the core potential, $Y_{core} = Y(r = 0)$. The fractional well depth (FWD) is defined as FWD $= 1-Y_{min}$. (**b**) A double potential well structure. In this case, FWD is defined as FWD $= 1-Y_{min}$, and the double well depth (*DWD*) as $Y_{peak}-Y_{min}$. Here, Y_{peak} coincides with Y_{core} [24]

Table 13.2 Summary of trends observed from modeling on the relationships between the control variables and the observables [24]

Control	Fractional well depth	Double well depth
Injected particle perveance, $P_0 = I_0\|\phi_g\|^{-3/2}$	$P\uparrow \rightarrow$ FWD$\uparrow$	$P\uparrow$ DWD$\uparrow$
Trapped particle perveance, β	$\beta\uparrow \rightarrow$ FWD$\uparrow$	*Optimum* $0 < \beta << 1$ for DWD
Trapped particles, $\sigma_{j,o}$, $j = 0$	$\sigma_{0,o}\downarrow \rightarrow$ FWD$\uparrow$	$\sigma_{0,o}\uparrow \rightarrow$ DWD$\uparrow$ plateaus for $\sigma_{0,o} \sim 1$
Injected particles, $\sigma_{j,o}$, $j = 1$	$\sigma_{1,o}\downarrow \rightarrow$ FWD$\uparrow$	$\sigma_{1,o}\downarrow \rightarrow$ DWD$\uparrow$

13.4.1 Analytical Study of the Virtual Electrode Structure

In another related study, Momota and Miley [27] used an analytical solution to study the angular momentum effects in ion-injected potential wells. Double well potential structure (virtual cathode formation) was studied for stationary spherical IECs using the nonlinear Poisson's equation and particle densities derived from kinetic theory. A novel method to obtain a spherically symmetric stationary distribution function was introduced, and an integral–differential equation was simplified by applying a relevant approximated formula for the integral. Electron and ion beams were assumed collision-free, and their velocities were roughly aligned toward the spherical center, but with a slight divergence. Analyses showed that the angular momentum of ions and the smaller one of the electrons created a virtual cathode (i.e., a double well structure) of the electrostatic potential on a potential hill near the center. The density limit of trapping ions in the well was exhibited, and conditions relevant to form a deep potential well were elaborated. These results showed trends in rough agreement with the numerical studies of Tzonev and colleagues. The techniques developed may be useful for future analytical study of these effects.

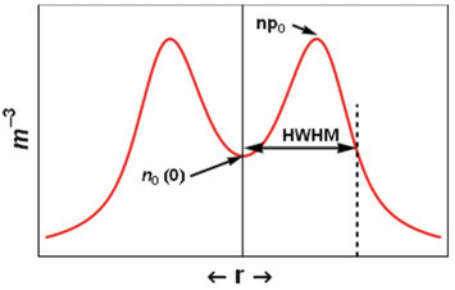

Fig. 13.11 An injected particle radial density profile, $n_0(r)$, for the case in which mutual repulsion of the injected particles results in significant space charge spreading of the core. In this case, the peak density, np_0. occurs at a radius $r \neq 0$ and $n_0(0) \neq np_0$ [24]

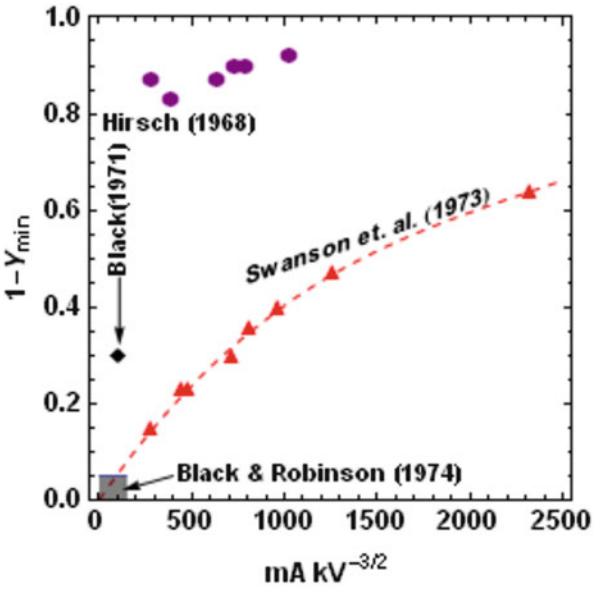

Fig. 13.12 Summary of results from early e-beam probe measurements of FWD in spherical IEC devices [24]. Here, $1-Y_{min}$ is a measurement of the well depth versus applied voltage

13.4.2 Experimental Potential Well Studies

Most notable in this early work is the seminal work by Hirsch [13]. Hirsch detected a steady-state neutron output of ~ 10^8 n/s from D–D reactions and ~10^{10} n/s from D–T reactions. Spatial fluctuation of neutrons and x-ray collimation data seemed to support the early hypothesis of an oscillating, or layered, virtual electrode structure [13]. The rest of the experimental work in this period generally falls into one of the two categories: (1) e-beam probe measurements of fractional well depth (FWD) in spherical IEC devices [28–31] and (2) injected or trapped particle density measurements [14, 15, 32–34]. Electron beam probe measurements were performed by Hirsch [28], Black and Robinson [30], and Swanson [29]. The results of the e-beam experiments are shown in Fig. 13.12. It should be noted that Gardner attempted to duplicate the work of Hirsch, but was not able to achieve equivalent yields [34].

Table 13.3 Summary of single potential well measurements in spherical IEC devices [24]

Investigator	Nadler (1992)	Thorson (1996)	Kachan (2003)
Device	AGD IXL SIEC	AGD IXL SIEC	GD IXL SIEC
Diagnostic	Proton collimation	Emissive probe	Single probe
mA $kV^{3/2}$	0.012–0.073	1.79–3.5	~0.35
η	80–0.97 %	0.85–0.94 %	–
mTorr	1–5	0.1–0.2	5
Inner grid Ø	15.2 cm	10 cm	2 cm
Outer Ø	61 cm	40 cm	16 cm
Notable result	0.1–0.47 FWD	0.38–0.78 FWD	0.30 FWD
Comments	2 ion gun source Quantitative FWD estimates based on ID orbital model	A third grid employed w/electron emitters	RF ion generation 2 ring cathode

AGD assisted glow discharge, *GD* glow discharge, *SIEC* spherical IEC, *FWD* fractional well depth

The problem was attributed to a failure to regain the excellent beam focus achieved by Hirsch. However, a recent effort to reproduce Hirsch's results was somewhat successful at the University of Wisconsin, Madison [35].

Several virtual anode experimental measurements have been made in assisted glow discharge (gridded IEC devices with intense ionization) by Nadler [36], Thorson [37, 38], and Khachan [39]. The quantitative FWD estimates by Nadler are uncertain due to the reliance on 1-D orbital model predictions and the relatively small input power. In addition, the detection of a virtual anode by Khachan [39], in an essentially "Star" mode operation, seems to be in direct contradiction with Thorson [38], who noted a flat potential profile in "Star" mode, and Yoshikawa and colleagues [40], who noted negligible electric fields within the core region of a "Star" mode device. However, Khachan's [39] cathode is distinct from others, in that it simply consisted of two parallel conducting rings separated by only 2 cm. Experimental detection of virtual anodes is summarized in Table 13.3 [24].

In parallel to virtual anode measurements, double potential well sightings have been somewhat inconsistent and often provoke skepticism. Several indications of double potential well structures have been reported, but many of the measurements involve indirect measurements, contain significant errors, require assumptions that are not strictly true, and/or are only qualitative in nature [13, 17, 32, 41, 42]. Recently, double potential wells of substantial depth (~20–30 %) had been reported in "Star" mode based on an oscillation in the radial fusion profile [42], but an alternative mechanism for this oscillation in the spatial profile of the fusion output has been proposed [43, 44]. In spite of this, these results cannot be totally disregarded as several of these measurements consistently indicate the formation of double wells as the input power, P_0, increases [40–42, 45]. In some cases, the double wells are detected after one has transitioned completely out of "Star" mode in the direction of increasing pressure [40, 45]. These double potential well measurements are summarized in Table 13.4.

Table 13.4 Summary of experimental double potential well measurements in spherical IEC devices [24]

Investigators	Hirsch (1967)	Swanson et al. (1973)	Meeker et al. (1973)	Meeker et al. (1973)	Satsangi (1996)	Gu et al. (1996)	Yoshikawa et al. (1999)	Gu and Miley (2000)	Dobson and Hrbub (2004)
Device	ES IXL SIEC	AGD EXL SIEC pulsed	AGD EXL CIEC pulsed	AGD EXL CIEC pulsed	GD IXL SIEC	GD IXL SIEC pulsed	GD IXL SIEC	GD IXL SIEC	GD IXL SIEC
Diagnostic	Neutron, X-ray collimation	e-beam deflection	μ-wave res.; laser heterodyne	μ-wave res.; laser heterodyne	Light coll.; neutron counts	Global neutron counts	Stark shift via LIF	Proton coll.	μ-wave interfer.
mA $kV^{3/2}$	0.0054–0.061	5.06	5,657–42,426	1,414–18,385	0.061–0.632	> 2.2	1.95	1.38	28–49
η	–	93 %	82 %	82 %	95 %	–	95–96 %	82 %	97–98 %
mTorr	0.1–7.8	2–10	0.5–15	0.5–15	4–60	–	31	5–20	15–30
Inner grid Ø	11.4 cm	6.35 cm	8 cm	8 cm	3.5 cm	–	5.5 cm	3.7 cm	15.2/22.9 cm
Outer Ø	17.8 cm	20 cm	15 cm	15 cm	31 cm	31 cm	34 cm	60 cm	60 cm
Notable result	Fluctuating neutron, x-ray profiles	0.3 % DWD	Dip in n_0 at center	Peak in n_1 at center	Ion energy ↑ as mA ↑	Non-linear npr scaling with I	2.67 % DWD	22–27 % DWD	Dip in transverse n_1 near 0.5 R_g

In summary, there are competing results reported by various researchers showing results that encourage and counter the formation of deep wells in IEC devices designed for reactors using beam–beam dominated fusion. However, much more work needs to be done along these lines to fully identify the optimal ion injection strategy for deep wells with minimum power input. As stressed earlier, the potential well parameter must also be combined with a consistent calculation of the energy gain Q, following the methods of Chacon and colleagues to establish a complete picture of energy gain possible in a reactor type ion-injected IEC. Note that potential well formation by electron injection faces similar problems. The Polywell concept uses a magnetic field to provide a large volume well, but it encounters issues with electron leakage through loss cones. In all of these cases, a full analysis of the well depth and shape plus the confined ion distribution function is essential for complete evaluation.

13.5 Stability Analysis of Non-Maxwellian Trapped Plasma

In addition to achieving adequate potential well trapping for net energy production, the question of stability of the non-Maxwellian plasma in the well must be considered. (Note that "stability" is a separate question from the thermalization of the beam-like distribution in the IEC discussed by Nevins and Chacon. However, these are coupled nonlinear problems due to the fact that the distribution function used for both calculations should be consistent.) In earlier studies, Krall showed that the distribution in the Bussard-type Polywell IEC is stable against key instabilities such as the classical two-stream instability. These studies were presented in the internal company reports and not openly published. However, some information is given in reference [46], which indicates that these instabilities can be avoided. More recently, in his thesis done at the University of Illinois, H. J. Kim did an in-depth study of two stream-like instabilities in the ion-injected-type IEC [47]. His work is encouraging in that he identified a possible "window of stability" which depends on the injected energy distribution and angular velocity spread. This result is summarized in Fig. 13.13. As shown there, the growth rate, γ, for the case shown is manageable if β is held below about 10^{-1}.

These results come from numerical studies that are discussed next.

13.5.1 Particle-In-Cell (PIC) Code Stability Analysis

It is instructive to briefly review Kim's computational method, because similar studies should be useful in future studies of specific IEC configurations. A particle-in-cell (PIC) method with explicit time integration generally dominated earlier

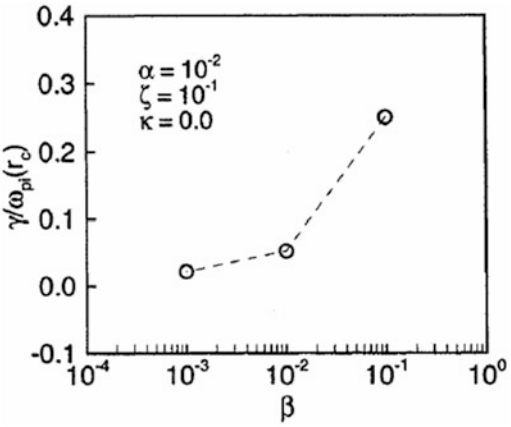

Fig. 13.13 Plot of the growth rate, γ, normalized by the plasma frequency ω_{pi}, of spherically converging/diverging ion beam instability for the variation of the angular velocity spread, i.e., for $\beta = T/|e\phi_c|$. All parameters are defined in reference [47]

plasma simulations. However, this method is inappropriate in multiple time scale problems such as encountered in the IEC potential trap. The explicit time-step algorithms become numerically unstable when the fastest time scale supported by the model cannot be resolved. Indeed, the fastest time scale may be orders of magnitude faster than the dynamic time scale of interest. The simulation also has to resolve the smallest length scale of system to avoid finite-grid instabilities that require resolution of spatial scales comparable to the Debye length. In order to improve the conservations property of implicit moment particle-in-cell algorithm, H. J. Kim developed a fully implicit particle-in-cell scheme and implemented it using a Jacobian-free Newton–Krylov algorithm. This approach does not require actual formation and storage of the Jacobian matrix, minimizing the computational time [47]. In this method, all quantities for both the particle and the field equations are consistent at each time step, enabling accurate energy conservation.

H. J. Kim's study verified that the algorithm correctly handles the typical electrostatic modes. For example, the results agree with the linear dispersion relations for simple limits of two cold electron counter-streaming instabilities, electron Landau damping, and ion acoustic waves. The simulation experience presented here demonstrates the energy conservation property of the systems and the efficacy of a nonlinear solver combined with an efficient preconditioning which is derived from the nonlinear Poisson's equation and particle description relations. For example, in treating ion acoustic waves, the maximum variation in the total energy is much less than 0.1 %.

H. J. Kim performed a normal mode analysis of the ion–ion counter-streaming instability in a spherical IEC in order to gain insights into the ion-injected IEC equilibrium configuration. To do this, he assumed that the electrostatic confinement equilibrium ion beams are proportional to $1/r^2$, effectively neutralizing the background electron density. It is evident from the analysis of cold ion beams that two-stream instability in finite spherical systems may be excited for small beam velocities compared to those of homogeneous and infinite plasma. When an ion

beam is hot, the waves excited by the instability are ion acoustic-type waves, and a certain threshold temperature ratio is required before the wave will become unstable.

Kim also developed a two-dimensional perturbative (δf) particle-in-cell algorithm to simulate the electrostatic interaction of electrons and ions in spherical inertial electrostatic confinement. δf scheme is applied, because the noise level in δf algorithm is significantly reduced compared with conventional particle-in-cell simulation. Because a particle-in-cell simulation in two or three-dimensions is very computationally and memory intensive, it is necessary to seek computational methods and options which lead to solutions with a reasonable amount of computing time. To do this, a distributed computing approach is implemented by using parallel libraries. Applying uniform grid spacing in spherical coordinates may lead to a stability problem due to singularity at the spherical center. In order to avoid the singularity issue, a two-dimensional rectangular domain and an immersed boundary method are applied so that a spherical domain inside the cathode gird of spherical electrostatic confinement is simulated by r–z coordinates. It is evident from the result that the instability growth rate decreases as the longitudinal energy spread of ion distribution function is reduced due to strong Landau damping by parallel kinetic effects. The growth rate does not change dramatically as a mode of angular perturbation increases.

In summary, the results summarized earlier in Fig. 13.13 indicate that the two-stream instability is stabilized if the angular momentum spread of the beam ions is reduced by enhanced ion densification at the center of the device. This is very encouraging for future IEC development. However, an experimental study should be performed to verify this result.

13.5.2 Energy Balance Study

Todd Rider reported a quite different type of energy balance analysis for IEC plasmas [48]. The prior studies discussed here used various methods to evaluate up-down scattering in various potential well configurations. However, Rider considered a "block diagram" type energy flow balance to determine the net gain from a power unit. In such an analysis the fusion reaction rates and scattering rates plus the electron–ion equilibration rates enter average reaction rate (i.e., $<\sigma v>$) quantities averaged over the distribution functions for ions and electrons. Because the distribution function needed for averaging is not known, an assumed form must be used. In traditional magnetic confinement analyses, a Maxwellian distribution function has generally been assumed. This has provided fairly accurate $<\sigma v>$ quantities because such systems are indeed near thermal equilibrium. However, as stressed repeatedly here, the IEC plasma is a non-equilibrium state.

That makes an analysis of the type attempted by Rider very challenging and leaves it open for possible criticism. In fact, it appears that Rider used Maxwellian averages, and critics generally cite this as the cause for his pessimistic results. Rider was particularly interested in the claim that due to its beam-like non-Maxwellian

plasma, the IEC can burn "advanced fusion fuels" such as D–^{3}He and p–B^{11} easier than traditional Maxwellian-type plasma devices (i.e., Tokamaks). Thus, he considered use of a variety of fuels, including D–T, D–D, D–^{3}He, ^{3}He–^{3}He, p–B^{11}, and p–^{6}Li. Due to their high-Z components, all of these fuels face significant energy losses via Bremsstrahlung. These losses were evaluated using the traditional formula for Bremsstrahlung emission by the scattered electrons. This rate depends heavily on the electron–ion temperature ratio, which in turn depends strongly on the $<\sigma v>$ values assumed for energy exchange between ions and electrons. Using the Maxwellian averaged energy exchange rates, Rider found that Bremsstrahlung losses would be prohibitively large for ^{3}He–^{3}He, p–B^{11}, and p–^{6}Li reactors, and would also be a considerable fraction of the fusion power for D–^{3}He and D–D reactors. As a result he concluded that it does not appear possible for the dense central region of a reactor-grade IEC device to maintain a significantly non-Maxwellian ion distribution or to keep a low electron to ion temperature ratio. The problem is, however, that the assumed rate constants would naturally force this situation and conclusion.

Rider's analysis also treats the energy carried out by both ion and electron losses with a similar rate assumption. Electron losses tended to dominate for electron-injected systems. Even by using one of the best electron confinement systems proposed for such devices, a polyhedral cusp magnetic field, Rider found that the electron losses proved to be intolerable for all fuels except perhaps D–T. Based on these results, he concluded that for either ion- or electron-injected IEC systems to be used as fusion reactors, it will be necessary to find methods to circumvent these problems, especially the excessive Bremsstrahlung losses.

In view of the questions about the effect of Rider's use of Maxwellian average $<\sigma v>$ rates, the accuracy of his conclusions cannot be evaluated. To determine the accuracy of this very basic energy analysis, his treatment should be redone with the revised reaction rate data based on averaging the rate coefficients over a more realistic energy distribution. However, such a study has not yet been reported.

13.6 Beam–Background IEC Fusion Rate Simulations

Several simulation studies noted in earlier chapters have focused on current low-level neutron source types of IECs. In this case, as opposed to future power reactors, the background gas is of sufficient pressure to result in beam–background scaling of the fusion rate (i.e., theoretically, as noted in Chap. 8, this gives ion current x pressure scaling). This must be modified because charge exchange with background gas becomes a significant factor in determination of the reaction rates. Pioneering simulations of IECs operating in this mode have been done by Santarius and colleagues at the University of Wisconsin, Madison; by Ohnishi and colleagues at Kansai and Kyoto universities; and Horioka and Tomiyasu and colleagues at the Tokyo Institute of Technology [49–53].

Here, to gain insight into the issues involved, we briefly review a study by Miley and colleagues [54]. They used an analytical model for charge exchange collisions

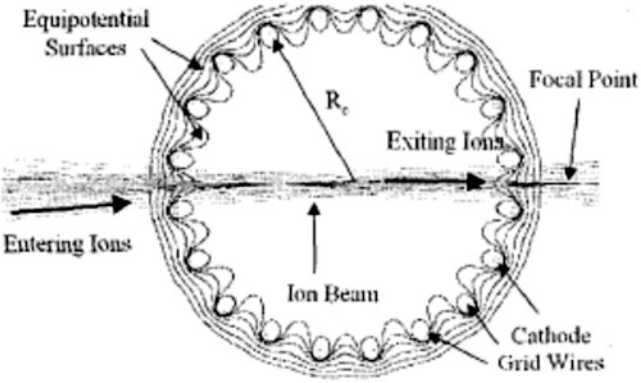

Fig. 13.14 Diagram showing equipotential surfaces of the IEC cathode grid and their focusing effect on a beam of ions in the "Star" mode discharge [54]

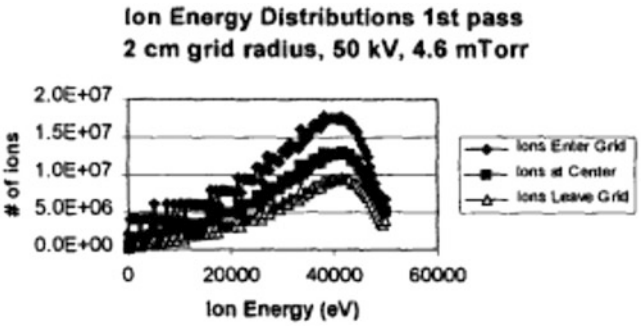

Fig. 13.15 Results for calculations for the first pass of ion energy distributions [54]

in the IEC plasma to calculate fusion neutron generation rates. Results from the model simulating a 10-mA deuterium ion current in a 30-cm-diameter IEC device at 50 kV roughly matched the experimental results of 10^6 fusion neutrons per second. The model was also used to find the effects of grid diameter on neutron yield as discussed in Chap. 6. Further, the model provides more insight into operation in the "Star" mode. This effect is further summarized from these calculations as shown in Fig. 13.14.

For higher pressure operation, charge exchange severely limits the number of passes possible through the grid despite the very high effective transparency achieved in the "Star" mode. This is emphasized by results for the calculations shown in Fig. 13.15 [54].

These results are for the UIUC IEC "A-device" with conditions of 50 kV, 10 mA, and 4-cm grid diameter, and with the background gas pressure at about 4.6 mTorr [54]. At this pressure, charge exchange (CX) collisions occur quite frequently for the case of D^+ ions. In their first pass through the IEC, about half

of the ions undergo CX within the cathode region and are lost. After only four passes, most of the remaining ions have lost a large amount of their original potential energy, and the fusion rate from subsequent passes becomes negligible. D_2^+ ions and also D_3^+ ions are naturally produced at diminishing quantities in ionization reactions such as those producing D^+. For D_2^+ ions with a smaller CX cross section, it takes about 20 passes for most of the D_2^+ ions to lose their energy and be lost to the grid. Deuterium anions (D_2^-) are also produced in an IEC device; as explained in Chap. 12, the electrons attach with the neutrals and form anions that stream outward, thus carrying away energy from the system. However, such anions are known to cause fusion on the surface of the chamber walls along with the charge exchanged neutrals, especially if the walls are coated with deuterium retaining materials such as titanium [55].

In summary, the design of an optimal beam–background IEC neutron source is seen to be quite different for a power producing IEC. In the former, the grid parameters, grid/vessel diameter ratio, chamber diameter, surface conditions, background pressure, current, and voltage all become important parameters. In power producing devices, the ion injector parameters including current, energy relative to the depth of the well potential, and the angular momentum involved, along with the chamber diameter determine performance.

13.7 Comments About IEC Reactor Development

The applications for IEC as a neutron source and some related sources (such as protons and x-rays) are well established for practical applications, as discussed in Chap. 12. However, a long-term goal is to develop a power producing IEC, and better yet to do so by taking advantage of the unique ability of the IEC to use a non-Maxwellian plasma to burn advanced fuels to minimize radioactive and radiation emission involvement. However, the best current IEC device results are 5 or 6 orders of magnitude down in energy gain from Q (energy out/in) = 1.0, i.e., "breakeven." Thus, it appears that such a hope is many years off, especially with steady-state devices. However, alternate versions of IEC device such as the Polywell, pulsed devices such as the POPS concept and high-pressure IEC devices explained in earlier chapters seem to hold better promise. Fortunately, even the steady-state IEC devices can be scaled up in energy gain while keeping a small size because the losses are in velocity space (i.e., via ion up-scattering out of the potential well trap). This is in sharp contrast to Tokamaks where losses occur via diffusion across the outer surface, so reduction of energy losses has been achieved by going to the massively large International Experimental Thermonuclear Reactor (ITER) type devices. The problems and costs for construction of ITER have thrown its development into the distant future, making this approach ineffective for addressing the present energy crisis. Plus, ITER-type plants represent very expensive, large, centralized power units, while the current trend in alternate power sources is toward smaller, distributed power units. To provide insight into the IEC

vision for power, we discuss next some conceptual approaches for a near-term IEC breakeven experiment to prove the physics of operation with aneutronic p–B^{11} fuel. If such a program can be initiated aggressively and proved successful, the IEC could have a major impact on the energy crises.

13.7.1 IEC Aneutronic Fusion

The IEC is one of the few approaches to fusion that has the potential of burning aneutronic fuels such as D–^{3}He and p–B^{11} (boron-11 isotope) in a scalable device. These fuels result in charged particle reaction products which allow efficient use of direct energy conversion technology with no greenhouse emissions and minimal radioactivity or radioactive wastes.

While confinement issues are easier with D–^{3}He, the need to obtain ^{3}He from lunar mining or from breeder reactors makes p–B^{11} most desirable, with its plentiful fuel availability. The goal would be to develop a revolutionary small IEC fusion power unit that could be commercialized in time to impact the current energy crisis. This device would burn relatively inexpensive aneutronic p–B^{11} fuel, avoiding issues of tritium breeding and radioactivity that the D–T burning ITER-type magnetic confinement devices face. The main challenge for doing this involves the basic plasma physics, because once that is achieved, the technology of constructing a power plant seems relatively straightforward due to the simple structure of IEC devices. The physics involved must focus on ways to create a deep potential electrostatic well for improved confinement in either an ion- or electron-injected IEC device. This physics will probably build on one of the possible approaches already discussed in this book. We will briefly touch on these here.

13.7.2 Ion Injection with Controlled Angular Momentum

As noted in Chap. 2, work at the University of Illinois has considered a multiple gun ion injection approach using specially designed ion guns to inject ions into the IEC with strong focus and controlled angular momentum. This builds on a combination of prior small-scale experiments with gun injected IECs and simulation of their scale-up to power production using particle-in-cell (PIC) codes and particle tracking analysis. The goal would be to maintain a tight ion focus so that the potential well achieves a small, tight, high-density fusing core. In principle, energy breakeven could be demonstrated with a core occupying a volume of only a few cubic centimeters with a few watts in and out! This is not currently possible, but the use of improved gun injected technology to obtain breakeven in a dense plasma core in the IEC of 10s of cc volume and with 20–25 kW input power seems to be a practical goal. This proof-of-principle device would demonstrate the physics of energy production and provide the basis for going rapidly to practical IEC power plants.

However, moving to large power levels such as MWs faces additional physics challenges with this approach. As shown by the simulations by Tzonev and colleagues in Chap. 13 [10], adding angular momentum to enlarge the core volume, hence power level, is input energy intensive. From that perspective, larger potential core volumes offered to be a Polywell-type IEC would be advantageous.

The six-gun experiment SIGFE, discussed in Chap. 10, is a very similar approach to the gun injected research done at the University of Wisconsin, Madison. However, the gun design is different from the one employed at Illinois, and the SIGFE goal thus far has focused on the reproduction of the earlier Hirsch gun experiment. Still, this effort is providing much basic physics data for gun injection.

13.7.3 The Polywell Approach

As discussed in Chap. 2, the Polywell approach resolves the problem of achieving larger ion trap volumes by using a magnetic field to confine the electrons in a defined volume where the potential trap is formed [46]. This has the advantage that the magnet design can start with smaller volumes for breakeven studies and relatively easily be scaled up to larger volume devices. Still, this faces a major physics challenge involving achieving sufficient electron density to close the loss cones, i.e., create a "wiffle ball" mode. To do that, it appears that very high electron injection currents or alternate plasma formation must be provided, requiring large energy inputs. Once the "wiffle ball" mode is achieved, however, the input power can be significantly reduced because the electron energy losses are reduced by closure of the loss cones. The private company EMC^2 has funding for experiments designed to study and hopefully overcome these problems. However, information about their project is not publicly available at this time. Some additional information about Polywell studies has been found by other IEC groups. For example, Khachan's group at the University of Sydney reported initial experiments on a unique small-sized Polywell-type device [56].

13.7.4 Multi-Grid IEC

As discussed in Chap. 8, the multi-grid design proposed by Sedwick and colleagues is intended to overcome the focus problem and virtual well formation. Computations and experiments performed to date are encouraging. However, the practical issues of maintaining such a grid structure in a fusion power plant have not been addressed. Active grid cooling would seem essential but such designs have yet to be studied.

13.7.5 Lens-Focused IEC

Klein's MARBLE approach described in Chap. 9 was designed to address many of the physics issues relative to other IEC gridded devices. The MARBLE design provides a unique configuration, and though the initial experiments discussed were encouraging, they identified some very challenging remaining physics issues.

13.7.6 POPS and the Penning Trap IEC

Both of these concepts (discussed in Chaps. 2 and 10) were developed at Los Alamos National Laboratory (LANL). These concepts are both at a low experimental level, but are well defined theoretically. POPS is a very important approach to a power reactor, but sacrifices the ability to use a non-Maxwellian distribution to burn advanced fuels for improved confinement by maintaining the plasma at local thermodynamic equilibrium at all times. Still, this trade-off offers another approach to very interesting fusion power with D–T or D–D fusion fuel. The Penning trap IEC could also be important for the demonstration of breakeven in a very small volume, low power level device. Scale-up to higher, more useful power levels poses some technological issues that have not yet been studied. The extensive BAFP studies of the Penning trap discussed earlier in this chapter provide important insight into this approach.

13.7.7 Vision of a Future p–B^{11} Fusion Plant

In the ultimate power plant, the preferred fusion reaction would employ aneutronic p–B^{11} fuel, which fuses to produce energetic alpha particles with no neutrons and minimal radioactivity. This eliminates radioactive tritium breeding and corresponding tritium inventory, activation, and damage to reactor structural materials, and the massive shielding and radiation protection in traditional fission and D–T fusion reactor systems. In this case, hydrogen and boron-11 undergo fusion according to

$$p + B^{11} \rightarrow 3\alpha. \tag{13.1}$$

Due to its inherent non-Maxwellian (beam-like) plasma, the IEC is especially well suited for burning a fuel such as p–B^{11} which requires high energies (~180 keV, see Fig. 13.16). In operation, a bulk of the IEC driving energy is given to ions so an applied voltage of ~180 keV provides ion energies near the peak of the p–B^{11} cross section. In contrast, in Maxwellian-type plasmas typical of magnetic confinement devices, energy is expended to create ions over a wide distribution of energies. Thus,

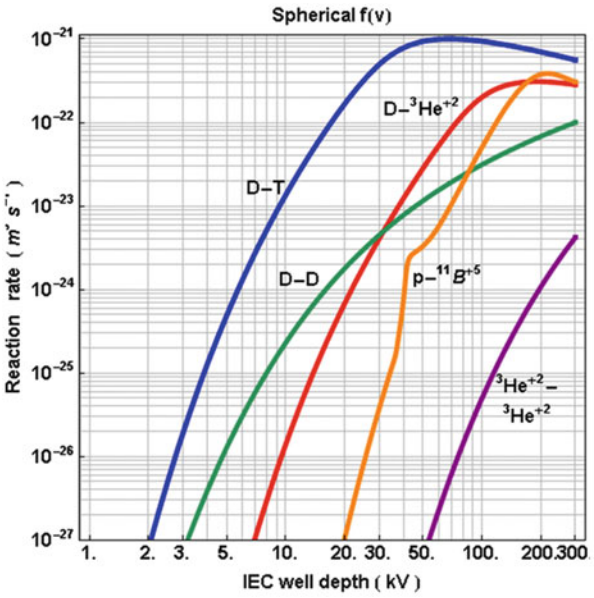

Fig. 13.16 Cross section of p–B^{11} fusion energy requirements [2]

Tokamaks are designed to operate at much lower ion energies (~20–30 keV) suitable for D–T fusion. The key physics challenge then for the IEC is to achieve strong ion trapping (i.e., large number of recirculations) in the potential well. This trapped plasma must meet the Lawson Criterion for energy to breakeven with p–B^{11}, $n\tau \sim 10^{16}$ cm^{-3}/s (two orders of magnitude above the requirement for D–T fusion). Here, n is the ion density and τ is the ion confinement time. Assuming the converged core density in the potential well of $\sim 10^{16}$ cm^{-3}, ion trap times of ~1 s are required. While very demanding, optimistic projections suggest that with proper ion injection and deep well formation, an IEC could potentially achieve this goal.

In contrast to Tokamaks, which can operate with an ignited plasma, the IEC must have continued electric input power to maintain the grid voltage (or an equivalent with virtual electrodes). John Lawson termed the name "wet wood burner" for such operation [2]. In order to maintain the operation, a fraction of the electric output produced must be recirculated to the IEC device. In doing this, energy losses occur in converting the output power (e.g., charged alpha particles from the p–B^{11}) to electricity. Converting the form of this electricity (typically a high voltage, low current DC electric output, depending on the conversion method) to conditions needed for driving, the IEC introduces another inefficiency, as does its "injection" into the device via ion "guns" and creating the grid voltage and current. For breakeven, the net recirculating power must balance the power output; or for power production to the grid, the output must exceed the recirculating power. These conditions can be relatively easily analyzed, as discussed in reference [2].

Once a p–B^{11} breakeven experiment in a small volume with a small total power is demonstrated, scale-up to a larger power level with electric production could proceed rapidly. The technology development largely involves the design and

engineering of subsystems needed for the balance-of-plant (BOP) design. Many of these can employ conventional equipment, but several require new developments. These include the hydrogen–boron fuel injection system, the direct energy conversion system to convert the charged particle product energy to electricity, and the exhaust plasma collection/recovery system. Also, the chamber wall must use advanced cooling methods to handle the large surface heating caused by the Bremsstrahlung emission hitting it. There are no "show stoppers" however, so the road map to fusion power seems clear. Because a relatively small power plant seems possible, construction and plant costs would allow fast development.

Clearly, the material in this section is extremely speculative. The intent is to provide a vision of the path to an IEC power plant. Much work remains to find if this vision can be transformed into reality.

13.8 Summary

Various semi-analytic and computer simulations of plasma confinement in the potential traps created by various IEC devices have been discussed. Key issues such as ion thermalization times, energy balances, and instabilities creased by deviations from equilibrium conditions have been addressed. However, various studies have come to contradictory conclusions, though the possibility of achieving a reactor grade confined plasma is not ruled out. Doing this with the "ideal" aneutronic fuel, p–B^{11}, is extremely demanding and brings in added issues such as maintaining a high ratio of ion to electron "temperature" to suppress Bremsstrahlung emission. To ultimately settle these issues, more aggressive experiments are required. Fortunately, the simple structure and possibility of studying breakeven in a small volume device makes rapid studies of the practicality of IEC power reactors possible. In the process, improved designs for "spin-off" applications such as higher flux neutron sources could be developed. Thus, IEC fusion remains one of the most fascinating fields for study and development. Hopefully, this book will provide background information to further aid this technology.

References

1. Lawson JD (1957) Some criteria for a power producing thermonuclear reactor. Proc Phys Soc B 70:6
2. Miley GH (1972) Fusion energy conversion. ANS, LaGrange
3. Nevins WM (1995) Can inertial electrostatic confinement work beyond the ion–ion collisional time scale? Phys Plasmas 2(10):3804–3819
4. Barnes DC, Mitchell TB, Schauer MM (1997) Beyond the Brillouin limit with the Penning fusion experiment. Phys Plasmas 4:1745
5. Tiouririne TN, Barnes DC (1995) Optimization of SCIF fusion systems. Bull Am Phys Soc 40:1665

6. Chacon L, Miley GH, Barnes DC, Knoll DA (2000) Energy gain calculations in penning fusion systems using a bounce-averaged Fokker–Planck model. Phys Plasmas 7(11):4547
7. Chacon L, Barnes DC, Knoll DA (1998) An implicit bounce-averaged Fokker-Planck (BAFP) code to model spherical inertial electrostatic confinement (IEC) fusion systems. In: International Sherwood fusion theory conference, Atlanta, 23–25 Mar
8. Miley G, Chacon L, Barnes D, Knoll D (2000) An implicit energy-conservative 2D Fokker-Planck algorithm. J Comput Phys 157:654–682
9. Ohnishi M et al (1996) Multi-potential well formation and neutron production in inertial-electrostatic confinement fusion by numerical simulations. In: Proceedings of 16th IEEE/NPSS symposium on fusion engineering, vol 2. Piscataway, pp 1468–1471
10. Tzonev IV, DeMora JM, Miley GH (1996) Effect of large ion angular momentum spread and high current on inertial electrostatic confinement potential structures. In: Proceedings of 16th IEEE NPSS symposium on fusion engineering, IEEE paper 95CH35852, Piscataway, New Jersey, pp 1476–1481
11. Bussard RW, Jameson LW, King KE (1992) Ion-acoustic waves and Ion wave group trapping in IEC systems. Bull Am Phys Soc 37(6):1582
12. Elmore WC, Tuck JL, Watson KM (1959) On the inertial-electrostatic confinement of a plasma. Phys Fluids 2(3):239–246
13. Hirsch RL (1967) Inertial-electrostatic confinement of ionized fusion gases. J Appl Phys 38(11):4522
14. Dolan TJ, Verdeyen JT, Meeker DJ, Cherrington BE (1972) Electrostatic-inertial plasma confinement. J Appl Phys 43(4):1590–1600
15. Dolan TJ (1975) Electrostatic-inertial plasma confinement. Ph.D. dissertation, University of Illinois-Urbana-Champaign
16. Cherrington BE, Verdeyan JT, Swanson DA (1975) Recent developments in electrostatic confinement-theoretical. Ann N Y Acad Sci 251:139
17. Swanson DA (1975) Theoretical study of a spherical inertial electrostatic plasma confinement device. Ph.D. dissertation, University of Illinois at Urbana-Champaign
18. Hu KM, Klevans EH (1974) On the theory of electrostatic confinement of plasmas with ion injection. Phys Fluids 17(1):227
19. Black WM, Klevans EH (1974) Theory of potential-well formation in an electrostatic confinement device. J Appl Phys 45(6):2502
20. Imel GR (1973) A theoretical model of a spherical electrostatic confinement device. M.S. thesis, Pennsylvania State University
21. Klevans EH (1975) Theoretical models of electrostatic confinement experiments. Ann N Y Acad Sci 251:190
22. Langmuir I, Blodgett KE (1924) Currents limited by space charge between concentric spheres. Phys Rev 24:49
23. Farnsworth PT (1968) Method and apparatus for producing nuclear fusion reactions. US Patent # 3,386,883, June 1968
24. Meyer R. Inertial electrostatic confinement: theoretical and experimental studies of spherical devices. Ph.D. thesis, Department of Nuclear Engineering, University of Missouri-Columbia
25. Hockney RW (1968) Formation and stability of virtual electrodes in a cylinder. J Appl Phys 39(9):4166
26. Barnes CW (1975) Computer simulation of electrostatic confinement of plasmas. Ann N Y Acad Sci 251:370
27. Miley GH, Momota H (2001) Virtual cathode in a stationary spherical inertial electrostatic confinement. Fusion Sci Technol 40:56–65
28. Hirsch RL (1968) Experimental studies of a deep, negative, electrostatic potential well in spherical geometry. Phys Fluids 11(11):2486
29. Swanson DA, Cherrington BE, Verdeyen JT (1973) Potential well structure in an inertial electrostatic plasma confinement device. Phys Fluids 16(11):1939
30. Black WM, Robinson JW (1974) Measuring rotationally symmetric potential profiles with an electron-beam probe. J Appl Phys 45(6):2479

31. Black WM (1971) Potential well formation in an electrostatic confinement device. Ph.D. dissertation, Pennsylvania State University
32. Meeker DJ, Verdeyen JT, Cherrington BE (1973) Measurement of electron density in a cylindrical inertial electrostatic plasma confinement device. J Appl Phys 44(12):5347–5355
33. Grush WH (1973) Electrical density measurement of an electrostatically-confined, spherically symmetric, helium plasma using a microwave cavity resonance shift technique. M.S. thesis, Pennsylvania State University
34. Gardner AL, Hatch DM, Chan AIY, Evans RP (1975) Measurement of a spherical electrostatic confinement system employing six ion guns. Ann N Y Acad Sci 251:179
35. Santarius J et al (2012) Overview of University of Wisconsin Inertial-Electrostatic Confinement (IEC) Research. In: 54th annual APS plasma physics meeting, Providence, Rhode Island, Oct 28–Nov 2
36. Nadler JH (1992) Space-charge dynamics and neutron generation in an inertial-electrostatic confinement device. Ph.D. dissertation, University of Illinois-Urbana-Champaign
37. Thorson TA, Durst RD, Fonck RJ, Wainwright LP (1997) Convergence, electrostatic potential, and density measurements in a spherically convergent ion focus. Phys Plasmas 4(1):4–15
38. Thorson TA (1996) Ion flow and fusion reactivity characterization of a spherically convergent ion focus. Ph.D. dissertation, University of Wisconsin-Madison
39. Khachan J (2003) Spatial distribution of ion energies in an inertial electrostatic confinement device. Phys Plasmas 10(3):596
40. Yoshikawa K, Takiyama K, Koyama T, Taruya K, Masuda K, Yamamoto Y, Toku T, Kii T, Hashimoto H, Inoue N, Ohnishi M, Horiike H (2001) Measurement of strongly localized potential well profiles in an inertial-electrostatic fusion neutron source. Nucl Fusion 41 (6):717–720
41. Satsangi AJ (1996) Light intensity measurements of an inertial electrostatic confinement fusion plasma. M.S. thesis, University of Illinois-Urbana-Champaign
42. Gu Y, Miley GH (2000) Experimental study of potential structure in a spherical IEC fusion device. IEEE Trans Plasma Sci 28(1):331
43. Matsuura H, Takaki T, Nakao Y, Kudo K (2001) Radial profile of neutron production rate in spherical inertial electrostatic confinement plasmas. Fusion Technol 39:1167
44. Krupakar Murali S, Santarius JF, Kulcinski GL (2011) Effects of the cathode grid wires on fusion proton measurements in inertial-electrostatic confinement devices. IEEE Trans Plasma Sci 39(2):749–755
45. Dobson CC, Hrbub I (2004) Electron density and two-channel neutron emission measurements in steady-state spherical inertial-electrostatically confined plasmas, with review of the one-dimensional kinetic model. J Appl Phys 96(1):94–107
46. Krall N (1992) The Polywell: a spherically convergent ion focus concept. Fusion Technol 22: 42–49
47. Kim HJ (2004) LANL Research on Newton-Krylov Solver. NPRE 597 Independent Study, Department of Nuclear, Plasma and Radiological Engineering, University of Illinois at Urbana-Champaign, July 2004
48. Rider TH (1995) A general critique of inertial-electrostatic confinement fusion systems. Phys Plasmas 2(6):1853
49. Tomiyasu K, Santarius JF, Kulcinski GL (2003) Numerical solution for UW-IEC device. In: 6th annual U.S.–Japan IEC workshop, Yokohama
50. Ashley RP, Kulcinski GL, Santarius JF, Murali SK, Piefer G et al (2001) Steady-state D-^{3}He proton production in an IEC fusion device. Fusion Technol 39(2):546
51. Ashley RP, Kulcinski GL, Santarius JF, Murali SK, Piefer G (1999) D-3He fusion in an inertial electrostatic confinement device. In: 18th IEEE symposium on fusion engineering, Albuquerque
52. Ohnishi M et al (1996) Multiple-potential well formation and neutron production in inertial-electrostatic confinement fusion by numerical simulations. In: 16th IEEE symposium on fusion engineering, Piscataway
53. Horioka K et al. Effects of virtual anode formation on the beam optics of grid-controlled vacuum arc ion source. Department of Energy Sciences, Tokyo Institute of Technology

54. Miley GH, DeMora JM, Jurczyk BE, Nieto M (1999) Computational studies of collisional processes in inertial electrostatic glow discharge fusion devices. In: 18th symposium on fusion engineering, Albuquerque, New Mexico, pp 23–26
55. Radel R (2007) Detection of highly enriched uranium and tungsten surface damage studies using a pulsed inertial electrostatic confinement fusion device. Ph.D. thesis, Department of Engineering Physics, University of Wisconsin, Madison
56. Khachan J (2010) Overview of IEC at the University of Sydney. In: 12th annual U.S.–Japan workshop

Index

G.H. Miley and S.K. Murali, *Inertial Electrostatic Confinement (IEC) Fusion: Fundamentals and Applications*, DOI 10.1007/978-1-4614-9338-9,